RESEARCH

2008-08

Development of Improved Test Rolling Methods for Roadway Embankment Construction

LRRB
LOCAL ROAD RESEARCH BOARD

Take the steps... Research...Knowledge...Innovative Solutions!

Transportation Research

Technical Report Documentation Page

1. Report No.	2.	3. Recipients Accession No.
MN/RC 2008-08		

4. Title and Subtitle	5. Report Date
Development of Improved Test Rolling Methods for Roadway Embankment Construction	February 2008
	6.

7. Author(s)	8. Performing Organization Report No.
Hambleton, J.P, and Drescher, A.	

9. Performing Organization Name and Address	10. Project/Task/Work Unit No.
University of Minnesota Department of Civil Engineering 500 Pillsbury Drive SE Minneapolis, Minnesota 55455	11. Contract (C) or Grant (G) No. (c) 81655 (wo) 186

12. Sponsoring Organization Name and Address	13. Type of Report and Period Covered
Minnesota Department of Transportation 395 John Ireland Boulevard Mail Stop 330 St. Paul, Minnesota 55155	Final Report 14. Sponsoring Agency Code

15. Supplementary Notes
http://www.lrrb.org/PDF/200808.pdf

16. Abstract (Limit: 200 words)

Test rolling is a quality assurance test in which penetration of the wheels of a heavy vehicle into subgrade soils is used as a measure of the adequacy of compaction. Current criteria for acceptable test roller penetration are empirical. Two theoretical approaches for modeling test rolling are developed. One is analytic and the other is numerical, based on the finite element code ABAQUS. Both approaches relate wheel penetration to wheel geometry, wheel load, and soil strength parameters (friction angle and cohesion). Elastic soil properties are included in the numerical simulations but play a secondary role. The models accommodate both rigid and flexible wheels. Homogeneous and layered soil structures are considered. Scaled laboratory tests support the theoretical predictions, although full validation requires execution of extensive full scale field testing. The models developed can be used to enhance interpretation of test rolling data and assess the effects of test roller modifications.

17. Document Analysis/Descriptors		18. Availability Statement
test rolling wheel penetration analytic method ABAQUS	subgrade strength finite element method	No restrictions. Document available from: National Technical Information Services, Springfield, Virginia 22161

19. Security Class (this report)	20. Security Class (this page)	21. No. of Pages	22. Price
Unclassified	Unclassified	288	

Development of Improved Test Rolling Methods for Roadway Embankment Construction

Final Report

Prepared by:

James Hambleton
Andrew Drescher

University of Minnesota
Department of Civil Engineering

February 2008

Published by:

Minnesota Department of Transportation
Research Services Section
395 John Ireland Boulevard, MS 330
St. Paul, Minnesota 55155-1899

Acknowledgements

Financial support provided by the Local Road Research Board is gratefully acknowledged. This work was carried out in part using computing resources provided by the University of Minnesota Supercomputing Institute.

Table of Contents

List of Tables

List of Figures

Notation

Roman Symbols

A	footing contact area; wheel contact area
b	wheel width
B	plane footing width; smaller dimension of rectangular footing
c	Mohr-Coulomb soil cohesion for homogenous soil
c'	effective Mohr-Coulomb soil cohesion for homogenous soil
c_1	Mohr-Coulomb soil cohesion of upper layer in layered soil
c_2	Mohr-Coulomb soil cohesion of lower layer in layered soil
c_{DP}	Drucker-Prager soil cohesion
c_u	undrained shear strength
d	wheel diameter; initial wheel diameter for flexible wheel
d_e	equivalent wheel diameter
d_h	hub diameter of pneumatic tire
D	footing depth
E_s	soil elastic modulus
E_w	tire carcass elastic modulus
$F_{cs}, F_{qs}, F_{\gamma s}$	shape factors for bearing capacity formula
$F_{cd}, F_{qd}, F_{\gamma d}$	depth factors for bearing capacity formula
$F_{ci}, F_{qi}, F_{\gamma i}$	inclination factors for bearing capacity formula
$\overline{F_{ci}}, \overline{F_{qi}}, \overline{F_{\gamma i}}$	modified inclination factors for bearing capacity on sloping ground
h	contact length of wheel
H	influence depth
L	longer dimension of rectangular footing
K_s	factor depending on ϕ in influence depth computations
N_c, N_q, N_γ	bearing capacity factors
$\overline{N_c}, \overline{N_q}, \overline{N_\gamma}$	modified bearing capacity factors for bearing capacity on sloping ground
q	surcharge at footing depth
q_u	ultimate bearing capacity (average stress)
r_f	radius of wheel edge fillet
s	wheel sinkage
t	simulation time
Q	total wheel force
Q_H	horizontal component of wheel force
Q_V	vertical component of wheel force (wheel weight)
t_{side}	thickness of tire sidewall
t_{trans}	thickness of tire transition section
t_{tread}	thickness of tire tread
V_d	volume of soil displaced by wheel
V_u	volume of soil displaced upward as a result of wheel penetration

x	horizontal coordinate in rut profile
y	vertical coordinate in rut profile

Greek Symbols

α	contact angle
α_e	equivalent contact angle
β	wheel force inclination angle measured from vertical
ε	uniaxial strain
ϕ	Mohr-Coulomb angle of internal friction for homogeneous soil
ϕ'	effective Mohr-Coulomb angle of internal friction for homogeneous soil
ϕ_1	Mohr-Coulomb angle of internal friction of upper layer in layered soil
ϕ_2	Mohr-Coulomb angle of internal friction of lower layer in layered soil
ϕ_{DP}	Drucker-Prager angle of internal friction
γ	soil unit weight for homogenous soil
γ_1	soil unit weight of upper layer in layered soil
η	coefficient for equivalent foundation depth
λ_i	wheel flexibility coefficient for indentation
λ_r	wheel flexibility coefficient for rolling
μ	coefficient of friction for wheel and soil
ν_s	soil Poisson's ratio
ν_w	tire carcass Poisson's ratio
θ	polar coordinate
ρ	soil density
σ	uniaxial stress
σ_o	uniaxial yield strength
σ_1	major principal stress
σ_2	intermediate principal stress
σ_3	minor principal stress; confining pressure in triaxial compression test
σ_f	normal stress on failure plane
σ_n	normal component of contact stress
σ_t	tangential component of contact stress
τ_f	shear stress on failure plane
τ_{max}	shear stress limit for tangential contact stresses
ψ	soil dilation angle

Executive Summary

Test rolling is a technique used for quality assurance testing in road construction practice. In this test, a heavy vehicle is operated on the subgrade of the embankment, and the penetration depth of the wheels is used as a measure of soil consistency on a pass/fail basis. As opposed to other tests used in road construction, test rolling is capable of providing a continuous record of measurement, and can be used to inspect large areas and detect inadequately compacted soils.

Current quality assessment criteria are empirical, and do not relate the measurements to soil properties, wheel geometry, and wheel weight. The research described in this report aims at formulating mechanistic models of test rolling, thereby providing rationale and means for improved test interpretation and equipment modifications.

Two theoretical approaches for modeling test rolling are developed. The first, based on the bearing capacity formula, is more approximate yet analytic and thus convenient for use. The second is numerical, based on the finite element software ABAQUS, and case specific. The models allow for realistic predictions of how much the wheel of a test roller with a given load and wheel geometry will penetrate (sink) into a soil with known material properties. The models also allow for analysis of the inverse problem, i.e., evaluating soil properties from measured wheel penetration. Homogeneous and layered soils are considered. Appropriate formulas and graphs are generated that can be used directly in the analysis of current and future test rolling procedures, as well as evaluation of the effects of test modifications.

As soil deformation resulting from wheel penetration is predominantly permanent (i.e., the result of soil failure) and visible as rutting, soil strength parameters (cohesion and/or friction angle) play a central role in the theoretical models and soil elasticity is secondary. This also implies that test rolling is a means of evaluating *in situ* soil strength parameters rather than elastic parameters such as resilient modulus.

Theoretical wheel penetration predictions are compared with results of scaled laboratory tests, in which rigid wheels are rolled over granular or cohesive soil. Experimental findings support the theoretical results. Limited field tests point to necessary test rolling improvements and to the need for undertaking an experimental program to assess the accuracy of the theoretical models in various field conditions.

Chapter 1

Introduction

1.1 Background

Test rolling is an approach used in roadway embankment construction to verify the adequacy of compaction of subgrade materials prior to placement of the base and pavement layers. According to Minnesota Department of Transportation (Mn/DOT) *Standard Specifications for Construction* (2000), Specification 2111, a heavy two-wheeled vehicle is towed across the subgrade (Fig. 1.1), and the penetration of the rolling wheels into the subgrade is recorded. Subgrade compaction is considered satisfactory if the penetration is smaller than a specified limit, and reworking of the subgrade is required in the event that penetration is larger than the limit. The large areas which may be tested and the ease with which problem areas are identified are the alluring advantages of test rolling over other verification procedures. The specific equipment and criteria for acceptable penetration vary between localities within the U.S., and many state agencies have no test rolling specifications.

Following the terminology discussed by Crovetti (2002), *proof rolling* and *test rolling* are considered similar in concept, though distinguished by the type of equipment and purpose of the test. *Proof rolling* typically involves use of a smooth-wheel or pneumatic rubber-tired construction roller, and in addition to identifying areas of weak subgrade, the test is intended to correct minor compaction inadequacies. In contrast, *test rolling* usually utilizes a vehicle with widely-spaced, narrow wheels such as a standard construction dump truck, in which the configuration is not intended to increase compaction, but rather identify weak areas exclusively.

In its fundamental form, test rolling consists of towing or driving a deformable wheel, upon which a known load is applied, on deformable soil. Throughout this report, the term *soil* refers generically to the subgrade material, which may be composed of clay, sand, or some other soil type. The test rolling problem is inherently one of soil-wheel interaction, since deformation depends on characteristics of both the wheel and soil. The depth to which a rolling wheel penetrates the soil during operation (i.e., the distance from the undisturbed soil surface to the bottom of the tire) is commonly referred to as *sinkage* in literature on soil-wheel interaction, where the term *rut* describes the depth of the permanent imprint which remains after passage of the wheel (Fig. 1.2). The current Mn/DOT test rolling specification nominally utilizes sinkage when specifying acceptable test roller penetration, which results from both permanent and (small) elastic soil deformation. However, test roller penetration in practice is typically measured by recording the vertical displacement of the test roller axle (referred to the ground surface) and axle displacement should be considered strictly the same as sinkage only when the wheel is rigid.

When unacceptable test roller wheel penetration occurs, the permanent deformation induced by the rolling wheel becomes clearly visible and is three-dimensional in its geometric form, as

illustrated in Figs. 1.2 and 1.3. Material is upheaved in front of the wheel and significant volumes of material are pushed to the sides, leaving well-defined side berms. The volume and geometry of the forward upheaval, side berms, and the depth of the rut depend on the applied load and properties of the soil and wheel.

The test rolling problem is the inverse of the so-called *vehicle mobility* problem. In the vehicle mobility problem, the soil mechanical properties are known *a priori* and are used to predict vehicle performance variables like sinkage and pull force. In test rolling, the soil properties are unknown, and the idea is to relate measured sinkage and rut depth to the soil mechanical properties, knowing the test roller characteristics like wheel force and wheel size. A theory linking soil properties to sinkage and rut depth is highly desirable for interpreting test rolling results, although no generally accepted theory has emerged from previous research on soil-wheel interaction.

Figure 1.1. Test rolling at TH 212 construction site in Chaska, Minnesota on Oct. 5, 2006

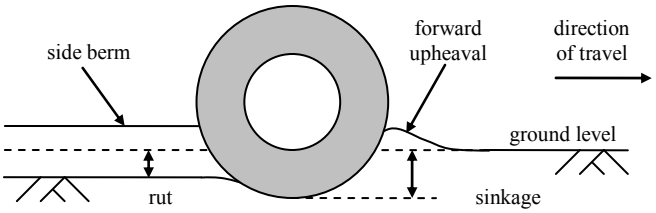

Figure 1.2. Schematic of deformation resulting from test roller wheel penetration

(a) (b) (c)

Figure 1.3. Ruts left by Mn/DOT test roller in granular soil: (a) passing soil; (b) soil near failing; (c) failing soil.

1.2 Objective and Scope

The objectives of the Development of Improved Test Rolling Methods for Roadway Embankment Construction Project were to gain an understanding of the deformation mechanisms involved in the test rolling process, formulate a theoretical model for test roller wheel penetration, relate the theory to experiments, and use the results of the research in recommendations for possible changes to current test rolling procedures used in embankment construction practices. In particular, the project investigated the effects of the various parameters involved, including weight of the test roller, wheel type and size, soil mechanical properties, and soil layering.

Two distinct approaches were used to arrive at a theoretical model of the test rolling process. The first is an approximate analytic method based on classical bearing capacity theory, which gives algebraic relationships between wheel force (weight), wheel size, wheel flexibility parameters, soil properties, and sinkage. The second approach is premised on comprehensive, three-dimensional numerical simulation using the finite element code ABAQUS. The theoretical models pertain to indentation of a rigid/flexible wheel as well as the case of a rolling rigid/flexible wheel in the towed condition. Indentation (i.e., a non-rolling wheel) was considered both for its importance as a fundamental deformation mechanism and as a basis for extension

and comparison to the rolling case. The case of a towed wheel was addressed because the current Mn/DOT test rolling specification requires that the test roller is towed, although the analysis also applies to wheels on a self-propelled vehicle that are not driving or braking (e.g., steerage wheels). The test rolling process was considered slow enough to be treated as quasi-static in both the analytic and numerical models, such that inertial forces and rate effects are disregarded.

Using the theoretical models, parametric study was performed to evaluate the effects of the variables involved in test rolling on roller penetration. Particular emphasis was placed on how changes to the weight and wheel size of test roller affect wheel penetration and how wheel penetration varies with soil type.

Experimental data from lab-scaled field tests and limited full scale field tests were collected to validate the theoretical models. Data were collected for both a cohesive soil and a granular soil. For the lab-scaled tests, subsequent laboratory testing was performed to determine the soil mechanical properties needed for the theoretical predictions. Theoretical predictions are also compared with supplemental data found in the literature.

Results from the parametric study and from the comparison between test data and theoretical predictions are subsequently used to formulate conclusions and recommendations regarding test rolling practice.

1.3 Organization

This report consists of 8 chapters, with additional material included in appendices. Chapter 2 is dedicated to the analysis of previous research on deformation caused by a rolling wheel, which consists of empirical and theoretical models and experimental findings. In Chapter 3, the analytic and numerical test rolling models are presented. Chapter 4 presents the parametric study performed for the theoretical models developed in Chapter 3. In Chapter 5, the results of the lab-scaled and full scale field tests are presented. Chapter 6 describes the laboratory tests performed to determine the physical and mechanical properties of the soils used in the lab-scaled field tests. In Chapter 7, a comparison and assessment of the lab-scale tests and theoretical predictions is presented. The limited data from full scale field tests were also used in the comparison. Chapter 8 gives conclusions resulting from the project, as well as recommendations in terms of potential changes to the current Mn/DOT test rolling method and how the theoretical models may be used. The appendices contain specific results, tables, graphs, and illustrative examples demonstrating the usefulness of the theoretical models.

Chapter 2

Analysis of Previous Findings

This chapter summarizes nationwide test rolling practices and synthesizes a large quantity of documented research on the study of deformation caused by a rolling wheel. The University of Minnesota's library search engine (MNCAT) was used to find relevant books, journals, and conference proceedings. Compendex, an online database for scholarly science and engineering publications, was used to find journal articles. Internet search engines were used to investigate online resources, particularly publications from government agencies such as the Wisconsin Department of Transportation (Wis/DOT) and the Corps of Engineers.

Test rolling procedures employed nationwide are summarized in Section 2.1. In Section 2.2, scholarly articles on the subject of soil-wheel interaction are discussed. In total, approximately 80 sources of documented research relevant to test rolling were obtained and analyzed. These sources are topically subdivided in Section 2.2 into the following three categories: (1) experimental studies, (2) semi-analytical or analytical models, and (3) numerical modeling. In Section 2.3, general conclusions from the analysis of previous work are provided.

2.1 Nationwide Test Rolling Procedures

The Mn/DOT specification (Minnesota 2000) requires use of a towed trailer weighing a total of 267 kN (30 tons), with two pneumatic tires spaced 1.8 m (6 ft) on center. The tire size can be either 18×34 or 18×25, and the tires must be inflated to a pressure of 650 kPa (95 psi). Soil compaction is considered satisfactory for all soils when sinkage is not greater than 50 mm (2 in.), except an additional 25 mm (1 in.) is allowed for granular soils to be stabilized after test rolling.

Test rolling procedures employed in states other than Minnesota are similar in character to that specified by Mn/DOT but vary in implementation and acceptance criteria for roller penetration. Typically, a heavily-loaded dump truck with a total weight of 180 to 360 kN (20 to 40 tons) is used to perform test rolling, given the availability of such equipment in construction. Acceptance criteria are usually visual and often left to the discretion of project engineers. Where specified, the acceptable sinkage or rutting varies from zero depth to up to about 75 mm (3 in.). The most significant differences between the Mn/DOT test rolling procedure and those generally used in other states are as follows: Mn/DOT requires a relatively large 133 kN (15 tons) wheel load using a specialized two-wheeled roller, identifies specific acceptance criteria in terms of sinkage, and specifies that the roller should be towed rather than self-propelled.

A thorough, largely experimental investigation into appropriate penetration limits for test rolling was undertaken by Wis/DOT between 1998 and 2002 (Crovetti 2002). The California

Bearing Ratio (CBR), determined from laboratory tests and correlations with dynamic cone penetrometer (DCP) measurements from the field, were empirically related to test roller penetration. This correlation was used to prescribe a specific minimum sinkage corresponding to a minimum allowable CBR. The following were recommended for test rolling:

i. Since adequate compaction is relatively easily achieved for granular materials, test rolling should be used for moisture sensitive clays and silts.
ii. The sinkage should be no more than 40 mm (1.5 in.), based on a minimum CBR of 6 and the following test roller configuration:
    a. sinkage measured at the wheels of the front axle of a standard quad-axle dump truck, with a wheel load of 53 kN (6 tons)
    b. standard front axle tires inflated to 760 to 860 kPa (110 to 125 psi)

Some numerical modeling was performed during the Wis/DOT study using nonlinear and stress-dependent finite element modeling, although the details of this work could not be obtained. Although the results of this effort evidently did not weigh into the recommendations for sinkage acceptance criteria, the numerical simulation offered some insight into the effects of layering. According to the simulation, upper layer stiffness had a significant impact on the wheel sinkage, while lower layer stiffness had a relatively small effect. Although the geometries used in the modeling are unspecified by Crovetti (2002), he later concludes based on substantiating experimental evidence that test rolling, in the configuration used, is effective at identifying weak soil within 30 cm (12 inches) of the surface.

2.2 Overview of Scholarly Literature

Serious attention was given to the problems surrounding soil-wheel interaction beginning in the 1960's with the publication of *Theory of Land Locomotion* 1956, *Off-the-Road Locomotion* (1960), and *Introduction to Terrain-Vehicle Systems* (1969) by Bekker. This same period also marks the inception of the *Journal of Terramechanic*s. *Terramechanics* has become the field which quite generally embraces the study of terrain-vehicle interaction. *Theory of Ground Vehicles* (2001) and *Terramechanics and Off-Road Vehicles* (1989) by Wong constitute the most recent reviews of the state of the art. The aggregation of soil-wheel interaction problems in the field of terramechanics allows for ready identification of the state of the art.

Several attempts to predict the soil deformation induced by a rolling wheel are presented in the literature. The theory of elasticity, theory of plasticity, and finite element method have been used to varying degrees of success, but the most used and widely accepted models are empirical in nature. Section 2.2.1 summarizes some common practices for evaluating the soil and wheel properties. Laboratory and field experiments on soil-wheel interaction are described in Section 2.2.2. In Section 2.2.3, the most prevalent models for predicting sinkage are presented.

2.2.1 Mechanical Properties of Soil-Wheel System

2.2.1.1 Mechanical Properties of Soil

Appropriate characterization of the mechanical properties of soil is of utmost importance soil-wheel interaction, and several methods have been proposed for quantifying deformation and

strength parameters. In soil mechanics, the classical methods comprise direct shear, one-dimensional compression, triaxial compression, and unconfined compression tests. These laboratory methods allow for determining parameters such as Young's modulus, Poisson's ratio, compression index, angle of internal friction, and cohesion. Field tests such as the cone penetration test (CPT), standard penetration test (SPT), and the vane test have also found application. In terramechanics, two specific methods, the *bevameter* and *cone penetrometer* tests, are used frequently (Maclaurin 1987; Wong 1989). These tests, elaborated on in Sections 2.2.1.1.1 and 2.2.1.1.2, are used for evaluating the response of various types of terrain (soil, snow, etc.) to wheel loads. In the following, the term *soil*, rather than *terrain*, will be used consistently to emphasize the particular interest of this project.

Soil parameters other than those resulting from the bevameter and cone penetrometer tests have been used by researchers, and their applicability depends on the particular problem being investigated. For instance, Muro (1993) references a dynamic plate loading test and slip sinkage test, each of which generate two additional soil-wheel system parameters. Also, the number of soil parameters greatly increases in contemporary nonlinear constitutive models, and appropriate tests have to be designed to arrive at their numerical values. Consensus on relevant soil parameters and how to measure them is one of the most enduring problems in terramechanics (Maclaurin 1987; Gee-Clough 1991).

2.2.1.1.1 Bevameter Tests

The bevameter tests, which are used to this day (e.g., Osetinksy and Shmulevich 2004; Shibly et al. 2005), were introduced by Bekker in 1960. The tests make use of two devices (Fig. 2.1). One device is used to perform a so-called *plate-sinkage test*, in which a rectangular plate of a size representing the contact area of running gear is pushed normally into the soil while measuring normal load-displacement data. The second device is used to perform a *shear test*, in which a thick-walled ring placed on the ground surface is rotated, under varying normal loads, while measuring shear load-displacement data.

The aim of the plate-sinkage test is to determine parameters governing the depth to which running gear displace normally into the soil. Three empirical parameters deduced from the plate-sinkage test are k_c, k_ϕ, and n (Bekker 1969). The purpose of the shear test is to determine parameters governing the resistance of the soil to shear induced by running gear. Angle of internal friction, cohesion, and an additional constant K are determined from curve-fitting empirical data collected with this shear test (Bekker 1969).

Although k_c and k_ϕ appear to be related to the angle of internal friction and cohesion, there is no clear connection to these strength parameters. Experiments performed by Willis et al. (1965) suggest that the parameters k_c and k_ϕ are dependent on the contact area of the plate used in the plate-sinkage test, so as to be inappropriate for use as true soil constants. Likewise, the cohesion and angle of internal friction measured with the bevameter shear test are, in the literature, ostensibly the same material strength parameters used in Mohr-Coulomb failure criterion, but in actuality, these very much depend on the configuration of the apparatus. In fact, they are parameters governing the shear response for a particular soil-machine arrangement.

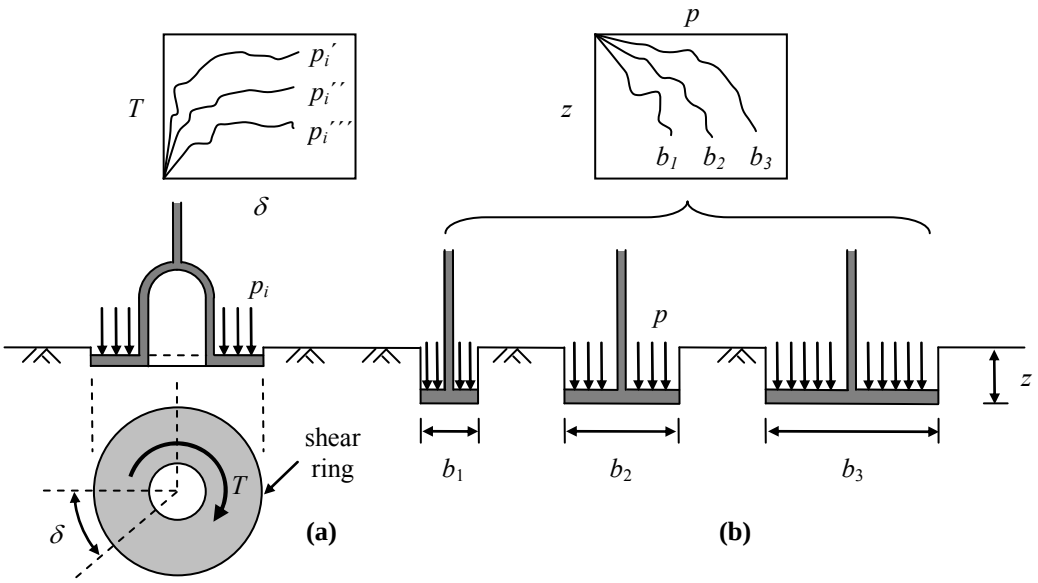

Figure 2.1. Schematic of bevameter tests (reproduced from Bekker 1969):
(a) shear test; (b) plate-sinkage test

2.2.1.1.2 Cone Penetrometer

The second test used often in terramechanics makes use of the *cone penetrometer*. In this test, a small cone affixed to the end of a rod is driven into the soil, and penetration resistance in terms of force is measured as a function of the depth of penetration. The technique was developed by the U.S. Army Corps of Engineers Waterway Experiment Station (WES) in the 1940's. The original cone penetrometer used by WES consists of a 30 degree right circular cone with a 3.23 cm^2 (0.5 in^2) base area (Wong 1989). One soil parameter arising from the cone penetrometer test is the *cone index* (CI). The cone index is often correlated to bulk density (Bygdén et al. 2004), which indicates the degree of compaction. Although the adequacy of the information obtained with the cone penetrometer continues to be questioned, it is still frequently used, owing to its simplicity (Maclaurin 1987). The cone penetrometer has been of greatest utility in empirical models.

The WES cone penetrometer test is distinctly different than the DCP test referred to in other sections of this report. The DCP referenced in Mn/DOT specifications (per ASTM D 6951) uses a 60 degree right circular cone with 3.14 cm^2 (0.49 in^2). In the DCP test, a mass is dropped from a specific height, and information regarding the number of blows and depth of penetration is recorded. In contrast, the WES cone penetrometer used commonly in terramechanics is a static test in which load is applied gradually.

2.2.1.2 Mechanical Properties of Wheel

The mechanical response of a flexible wheel in the context of soil-wheel interaction is a field of study unto itself (cf. Nakashima and Wong 1993), although the assumption of a rigid wheel is commonly introduced to simplify computation. The assumption of a rigid wheel is valid even for

a pneumatic tire when the tire inflation pressure and carcass stiffness are large compared to the deformability of the soil (Bekker 1960). Without wheel rigidity, the problem is complicated by the fact that both the wheel and soil deform under loading.

Soil-wheel models which consider elastic deformation of the wheel vary greatly. Most predictions rely on an experimentally determined relationship between tire deformation and applied load. Contact profiles between the wheel and soil are usually either assumed or experimentally determined (cf. Fujimoto 1977; Karafiath and Nowatzki 1978; Qun et al. 1987; Osetinksy and Shmulevich 2004).

2.2.2 Experiments on Soil-Wheel Interaction

The study on acceptable test roller penetration performed for Wis/DOT (Crovetti 2002) is perhaps the only documented experimental investigation performed specifically with test rolling in mind. The execution and findings of this study are discussed in Section 2.1. This section gives a survey of related experimental research on soil-wheel interaction, taken from scholarly journals and books.

Freitag (1965) conducted numerous experiments in an effort to characterize empirically the relationships between various non-dimensional parameters arising from dimensional analysis of soil-wheel interaction in the general context of vehicle mobility. He used multiple pneumatic wheel sizes operating in clay and fine sand. Experimental results for many tests are tabulated, which include sinkage, tire deflection, pull force, and several other parameters for multiple wheel loads and tire configurations.

Onafeko and Reece (1967) and Krick (1969) measured the normal and tangential stress distribution on the circumference of a rigid wheels operating in sandy material by placing stress transducers on the wheel. Measured normal stresses were compressive and distributed somewhat asymmetrically. However, tangential stresses were found to change direction at a point along the contact length of the wheel (Fig. 2.2). This change in direction is in agreement with later studies of the soil deformation field, which identify forward and backward particle flow zones as illustrated in Fig. 2.3, reproduced from Wong (2001). Krick also showed that stresses are nearly uniform across the width of the wheel, though higher at the edge of the wheel due to stress concentration.

Windisch and Yong (1970) measured the deformation field beneath a towed rigid wheel in a clayey material using X-ray techniques. Plane-strain experiments were conducted by placing lead markers in the soil and measuring marker displacement by superposition of successive X-ray photographs. The results show that a particle at the soil surface will move forward, downward, and backward in an open loop.

Raghavan and McKyes (1978) arrived at empirical predictions of dry density based on location within the soil, applied pressure, and moisture content for a clay soil. Tests were conducted using several standard tractor tire sizes, with contact pressures ranging from 16 to 62 kPa (1.7 to 9.0 psi). Data was acquired via in situ tests conducted to depths of 50 cm (20 in.) below the centerline of the wheel path and 50 cm (20 in.) away from the centerline of the wheel path. Several vehicle and pneumatic tire types were used, and the effect of multiple passes was considered. The correlations presented are based on several thousand measurements.

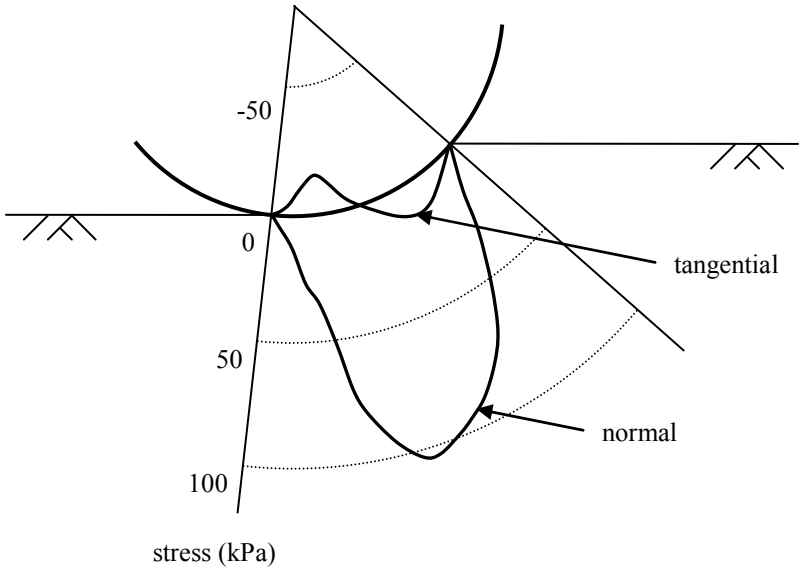

Figure 2.2. Distribution of normal and tangential stresses beneath a towed wheel (example from Onafeko and Reece 1967)

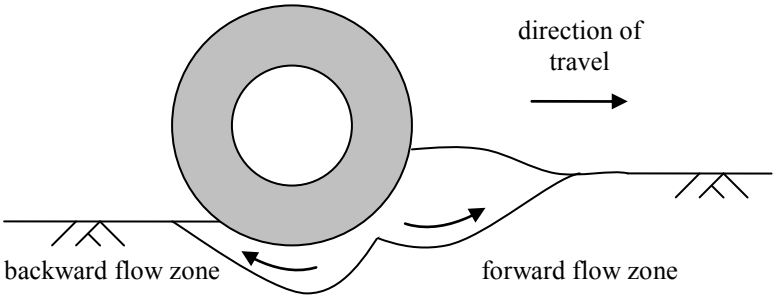

Figure 2.3. Schematic of flow zones beneath rolling wheel (Wong 2001)

Raghavan et al. (1978) showed that in clay soils large wheel slip causes significantly greater sinkage than that caused when the wheel is not slipping. The driven wheel condition was investigated using several tractor types.

Gee-Clough (1979) published an experimental study on the effects of wheel width and wheel diameter for a rigid wheel operating in dry sand. The focus of the paper was analysis and verification of the semi-empirical predictions of rolling resistance. Experiments were conducted using wooden wheels with diameters ranging from 13 to 23 cm (5.1 to 9.0 in.). Width-to-diameter ratios ranged from 0.11 to 0.96. Tests were conducted by enforcing sinkage ranging from nearly 0 to 6 cm (2.4 in.). Results show that the "bulldozing" or forward upheaval effect, in which a volume of material is accumulated in front of a rolling wheel (Fig. 1.2), is significant for wheels with large width-to-diameter ratios operating in sand.

Although the focus of the research was not the soil deformation field, Abebe et al. (1989) present images of the displacement field in sandy loam beneath a rigid wheel. For a rigid wheel 40 cm (16 in.) in diameter and 50 cm (20 in.) in width and wheel loads of 0.5 and 0.6 kN (112

and 135 lbs), deformation was found to occur most significantly within a depth of 15 cm (5.9 in.). Results indicated that most sinkage and compaction occurs within the first passing of the wheel, with effects rapidly decreasing in subsequent passes.

Block (1991) and Block et al. (1994) measured soil stresses at discrete locations beneath the path of a rigid wheel in a sandy soil and a clayey soil using stress transducers. The wheel had a diameter of 137 cm (54 in.) and width of 30 cm (12 in.), and wheel loads ranged from 5.8 to 11.6 kN (1300 to 2600 lbs). They concluded that the soil type had a moderate influence on the development of stresses directly beneath the wheel at depths from 15 to 30 cm (6 to 12 in.), where stresses in the clayey soil were on average slightly higher than those induced in the sandy soil. At the same locations relative to the wheel, the presence of a stiff underlying layer was found to generally reduce stresses developed in the sand and have negligible effects for the clay. Wheel slip was found to have no effect on stress development within the soil at the locations where measurements were taken.

Schwanghart (1991) experimentally determined the contact area and contact pressure distribution beneath several pneumatic wheel types at varying inflation pressures. He proposed an empirical method for predicting contact areas and contact pressures. His results show that contact area is approximately a linear function of wheel load up to loads of 35 kN (4 tons) for tires with diameters ranging from 100 to 150 cm (40 to 60 in.). Contact pressures were also found to vary linearly as function of tire inflation pressure for pressures between 0 and 250 kPa (36 psi) and similar wheel loads. Schwanghart's experiments validate observations made by previous researchers (Bekker 1969; Wong 1989) that contact pressure may be significantly different than tire inflation pressure, although it is a common assumption that they are equal. The disparity is attributed to the stiffness of the tire carcass.

Adebiyi et al. (1991) give sinkage values for a standard-sized pneumatic tire operating in a sandy loam at loads up to approximately 1.5 kN (340 lbs). Two different moisture contents were investigated. Sinkage was slightly higher at all loads investigated for the higher moisture content.

Çarman (1994) measured sinkage, bulk density, and cone index for standard tractor tires operating in a silty-loam, as well as shear strength using a shear vane. Wheel loads ranged from 7 to 14 kN (1,600 to 3,200 lbs). This study concentrated on the effect of wheel load and vehicle velocity on compaction, comparing results obtained for velocities ranging from 0.78 to 2.5 m/s (1.7 to 5.6 mph). Increased vehicle velocity was found to reduce the sinkage, as well as cone index, bulk density, and shear strength measured in the wheel track. However, the influence of vehicle velocity was determined to be small compared to the effect of wheel load.

Arvidsson and Ristic (1996) measured rut depth and profile, penetration resistance, and vertical soil stresses for several standard pneumatic tractor tire types operating in dry sand, focusing on the influence of tire pressure. The wheel load was 25.4 kN (5,700 lbs). Soil stresses were measured at depths from 20 to 40 cm (8 to 16 in.) beneath the tire and up to 27 cm (11 in.) away from the centerline of the tire. Rut depth, as well as vertical soil stress (using the mean of stresses measured at the various locations) and penetration resistance measured in the wheel track using a cone penetrometer, was found to increase with increasing tire pressure.

In a comparison of the effects a construction roller and tracked vehicle on compaction, Muro et al. (1998) measured sinkage, dry density distribution versus depth, and vertical stress versus depth for a sandy soil. The effects of multiple passes were investigated. Dry density was measured using a cone penetrometer, and vertical stress was measured using load cells. Measurements were taken at depths up to 60 cm (24 in.). For the 10 kN (2,200 lbs) commercial

construction roller used in the experiment, vertical stresses in the soil caused by the roller were found to be appreciable only in the first 40 cm (16 in.) of soil.

Botta et al. (2002) measured bulk density and cone index in a fine clay before and after single passage of a four-wheeled tractor with standard-sized pneumatic tires. Wheel loads ranged from 18 to 32 kN (4,000 to 7,200 lbs). Changing wheel sizes and configurations affected soil compaction only to a depth of 20 cm (8 in.). Compaction at depths ranging from 20 to 60 cm (8 to 24 in.) was found to be directly related to applied wheel load. Abu-Hamdeh et al. (2000) conducted a similar investigation, though they concluded that tire inflation pressure affects soil compaction at soil depths up to 50 cm (20 in.).

Maciejewski and Jarzębowski (2004) performed an extensive investigation of compaction of a medium-dense cohesive soil under a rolling rigid cylinder, both driven and towed. The diameter of the cylinder was 32 cm (13 inches), and tests were conducted at wheel loads ranging from nearly 0 to 4 kN (900 lbs). Experiments were conducted in a soil box with a transparent wall, and the deformation field was determined by observing markers in the soil in its original and deformed configurations. The apparatus applied constant load to the wheel at various controlled values of wheel slip. The following conclusions for a cohesive soil may be drawn from this work:

i. sinkage induced by a towed wheel is less than that induced by a driven wheel
ii. the flow pattern in cohesive soil is consistent with that in granular soil (Fig. 2.3)
iii. soil behind the towed wheel undergoes localized failure in nearly vertical cracks, but only at sufficiently large loading and soil layer thickness
iv. most soil compaction resulting from wheel loading is achieved in the first passage
v. the level of compaction depends most strongly on applied wheel load (i.e., compaction achieved with single passage of wheel with large load is greater than compaction from repeated loading under relatively light wheel)

2.2.3 Sinkage Models

2.2.3.1 Empirical Models

The bevameter tests (see Section 2.2.1.1.1) provide a basis for most empirical predictions of wheel sinkage. The three soil parameters determined from the plate-sinkage test are evaluated by curve-fitting a pressure-sinkage relationship of the following form (Bekker 1960):

$$p = \left(\frac{k_c}{b_p} + k_\phi \right) z^n \tag{2.1}$$

where p is the average pressure acting on rectangular plate, k_c, k_ϕ and n are empirical constants, z is the plate sinkage, and b_p is the width of plate used in plate-sinkage test.

Onafeko and Reece (1967) proposed replacing the pressure-sinkage relationship of Eq. (2.1) with a more dimensionally consistent form

$$p = \left(ck_c^{'} + \gamma b k_\phi^{'} \right) \left(\frac{z}{b_p} \right)^n \tag{2.2}$$

where c is the cohesion, γ is the unit weight of soil, and k_c' and k_ϕ' are empirical constants.

Researchers have applied the empirical pressure-depth relationship from the plate-sinkage test to the soil-wheel problem in numerous ways. It is common to assume that there is a direct correspondence between stresses acting at a point on the circumference of the wheel and the depth of that point. That is, Eq. (2.1) or (2.2) are used to relate stress on the wheel to depth, and the stresses are integrated over the soil-wheel interface to calculate wheel force. For instance, assuming that stresses acting on the wheel are radial only (no shear) and are exactly the pressures determined from the pressure-depth relationship (2.1), the following formula is obtained (Bekker 1960):

$$z = \left[\frac{3W}{b(3-n)\left(\frac{k_c}{b_p} + k_\phi \right)\sqrt{d}} \right]^{\frac{2}{2n+1}} \tag{2.3}$$

where W is the total applied load, b is the wheel width, and d is the wheel diameter. The applicability of results derived from the plate loading tests for the rolling-wheel problem has been questioned by several researchers (Dagan and Tulin 1969; Gee-Clough 1991), although the merit of the approach is made evident by Eq. (2.3), which is quite simple and easy to implement.

Several researchers have expanded on empirical models in various ways. Perhaps the most comprehensive of these is a model proposed by Muro (1993) which relates sinkage to force and torque acting on a wheel. The model makes use of 15 parameters from four separate tests, including a static plate loading and unloading test, a dynamic plate loading test, a plate traction test (bevameter shear test), and a slip sinkage test. Additional semi-empirical models have been proposed by Poletayev (1964), McRae (1964), Willis (1965), Kogure (1976), Fujimoto (1977), Wong et al. (1984), Osetinksy and Shmulevich 2004, and Shibly et al. (2005).

2.2.3.2 Analytical Models

Analytical models have been formulated using elasticity and plasticity approaches. Implementation of elasticity has lead to variations on the classical contact problems of mechanics for predicting local deformations (Karafiath and Nowatzki 1978). Solutions using elasticity give reasonable predictions of local deformation for relatively small wheel loads and are used widely to predict soil stresses induced from large loads in regions sufficiently far away from the point of loading (e.g., Boussinesq's solution). Plasticity approaches by their vary nature apply when the problem is characterized by material failure, such that they are applicable for predicting stresses and permanent deformations when loads are high enough to fail the soil. For most problems of interest in soil-wheel interaction, the soil does indeed fail in regions close to the wheel. The forward and backward flow zones shown schematically in Fig. 2.3 are regions of

such plastic deformation. Several of the most significant analytical studies using elasticity or plasticity approaches are presented here.

Roberts (1971) presented solutions for a pneumatic tire and rigid wheel traveling at constant speed over a two-dimensional elastic half-space. The pneumatic tire was assumed to impose a region of uniform pressure over a predetermined contact length. The purpose of this paper was to present the displacements and stresses arising from consideration of a dynamic contact problem, which are of concern when the wheel is moving at considerable speeds. Roberts refers the reader to solutions of classical contact problems for determining depth of indentation. Lansing (1966) earlier presented similar solutions to the problem of a concentrated normal load moving at constant speed.

Evans (1964) combined elasticity calculations with bearing capacity theory to predict the pressure-sinkage relationship for a tracked vehicle. Calculations based on elasticity were used to predict sinkage at small loads, and bearing capacity theory was used to determine the limiting value of the pressure-sinkage curve. The two regimes (small load and limit load) were then connected with an assumed function to obtain a complete pressure-sinkage relationship. The analysis implicitly assumed the case of uniform load applied along an infinitely long strip (plane strain condition).

Dagan and Tulin (1969) published an approximate plane strain plasticity analysis for a driven wheel, applying the equations of plastic flow for a rigid, perfectly plastic material. The wheel was assumed to be moving through the incompressible soil (e.g., saturated clay) at constant velocity and with a specified sinkage. Particle velocities and normal stresses on the wheel were computed for a specified distribution of shear stresses on the soil-wheel interface. Rough agreement between computed wheel load resulting from the stresses and experimentally determined wheel load was found for one particular problem, but no load-sinkage relationships were presented.

Karafiath (1971) and Nowatzki and Karafiath (1978, 1974) gave perhaps the most thorough application of plasticity to the problem of soil-wheel interaction. Using the slip lines method applicable to a rigid-perfectly plastic material and plane strain conditions, the stress field in the soil beneath a rigid wheel and the stress distribution on the surface of the wheel were determined for a given sinkage. Linear and nonlinear failure criteria were used. The wheel geometry and soil properties, interface friction between the wheel and soil, and location of the transition point between forward and backward flow zones (as shown in Fig. 2.3) were used as inputs. For a given sinkage, the corresponding wheel load was computed by integrating the stresses acting on the wheel. Nowatzki and Karafiath (1974) give several load-sinkage curves corresponding to different values of wheel slip for a small wheel operating in sand. They found reasonable agreement between analytical and experimental results.

Elsamny and Ghobarah (1972) performed a plane strain analysis similar to that of Nowatzki and Karafiath, though less comprehensive. The stress field beneath a rigid wheel was computed assuming full wheel slip, but no load-sinkage curves were generated.

Researchers have applied conventional bearing capacity theory to the soil-wheel problem in various ways. Hetherington and Littleton (1978) and Kim and Shin (1986) proposed formulas for predicting rolling resistance using, among other things, Terzaghi's bearing capacity theory to predict stresses acting on a rigid, rolling wheel. For example, Hetherington and Littleton assumed that the vertical stress acting on a wheel operating in sand is given by $\gamma N_q z$, where N_q is one of Terzaghi's bearing capacity factors for a strip footing. Kim and Shin used bearing

capacity formulas in a similar way, but the procedure is somewhat obscured by experimentally-motivated relationships taken from other sources.

2.2.3.3 Numerical Models

Perumpral et al. (1971) implemented the finite element method (FEM) to predict the soil stresses and deformation caused by a stationary wheel and a rolling wheel. For the static wheel analysis, wheel loading was simulated assuming a circular (axisymmetric) contact area of uniform pressure. A bilinear elastic stress-strain relationship was used for the soil in the static analysis. For the moving wheel, plane strain analysis was performed assuming a rigid wheel and a linearly elastic stress-strain relationship. The analysis was performed by prescribing the boundary stresses (radial and shear stresses acting on the soil-wheel interface) based on experimental results obtained by Onafeko and Reece (1967). Soil stresses and displacements were presented for a particular wheel geometry and assumed sinkage.

Chung and Lee (1975) used a viscoelastoplastic constitutive model for the soil to determine the stresses and displacements beneath a rigid rolling wheel. The constitutive model requires four elastic parameters, one plastic parameter, and one viscous parameter. Plane strain FEM analysis was used, also by specifying boundary stresses based on the experimental results obtained by Onafeko and Reece (1967). Displacement and stress fields were shown for some soil-wheel arrangements.

Yong and Fattah (1976) considered plane strain soil deformation induced by a rolling rigid wheel. In their FEM analysis, displacements at the soil-wheel interface as measured in tests were assumed. A nonlinear constitutive relationship was used for the soil. Velocities and strain rates were computed, and contours of velocities were presented.

Yong et al. (1978) expanded on the analysis of Perumpral et al. (1971) and Yong and Fattah (1976) by accounting for the deformability of the wheel. First, the tractions induced by the wheel were computed as a contact problem of an elastic wheel on a rigid surface. The computed tractions were approximated by a parabolic distribution. Next, the tractions were applied to the soil, which was modeled as a nonlinear elastic material. Velocities and strain rate fields were constructed.

Pollock et al. (1986) implemented FEM to investigate the effects of multiple passes of a wheel on soil compaction. The wheel was assumed to exert a uniform pressure over a circular area, allowing for axisymmetric analysis. Upon loading, soil behavior was analyzed by prescribing the hyperbolic constitutive model described by Duncan and Chang (1970). Upon unloading, the material was treated as linear elastic. Graphs representing volumetric strains within the soil were presented.

Gassman et al. (1989) used the finite element program ANSYS to determine compaction resulting in a layered soil under plane strain conditions. Like previous researchers, the analysis was performed by applying uniformly distributed tractions over a specified area on the soil-wheel interface. An elastoplastic soil constitutive relationship was used in the computations, and elastic and plastic strain distributions within the soil were constructed.

Saliba (1990) used FEM with a viscoelastoplastic constitutive model for the soil. Five soil parameters were required for the model, including Young's modulus, Poisson's ratio, angle of internal friction, cohesion, and a fluidity parameter to capture viscous effects. Plane strain analysis was performed by prescribing pressure over a region on the soil surface. The effects of

tire inflation pressure and soil layering were considered. The effects of inflation pressure were evaluated by varying the magnitude and distribution of pressures applied to the soil surface. Several plots of computed rut profiles were presented.

Nakashima and Wong (1993) constructed a three-dimensional model of a pneumatic tire using FEM, with an interest in accurately predicting the geometry of the contact area between the tire and soil. This study was intended as a precursor to more involved procedures for studying soil-wheel interaction through FEM, focusing on construction and validation of the tire model. No results for the tire operating on a deformable material were obtained.

Chi et al. (1993) performed a FEM analysis similar to that of Perumpral et al.(1971), Pollock et al.(1986), and Gassman et al. (1989) to predict soil compaction resulting from vehicle loading, except that the analysis was extended to three dimensions. The model used the hyperbolic stress-strain relationship for soil developed by Duncan and Chang (1970). Uniform pressures representative of several types of wheels and tracks were applied to the soil surface. Several plots of bulk density increase in the soil were presented.

Foster et al. (1995) used FEM to investigate soil stresses and deformations caused by a stationary wheel and a rolling wheel. Plane strain analysis was performed assuming nonlinear elastic soil behavior and a rigid wheel. The codes NASTRAN and ABAQUS were used to perform the analysis. In the case of the stationary wheel, a concentrated force was applied to the center of the wheel, and resulting deformation and stress fields in the soil were computed. For the rolling wheel, the rolling action was simulated by imposing representative displacements at the soil surface. Loads and rut depths were tabulated for the static wheel case, as well as stresses at some locations for the static and moving wheels.

Liu and Wong (1996) performed a plane strain analysis using FEM for the case of a rigid wheel. In the analysis, a vertical load was applied to the wheel, and then the wheel was moved horizontally across the simulated soil surface, inducing an assumed exponential distribution of shear stresses. An elastoplastic constitutive relationship was used for the soil, in which four elastic parameters and four plastic parameters were required. Soil-wheel interface stresses and deformation fields within the soil were computed. Some reservation as to the accuracy of modeling localized deformation with the elastoplastic models was expressed.

Chiroux et al. (2005) performed FEM analysis using ABAQUS similar to that of Liu and Wong (1996), except that the model was developed in three dimensions. The wheel was assumed to be rigid, and soil was modeled as an elastoplastic material requiring two elastic parameters and three plastic parameters. A vertical load was applied to the wheel, and then the wheel was moved horizontally at a specified velocity. The analysis was run for several wheel loads and velocities. A dry friction law was prescribed for the interaction between the wheel and soil. Rut depth as a function of wheel load was computed for some cases. Three-dimensional visualization illustrated the development of the rut profile. Soil rebound after passage of the wheel was found to be excessive and in disagreement with experiments, even though considerable attention was given to selecting realistic parameters.

2.3 Remarks on Previous Work

In terms of understanding how the test roller variables and soil properties affect test roller wheel penetration, analysis of current test rolling procedures offers very limited information. Current procedures appear to have been developed primarily from experience or empirical data.

Diversity in specifications for equipment and soil acceptance criteria employed in different states in the U.S. illustrates the general lack of understanding of the mechanics of test rolling. This lack of understanding is also reflected in the scholarly literature referenced in Section 2.2. The dependence of wheel penetration on wheel weight, wheel geometry, and soil properties was analyzed in only a few papers, although the results provide a good starting point for deeper analysis. Experimental observations and data obtained by previous researchers are of use in setting and validating models relating test roller penetration to soil quality.

Much research has been concerned with vehicle and wheel performance characteristics other than sinkage and rutting. For example, the distribution of stresses at the soil-wheel interface and within the soil itself was of interest to many researchers, as well as the strains within the soil. This information is of limited direct use in the test rolling problem, where the objective is to relate wheel penetration to soil mechanical properties.

One of the lingering problems in terramechanics and test rolling in particular is adequate characterization of soil mechanical properties. Early on in terramechanics, emphasis was placed on field tests (e.g., the bevameter tests). This resulted in the predomination of empirical methods, as results of the field tests were virtually always viewed simply as soil index parameters. Little effort has been directed towards obtaining fundamental material constants for the soil, as in soil mechanics. The problem of selecting appropriate soil properties is again demonstrated by the difficulties arising in numerical analyses using FEM. Researchers have employed a number of different soil constitutive models with varying degrees of complexity, although no single model has emerged as the definitive choice for capturing soil response in soil-wheel interaction.

Most proposed analytic and numerical models for soil-wheel interaction have been limited to the plane strain condition, and whether the three-dimensional deformation induced by a wheel can be neglected is debatable. In the instances of three-dimensional analyses, axisymmetric loading have been assumed. Expanding the models to non-axisymmetric, three-dimensional analysis has been recommended by several researchers (Hetherington 1980).

Chapter 3

Theoretical Models

This chapter details the formulation of the theoretical models developed to characterize the test rolling process. Two distinct approaches were used: an approximate analytic method and numerical simulation. For the analytic method, classical bearing capacity theory, a result of Limit Analysis, was used to obtain closed-form relationships between test roller characteristics (weight, wheel geometry, etc.), soil properties, and sinkage for wheel indentation and steady-state rolling. Although the rolling case is the main problem of interest, indentation (i.e., a non-rolling wheel) was considered for its importance as a fundamental deformation mechanism and as a basis for extension and comparison to the rolling case. Under steady-state rolling conditions, rolling is considered to have progressed long enough such that the sinkage is unvarying under the constant wheel force (weight). In the numerical simulations, the finite element code ABAQUS was used to simulate both indentation and rolling processes.

Although the test roller is moving at some velocity, the test rolling process is considered slow enough to be treated as quasi-static in both the analytic and numerical models. Inertial forces and rate effects are therefore disregarded. Furthermore, the case of a towed wheel is addressed, in which torque about the wheel axle is negligible. When wheel torque is present, the wheel is being either driven or braked. The current Mn/DOT test rolling specification (Minnesota 2000) requires that the test roller is towed, and even in the case of self-propelled vehicles, many have wheels in the towed condition (e.g., steerage on dump trucks).

Both rigid and flexible wheels are considered. In the analytic method, wheel flexibility is accommodated in an approximate way by introducing a wheel flexibility parameter. In the numerical simulations, a pneumatic tire is simulated, where tire inflation pressure and carcass stiffness are explicitly accounted by modeling the tire as a pressurized shell structure.

Section 3.1 explains the material models used in the analytic method and the numerical simulations. Section 3.2 gives the details of the analytic method for wheel indentation and rolling on homogeneous soil. Section 3.3 explains the numerical simulations of wheel indentation and rolling on homogeneous soils. In Section 3.4, the effect of layering in the analytic method and numerical simulation is considered. General remarks regarding the theoretical models are in Section 3.5.

Appendix A contains a summary of the formulas for practical consideration, whereas the full details of model development are given in Section 3.1.

3.1 Material Models

3.1.1 Analytic Method

Soil in the analytic method is intrinsically modeled as a rigid-perfectly plastic material. Fig. 3.1 shows the uniaxial stress (σ) versus strain (ε) response of a rigid-perfectly plastic material. *Rigid* implies that there is no deformation prior to yielding, and *perfectly plastic* indicates that there is no hardening or softening effects (i.e., the yield stress σ_o is constant for all values of strain). At yield stress σ_o, unlimited plastic or permanent strains may result, and the material does not deform when the applied stress is lowered. In the stress-strain diagram of Fig. 3.1, unloading and reloading are represented by a vertical line segment at constant strain.

When multiple stress components are present, the concept of yield stress is replaced by a yield criterion, which prescribes yielding based on some combination of stresses. The analytic method is based on the Mohr-Coulomb yield criterion frequently applied to soils in general

$$\tau_f = c + \sigma_f \tan\phi \tag{3.1}$$

where τ_f and σ_f are respectively the shear and normal stresses on the failure plane at yielding, c is cohesion, and ϕ is the angle of internal friction. Eq. (3.1) is alternatively written in terms of principal stresses as

$$\sigma_1 = \sigma_3 \tan^2\left(45^\circ + \frac{\phi}{2}\right) + 2c\tan\left(45^\circ + \frac{\phi}{2}\right) \tag{3.2}$$

where σ_1 and σ_3 are the major and minor principal stresses, respectively. Eq. (3.1) or Eq. (3.2) with $\phi = 0$ is known as the Tresca yield criterion, often used to model the undrained response of saturated clays.

Throughout this report, the parameters ϕ and c are considered to be interchangeable with ϕ' and c', the so-called *effective* material properties that account for pore water pressure. Likewise, no distinction is made between c and c_u, where c_u is the *undrained shear strength* discussed commonly in the context of saturated clays. The parameters ϕ and c should be chosen to reflect soil response under the relatively fast loading conditions present in test rolling (e.g., $\phi = \phi'$ for free draining sand and $c = c_u$ for saturated clay), although the notational convention of this report is simply to use ϕ and c.

Cohesion and friction angle are the only material parameters entering the analytic method in addition to the unit weight γ. The analytic method cannot be used to predict elastic soil response and applies to the case where elastic deformation is small compared to permanent deformation.

3.1.2 Numerical Simulation

An elastoplastic material model was used for the soil in the ABAQUS simulations. Unlike the rigid-perfectly plastic model, the elastoplastic model allows for elastic deformation of the material prior to yielding and during unloading/reloading. Although hardening or softening can

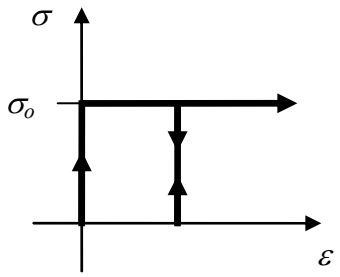

Figure 3.1. Stress-strain response of a rigid-perfectly plastic material

be incorporated in ABAQUS, perfectly plastic behavior was assumed for simplicity. Fig. 3.2 shows the uniaxial stress (σ) versus strain (ε) response of an elastoplastic material with perfect plasticity.

Isotropic linearly elastic response is assumed, so that the elastic part of soil deformation is described by two material constants: the soil Young's modulus E_s and soil Poisson's ratio ν_s. Although the term *Young's modulus* is used here for consistency with classical theory of elasticity, the term *resilient modulus* often used in practice may also be used to describe the same parameter.

Because of inherent difficulties in implementing the Mohr-Coulomb and Tresca yield conditions numerically, other yield conditions which closely approximate them are used. In the numerical simulations, the von Mises and Drucker-Prager models replace the Tresca and Mohr-Coulomb models, respectively. The von Mises yield condition may be written in terms of principal stresses as

$$\frac{1}{\sqrt{2}}\sqrt{(\sigma_1-\sigma_2)^2+(\sigma_2-\sigma_3)^2+(\sigma_3-\sigma_1)^2}=\sigma_o \tag{3.3}$$

where σ_2 is the intermediate principal stress and σ_o is the yield strength of the material in uniaxial tension or compression. The left-hand side of Eq. (3.3) is a stress invariant, referred to in this report as *generalized shear stress*. Using $\sigma_o = 2c$ or $\sigma_o = \sqrt{3}c \approx 1.73c$, the von Mises yield surface either circumscribes or inscribes, respectively, the Tresca yield surface.

The Drucker-Prager yield criterion is

$$\frac{1}{\sqrt{2}}\sqrt{(\sigma_1-\sigma_2)^2+(\sigma_2-\sigma_3)^2+(\sigma_3-\sigma_1)^2}-\frac{1}{3}\tan\phi_{DP}(\sigma_1+\sigma_2+\sigma_3)=\sigma_o \tag{3.4}$$

where ϕ_{DP} is the Drucker-Prager internal friction angle. Note that when $\phi_{DP} = 0$, the pressure-independent von Mises yield condition is recovered. The Drucker-Prager yield criterion matches the Mohr-Coulomb criterion in triaxial compression when

$$\sigma_o=\frac{6c\cos\phi}{3-\sin\phi} \quad , \quad \tan\phi_{DP}=\frac{6\sin\phi}{3-\sin\phi} \tag{3.5}$$

and in triaxial extension when

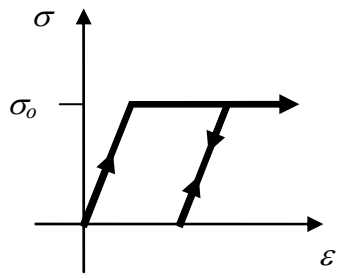

Figure 3.2. Stress-strain response of an elastoplastic material with perfect plasticity

$$\sigma_o = \frac{6c\cos\phi}{3+\sin\phi} \quad , \quad \tan\phi_{DP} = \frac{6\sin\phi}{3+\sin\phi} \tag{3.6}$$

In ABAQUS, a so-called *modified Drucker-Prager* yield condition is also available. This yield condition provides a somewhat closer match to the Mohr-Coulomb yield condition used in the analytic method than the Drucker-Prager yield condition. For most simulations discussed in this report, the Drucker-Prager yield condition was used. Where the modified version was used, an explicit statement to that effect is included.

A dilation angle, denoted ψ, is also specified in the Drucker-Prager material model as appropriate to reproduce realistic volumetric strains and give computational stability. The dilation angle ranges between $0 \leq \psi \leq \phi_{DP}$. Two assumptions regarding the dilation angle are common: $\psi = \phi_{DP}$ and $\psi = 0$. The former (associated flow) may be appropriate when studying incipient failure problems but results in unrealistically large strains when modeling a process, such as indentation and rolling. For this reason, $\psi = 0$ was assumed in the numerical simulations.

When the wheel is rigid, no material parameters are needed. For the case of a flexible wheel, a pneumatic tire is simulated. The hub of the tire is assumed rigid, such that only the flexible tire carcass requires specification of material. The carcass of the pneumatic tire modeled in ABAQUS was assumed to be composed of linearly elastic material characterized by an elastic modulus E_w and Poisson's ratio ν_w.

3.2 Analytic Method

The analytic method is based on the concept of bearing capacity of shallow foundations and the formula widely used in geotechnical practice. Bearing capacity is identified as the ultimate average stress, denoted q_u, acting at the foundation-soil interface when the soil fails plastically. The original bearing capacity formula due to Terzaghi (1943) applies to a strip footing and is approximate in postulating additivity of the contributions of soil cohesion, surcharge, and weight. The formula derives from fundamental works, presented by Prandtl (1921) and Reissner (1924), on punch indentation into a rigid-perfectly plastic material obeying the Tresca or Mohr-Coulomb yield condition (Fig. 3.3).

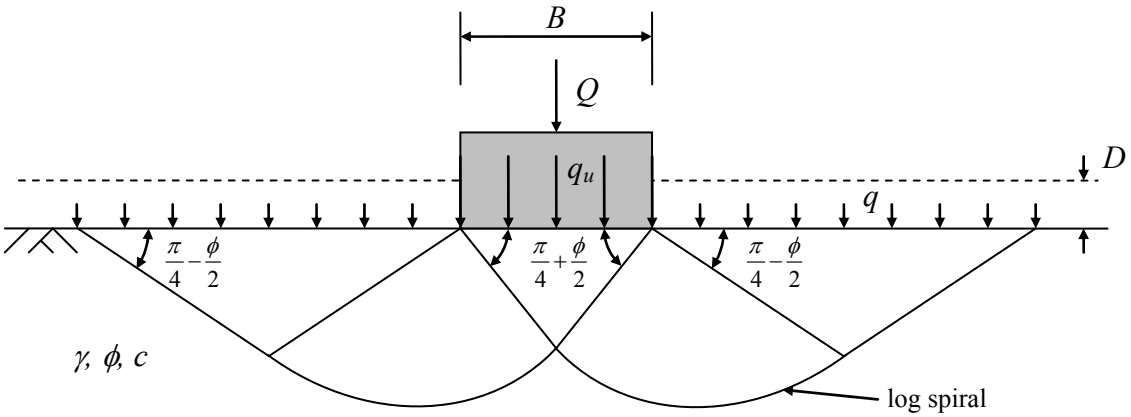

Figure 3.3. Prandtl solution for shallow strip footing

Terzaghi's formula was modified by Meyerhof (1963) to apply to rectangular footings, as well as to account for shear resistance above the depth of embedment and non-vertical loading. The so-called *generalized bearing capacity formula* of Meyerhof has the following form (cf. Das 2005)

$$q_u = cN_c F_{cs} F_{cd} F_{ci} + qN_q F_{qs} F_{qd} F_{qi} + \frac{1}{2}\gamma B N_\gamma F_{\gamma s} F_{\gamma d} F_{\gamma i} \tag{3.7}$$

where c is the soil cohesion, γ is the soil unit weight, B is the smaller dimension of a rectangular footing, and q is the surcharge (pressure) of the soil acting at the depth D of the footing, given by

$$q = \gamma D \tag{3.8}$$

In Eq. (3.7), N_c, N_q, and N_γ are the bearing capacity factors dependent solely on the friction angle ϕ, and F_{cs},...,F_{qd},...,$F_{\gamma i}$... are the shape, depth, and inclination factors, respectively. These factors were derived from theoretical considerations and empirical data, and various forms have been presented in the literature (cf. Caquot and Kerisel 1953; Meyerhof 1963; De Beer 1970; Hansen 1970; Vesic 1973; Zhu and Michalowski 2005). In this analysis, the factors presented by Das (2005) are used. They are repeated below.

Bearing capacity factors:

$$N_q = \tan^2\left(\frac{\pi}{4}+\frac{\phi}{2}\right)e^{\pi\tan\phi} \quad ; \quad N_c = \left(N_q - 1\right)\cot\phi \quad ; \quad N_\gamma = 2\left(N_q + 1\right)\tan\phi \tag{3.9}$$

Shape factors:

$$F_{cs} = 1 + \frac{B}{L}\frac{N_q}{N_c} \quad ; \quad F_{qs} = 1 + \frac{B}{L}\tan\phi \quad ; \quad F_{\gamma s} = 1 - 0.4\frac{B}{L} \tag{3.10}$$

Depth factors:

$$\left.\begin{aligned} F_{cd} &= 1 + 0.4\frac{D}{B} \\ F_{qd} &= 1 + 2\tan\phi\left(1-\sin\phi\right)^2\frac{D}{B} \\ F_{\gamma d} &= 1 \end{aligned}\right\} \quad \text{for } \frac{D}{B} \le 1 \tag{3.11}$$

$$\left.\begin{aligned} F_{cd} &= 1 + 0.4\tan^{-1}\left(\frac{D}{B}\right) \\ F_{qd} &= 1 + 2\tan\phi\left(1-\sin\phi\right)^2\tan^{-1}\left(\frac{D}{B}\right) \\ F_{\gamma d} &= 1 \end{aligned}\right\} \quad \text{for } \frac{D}{B} > 1 \tag{3.12}$$

Inclination factors:

$$F_{ci} = F_{qi} = \left(1-\frac{2\beta}{\pi}\right)^2 \quad ; \quad F_{\gamma i} = \left(1-\frac{\beta}{\phi}\right)^2 \tag{3.13}$$

In Eqs. (3.10), L is the longer dimension of a rectangular footing ($B \le L$), and β in Eqs. (3.13) is the load inclination angle measured from the vertical. Notice that the factor F_{cd} is discontinuous at $D/B = 1$ by an amount 0.085. However, it will be shown later that $D/B \le 1$ for practical purposes so that only Eqs. (3.11) apply.

The formula for the average ultimate stress q_u obtained after substituting Eqs. (3.8)-(3.13) into (3.7) is

$$\begin{aligned} q_u = {} & cN_c\left(1+\frac{B}{L}\frac{N_q}{N_c}\right)\left[1+0.4\frac{D}{B}\right]\left(1-\frac{2\beta}{\pi}\right)^2 \\ & + \gamma D N_q\left(1+\frac{B}{L}\tan\phi\right)\left[1+2\tan\phi\left(1-\sin\phi\right)^2\frac{D}{B}\right]\left(1-\frac{2\beta}{\pi}\right)^2 \\ & + \frac{1}{2}\gamma B N_\gamma\left(1-0.4\frac{B}{L}\right)\left(1-\frac{\beta}{\phi}\right)^2 \end{aligned} \tag{3.14}$$

for $D/B \le 1$ and

$$q_u = cN_c\left(1+\frac{B}{L}\frac{N_q}{N_c}\right)\left[1+0.4\tan^{-1}\left(\frac{D}{B}\right)\right]\left(1-\frac{2\beta}{\pi}\right)^2 + \gamma DN_q\left(1+\frac{B}{L}\tan\phi\right)\left[1+2\tan\phi\left(1-\sin\phi\right)^2\tan^{-1}\left(\frac{D}{B}\right)\right]\left(1-\frac{2\beta}{\pi}\right)^2 + \frac{1}{2}\gamma BN_\gamma\left(1-0.4\frac{B}{L}\right)\left(1-\frac{\beta}{\phi}\right)^2 \quad (3.15)$$

for $D/B > 1$. In the test rolling problem, the total force Q rather than average stress q_u is of interest. The former is calculated as a product of the contact area and the average ultimate stress

$$Q = q_u A \quad (3.16)$$

The intent of the theoretical modeling in this report is to arrive at load-sinkage relationships, although the bearing capacity calculations predict a single value of ultimate load for a rigid footing with fixed contact area and depth. The key component linking the ultimate load calculations to the process of wheel indentation and rolling is the evolution of the contact area between the wheel and soil. When a wheel penetrates soil, the soil-wheel contact region grows in area and evolves in shape. With respect to the bearing capacity formula, the growth of the contact area is equivalent to an increasing foundation area. Thus, ultimate load calculated with the bearing capacity equations grows as the wheel penetration, or sinkage, increases. Essentially, it is postulated that an instant during indentation or rolling can be understood as a yielding state requiring average ultimate bearing capacity q_u. The full process of indentation is thus considered as a sequence of yielding states, and steady-state rolling similarly corresponds to a steady yielding state.

In contrast to footings, the contact region between a wheel and soil is not flat. If penetration of the wheel is small in relation to wheel's diameter, considering contact area as a horizontal cross section of the wheel seems fully warranted. This contact area, however, depends on both the shape of the wheel and its deformability, related to wheel construction and inflation pressure for pneumatic tires. Pneumatic tires vary considerably in construction and shape and commonly possess contoured treaded surfaces. In the following, only simplified shapes of the wheel are considered. Although the analytic model applies most readily to rigid wheels, a method for analyzing flexible wheels is also presented.

3.2.1 Rigid Wheel Indentation

The concept of a fully rigid wheel has been employed extensively by researchers interested in soil-wheel interaction (e.g., Bekker 1969; Karafiath and Nowatzki 1978; Muro 1993) and applies to the case where the wheel is very stiff relative to the soil. It is used in the present analysis to simplify calculations and provide a reference when analyzing a flexible wheel. Only the soil deforms when the wheel is rigid, with the shape of the wheel fixed. To investigate the influence of tire shape, two particular geometries are considered: the right cylinder and the torus. Fig. 3.4 illustrates these cases, and the relevant geometric parameters: sinkage s, wheel diameter d, wheel width b, contact length h, and contact angle α.

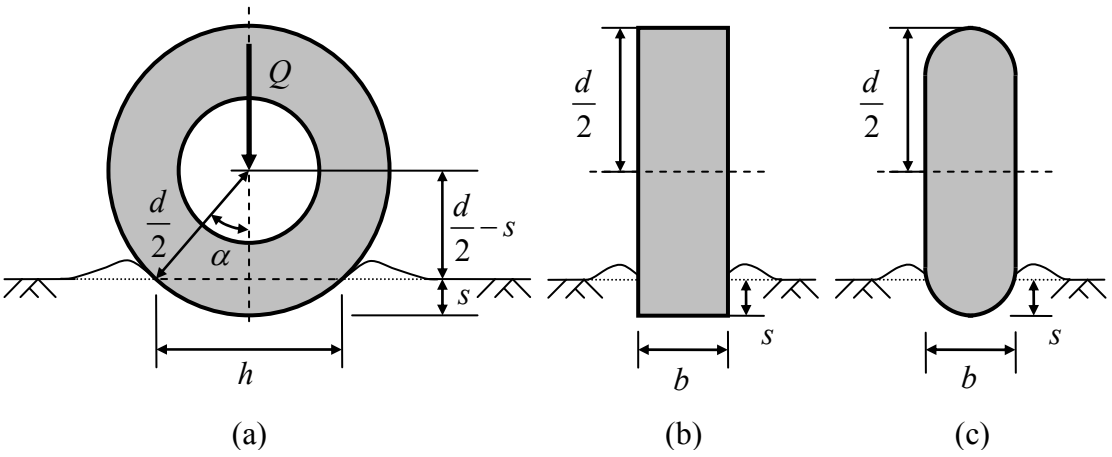

Figure 3.4. Schematic of rigid wheel indentation for right-cylindrical and toroidal wheels: (a) cross section in plane of wheel diameter; (b) cross section of right-cylindrical wheel; (c) cross section of toroidal wheel

3.2.1.1 Indentation of Right-Cylindrical Wheel

The process of indentation of a right-cylindrical wheel as it is reflected in the changing contact area is illustrated in Fig. 3.5. The solid lines trace the wheel as it is viewed from above, so that the sense of wheel displacement is orthogonal to the page. For the case of a right-cylindrical wheel, the length of the contact area along the wheel width (b) remains fixed, while the other side of the rectangular area evolves as governed by the sinkage s and wheel diameter d.

When the wheel indents the soil, it displaces a certain amount of material outside the contact area (Fig. 3.4).This material is neglected in determining the contact area, because the exact configuration of the deformed soil is unknown. Therefore, the contact length h is given by

$$h = 2\sqrt{ds - s^2} \tag{3.17}$$

and contact area A is

$$A = bh = 2b\sqrt{ds - s^2} \tag{3.18}$$

The equivalent footing lengths B and L in Eqs. (3.14) and (3.15) are conditionally defined in terms of h and b as

$$\left.\begin{matrix} B = h \\ L = b \end{matrix}\right\} \text{ for } h < b \quad , \quad \left.\begin{matrix} B = b \\ L = h \end{matrix}\right\} \text{ for } h \geq b \tag{3.19}$$

Although it is not considered in computing h, the resistance added by the upheaved material is

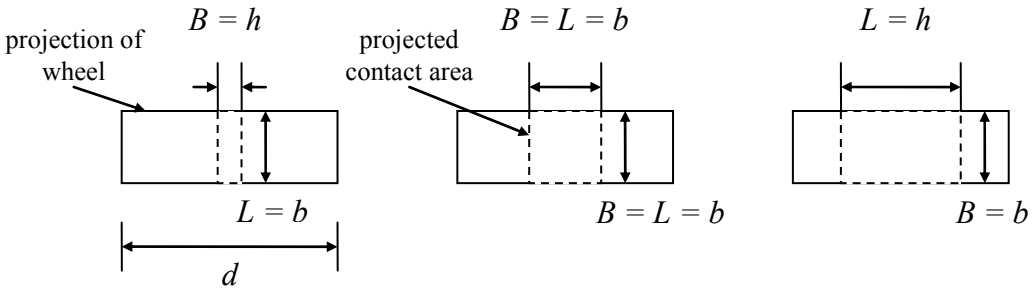

Figure 3.5. Evolution of contact area in wheel indentation process for right-cylindrical wheel

accounted for through the equivalent footing depth D, which is assumed to depend solely on the displaced material. For a fully-saturated (incompressible) clay-type material, the volume of material occupied by the wheel equals the volume displaced upwards. For granular materials, however, the material may dilate or contract, and the displaced volume does not necessarily equal the volume displaced upwards.

Material dilation (contraction) tends to increase (decrease) the amount of material displaced upward and decrease (increase) the density, and in the bearing capacity solution, these effects tend to offset one another. With this, it is reasonable to keep the unit weight fixed and assume that the volume displaced by the wheel equals the volume displaced upwards. Referring to Fig. 3.3 for the bearing capacity plasticity solution considered by Prandtl (1921), the displaced volume can be roughly approximated by the set of rectangular prisms shown in Fig. 3.6.

As a first step, a formula for D is theoretically derived by assuming the soil displacement mechanism shown in Fig. 3.6 and equating the volume of soil displaced by the wheel with the volume displaced upwards. This formula for D is then slightly modified. This modification, discussed in more detail in Section 3.5, is introduced to obtain better agreement with experimental results and the results from numerical simulation.

The lengths h_f and b_f in Fig. 3.6 are related through

$$h_f = \frac{h}{\eta} \quad ; \quad b_f = \frac{b}{\eta} \tag{3.20}$$

The parameter η in Eq. (3.20) is introduced for convenience and is given by

$$\eta = \frac{\sin\left(\frac{\pi}{4} - \frac{\phi}{2}\right)}{\sin\left(\frac{\pi}{4} + \frac{\phi}{2}\right)} e^{-\frac{\pi}{2}\tan\phi} \tag{3.21}$$

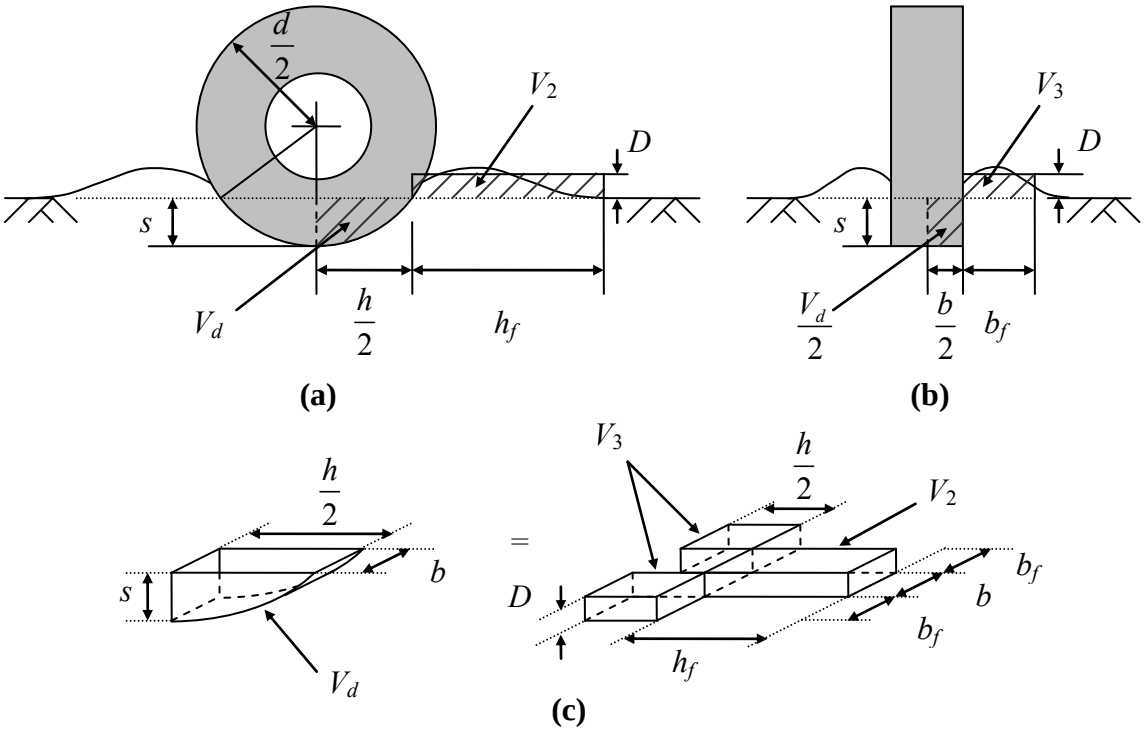

Figure 3.6. Schematic of soil displaced by wheel:
(a) cross section in plane of wheel diameter; (b) cross section in plane of wheel width;
(c) approximated volume of displaced soil

Considering one half of the wheel, the volume of soil displaced by the wheel (see Fig. 3.6) is

$$V_d = \frac{1}{8}bd^2\alpha - \frac{1}{4}bh\left(\frac{d}{2} - s\right) \tag{3.22}$$

and the equivalent volume of soil displaced upwards (see Fig. 3.6) is

$$V_u = V_1 + V_2 = \frac{2bhD}{\eta} \tag{3.23}$$

Setting $V_d = V_u$ gives

$$D = \eta\left[\frac{d^2\alpha}{16h} - \frac{1}{8}\left(\frac{d}{2} - s\right)\right] = \eta\left[\frac{d^2}{32\sqrt{ds - s^2}}\cos^{-1}\left(1 - 2\frac{s}{d}\right) - \frac{1}{8}\left(\frac{d}{2} - s\right)\right] \tag{3.24}$$

A series expansion of Eq. (3.24) about zero gives

$$D = \eta\left[\frac{1}{6}s + \frac{1}{30}\frac{s^2}{d} + O\left(s^3\right)\right] \tag{3.25}$$

Truncating the series after the first term results in the sufficiently accurate expression

$$D = \frac{1}{6}\eta s \tag{3.26}$$

Fig. 3.7 illustrates the reduction in D with increasing ϕ, which is a result of material being displaced thinly over a larger area. The figure also shows how h_f and b_f, which govern the area of the displaced volume, increase with ϕ. It is clear in Fig. 3.7 that the depth D is a very small fraction of the sinkage when ϕ is large.

The Prandtl failure mechanism strictly applies to the case of a weightless soil, and the presence of gravity tends to decrease the overall size of the mechanism. Also, the Prandtl mechanism is based on an associated flow rule. Non-associated flow, which is more realistic for sands, also tends to shrink the size of the mechanism. This implies that the real area over which material is displaced is smaller and D is greater than estimated by Eq. (3.26). For cohesive soils with $\phi = 0$, the depth D only enters through the depth factor F_{cd}, so that the final results do not depend strongly on how D is estimated. For granular materials with $\phi > 0$, the second term of the bearing capacity formula (3.14) or (3.15) is multiplied by D, such that accurate estimation of D is rather important.

For the limiting case $D = s/6$ pertaining to $\phi = 0$, Fig. 3.8 illustrates the variation of D/B with s/d for low, normal, and high wheel aspect ratios and also shows the difference between the exact and linearized expressions for D. Note s/d is as large as 0.5 the figure for illustrative purposes, although s/d larger than 0.1 are considered outside the range of interest. It is clear that $D/B \leq 1$ for small sinkage and typical wheel aspect ratios. Since $D/B \leq 1$, the depth factor is given by Eq. (3.11), and Eq. (3.14) applies.

The bearing capacity formula (3.14) together with the equivalent footing parameters from Eqs. (3.19) through (3.18) and Eq. (3.26) give an explicit expression for the wheel force Q. From symmetry of the indentation problem, the inclination angle β vanishes, so that the horizontal component of the wheel force Q_H is zero and the vertical component Q_V is equal to the total force Q. For clarity in later sections, the symbol Q_V is now used, and the wheel force is expressed as

$$\begin{aligned} Q_V = 2b\sqrt{ds - s^2}\Bigg\{ & cN_c\left(1 + 2\frac{\sqrt{ds - s^2}}{b}\frac{N_q}{N_c}\right)\left(1 + 0.03\frac{\eta s}{\sqrt{ds - s^2}}\right) \\ & + 0.17\gamma\eta s N_q\left(1 + 2\frac{\sqrt{ds - s^2}}{b}\tan\phi\right)\left[1 + 0.17\tan\phi\left(1 - \sin\phi\right)^2\frac{\eta s}{\sqrt{ds - s^2}}\right] \\ & + \gamma\sqrt{ds - s^2}N_\gamma\left(1 - 0.8\frac{\sqrt{ds - s^2}}{b}\right)\Bigg\} \end{aligned} \tag{3.27}$$

for $2\sqrt{ds - s^2} < b$ and

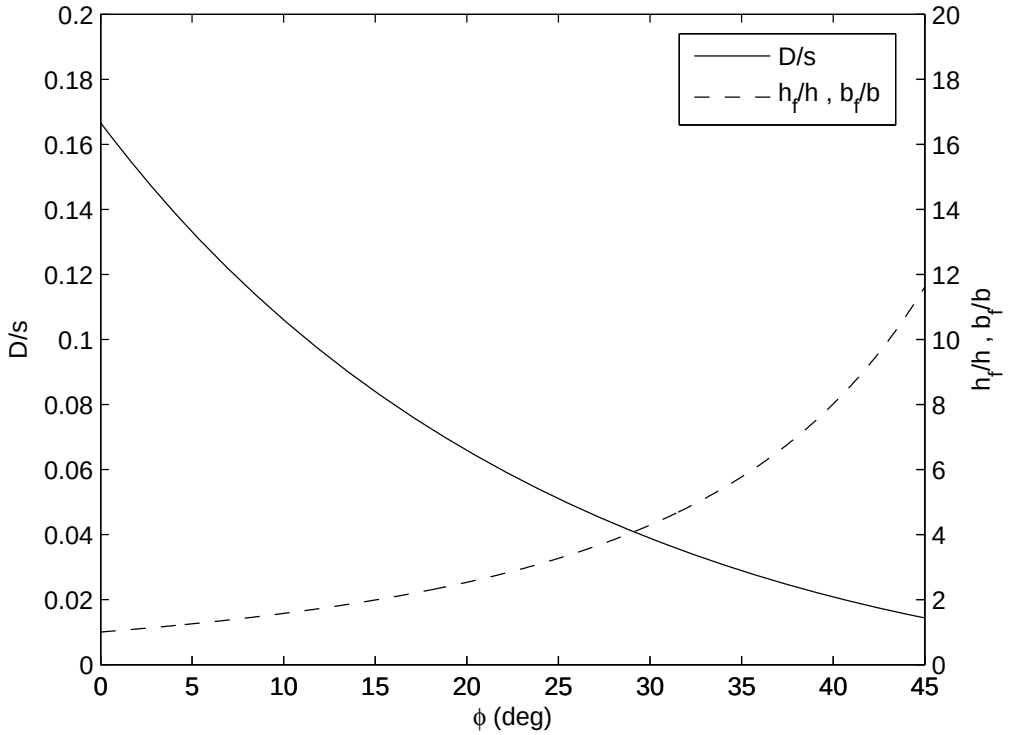

Figure 3.7. Effect of friction angle on theoretical equivalent footing depth

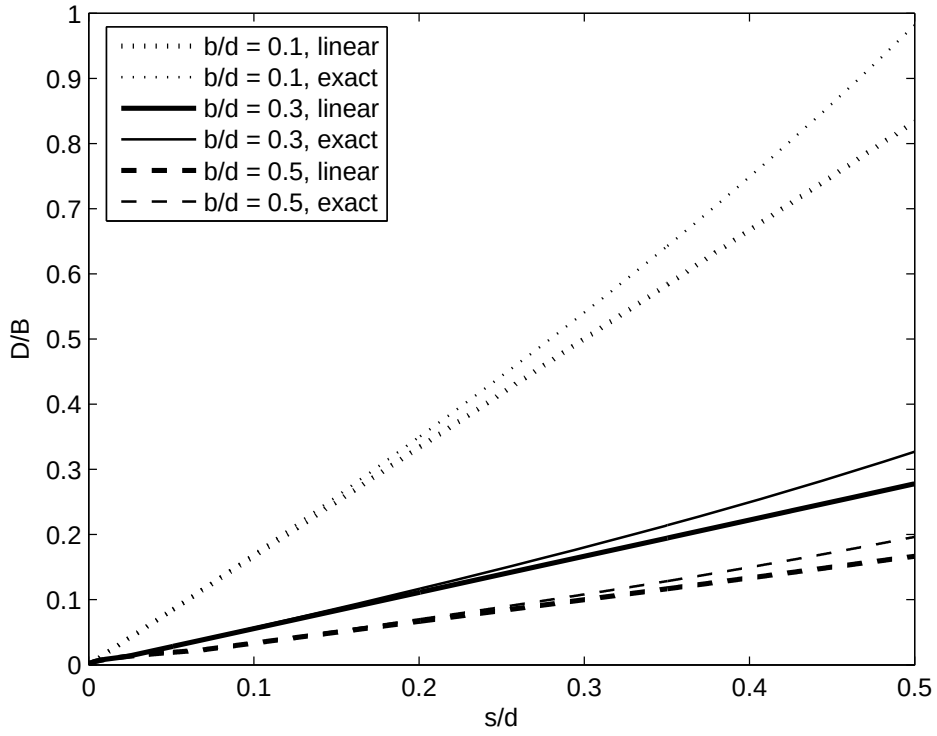

Figure 3.8. Plot of exact and linearized forms of theoretical *D*/*B* for several wheel aspect ratios (limiting case $\phi = 0$)

$$Q_V = 2b\sqrt{ds - s^2}\left\{cN_c\left(1 + 0.5\frac{b}{\sqrt{ds - s^2}}\frac{N_q}{N_c}\right)\left(1 + 0.07\frac{\eta s}{b}\right)\right.$$
$$+ 0.17\gamma\eta sN_q\left(1 + 0.5\frac{b}{\sqrt{ds - s^2}}\tan\phi\right)\left[1 + 0.33\tan\phi\left(1 - \sin\phi\right)^2\frac{\eta s}{b}\right] \qquad (3.28)$$
$$\left. + \gamma bN_\gamma\left(0.5 - 0.1\frac{b}{\sqrt{ds - s^2}}\right)\right\}$$

for $2\sqrt{ds - s^2} \geq b$. These equations may be rewritten in dimensionless form as

$$\frac{Q_V}{\gamma d^3} = 2\frac{b}{d}\sqrt{\frac{s}{d} - \frac{s^2}{d^2}}\left\{\frac{c}{\gamma d}N_c\left(1 + 2\frac{d}{b}\frac{N_q}{N_c}\sqrt{\frac{s}{d} - \frac{s^2}{d^2}}\right)\left(1 + 0.03\eta\sqrt{\frac{\frac{s}{d}}{1 - \frac{s}{d}}}\right)\right.$$
$$+ 0.17\eta N_q\frac{s}{d}\left(1 + 2\frac{d}{b}\sqrt{\frac{s}{d} - \frac{s^2}{d^2}}\tan\phi\right)\left[1 + 0.17\tan\phi\left(1 - \sin\phi\right)^2\eta\sqrt{\frac{\frac{s}{d}}{1 - \frac{s}{d}}}\right] \qquad (3.29)$$
$$\left. + N_\gamma\sqrt{\frac{s}{d} - \frac{s^2}{d^2}}\left(1 - 0.8\frac{d}{b}\sqrt{\frac{s}{d} - \frac{s^2}{d^2}}\right)\right\}$$

for $2\frac{d}{b}\sqrt{\frac{s}{d} - \frac{s^2}{d^2}} < 1$ and

$$\frac{Q_V}{\gamma d^3} = 2\frac{b}{d}\sqrt{\frac{s}{d} - \frac{s^2}{d^2}}\left\{\frac{c}{\gamma d}N_c\left(1 + 0.5\frac{\frac{b}{d}}{\sqrt{\frac{s}{d} - \frac{s^2}{d^2}}}\frac{N_q}{N_c}\right)\left(1 + 0.07\eta\frac{s}{d}\frac{d}{b}\right)\right.$$
$$+ 0.17\eta\frac{s}{d}N_q\left(1 + 0.5\frac{\frac{b}{d}}{\sqrt{\frac{s}{d} - \frac{s^2}{d^2}}}\tan\phi\right)\left[1 + 0.33\tan\phi\left(1 - \sin\phi\right)^2\eta\frac{s}{d}\frac{d}{b}\right] \qquad (3.30)$$
$$\left. + \frac{b}{d}N_\gamma\left(0.5 - 0.1\frac{\frac{b}{d}}{\sqrt{\frac{s}{d} - \frac{s^2}{d^2}}}\right)\right\}$$

for $2\frac{d}{b}\sqrt{\frac{s}{d}-\frac{s^2}{d^2}} \geq 1$.

Plots of Eqs. (3.29) and (3.30) are shown in Figs. 3.9 and 3.10 for the cases $\phi = 0$ and $c = 0$, respectively. Notice that the "kink" in the force-sinkage curves coincides with the point $h = b$ and is a result of the conditional dependence of the equivalent footing lengths B and L. The aspect ratio B/L increases from zero to one as s/d goes from zero to that required for $h = b$, at which point B/L decreases as the inverse without continuity of the first derivative. Also, B multiplies the N_γ term in the bearing capacity formula, which is initially increasing as h until it becomes fixed at b.

The force-sinkage curves for cohesive material plotted in (Fig. 3.9) are clearly nonlinear and appear concave downward in the force-sinkage plot. This characteristic trend is found throughout this report. The same trend is visible for frictional material (Fig. 3.10), although the nonlinearity is not as severe as with $\phi = 0$. This tendency is tied strongly to the relationship between contact area and sinkage (Eq. (3.18)).

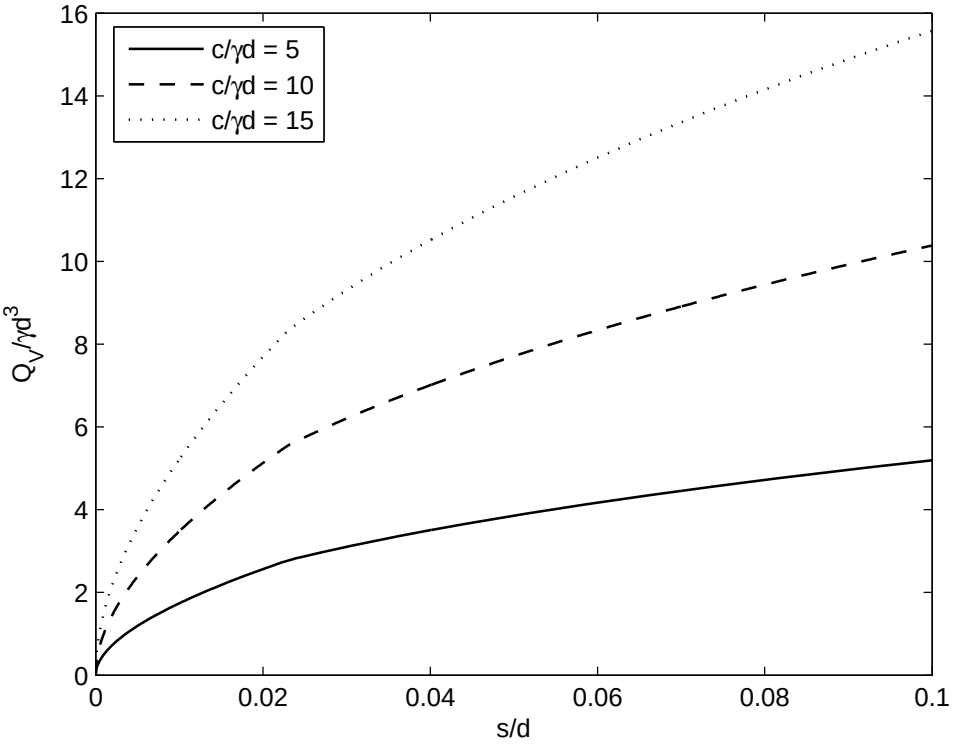

Figure 3.9. Vertical force versus sinkage for rigid wheel indentation with $\phi = 0$ ($b/d = 0.3$)

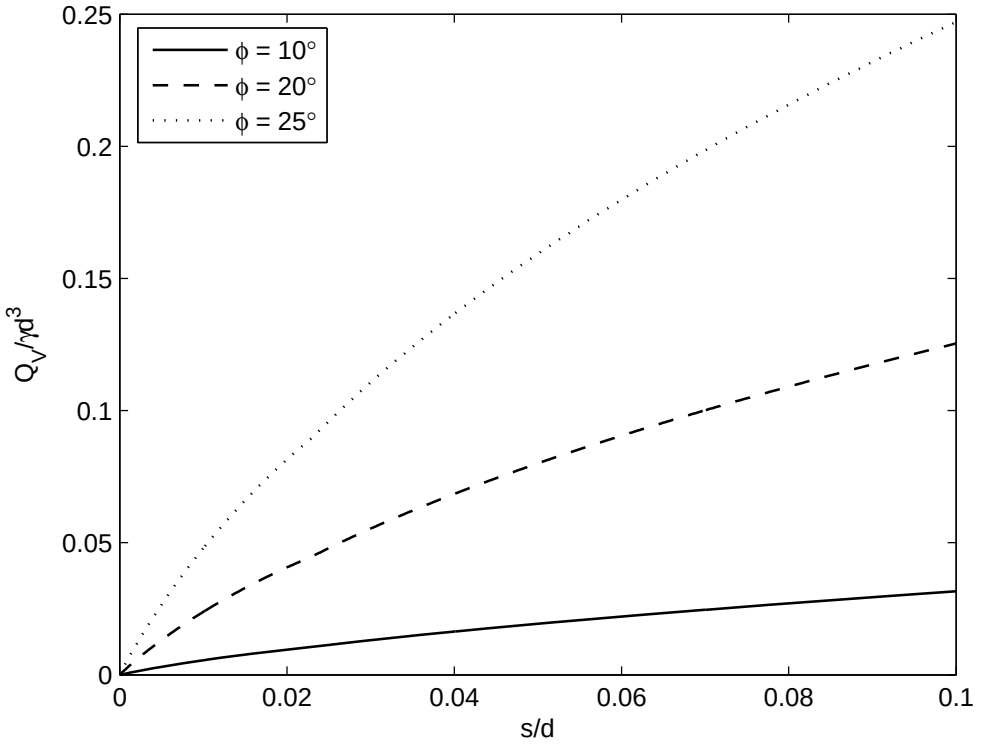

Figure 3.10. Vertical force versus sinkage for rigid wheel indentation with $c = 0$ ($b/d = 0.3$)

3.2.1.2 Indentation of Toroidal Wheel

Indentation of a toroidal wheel is analogous to indentation of a right-cylindrical wheel, with the important distinction that the true contact area is no longer rectangular and the width of the contact area is also a function of sinkage (Fig. 3.11).

Since the bearing capacity formula applies to a rectangular contact area, the non-rectangular areas shown in Fig. 3.11 are approximated by circumscribed rectangles. A more refined prescription of the contact area is conceptually no more difficult to implement, but the circumscribed rectangular suffices for the present investigation of the effect of a rounded wheel. The definition of h for a right-cylindrical wheel given by Eq. (3.17) still applies, and the contact area A is now

$$A = b_c h = 2b_c\sqrt{sd - s^2} \tag{3.31}$$

where b_c is the changing contact width given as

$$b_c = \begin{cases} 2\sqrt{bs - s^2} & \text{for } s < b/2 \\ b & \text{for } s \geq b/2 \end{cases} \tag{3.32}$$

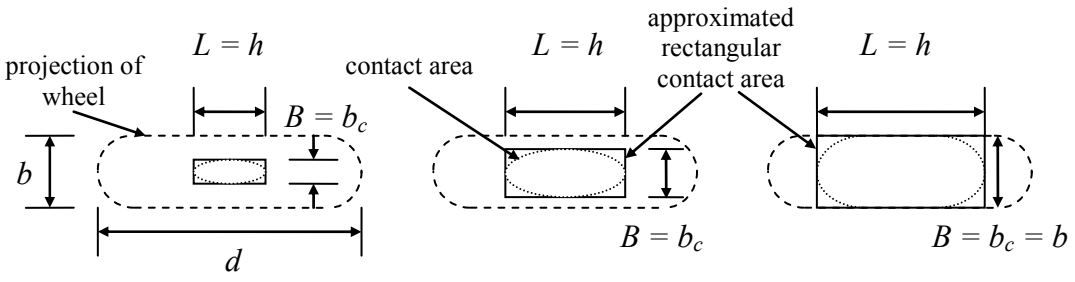

Figure 3.11. Evolution of contact area in wheel indentation process for toroidal wheel

Toroidal wheels must have $b < d$, and this results in the condition that $h > b_c$ for all s. We therefore have the unconditional definitions $L = h$ and $B = b_c$, unlike the case for the right-cylindrical wheel.

For indentation of a right-cylindrical wheel, the volume of displaced soil was evaluated for the purpose of determining an approximation for the equivalent footing depth D. An expression for the exact volume of soil displaced by a toroidal wheel would be complicated and unwieldy, and the expression for D proposed for indentation of a right-cylindrical wheel is itself approximate. For these reasons, we use the same definition of D as was determined for the right-cylindrical wheel, acknowledging that since the volume of soil displaced by the toroidal wheel is smaller, D is perhaps somewhat overestimated.

As with the right-cylindrical wheel, the condition $D/B \le 1$ is satisfied for practical values of s and typical wheel geometries, so that Eq. (3.14) applies. Again, $\beta = 0$ and $Q = Q_V$ by virtue of symmetry. Substituting the above into Eqs. (3.14) and (3.16), the following force-sinkage relationships are obtained:

$$\begin{aligned} Q_V = {} & 4\sqrt{bs-s^2}\sqrt{ds-s^2}\left\{cN_c\left(1+\frac{\sqrt{bs-s^2}}{\sqrt{ds-s^2}}\frac{N_q}{N_c}\right)\left[1+0.03\frac{\eta s}{\sqrt{bs-s^2}}\right]\right. \\ & +0.17\gamma\eta sN_q\left(1+\frac{\sqrt{bs-s^2}}{\sqrt{ds-s^2}}\tan\phi\right)\left[1+0.17\tan\phi\left(1-\sin\phi\right)^2\frac{\eta s}{\sqrt{bs-s^2}}\right] \\ & \left.+\gamma\sqrt{bs-s^2}N_\gamma\left(1-0.4\frac{\sqrt{bs-s^2}}{\sqrt{ds-s^2}}\right)\right\} \end{aligned} \tag{3.33}$$

for $s < b/2$ and

$$Q_V = 4\sqrt{bs-s^2}\sqrt{ds-s^2}\left\{cN_c\left(1+0.5\frac{b}{\sqrt{ds-s^2}}\frac{N_q}{N_c}\right)\left[1+0.07\frac{\eta s}{b}\right]\right.$$
$$+0.17\gamma\eta sN_q\left(1+0.5\frac{b}{\sqrt{ds-s^2}}\tan\phi\right)\left[1+0.33\tan\phi\left(1-\sin\phi\right)^2\frac{\eta s}{b}\right] \quad (3.34)$$
$$\left.+\gamma bN_\gamma\left(0.5-0.2\frac{b}{2\sqrt{ds-s^2}}\right)\right\}$$

for $s \geq b/2$.

Note that Eqs. (3.33) and (3.34) have dimensionless forms like Eqs. (3.29) and (3.30), but along with the dimensionless counterparts of remaining equations in Chapter 3, these forms are not presented to avoid repetition. The resulting dimensionless parameters are still used for plotting and discussion.

Fig. 3.12 shows several force-sinkage relationships for indentation with toroidal wheels as compared with right-cylindrical wheels. Initially, the forces for a given indentation are significantly different, with the force for the toroidal wheel being much less as a result of the smaller contact area. In other words, less force is required to indent a toroidal wheel. With an increase in sinkage, the forces predicted for a right-cylindrical and toroidal wheel with the same width and diameter become close and are identical for $s > b/2$. Notice also the shape of the curve for a toroidal wheel penetrating a purely frictional material, where the depth D has a great influence initially and causes inflection.

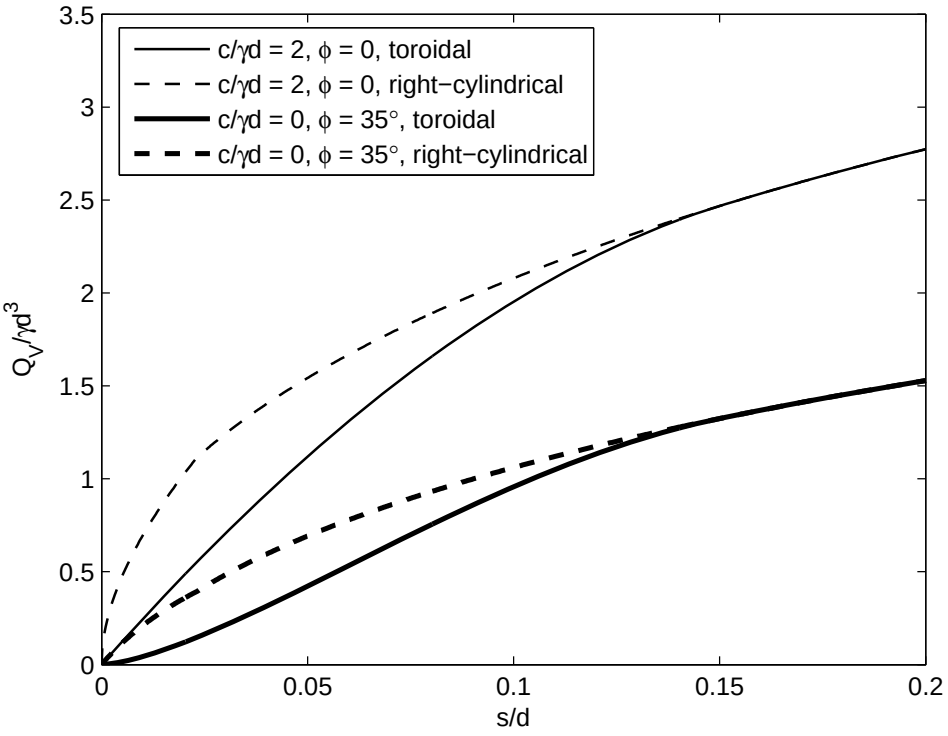

Figure 3.12. Comparison of force-sinkage curves for right-cylindrical wheel and toroidal wheel ($b/d = 0.3$)

This result gives insight into the effect of irregular tire geometries. For example, one may wish to use the right-cylindrical geometry to approximate a wheel with rounded edges, but an overprediction of the load should be expected, especially at low sinkage. The magnitude of this overprediction depends on the extent and shape of the rounding.

3.2.2 Rigid Wheel Rolling

In the analysis of rolling, only an advanced, steady state of rolling of a towed wheel is considered. In the indentation process, one can imagine tracing a continuous force-sinkage curve as the wheel penetrates the soil. The analogy for steady-state rolling would be to slowly increase the force or sinkage as the wheel is rolling forward. Although such a process is conceivable, the relationship between force and sinkage for a steady state is assessed in the following sections, without regard for the transient process required to reach that state. Note also that only right-cylindrical wheels are considered here, but like indentation, extension to other geometries is conceptually straightforward.

The assumed soil-wheel configuration for steady-state rolling is shown in Fig. 3.13. Although the idealized contact geometry for this analysis may seem oversimplified, it has been used fairly successfully in terramechanics for rolling analysis (cf. Willis et al. 1965; McRae 1964) in the context of semi-empirical methods. Specifically, the assumption that the contact region extends from the lowermost part of the wheel to the part intersected by the undisturbed soil surface appears to be satisfactory.

An important difference between wheel rolling and wheel indentation is that the total force Q is no longer vertical but inclined at an angle β. In the approximate analysis employing the bearing capacity concept, the inclination of the average ultimate stress is unknown. In reality, the angle β is determined by the distribution of the normal stress σ_n and shear stress σ_t acting on the wheel as a result of contact (Fig. 3.13).

Using a polar coordinate system with the origin at the center of the wheel and θ defined as shown in Fig. 3.13, the following apply

$$Q_V = -\frac{bd}{2}\int_0^{\alpha}\left(\sigma_t \sin\theta + \sigma_n \cos\theta\right)d\theta \quad ; \quad Q_H = \frac{bd}{2}\int_0^{\alpha}\left(\sigma_t \cos\theta - \sigma_n \sin\theta\right)d\theta \tag{3.35}$$

$$\beta = \tan^{-1}\left(\frac{Q_H}{Q_V}\right) \tag{3.36}$$

$$Q_V = Q\cos\beta \quad ; \quad Q_H = Q\sin\beta \tag{3.37}$$

where Q_V and Q_H are the horizontal components of the wheel force. Note that it is assumed in Eqs. (3.35) that the stresses are constant across the wheel width. Normal stress measurements by Krick (1969) for a towed, rigid wheel operating in a sandy agricultural soil indicate that this assumption is reasonable, although the normal stresses are expectedly higher near the wheel edge. For a towed wheel with no torque, the shear stresses must satisfy

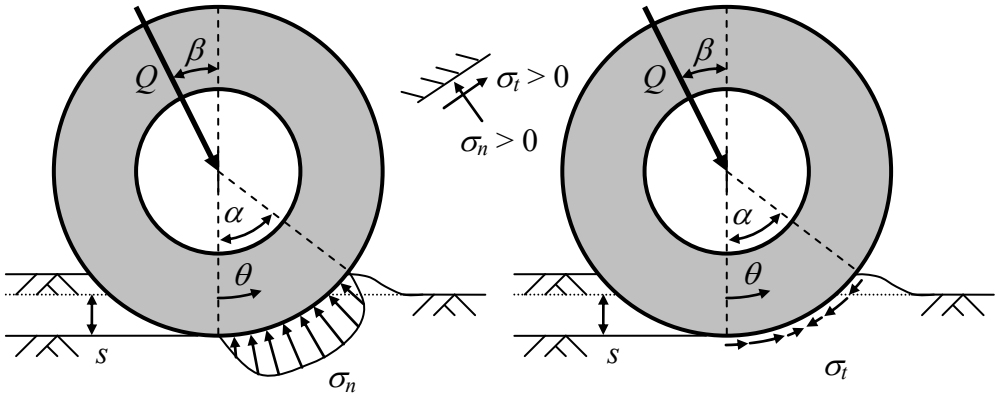

Figure 3.13. Schematic of contact stresses acting on rolling rigid wheel: (a) normal stresses; (b) shear stresses

$$\frac{d^2}{4}\int_0^{\alpha}\sigma_t d\theta = 0 \text{ or } \int_0^{\alpha}\sigma_t d\theta = 0 \tag{3.38}$$

requiring that the shear stresses be either zero everywhere or pointwise positive and negative as illustrated in Fig. 3.13b.

Onafeko and Reece (1967) and Krick (1969) measured the normal and shear contact stresses on towed rigid wheels operating in sandy agricultural soils. Their results show that indeed the shear stresses reverse at some point on the face of the wheel when the wheel is towed, as required by Eq. (3.38). Furthermore, it is a reasonable approximation based on their measurements to say that the shear stresses are antisymmetrically distributed about the ray $\theta = \alpha/2$ and that the normal stresses are symmetrically distributed about the same ray (as depicted in Fig. 3.13). From Eqs. (3.35)-(3.36), it follows that

$$\beta = \frac{\alpha}{2} \tag{3.39}$$

The angle α is related to s through

$$\alpha = \cos^{-1}\left(1 - 2\frac{s}{d}\right) \tag{3.40}$$

A series expansion of Eq. (3.40) about zero gives

$$\alpha = 2\sqrt{\frac{s}{d}} + O\left(s^{3/2}\right) \tag{3.41}$$

Using Eq. (3.39) and keeping only the first term of (3.41) results in the simple expression

$$\beta = \sqrt{\frac{s}{d}} \tag{3.42}$$

Notice that even if the shear stresses are not antisymmetric about $\theta = \alpha/2$, the same result (3.42) applies if the shear stresses are negligible and only the normal stresses are symmetric. Using the data given by Onafeko and Reece (1967), the actual values of β determined from direct measurements of Q_V and Q_H agree with the values predicted by Eq. (3.42) to within -9 to 4 %.

Two different methods for implementing bearing capacity theory are presented. In the first, the wheel is essentially replaced by a footing that is horizontal with the load inclined at the angle β relative to the footing. In the second method, the load is considered perpendicular to the footing, but the footing itself is inclined at the angle β. These approaches are therefore referred to as the "inclined load" and "inclined footing" methods, respectively.

3.2.2.1 Inclined Load Method

In the inclined load method, the wheel is considered equivalent to a horizontal rectangular footing that is loaded at the angle β. The procedure for applying the bearing capacity formula is analogous to indentation, except $\beta \neq 0$ and the contact area assumed to be half of that for indentation. Because $\beta \neq 0$, the inclination factors given by Eqs. (3.13) apply with $F_{ci} = F_{qi} \neq 1$ and $F_{\gamma i} \neq 1$. The contact length h is taken as shown in Fig. 3.14, related to the sinkage s through

$$h = \sqrt{sd - s^2} \tag{3.43}$$

and projected contact area A is now

$$A = bh = b\sqrt{sd - s^2} \tag{3.44}$$

The equivalent footing lengths B and L are again related to h and b by

$$\left.\begin{matrix} B = h \\ L = b \end{matrix}\right\} \text{ for } h < b \quad , \quad \left.\begin{matrix} B = b \\ L = h \end{matrix}\right\} \text{ for } h \geq b \tag{3.45}$$

Although the distribution of displaced soil is perhaps different from that assumed for indentation due to the rolling process, the same approximate expression for D is used:

$$D = \frac{1}{6}\eta s \tag{3.46}$$

As with indentation, Eq. (3.14) with $D/B \leq 1$ applies for practical problems, and attention is restricted to Eq. (3.14).

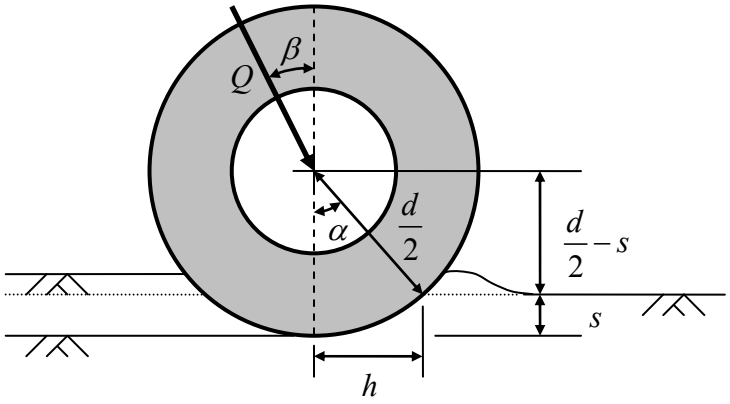

Figure 3.14. Schematic of steady-state rolling with rigid wheel and h defined using inclined load method

Using the expression for β given by Eq. (3.42) and substituting the preceding results into Eqs. (3.14) and (3.16) gives the following force-sinkage relationships for a rolling wheel:

$$Q = b\sqrt{sd - s^2}\left\{cN_c\left(1 + \frac{\sqrt{sd - s^2}}{b}\frac{N_q}{N_c}\right)\left[1 + 0.07\frac{\eta s}{\sqrt{sd - s^2}}\right]\left(1 - 0.64\sqrt{\frac{s}{d}}\right)^2\right.$$
$$+ 0.17\gamma\eta s N_q\left(1 + \frac{\sqrt{sd - s^2}}{b}\tan\phi\right)\left[1 + 0.33\tan\phi\left(1 - \sin\phi\right)^2\frac{\eta s}{\sqrt{sd - s^2}}\right] \tag{3.47}$$
$$\left.\times\left(1 - 0.64\sqrt{\frac{s}{d}}\right)^2 + \gamma\sqrt{sd - s^2}N_\gamma\left(0.5 - 0.2\frac{\sqrt{sd - s^2}}{b}\right)\left(1 - \frac{1}{\phi}\sqrt{\frac{s}{d}}\right)^2\right\}$$

for $2\sqrt{ds - s^2} < b$ and

$$Q = b\sqrt{sd - s^2}\left\{cN_c\left(1 + \frac{b}{\sqrt{sd - s^2}}\frac{N_q}{N_c}\right)\left[1 + 0.07\frac{\eta s}{b}\right]\left(1 - 0.64\sqrt{\frac{s}{d}}\right)^2\right.$$
$$+ 0.17\gamma\eta s N_q\left(1 + \frac{b}{\sqrt{sd - s^2}}\tan\phi\right)\left[1 + 0.33\tan\phi\left(1 - \sin\phi\right)^2\frac{\eta s}{b}\right] \tag{3.48}$$
$$\left.\times\left(1 - 0.64\sqrt{\frac{s}{d}}\right)^2 + \gamma b N_\gamma\left(0.5 - 0.2\frac{b}{\sqrt{sd - s^2}}\right)\left(1 - \frac{1}{\phi}\sqrt{\frac{s}{d}}\right)^2\right\}$$

for $2\sqrt{ds - s^2} \geq b$. The total force Q given by Eqs. (3.47) and (3.48) can be decomposed into its vertical and horizontal components Q_V and Q_H using

$$Q_V = Q\cos\left(\sqrt{\frac{s}{d}}\right) \quad ; \quad Q_H = Q\sin\left(\sqrt{\frac{s}{d}}\right) \tag{3.49}$$

The vertical component Q_V is identical to the weight acting on the wheel. The horizontal component Q_H is associated with resistance to the forward motion of the test roller caused by test roller sinkage.

Fig. 3.15 compares the force-sinkage curves for steady-state rolling and indentation. At a given sinkage, Q_V for rolling is significantly less than Q_V for indentation as a result of the reduced contact area and inclined loading. Without the effect of inclined loading, Q_V in the rolling case is simply half of Q_V in indentation for the same s. The effect of the inclination factor in the rolling case is evident as it decreases the force with increasing sinkage, even causing the force to start decreasing at some s/d. Also plotted is Q_H for the rolling case, which steadily increases as the sinkage increases.

Although the analytic method is expected to be valid only for small s/d, the unrealistic decline in Q_V predicted by Eqs. (3.47) and (3.48) indicates that the reduction in wheel force caused by the inclination factors (3.13) may be too severe. It is known that the inclination factors (3.13) tends to underpredict ultimate bearing capacity, and Meyerhof and Koumoto (1987) gave revised inclination factors which reduce the ultimate bearing capacity less than the factors (3.13). Rather than use alternative inclination factors from the literature, modified inclination factors are derived in the next section, in which the wheel is viewed as analogous to a footing on sloping ground.

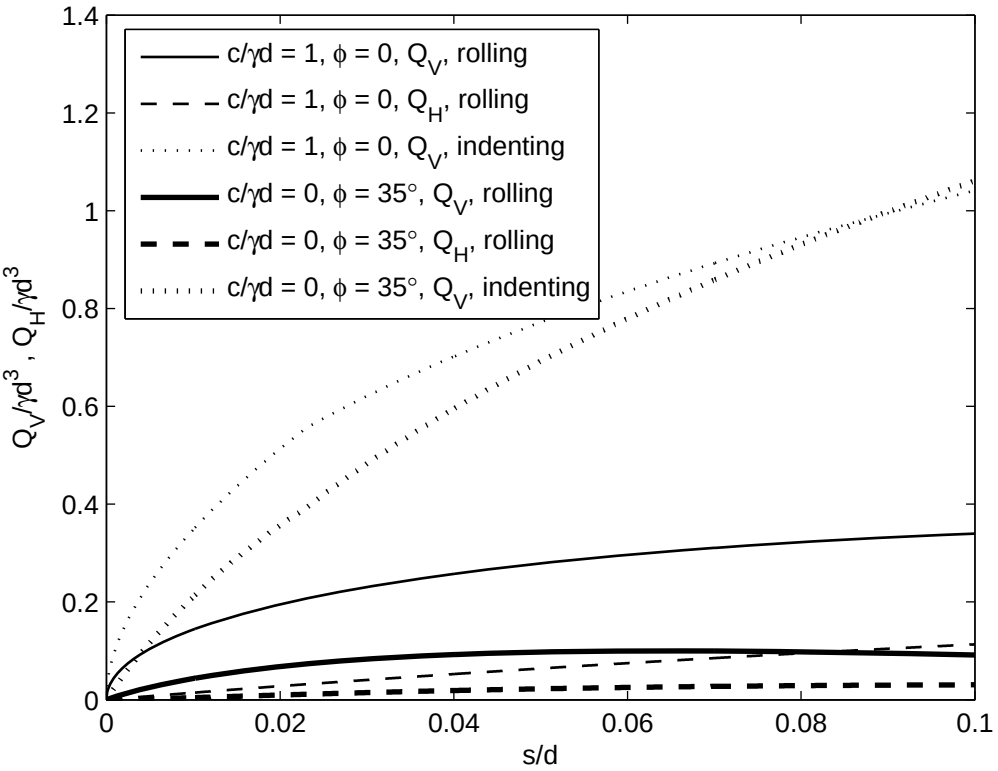

Figure 3.15. Comparison of force-sinkage curves for steady-state rolling and indentation ($b/d = 0.3$)

3.2.2.2 Inclined Footing Method

In the inclined footing approach, it is supposed for a rolling wheel (Fig. 3.16a) that the true soil failure mechanism has similarity to the case in which the footing itself is inclined at an angle β and the total force remains perpendicular to the footing. With this, the configuration is like the ultimate bearing capacity problem for a shallow footing on sloping ground (Fig. 3.16b). Although this problem is not as well understood as the case of horizontal ground, solutions with sloping ground which may be used in the framework of the bearing capacity formula (3.7) are available in the literature.

Because gravity acts vertically in Fig. 3.16a, gravitational forces are inclined in the equivalent bearing capacity problem of Fig. 3.16b. Of course, previous work regarding shallow foundations on slopes has been for gravity acting vertically, and the equivalent bearing capacity problem is therefore not strictly identical to that considered in conventional theory. In the following, this discrepancy is neglected on the basis that β is small for small s.

The bearing capacity formula (3.7) for level ground can be adapted to work for a sloped ground surface by modifying the bearing capacity factors N_c, N_q, and N_γ. Chen (1975) shows that for a strip footing on a slope, the factor N_c should be modified using

$$\overline{N_c} = \cot\phi\left[e^{(\pi-2\beta)\tan\phi}\tan^2\left(\frac{\pi}{4}+\frac{\phi}{2}\right)-1\right] = \cot\phi\left[e^{-2\beta\tan\phi}N_q-1\right] \tag{3.50}$$

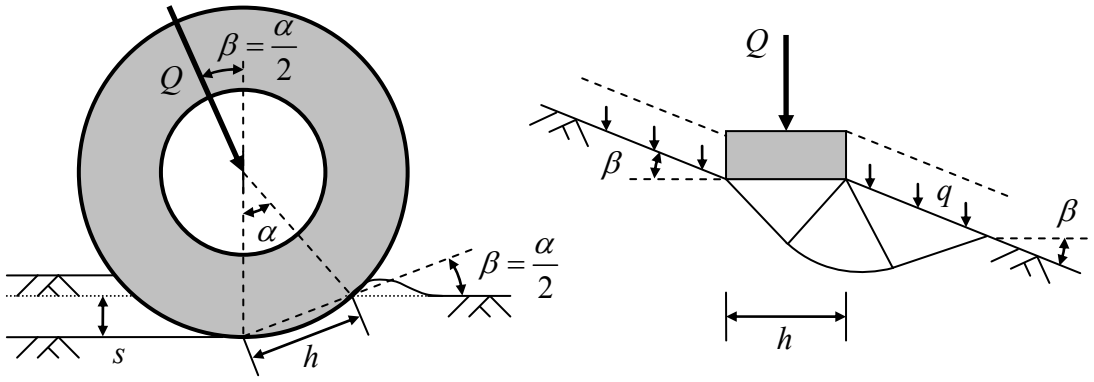

(a) (b)

Figure 3.16. Steady-state rolling as footing on a slope: (a) soil-wheel configuration; (b) strip footing on sloping ground

The modified factor is designated by $\overline{(\ )}$ and $\beta \geq 0$ is the angle of elevation of the slope, equal to the angle of inclination of the load in this case (see Fig. 3.16). Notice that Eq. (3.50) reduces to

$$\overline{N_c} = 2 + \pi - 2\beta \approx 5.14 - 2\beta \tag{3.51}$$

for the case $\phi = 0$. Hansen (1970) proposed that the factors N_q and N_γ should be modified as follows

$$\overline{N_q} = N_q \left(1 - \tan\beta\right)^2 \quad , \quad \overline{N_\gamma} = N_\gamma \left(1 - \tan\beta\right)^2 \tag{3.52}$$

Using the inclined footing method, it is appropriate to choose the contact length h as the length of the chord subtending α (Fig. 3.14a), such that h is related to s and d through

$$h = \sqrt{ds} \tag{3.53}$$

Altogether, the inclined footing method is the same as the inclined load method with the exceptions that h is slightly greater and the inclination factors (3.13) are replaced by the modified inclination factors

$$\overline{F_{ci}} = \frac{\overline{N_c}}{N_c} = \frac{N_q e^{-2\beta \tan\phi} - 1}{N_q - 1} \tag{3.54}$$

$$\overline{F_{qi}} = \frac{\overline{N_q}}{N_q} = \overline{F_{\gamma i}} = \frac{\overline{N_\gamma}}{N_\gamma} = \left(1 - \tan\beta\right)^2 \tag{3.55}$$

The modified inclination factors (3.54) and (3.55) are plotted in Figs. 3.17 and 3.18 along with the inclination factors (3.13) for $\phi = 30$ deg and $\phi = 15$ deg, respectively. The factor $\overline{F_{ci}}$ is larger than F_{ci} for small ϕ, becoming roughly the same at $\phi \approx 33$ deg. The factor $\overline{F_{qi}}$ is consistently smaller than F_{qi}. The factor $\overline{F_{\gamma i}}$ is larger than $F_{\gamma i}$, especially for small ϕ.

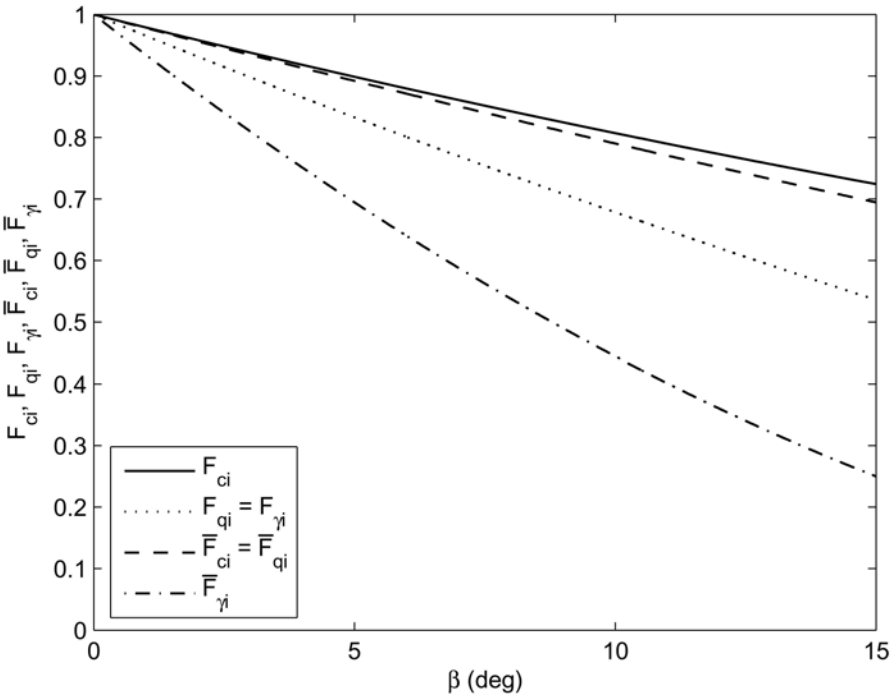

Figure 3.17. Comparison between modified inclination factors for inclined slope and inclination factors for horizontal ground with $\phi = 30^{\circ}$

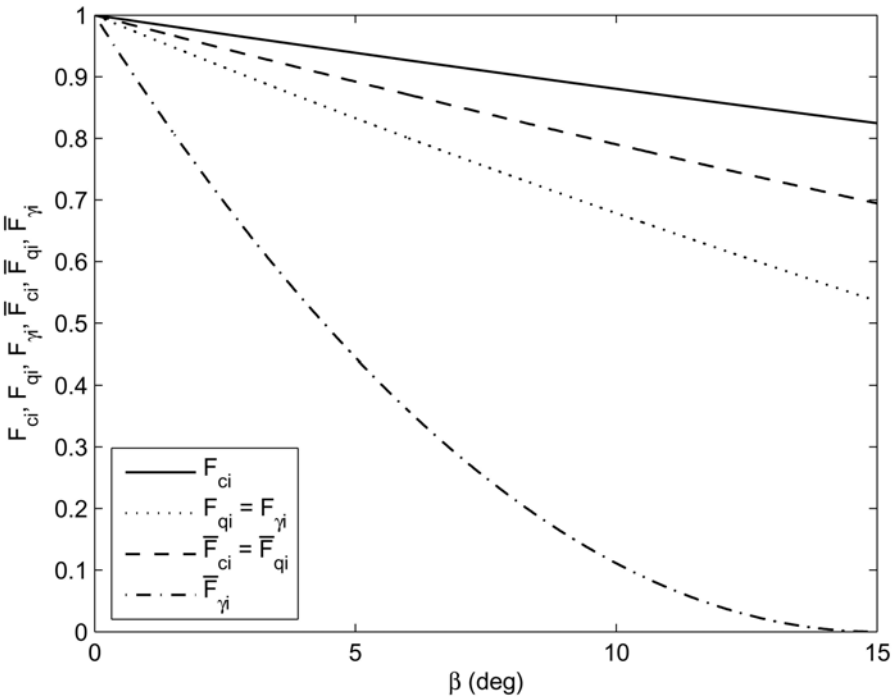

Figure 3.18. Comparison between modified inclination factors for inclined slope and inclination factors for horizontal ground with $\phi = 15^{\circ}$

Little work has been done to determine shape and depth factors for the case of a footing on a slope. In this approximate method, the same shape and depth factors that pertain to horizontal footing are used (Eqs. (3.10)-(3.11)). Since β is small in this analysis, this error is expected to be small. Replacing the inclination factors in (3.47) and (3.48) with the modified inclination factors (3.54) and (3.55) and the modified expression for h (Eq. (3.53)) gives the following force-sinkage relationships:

$$Q = b\sqrt{ds}\left\{cN_c\left(1+\frac{\sqrt{ds}}{b}\frac{N_q}{N_c}\right)\left(1+0.07\frac{\eta s}{\sqrt{ds}}\right)\left(\frac{N_q e^{-2\sqrt{\frac{s}{d}}\tan\phi}-1}{N_q-1}\right)\right.$$
$$+\left[0.17\gamma\eta s N_q\left(1+\frac{\sqrt{ds}}{b}\tan\phi\right)\left(1+0.33\tan\phi\left(1-\sin\phi\right)^2\frac{\eta s}{\sqrt{ds}}\right)\right. \tag{3.56}$$
$$\left.\left.+\gamma\sqrt{ds}N_\gamma\left(0.5-0.2\frac{\sqrt{ds}}{b}\right)\right]\left[1-\tan\left(\sqrt{\frac{s}{d}}\right)\right]^2\right\}$$

for $2\sqrt{ds} < b$ and

$$Q = b\sqrt{ds}\left\{cN_c\left(1+\frac{b}{\sqrt{ds}}\frac{N_q}{N_c}\right)\left(1+0.07\frac{\eta s}{b}\right)\left(\frac{N_q e^{-2\sqrt{\frac{s}{d}}\tan\phi}-1}{N_q-1}\right)\right.$$
$$+\left[0.17\gamma\eta s N_q\left(1+\frac{b}{\sqrt{ds}}\tan\phi\right)\left(1+0.33\tan\phi\left(1-\sin\phi\right)^2\frac{\eta s}{b}\right)\right. \tag{3.57}$$
$$\left.\left.+\gamma b N_\gamma\left(0.5-0.2\frac{b}{\sqrt{ds}}\right)\right]\left[1-\tan\left(\sqrt{\frac{s}{d}}\right)\right]^2\right\}$$

for $2\sqrt{ds} \geq b$.

The vertical and horizontal components of force may be computed using Eqs. (3.49). Fig. 3.19 plots Eqs. (3.56) and (3.57) as compared with Eqs. (3.47) and (3.48), taking the vertical component of force Q_V. The force predicted is significantly greater considering the footing, rather than the force, to be inclined. In addition, the force in the inclined footing method is increasing over a broader range of s/d than with the inclined load approach.

When $\phi = 0$, $N_\gamma = 0$ strictly applies to the case $\beta = 0$. When the footing is on a slope, the failure mechanism does not possess the proper symmetry for $N_\gamma = 0$. It can be shown, however, that the unit weight for the case $\phi = 0$ has a minimal effect on the force, and for this reason, the unit weight for a purely cohesive soil can be neglected and the third term in the bearing capacity formula can therefore be disregarded.

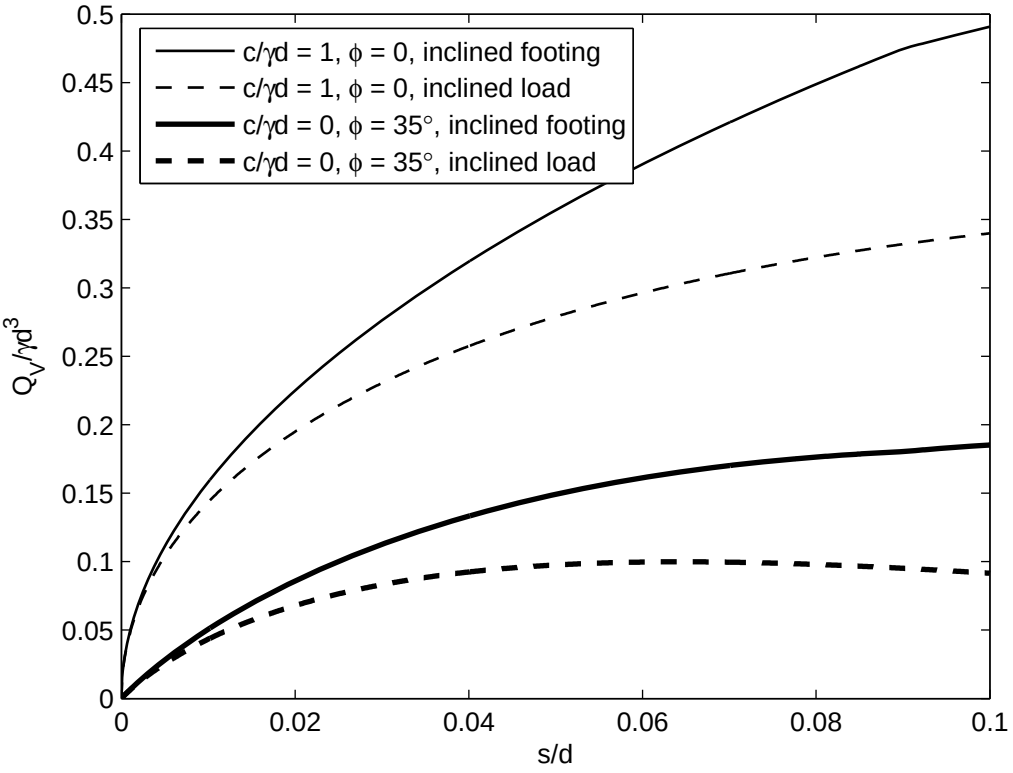

Figure 3.19. Comparison of force-sinkage curves for steady-state rolling using inclined footing method and inclined force method ($b/d = 0.3$)

3.2.3 Flexible Wheel Indentation

In contrast to the rigid wheel, both the soil and the wheel deform during indentation of a flexible wheel. This section is presented largely with pneumatic tires in mind since they are the most prevalent type of flexible wheel, although the simplified analysis addresses other types of flexible wheels equally well. Tires which are approximately right-cylindrical are considered. The shape of the deformed tire depends upon the soil properties, tire construction, and inflation pressure, as well as the applied wheel force. Fig. 3.20 illustrates the manner in which a typical pneumatic tire deforms when indenting soil. The bottom part of the tire flattens, while the upper part expands relatively uniformly and radially.

It should be stressed that one cannot precisely determine the deformed shape of the tire without solving the boundary value problem for the wheel and soil as two deformable bodies in contact. For the analytic method, an approach which fits within the structure of previous consideration for rigid wheels is sought. Prescribing how the contact region between the wheel and the soil evolves is the essential component needed to use the bearing capacity formula for determining force-sinkage relationships.

Based on previous work in terramechanics (Fujimoto 1977; Qun et al. 1987) and experimental observations, it is first postulated that the part of the wheel in the contact region

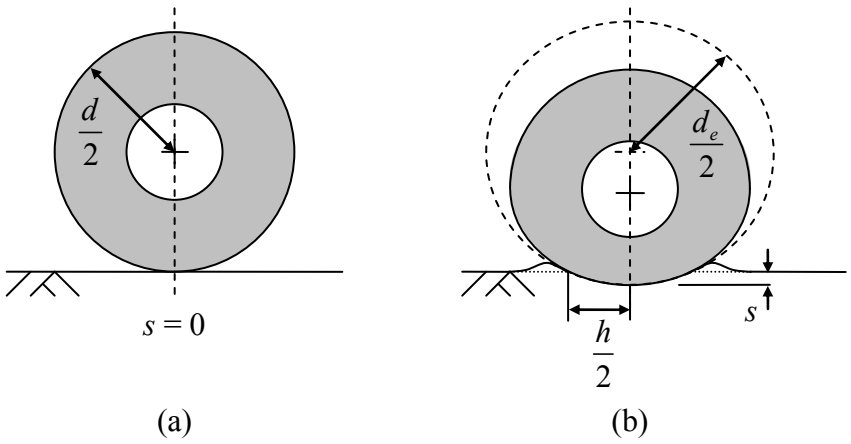

Figure 3.20. Schematic of flexible wheel indentation: (a) initial configuration; (b) deformed configuration

deforms under loading to the arc of a circle with a larger diameter than the initial diameter of the wheel (Fig. 3.20b). The equivalent diameter d_e of this larger circle governs the evolution of the contact area as it changes throughout the indentation process. In particular, d_e increases as the load on the tire increases, so as to flatten the wheel and increase the contact area from that for a rigid wheel of the same initial geometry.

Possible forms for d_e as a function of Q_V are shown in Fig. 3.21. The motivation for considering d_e as a function of Q_V only, as opposed to s for instance, comes from consideration of the case where the wheel is flexible and the soil is rigid. In this case, the wheel deforms under the load Q_V without any sinkage, so d_e cannot depend on s alone.

The behavior shown in Fig. 3.21a is that of a tire which deforms to some extent before behaving like a rigid wheel of a larger diameter with further loading. This appears to be the common case for relatively stiff tires indenting soft soils. Fig 3.21b might reflect a flexible tire which preferentially flattens rather than indents the soil and perhaps has an associated maximum developable load. A non-monotonic relationship like that in Fig. 3.21c is possible and may be a result of the changing distribution of contact stresses, but the curve must be initially increasing.

Without basis for choosing a higher order form and for the sake of simplicity, a linear relationship of the form shown in Fig. 3.21d is used:

$$d_e = d + \lambda_i Q_V \tag{3.58}$$

This introduces the single additional parameter λ_i, a wheel flexibility coefficient. The subscript i is used to distinguish this parameter from the one used later in the analysis of a flexible, rolling wheel. Based on observations about the behavior of pneumatic tires operating in soil (cf. Bekker 1960; Fujimoto 1977), one expects that increasing inflation pressure, increasing carcass stiffness, or decreasing soil strength tend to reduce the flexibility coefficient λ_i.

The definition of the contact length h given by Eq. (3.17) again applies after replacing the initial wheel diameter d with the equivalent wheel diameter d_e:

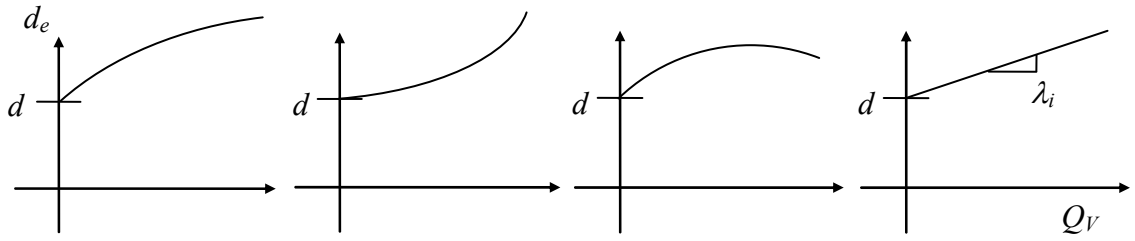

Figure 3.21. Possible forms for d_e as a function of Q_V

$$h = 2\sqrt{d_e s - s^2} = 2\sqrt{s\left(d + \lambda_i Q_V\right) - s^2} \tag{3.59}$$

As with the case of rigid wheel indentation, the contact area is given by

$$A = bh = 2b\sqrt{s\left(d + \lambda_i Q_V\right) - s^2} \tag{3.60}$$

Typically, the width of a right-cylindrical pneumatic tire does not change substantially as the tire is loaded, although the sidewall may bulge somewhat at a distance above the bottom of the tire. It is assumed that these effects are negligible and that wheel deformation occurs only in the radial cross-section shown in Fig. 3.20. The parameters B and L are again given by

$$\left.\begin{aligned} B &= h \\ L &= b \end{aligned}\right\} \text{ for } h < b \quad , \quad \left.\begin{aligned} B &= b \\ L &= h \end{aligned}\right\} \text{ for } h \geq b \tag{3.61}$$

The expression for D is taken as the same as that derived for indentation of a rigid, right-cylindrical wheel:

$$D = \frac{1}{6}\eta s \tag{3.62}$$

For $\lambda_i = 0$, the wheel is rigid and Eq. (3.62) is exact in that it follows directly from the derivation of Section 3.2.1.1. For $\lambda_i > 0$, Eq. (3.62) is not strictly correct in the sense of the derivation, but should give a reasonable approximation of D.

As with previous cases, $D/B \leq 1$ for realistic sinkage and wheel geometries, so that Eq. (3.14) unconditionally applies. Using Eqs. (3.59)-(3.62) in Eqs. (3.14) and (3.16) gives

$$Q_V = 2b\sqrt{s\left(d+\lambda_i Q_V\right)-s^2}\left\{cN_c\left(1+2\frac{\sqrt{s\left(d+\lambda_i Q_V\right)-s^2}}{b}\frac{N_q}{N_c}\right)\right.$$
$$\times\left[1+0.03\frac{\eta s}{\sqrt{s\left(d+\lambda_i Q_V\right)-s^2}}\right]+0.17\gamma\eta N_q s\left(1+2\frac{\sqrt{s\left(d+\lambda_i Q_V\right)-s^2}}{b}\tan\phi\right)$$
$$\times\left[1+0.17\tan\phi\left(1-\sin\phi\right)^2\frac{\eta s}{\sqrt{s\left(d+\lambda_i Q_V\right)-s^2}}\right]+\gamma N_\gamma\sqrt{s\left(d+\lambda_i Q_V\right)-s^2} \tag{3.63}$$
$$\left.\times\left(1-0.8\frac{\sqrt{s\left(d+\lambda_i Q_V\right)-s^2}}{b}\right)\right\}$$

for $2\sqrt{s\left(d+\lambda_i Q_V\right)-s^2} < b$ and

$$Q_V = 2b\sqrt{s\left(d+\lambda_i Q_V\right)-s^2}\left\{cN_c\left(1+0.5\frac{b}{\sqrt{s\left(d+\lambda_i Q_V\right)-s^2}}\frac{N_q}{N_c}\right)\right.$$
$$\times\left[1+0.07\frac{\eta s}{b}\right]+0.17\gamma\eta N_q s\left(1+0.5\frac{b}{\sqrt{s\left(d+\lambda_i Q_V\right)-s^2}}\tan\phi\right) \tag{3.64}$$
$$\left.\times\left[1+0.33\tan\phi\left(1-\sin\phi\right)^2\frac{\eta s}{b}\right]+\gamma bN_\gamma\left(0.5-0.1\frac{b}{\sqrt{s\left(d+\lambda_i Q_V\right)-s^2}}\right)\right\}$$

for $2\sqrt{s\left(d+\lambda_i Q_V\right)-s^2} \geq b$.

Eqs. (3.63) and (3.64) are implicit with respect to the wheel force but can be easily solved numerically using standard mathematics software or a spreadsheet. Fig. 3.22 gives the force-sinkage relationship for several values of λ_i. Eqs. (3.27) and (3.28) for a rigid wheel are recovered with $\lambda_i = 0$. With $\lambda_i > 0$, the wheel force Q_V is greater than that for a rigid wheel at the same sinkage. This gives the expected result that the force required to indent a flexible wheel is greater than the force needed to indent a rigid wheel the same amount.

The assumption that the tire deforms to the arc of a circle is arguably one of the simplest. One could readily incorporate higher order curves which may require additional parameters, although this adds unwarranted complexity in this analysis, in view of the fact that any one of these parameters is most likely difficult to determine. Analysis of non-right-cylindrical wheels may have the added complexity of non-negligible flexibility in the cross section of the wheel width, but the procedure used in this formulation may be extended to account for flexibility in both cross sections. For example, one should expect that a flexible, toroidal wheel flattens in both cross sections as load is applied, and this could be readily addressed by introducing two flexibility coefficients, one for both cross sections.

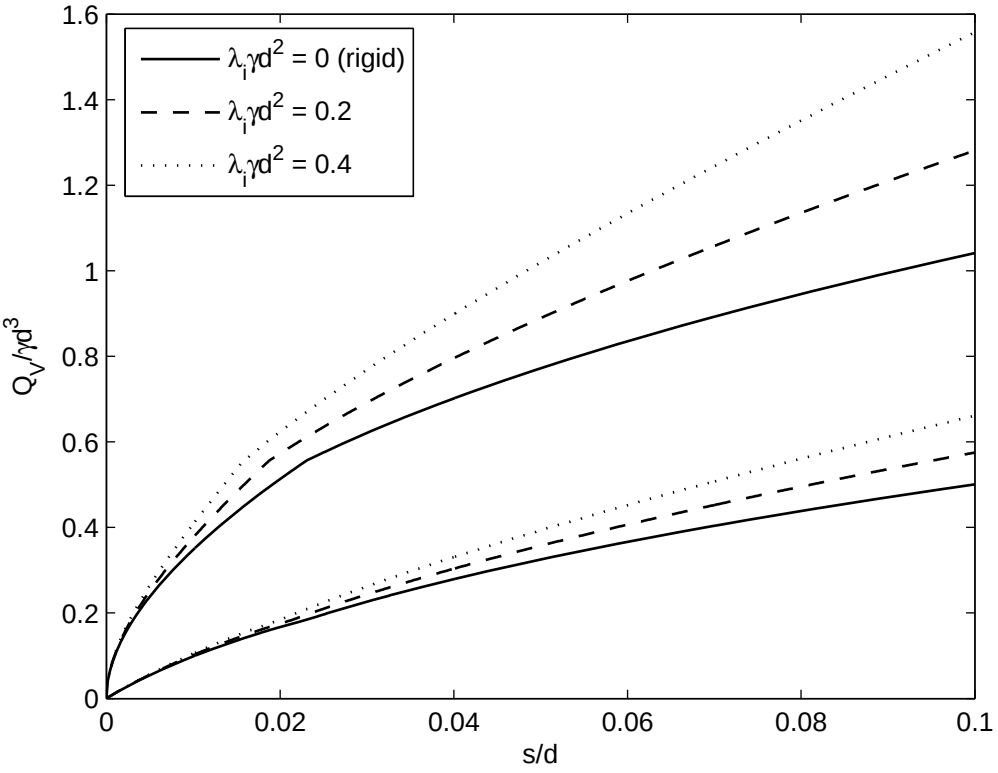

Figure 3.22. Force-sinkage curves for flexible wheel indentation (upper curves are with $c/\gamma d = 1$, $\phi = 0$ and lower curves are with $c/\gamma d = 0$, $\phi = 30$ deg; $b/d = 0.3$)

A fundamental assumption made in the proposed analysis is that the bearing capacity formula (3.7), which pertains to a flat footing of fixed contact area and depth, can be used to give an approximation of the average stress over a curved wheel surface. Since a flexible wheel tends towards a flatter surface as it is loaded, it may in fact be that the approximate analytic approach applies more aptly to the case of flexible wheels than rigid wheels.

3.2.4 Flexible Wheel Rolling

The same essential assumptions used to move from rigid wheel indentation to rigid wheel rolling apply here. Only the inclined footing method as it was described in Section 3.2.2.2 is presented here, although moving from the inclined footing method to the inclined load method is simply a matter of adjusting the contact length h and replacing the modified inclination factors (3.54) and (3.55) with the original factors (3.13). As with flexible wheel indentation, it is assumed that the wheel deforms to the arc of circle with diamater d_e, which is larger than the initial diameter d, upon loading (Fig. 3.23).

Using the same assumptions and reasoning that as for flexible wheel indentation, the equivalent wheel diameter takes the form

$$d_e = d + \lambda_r Q \tag{3.65}$$

where Q is the total wheel force and λ_r is the rolling wheel flexibility coefficient. Although one might expect that the flexibility coefficient for rolling is approximately the same as for indentation, the subscripts r and i are used respectively in allowing that they may be different. Due to the approximate symmetry and antisymmetry of normal and shear stresses considered in Section 3.2.2, using the inclined force Q for which the line of action is approximately parallel to the line of symmetry/antisymmetry is more physically justified than using the vertical component Q_V.

For a rolling, flexible wheel and the an implementation using the inclined footing method, h is given by

$$h = \sqrt{d_e s} = \sqrt{s\left(d + \lambda_r Q\right)} \tag{3.66}$$

Guided by the same assumptions used in rigid wheel rolling and flexible wheel indentation, the same equations for the contact area A, equivalent footing lengths B and L, and equivalent footing depth D apply and are repeated here for convenience:

$$A = bh = b\sqrt{s\left(d + \lambda_r Q\right)} \tag{3.67}$$

$$\left.\begin{matrix} B = h \\ L = b \end{matrix}\right\} \text{ for } h < b \quad ; \quad \left.\begin{matrix} B = b \\ L = h \end{matrix}\right\} \text{ for } h \geq b \tag{3.68}$$

$$D = \frac{1}{6}\eta s \tag{3.69}$$

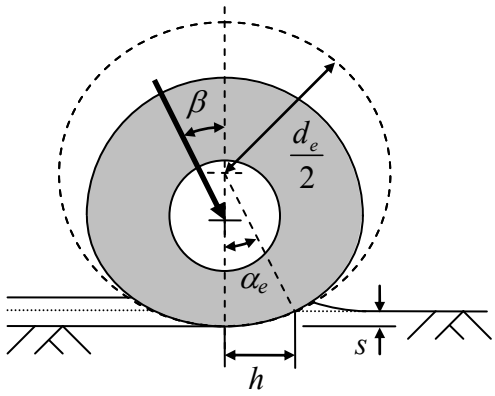

Figure 3.23. Schematic of rolling, flexible wheel

To determine the inclination angle β, the analysis considered in Section 3.2.2 is revisited. If the normal and shear contact stresses remain symmetrically and antisymmetrically distributed on the deformed surface described by the circle of diameter d_e, the condition that there is no torque transmitted between the wheel and axle is contradicted. Without an experimental or theoretical basis for adjusting β, this contradiction is accepted, understanding that the analysis used to determine β for a rigid wheel is approximate. With this, β is given by

$$\beta = \frac{\alpha_e}{2} = \frac{1}{2}\cos^{-1}\left(1-2\frac{s}{d_e}\right) \approx \sqrt{\frac{s}{d_e}} = \sqrt{\frac{s}{d+\lambda_r Q}} \tag{3.70}$$

where α_e is the equivalent contact angle subtended by the contact region (Fig. 3.23). Again, $D/B \leq 1$ for practical problems so that Eq. (3.14) applies. Substituting Eqs. (3.66)-(3.70) into Eqs. (3.14) and (3.16) gives the following force-sinkage relationships for a rolling, flexible wheel:

$$\begin{aligned} Q = b\sqrt{s\left(d+\lambda_r Q\right)}\Bigg\{ & cN_c\left(1+\frac{\sqrt{s\left(d+\lambda_r Q\right)}}{b}\frac{N_q}{N_c}\right)\left(1+0.07\frac{\eta s}{\sqrt{s\left(d+\lambda_r Q\right)}}\right)\left(\frac{N_q e^{-2\sqrt{\frac{s}{d+\lambda_r Q}}\tan\phi}-1}{N_q-1}\right) \\ & + \Bigg[0.17\gamma\eta s N_q\left(1+\frac{\sqrt{s\left(d+\lambda_r Q\right)}}{b}\tan\phi\right)\left(1+0.33\tan\phi\left(1-\sin\phi\right)^2\frac{\eta s}{\sqrt{\left(d+\lambda_r Q\right)s}}\right) \\ & + \gamma\sqrt{s\left(d+\lambda_r Q\right)}N_\gamma\left(0.5-0.2\frac{\sqrt{s\left(d+\lambda_r Q\right)}}{b}\right)\Bigg]\left[1-\tan\left(\sqrt{\frac{s}{d+\lambda_r Q}}\right)\right]^2\Bigg\} \end{aligned} \tag{3.71}$$

for $\sqrt{s\left(d+\lambda_r Q\right)} < b$

$$\begin{aligned} Q = b\sqrt{s\left(d+\lambda_r Q\right)}\Bigg\{ & cN_c\left(1+\frac{b}{\sqrt{s\left(d+\lambda_r Q\right)}}\frac{N_q}{N_c}\right)\left(1+0.07\frac{\eta s}{b}\right)\left(\frac{N_q e^{-2\sqrt{\frac{s}{\left(d+\lambda_r Q\right)}}\tan\phi}-1}{N_q-1}\right) \\ & + \Bigg[0.17\gamma\eta s N_q\left(1+\frac{b}{\sqrt{s\left(d+\lambda_r Q\right)}}\tan\phi\right)\left(1+0.33\tan\phi\left(1-\sin\phi\right)^2\frac{\eta s}{b}\right) \\ & + \gamma b N_\gamma\left(0.5-0.2\frac{b}{\sqrt{s\left(d+\lambda_r Q\right)}}\right)\Bigg]\left[1-\tan\left(\sqrt{\frac{s}{d+\lambda_r Q}}\right)\right]^2\Bigg\} \end{aligned} \tag{3.72}$$

and $\sqrt{s\left(d+\lambda_r Q\right)} \geq b$.

After solving Eqs. (3.71) and (3.72), the total wheel force Q is resolved into its vertical and horizontal components Q_V and Q_H using

$$Q_V = Q\cos\left(\sqrt{\frac{s}{d+\lambda_r Q}}\right) \quad , \quad Q_H = Q\sin\left(\sqrt{\frac{s}{d+\lambda_r Q}}\right) \tag{3.73}$$

The vertical component of force is plotted in Figs. 3.24 for example data. One can again clearly see that more vertical force is required for a flexible wheel than for a rigid wheel at the same sinkage.

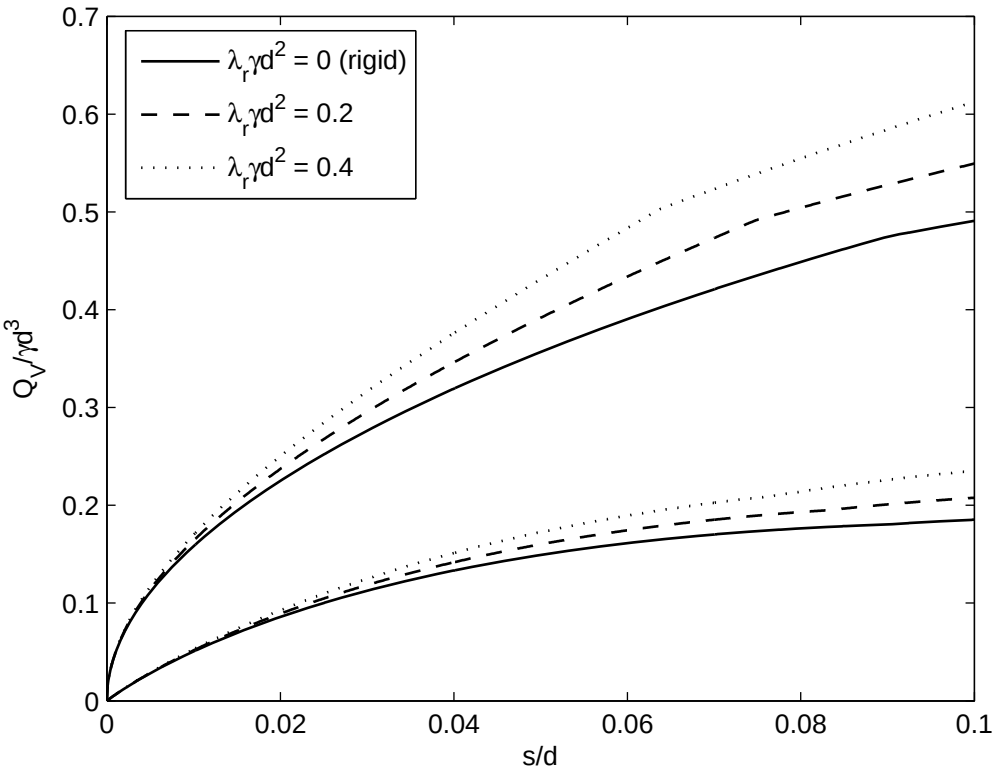

Figure 3.24. Force-sinkage curves for rolling, flexible wheel (upper curves are with $c/\gamma d = 1$, $\phi = 0$ and lower curves are with $c/\gamma d = 0$, $\phi = 35$ deg; $b/d = 0.3$)

3.3 Numerical Simulation

Three computer codes were considered for numerical modeling: ABAQUS/Standard, ABAQUS/Explicit, and FLAC^{3D}. ABAQUS/Standard is a general-use finite element code using an implicit solution scheme. ABAQUS/Explicit is a time-stepping dynamics finite element code. FLAC^{3D} is also a dynamic code which uses an explicit, time-stepping solution method and is specialized for modeling soils and rocks. ABAQUS/Standard gives true static solutions, while the other two codes provide quasi-static solutions to static problems using slow and smooth application of external forces and displacements.

ABAQUS/Explicit was found to be superior to both ABAQUS/Standard and FLAC^{3D} for the test rolling models. Because the models involve large, plastic deformations, the implicit solution scheme used by ABAQUS/Standard is computationally inefficient and often fails to converge to a solution. The large element distortions that result from the rolling process require that the mesh be corrected throughout the analysis to give accurate results. The adaptive meshing algorithm in ABAQUS/Explicit is capable of correcting element distortions, while ABAQUS/Standard and FLAC^{3D} do not provide means to accurately solve problems involving such extreme deformations. All references to ABAQUS in the remainder of this report pertain to the specific code ABAQUS/Explicit.

3.3.1 Rigid Wheel Indentation

The reference configuration used in ABAQUS for three-dimensional analysis of rigid wheel indentation is shown in Fig. 3.25. A coordinate system with the origin centered directly beneath the wheel is used, with coordinate directions as shown. There are two planes of symmetry for the indentation problem, one in the *x*-*z* plane and one in the *y*-*z* plane, so that only one quarter of the domain of the full problem is simulated. One half of the wheel, rather than one quarter, is shown in Fig. 3.25 because of the way the wheel is modeled.

The wheel was simulated using an analytical rigid shell, where *analytical* (a term used in the ABAQUS reference manuals) in this case means that it is not discretized into finite elements. The term *shell* implies that the wheel is represented by a surface in three-dimensional space. The interior of the shell is visible in the isometric view of Fig. 3.25a. The wheel is right-cylindrical with an edge fillet of radius r_f. A non-zero fillet radius is required to avoid numerical problems arising in the algorithm used to model contact between the wheel and the soil. Since the wheel is rigid, boundary conditions are prescribed on a single reference point which governs the response of the entire body.

The soil was discretized using C3D8R elements, which are linear 8-node reduced integration hexahedral elements for three-dimensional solids. The soil was partitioned into two regions of different element sizes, as shown in Fig. 3.25, to accommodate the large displacement and stress gradients occurring near the wheel. The two regions were connected using the surface-based tie constraint available in ABAQUS for rapid mesh transition.

Like the numerical simulations discussed in later sections, the mesh was tailored somewhat to the specific problem of interest and varies with aspect ratio b/d, indentation depth, and material properties. For $b/d \approx 0.3$ and $r_f/d \approx 0.04$ as shown in Fig. 3.25, the overall soil domain was taken as a cube with edge length roughly $1.5d$, and the region of small elements was taken as a cube with length $0.5d$. The elements in the model were nearly cubic, which is a desirable aspect

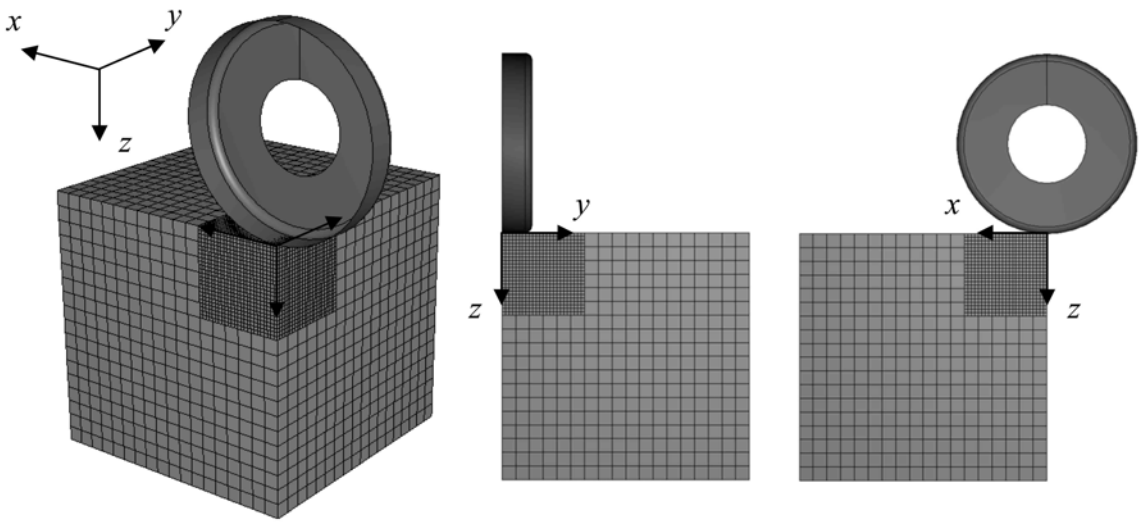

Figure 3.25. Soil and wheel model used in numerical simulation of rigid wheel indentation: (a) isometric view; (b) view along positive x-axis; (c) view along positive y-axis

of the mesh grading used. The larger elements had an edge length of approximately $0.08d$, and the smaller elements had length $0.02d$. The total number of elements for the configuration shown in Fig. 3.25 was roughly 20,000.

Symmetry boundary conditions were applied to the soil in the x-z and y-z planes by enforcing zero nodal displacements in the y and x-directions, respectively. The soil face in the x-y plane was traction-free, except where tractions developed as a result of contact. The free surface of the soil and the wheel were defined as a contact pair, with tangential stresses developing according to a dry friction law. For simplicity, a single coefficient of friction μ was used for both sticking and sliding contact. The contact definition applies to all simulations discussed in Section 3.3. On the soil faces not visible in Fig. 3.25, out-of-plane displacements alone were fixed, with the soil free to move in the remaining two degrees of freedom.

To introduce the unit weight of the soil, a uniform body force was first applied to the soil in the z-direction. After the unit weight was introduced, the wheel was displaced into the soil in the z-direction at a constant velocity. The adaptive meshing algorithm was used while the wheel was being indented to preserve the aspect ratio of the elements.

Since inertial effects are present in the numerical code used, the rate at which loads are applied is important. When the rate is too high, inertial forces which would not develop in the static process may result. Rates that are too low produce unnecessarily long computation times. For rigid wheel indentation, the unit weight was introduced over a period of $60d(\rho/E_s)^{1/2}$ and the wheel was indented an amount $s/d = 0.1$ over a period of $180d(\rho/E_s)^{1/2}$, where ρ is the soil density (related to γ through $\rho = \gamma/g$, where $g = 9.81$ m/s^2 $= 32.2$ ft/s^2 is acceleration due to gravity). Like the rest of the models in Section 3.3, the actual time periods used in a particular simulation were greater than or equal to the given values.

Due to the dynamic analysis, a mass is necessarily assigned to the wheel in the model, and density is assigned to the soil. They were chosen as realistic values where practical for the rigid wheel indentation model and the remaining models. Although the wheel mass and soil density

would be important with fast loading, they are relatively unimportant for quasi-static analysis and can be chosen somewhat arbitrarily.

Example output from the rigid wheel indentation simulation for a cohesive (von Mises) material is shown in Figs 3.26 and 3.27. The generalized shear stress field shown in Fig. 3.26a indicates how close the soil is to yielding. Where the contour is darkest, the material is in a state of yielding. Note that the wheel is not rendered in Fig. 3.26 for clarity. The trend in the force-sinkage curve from the indentation simulation (Fig. 3.27) is very similar to the trends found using the analytic method.

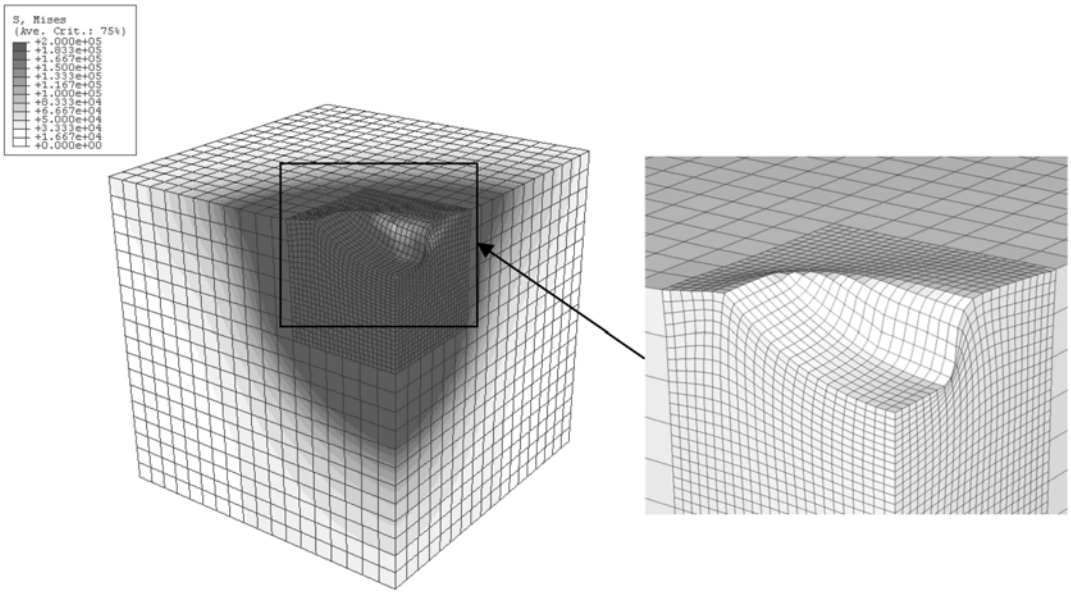

(a) (b)

Figure 3.26. Example output from numerical simulation of rigid wheel indentation; (a) contours of generalized shear stress, (b) close-up of highly-deformed soil region

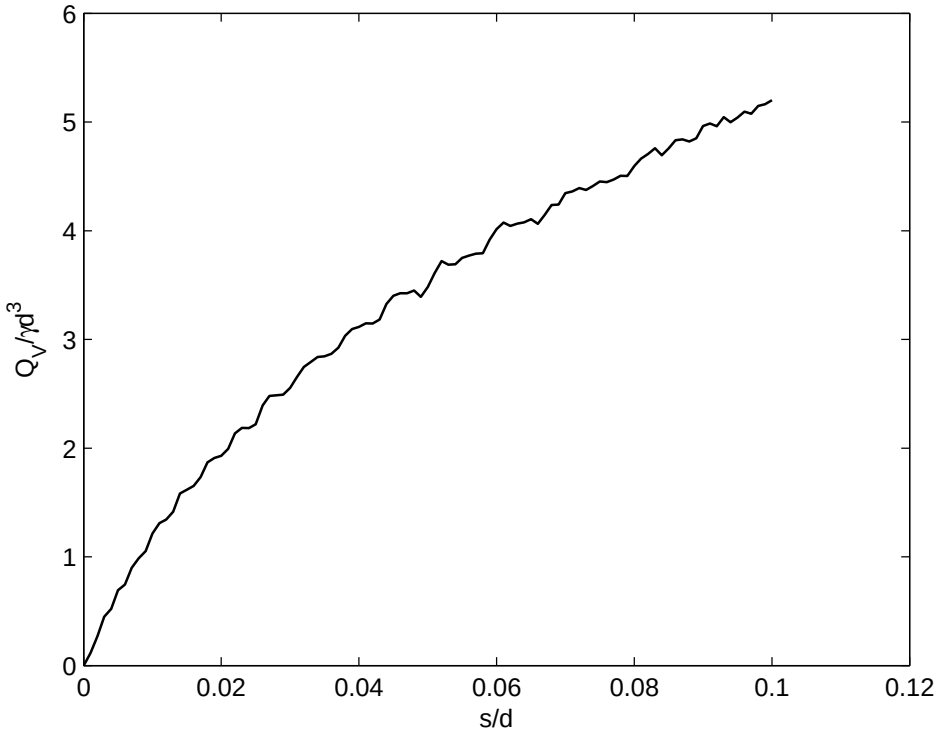

Figure 3.27. Example of force-sinkage curve from rigid wheel indentation on cohesive soil

3.3.2 Rigid Wheel Rolling

The reference configuration used for rigid wheel rolling is shown in Fig. 3.28. A coordinate system with the origin at the leftmost corner of the soil region visible in the figure is used, with coordinate directions as shown. The *y*-*z* plane, the midplane of the full wheel, is the only plane of symmetry in the rolling problem, allowing for one half of the full problem to be simulated as depicted. The rigid wheel used in the rolling case is identical to that used for indentation. The wheel in Fig. 3.28 is oriented relative the reader as in Fig. 3.25 for indentation and rolls in the *y*-direction during the simulation.

During the test rolling process, the test roller typically rolls from a region of competent soil in which very little penetration occurs into a region of soft soil in which it penetrates more readily. To simulate this, the soil was partitioned into a "stiff" region and a "soft" region as shown in Fig. 3.28. In this context, the relative "stiffness" or "softness" of the soils can involve elastic properties, plastic properties, or both, but in any case, the wheel penetrates deeper into the soft material than the stiff material.

Again, the soil discretization consisted of two regions of different element sizes connected through the tie constraint. In the *x*-*z* plane, the overall soil domain was a square with edge length roughly 1.5*d*, with the region of smaller elements taken as a square with length 0.5*d*. The length of the soil region parallel to the *y*-axis was roughly 3.5*d*. The interface between the stiff and soft soil was at $y \approx 0.75d$, and the wheel was initially located at $y \approx 0.4d$. Since the rolling process occurs over a longer period than indentation and smaller increments are needed in the time-

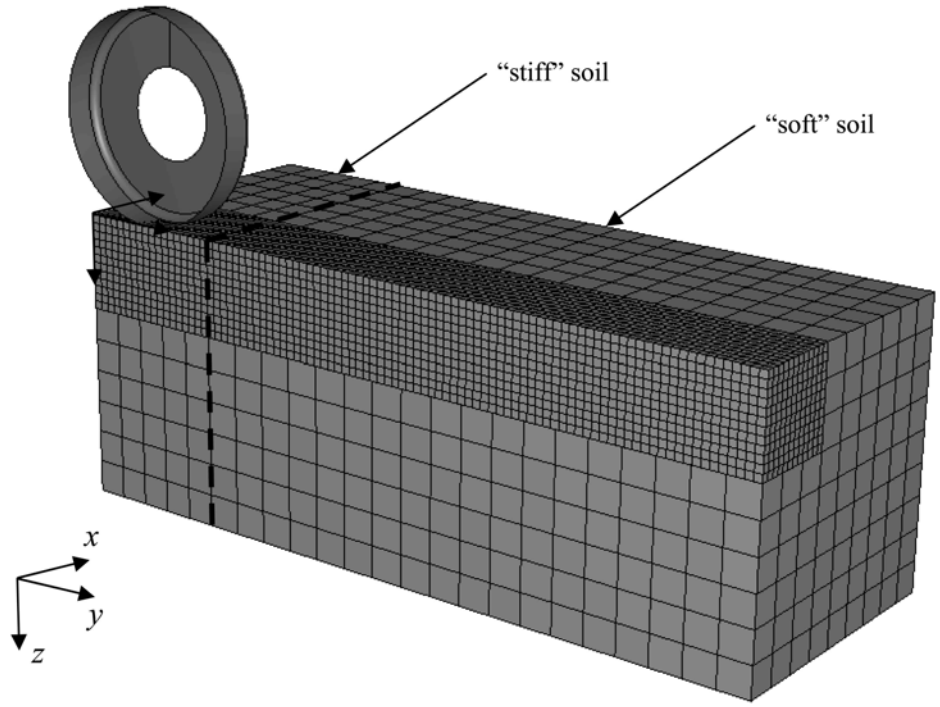

Figure 3.28. Soil and wheel model used in numerical simulation of rigid wheel rolling

stepping process due to greater element distortion, a coarser mesh than the one employed for indentation was used. For the model shown in Fig. 3.28, with $b/d \approx 0.3$ and $r_f/d \approx 0.04$, the larger elements had an edge length of approximately $0.16d$, and the smaller elements had length $0.04d$. The total number of elements was therefore about 15,000.

In addition to the symmetry boundary condition applied to the soil in the y-z plane, out-of-plane displacements were fixed on all faces, except the free surface in the x-y plane. All displacements and rotations of the wheel were fixed except displacements in the y- and z-directions and rotation about the x-direction, so that the wheel could displace into the soil, move forward, and rotate freely. Free rotation is an essential part of simulating the towed condition, in which no torque (about the x-direction) is exerted on the wheel. The wheel rotates as a natural consequence of its frictional interaction with the soil.

As in the simulation of indentation, a uniform body force representing unit weight was first applied to the soil. Next, a concentrated force in the positive z-direction was applied to the wheel to simulate the axle load introduced by the weight of the test roller. This force is Q_V, the vertical component of the wheel force, which after being applied remained constant. The vertical force Q_V was applied while the wheel was kept stationary on the stiff material. After Q_V was applied, the wheel was given a linear velocity in the y-direction, ramping smoothly from zero velocity to a constant value. The wheel reached a constant linear velocity just before the wheel entered the region of soft soil. In the fourth and final stage of simulation, the wheel continued to roll forward at a constant linear velocity, with a constant vertical force Q_V, through the soft soil. In rough terms, the soil unit weight was applied over a period $60d/(\rho/E_s)^{1/2}$, the force Q_V was applied over $180d(\rho/E_s)^{1/2}$, constant velocity was reached in $180d(\rho/E_s)^{1/2}$, and constant velocity was maintained for a period $1000d(\rho/E_s)^{1/2}$. The wheel velocity was chosen such that the wheel traversed most of the soil region in the y-direction.

Example output is shown in Figs. 3.29-3.31 for a cohesive material. In Fig. 3.29, some of the soil appears to penetrate the wheel. Part of this is due to poor rendering of the output, but indeed, some elements are partly within the wheel across the edge fillet in the contact region. This is as a result of the contact algorithm, in which the soil nodes, rather than the faces of the soil elements, interact with the wheel surface. This mild interpenetration can be reduced by refining the soil mesh or a similar means but does not appear to have a significant impact on the overall wheel forces and displacements, which are of primary interest.

Fig. 3.31 shows how s, the primary variable of interest, changes throughout the simulation. Also shown is the horizontal wheel force Q_H, which is of lesser interest but can be extracted from the simulations nonetheless. In the figure, s and Q_H are plotted versus u_y, the wheel displacement in the y-direction. Two regimes are evident. In the first regime corresponding to the period when the wheel has just entered the region of soft soil (u_y δ 1), s and Q_H steadily increase. In the second regime (u_y τ 1), s and Q_H are basically constant. The values of s and Q_H in the second regime correspond to steady state. Each simulation thus generates a single value of steady-state s corresponding to a prescribed Q_V. This is dissimilar to a simulation of indentation, in which the complete Q_V-s history is obtained, and also different from Section 3.2.2, in which the analytic method was used to obtain complete Q_V-s curves.

A different approach to the numerical simulations was used to obtain a complete Q_V-s relationship for the rolling case. In this simulation, the entire soil domain consisted of "soft" soil, and rather than apply constant Q_V to the wheel, the wheel was displaced into the soil at a constant rate while rolling forward at the specified linear velocity. Since the rate at which the wheel was displaced into the soil was small, the conditions were essentially the same as those at steady state at each instant during the simulation. In this way, a single simulation could generate a virtually continuous force-sinkage history for steady rolling conditions. Fig. 3.32 compares the continuous Q_V-s history obtained for a rolling, rigid wheel with the continuous analysis with steady-state s resulting from the simulation with constant Q_V for a cohesive soil and $b/d \approx 0.3$.

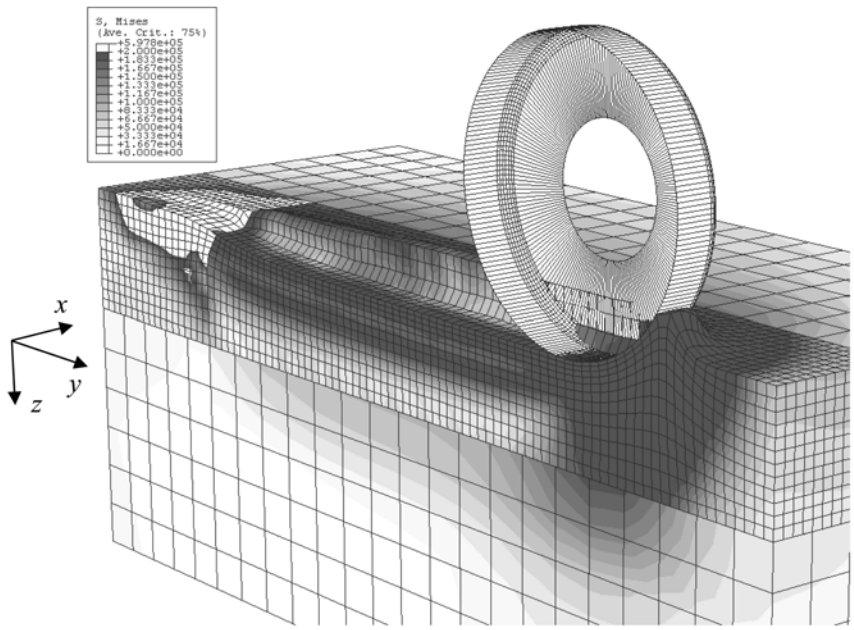

Figure 3.29. Example of deformed configuration and contours of generalized shear stress from numerical simulation of rigid wheel rolling

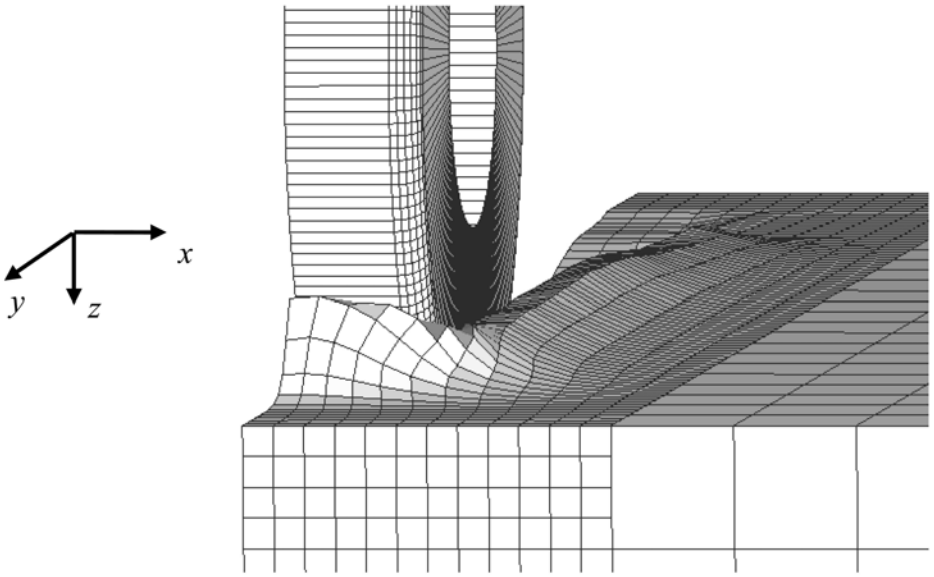

Figure 3.30. Example of soil deformation near wheel in numerical simulation of rigid wheel rolling

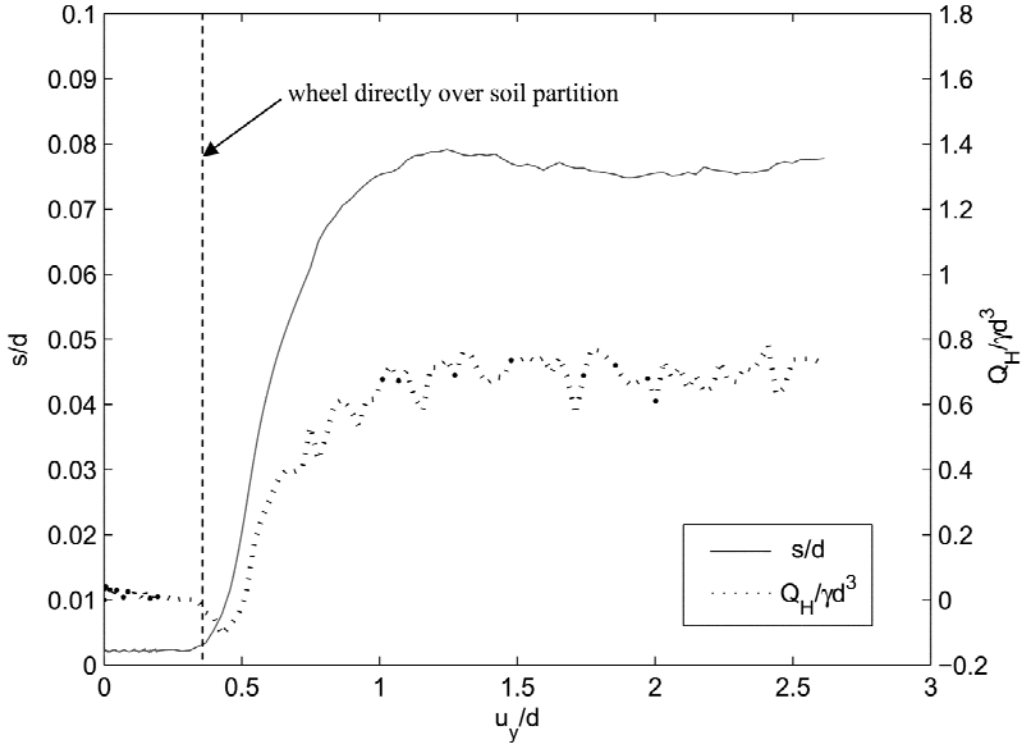

Figure 3.31. Example of s and Q_H versus wheel displacement in the y-direction (the direction of rolling) from numerical simulation of rigid wheel rolling

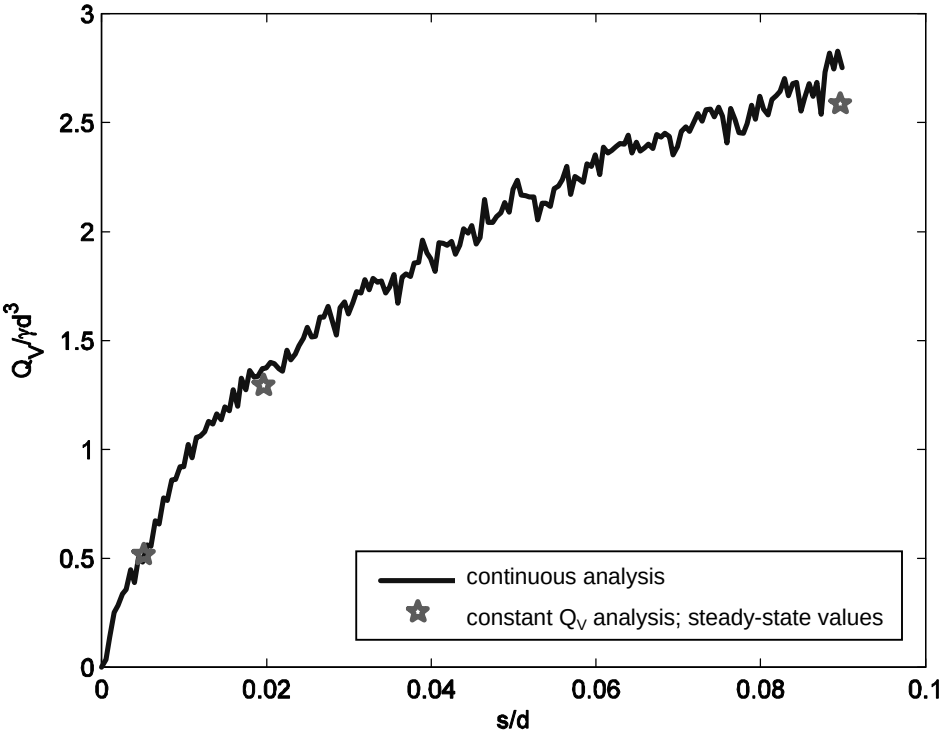

Figure 3.32. Q_V versus s from simulation of rigid wheel rolling using continuous analysis as compared with steady-state s from simulation with constant Q_V

3.3.3 Pneumatic Tire Indentation

The reference configuration used for the pneumatic tire indentation simulation was similar to that for rigid wheel indentation, with the same basic dimensions and meshing used for the soil. The simulated pneumatic tire is shown in Fig. 3.33, the analogue to the rigid wheel in Fig. 3.25a. The tire reference configuration consisted of a flexible carcass, modeled as an elastic rather than rigid shell, affixed to a rigid hub with diameter d_h. This configuration represents the realistic construction of a pneumatic tire, and like the case where the entire wheel is rigid, boundary conditions may be prescribed on a single reference point on the hub. Due to symmetry of the indentation problem, only one quarter of the full soil and tire was modeled, though one half of the wheel hub is shown in the figure.

The construction of the simulated pneumatic tire is shown in Fig. 3.34. The tire carcass was assumed to be composed of three different shell sections: a tread, a transition section for the edge fillet, and sidewall. These sections have associated thicknesses t_{tread}, t_{trans}, and t_{side}, respectively. Section thicknesses were taken as $t_{tread} = 0.046$d, $t_{trans} = 0.6t_{tread}$, and $t_{side} = 0.2t_{tread}$. The thickness was crucial in determining the stiffness of the individual sections, but since the carcass was modeled as a shell, the apparent thickness of the carcass was zero in relation to the rest of the model. After fixing the section thicknesses, the Young's modulus E_w and Poisson's ratio ν_w of the tire carcass were chosen to give realistic overall tire flexibility.

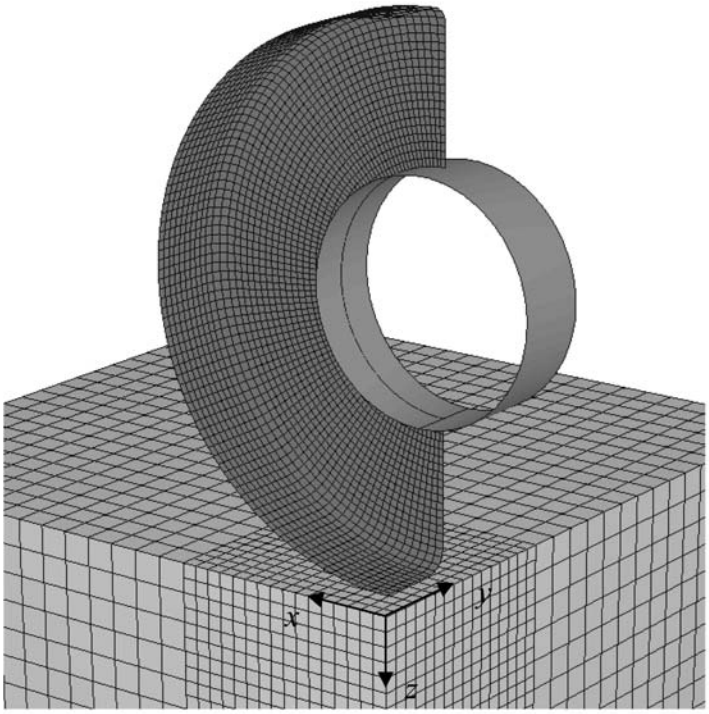

Figure 3.33. Wheel model used in numerical simulation of pneumatic tire indentation

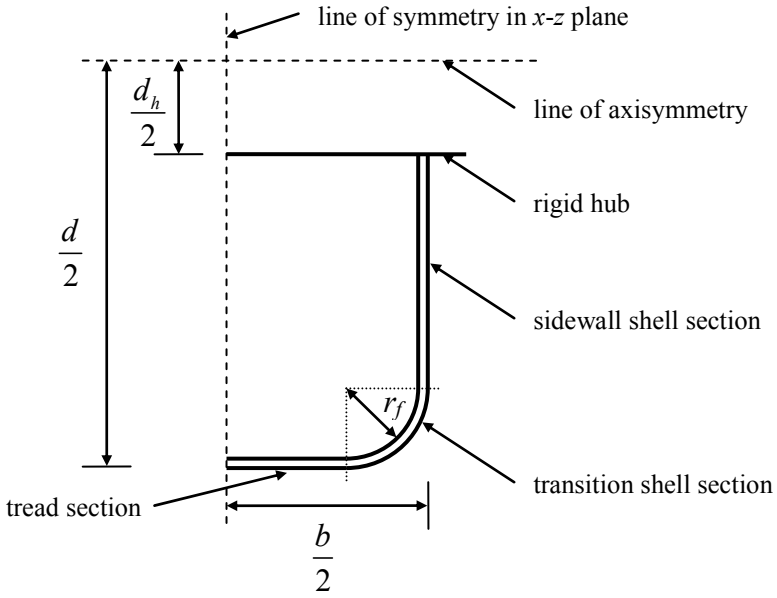

Figure 3.34. Schematic of shell configuration used for pneumatic tire in numerical simulations

The carcass was discretized using the S4R general-purpose 4-node reduced integration shell elements available in ABAQUS, using the sweep meshing technique to obtain radially uniform elements. The soil was discretized in the same way as for rigid wheel indentation. In the pneumatic tire indentation model, both the wheel and the soil are discretized, and for the contact algorithm used in ABAQUS, one of the discretized surfaces should have more densely spaced nodes than the other. Since the carcass does not undergo plastic deformation, it was elected to make the wheel mesh finer than the soil mesh by a factor of two. The resulting discretization for the wheel consisted of roughly 6,000 elements. Note that the mesh shown in Fig. 3.33 is somewhat coarser for clarity.

Symmetry and fixity boundary conditions were applied to the soil as in the rigid wheel indentation model. In the pneumatic tire model, symmetry conditions were applied to the tire carcass in the x-z and y-z planes, which required fixing both displacement and rotation degrees of freedom on nodes of the carcass elements as appropriate. The tire carcass was fixed to the wheel hub using the tie constraint. Only compatibility of displacements was enforced, with rotation relative to the hub being allowed (i.e., the hub and sidewall were not fixed at a right angle in a section view like Fig. 3.34).

The indentation process was simulated as described in Section 3.3.1, with an added "inflation" step preceding the indentation process. In the inflation step, a uniform pressure p was applied to the interior of the tire carcass over a period of $240d(\rho/E_s)^{1/2}$. After being applied, the pressure remained fixed throughout the analysis. In reality, the tire pressure increases slightly as wheel force is applied. Several supplementary simulations were performed considering the interior of the tire as a cavity filled with fluid obeying the ideal gas law, but the small fluctuations in tire pressure suggested that applying a constant pressure is appropriate. During the inflation step, the tire expands significantly. To avoid premature contact with the soil, the tire was initially offset from the soil as shown in Fig. 3.33. In the last analysis step, the tire was indented into the soil by displacing the hub in the z-direction at a constant velocity over a period of $240d(\rho/E_s)^{1/2}$.

Fig. 3.35 shows example output from the pneumatic tire indentation model using for cohesive soil. Although it is not rendered as such in the figure, the hub is a smooth surface in the analysis. A Q_V-s curve like that shown in Fig. 3.27 may be obtained from the simulation of pneumatic tire indentation, noting that the sinkage (the distance between the lowermost part of the wheel and the undisturbed soil surface) is not the same as the hub displacement.

The model for the pneumatic tire was developed in an effort to reproduce the behavior of the tire required in the current Mn/DOT test rolling specification (Minnesota 2000). Photos of an observed test roller tire are shown in Fig. 3.36. The deformed shape of the pneumatic tire simulated in ABAQUS, under approximately the same loading and inflation pressure as required by the current specification, is shown in Fig. 3.37. Flattening of the simulated tire with decreasing inflation pressure was also verified in separate analyses to ensure that the carcass did not carry an excessive portion of the wheel force.

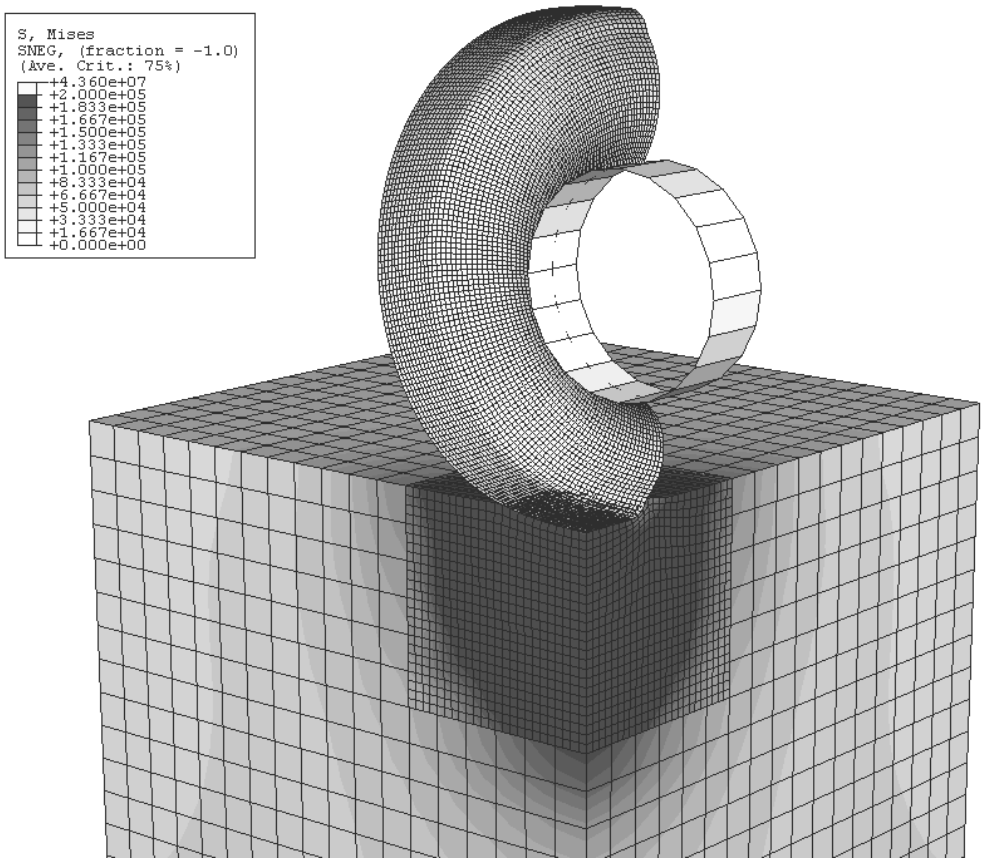

Figure 3.35. Deformed configuration and contours of generalized shear stress from simulation of pneumatic tire indentation

Figure 3.36. Photos of pneumatic tire for current test roller configuration

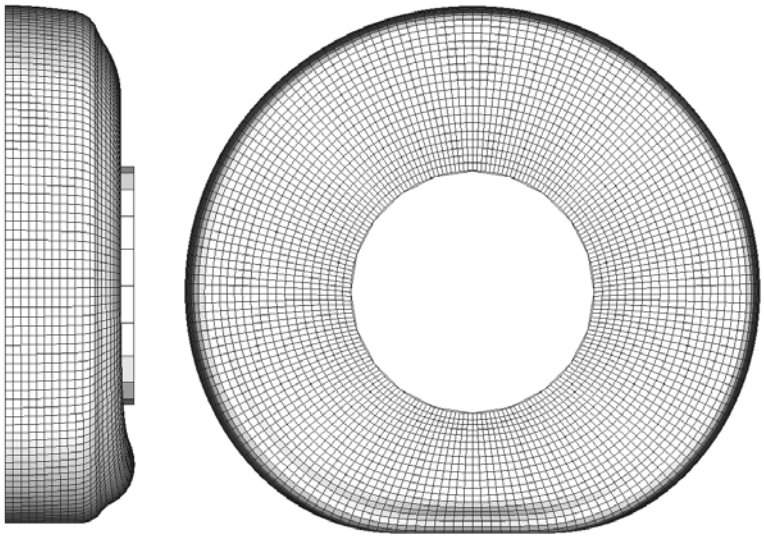

Figure 3.37. Deformed shape of simulated test roller tire

3.3.4 Pneumatic Tire Rolling

The numerical simulation used for pneumatic tire rolling is a straightforward extension of the previous cases. The reference configuration for rigid wheel rolling (Fig. 3.28) was used, with the rigid wheel replaced by the pneumatic tire described in Section 3.3.3. For a wheel mesh twice as fine as the soil, approximately 2,500 elements were needed, where naturally one half of the wheel was modeled rather than one quarter.

The rolling process was simulated as described in Section 3.3.2, with an added inflation step (discussed in Section 3.3.3) preceding application of the vertical wheel force. Since the analysis is dynamic and the simulated tire behaves elastically, the tire tended to "bounce" when loaded on the stiff soil region. Bouncing is most readily avoided by positioning the tire such that it nearly comes into contact with the soil after inflation. However, the geometry of the inflated pneumatic tire depends on the tire's initial dimensions, elastic properties, and inflation pressure. An analysis to determine the inflated dimensions of the wheel, which requires very little time relative to the overall computation time for pneumatic tire rolling, should be performed ahead of time when the tire configuration is changed. Note that this issue is not a concern for the indentation simulations, which are displacement-controlled, or the case of rigid wheel rolling, in which the wheel has fixed dimensions and stores no energy.

Fig. 3.38 shows example output from a simulation of pneumatic tire rolling. Wheel displacements and forces may be extracted from the simulation output, as in Figs. 3.31-3.32, noting that sinkage and vertical hub displacement (or axle displacement) are two separate variables.

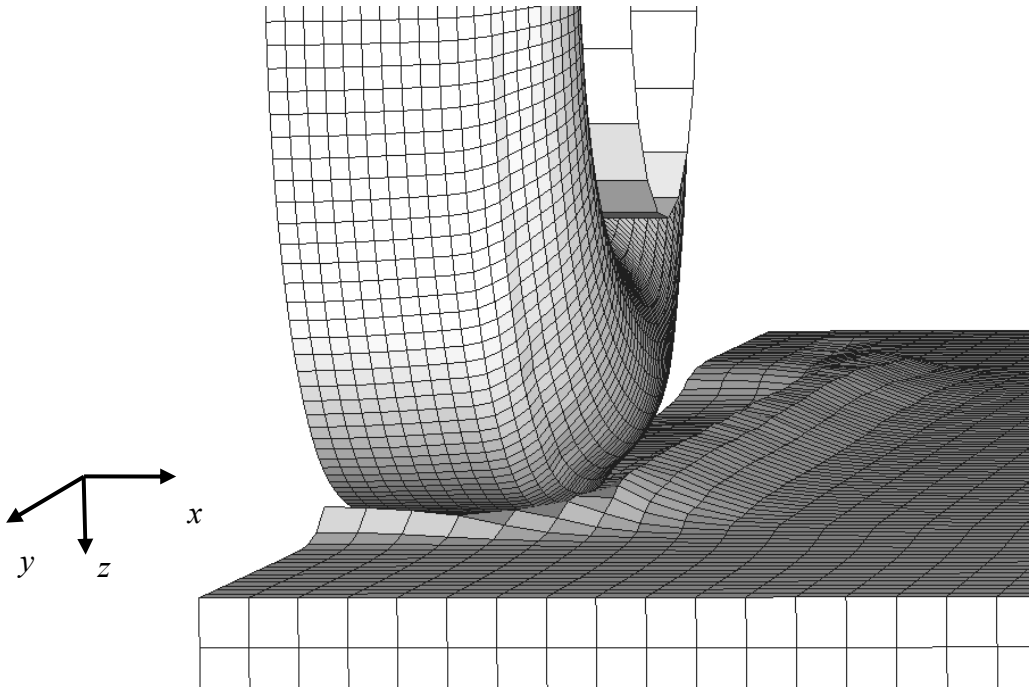

Figure 3.38. Soil deformation near wheel from simulation of pneumatic tire rolling

3.4 Soil Layering

In road construction, soil thickness and layering are important factors. An arbitrary number of distinct layers with differing properties may be easily incorporated into the numerical simulation, and such simulations are described further in Chapter 4. Layering is not as readily addressed in the analytic method, although there is a body of literature on the effect of layering on the bearing capacity of shallow foundations that can be employed to approximate layering effects for a wheel operating on soil.

In this section, analytic formulas for predicting the influence depth of a test roller are derived. Influence depth is considered to be the depth at which a strong or weak underlying layer begins to influence sinkage of a test roller. The concepts employed in obtaining the formulas are closely related to the approximate analytic technique presented in Section 3.2. Only the case of a rolling, rigid wheel is considered (using the inclined footing approach of Section 3.2.2.2), although implementation for other cases is straightforward.

Das (1995) summarizes work by Meyerhof (1974) and Meyerhof and Hanna (1978) regarding the bearing capacity of shallow foundations on layered soils. The formulas in Das pertain to a rectangular footing with vertical loading, though it is postulated that they may be used to arrive at an approximation of the influence depth of a rolling wheel in much the same way as considered in Section 3.2. Section 3.4.1 pertains to the case of dense sand over weak clay, Section 3.4.2 is for strong clay over weak clay, and Section 3.4.3 addresses the generic case of a weak layer overlying strong material.

3.4.1 Dense Sand over Weak Clay

For a dense sand with material properties $\phi_1 > 0$ and $c_1 = 0$ overlying a weak clay with $\phi_2 = 0$ and $c_2 > 0$, bearing capacity q_u may be computed as (Das 1995)

$$\begin{aligned} q_u &= 5.14\left(1+0.2\frac{B}{L}\right)c_2 + \left(1+\frac{B}{L}\right)\gamma_1 H^2\left(1+\frac{2D}{H}\right)K_s\frac{\tan\phi_1}{B} + \gamma_1 D \\ &\le \gamma_1 D N_{q1} + \frac{1}{2}\left(1-0.4\frac{B}{L}\right)\gamma_1 B N_{\gamma 1} \end{aligned} \tag{3.74}$$

where B, L, and D are the foundation parameters previously defined, H is the thickness of the sand layer, γ_1 is the unit weight of the sand layer, and N_{q1} and $N_{\gamma 1}$ are the bearing capacity factors computed as

$$N_{q1} = \tan^2\left(\frac{\pi}{4}+\frac{\phi_1}{2}\right)e^{\pi\tan\phi_1} \tag{3.75}$$

$$N_{\gamma 1} = 2\left(N_q+1\right)\tan\phi_1 \tag{3.76}$$

The factor K_s depends on ϕ and the ratio $\delta = (10.28c_2)/(\gamma_1 B N_{\gamma 1})$ as shown in Fig. 3.39 (reproduced from Das 1995). An expression for K_s could not be found, so interpolation must be

used in conjunction with the data given in the figure. As the equivalent foundation parameters B, L, and D pertain to test rolling using the analytic method (see Section 3.2.2.2), they are taken for a rolling, rigid wheel as

$$\left.\begin{matrix} B=\sqrt{ds} \\ L=b \end{matrix}\right\} \text{ for } \sqrt{ds}\le b \quad ; \quad \left.\begin{matrix} B=b \\ L=\sqrt{ds} \end{matrix}\right\} \text{ for } \sqrt{ds}>b \tag{3.77}$$

$$D=\frac{1}{6}\eta s \tag{3.78}$$

The left-hand side of the inequality in Eq. (3.74) is for the situation in which the failed soil extends into the underlying clay layer. The right-hand side applies to the case when failure occurs only in the sand layer (and the presence of the weak layer has no effect on bearing capacity). Of interest in test rolling is the depth H at which the weak layer will begin to influence bearing capacity. This depth may be determined by setting the left-hand side of the inequality in Eq. (3.74) equal to the right-hand side and solving for H. It is straightforward to find an explicit solution of the form $H = f_{sand}(\phi_1,\gamma_1,c_2,b,d,s)$ using the quadratic formula, although the resulting expression is rather cumbersome. The formula is not given here but can be found in Appendix A.

The wheel force Q_V does not appear at first glance to enter the formulas for H, since H is related only to the soil properties, wheel geometry, and s. The sinkage s, however, is related to Q_V. Section 3.2 was dedicated to finding this relationship for a homogeneous soil. Using this relation (e.g., Eqs. (3.56) and (3.57) for the inclined footing method), influence depth may be plotted as a function of Q_V rather than s, accepting that there is some discrepancy arising because the formulas for H disregard the effects of inclined loading. The end result is a plot like Fig 3.40, which shows, as a function of Q_V, the depth H at which a soft clay layer will begin to influence test roller sinkage. Viewed in this way, it is natural to think of H as an *influence depth*, which is the terminology used throughout this report.

When the sinkage is small (Fig 3.40), the formula predicts that the weak underlying layer must be very close to the surface to have an effect. As the sinkage becomes larger the footprint of the wheel becomes larger, the extent of failed soil increases, and the depth at which the weak layer has an effect consequently grows.

3.4.2 Strong Clay over Weak Clay

For the case of a strong clay layer ($\phi_1 = 0$ and $c_1 > 0$) overlying a weak clay ($\phi_2 = 0$ and $c_2 > 0$), Das (1995) gives the following

$$\begin{aligned} q_u &= 5.14\left(1+0.2\frac{B}{L}\right)c_2+\left(1+\frac{B}{L}\right)\left(\frac{2c_aH}{B}\right)+\gamma_1 D \\ &\le 5.14\left(1+0.2\frac{B}{L}\right)c_1+\gamma_1 D \end{aligned} \tag{3.79}$$

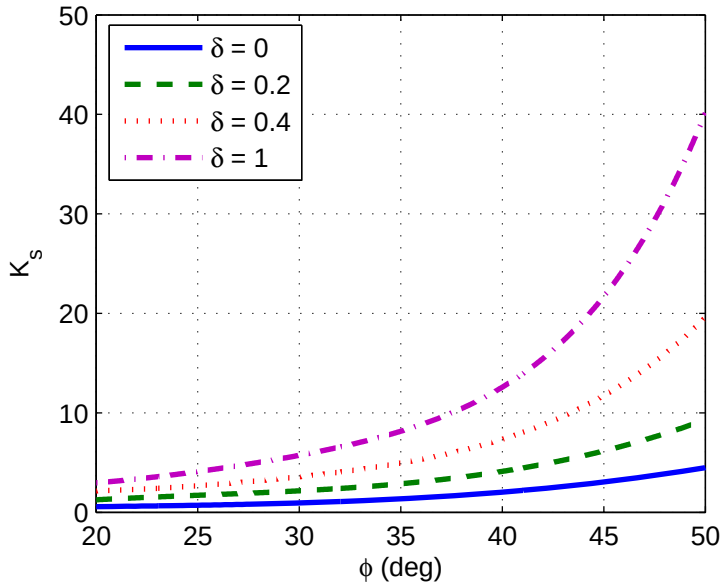

Figure 3.39. Variation of K_s with ϕ_1 for various $\delta = (10.28c_2)/(\gamma_1 B N_{\gamma 1})$ according to Das (1995)

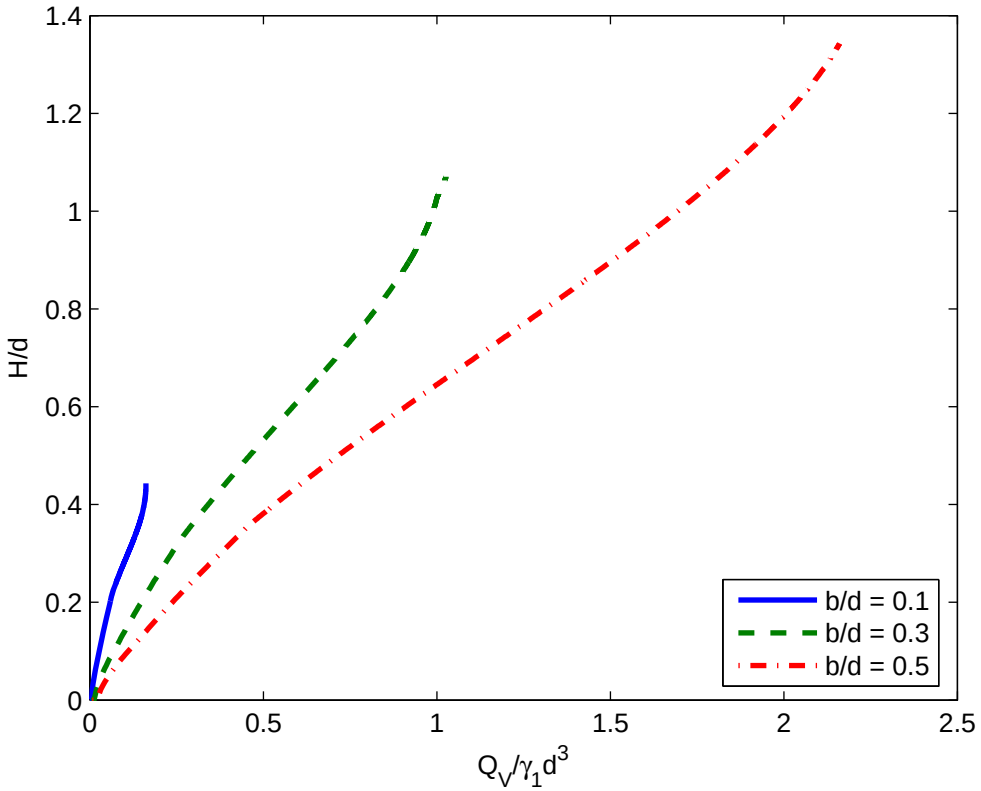

Figure 3.40. Influence depth versus wheel force for dense sand over weak clay and rolling, rigid wheel ($\phi_1 = 45°$, $c_2/\gamma_1 d = 0.5$)

where c_a depends on c_2/c_1 as shown in Fig. 3.41. No expression for c_a could be found, so a regression analysis was performed to obtain the following:

$$\frac{c_a}{c_1} = 0.321\left(\frac{c_2}{c_1}\right)^3 + 1.023\left(\frac{c_2}{c_1}\right)^2 + 1.08\left(\frac{c_2}{c_1}\right) + 0.621 \tag{3.80}$$

As with the previous case of sand overlying clay (Section 3.4.1), an expression for H may be obtained by setting the left-hand side of the inequality in Eq. (3.79) equal to the right-hand side and solving. The equivalent foundation parameters B, L, and D are again taken as in Eqs. (3.77) and (3.78). The resulting formula has the form $H = f_{clay}(c_1,c_2,b,d,s)$. The resulting formula is given in Appendix A.

As discussed in Section 3.4.1, H can ultimately be plotted versus Q_V by using the Q_V-s relationships from Section 3.2 (e.g., Eqs. (3.56) and (3.57) for the inclined footing method). An example of the resulting H-Q_V relationship is shown in Fig. 3.42. In the figure, Q_V is normalized by c_1d^2 rather than $\gamma_1 d^3$, since γ_1 vanishes in the formula for H. Comparison between Figs. 3.40 and 3.42 reveals that that the depth of influence H for the case of strong clay over weak clay is generally less (roughly one half) than in the case of the sand over weak clay (except for very small s).

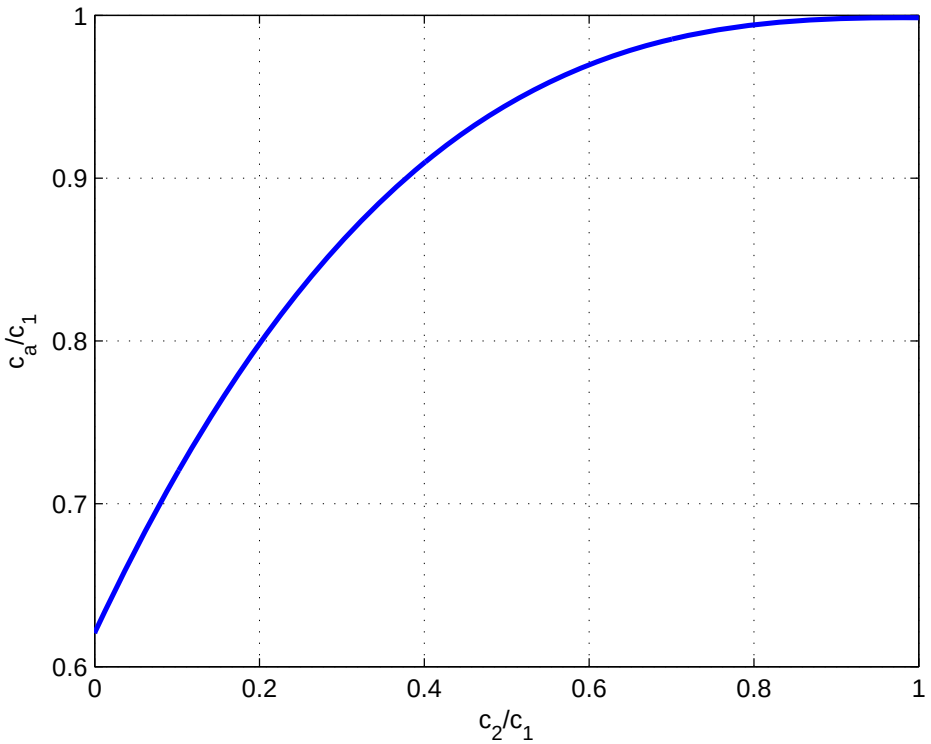

Figure 3.41. Variation of c_a/c_1 with c_2/c_1 for strong clay over weak clay (Das 1995)

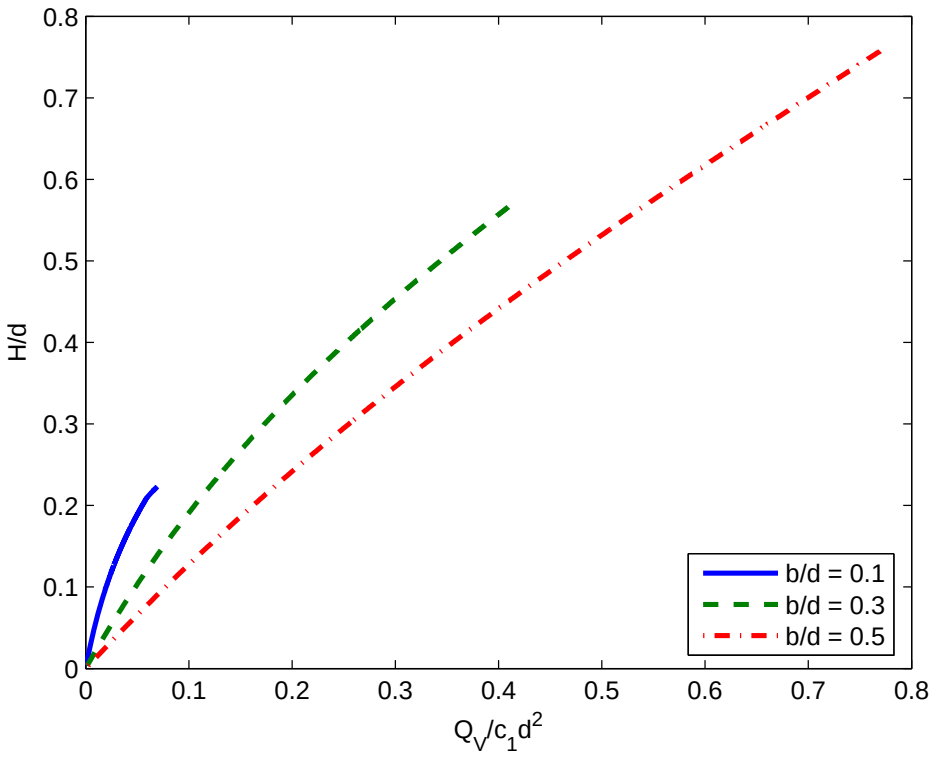

Figure 3.42. Influence depth versus wheel force for strong clay over weak clay and rolling, rigid wheel ($c_1/c_2 = 15$)

3.4.3 Weak Soil over Strong Soil

Eqs. (3.74) and (3.79) in the previous sections pertain to a strong layer overlying a weak layer. Meyerhof and Hanna (1978) also considered the case of a weak layer over a strong layer, however, the empirical nature of their work prohibits quantitative analysis for evaluating H in this case. According to Meyerhof and Hanna, H/B for weak soil over strong soil ranges from 1 for a clay to 2 for a sand with strip footings (B/L small). For circular footings ($B = L$), H/B is about 1 for all soil types. Since the footprint of a typical wheel at operating values of s is closer to a square ($B = L$) than a thin rectangle, $H/B = 1$ is likely a fair approximation. The influence depth H is then simply the foundation width B, given for a rolling rigid wheel by Eq. (3.77).

Employing the Q_V-s relationships from Section 3.2 (e.g., Eqs. (3.56) and (3.57)), plots of H versus Q_V may be obtained. In Fig. 3.43, the H-Q_V relationship is shown for a sand layer that is relatively weaker than the underlying layer of sand or clay. Fig. 3.44 is an example for clay that is weak relative to the underlying layer of sand or clay. The influence depth for the case of a weak layer over strong material is considerably less than in the case of a strong layer over a weak layer (Sections 3.4.1 and 3.4.2).

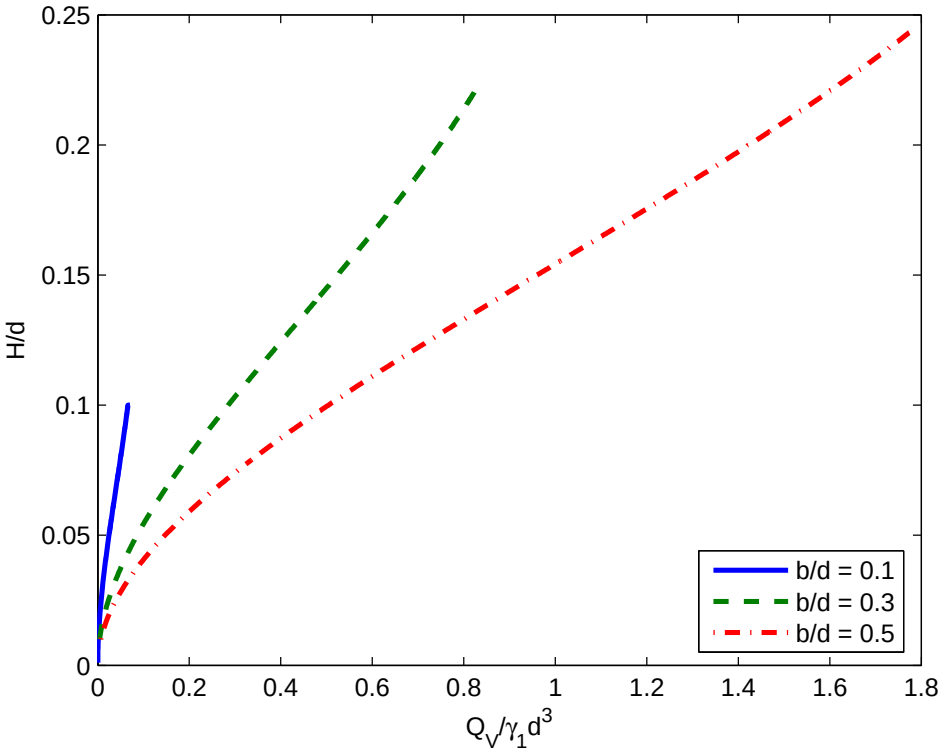

Figure 3.43. Influence depth versus wheel force for relatively weak sand (ϕ_1= 45º, c_1 = 0) overlying strong layer of sand or clay (rolling, rigid wheel)

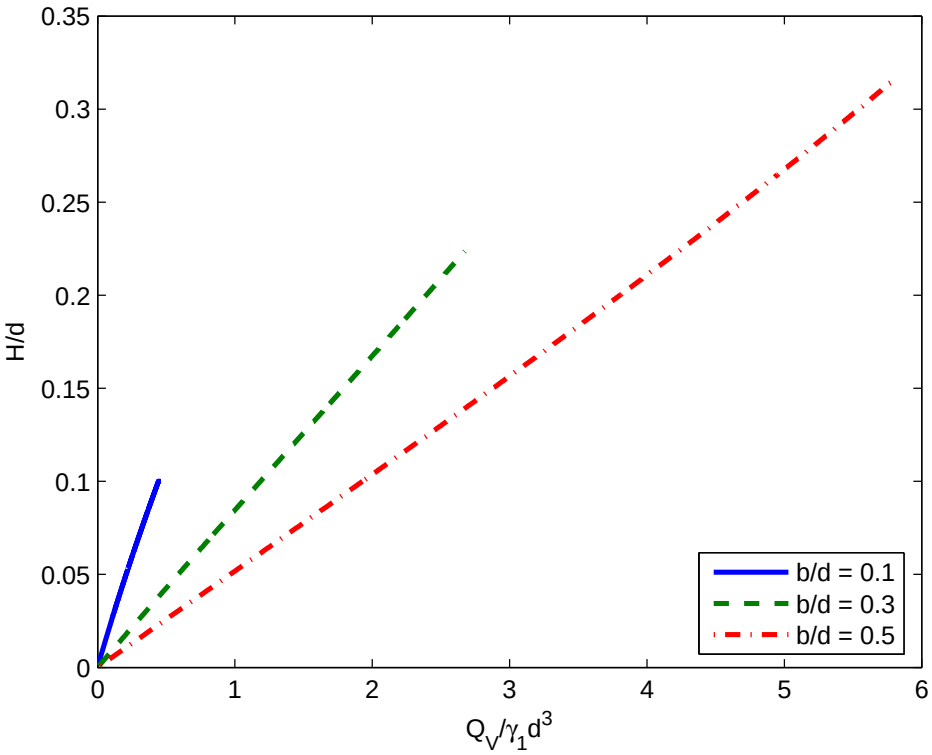

Figure 3.44. Influence depth versus wheel force for relatively weak clay (ϕ_1 = 0, $c_1/\gamma_1 d$ = 7.5) overlying strong layer of sand or clay (rolling, rigid wheel)

3.5 Remarks on Theoretical Models

In this chapter, analytic and numerical models for indentation and rolling of both rigid and flexible wheels were developed. The analytic method provides highly-desirable, closed-form predictions of wheel sinkage under loading but requires several simplifying approximations. The numerical simulation can accommodate many factors without the need for introducing the same approximations made in the analytic method, though the simulations are time-consuming and can only give case-wise results.

The analytic method is based on ultimate bearing capacity theory for shallow foundations, which itself possesses inaccuracies. In particular, appropriate forms for the shape, depth, and inclination factors, as well as the bearing capacity factor N_γ, are still a source of controversy. The factors used in design of foundations often tend to conservatively underestimate bearing capacity. It follows that further improvements to bearing capacity theory can be directly implemented in the context of the analytic method to refine the predictions.

In the analytic method, the theoretical expression derived for the equivalent footing depth D was (Section 3.2.1.1)

$$D = \frac{1}{6}\eta s \tag{3.81}$$

where η is given as a function of ϕ:

$$\eta = \frac{\sin\left(\frac{\pi}{4} - \frac{\phi}{2}\right)}{\sin\left(\frac{\pi}{4} + \frac{\phi}{2}\right)} e^{-\frac{\pi}{2}\tan\phi} \tag{3.82}$$

In relation to a wheel operating on soil, D is essentially accounts for resistance added by material displaced by the wheel and to some extent changes in the nature of the failure mechanism. Based on comparison with experimental data and numerical simulations (discussed in Chapter 7), the theoretical expression (3.81) appears to underestimate the added resistance of displaced material. This is particularly true for sands, where the assumption of associativity on which Eqs. (3.81) and (3.82) were derived leads to very small D. In the analytic formulas, D plays a minor role for cohesive materials ($\phi = 0$).

A reasonable correction to Eqs. (3.81) that is justified by the numerical simulations and experimental results is simply to replace η with a fixed constant. In the case of sand, taking η as a constant is akin to saying that the material is completely non-associated ($\psi = 0$), which is closer to reality for most sands. Comparison between predictions using the analytic method and results from experiments and numerical simulations revealed that $\eta = 6$ is an apt choice for η. The resulting formula for $\bar{D}$, the modified equivalent foundation depth, is simple and reasonable:

$$\bar{D} = s \tag{3.83}$$

This modification to the analytic method can be regarded as a "fine tuning" of the model to obtain a quantitative agreement with experiments. The overall trends in the predictions (discussed in Chapter 4) are not affected by D. The plots pertaining to the analytic method in Chapter 4, Appendix H, and Appendix I were generated using D as in Eqs. (3.81) and (3.82). The plots in Chapter 7 are with $\bar{D}$ as in Eq. (3.83).

Chapter 4

Parametric Study

In this chapter, parametric study is performed on the theoretical models developed in Chapter 3 to understand the effects of soil mechanical properties, wheel load, wheel geometry, soil layering, and other effects on the wheel penetration of a test roller. As in Chapter 3, both indentation and steady-state rolling processes were investigated, as the former may have applicability in the initial stages of soil failure and is used for extension and comparison to the rolling case.

A rigid, right-cylindrical wheel was considered in the parametric analysis, although the theoretical models were developed to accommodate wheel flexibility. A rigid (or nearly rigid) wheel is the preferred wheel type for test rolling, and it is believed that one of the foremost improvements to the current Mn/DOT test roller (Minnesota 2000) will be to change from a pneumatic tire to a rigid wheel. Wheel flexibility adds tremendous difficulty to the analysis and only obscures field measurements.

Two separate approaches to modeling the test rolling problem were presented in Chapter 3: an analytic method and numerical simulations using the finite element code ABAQUS. Section 4.1 discusses the parameters which enter into the two formulations. In Section 4.2, important implications of the theoretical models are discussed. In Sections 4.3 and 4.4, the effects of the various parameters in the theoretical models are discussed in detail. Some comparison between results obtained with the analytic method and the numerical simulations is also given in Section 4.5. A short summary of findings from the parametric analysis and additional comments are in Section 4.6.

4.1 Model Parameters

4.1.1 Analytic Method

The analytic method developed in Chapter 3 has the following form, considering a rigid wheel:

$$s = F\left(Q_V, \phi, c, \gamma, b, d\right) \tag{4.1}$$

where Q_V is the vertical component of wheel force (wheel weight), ϕ is the Mohr-Coulomb angle of internal friction, c is Mohr-Coulomb cohesion, γ is soil unit weight, b is wheel width, and d is wheel diameter. The particular function F in (4.1) is different for the indentation and rolling processes. A dimensionless form for Eq. (4.1) that was used in Chapter 3 is

$$\frac{s}{d} = \Pi\left(\frac{Q_V}{\gamma d^3}, \phi, \frac{c}{\gamma d}, \frac{b}{d}\right) \tag{4.2}$$

The dimensionless variables in (4.2) are used where appropriate throughout this section. The total number of parameters is reduced from 7 in the dimensional form to 5 in the dimensionless form. With fewer variables to consider, the parametric analysis is simpler in terms of the dimensionless variables.

The dimensionless variables are significant in terms of how the test rolling problems scales. Consider, for example, the following two test rolling scenarios:

1. Q_V = 68 kN (7.6 tons), d = 1.5 m (60 in.), and b = 0.45 m (18 in.) operating on a soil with ϕ = 10º, c = 60 kPa (8.7 psi), and γ = 20 kN/m^3 (127 pcf)
2. Q_V = 11 kN (1.2 tons), d = 0.9 m (36 in.), and b = 0.3 m (12 in.) operating on a soil with ϕ = 10º, c = 27 kPa (4 psi), and γ = 15 kN/m^3 (95 pcf)

Using Eqs. (3.56) and (3.57) for rigid wheel rolling, s = 55 mm (2.2 in.) for the first test roller and s = 33 mm (1.3 in.) for the second test roller. These two seemingly dissimilar problems can be reduced to a single set of dimensionless variables: s/d = 0.036, $Q_V/\gamma d^3$ = 1, γ = 30º, $c/\gamma d$ = 2, and b/d = 0.3. Specifying all the dimensional variables separately is therefore unnecessary. The dimensionless parameters, sometimes called *similarity variables*, contain the core information of the problem and do not dependent on a choice for units of measurement.

Only the inclined footing approach to the rolling problem (Section 3.2.2.2) was used in the parametric study, as it is believed to more correctly reflect the physics of the rolling wheel problem and ultimately provides better agreement with results from experiments and numerical simulation.

4.1.2 Numerical Simulations

As a result of the material models and soil-wheel interface properties used in the numerical simulations (see Sections 3.1 and 3.3), the results of the numerical simulations for a rigid wheel have the following form:

$$s = F\left(Q_V, \phi_{DP}, c_{DP}, E_s, \nu_s, \gamma, b, d, \mu\right) \tag{4.3}$$

where ϕ_{DP} is the Drucker-Prager angle of internal friction, c_{DP} is the Drucker-Prager cohesion, E_s is the soil Young's modulus, ν_s is the soil Poisson's ratio, and μ is the coefficient of friction at the soil-wheel interface. As discussed in Section 3.3, a non-zero fillet radius r_f (not included in Eq. (4.3)) is also required in the numerical simulations, which was assumed to be $r_f \approx b/12$.

Reducing Eq. (4.3) to a dimensionless form similar to the one considered for the analytic emthod (Section 4.1.1) gives

$$\frac{s}{d} = \Pi\left(\frac{Q_V}{\gamma d^3}, \phi_{DP}, \frac{c_{DP}}{\gamma d}, \frac{E}{\gamma d}, \nu, \frac{b}{d}, \mu\right) \tag{4.4}$$

The parameters in (4.4) are used throughout the remainder of the report for the numerical simulations.

While the analytic approach gives results for any combination of ϕ and c, the numerical simulations cannot be used to predict behavior for purely frictional soils with $c_{DP} = 0$ due to computational instabilities that result in the plasticity reduction algorithm. The cohesion c_{DP} in the parametric study was therefore restricted to values greater than zero.

4.1.3 Typical Values

This section summarizes the range of values of the critical variables entering into the theoretical models. Table 4.1 gives the tire size specified for the current Mn/DOT test roller (Minnesota 2000), as well as some other typical tire sizes. Tables 4.2 and 4.3 give values of c and ϕ for naturally occurring cohesive ($\phi = 0$) and frictional soils ($c = 0$), respectively. Table 4.4 summarizes strength data obtained through triaxial compression tests by Swenson et al. (2006) for several fine-grained soils with moisture contents and densities typically encountered in road construction. Table 4.5 summarizes strength data acquired from triaxial compression tests by Davich et al. (2004) for several granular soils containing fine particles (2% to 21% by mass). Table 4.6 gives typical values of E_s from Das (1995).

The data collected by Davich et al. was also for moisture contents and densities representative of values occurring in the field. The parameters ϕ and c obtained by Swenson et al. and Davich et al. were based on a limited quantity of data, as the focus of these studies was on soil resilient modulus and not soil strength. In some cases, only two triaxial compression tests were conducted to estimate both ϕ and c (the minimum number of tests required), and the accuracy of the values is somewhat questionable as a result. Nevertheless, the data is helpful in indicating the range of ϕ and c.

Based on the data listed in Tables 4.2-4.6 and personal communication with the Mn/DOT Office of Materials, the values shown in Table 4.7 were considered as the basis for parametric study.

Table 4.1. Typical tire sizes

wheel type	**width, *b* (m)**	**diameter, *d* (m)**
current Mn/DOT test roller	~ 0.5	~ 1.5
light truck	0.25	0.8
commercial truck	0.3	1.1
articulated and rigid hauling trucks	0.7	2.2

Table 4.2. Consistency and c for naturally occurring cohesive soils with $\phi = 0$ (Das 1983)

consistency	***c* (kPa)**
very soft	0 to 12
soft	12 to 24
medium	24 to 48
stiff	48 to 96
very stiff	96 to 192
hard	> 192

Table 4.3. Typical values of ϕ for naturally occurring frictional soils with $c = 0$ (Das 1983)

type of soil	**ϕ (deg)**
sand: round grains	
loose	28 to 30
medium	30 to 35
dense	35 to 38
sand: angular grains	
loose	30 to 35
medium	35 to 40
dense	40 to 45
sandy gravel	34 to 48

Table 4.4. Statistics on ϕ and c from fine-grained soils tested by Swenson et al. (2006)

	ϕ (deg)	**c (kPa)**
minimum	18	23
maximum	57	212
mean	36	100

Table 4.5. Statistics on ϕ and c from sands (with fine particles) tested by Davich et al. (2004)

	ϕ (deg)	**c (kPa)**
minimum	39	0
maximum	60	56
mean	49	20

Table 4.6. Range of Young's modulus from Das (1995).

material	E_s (MPa)	
	min	max
loose sand	10	24
dense sand	34	55
silty sand	10	17
soft clay	4	21
stiff clay	41	97

Table 4.7. Range of material parameters considered as basis for parametric study

soil type	c (kPa)			ϕ (deg)			E (MPa)		
	min	typical	max	min	typical	max	min	typical	max
cohesive	20	100	200	0	30	50	15	50	125
granular	0	20	50	30	45	60	20	55	130

4.2 General Aspects of Theoretical Models

In Chapter 3, emphasis was placed on obtaining force-sinkage relationships for given wheel geometry and soil properties. Example force-sinkage predictions using the analytic method for indention are shown in Fig. 4.1. It was natural in Chapter 3 to plot Q_V versus s since the derived formulas give Q_V as an explicit function of s, and s cannot be written explicitly in terms of the other variables. However, s is the primary variable of interest in test rolling. For this reason, s is usually plotted versus Q_V where the force-sinkage relationship is discussed in this chapter.

Furthermore, wheel force is fixed during test rolling (according to the weight of the test roller), such that the force-sinkage relationship as such is usually not of particular interest. Of interest in test rolling is the relationship between soil properties and sinkage for a given wheel force. This relationship is also embedded in the analytic method, and plots such as Fig. 4.2 that show sinkage as a function of soil properties may be easily obtained. Note that the corresponding points in Figs. 4.1 and 4.2 have been marked as asterisks to illustrate the connection between the data in the plots. A tremendous advantage of the analytic method over the numerical simulations is that plots such as Fig. 4.2 can be readily generated for an arbitrary set of parameters. A numerical simulation is capable of giving only a single point in a plot like Fig. 4.2, because soil properties are necessarily fixed in each simulation.

For illustrative purposes, the data in Fig. 4.2 is reproduced in Fig. 4.3 except given in terms of the dimensionless parameters discussed in Section 3.1. Examination reveals that the same information is contained in the two figures.

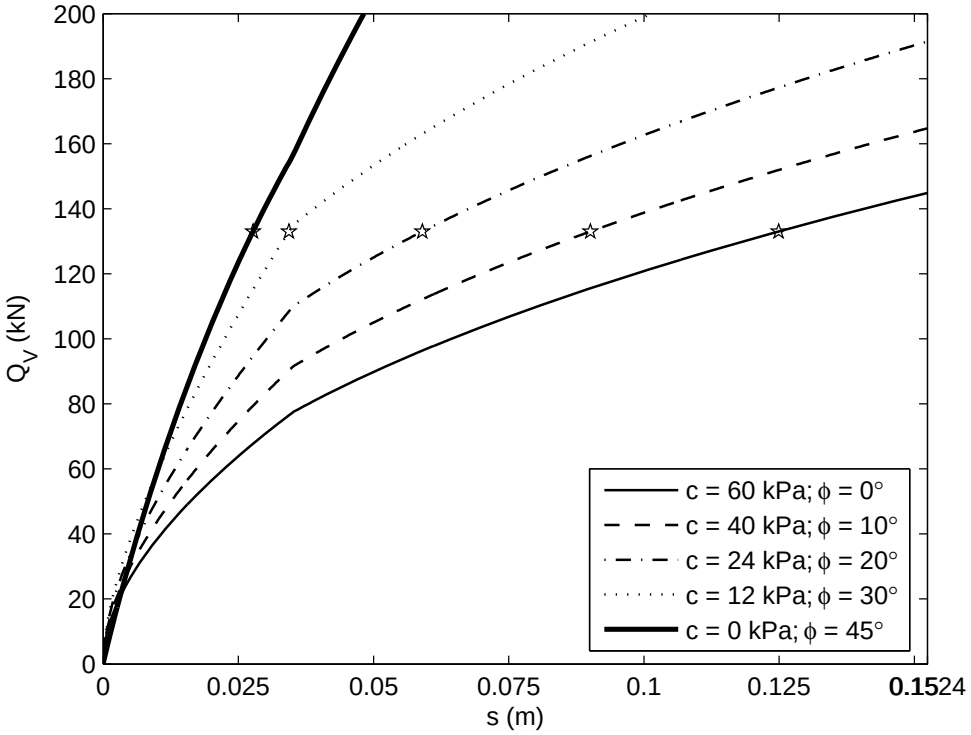

Figure 4.1. Force versus sinkage using analytic method for indentation (d = 1.52 m, b = 0.457 m, and γ = 20 kN/m^3)

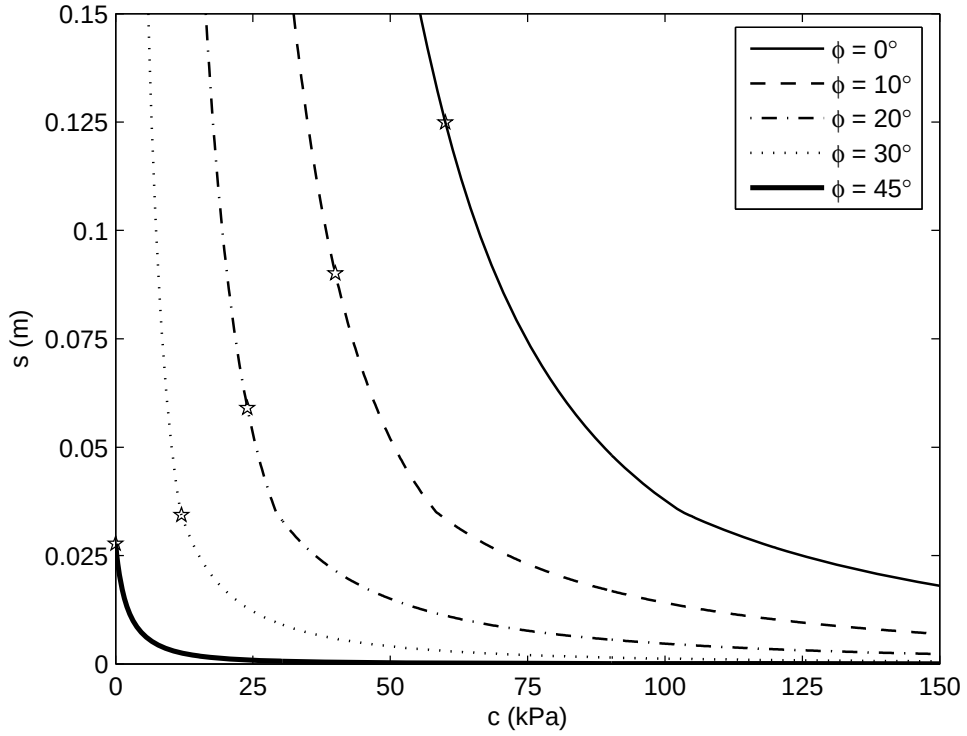

Figure 4.2. Sinkage versus soil properties using analytic method for indentation (Q_V = 133 kN, d = 1.52 m, b = 0.457 m, and γ = 20 kN/m^3)

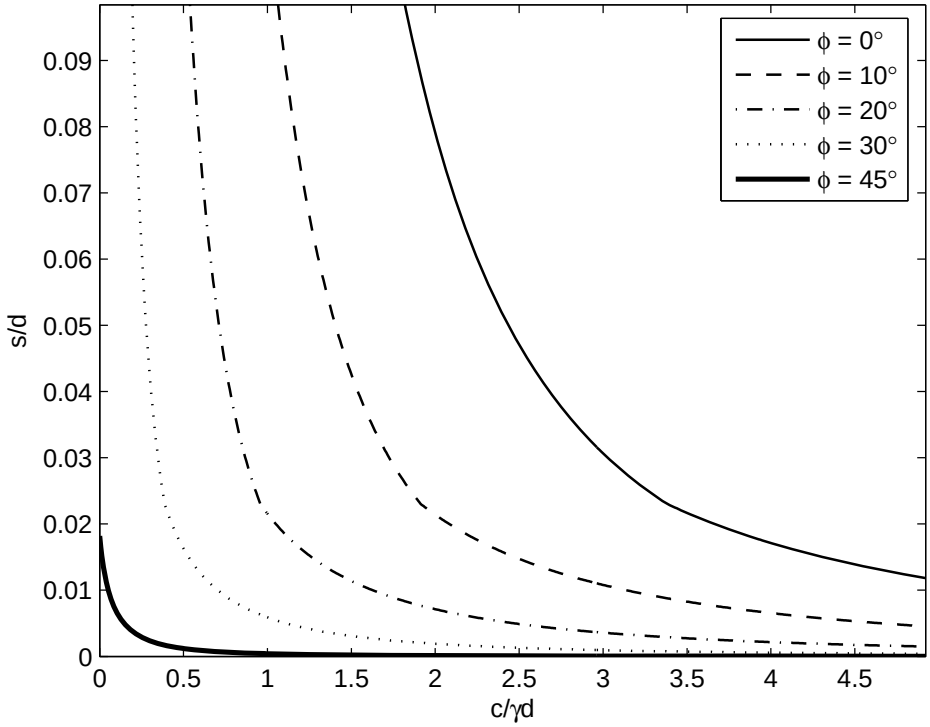

Figure 4.3. Dimensionless sinkage versus soil properties using analytic method for indentation ($Q_V/\gamma d^3 = 1.88$ and $b/d = 0.3$)

A numerical simulation of indentation gives a nearly continuous force-sinkage relationship such as those in Fig. 4.1. For rolling, two different types of numerical simulation were employed, as described in Section 3.3.2. In the first type, a constant value of Q_V was applied to the wheel, and the wheel rolled from a stiff region of soil into a soft region. An end result of this first type of simulation is a single value of steady-state s corresponding to the specified Q_V. In the second type of simulation, the wheel was displaced into the soil at a specified rate in order to obtain a complete Q_V-s history. This second type of simulation was used extensively in the parametric study to facilitate extraction of more information from the simulations.

To conveniently present and manipulate the results of the numerical simulations, the force-sinkage data from each simulation was fitted with a curve of the form

$$\frac{Q_V}{\gamma d^3} = \kappa_1 \sqrt{\frac{s}{d}} + \kappa_2 \frac{s}{d} + \kappa_3 \left(\frac{s}{d}\right)^2 + \kappa_4 \left(\frac{s}{d}\right)^3 \tag{4.5}$$

where κ_1, κ_2, κ_3, and κ_4 are constants determined from least-squares fitting. The form (4.5) could accurately capture the results from the numerical simulations for both indentation and rolling. Figs. 4.4-4.6 show the data obtained from numerical simulation and the corresponding curve fit for several different cases.

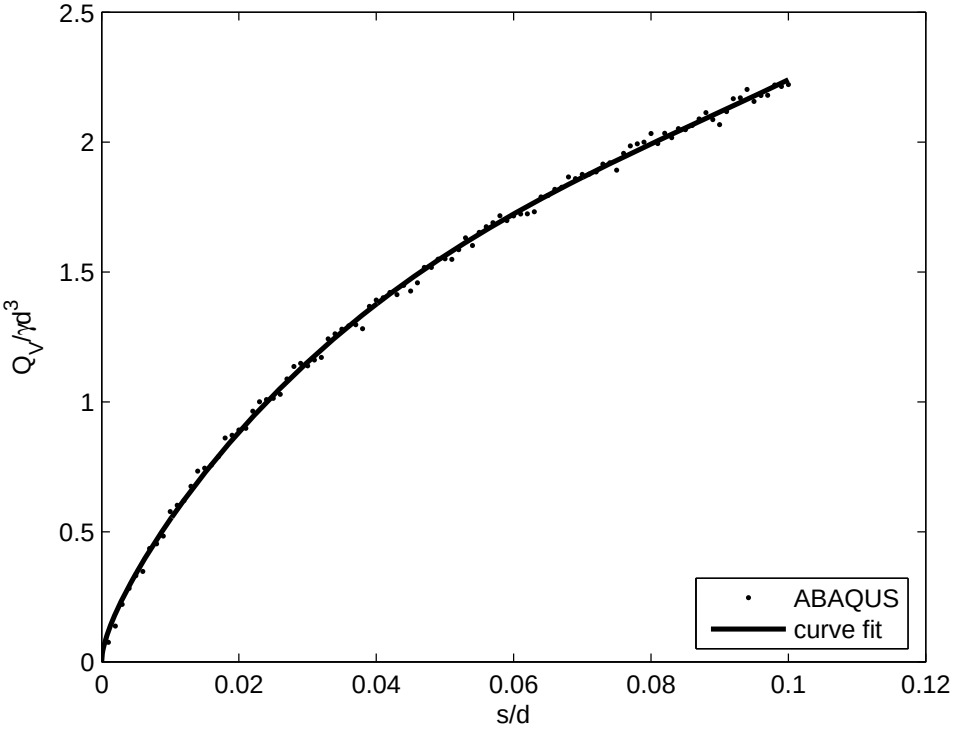

Figure 4.4. Force-sinkage output from simulation of indentation on cohesive soil ($b/d = 0.3$, $\phi_{DP} = 0$, $c_{DP}/\gamma d = 3.3$, $E/\gamma d = 1300$, $\nu = 0.35$, $\mu = 0.8$)

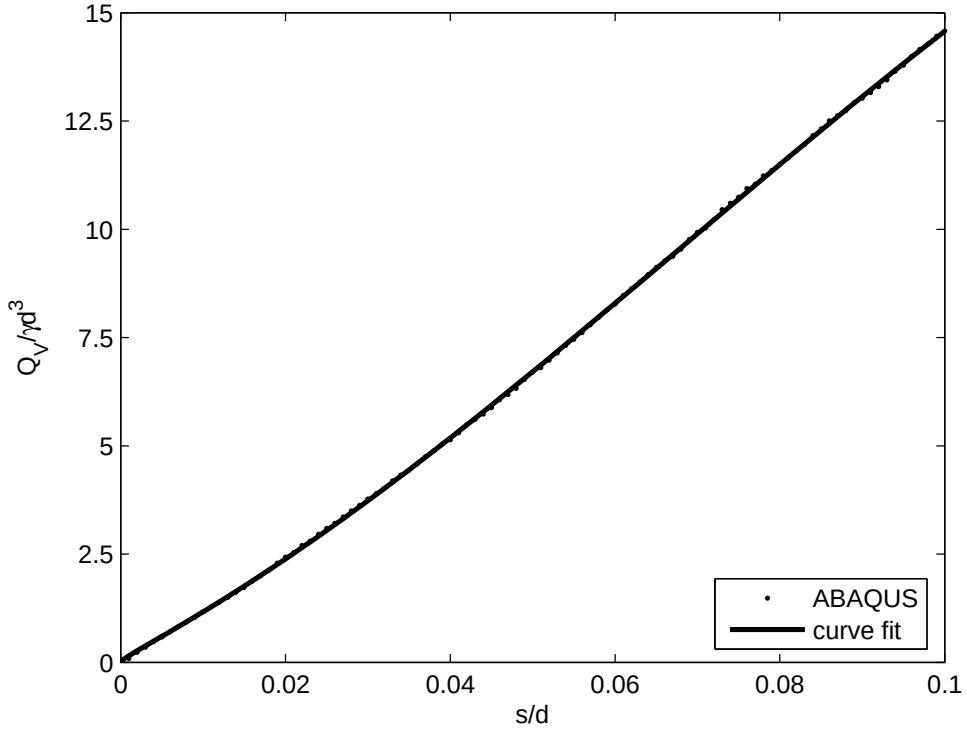

Figure 4.5. Force-sinkage output from numerical simulation of indentation on frictional soil ($b/d = 0.3$, $\phi_{DP} = 55.2°$, $c_{DP}/\gamma d = 0.98$, $E/\gamma d = 1300$, $\nu = 0.35$, $\mu = 0.8$)

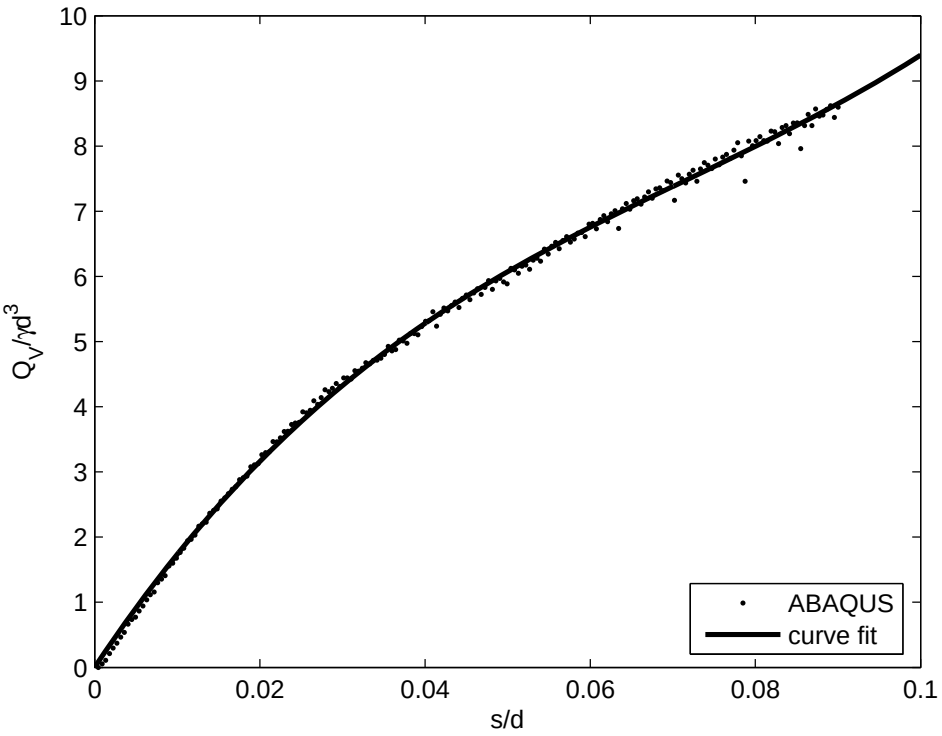

Figure 4.6. Example force-sinkage output from numerical simulation of rolling on frictional soil ($b/d = 0.3$, $\phi_{DP} = 27.5°$, $c_{DP}/\gamma d = 12.8$, $E/\gamma d = 1300$, $\nu = 0.35$, $\mu = 0.8$)

4.3 Effect of Parameters: Analytic Method

4.3.1 Indentation

Fig. 4.7 shows the relationship between s and soil properties for $Q_V/\gamma d^3 = 1$ and $b/d = 0.3$, as predicted using the analytic method for indentation. While the wheel load and wheel geometry impact the specific value of the s, the form of the curves in Fig. 4.7 is always essentially the same. Namely, the sinkage drops very sharply with increasing c along any of the curves of constant ϕ. In other words, a small addition of cohesion to a soil dominated by friction reduces the sinkage tremendously. A small addition of friction to a soil with large cohesion (the right side of Fig. 4.7) does not, however, have such a significant impact on the sinkage.

Notice in Fig. 4.7 how several of the curves of constant ϕ intercept the y-axis. The intercept is the sinkage for a purely fictional soil ($c = 0$). When ϕ is large, the pronounced effect of a small variation in ϕ is evident in the figure. For example, the change in s between $\phi = 35°$ and $\phi = 40°$ is $\Delta s/d \approx 0.06$. This is a considerable amount, owing to a mere 5° change in the friction angle.

In Fig. 4.8, the wheel force is doubled from $Q_V/\gamma d^3 = 1$ (as in Fig. 4.7) to $Q_V/\gamma d^3 = 2$. As should be expected, the sinkage increases substantially. Twice the wheel force, however, does not necessarily result in twice the sinkage. In the analytic method, Q_V depends (roughly) on the square root of the sinkage when $\phi = 0$, such that 2 times the wheel force results in around 4 (2^2) times the sinkage. With $c = 0$, Q_V does vary almost linearly with the sinkage, so that 2 times the wheel force results in roughly 2 times the sinkage.

Fig. 4.9 shows the effect of reducing the wheel width to $b/d = 0.1$. Again, reducing the wheel width by a factor of 3 does not necessarily increase the sinkage by a factor of 3. This can be attributed to the fact that the *force* roughly decreases linearly with a decrease in the width (at constant sinkage), and Q_V varies with the sinkage as mentioned previously (e.g., $Q_V \sim s^{1/2}$ for $\phi = 0$ and $Q_V \sim s$ for $c = 0$).

Fig. 4.10 compares two sets of force-sinkage curves to illustrate the effect of the soil unit weight (showing the effect is more difficult in a plot like Fig. 4.7). The curves with the heavy lines are computed with a unit weight that is 0.7 times the unit weight used to compute the fine lines (e.g., $\gamma = 14$ kN/m^3 (90 pcf) versus $\gamma = 20$ kN/m^3 (130 pcf)). The figure shows that there is virtually no difference in the force-sinkage relationship for cohesive soils but that the unit weight is important for purely frictional materials. This comes as no surprise, since unit weight is required for purely frictional materials to have any strength. For frictional materials, the analytic method predicts that the wheel force should scale linearly with the unit weight. This is reflected in the figure by the curves with $c = 0$, in which the wheel force is reduced by 70% with the 70% reduction in unit weight at a given sinkage.

In Appendix H, numerous dimensional plots which were generated using the analytic method for indentation are shown. In these figures, the dimensional parameters are varied independently to lend more physical insight into their effects, since dimensionless parameters are not particularly convenient for practical application.

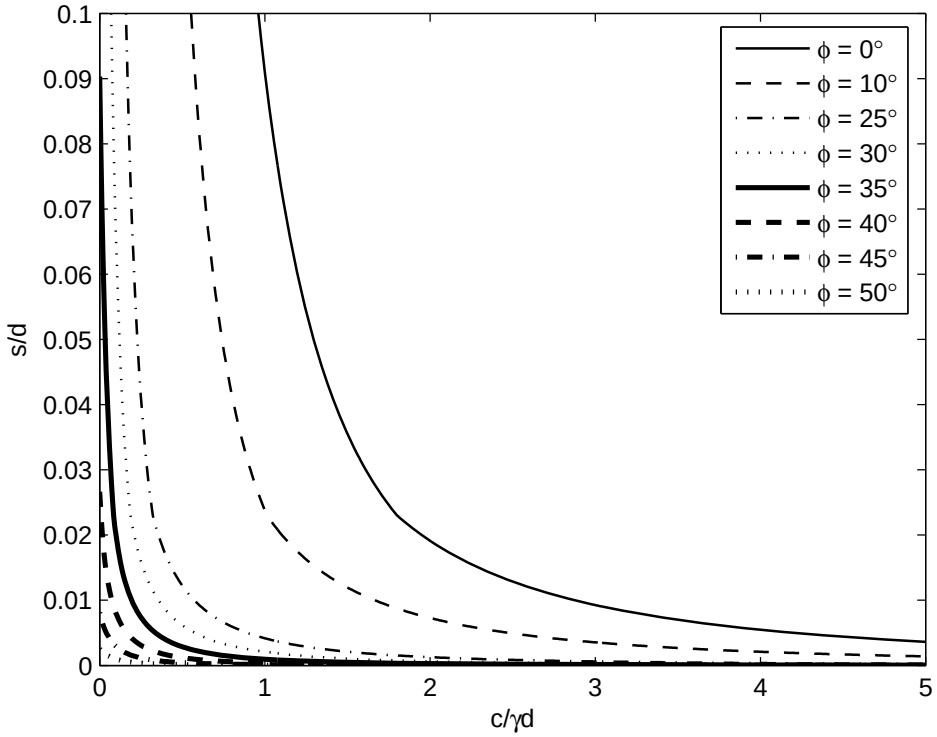

Figure 4.7. Sinkage predicted using analytic method for indentation with $Q_V / \gamma d^3 = 1$ and $b/d = 0.3$

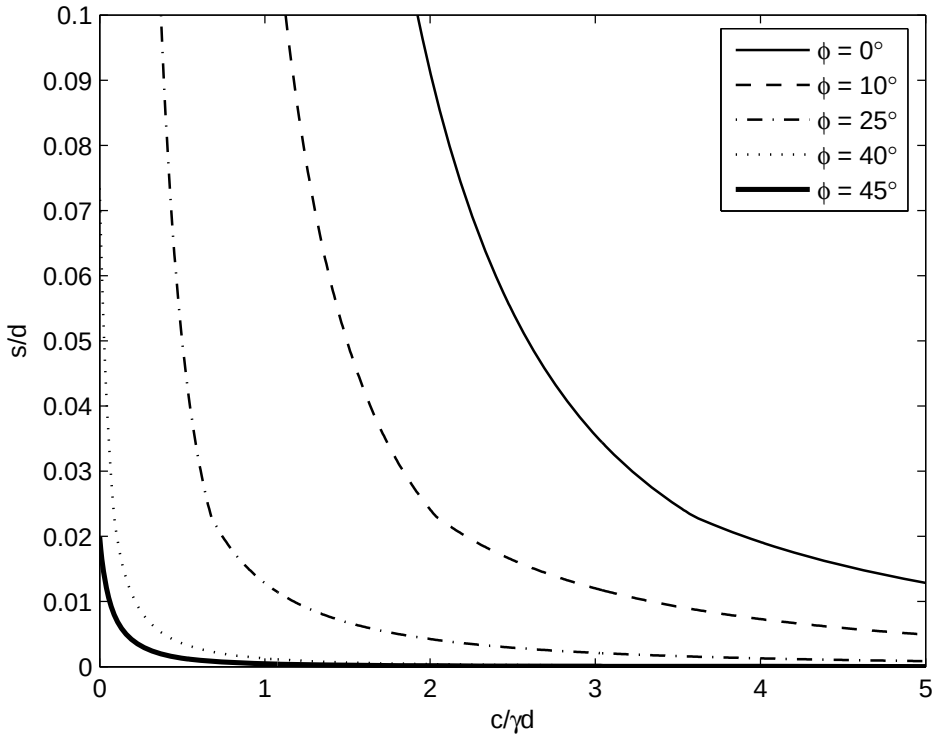

Figure 4.8. Sinkage predicted using analytic method for indentation with $Q_V / \gamma d^3 = 2$ and $b/d = 0.3$

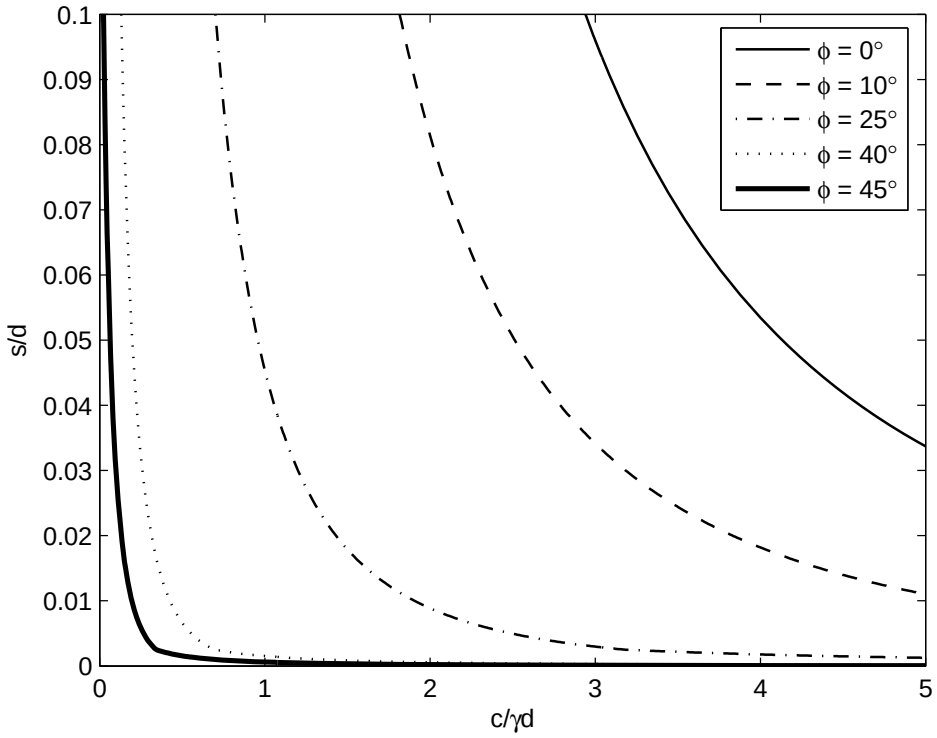

Figure 4.9. Sinkage predicted using analytic method for indentation with $Q_V / \gamma d^3 = 1$ and $b/d = 0.1$

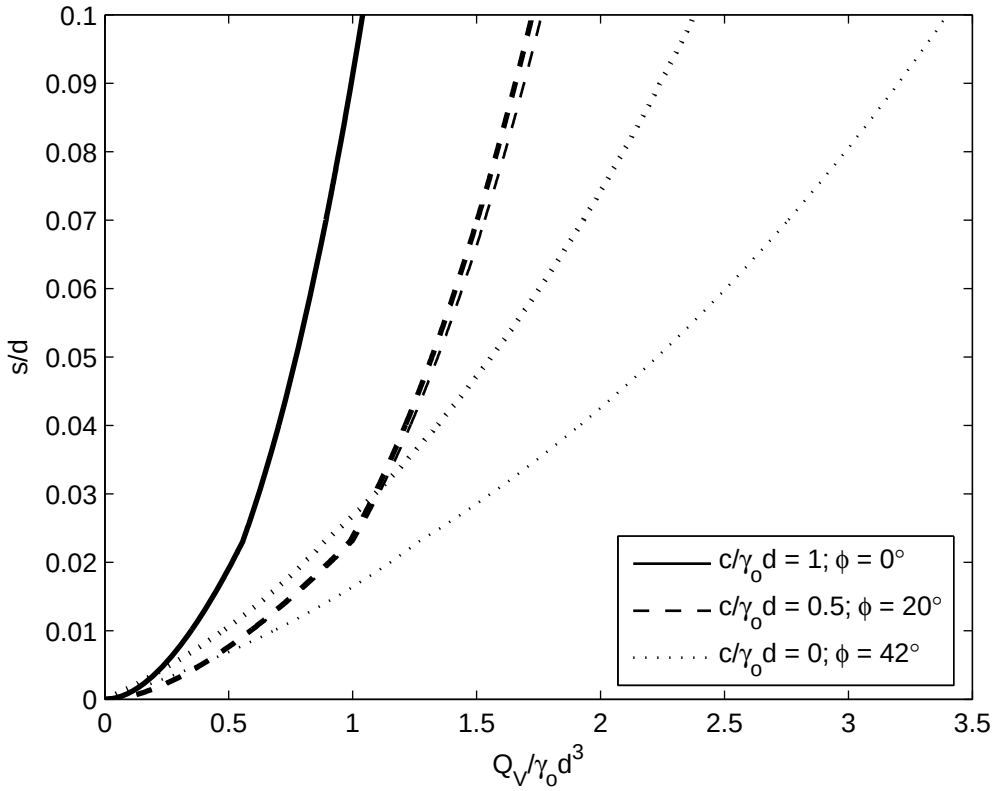

Figure 4.10. Effect of unit weight in analytic method for indentation; fine lines are with $\gamma = \gamma_o$ and heavy lines are with $\gamma = 0.7\gamma_o$ ($b/d = 0.3$)

4.3.2 Rolling

The essential differences between indentation and steady-state rolling are that the contact area is reduced (assumed to be half that from the analogous indentation process) and that the total force is inclined. Both of these have the effect of increasing sinkage at a given wheel force as compared with indentation, with the reduced contact area having a stronger effect than the effect of inclining the force. Fig. 4.7 and 4.11 are plotted using the same parameters, where Fig. 4.11 is for steady state rolling. The sinkage is significantly larger in Fig. 4.11 due to the reduced contact area and inclination of the wheel force, but the trends in the sinkage with respect to ϕ and c are very similar.

While there are some subtle differences arising between the analytic predictions for indentation and rolling, Figs. 4.11-4.13 show the wheel force and wheel width have similar effects on steady-state rolling as they do for indentation. Unit weight has the same effect for both indentation and rolling, as well.

As with indentation, numerous dimensional plots generated using the analytic method for steady-state rolling are in Appendix I to show the effect of varying the parameters in practical terms.

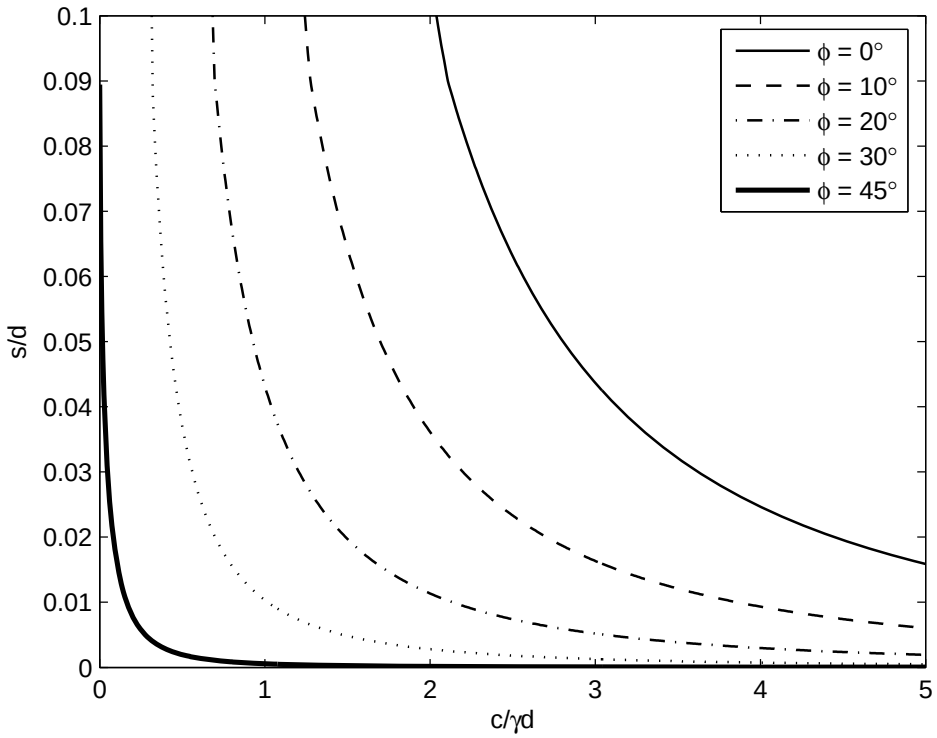

Figure 4.11. Sinkage predicted using analytic method for rolling with $Q_V / \gamma d^3 = 1$ and $b/d = 0.3$

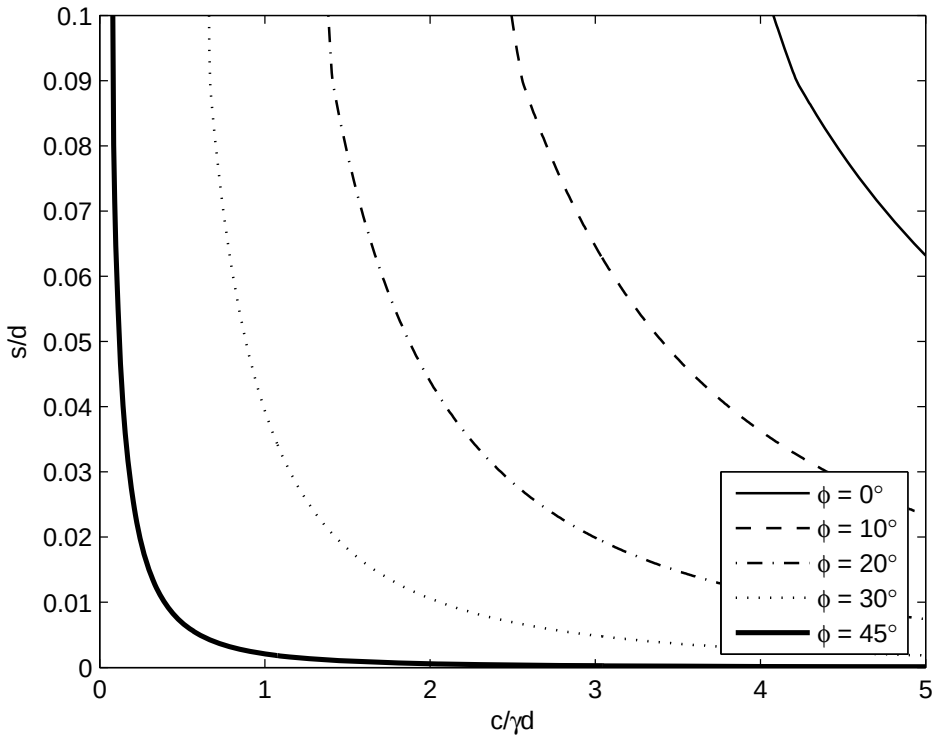

Figure 4.12. Sinkage predicted using analytic method for rolling with $Q_V / \gamma d^3 = 2$ and $b/d = 0.3$

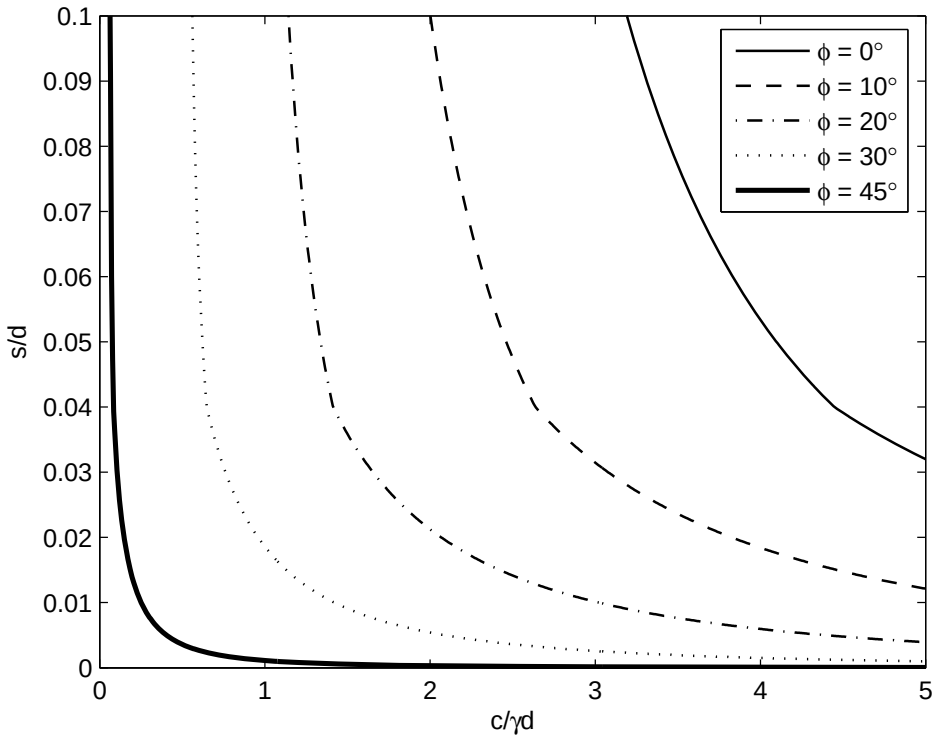

Figure 4.13. Sinkage predicted using analytic method for rolling with $Q_V / \gamma d^3 = 1$ and $b/d = 0.2$

4.4 Effect of Parameters: Numerical Simulations

4.4.1 Material Properties

Table 4.8 gives the materials parameters used in the numerical simulations. These parameters were chosen based on the range of parameters in Table 4.7. Note that the instance $c = 0$ could not be investigated in the numerical simulations because of issues regarding computational stability. Also, the Young's modulus never exceeded 60 MPa (although the maximum is listed as 130 MPa in Table 4.7) because the difference in computational results was found to be negligible for larger moduli and computation times are greatly increased with large elastic moduli due to the particular solution scheme used. The Mohr-Coulomb strength parameters in Table 4.8 were translated into Drucker-Prager strength parameters (c_{DP} and ϕ_{DP}) by matching at a point between triaxial compression and extension.

4.4.2 Indentation

Numerical simulations of indentation were performed for 30 different cases to evaluate the effect of soil properties, wheel geometry, and soil-wheel interface friction. The parameters used in the simulations are tabulated in Appendix B. A table giving the Mohr-Coulomb parameters that match the Drucker-Prager parameters in triaxial compression is also included in Appendix B for reference. The correlation coefficients determined for each of the cases (according to Eq. (4.5)) are in Appendix E. Case numbers 1-12 were run to investigate the effect of the strength parameters ϕ_{DP} and c_{DP} (Table 4.8 with $E = 40$ MPa). Cases 2, 5, 8, 10, and 12 are also used as the basis for comparison when varying remaining parameters. In cases 13-27, the interface friction, unit weight, and wheel width are varied (the effect of Young's modulus was investigated only in the rolling cases due to computational expense).

Table 4.8. Material properties considered in parametric study with numerical simulations

c (kPa) / ϕ (deg)	**0**	**20**	**50**	**100**	**200**
0			$E = 40$ MPa	$E = 15$; 40; 60 MPa	$E = 40$ MPa
15			$E = 40$ MPa	$E = 15$; 40; 60 MPa	$E = 40$ MPa
30		$E = 40$ MPa	$E = 15$; 40; 60 MPa	$E = 40$ MPa	
45		$E = 15$; 40; 60 MPa	$E = 40$ MPa		
60		$E = 15$; 40; 60 MPa			

Fig. 4.14 shows the results of indentation simulations 1-12 for $Q_V/\gamma d^3 = 2$. Each simulation generated a single curve of force versus sinkage, but the figure, which gives s as a function of ϕ_{DP} and c_{DP} for a given wheel weight, is a convenient way of looking at the data (as in Section 4.3). The figure is the counterpart of Fig. 4.8, which was generated using the analytic method. The same trends that appeared in Fig. 4.8 are clearly visible in Fig. 4.14, and similar conclusions as were discussed in Section 4.3.1 may be drawn regarding the trends resulting from variations in ϕ_{DP} and c_{DP}.

Fig. 4.15 shows the numerical results at half the wheel force as in Fig. 4.14. As with the analytic prediction, the sinkage is significantly less at half the force, and it is clear that this has a different effect depending on the material properties. For the material with $\phi_{DP} = 0$ and $c_{DP}/\gamma d = 3.3$, the sinkage is reduced by a factor of 4 by reducing the wheel force by a factor of 2. For the more frictional materials, the sinkage reduces by a factor of 2 when the wheel force is halved. In this regard, variation in the wheel force shows a similar effect in the numerical simulations as in the analytic method. However, if we look at the cohesive material with $\phi_{DP} = 0$ and $c_{DP}/\gamma d = 13.1$, the sinkage also reduces by a factor of 2. This is most likely due to elasticity, which has some effect at very small s.

Fig. 4.16 shows the effect of reducing the interface friction coefficient from $\mu = 0.8$ to $\mu = 0.4$. The figure shows that the decrease in interface friction tends to slightly increase the sinkage (0 to 4%), having a greater effect at large sinkage. The minor differences suggest that the coefficient of interface friction is a relatively unimportant parameter.

Fig. 4.17 illustrates that unit weight also has very little influence on the sinkage for a given wheel force (0 to 2%). As with the prediction from the analytic method, the unit weight affects frictional materials more than cohesive materials (this is more evident when Fig. 4.17 is plotted over a larger range of $Q_V/\gamma d^3$, though such loads are impractically large). The cohesion could not be taken small enough in the numerical simulations to see how the unit weight affects a purely frictional material ($c_{DP} = 0$).

Fig. 4.18 shows the increase in sinkage resulting from a decrease in wheel width (from $b/d = 0.3$ to $b/d = 0.2$). Decreasing the wheel width by a factor of 1.5 causes the sinkage to increase by a factor of 1.3 to 1.8 for a given wheel force. Like the analytic predictions, the extent of the effect of varying the wheel width depends on the material properties: frictional materials are less affected by the wheel width than cohesive materials.

The effect of Poisson's ratio is shown in Fig. 4.19. The figures reveal that the Poisson's ratio is not a particularly important parameter, although it does affect the process when the sinkage is small and elastic effects are significant. An increase in Poisson's ratio decreases the sinkage slightly, especially at relatively low wheel forces.

Figs. 4.14-4.19 are reproduced in Appendix J in terms of dimensional parameters for convenience.

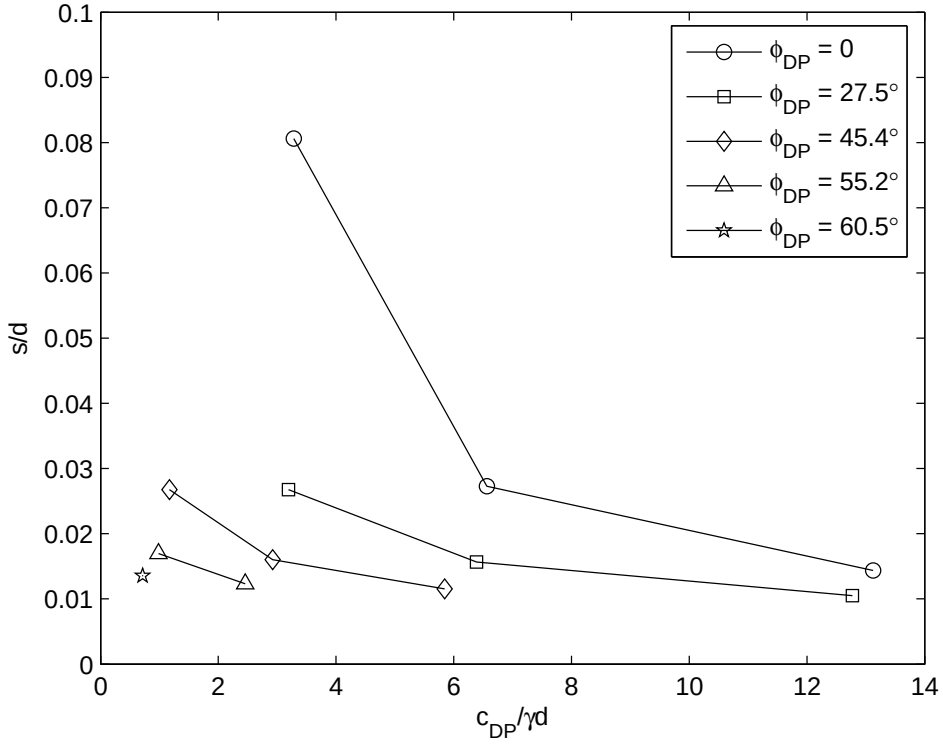

Figure 4.14. Sinkage from numerical simulations of indentation; cases 1-12; $Q_V/\gamma d^3 = 2$

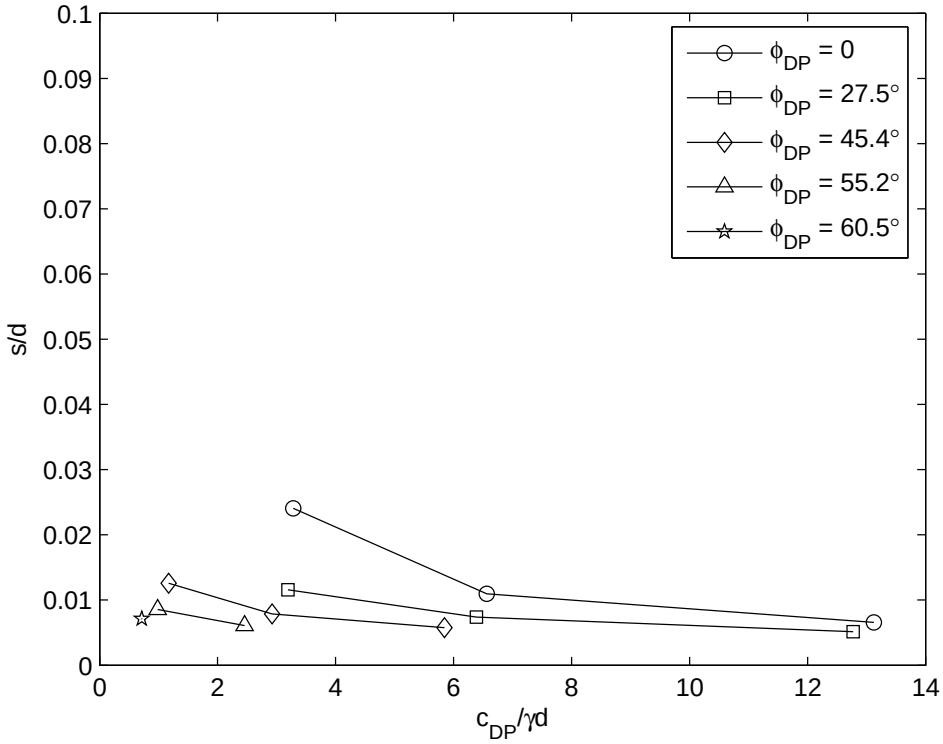

Figure 4.15. Sinkage from numerical simulations of indentation; cases 1-12; $Q_V/\gamma d^3 = 1$

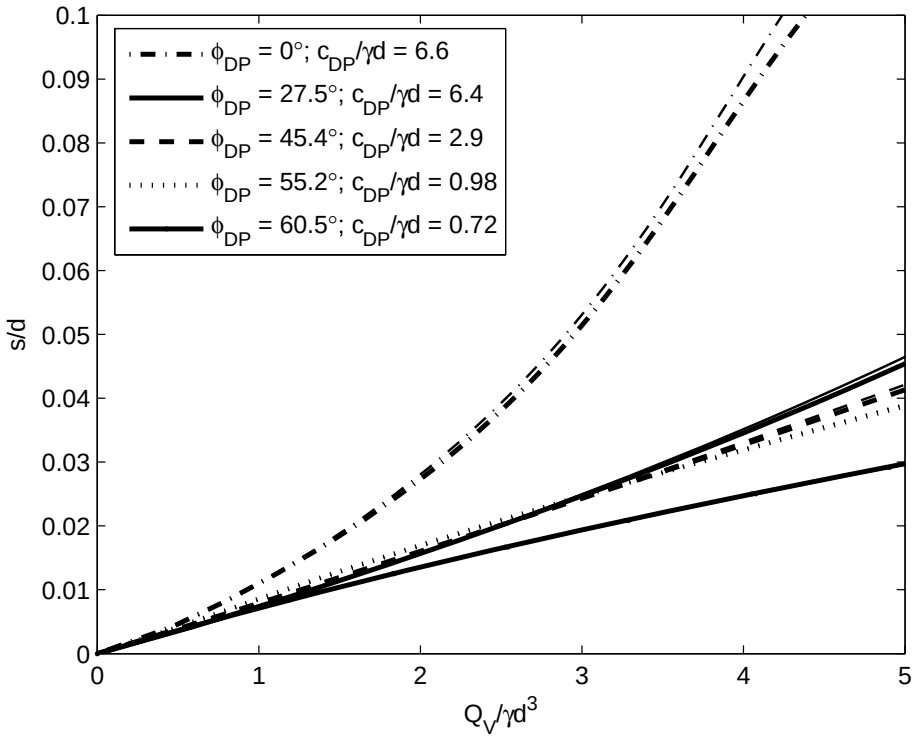

Figure 4.16. Effect of interface friction in numerical simulations of indentation; heavy lines are for $\mu = 0.8$ and fine lines are for $\mu = 0.4$

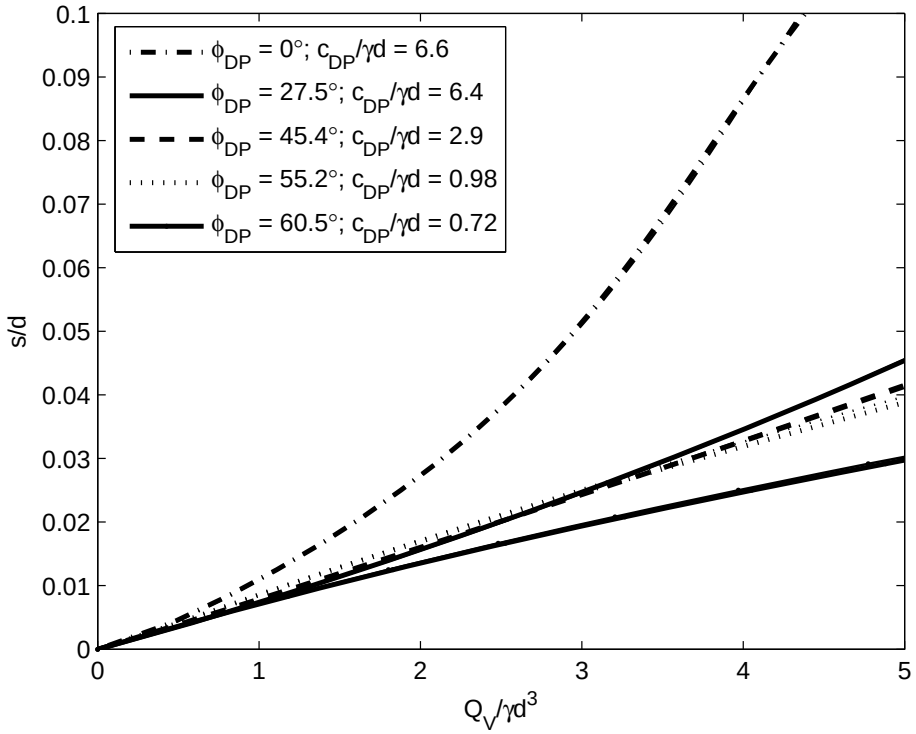

Figure 4.17. Effect of unit weight in numerical simulations of indentation; heavy lines are for $\gamma = 20$ kN/m^3 and fine lines are for $\gamma = 14$ kN/m^3 ($\gamma = 20$ kN/m^3 used for normalization)

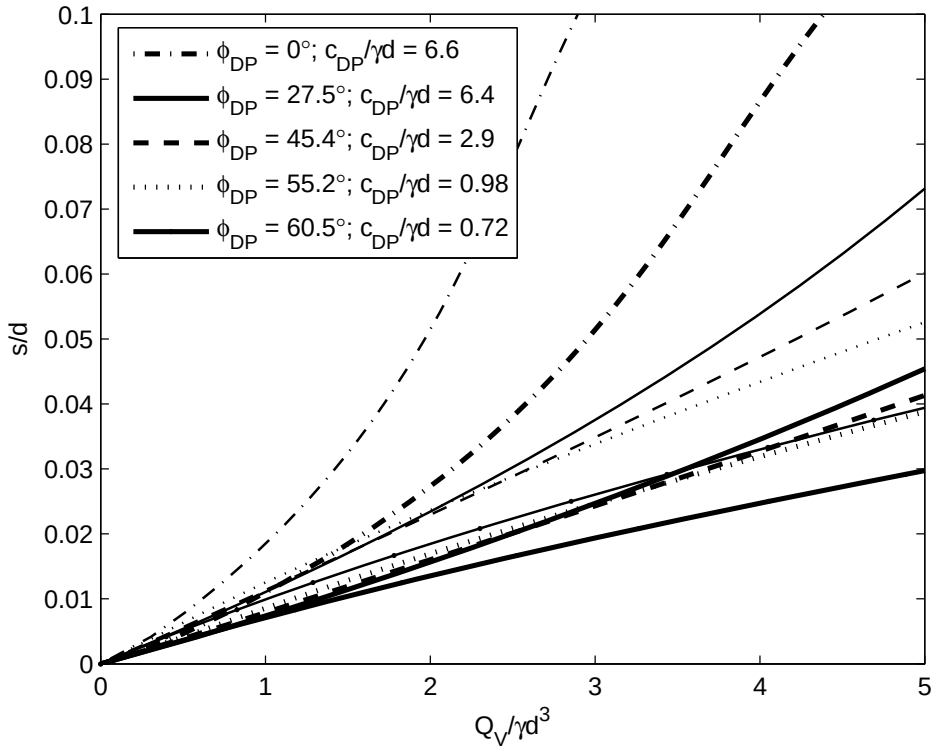

Figure 4.18. Effect of wheel width in numerical simulations of indentation; heavy lines are for $b/d = 0.3$ and fine lines are for $b/d = 0.2$

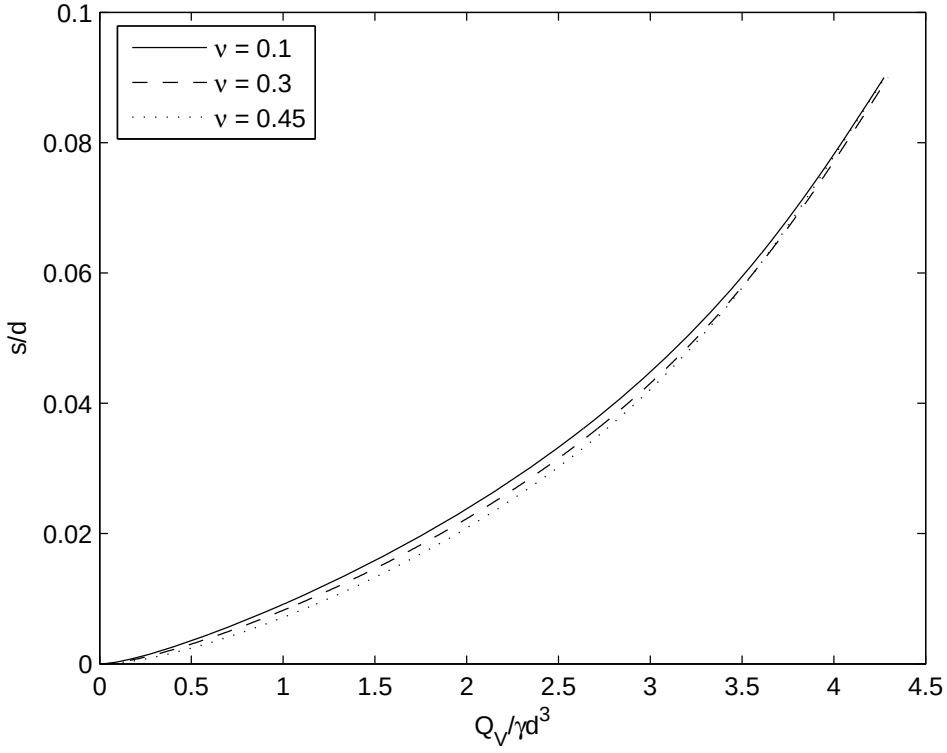

Figure 4.19. Effect of Poisson's ratio in numerical simulations of indentation; cases 28-30

4.4.3 Rolling

Numerical simulations of indentation were run for 43 different cases. The parameters used in the simulations are tabulated in Appendix C, together with a table giving the Mohr-Coulomb parameters that match the Drucker-Prager parameters in triaxial compression. The correlation coefficients determined for each of the cases (according to Eq. (4.5)) are in Appendix F. As with indention, case numbers 1-12 were run to investigate the effect of the strength parameters ϕ_{DP} and c_{DP}. Cases 2, 5, 8, 10, and 12 were used as the basis for comparison when varying remaining parameters. In cases 13-43, the Young's modulus, unit weight, interface friction, wheel width, and wheel diameter were varied.

Fig. 4.20 gives sinkage at $Q_V/\gamma d^3 = 2$ as determined from the numerical simulations of rolling (cases 1-12), exhibiting the same trends as seen previously. The trends are more clearly visible in Fig. 4.20 than they perhaps were in Fig. 4.14 for indentation, since more deformation occurs in the rolling case under the same vertical wheel force. Fig. 4.21 shows the result of lowering the wheel force to $Q_V/\gamma d^3 = 1$. The same effects as discussed in Section 4.4.2 are evident.

Fig. 4.22 shows the effect of reducing the Young's modulus (from 40 MPa to 15 MPa or $E/\gamma d = 1312$ to $E/\gamma d = 492$). The modulus plays an important roll when the sinkage is small. As the wheel force increases and the resulting sinkage increases, the elastic part of the deformation becomes, in general, a less significant part of the total deformation. This is particularly apparent in the case of the frictionless soil, for which the reduction in the modulus is practically unimportant for relatively large sinkage. It is interesting that reducing the modulus appears to have a greater effect on more frictional materials. From the reduction in the modulus, the maximum change in the sinkage for $0 < Q_V/\gamma d^3 < 2$ ($0 < Q_V < 140$ kN with $\gamma = 20$ kN/m^3 and $d = 1.524$ m) is about $s/d = 0.01$ ($s = 0.015$ m with $d = 1.52$ m).

Fig. 4.23 gives the effect of increasing the Young's modulus by a factor of 1.5 (from 40 MPa (5800 psi) to 60 MPa (8700 psi)). This increase in the modulus results in a fairly insignificant increase in the sinkage. Elastic effects may be considered unimportant in terms of the overall sinkage for practical wheel loads and $E/\gamma d \tau 1300$ ($E \tau 40$ MPa (5800 psi) with $\gamma = 20$ kN/m^3 (127 pcf) and $d = 1.52$ m (60 in.)).

Figs. 4.24-4.26 show that the unit weight, wheel width, and soil-wheel interface friction have very similar effects on sinkage in the rolling process as they did in the case of indentation. The wheel width affects the sinkage greatly, while the unit weight and interface friction are fairly inconsequential compared to the effects of other parameters.

Figs. 4.20-4.26 are reproduced in Appendix K in terms of dimensional parameters for convenience.

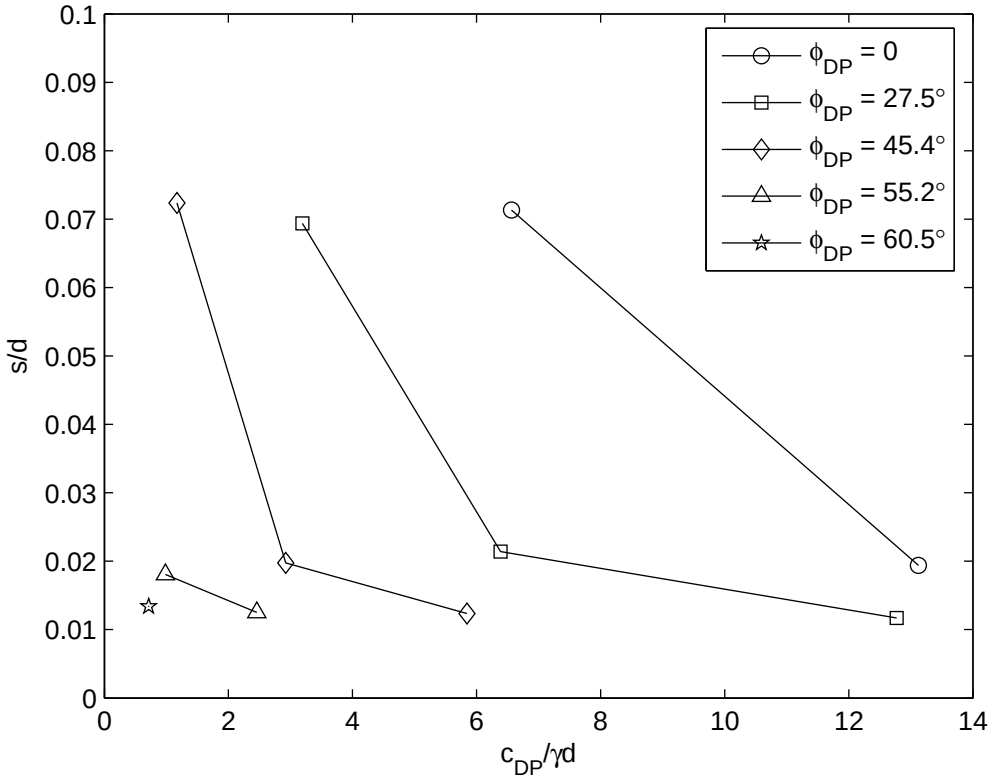

Figure 4.20. Sinkage from numerical simulations of rolling; cases 1-12; $Q_V/\gamma d^3 = 2$

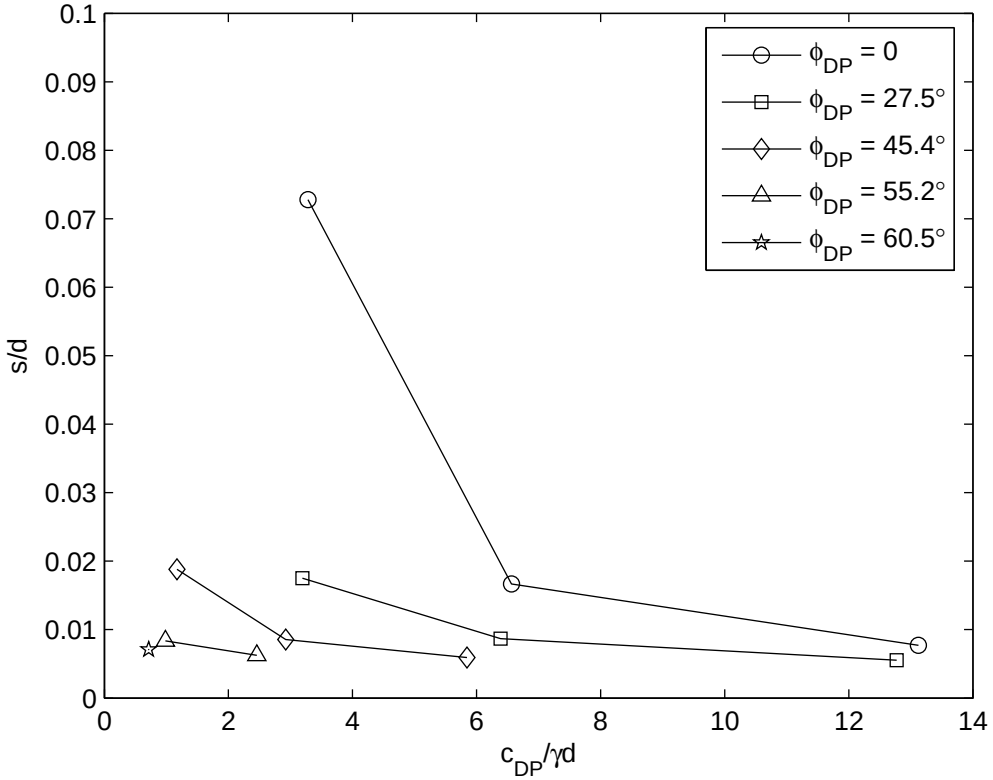

Figure 4.21. Sinkage from numerical simulations of rolling; cases 1-12; $Q_V/\gamma d^3 = 1$

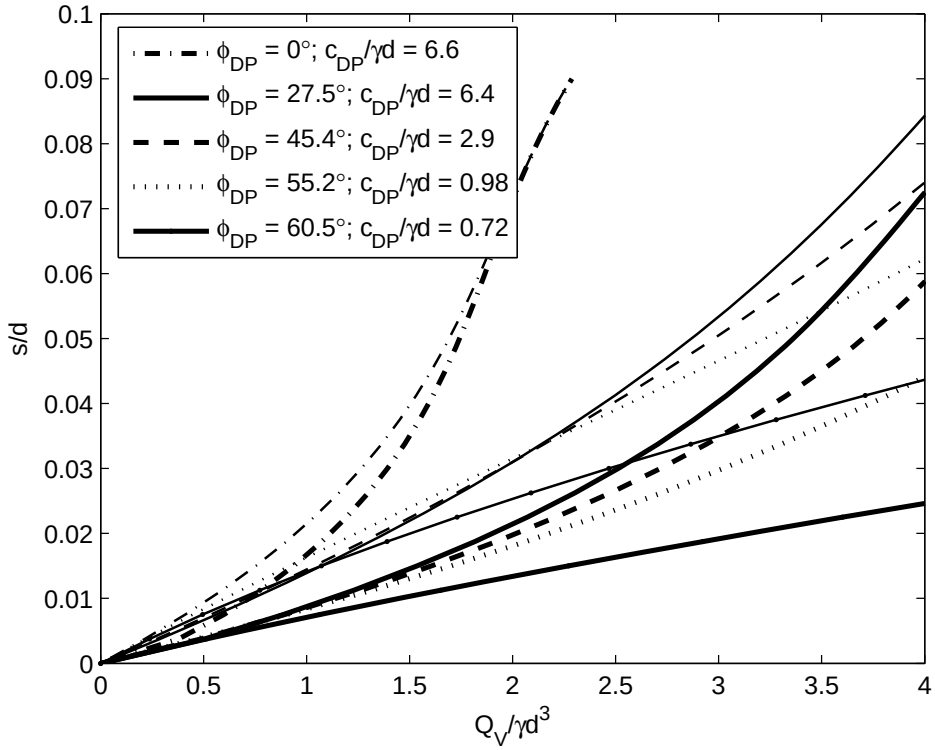

Figure 4.22. Effect of low Young's modulus in numerical simulations of rolling; heavy lines are for $E/\gamma d = 1312$ and fine lines are for $E/\gamma d = 492$

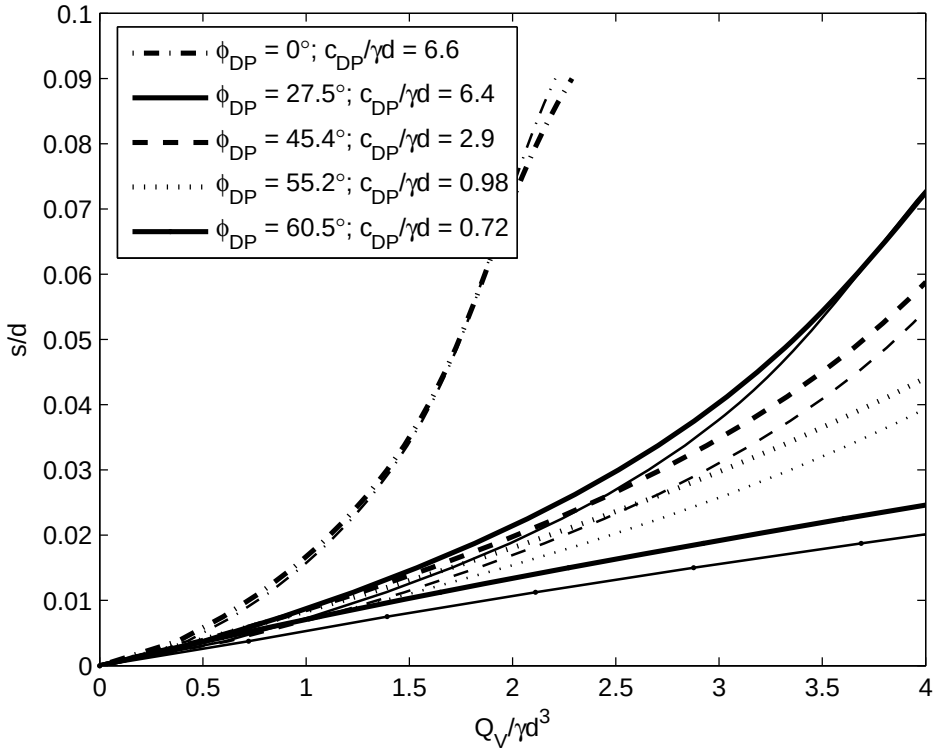

Figure 4.23. Effect of high Young's modulus in numerical simulations of rolling; heavy lines are for $E/\gamma d = 1312$ and fine lines are for $E/\gamma d = 1968$

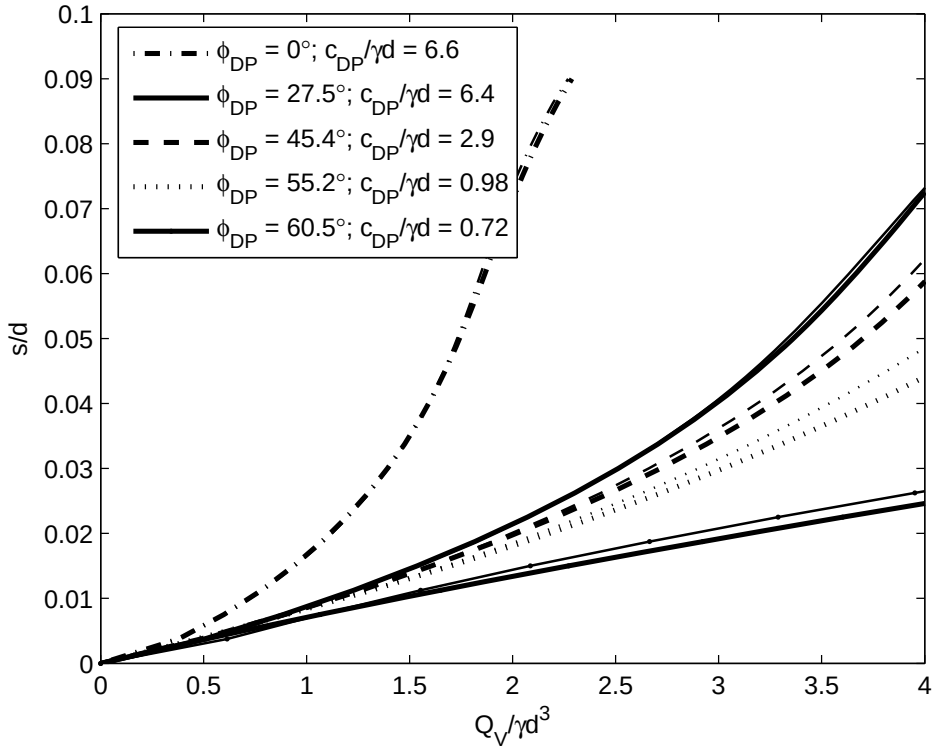

Figure 4.24. Effect of unit weight in numerical simulations of rolling; heavy lines are for $\gamma = 20$ kN/m^3 and fine lines are for $\gamma = 14$ kN/m^3 ($\gamma = 20$ kN/m^3 used for normalization)

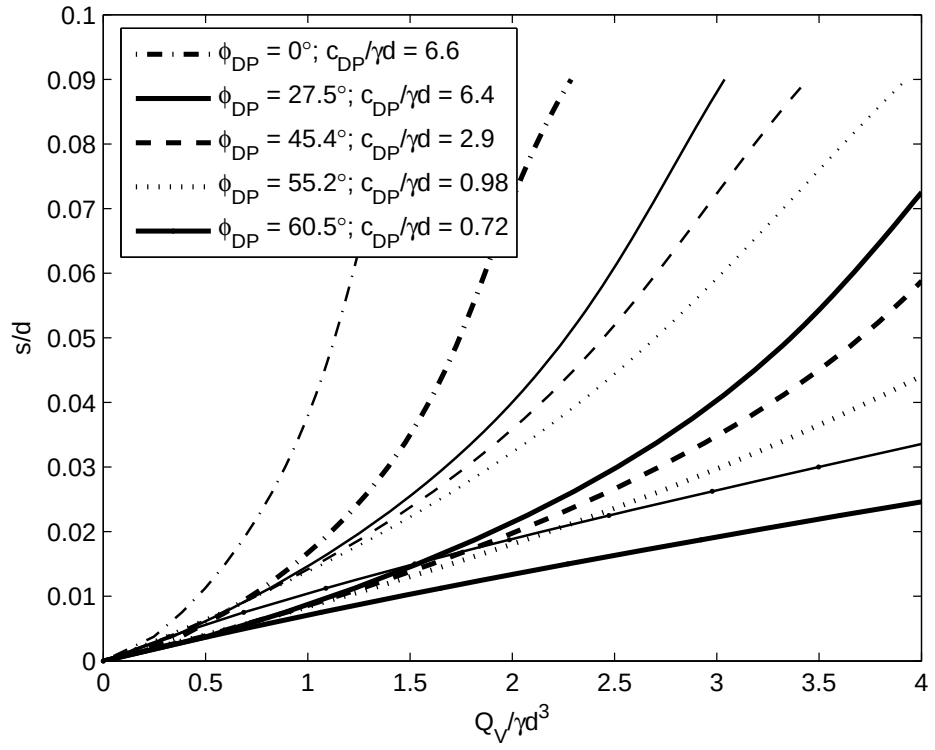

Figure 4.25. Effect of wheel width in numerical simulations of rolling; heavy lines are for $b/d = 0.3$ and fine lines are for $b/d = 0.2$

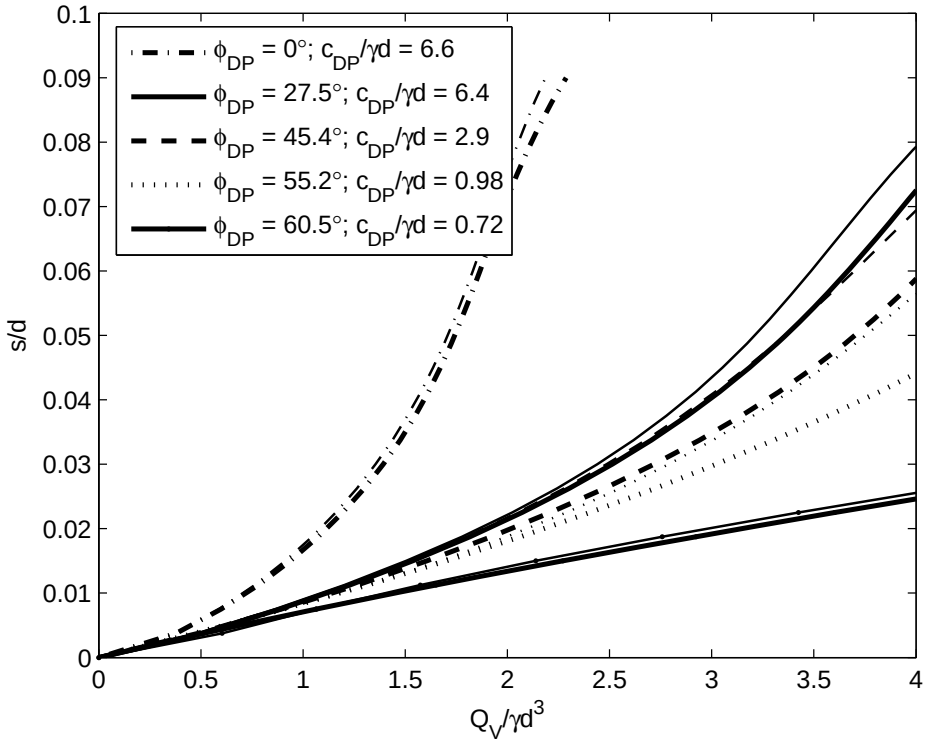

Figure 4.26. Effect of interface friction in numerical simulations of rolling; heavy lines are for $\mu = 0.8$ and fine lines are for $\mu = 0.4$

4.4.4 Effect of Layering on Rolling

Numerical simulations were run for 20 different cases to look at the effect of layering. This was accomplished by partitioning the soil domain in ABAQUS into 3 layers with thicknesses as shown in Fig. 4.27. Varying soil properties were assigned to the layers, and by assigning the same properties to two adjacent layers, a single layer with increased thickness could be formed.

Displacements at the bottom of the third layer were fixed, and this fixity condition is equivalent to having a perfectly rigid layer beneath the third layer. To determine whether this layer was at sufficient depth such that the soil deformation mechanisms beneath the wheel were not significantly affected, an additional numerical simulation was performed in which a very soft clay-type layer ($\phi = 0$, c = 10 kPa (1.5 psi) and E = 4 MPa (580 psi)) with thickness 4 m (13 ft) was introduced below the third layer (Fig. 4.28). Compared to the simulation with a rigid foundation beneath the third layer, the sinkage of a simulated wheel representative of the current test roller (Q_V = 134 kN (15 tons), d = 1.52 m (60 in.), b = 0.46 m (18 in.)) was practically unaffected by the presence of the soft layer. In fact, the minor difference (roughly 5 mm (0.2 in.)) in vertical wheel displacement could be attributed entirely to elastic contraction of the very soft layer, and not differences appearing in the upper soil layers. This reveals an important point regarding test rolling, which is that test rolling measurements are *relative* and not *absolute*. With a soft underlying foundation, the wheel and upper soil layers displace together, although displacement of the wheel relative to the upper soil layer remains essentially unchanged.

Appendix D gives the soil properties used in the simulations of a layered system. Six different scenarios were investigated: (1) weak frictional soil over strong frictional soil; (2) strong frictional soil over weak frictional soil; (3) weak cohesive soil over strong cohesive soil; (4) strong cohesive soil over weak cohesive soil; (5) flexible soil over stiff soil; (6) and stiff soil over flexible soil. In each of the six scenarios, two different structures were considered. In the first, layer numbers 2 and 3 were assigned the same soil properties to form one thin layer over one thick layer. In the second, layer numbers 1 and 2 were assigned the same soil properties to form a thick layer over a thin layer. The first 12 simulations listed in Appendix D pertain to layers with moderate differences in relative strength and are discussed in Section 4.4.4.1. The last 8 simulations, discussed in Section 4.4.4.2, were performed to consider the effects of layers that are very weak or very strong relative to one another.

4.4.4.1 Layers with Moderate Difference in Strength

The results of the simulations for the layered soil (cases 1-12 in Appendix D) are interpreted by comparing with results from simulations with soil composed homogeneously of the soil properties assigned to the uppermost layer. Since the soil is in that case uniform through the entire depth of the model, results are denoted as "1.2d" in the figures. Also, the results from the numerical simulations are given directly in this section, since the curve fit was found to miss some of the subtleties present in the output for layered soil.

Fig. 4.29 compares sinkage versus vertical force for the case of a weak frictional soil over a strong frictional soil. The difference between the results is basically indistinguishable within the numerical noise in the output. This implies that the added depth of the weak layer is not "detected" by the test roller, and that the influence depth of the test roller is therefore less than $0.4d$ for $Q_V/\gamma d^3 < 2$

Figure 4.27. Soil layer designations and thicknesses in numerical simulations

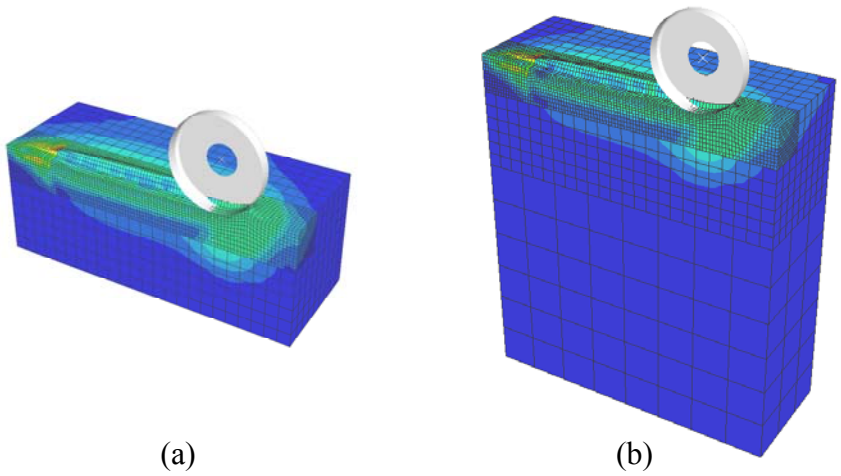

(a) (b)

Figure 4.28. Simulations used to investigate effect of soft underlying foundation: (a) rigid foundation; (b) soft foundation

Fig. 4.30 shows the effect of a strong frictional soil over a weak frictional soil. In this case, there is a noticeable increase in the sinkage when the strong layer is underlain by a weak layer; however this difference only occurs at impractically large wheel forces. For a practical range of wheel forces ($0 < Q_V/\gamma d^3$ δ 4), there is virtually no difference, suggesting that the test roller will fail to discern weak layers below 0.4*d*.

Figs. 4.31 and 4.32 show the cases of a weak cohesive layer over strong cohesive layer and a strong cohesive soil over a weak cohesive soil, respectively. Again, there is no noticeable difference in the results. Given the results for the frictional materials, this is not surprising, since the plastic zone in a cohesive material tends to be smaller than in a frictional material.

Fig. 4.33 gives the results for a flexible layer underlain by a stiff layer. Over a practical range of wheel force ($0 < Q_V/\gamma d^3$ δ 4), there is a notable difference when the flexible layer is increased in thickness from 0.4*d* to 0.8*d*, but not when the thickness in increased from 0.8*d* to 1.2*d*. This suggests that the influence depth of the test roller is between 0.4*d* to 0.8*d* in terms of elastic deformation, although the resulting differences in the sinkage are very small in terms of what one might be able to measure in the field. A similar trend is evident for the case of a stiff layer over a flexible layer (Fig. 4.34). There is a perceptible difference in the sinkage when the thickness of the flexible underlying layer is increased from 0.4*d* to 0.8*d*, although this difference may be impractical to measure.

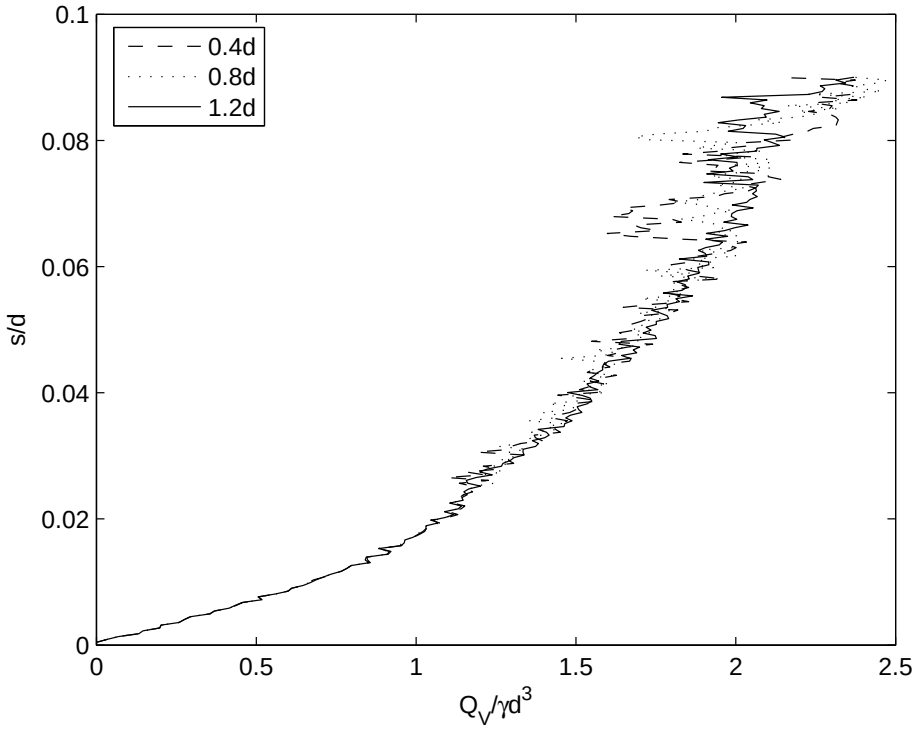

Figure 4.29. Effect of layering on sinkage with frictional soil: weak over strong; $E/\gamma d = 1312$, $\phi_{DP} = 45.4°$, and $c_{DP}/\gamma d = 1.17$ in top layer (thickness shown in legend); $E/\gamma d = 1312$, $\phi_{DP} = 55.2°$, and $c_{DP}/\gamma d = 0.98$ in bottom layer

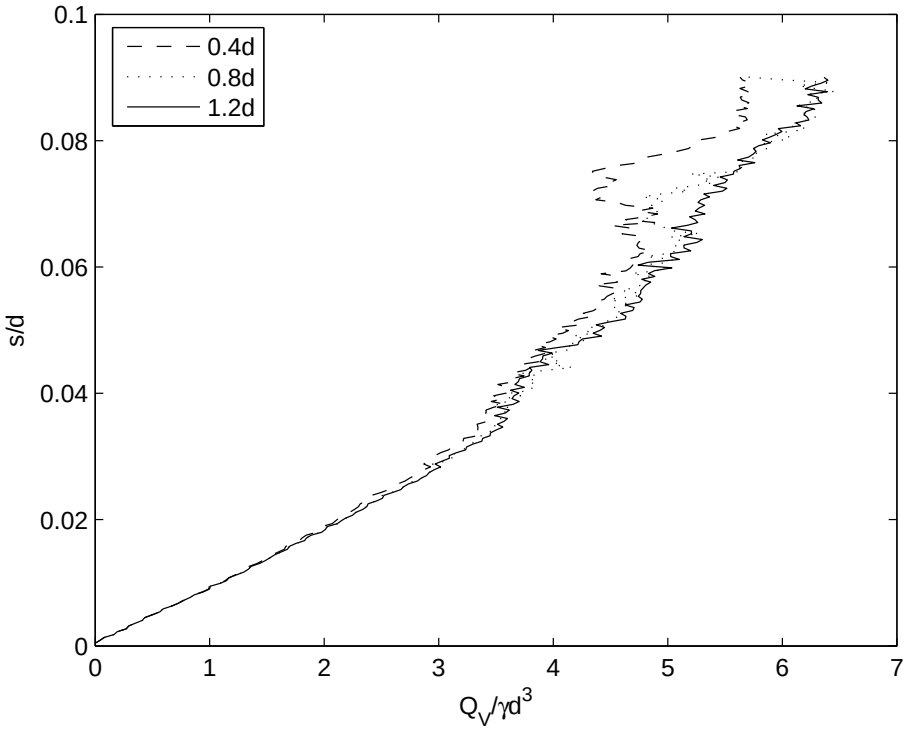

Figure 4.30. Effect of layering on sinkage with frictional soil: strong over weak; $E/\gamma d = 1312$, $\phi_{DP} = 55.2°$, and $c_{DP}/\gamma d = 0.98$ in top layer (thickness shown in legend); $E/\gamma d = 1312$, $\phi_{DP} = 45.4°$, and $c_{DP}/\gamma d = 1.17$ in bottom layer

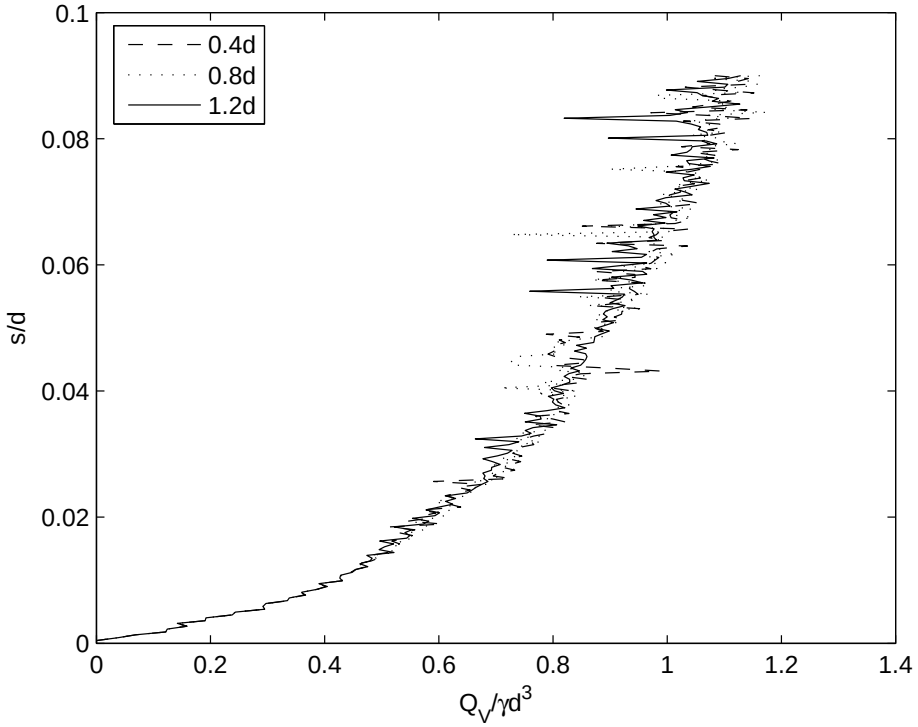

Figure 4.31. Effect of layering on sinkage with cohesive soil: weak over strong; $E/\gamma d = 1312$, $\phi_{DP} = 0$, and $c_{DP}/\gamma d = 3.28$ in top layer (thickness shown in legend); $E/\gamma d = 1312$, $\phi_{DP} = 0$, and $c_{DP}/\gamma d = 6.56$ in bottom layer

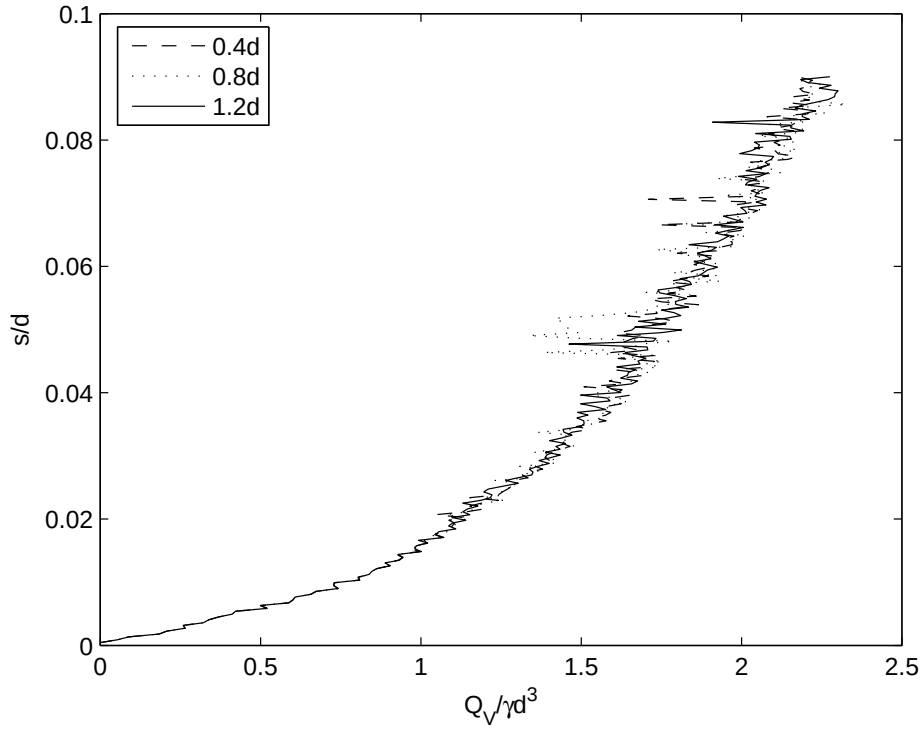

Figure 4.32. Effect of layering on sinkage with cohesive soil: strong over weak; $E/\gamma d = 1312$, $\phi_{DP} = 0$, and $c_{DP}/\gamma d = 6.56$ in top layer (thickness shown in legend); $E/\gamma d = 1312$, $\phi_{DP} = 0$, and $c_{DP}/\gamma d = 3.28$ in bottom layer

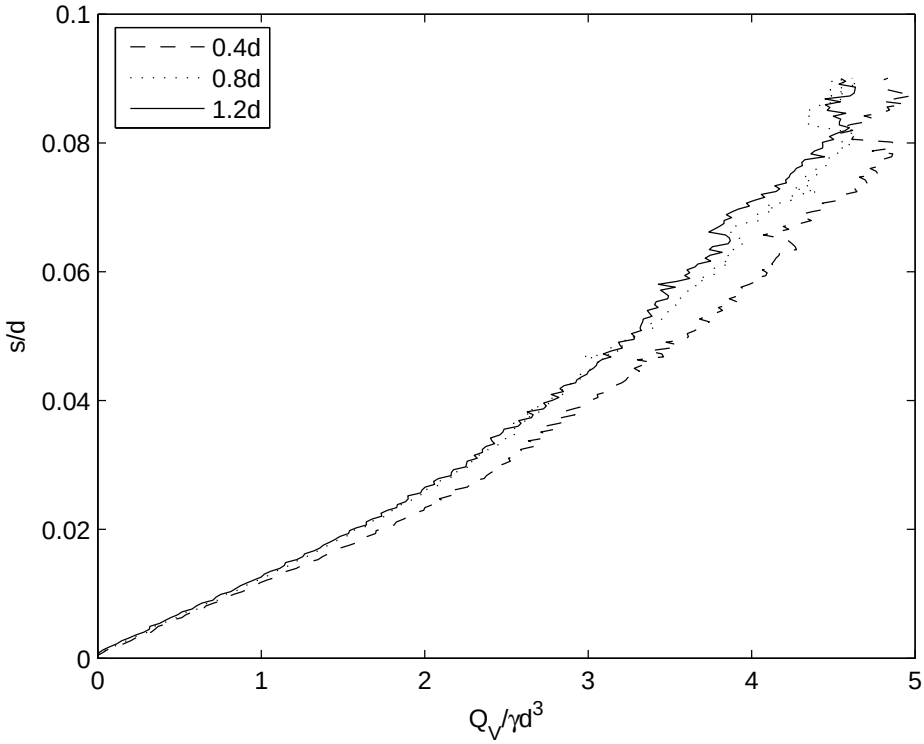

Figure 4.33. Effect of layering on sinkage: flexible over stiff; $E/\gamma d = 656$, $\phi_{DP} = 45.4°$, and $c_{DP}/\gamma d = 2.92$ in top layer (thickness shown in legend); $E/\gamma d = 1968$, $\phi_{DP} = 45.4°$, and $c_{DP}/\gamma d = 2.92$ in bottom layer

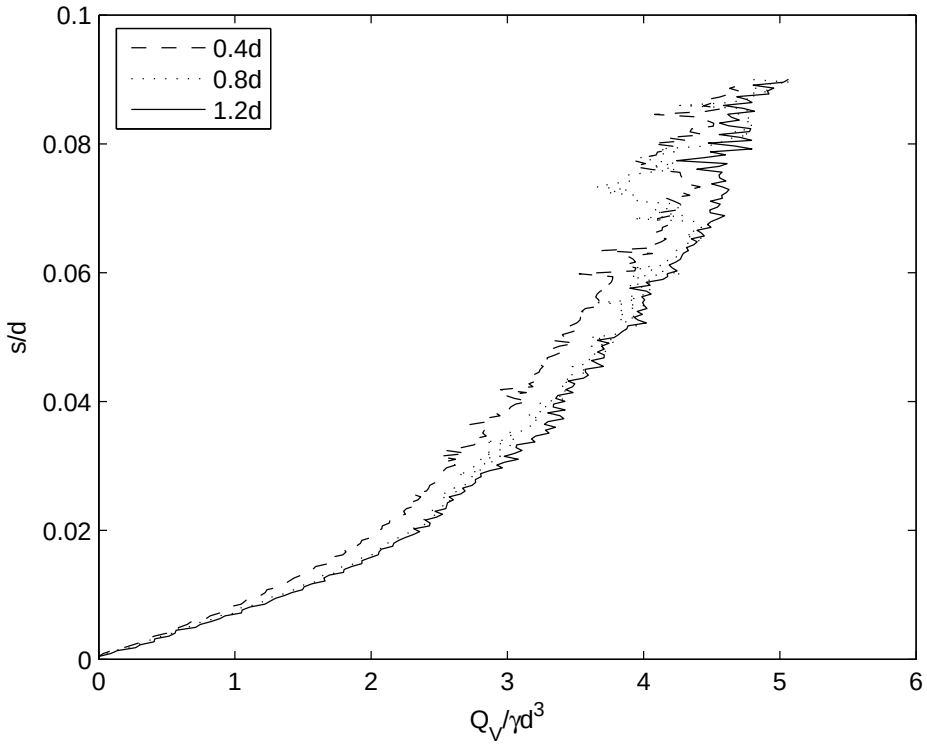

Figure 4.34. Effect of layering on sinkage: stiff over flexible; $E/\gamma d = 1968$, $\phi_{DP} = 45.4°$, and $c_{DP}/\gamma d = 2.92$ in top layer (thickness shown in legend); $E/\gamma d = 656$, $\phi_{DP} = 45.4°$, and $c_{DP}/\gamma d = 2.92$ in bottom layer

4.4.4.2 Layers with Major Difference in Strength

A total of 8 simulations (cases 13-20 in Appendix D) were performed to investigate the influence of very weak or very strong underlying soil layers. The simulation type in which a constant vertical force is applied to the wheel and the wheel rolls from a region of soft soil into a region of stiff soil (Section 3.3.2) was employed. Wheel geometry and load representative of the current test roller were used ($d = 1.52$ m (60 in.), $b = 0.46$ m (18 in.), and $Q_V = 133.5$ kN (15 tons)). The material properties used in the 8 simulations are shown in Appendix D. Cases 13-15 are for a weak clay underlying a dense sandy material, and cases 17-19 are for a weak clay underlying a strong clay. Case 16 represents a weak sandy material over strong clay, and case 20 is a strong clay layer over a weak clay.

Fig. 4.35 shows the results of the numerical simulations as s versus normalized simulation time t/t_o. The unit weight ($\gamma = 20$ kN/m^3 (127pcf)) was applied to the soil over $0 < t/t_o < 0.04$, the vertical force Q_V was applied to the wheel over $0.04 < t/t_o < 0.15$, the wheel velocity was ramped smoothly up to a constant value over $0.15 < t/t_o < 0.27$, and the wheel rolled through the region of soft soil at constant velocity for $0.27 < t/t_o < 1$. Figs. 4.36 and 4.37 show the deformed soil configuration and contours of generalized shear stress at time $t/t_o = 1$ for selected cases.

Case 13 (Fig. 4.36a) represents a homogenous sandy material with $\phi = 45°$ and $c/\gamma d = 0.33$. As discussed in Section 4.1.2, $c > 0$ to avoid numerical instabilities. The steady-state sinkage for this case, as seen in Fig. 4.35, is $s/d = 0.011$. When a soft clay layer ($\phi = 0$ and $c/\gamma d = 0.33$) is introduced at a depth of $0.8d$ below the surface (case 14), the steady-state sinkage increases only

slightly to s/d = 0.012. When the soft clay layer is at a depth of 0.4d below the surface (case 15), the sinkage increases drastically to around s/d = 0.092. The deformation induced in the sand layer and the soft clay for case 15 is shown in Fig. 4.36b. Results from cases 13-15 reveal that the test roller responds to weak material at a depth between 0.4d and 0.8d. It should be noted, however, that this does not apply to all cases of sand overlying a weak clay layer, since the response of the test roller will, in general, depend on the relative strengths of the two layers.

Case 17 (Fig. 4.37a) is for a relatively strong homogenous clay material with $\phi = 0$ and $c/\gamma d$ = 4.9, for which the steady-state sinkage from Fig. 4.35 is s/d = 0.027. When a soft clay layer (ϕ = 0 and $c/\gamma d$ = 0.33) is at a depth of 0.8d (case 18), the sinkage increases insignificantly to s/d = 0.028. When the soft layer is at 0.4d (case 19), the sinkage increases marginally to s/d = 0.034. Soil deformation for case 19 is shown in Fig. 4.37b. Clearly, the influence depth of the test roller is less in this scenario of strong clay over weak clay as compared with the previously considered case of sand over weak clay. For the strong clay overlying the weak clay, the influence depth appears to be 0.4d at most, although one again should expect that this depth varies with the relative strengths of the layers.

Cases 16 and 20 were simulated to investigate the influence of a very strong underlying layer ($\phi = 0$ and $c/\gamma d$ = 9.9), using ϕ = 45º and $c/\gamma d$ = 0.33 or $\phi = 0$ and $c/\gamma d$ = 4.9 in the uppermost layer. In both cases, the strong layer is at a depth of 0.4d. For both the sandy material (ϕ = 45º and $c/\gamma d$ = 9.9) and the clay material ($\phi = 0$ and $c/\gamma d$ = 4.9), no noticeable difference in sinkage is seen in Fig. 4.35 when compared with the results for homogenous material (cases 13 and 17, respectively). Effectively, the test roller does not respond to a strong layer at depths at or below 0.4d for both the sand and clay.

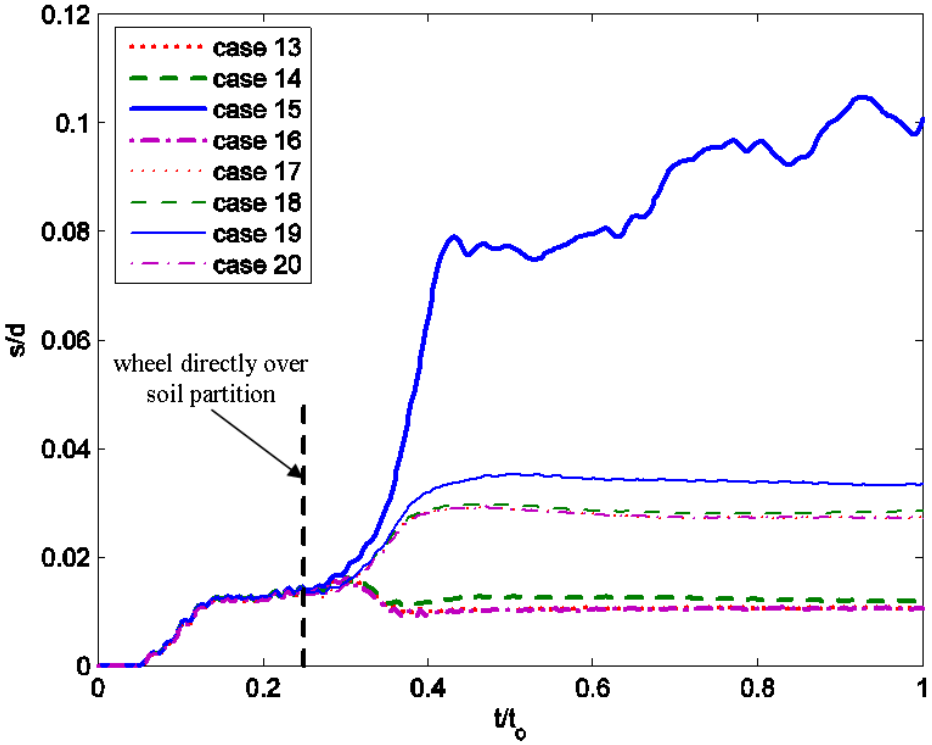

Figure 4.35. Sinkage from numerical simulations with very weak or very strong layers as sinkage versus normalized simulation time

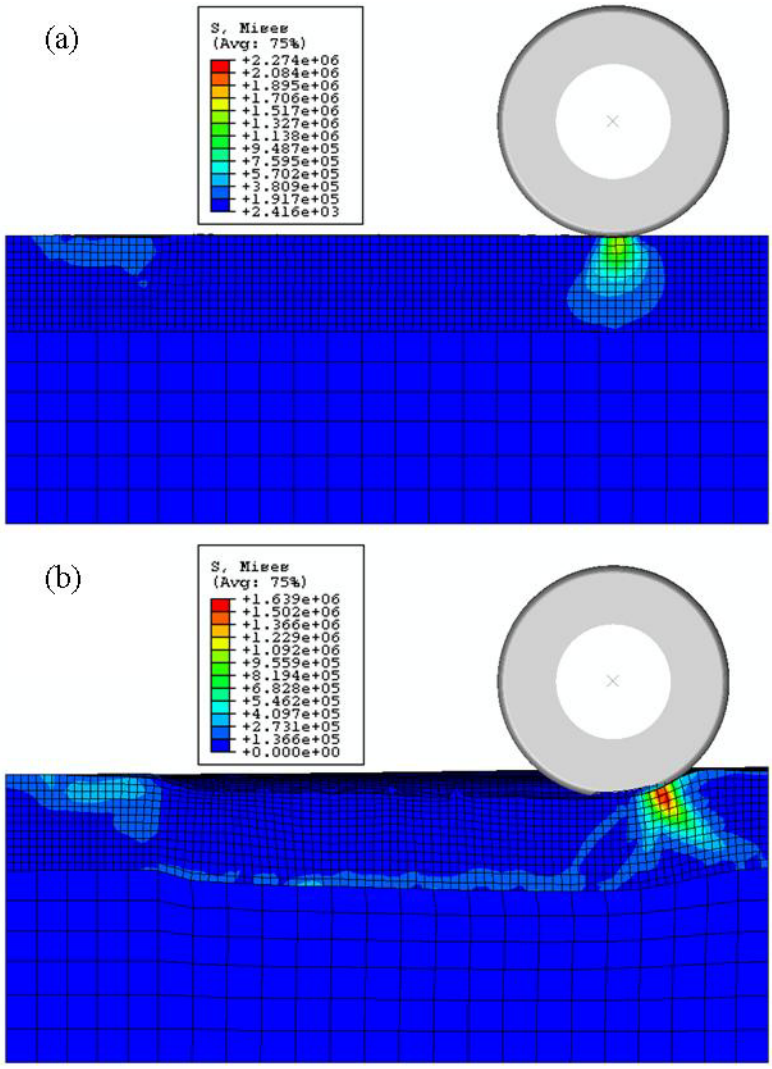

Figure 4.36. Deformed configurations and contours of generalized shear stress for (a) case 13 and (b) case 15 from Appendix D

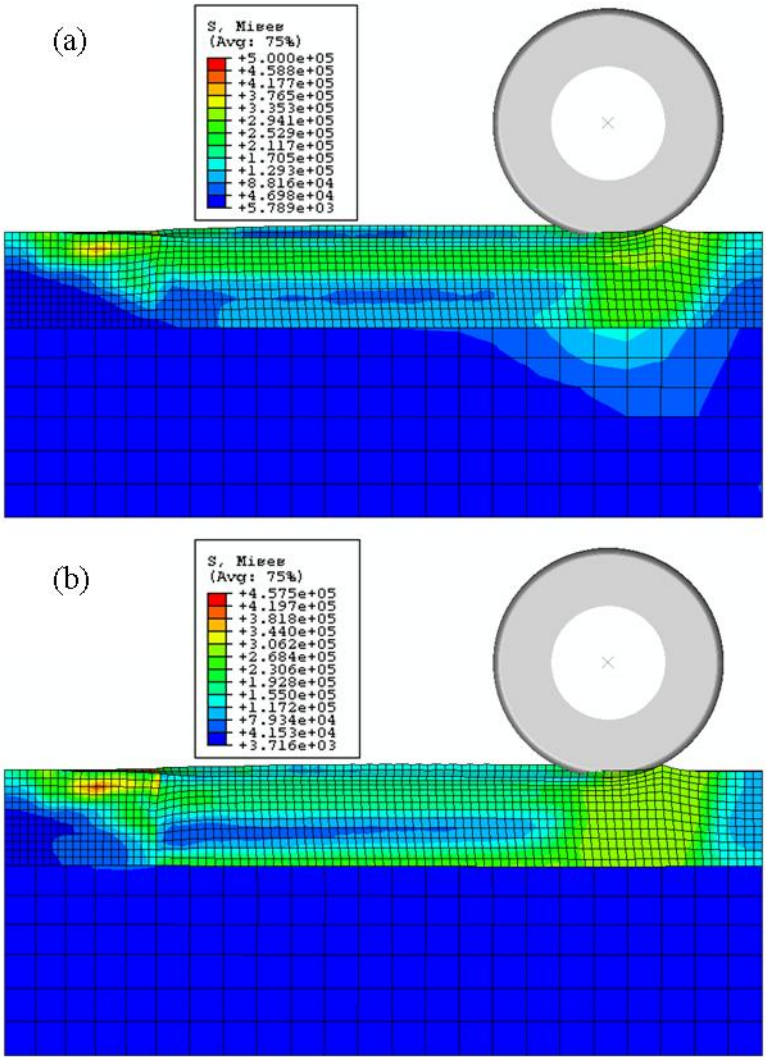

Figure 4.37. Deformed configurations and contours of generalized shear stress for (a) case 17 and (b) case 19 from Appendix D

4.6 Sinkage versus Rut Depth

Disambiguating the elastic and plastic components of the deformation resulting from a rolling wheel is a rather subtle problem. Wheel sinkage is clearly a consequence of both plastic and elastic deformation. That is, either a decrease in strength or a decrease in stiffness will lead to an increase in sinkage. The rut depth is invariably smaller than the sinkage, but not necessarily because the soil rebounds purely elastically after passage of the wheel. The rebound, defined as the difference between the sinkage and the rut depth, may also be a result of both plastic and elastic deformation. Nothing precludes the possibility that the rebound results, in part, from plastic flow. Indeed, the experimental work by Wong (1967), discussed in Section 2.2.2, indicates that material does flow plastically into the region behind the wheel.

Fig. 4.38 shows the results of several numerical simulations for a rolling, rigid wheel and clay-type soil (d = 1.52 m (60 in.), b = 0.46 m (18 in.), and $c = \sigma_o/2$ = 100 kPa (14.5 psi)). Sinkage and rut depth are plotted versus the soil Young's modulus. Two wheel weights, Q_V = 133.5 kN (15 tons) and Q_V = 66.75 kN (7.5 tons), were used in the simulations, with the former representative of the weight of the Mn/DOT test roller (Minnesota 2000). For very flexible materials with E δ 20 MPa (2900 psi), there appears to be a well-defined relationship between the rebound and Young's modulus. For soils with normal to high stiffness (E τ 20 MPa (2900 psi), the relationship becomes very weakly defined, and the rebound may be impractical to measure (< 1 cm (0.4 in.)). Interestingly, the effect of reducing the weight on the wheel by a factor of two is to simply shift the curves down by roughly a factor of four.

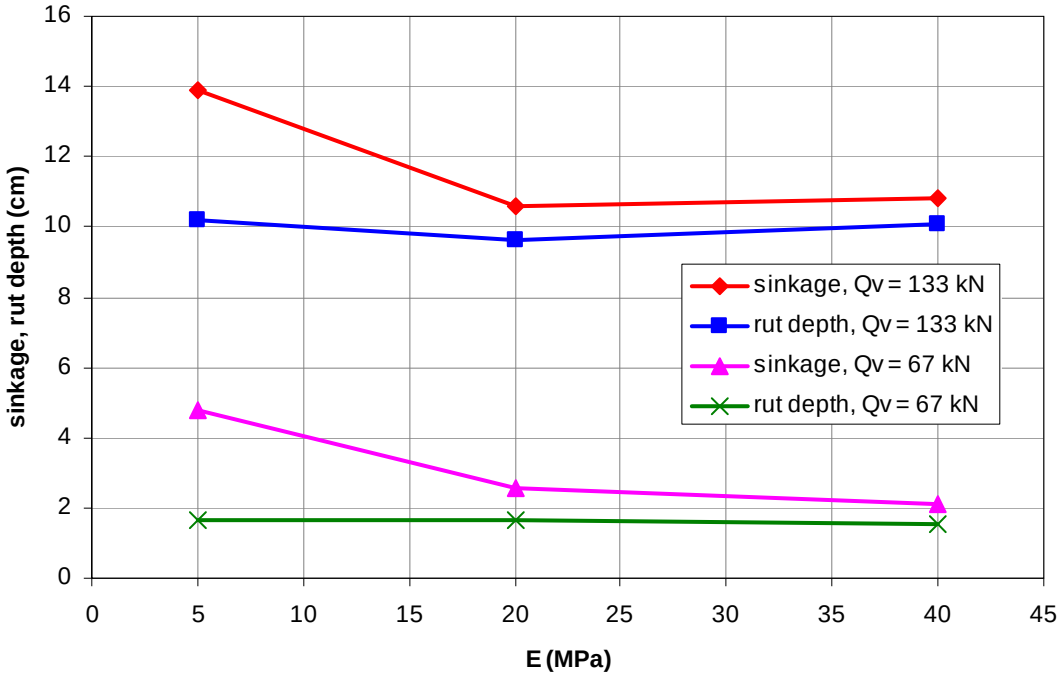

Figure 4.38. Sinkage and rut depth versus Young's modulus from simulations of rolling, rigid wheel

4.7 Remarks on Parametric Study

The parametric and sensitivity analysis using the theoretical models developed in Chapter 3 has shown that the wheel sinkage is most sensitive to wheel force (Q_V), wheel geometry (b and d), and soil strength parameters (ϕ and c or ϕ_{DP} and c_{DP}). The sinkage is relatively insensitive to the interface friction between the soil and wheel and the soil unit weight, although the unit weight does have a significant effect when the cohesion is very small. While the Poisson's ratio does not affect the sinkage substantially, a low elastic modulus can have a noticeable influence on the sinkage. With E = 15 MPa (2200 psi) and a wheel load and geometry representative of the current test Mn/DOT test roller (Q_V = 134 kN (15 tons), d = 1.52 m (60 in.), and b = 0.46 m (18 in.)) the numerical simulations showed that around 1 to 2 cm (0.4 to 0.8 in.) of sinkage could be attributed to elastic effects, assuming a rigid wheel. Such deformation may not be practical to accurately measure in the field, and while elastic effects plays some role, they are relatively insignificant compared to the effects of other parameters.

For a purely granular material (c = 0), a small addition of c, as when a small fraction of fines are added, reduces sinkage substantially. Sinkage is also quite sensitive to ϕ for granular materials (for which ϕ is large). That is, a slight increase in ϕ resulting from compaction causes the sinkage to decrease significantly. For cohesive soils (ϕ = 0), a small addition of ϕ has a moderate effect on sinkage, and the sinkage drops very sharply with increasing c (in fact, s and c roughly are inversely proportional).

Larger wheel weight leads to greater sensitivity of the sinkage with respect to a small variation in soil strength. That is, when the wheel weight is large, a small variation in soil strength can lead to a relatively large change in sinkage, whereas there is a relatively small change in sinkage resulting from the same variation with a small wheel weight.

For rigid wheels, the parametric study showed that the following approximate relationships hold between the sinkage, wheel weight, wheel width, and wheel diameter:

i. The relationship between sinkage and wheel weight for granular soils is linear. In cohesive soils this relationship is quadratic. This means that reducing the test roller weight by half will reduce the sinkage by one half in granular soils, and by one fourth in cohesive soils.
ii. Sinkage is inversely proportional to the width of the wheel for granular soils and inversely proportional to the width squared for cohesive soils. Thus, reducing wheel width by half leads to a two-fold increase in sinkage on granular soils and to a four-fold increase in sinkage on cohesive soils.
iii. Sinkage is inversely proportional to wheel diameter for both granular and cohesive soils. This implies a two-fold increase in sinkage in either soil for wheels whose diameter is reduced by half.

The parametric study on a layered soil structure with moderate relative differences in layer strength (Section 4.4.4.1) indicates that for a wheel load and geometry representative of the current test roller, the test roller is fairly insensitive to variations in the soil structure, in terms of both strength and elastic properties, below a depth of roughly half the wheel diameter (or 0.7 m with the current test roller). In other words, the numerical simulations indicate that a test roller will fail to discern weak soils below a depth of approximately half the wheel diameter.

Results obtained in Section 4.4.4.2 for a layered soil reaffirm that the simulations can capture what is known empirically about the present Mn/DOT test roller, which is that the test roller can identify very weak soils within a depth of 1.2 m (4 ft). The scenario most often encountered in the field is a sand layer underlain by a weak clay layer, and the simulations show that, in this particular case, test roller sinkage is indeed affected by the presence of a very weak clay layer less than 1.2 m (4 ft) of the surface. In the scenario of a strong clay overlying a very weak clay layer, which appears to be less frequently encountered in the field, the numerical simulations indicate that test roller is less sensitive to the weak layer, and that a weak clay layer may be as close as 0.6 m (2 ft) to the surface without significantly affecting sinkage. The simulations also show that sinkage is not as sensitive to a very strong underlying layer as it is to a very weak underlying layer, as a strong layer (sand or clay) introduced at a depth of 0.6 m (2 ft) had virtually no affect on the results.

Chapter 5

Indentation and Rolling Tests

This chapter presents data collected to validate the theoretical models presented in Chapter 3. Originally, field tests were to be conducted at a road construction site using a full scale test roller. For this purpose, visits were made to several sites at the TH 212 construction project near Chaska, Minnesota. A site at which test rolling was being conducted on a granular soil was visited on October 5, 2006. A site with cohesive soil was visited on October 24, 2006. While some field measurements were taken at these sites, neither of the full scale field tests were thoroughly completed, as the full scale field tests were deemed inadequate for the purposes of validating the theoretical models. Observed deficiencies of the field tests with regard to obtaining data for validation include the following:

- variable/unknown test roller tire construction
- field measurements obscured by damage to soil (see Figs. 5.1 and 5.2)
- unknown wheel force due to losses and sloshing of ballast for water-filled test roller
- severely limited number of measurements
- uncontrolled soil consistency
- difficulties in coordinating tests with contractor

For these reasons, the full scale field tests were ultimately replaced with lab-scaled field tests.

Scaled field tests were conducted in the laboratory using a rigid wheel rolling over a prepared bed of soil. The test soils are described in Section 5.1. The details of the testing procedure and the wheels used in the tests are discussed in Section 5.2. The results of the scaled field tests are presented in Section 5.3. Limited results from the full scale field tests are presented in Section 5.4. Some supplemental data found in the literature is given in Section 5.5.

5.1 Test Soils

Two soils were used in the scaled field tests: a cohesive soil and a granular soil. Samples of both the cohesive soil and the granular soil were tested previously as part of the Moisture Effects on PVD and DCP Measurements research project (Swenson et al. 2006). The cohesive soil was a naturally-formed clay taken from Duluth, Minnesota. The granular soil was Quikrete Sand No. 1113 produced by the Quikrete Company. Properties of the two soils are in Tables 5.1 and 5.2. The grain size distribution for the granular soil is given in Fig. 5.1.

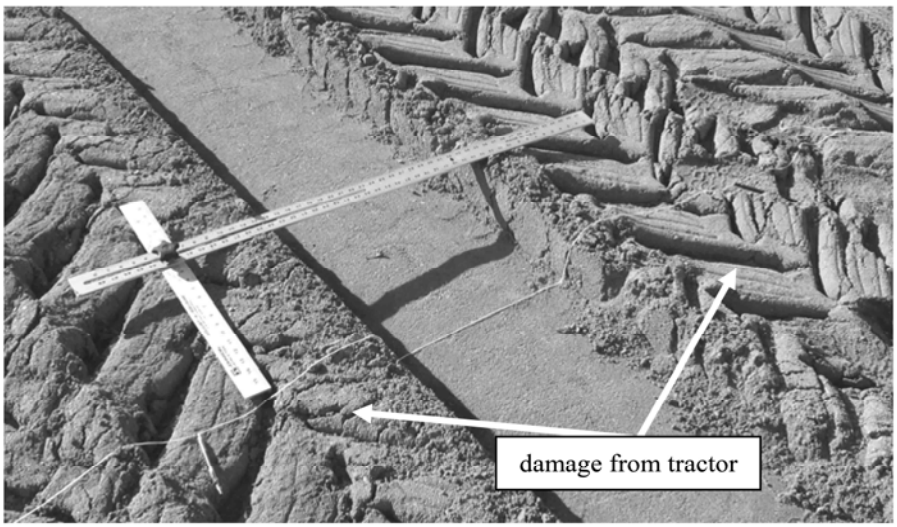

Figure 5.1. Damage to soil at field site with granular soil

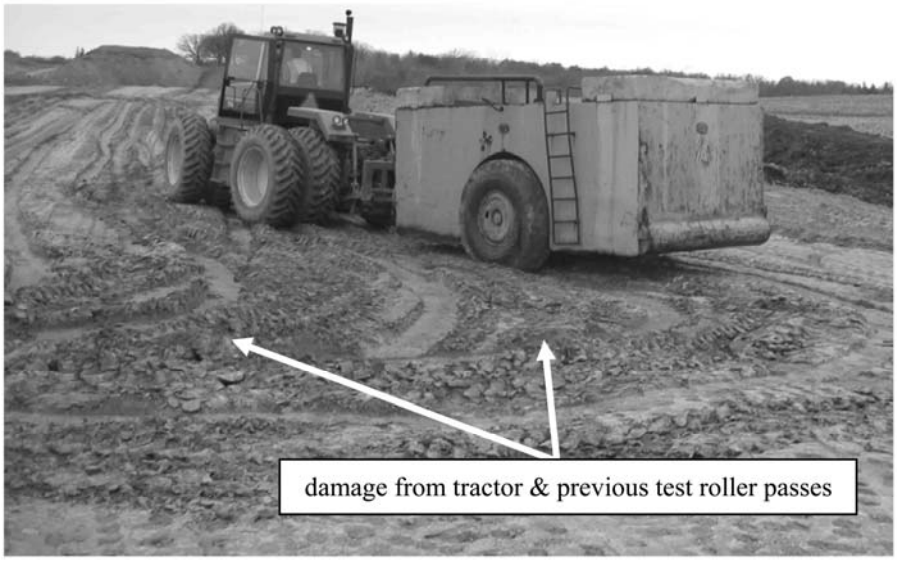

Figure 5.2. Damage to soil at field site with cohesive soil

These particular soils were chosen for their characteristics at opposing ends of the spectrum of engineering geomaterials. It was assumed in the theoretical models generated in Chapter 3 that soils can be characterized as elastoplastic (or rigid-perfectly plastic) using the Mohr-Coulomb or Drucker-Prager yield conditions. The plastic behavior of soils is therefore assumed to derive from either cohesion, internal friction, or both. While soils in general may possess both cohesion c and internal friction ϕ, the soils tested in the scaled field tests are the two extreme cases: the clay soil is purely cohesive ($\phi \approx 0$) under relatively fast loading and the sand is purely frictional ($c = 0$). If the theoretical models developed in Chapter 3 correctly predict the response for these two cases, it is reasonable to expect that the models should also give accurate predictions for the general case $c \neq 0$ and $\phi \neq 0$.

To achieve frictionless and nearly incompressible response, the cohesive soil was brought to a moisture content estimated to be near the point of saturation. This moisture content was estimated to be roughly 35%, which is just above the plastic limit of 32.7% (Table 5.1). To saturate the soil, air-dried material was manually crushed and combined with water in small batches using a commercial mixer.

Because moisture has little effect on the internal friction of sand, the sand was tested under air-dried conditions. Because density tends to increase internal friction, the sand was tested at two different densities. A low density was achieved by raining the sand during placement without additional compactive effort, while a high density was obtained through vibration of the material after placement.

Table 5.1. Selected properties for cohesive soil used in scaled field tests (Swenson et al. 2006)

average std. proctor dry unit weight (kN/m^3)	14.1
average optimum moisture content (%)	27
average liquid limit	84.6
average plastic limit	32.7
average % silt	19.0
average % clay	77.0
average R-value	10.9
Mn/DOT textural classification	C
AASHTO group	A-7-6

Table 5.2. Selected properties for granular soil used in scaled field tests (Przeslawski 2004)

mean diameter (mm)	0.5
uniformity coefficient	2.14
coefficient of gradation	0.88
min. dry unit weight (kN/m^3)	15.9
max. dry unit weight (kN/m^3)	17.8
AASHTO group	A-1-b

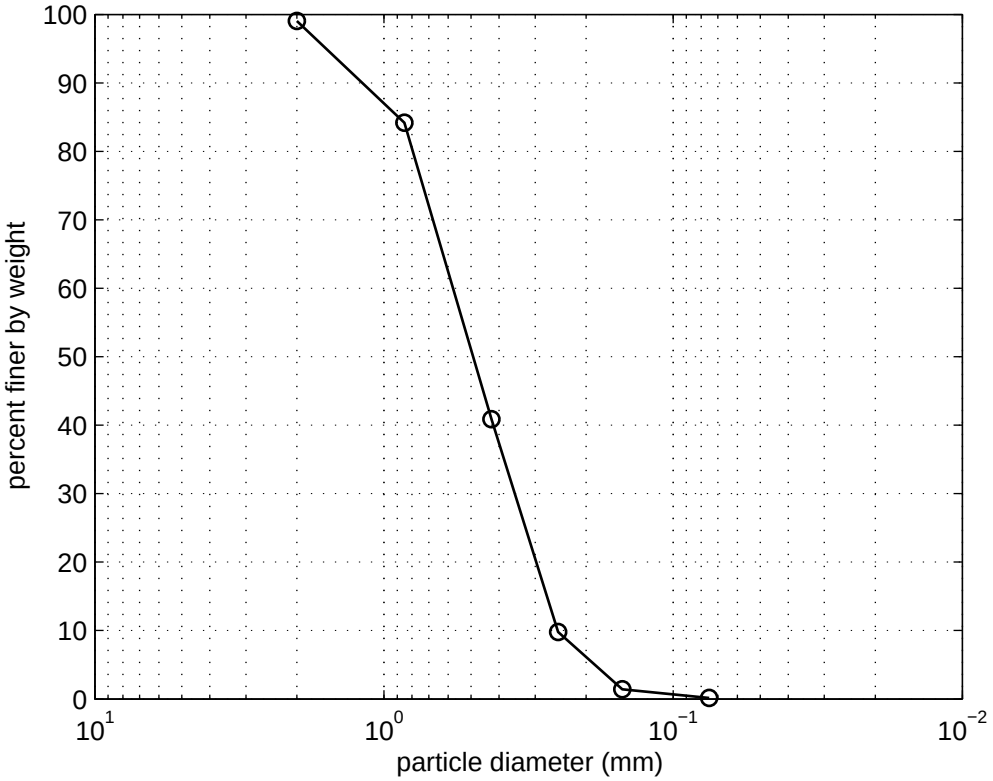

Figure 5.3. Measured grain size distribution for granular soil used in scaled field tests (Przeslawski 2004)

5.2 Test Procedures

The theoretical models developed in Chapter 3 apply to any length scale, provided the size of the wheel is large enough compared to the particle sizes of the soil to correctly approximate the response of the soil using a continuum model. Small-scale tests are much easier to control and conduct than large-scale tests. For this reason, as well as the deficiencies in the full scale field (see introduction to Chapter 5), small-scale tests were conducted in the laboratory. There is little reason to believe that the theoretical models, after validation via careful experimentation, should not apply to the full scale processes occurring in the field.

The testing apparatus for the scaled tests is shown in Fig. 5.4. The test soils were placed in a container with approximate length 300 mm (12 in.), width 250 mm (10 in.), and depth 100 mm (4 in.). The container was mounted to a linear bearing, allowing only translation of the test bed in one direction. The rail of the linear bearing was mounted to the loading ram of a standard load frame. The wheel was mounted to a 2.2 kN (500 lb) load cell attached to the upper part of the load frame, using the device shown in Fig. 5.4 to permit free rotation of the wheel (emulating the towed wheel condition). This setup allowed for the wheel to be displaced a controlled amount into the soil while measuring vertical wheel force

For the analytic method proposed in Chapter 2, the towed wheel case was considered through extension of the case of simple indentation of wheel. Indentation, additionally, may be a relevant process in the initial stages of soil failure during test rolling. Both indentation and rolling experiments were therefore conducted in the laboratory for validation purposes.

In the case of the indentation experiments, the wheel was simply displaced normally into the soil at a rate of approximately 0.1 mm/s (0.004 in./s) without translating the soil bed on the linear bearing. For the rolling experiments, the wheel was displaced into the soil a certain amount, and the bed was then translated at a constant velocity of roughly 3.5 mm/s (0.138 in./s) while measuring vertical force. The rolling experiments were therefore displacement-controlled, with the vertical wheel force (Q_V) under steady rolling conditions being the measured quantity of interest. While each indentation experiment generated a virtually continuous force-sinkage history, each rolling experiment generated one data point on the force-sinkage curve for a wheel rolling under steady conditions.

Two right-cylindrical aluminum wheels with differing sizes but the same aspect ratio b/d = 0.33 were tested. The wheels are shown in Fig. 5.5. Coarse-grained sandpaper was adhered to the contacting surfaces of the wheels to provide roughness. The smaller of the two wheels had dimensions b = 25.4 mm (1 in.) and d = 77.7 mm (3.06 in.), and the larger wheel had b = 38.3 mm (1.5 in.) and d = 115.4 mm (4.54 in.). Only the large wheel was used in the experiments on the sand due to a low signal-to-noise ratio in the measured vertical force that would have resulted with the small wheel.

In the case of the cohesive soil, the test bed was prepared before each test by first kneading and compacting the clay into the container in small (~25 mm (1 in.)) lifts. Once filled, a platen was placed over the soil, and then a force of 5 kN (1100 lb) was applied to the platen for 10 minutes. After the force was removed, a flat surface was created by drawing a thin wire across the surface of the container. The final state of the clay is visible in Fig. 5.4. Multiple tests were conducted by emptying the test bed after each individual test and repeating this preparation procedure. Specimens for laboratory testing discussed in Chapter 6 were extracted by pushing a tube with an inner diameter of 38.4 mm (1.5 in.) into the soil after a test, removing the tube, and

extruding the soil with a 38 mm piston (1.5 in). Samples were also extracted for the purpose of obtaining moisture content and density measurements.

For the granular soil, the soil was placed in the test bed at two different densities. For the low-density condition, the sand was simply rained into the test bed through a funnel in small (~10 mm (0.5 in.)) lifts. For the high-density condition, the sand was again rained into the container in small lifts, but after placement of each lift, the side of the test bed was lightly and repeatedly impacted using a rubber mallet. Before each test, the surface of the soil was struck flat by drawing a bar across the surface of the test bed. The entire soil bed was placed on a scale to determine the mass of the soil placed in the test bed, and the density was then deduced knowing the volume of the test bed (0.0065 m^3 (0.23 ft^3)).

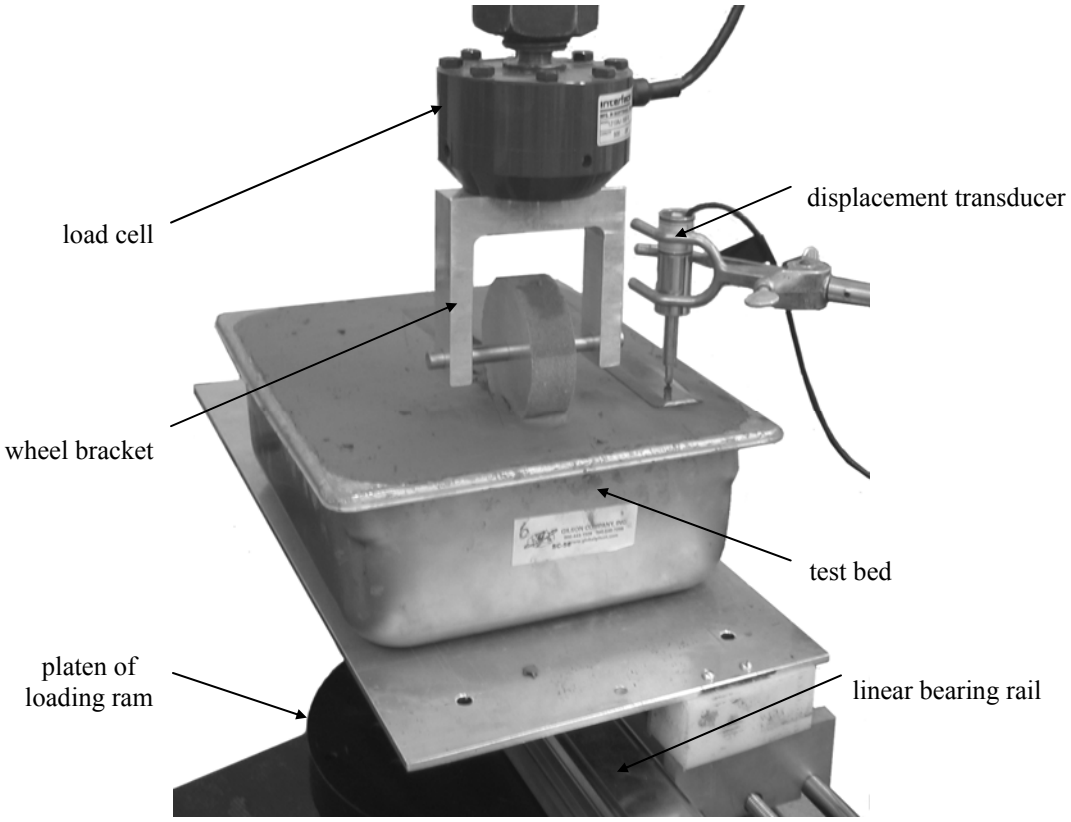

Figure 5.4. Apparatus used in scaled field tests (clay soil shown)

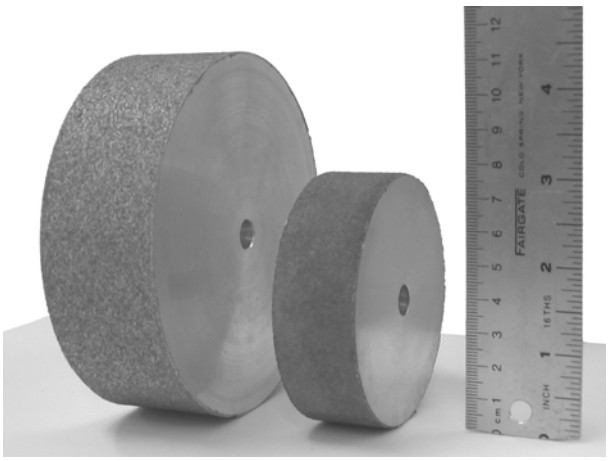

Figure 5.5. Wheels used in scaled field tests

5.3 Results of Scaled Tests

5.3.1 Cohesive Soil

5.3.1.1 Wheel Indentation

The results of the indentation tests on the cohesive soil are plotted in Fig. 5.6. The vertical force (Q_V) equals the total force (Q) in the case of indentation. The unit weight did not vary significantly throughout the tests, and the average moist unit weight of the soil was determined to be $\gamma = 18.5$ kN/m^3 (118 pcf). Measured moisture contents varied between 35% and 37%, with an average of 36.0% over the course of the tests. The dry unit weight was therefore about 13.6 kN/m^3 (86.6 pcf). These values reflect unit weight and moisture content measurements taken periodically throughout the course of both the indentation and the rolling tests, so they apply to the rolling tests as well.

5.3.1.2 Wheel Rolling

Example data from a rolling wheel test on the clay soil with the larger wheel and s = 8.2 mm (0.32 in.) is shown in Fig. 5.7. As shown, the record for a rolling experiment consists of data for two separate processes: (1) displacement of the wheel into the soil to a specified s and (2) rolling at constant s. The vertical wheel force Q_V when the force history has converged to a single value or is oscillating about a particular value is taken as the wheel force under steady conditions. The steady-state force-sinkage data obtained in this way for the two wheels is given in Tables 5.3 and 5.4 also plotted in Fig. 5.8. As discussed in Section 5.3.1.1, the average moist unit weight of the soil was determined to be $\gamma = 18.5$ kN/m^3 (118 pcf), and the average moisture content was 36.0%.

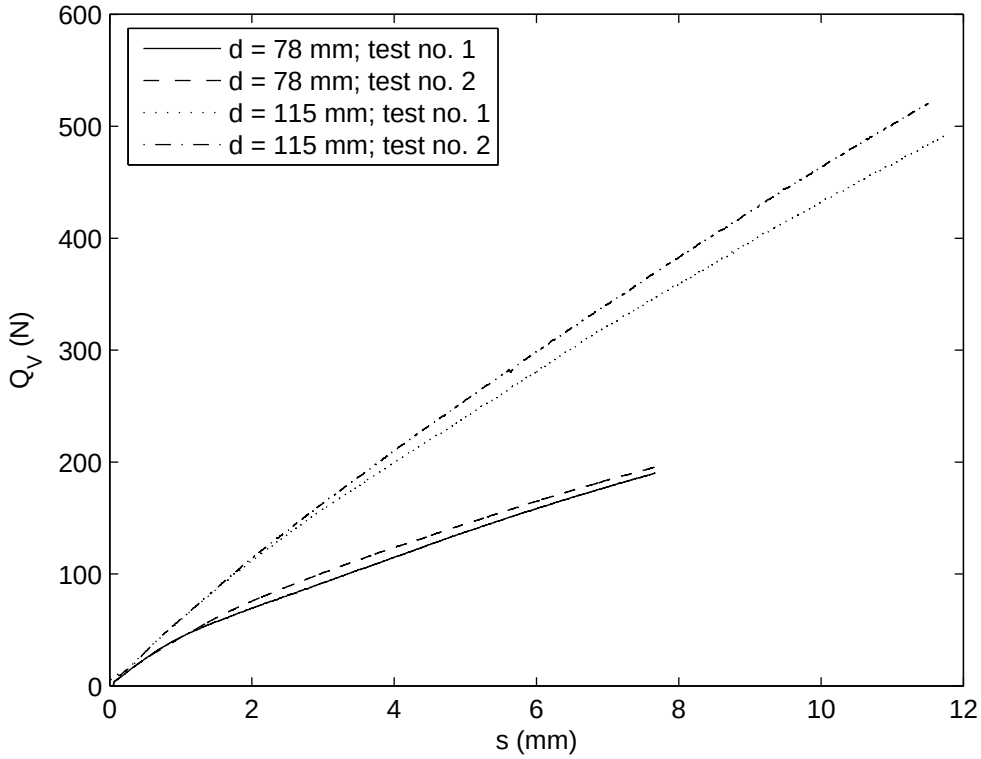

Figure 5.6. Force versus sinkage for indentation test on cohesive soil

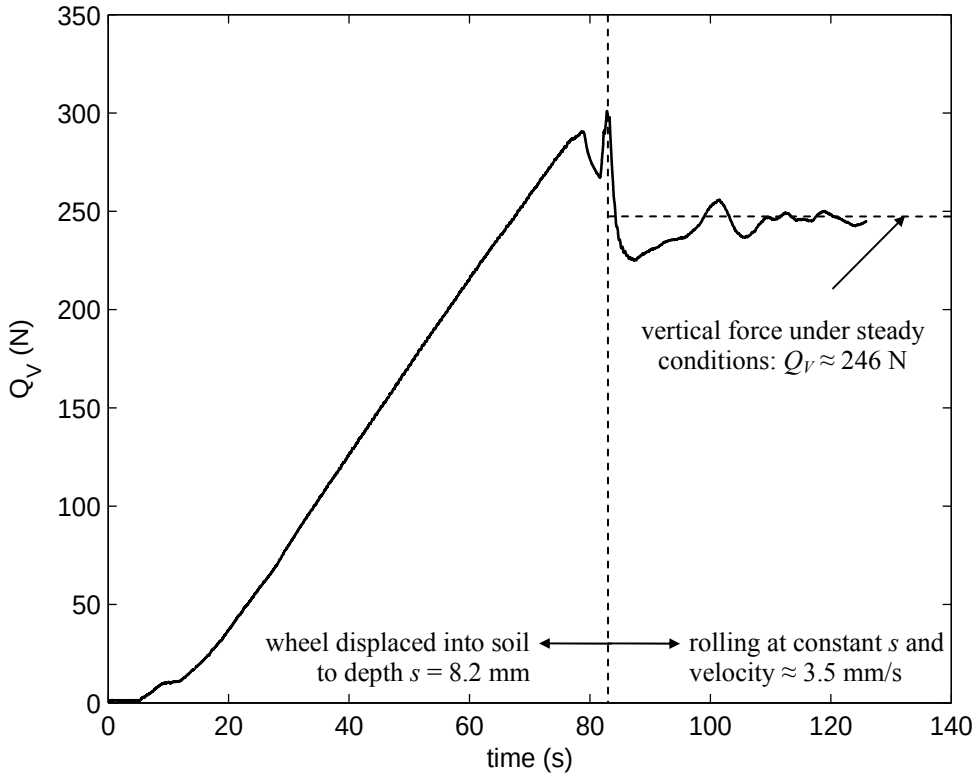

Figure 5.7. Example data from rolling test on cohesive soil

Table 5.3. Force-sinkage data from rolling tests on cohesive soil with small wheel (d = 78 mm)

***s* (mm)**	**Q_V (N)**
0.9	13
1.3	24
2.6	60
3.7	92
5.5	109
7.7	153
9.1	166

Table 5.4. Force-sinkage data from rolling tests on cohesive soil with large wheel (d = 115 mm)

***s* (mm)**	**Q_V (N)**
1.4	42
2.3	93
4.9	159
8.2	246
10.4	342
13.5	384

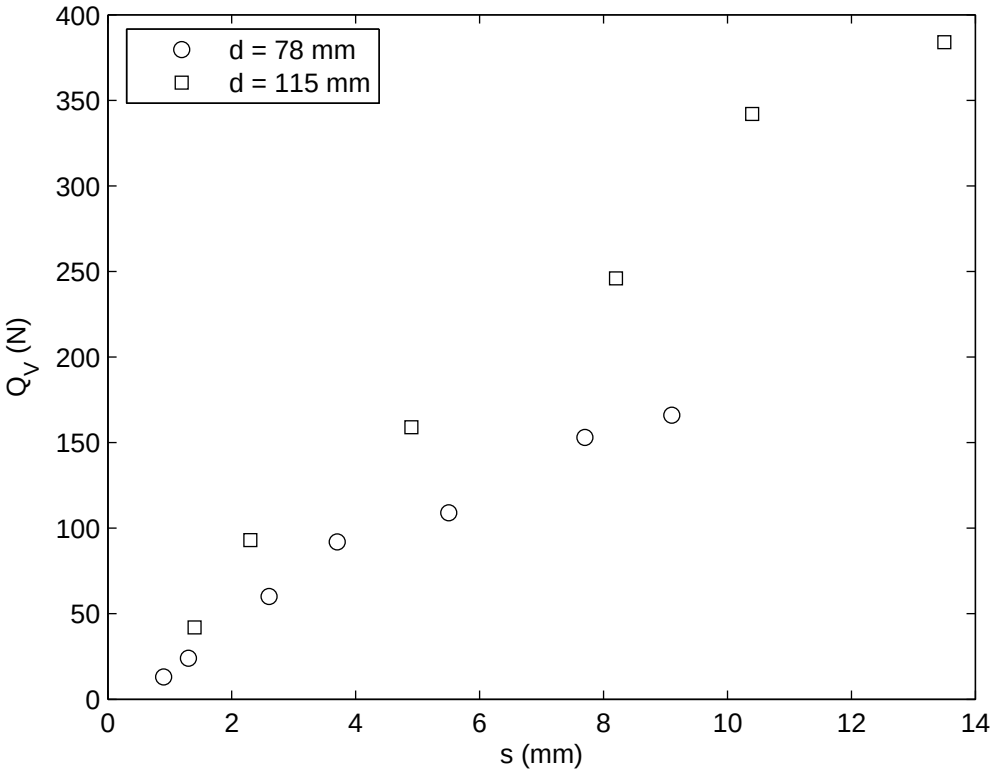

Figure 5.8. Force versus sinkage from rolling tests on cohesive soil

5.3.2 Granular Soil

5.3.2.1 Wheel Indentation

The results of the indentation tests on the granular soil are plotted in Fig. 5.9. As mentioned previously, only the large wheel with d = 115 mm (4.54 in.) was used in the tests. The soil was tested at two different densities. For the low-density soil, the dry unit weight averaged γ = 16.0 kN/m^3 (102 lb/ft^3), and for the high-density soil, the dry unit weight averaged γ = 17.4 kN/m^3 (111 lb/ft^3) without significant variation. Since the sand was tested under air-dried conditions, the moisture content of the sand was considered zero for all the tests and the moist unit weight was the same as the dry unit weight. Computing relative densities based on the minimum and maximum unit weights given in Table 5.2 gives relative densities of 5% and 81% for the low-density and high-density materials, respectively. The low-density sand was therefore *loose* and the high-density sand was *dense* (Das 2005). Again, these unit weights pertain to the rolling tests as well as the indentation tests.

5.3.2.2 Wheel Rolling

The data for the rolling tests on the granular soil was obtained in the same way as for the cohesive soil (Section 5.3.1.2). Tables 5.5 and 5.6 give the steady-state sinkage and vertical force

for the loose and dense states, respectively. The data is also plotted in Fig. 5.10. Refer to Section 5.3.2.1 for the measured soil densities.

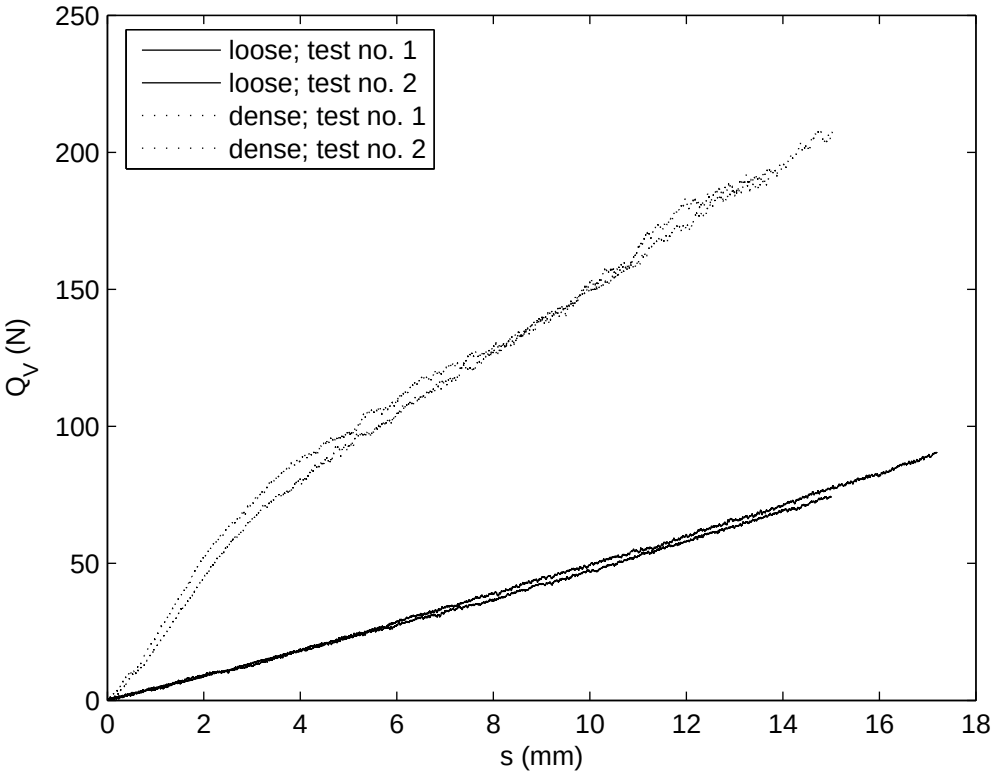

Figure 5.9. Force versus sinkage from indentation tests on granular soil

Table 5.5. Force-sinkage data from rolling tests on loose granular soil

***s* (mm)**	***Q_V* (N)**
2.0	3.8
2.7	4.4
5.3	7.1
8.7	10.0
10.7	13.1
13.8	15.1

Table 5.6. Force-sinkage data from rolling tests on dense granular soil

***s* (mm)**	**Q_V (N)**
2.3	13
6.4	23
11.4	33

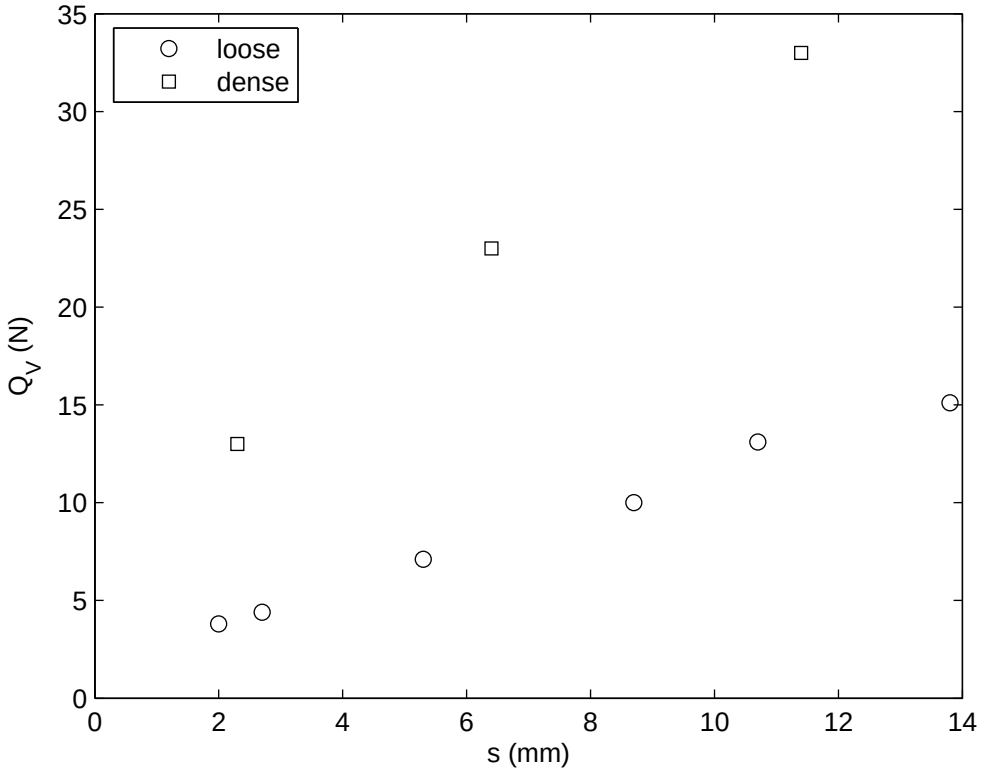

Figure 5.10. Force versus sinkage from rolling tests on granular soil

5.4 Partial Results for Full Scale Field Tests

In this section, results that were obtained from the field visits are presented. This section is by no means intended to represent a complete and consistent set of measurements, since the full scale field tests were replaced by the scaled field tests (for the reasons discussed in the introduction to Chapter 5) and were thus never finalized.

Limited test rolling data was collected at two field sites within the TH 212 construction project near Chaska, Minnesota. A site with granular soil was visited on October 5, 2006, and a site with cohesive soil was visited on October 24, 2006. Both of these visits were scheduled primarily for the purpose of observation, but some measurements were taken nonetheless. Specifically, several rut profiles were measured in regions which failed or nearly failed according to the present test rolling criteria. Since a dynamic cone penetrometer (DCP) was readily available, DCP data was then taken in the failing regions. Moisture content measurements were also taken, although soil unit weights were not measured because no apparatus for determining unit weight was available.

A photogrammetic technique was used to measure the rut profile. This entailed taking digital photographs of the rut from several different angles and then using photogrammetry software (Photomodeler Pro 5 by Eos Systems, Inc.) to obtain the three-dimensional spatial coordinates of the rut surface. For convenience, a string was positioned across the rut and the software was then used to obtain the spatial coordinates of the string (see Fig. 5.12). The spatial variation of the string in the vertical direction (denoted y) as a function of the horizontal distance along the string (denoted x) is of most interest.

While the DCP data was taken for the most part out of convenience, it is possible to correlate the DCP data to the strength parameters required for the theoretical models developed in Chapter 3. For example, Ayers et al. (1989) correlated DCP results to angle of internal friction (ϕ) for several granular materials, suggesting that a very strong correlation exists between friction angle and DCP penetration rate.

The same test roller was used at both sites. A photograph of one of the wheels on the test roller is shown in Fig. 5.11. The wheel diameter and wheel width were approximately 1.6 m (5.2 ft) and 0.46 m (1.5 ft), respectively.

5.4.1 Site with Granular Soil

After observing test rolling at the site with granular soil, two ruts at which the soil was at or near failing (in terms of the present test rolling criteria) were identified and profile measurements were taken. Rutting was particularly severe at the first location (shown in Fig. 5.12) and relatively mild at the second location (Fig. 5.14). The rut profiles for the large and small rut, determined from photogrammetric analysis, are shown in Figs. 5.13 and 5.15, respectively. It is clear in the figures that soil damage caused by the tractor pulling the test roller creates difficulty in referring the rut profile measurements to the ground surface. Acknowledging this difficulty, the large rut measured about 120 mm (4.7 in.) in depth and the small rut measured approximately 70 mm (2.7 in.) in depth according to the photogrammetric measurements.

For each of the two ruts, DCP measurements were taken at three different locations: one DCP test was performed on the soil in the rut, another was conducted just next to the rut, and a third was performed in the relatively well-compacted soil at the centerline of the roadway

embankment. DCP data for the large rut and the small rut are shown in Figs. 5.16 and 5.17, respectively. The data is also tabulated in Appendix M.

Moisture content was determined from extracted samples taken approximately 30 cm (1 ft) below grade where the DCP tests were performed. The results are in Table 5.7. While unit weight measurements were not taken, some data on the soil, which was given by the Mn/DOT inspector at the site, is in Appendix N. The data in Appendix N represents quality assurance measurements taken along the section of the roadway where the rut profiles were measured.

Figure 5.11. Test roller tire for test roller used at field sites

Figure 5.12. Large rut at site with granular soil

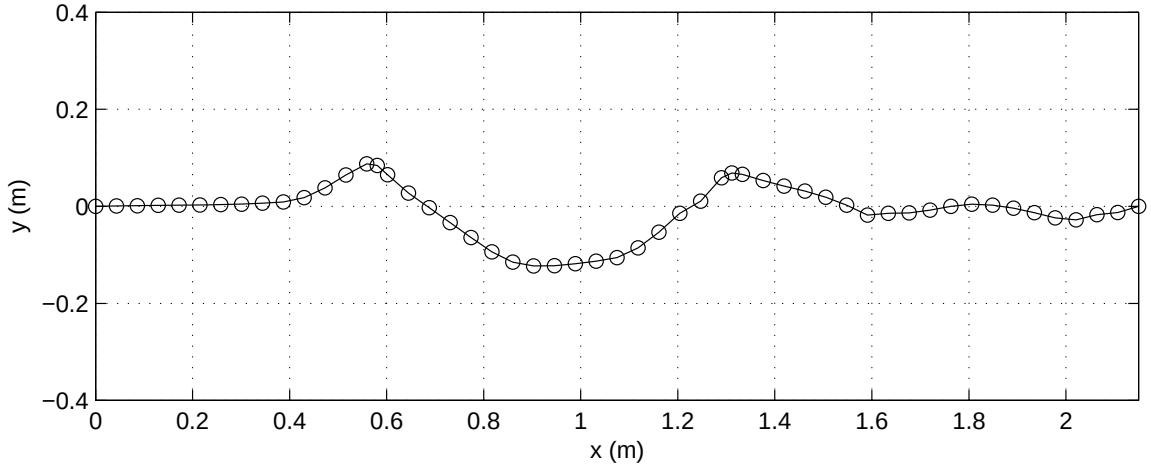

Figure 5.13. Rut profile determined for large rut at site with granular soil

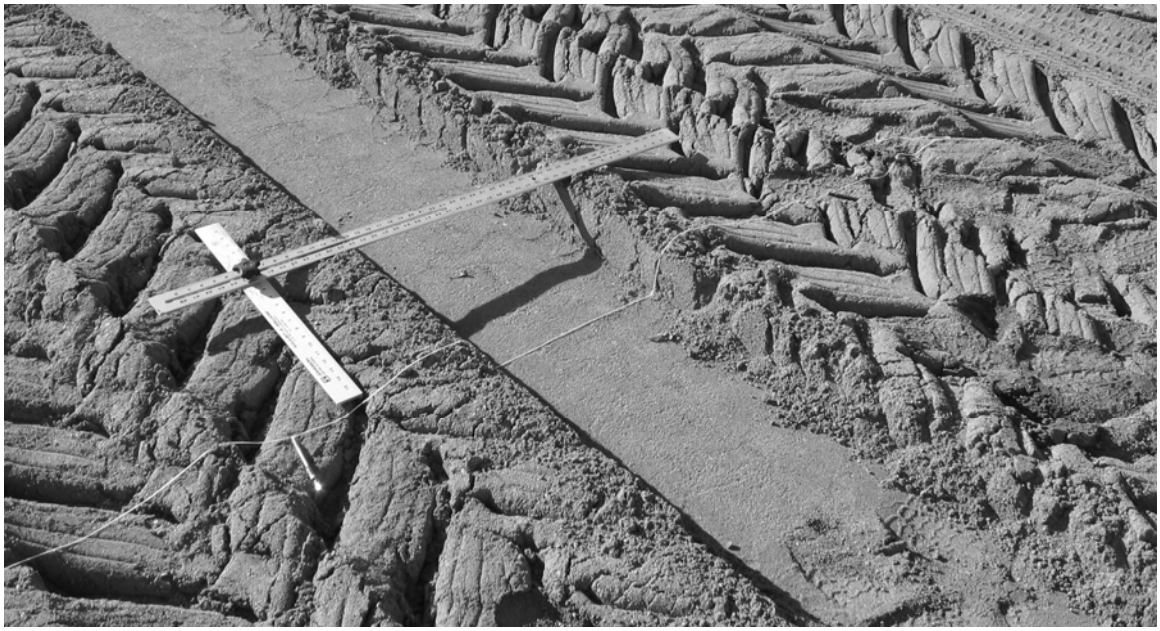

Figure 5.14. Small rut at site with granular soil

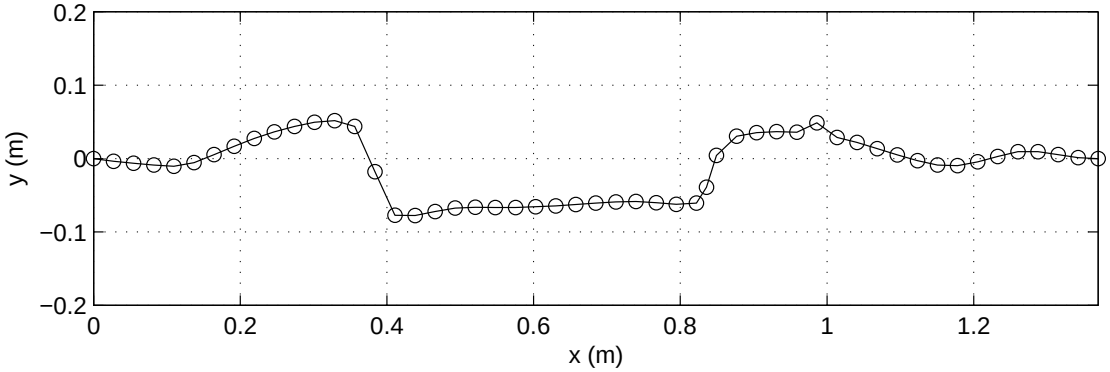

Figure 5.15. Rut profile determined for small rut at site with granular soil

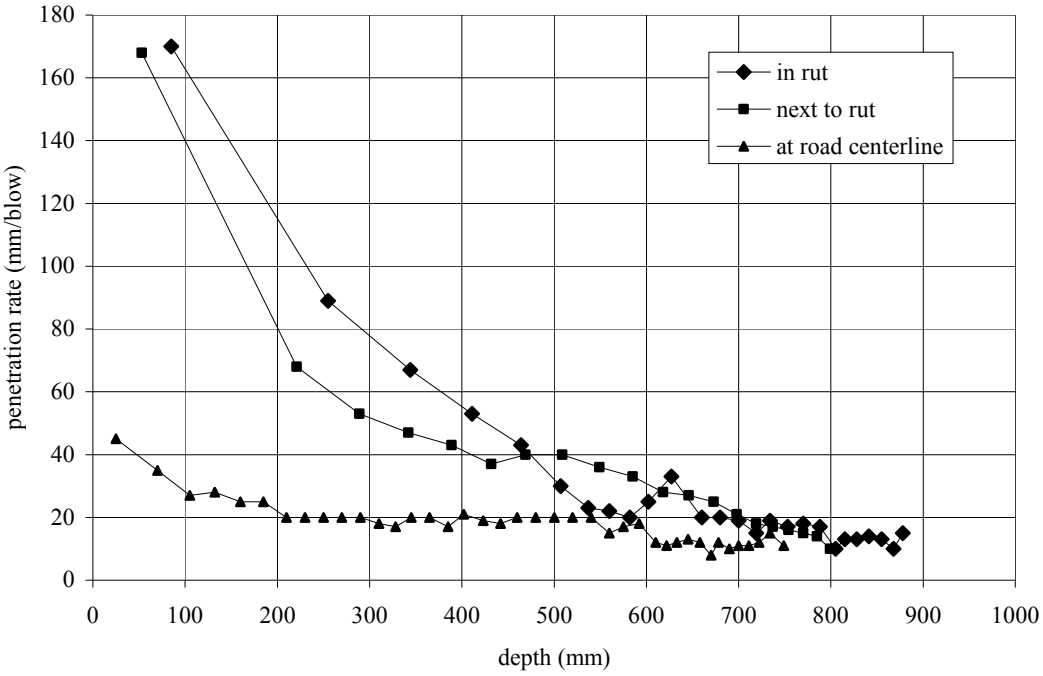

Figure 5.16. DCP data obtained for large rut at site with granular soil

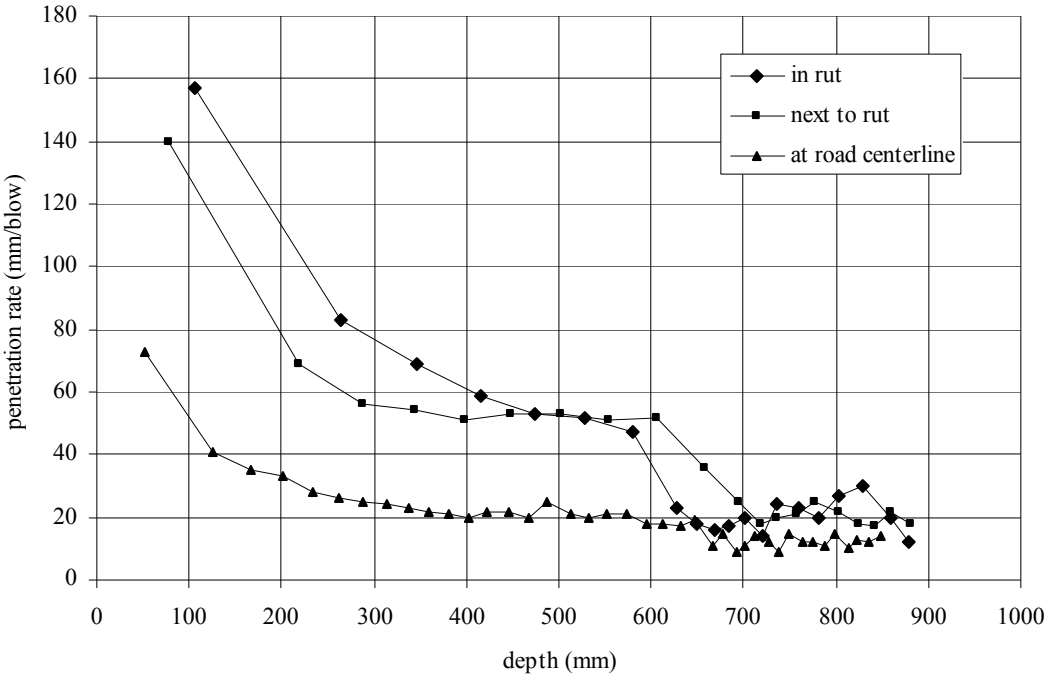

Figure 5.17. DCP data obtained for small rut at site with granular soil

Table 5.7. Moisture contents for site with granular soil

	moisture content (%)	
location	**large rut**	**small rut**
in rut	9.51	13.77
just outside rut	--	--
at road centerline	7.21	10.50

5.4.2 Cohesive Soil

At the site with cohesive soil, only the profile of one rut was measured. A photograph of the rut is in Fig. 5.18, and the rut profile determined from photogrammetric analysis is in Fig. 5.19. The soil surrounding the rut is not as damaged in the case of the cohesive soil as compared with the granular soil (Section 5.4.1), and rut depth can therefore be determined with greater confidence. The rut depth in the cohesive soil was about 90 mm (3.5 in.) according to photogrammetric measurement of the rut profile.

Two DCP tests were performed. One DCP test was performed on the soil in the rut and another was conducted just outside the rut. The DCP data is shown in Fig. 5.20 and tabulated in Appendix M. Moisture content was determined from a sample extracted at approximately 30 cm (1 ft) below grade in the rut. The moisture content was 17.1%. Other soil properties for the cohesive soil are unknown.

Figure 5.18. Rut at site with cohesive soil

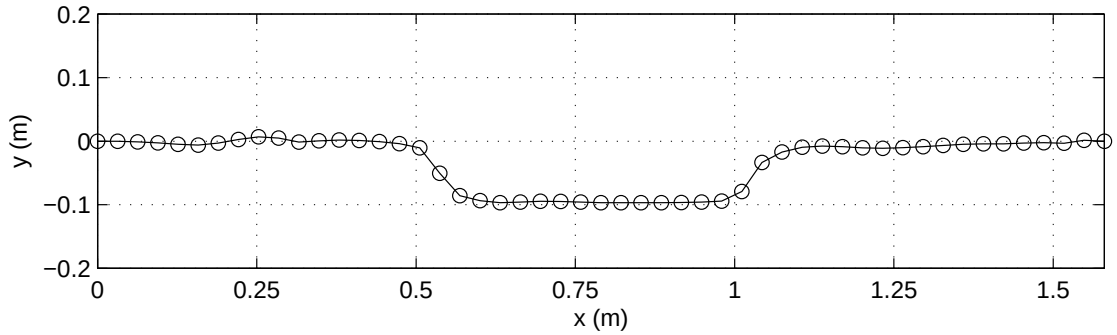

Figure 5.19. Rut profile determined for rut at site with cohesive soil

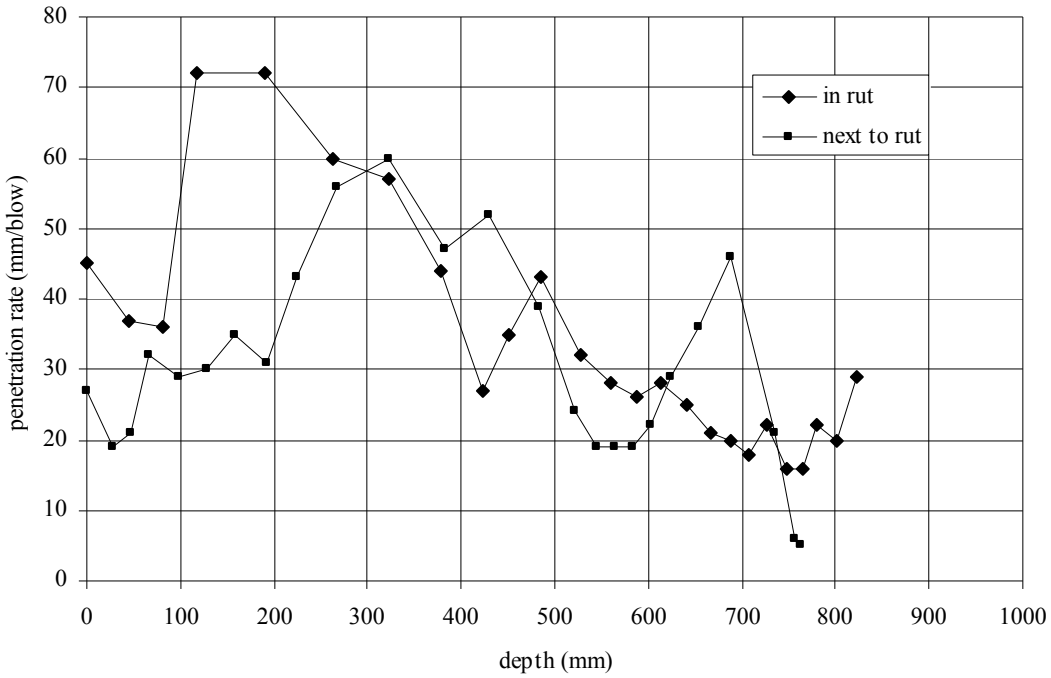

Figure 5.20. DCP data obtained for rut at site with cohesive soil

5.5 Supplemental Data

Willis et al. (1965) measured the sinkage for various towed, rigid wheels operating in granular and cohesive soils under varying vertical wheel force, presumably under steady conditions. The wheels used in the experiments were right-cylindrical, except the sides of the wheels were recessed to prevent frictional interaction between the wheel sides and the soil. Coarse sandpaper was adhered to the contacting surfaces of the wheels. The wheels had diameters of d = 50.8 cm (20 in.) and d = 40.6 cm (16 in.). For the tests on the granular soil, wheels with widths of b = 3.8 cm (1.5 in.) and b = 11.4 cm (4.5 in.) where used, and for the cohesive soil, the wheel widths were b = 3.8 cm (1.5 in.) and b = 7.6 cm (3 in.).

The granular soil was an unspecified sand with a moisture content of 5.5% and unit weight of γ = 14 kN/m^3 (90 lb/ft^3) after placement. The friction angle of the sand was determined to be ϕ = 34.6º. The cohesive material was an unspecified clay for which the moisture content and unit weight were not reported. The clay was found to have cohesion c = 22 kPa (3.2 psi) for the experiments with b = 3.8 cm (1.5 in.), which remained constant throughout the tests. The clay was reported to have lost moisture throughout the tests with b = 7.6 cm (3 in.), resulting in an increase in cohesion. A mean cohesion of 30 kPa was given for the experiments with b = 7.6 cm (3 in.). The reported friction angle of the clay was ϕ = 6.9º. No other material properties were given for the sand or the clay. It is somewhat ambiguous whether the friction angle and cohesion reported by the authors pertains to the Mohr-Coulomb strength parameters or the bevameter test parameters discussed in Section 2.2.1.1.1. Nonetheless, the given parameters are within the range of typical Mohr-Coulomb strength parameters for a medium-density sand and soft clay.

The experimental force-sinkage data given by Willis et al. (1965) are tabulated in Tables 5.8-5.15 and plotted in Figs. 5.21 and 5.22. Note that some of the data correspond to the actual experimental results and some are "fitted" data (denoted as such in the tables and figures). The authors did not present all of there exact experimental results to conserve space, but all of the data evidently exhibited trends strong enough to be well-represented by a few selected points.

Table 5.8. Force-sinkage data for sand and wheel with d = 40.6 cm and b = 3.8 cm; fitted (Willis et al. 1965)

s (cm)	Q_V (kN)
2.5	0.089
5.1	0.233
7.6	0.440
10.2	0.759

Table 5.9. Force-sinkage data for sand and wheel with d = 40.6 cm and b = 11.4 cm (Willis et al. 1965)

s (cm)	Q_V (kN)
0.9	0.085
1.5	0.177
3.3	0.355
3.4	0.445
4.0	0.535
6.1	0.543
4.7	0.712
5.6	0.802
5.8	0.891

Table 5.10. Force-sinkage data for sand and wheel with d = 50.8 cm and b = 3.8 cm (Willis et al. 1965)

s (cm)	Q_V (kN)
2.7	0.093
4.5	0.227
7.7	0.503
6.2	0.573
8.9	0.592
9.0	0.682
9.3	0.682
9.1	0.771
9.6	0.771
10.0	0.771
10.4	0.861
10.7	0.861
10.9	0.950
11.3	0.950
11.2	1.042

Table 5.11. Force-sinkage data for sand and wheel with d = 50.8 cm and b = 11.4 cm; fitted (Willis et al. 1965)

s (cm)	Q_V (kN)
1.3	0.176
2.5	0.385
3.8	0.630
5.1	0.940

Table 5.12. Force-sinkage data for clay and wheel with d = 40.6 cm and b = 3.8 cm; fitted (Willis et al. 1965)

s (cm)	Q_V (kN)
0.6	0.253
1.3	0.383
2.5	0.564
5.1	0.856
7.6	1.090

Table 5.13. Force-sinkage data for clay and wheel with d = 40.6 cm and b = 7.6 cm (Willis et al. 1965)

s (cm)	Q_V (kN)
0.2	0.408
0.5	0.678
0.7	0.899
0.9	1.118
1.5	1.345
2.6	1.565
3.2	1.784
3.9	2.010

Table 5.14. Force-sinkage data for clay and wheel with d = 50.8 cm and b = 3.8 cm; fitted (Willis et al. 1965)

s (cm)	Q_V (kN)
1.3	0.392
2.5	0.566
5.1	0.843
7.6	1.068
10.2	1.287

Table 5.15. Force-sinkage data for clay and wheel with d = 50.8 cm and b = 7.6 cm (Willis et al. 1965)

s (cm)	Q_V (kN)
0.4	0.534
0.8	0.792
1.4	1.059
1.9	1.334
2.4	1.334
2.9	1.557
3.0	1.557
3.3	1.810
4.3	2.028
5.2	2.268

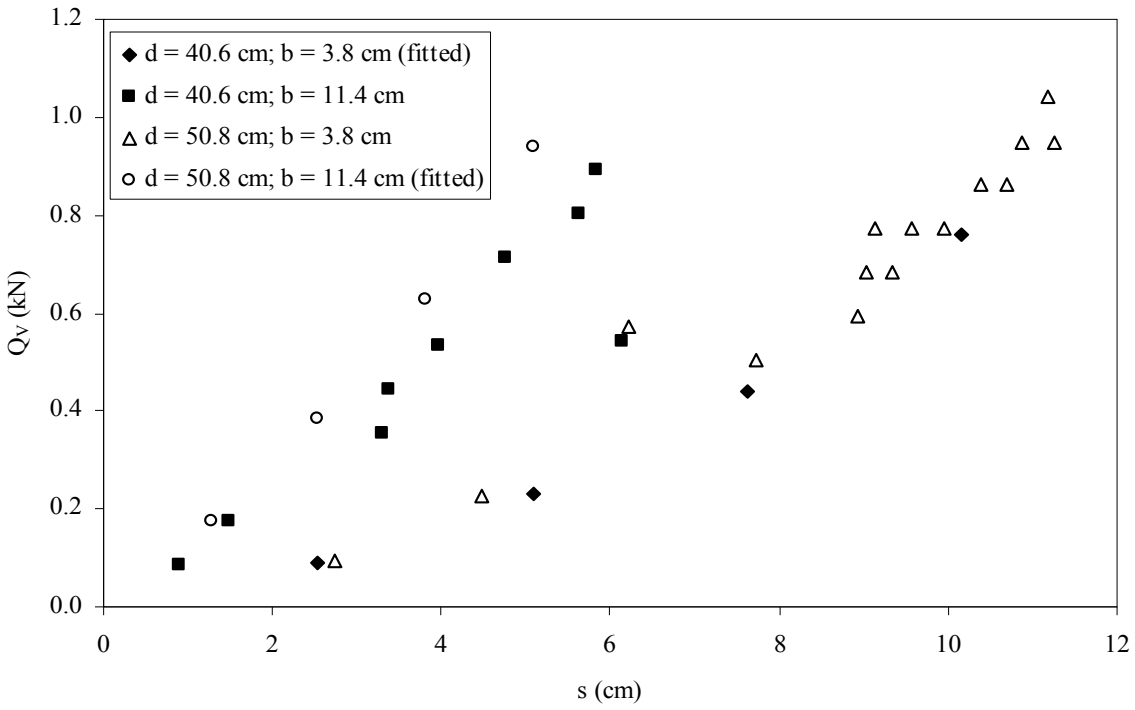

Figure 5.21. Force versus sinkage for rolling tests on sand (Willis et al. 1965)

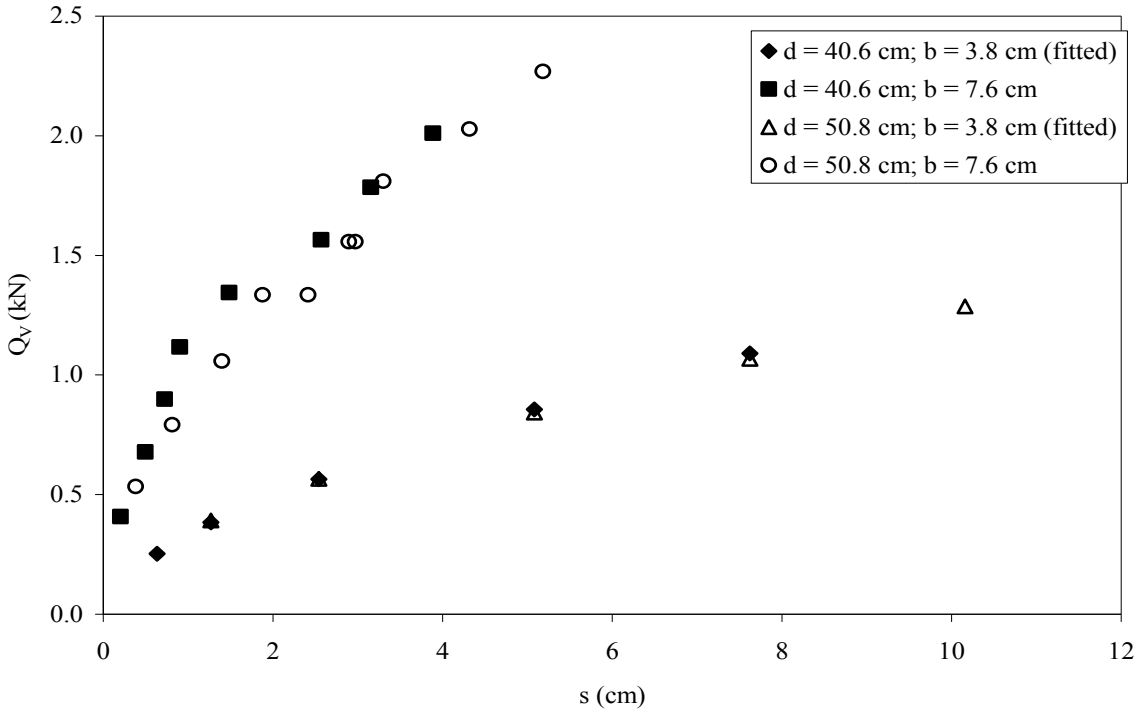

Figure 5.22. Force versus sinkage for rolling tests on clay (Willis et al. 1965)

Chapter 6

Laboratory Testing

This chapter presents the laboratory testing performed to determine the mechanical properties of the soils described in Chapter 5 on which scaled field tests were performed. In the scaled field tests, both a cohesive soil and a granular soil were used. Details regarding the classification and properties of the two soils can be found in Chapter 5.

Soil specimens and samples were collected in the scaled field tests for the purpose of laboratory testing. In the case of the cohesive soil, specimens were extracted from the soil test bed after completing an indentation or rolling test. For the granular soil, bulk samples were retained to prepare specimens for laboratory testing.

Section 6.1 explains the laboratory tests conducted on the soil specimens. In Section 6.2, the results of the laboratory tests are given, as well as their interpretation in terms of the material constants assumed in the soil constitutive models used in Chapter 3.

6.1 Test Procedures

6.1.1 Cohesive Soil

As discussed in Chapter 5, the cohesive soil was prepared in such a way that frictionless ($\phi = 0$) plastic behavior would be a reasonable approximation under relatively fast loading. With $\phi = 0$, the soil elastic modulus E_s and cohesion c may be easily and accurately determined from uniaxial compression tests. For this reason, uniaxial compression tests (cf. Das 2005 and ASTM D 2166) formed the basis for determining mechanical properties of the cohesive soil, although several triaxial compression tests were also performed in order to evaluate the assumption of frictionless response.

Shortly after the cohesive soil was mixed with water to achieve the target moisture content, three right-cylindrical specimens were prepared and subjected to standard unconsolidated-undrained triaxial compression tests (cf. Das 2005 and ASTM D 2850). The specimens were prepared by kneading the clay into a container, subjecting the soil to an overburden pressure of roughly 100 kPa (14.5 psi) for 10 minutes in a load frame, inserting 100 mm (4 in.) sampling tubes into the soil, and then extruding the soil specimens from the tubes. The samples were trimmed to a height of roughly 200 mm (8 in.). The triaxial tests were then performed using a load frame and conventional triaxial testing apparatus. The tests were displacement-controlled, with an axial displacement rate of about 0.1 mm/s (0.004 in./s).

The scaled field tests (Chapter 5), using two separate wheel sizes, were conducted within a period of roughly two months after the cohesive soil was mixed to the desired moisture content.

Indentation tests using the small wheel were conducted within several days after soil was mixed. The rolling tests with the small wheel were conducted approximately two weeks later. The indentation and rolling tests using the large wheel were conducted a total of about two months after the soil was mixed. In order to accommodate the possibility that the soil mechanical properties could change over time, uniaxial compression tests were conducted shortly after the indentation and rolling tests at each of these three different periods. There are thus three sets of results from uniaxial compression tests, each corresponding to a specific series of scaled field tests. The displacement-controlled uniaxial compression tests were conducted using a standard load frame and an axial displacement rate of 0.1 mm/s (0.004 in./s).

6.1.2 Granular Soil

In the scaled field tests, the granular soil was tested at two different densities. In the series of tests in which the sand was prepared in a loose state, the dry unit weight averaged 16.0 kN/m^3 (102 lb/ft^3). For the series of tests with the sand in the dense condition, the dry unit weight averaged 17.4 kN/m^3 (111 lb/ft^3). The sand was tested under air-dried conditions and the moisture content of the sand was considered zero for all the tests. Relative densities were on average 5% and 81% for the loose and dense materials, respectively.

Loose and dense specimens for the triaxial compression tests were prepared in a right-cylindrical, membrane-lined mold with a diameter of 35 mm (1.4 in.) and a height of 80 mm (3.2 in.). To prepare the loose specimens, the sand was rained into the mold in small (~15 mm (0.6 in.)) lifts through a funnel, gently leveling the soil in the mold with a tamper after each lift. To prepare the dense specimens, the sand was again rained into the mold in small lifts, and after placement of each lift, the sand was tamped to compact the soil. The density of each specimen was evaluated by determining the mass of the sand within the mold and measuring the diameter and height of the specimen after removal of the mold. The calculated densities and unit weights are given in Section 6.2.2.

In total, 10 specimens of the granular soil were prepared for the triaxial compression tests, with 5 prepared in a loose state and 5 prepared in a dense state. The specimens were subjected to standard consolidated-drained triaxial compression tests (cf. Das 2005). The test chamber through which the confining pressure was applied was filled with water, such that burette readings of the fluid leaving and entering the chamber as a result of dilation or contraction of the specimen could be taken. The average volumetric strain within a specimen throughout a triaxial compression test was computed based on the burette readings.

In addition to the triaxial compression tests, several direct shear tests were performed on loose soil specimens, primarily due to the fact that a loose state is more easily achieved with this test. Loose specimens were prepared by raining the sand through a funnel into a shear box with a length of 102 mm (4 in.), width of 102 mm (4 in.), and depth of 38 mm (1.5 in.). Soil density was determined after preparation of each specimen by measuring the mass and volume of the sand within the shear box. After preparing a specimen, the shear box was placed in a direct shear apparatus and subjected to a standard direct shear test (cf. Das 2005 and ASTM D 3080). A total of 7 direct shear tests, with varying applied normal stresses, were performed on loose sand specimens. Particular emphasis was placed on obtaining information over a low range of normal stresses.

6.2 Test Results

6.2.1 Cohesive Soil

Figs. 6.1 and 6.2 show the results of the triaxial compression tests performed on the cohesive soil. Fig. 6.1 gives the deviatoric stress-strain data from the triaxial tests, and Fig. 6.2 is the corresponding Mohr's plot showing the stress states at failure. The Mohr-Coulomb failure envelope interpreted for the soil is also given in Fig. 6.2. The clay was found to have internal friction with $\phi \approx 3°$. The low friction angle warrants the assumption of pressure independence and the use of uniaxial compression tests for determining mechanical properties.

The results of the uniaxial compression tests corresponding to the indentation tests with the small wheel are shown in Fig. 6.3, along with the approximated Young's modulus E_s = 2 MPa (290 psi) and uniaxial yield stress σ_o = 58 kPa (8.4 psi). Results for the rolling tests using the small wheel are shown in Fig. 6.4, and as depicted, material properties for the rolling tests with the small wheel are approximately E_s = 2 MPa (290 psi) and σ_o = 72 kPa (10.4 psi). Data from the uniaxial compression tests corresponding to the indentation and rolling tests with the large wheel are shown in Fig. 6.5 along with the approximated parameters E_s = 2.5 MPa (363 psi) and σ_o = 70 kPa (10.2 psi). The different form of the stress-strain curves between Figs. 6.3-6.5 and differences in the approximate material properties may be attributed to thixotropy and moderate moisture loss during storage of the clay.

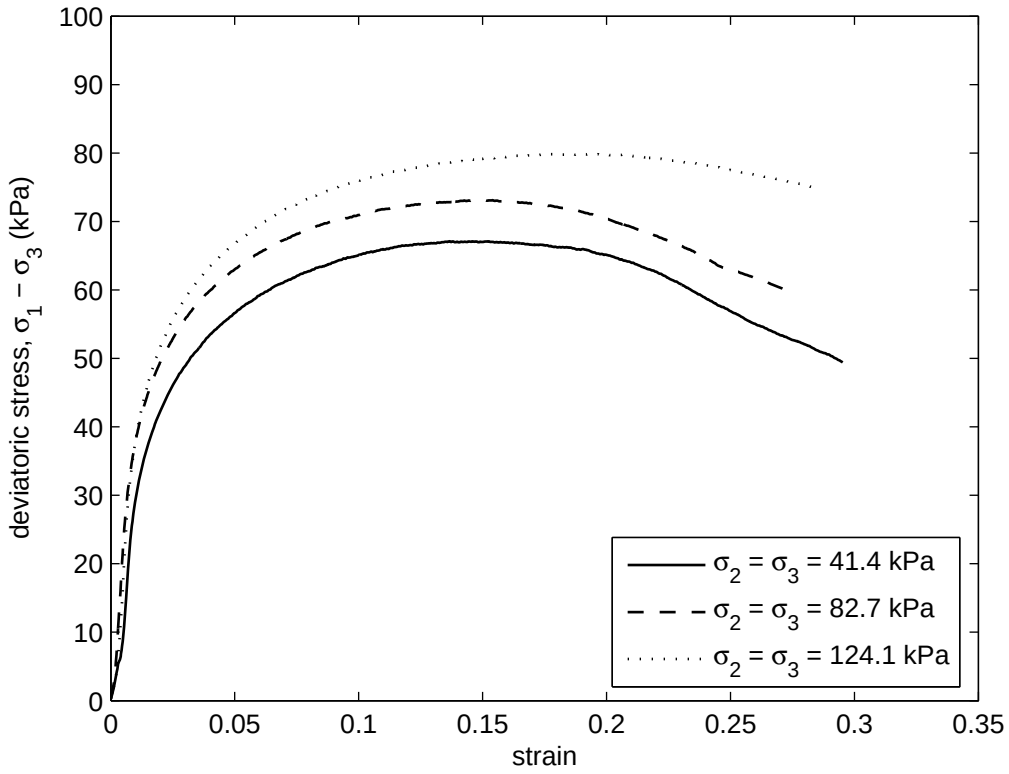

Figure 6.1. Deviatoric stress versus axial strain from triaxial tests on cohesive soil

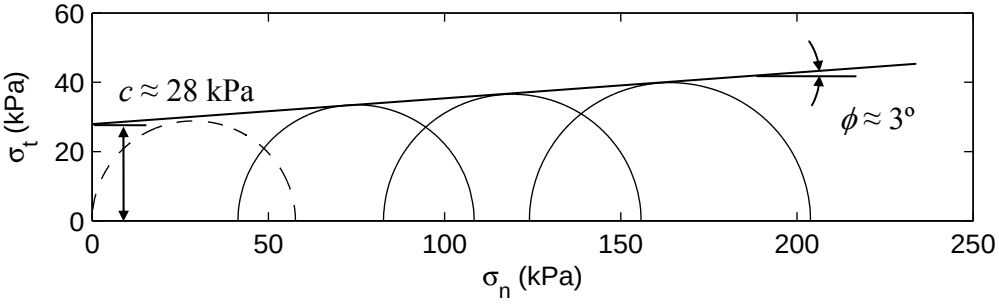

Figure 6.2. Mohr's plot and failure envelope from triaxial tests on cohesive soil (dashed line indicates results from corresponding uniaxial compression test)

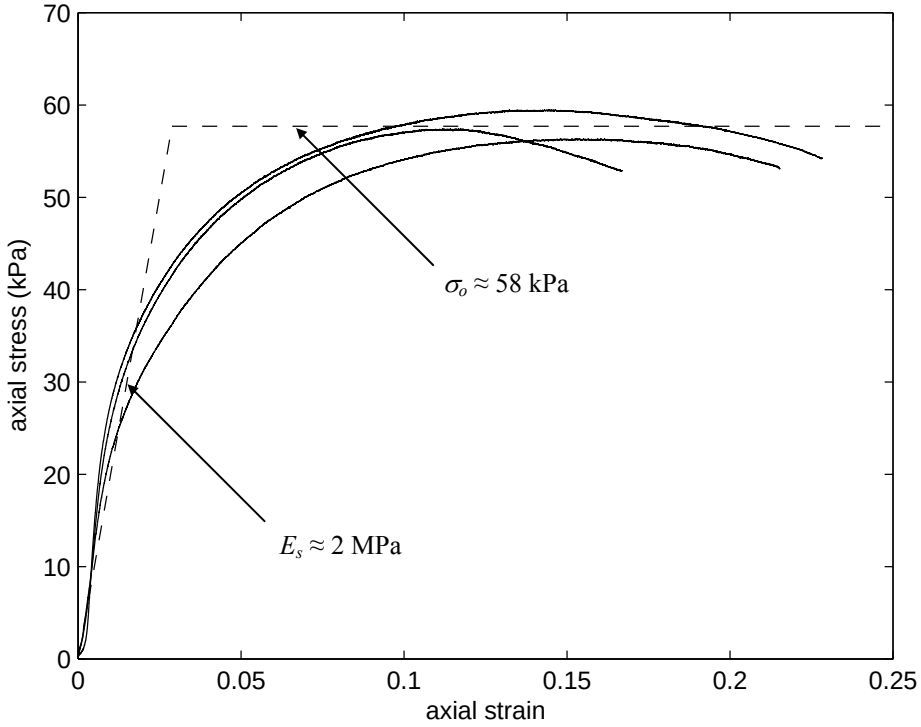

Figure 6.3. Uniaxial compression tests on cohesive soil used in indentation tests with small wheel

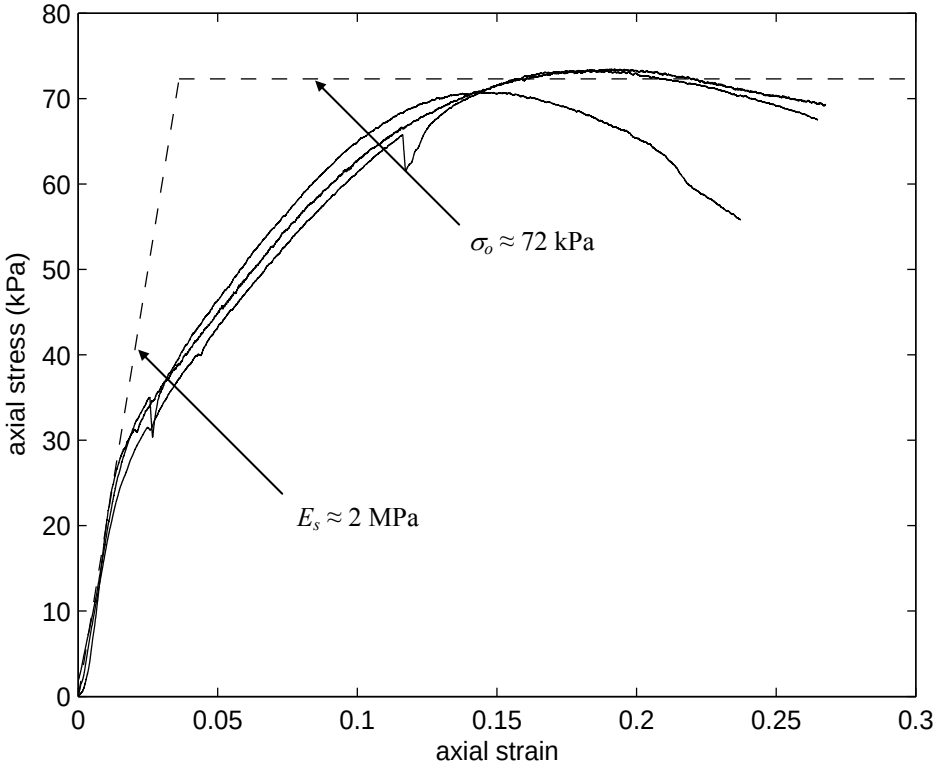

Figure 6.4. Uniaxial compression tests on cohesive soil used in rolling tests with small wheel

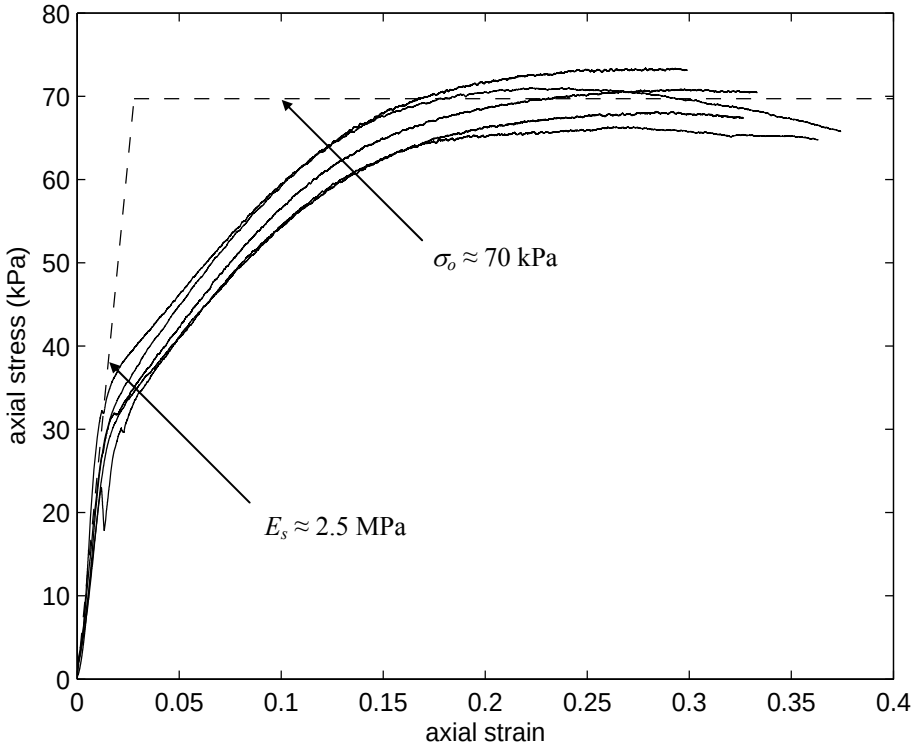

Figure 6.5. Uniaxial compression tests on cohesive soil used in indentation and rolling tests with large wheel

6.2.2 Granular Soil

The initial densities and unit weights measured for each of the specimens tested in triaxial compression are given in Tables 6.1 and 6.2. The average dry unit weight measured for the specimens prepared in a loose state was 16.8 kN/m^3 (107 pcf) and the average dry unit weight for the dense specimens was 17.7 kN/m^3 (113 pcf).

Figs. 6.6 and 6.7 give deviatoric stress versus axial strain for each of the triaxial compression tests. Figs. 6.8 and 6.9 show the calculated volumetric strain versus axial strain for each of the tests. Note that the curves in Figs. 6.8 and 6.9 are interpolated from about 15 readings taken throughout each test.

Fig. 6.10 shows the Mohr's plot with stress states at failure from the triaxial compression tests on the loose granular soil. It is shown that a best-fit Mohr-Coulomb failure envelope corresponds to a friction angle ϕ = 35.5º and apparent cohesion c = 4.0 kPa (0.58 psi). The apparent cohesion is an artifact arising because the true failure envelope is non-linear. The dry granular soil tested has no uniaxial compression strength, so the failure envelope should pass through the origin in the Mohr's plot. An alternative failure envelope with c = 0 is also shown in Fig. 6.10, with a corresponding approximate friction angle ϕ = 39º applicable over the range of confining pressures used in the tests.

Fig. 6.11 shows the Mohr's plot from the triaxial compression tests on the dense granular soil. Again, a best-fit Mohr-Coulomb failure envelope has ϕ = 42º and apparent cohesion c = 6.5 kPa (0.94 psi). The friction angle for the failure envelope with c = 0 has again a somewhat larger friction angle of roughly ϕ = 46º, applying over the confining pressures at which the tests were conducted. Notice that the friction angle is increased by approximately 7º when the sand is compacted from a loose state to a dense state.

Fig. 6.12 shows Young's modulus as a function of confining pressure from the triaxial compression tests. The moduli were computed by fitting a line to the initial, linear portion of the deviatoric stress-strain curves in Figs. 6.6 and 6.7.

Data from the direct shear tests conducted on the loose granular soil are presented in Table 6.3 and Figs. 6.13-6.14. In Table 6.3, the initial densities and unit weights of the specimens are shown. The average initial dry unit weight was 16.5 kN/m^3 (105 pcf), which is somewhat lower than the average unit weight achieved for the loose specimens prepared for the triaxial compression tests. Fig. 6.14 shows the Mohr's plot and approximated failure envelopes using the data from the direct shear tests. A best-fit Mohr-Coulomb failure envelope corresponds with ϕ = 32º and apparent cohesion c = 2 kPa (0.3 psi), with the apparent cohesion again indicating non-linearity of the failure envelope. A reasonable approximation of the failure envelope, over the range of normal stresses used in the tests, with c = 0 corresponds to $\phi \approx$ 36º.

Table 6.1. Initial densities of loose granular soil specimens in triaxial compression tests (values tabulated are for dry material)

Test No.	σ_3 (kPa)	ρ (kg/m^3)	γ (kN/m^3)
1	6.9	1707	16.74
2	13.8	1723	16.90
3	20.7	1704	16.71
4	27.6	1717	16.84
5	34.5	1707	16.74

Table 6.2. Initial densities of dense granular soil specimens in triaxial compression tests (values tabulated are for dry material)

Test No.	σ_3 (kPa)	ρ (kg/m^3)	γ (kN/m^3)
1	6.9	1788	17.53
2	13.8	1796	17.61
3	20.7	1795	17.61
4	27.6	1816	17.81
5	34.5	1810	17.75

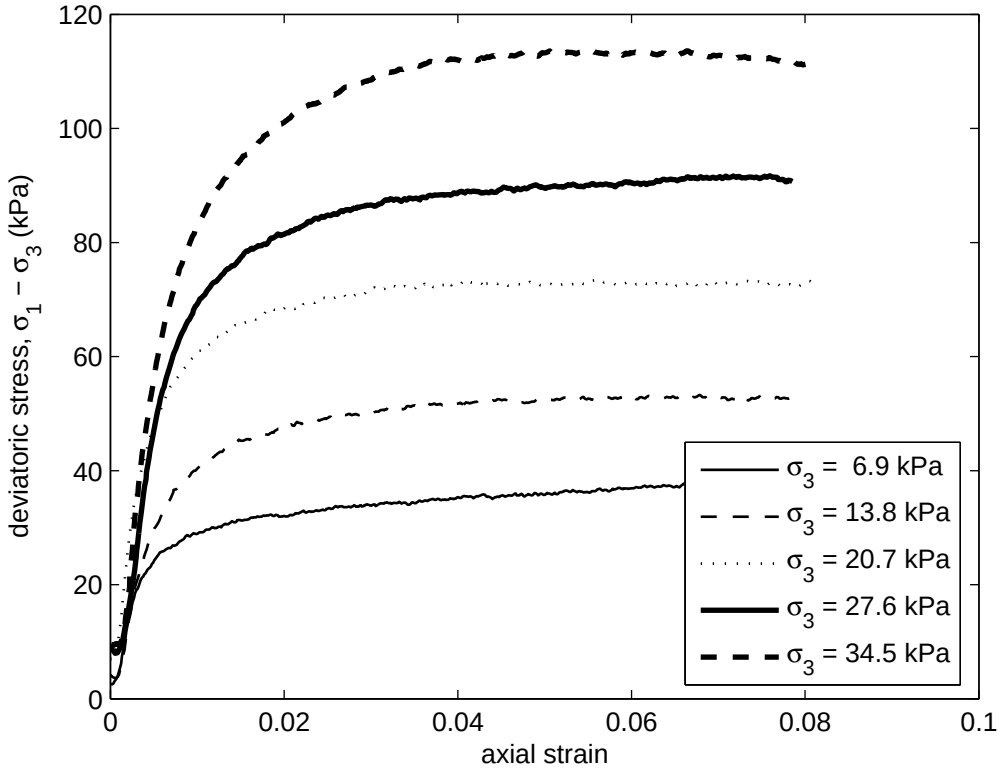

Figure 6.6. Deviatoric stress versus axial strain from triaxial compression tests on loose granular soil

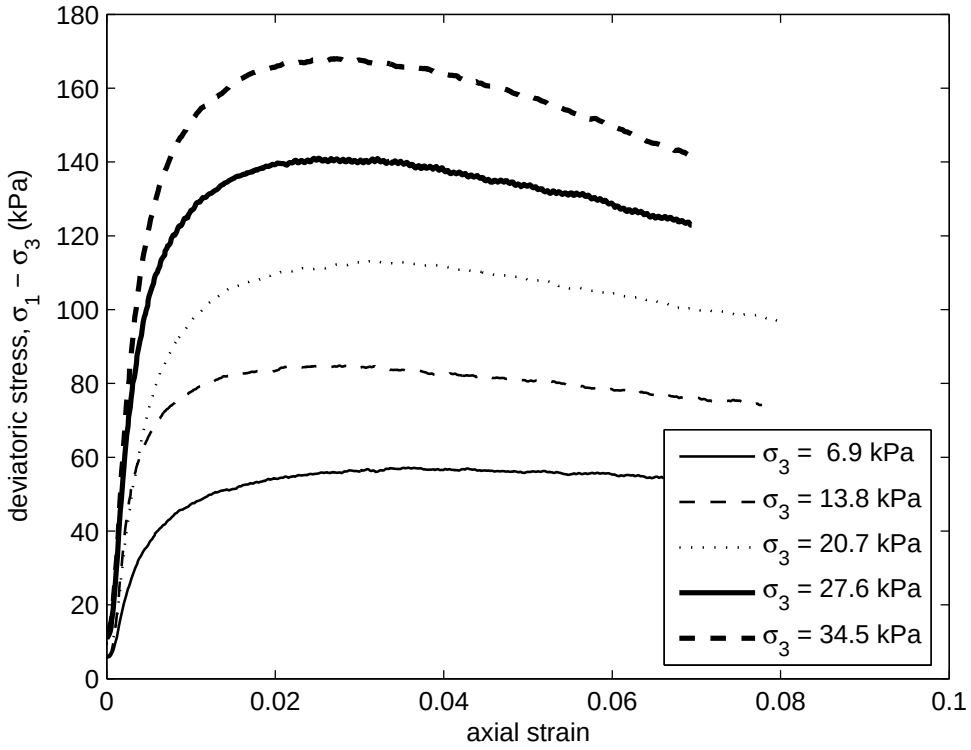

Figure 6.7. Deviatoric stress versus axial strain from triaxial compression tests on dense granular soil

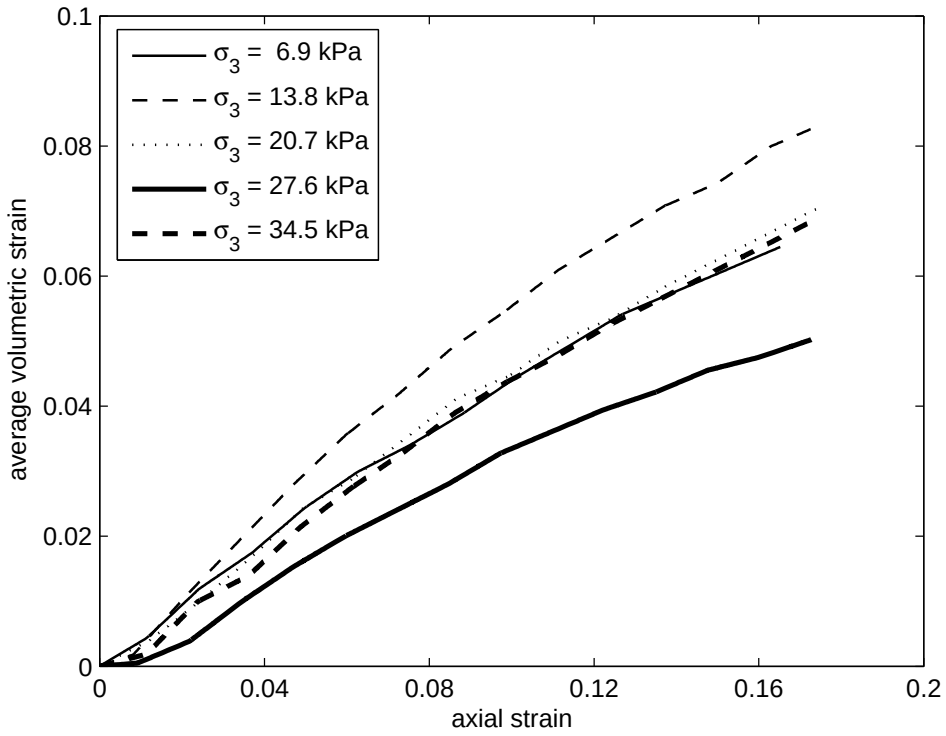

Figure 6.8. Average volumetric strain (interpolated) versus axial strain from triaxial compression tests on loose granular soil (positive volumetric strain implies dilation)

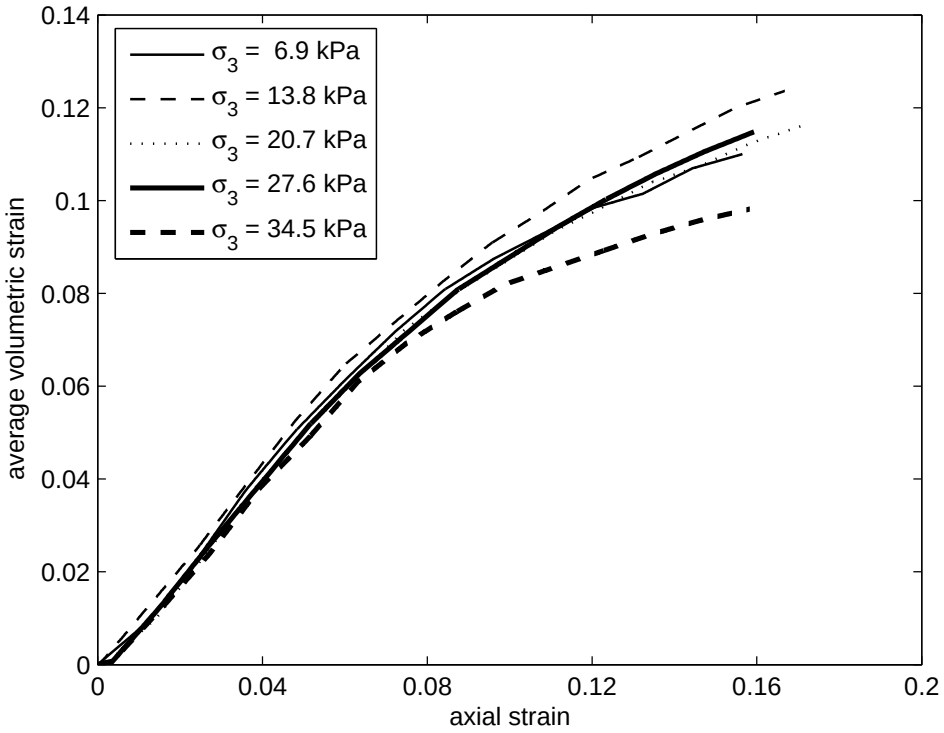

Figure 6.9. Average volumetric strain (interpolated) versus axial strain from triaxial compression tests on dense granular soil (positive volumetric strain implies dilation)

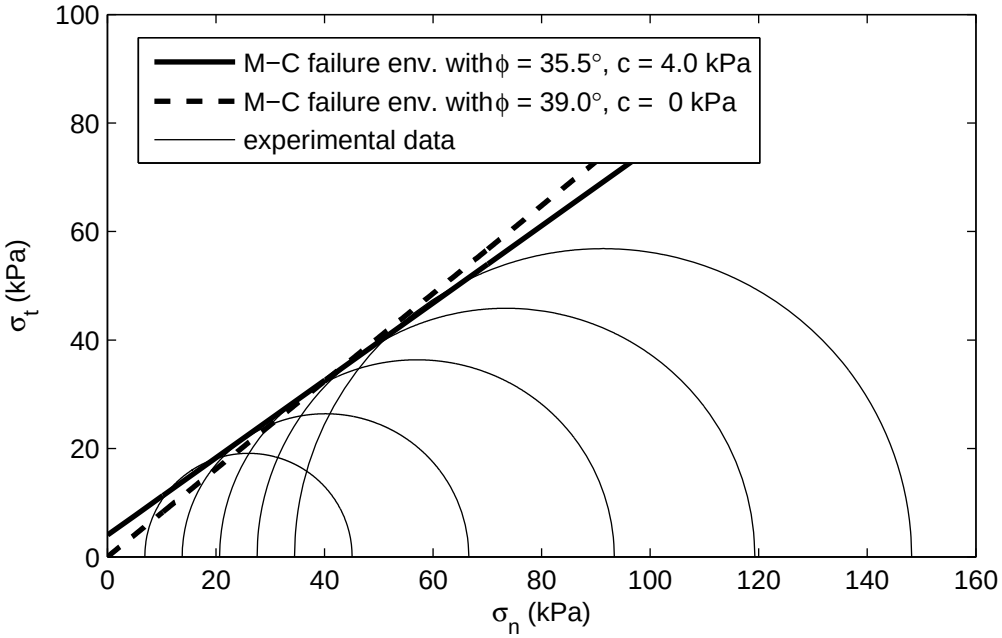

Figure 6.10. Mohr's plot for triaxial compression tests on loose granular soil

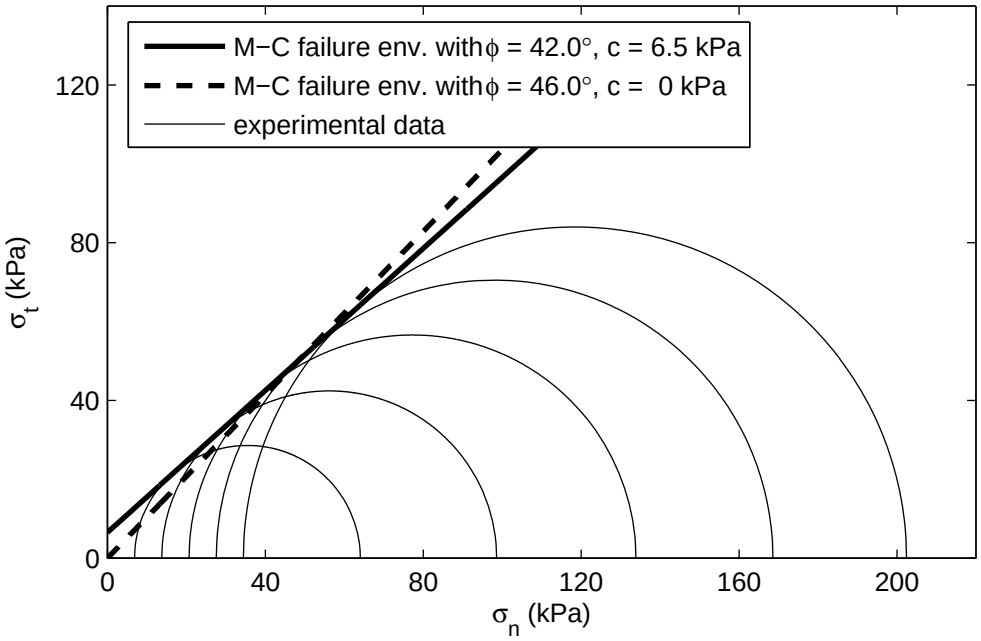

Figure 6.11. Mohr's plot for triaxial compression tests on dense granular soil

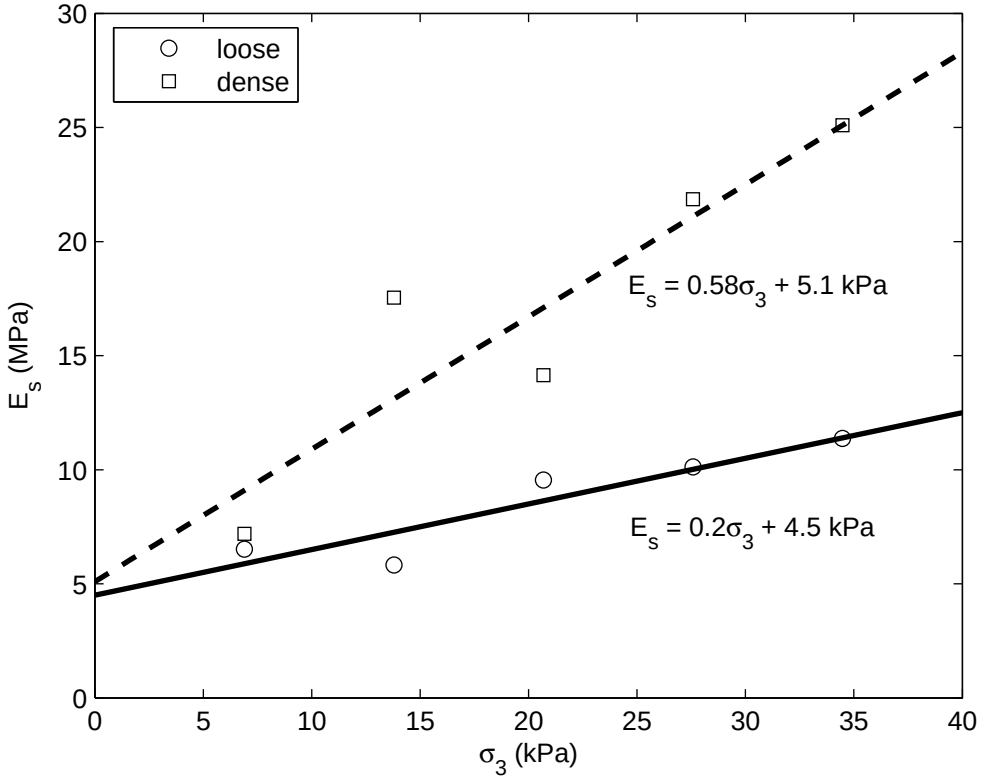

Figure 6.12. Young's modulus versus confining pressure from triaxial compression tests on granular soil

Table 6.3. Initial densities of loose granular soil specimens in direct shear tests
(values tabulated are for dry material)

Test No.	σ_n (kPa)	ρ (kg/m^3)	γ (kN/m^3)
1	3.2	1666	16.33
2	5.0	1687	16.54
3	9.2	1684	16.52
4	12.9	1678	16.45
5	17.5	1690	16.58
6	22.9	1694	16.61
7	49.1	1699	16.66

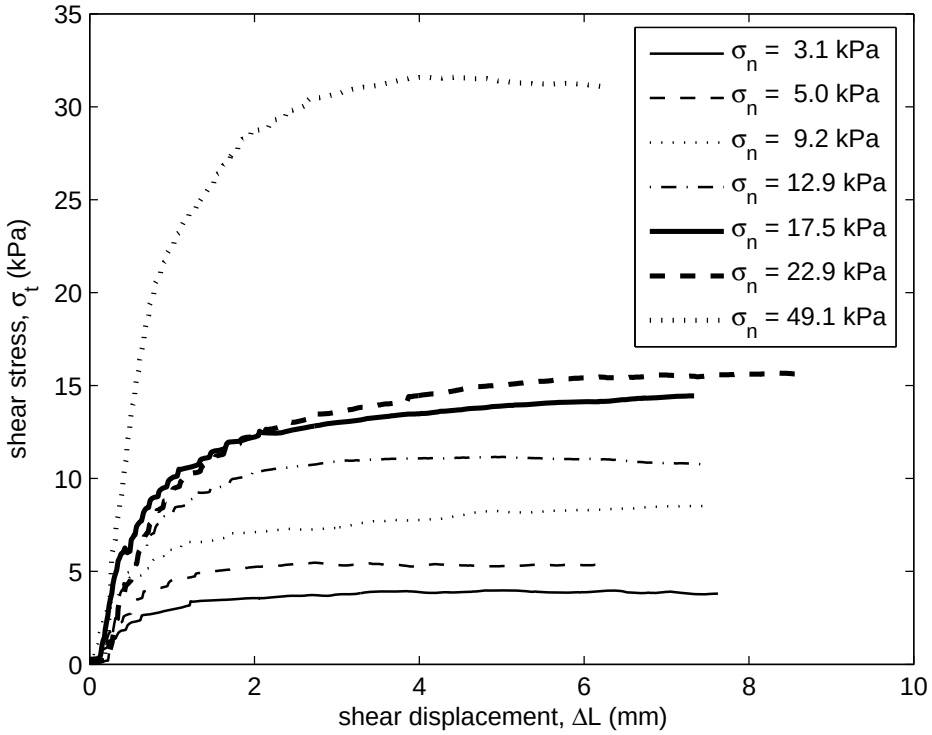

Fig. 6.13. Shear stress versus shear displacement from direct shear tests on loose granular soil

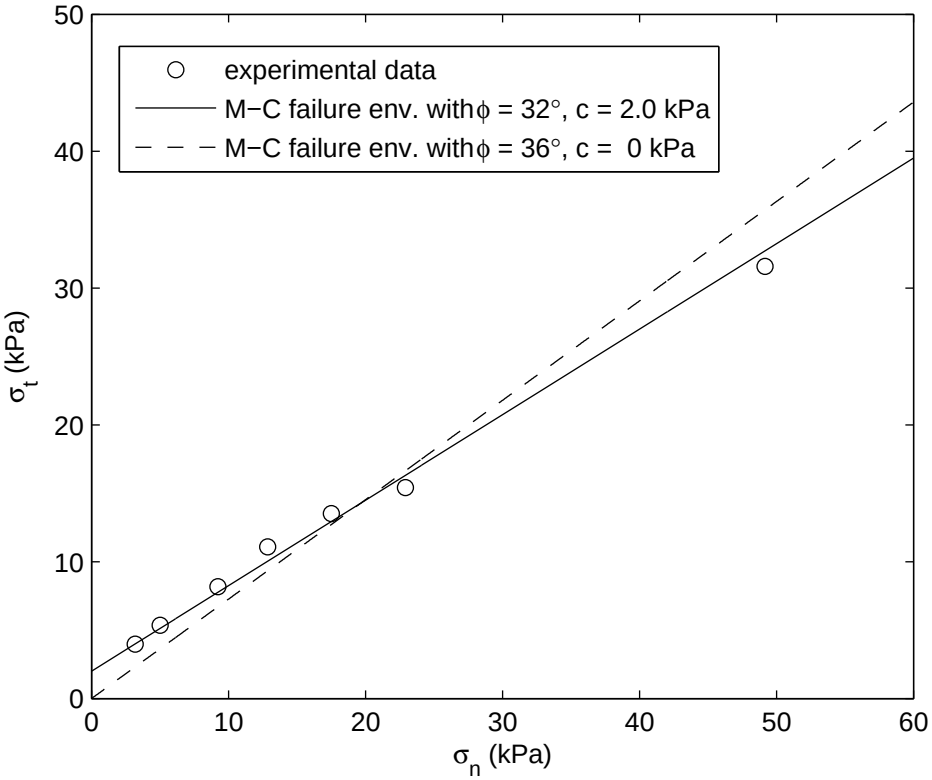

Fig. 6.14. Mohr's plot determined from direct shear tests on loose granular soil

Chapter 7

Comparison of Theoretical Predictions and Experimental Data

In this chapter, the theoretical predictions from Chapter 3 for wheel sinkage are compared with experimental data collected from lab-scaled field tests (Chapter 5). The soil mechanical properties determined from laboratory testing (Chapter 6) were used in the theoretical models to formulate sinkage predictions. The theoretical predictions and experimental data are compared in Sections 7.1-7.3, and the validity of the theoretical models is critically assessed in Section 7.4.

As mentioned in the introduction to Chapter 5, deficiencies in the field tests, including soil damage caused by tractor pulling the test roller and unknown tire construction, preclude use of the field data in validating the models. A comparison between the results of the field tests and the theoretical predictions is nevertheless made in Section 7.3, as insights can still be drawn from the limited field data. Lack of information in the field tests, regarding soil properties and test roller tire construction particularly, is necessarily compensated with some speculation.

Using the analytic method, the theoretical predictions obtained for comparison with experimental data are based on the slight modification discussed in Section 3.5, where the equivalent footing depth $D = \eta s / 6$ is replaced with the modified depth $\bar{D} = s$. Only the inclined footing method (Section 3.2.2.2) is used, as it gives better agreement with experimental and numerical results and is believed to more accurately reflect the true failure mechanism beneath a rolling wheel.

In the numerical simulations discussed in this chapter, the modified Drucker-Prager yield condition discussed in Section 3.1.2 was used to provide a closer match to the Mohr-Coulomb failure envelope than the Drucker-Prager yield condition.

7.1 Comparison of Predictions and Data from Scaled Field Tests

In this section, theoretical predictions are compared with experimental data obtained from the scaled field tests discussed in Section 5.3. The soil mechanical properties determined in Section 6.2 were used to formulate the theoretical predictions.

7.1.1 Cohesive Soil

7.1.1.1 Indentation

The experimental results for wheel weight (vertical force) Q_V as a function of wheel sinkage s with indentation of the small wheel (d = 78 mm (3 in.) and b = 25 mm (1 in.)) are plotted in Fig. 7.1 together with theoretical predictions from the analytic method and numerical simulations. Simulations with two different soil Young's moduli were conducted: E_s = 2 MPa (290 psi) is representative of the modulus measured experimentally and E_s = 50 MPa (7250 psi) is so large as to make elastic effects negligible. The Poisson's ratio was taken as ν_s = 0.45.

The predictions from the numerical simulation with E_s = 2 MPa (290 psi) agree with the experimental results very well. The analytic method qualitatively predicts the response, though tends to overestimate the wheel force for a given sinkage, especially at low sinkage. As revealed by the results of the numerical simulation with E_s = 50 MPa (7250 psi), the overestimation of wheel force at low sinkage using the analytic method can be attributed to the very low elastic stiffness of the soil. The prediction using the analytic method, which neglects elastic effects, is in good agreement with the results from the numerical simulation with a large elastic stiffness.

A similar comparison is made in Fig. 7.2 for the large wheel (d = 115 mm (4.5 in.) and b = 38 mm (1.5 in.)). The nature of the agreement between the experimental results and predictions is nearly identical to that observed for the small wheel.

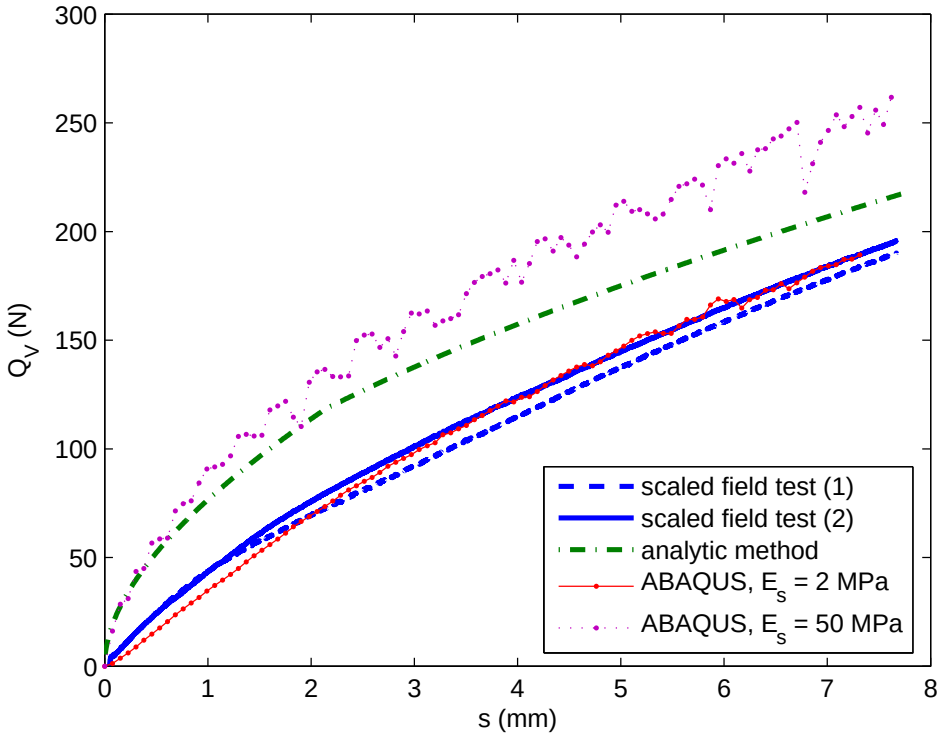

Figure 7.1. Comparison of theoretical predictions and test data on clay for indentation of wheel with d = 78 mm and b = 25 mm

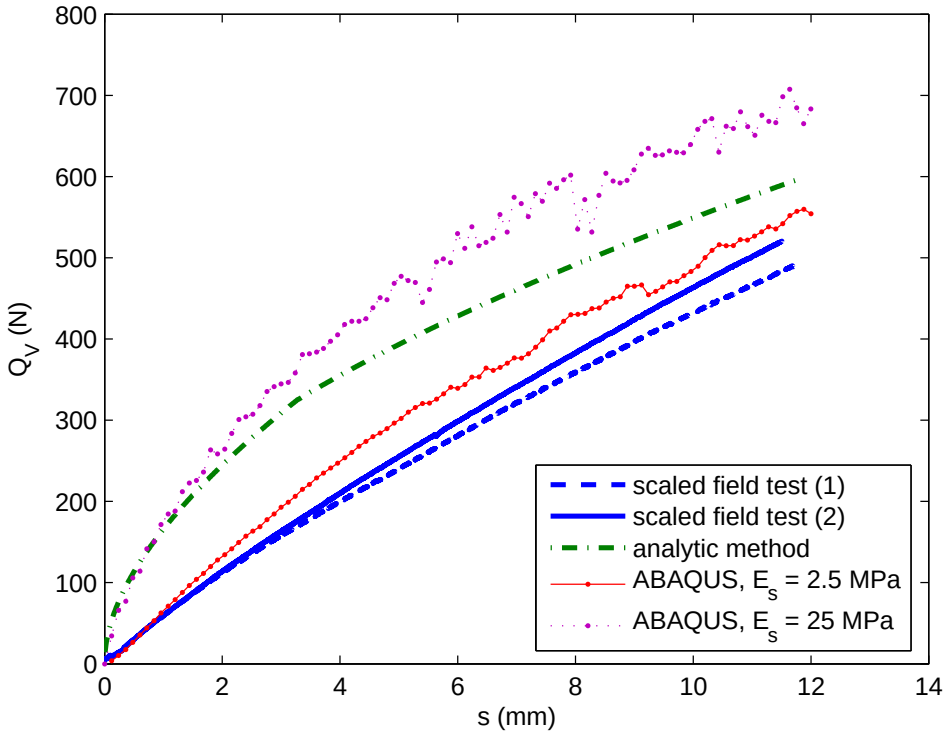

Figure 7.2. Comparison of theoretical predictions and test data on clay for indentation of wheel with d = 115 mm and b = 38 mm

7.1.1.2 Rolling

Test data and theoretical predictions are compared for the small wheel and large wheel rolling on the cohesive soil in Figs. 7.3 and 7.4, respectively. For the small wheel, two sets of numerical simulations were performed to investigate the significance of elastic effects.

Comparable agreement as was seen in the case of indentation is evident. The analytic method qualitatively predicts the response rather well, although it noticeably overestimates the wheel force at small sinkage. Results from the numerical simulation using the experimentally-measured modulus (E_s = 2 MPa (290 psi)) show good agreement, but also tend to overestimate the wheel force at small sinkage. This may be indicative of some error in the experimental measurements at very small sinkage (s ~ 1 mm (0.04 in.)), for which the values of wheel sinkage are approaching the measurement precision. Results from the numerical simulation with a relatively high modulus (E_s = 25 MPa (3600 psi)) agree well with prediction from the analytic method for which elasticity is neglected.

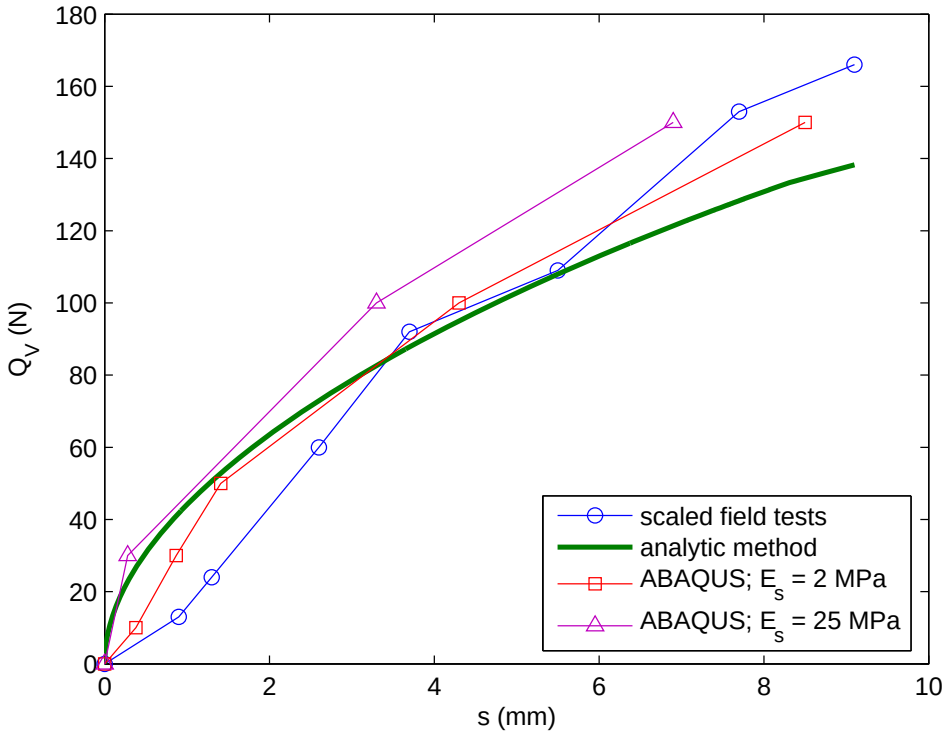

Figure 7.3. Comparison of theoretical predictions and test data on clay for rolling wheel with d = 78 mm and b = 25 mm

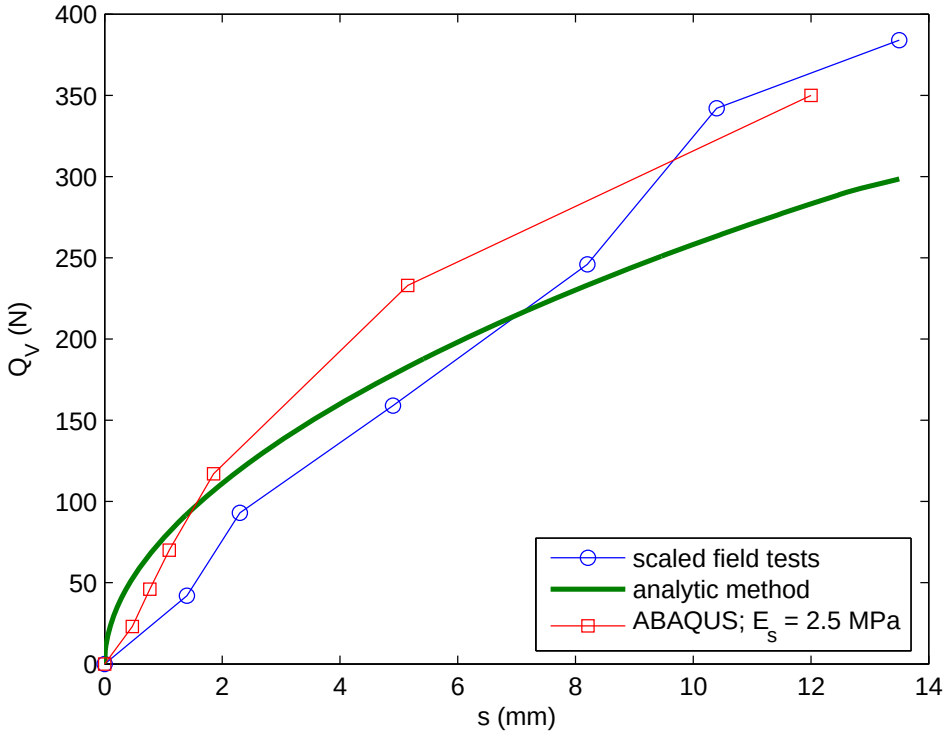

Figure 7.4. Comparison of theoretical predictions and test data on clay for rolling wheel with d = 115 mm and b = 38 mm

7.1.2 Granular Soil

7.1.2.1 Indentation

Test results for the large wheel (d = 115 mm (4.5 in.) and b = 38 mm (1.5 in.)) indenting loose sand are shown in Fig. 7.5 together with predictions using the analytic method. As mentioned in Section 6.2.2, there is some ambiguity concerning how to best fit a linear failure envelope to the triaxial test data for the sand. An envelope with the best fit (ϕ = 35.5º and c = 4.0 kPa (0.58 psi)) is characterized by some apparent cohesion, although non-zero cohesion is unrealistic for the purely frictional soil. A best-fit envelope with no cohesion has a friction angle around ϕ = 39º. In Fig. 7.5, predictions using the analytic method are therefore shown for three possible choices of material properties: (1) ϕ = 35.5º and c = 4.0 kPa (0.58 psi); (2) ϕ = 35.5º and c = 0 kPa; and (3) ϕ = 39º and c = 0 kPa. The unit weight used in the predictions is taken as the measured dry unit weight of γ = 16.0 kN/m^3 (102 pcf).

The prediction for ϕ = 35.5º and c = 4.0 kPa (0.58 psi) reveals that nonzero cohesion results in an unrealistically large prediction of wheel force for a given sinkage. When the cohesion is simply dropped and the friction angle remains at ϕ = 35.5º, the prediction using the analytic method is in excellent agreement with the test data. When the parameters for the best-fit envelope without cohesion (ϕ = 39º and c = 0 kPa) are used in the prediction, Q_V is significantly overestimated.

Not only does the prediction ϕ = 35.5º and c = 0 give the best match to experimental data, but these properties also appear to be the most reasonable for characterizing the loose sand. Direct shear tests were also conducted on the sand, and the friction angle was found to range between ϕ = 32º and ϕ = 36º. This supports ϕ = 35.5º, and even indicates that the friction angle may be somewhat lower 35.5º (which may lead to an even better theoretical prediction). Das (2005) gives that the friction angle typically ranges between 27º and 35º for loose sands.

Fig. 7.6 compares the theoretical predictions and test data for the dense sand. A similar ambiguity exists in determining ϕ and c as with the loose sand, and predictions for three sets of strength properties are again shown: (1) ϕ = 42.0º and c = 6.5 kPa (0.94 psi); (2) ϕ = 42.0º and c = 0 kPa; and (3) ϕ = 46º and c = 0 kPa. The measured dry unit weight γ = 17.4 kN/m^3 (111 pcf) is used in the predictions.

The nature of the agreement between the test data and the theoretical predictions for the dense sand is virtually the same as for the loose sand. Nonzero cohesion as in the best-fit envelope (ϕ = 42.0º and c = 6.5 kPa (0.94 psi)) leads to a drastic overestimation of Q_V for a given sinkage. When the cohesion is simply dropped (ϕ = 42.0º and c = 0), the prediction agrees with the test data very well. When the friction angle is increased to compensate for the dropped cohesion (ϕ = 46º and c = 0), the force Q_V is overestimated.

As with the loose sand, the lower value of friction angle ϕ = 42.0º with c = 0 leads to the best agreement for the dense sand, and this friction angle seems to be the most appropriate for the material. Das (2005) gives that the friction angle typically ranges between 35º and 45º for dense sands.

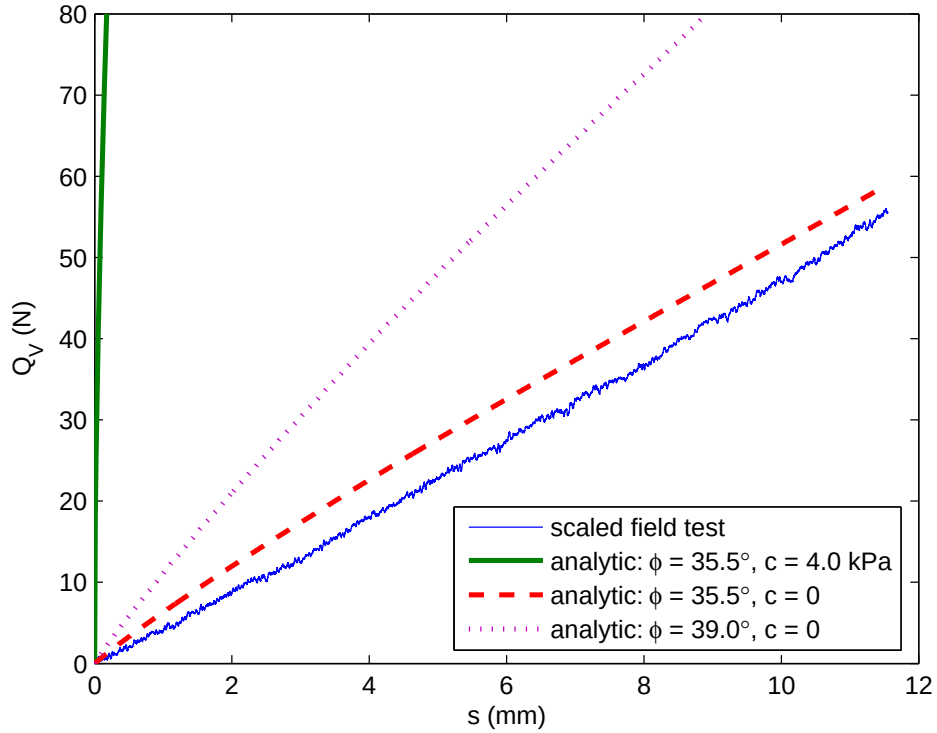

Figure 7.5. Comparison of theoretical predictions using analytic method and test data on loose sand for indentation of wheel with d = 115 mm and b = 38 mm

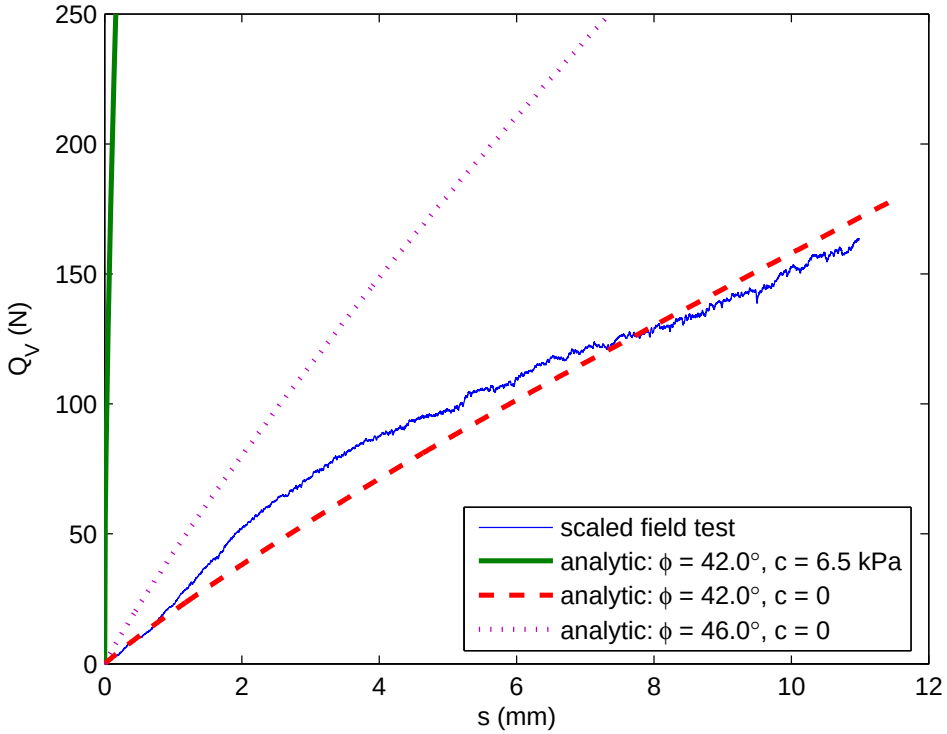

Figure 7.6. Comparison of theoretical predictions using analytic method and test data on dense sand for indentation of wheel with d = 115 mm and b = 38 mm

In Fig. 7.7, test data for indentation in the loose sand is compared with predictions from several numerical simulations. As with the comparison between test results and the predictions using the analytic method (Fig. 7.5), three sets of material properties were used in the simulations, employing the modified Drucker-Prager yield condition to match the Mohr-Coulomb strength parameters ϕ and c. Cohesionless material was approximated by taking a value of cohesion very close to zero, which is possible in the simulations of indentation (as opposed to rolling, where the minimum cohesion needed to maintain numerical stability is relatively large). Additional parameters used in the numerical simulation were E_s = 10 MPa (1450 psi), ν_s = 0.3, and γ = 16.0 kN/m^3 (102 pcf).

The theoretical predictions in Fig. 7.7 obtained from numerical simulation are similar to the predictions using the analytic method (Fig. 7.5). Again, the material properties $\phi = 35.5^o$ and $c \approx 0$ lead to the closest agreement with test data, although the agreement is somewhat worse as compared with that found using the analytic method. In Fig. 7.7, some numerical instability arising from the frictional nature of the material becomes apparent at s τ 6 mm (0.24 in.).

The simulations performed for the dense sand are compared with the test data in Fig. 7.8. Parameters not shown in the figure were fixed at E_s = 20 MPa (2900 psi), ν_s = 0.3, and γ = 17.4 kN/m^3 (111 pcf). The agreement between the predictions and the test data is again much like that observed using the analytic method (Fig. 7.6), with the simulation employing $\phi = 42.0^o$ and $c \approx 0$ giving the best match. Numerical instability arising in the simulations can again be seen, leading to early termination of the simulations in the case of the dense sand.

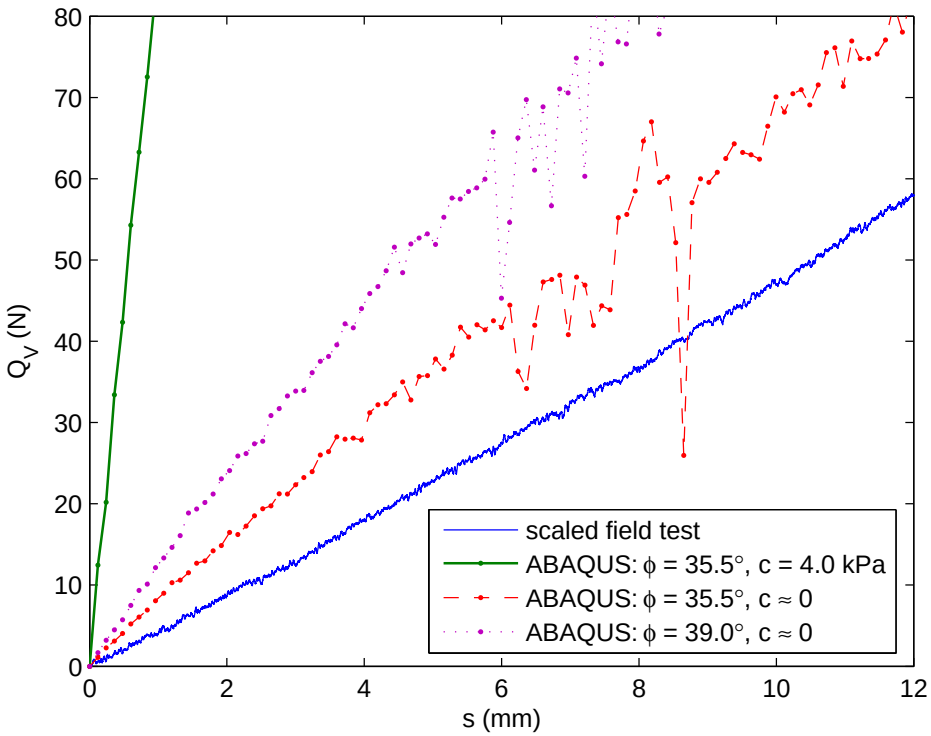

Figure 7.7. Comparison of theoretical predictions from numerical simulations and test data on loose sand for indentation of wheel with d = 115 mm and b = 38 mm

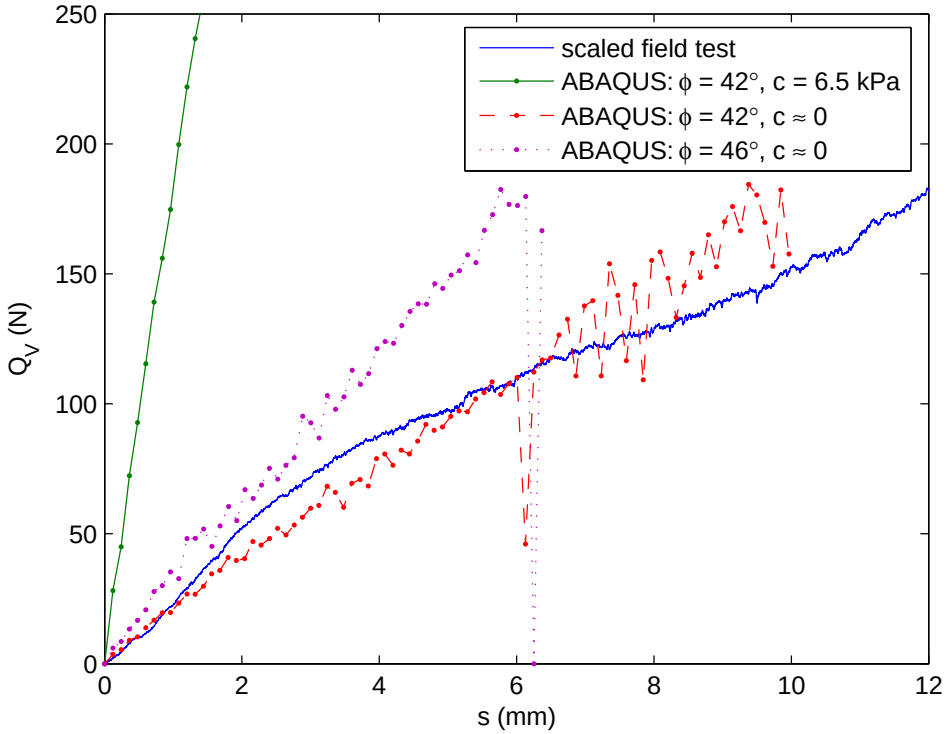

Figure 7.8. Comparison of theoretical predictions from numerical simulations and test data on dense sand for indentation of wheel with d = 115 mm and b = 38 mm

7.1.2.2 Rolling

Fig. 7.9 compares theoretical predictions using the analytic method with the data for the rolling tests on loose sand using the large wheel (d = 115 mm and b = 38 mm). The three possible choices for material parameters used in Section 7.1.2.1 for indentation are again employed. As with indentation, the prediction using $\phi = 35.5^{\circ}$ and c = 0 provides excellent agreement with the experimental data.

Fig. 7.10 compares predictions and test data for the dense sand. Again, the prediction provides a very good match to the test data when material properties are taken as $\phi = 42.0^{\circ}$ and c = 0.

Realistic rolling simulations could not be performed for the sand, since the cohesion required to maintain stability is considerable. As demonstrated in this and the previous section, the presence of non-negligible cohesion causes a large overestimation of the wheel force at a given sinkage for the purely frictional material considered.

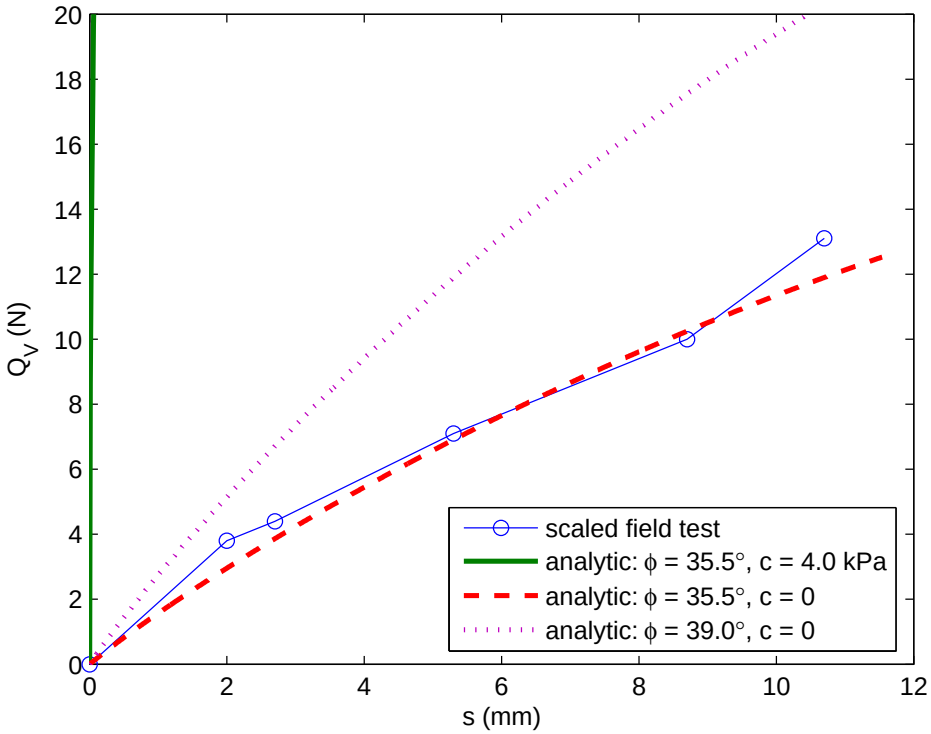

Figure 7.9. Comparison of theoretical predictions and test data on loose sand for rolling wheel with d = 115 mm and b = 38 mm

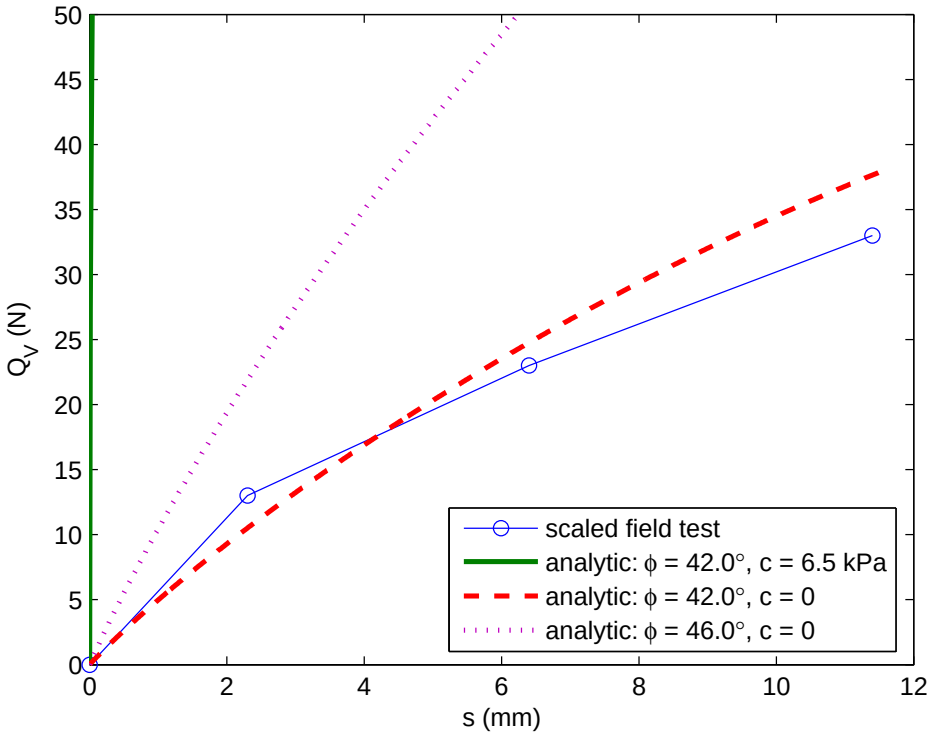

Figure 7.10. Comparison of theoretical predictions and test data on dense sand for rolling wheel with d = 115 mm and b = 38 mm

7.2 Comparison of Predictions and Supplemental Data

In this section, predictions using the analytic method are compared with the experimental data obtained by Willis et al. (1965) for several towed, rigid wheels operating in clay and sand. Pertinent details regarding the test setup and procedure are discussed in Section 5.5, as well as the soil mechanical properties.

The friction angle and cohesion determined by Willis et al. (1965) for the two soils were evaluated using a so-called "torsional shear annulus," so it is not clear whether these properties can be equated to the Mohr-Coulomb strength parameters. Nonetheless, the measured values appear to be reasonable for the soil types used in the experiments. Also, the authors collected data up to sinkage values that are quite large ($s/d \approx 0.25$). Only the data for $s/d \leq 0.1$ is considered in the comparison with theoretical predictions.

7.2.1 Cohesive Soil

Predictions and test data are compared for the cohesive soil and the wheel with b = 38 mm (1.5 in.) in Fig. 7.11. The figure shows excellent agreement between the predictions using the analytic method and the experimental data. Comparison is made between the predictions and test data for the wider wheels with b = 76 mm (3 in.) in Fig. 7.12. The test data is again closely predicted, albeit slightly worse in the case of the wheel with d = 406 mm (16 in.). This is most likely due to the change in soil cohesion throughout the tests resulting from drying of the soil (Willis et al. 1965). The test data in Fig. 7.12 indicates that the wheel with the large diameter sinks deeper into the soil than the wheel with the small diameter. This unrealistic trend is probably a result of the cohesion increasing throughout the individual tests.

7.2.2 Granular Soil

Figs. 7.13 and 7.14 compare predictions and test data for the granular soil. Agreement is fair to excellent for s/d δ 0.06, although it is evident for larger sinkage (0.06 δ s/d δ 0.1) that the predictions underestimate wheel force for a given sinkage. In fact, the trend in the test data for d = 508 mm (20 in.), which is concave upward in the figures, is different from that predicted using the analytic method, which is concave downward. Overall, the agreement between predictions and test data from Willis et al. (1965) for the granular soil can be characterized as fair.

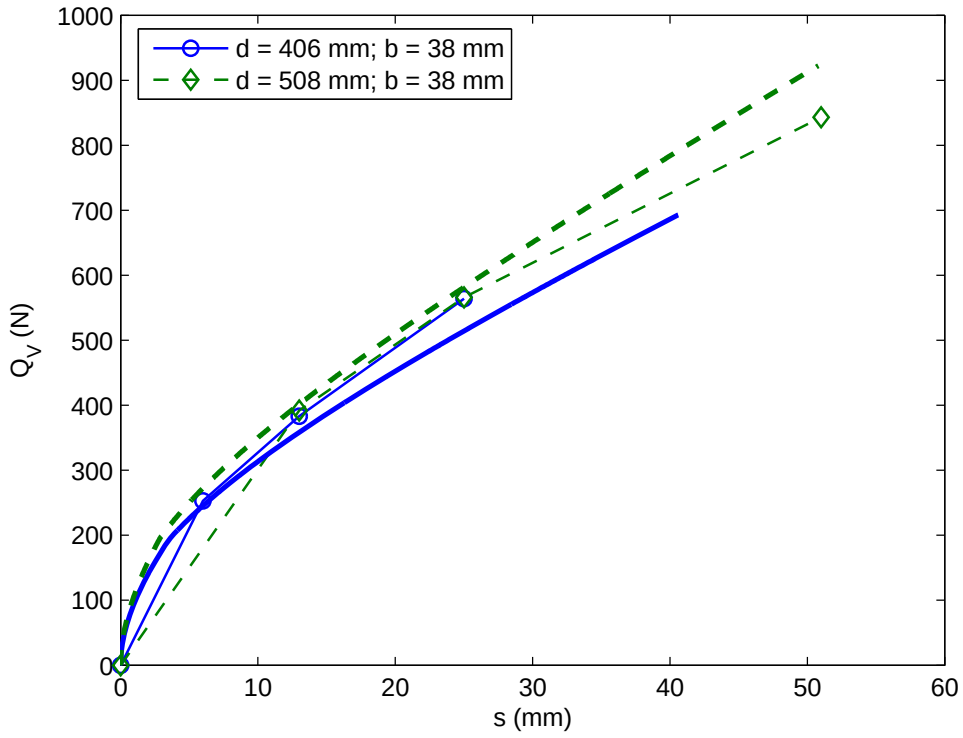

Figure 7.11. Comparison of test data from Willis et al. (1965) and predictions using analytic method for cohesive soil and wheels with b = 38 mm (connected points are test data; thick lines are predictions)

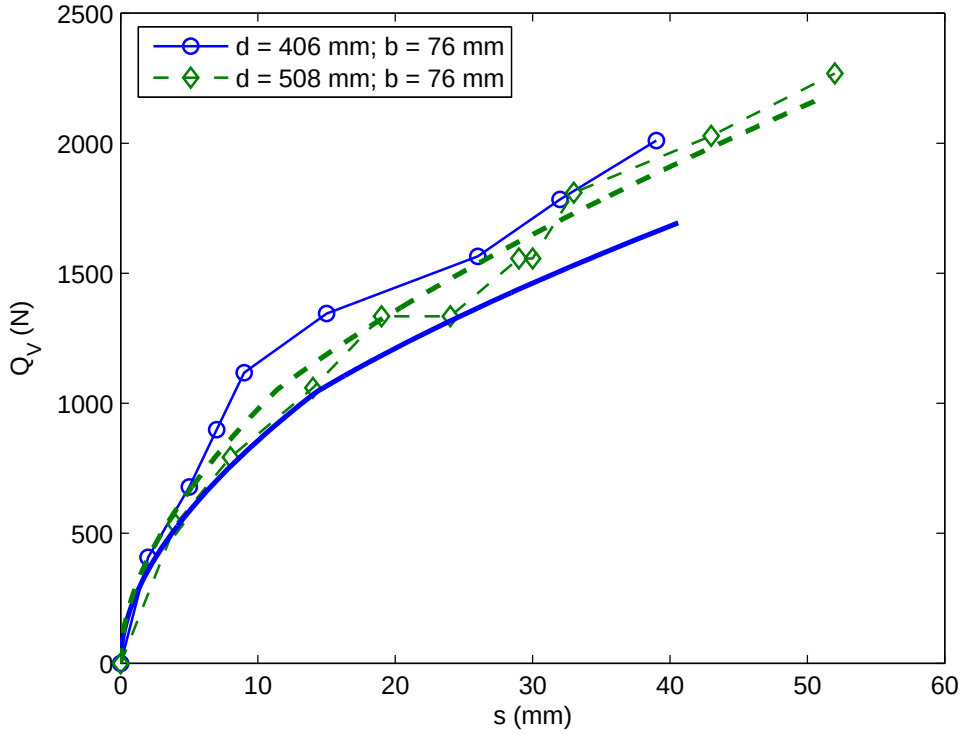

Figure 7.12. Comparison of test data from Willis et al. (1965) and predictions using analytic method for cohesive soil and wheels with b = 76 mm (connected points are test data; thick lines are predictions)

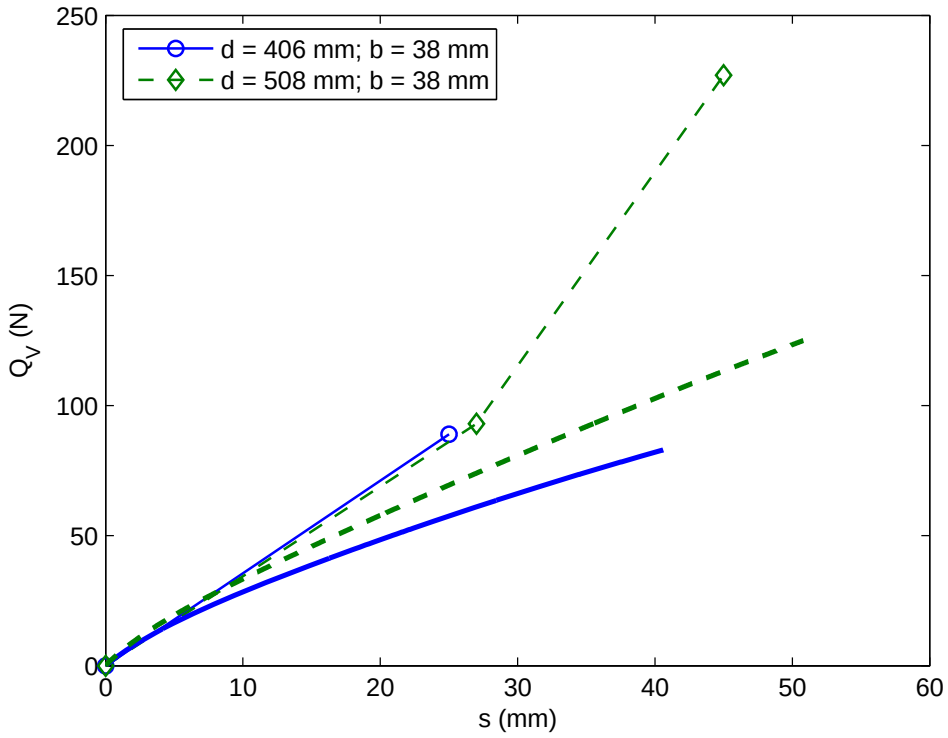

Figure 7.13. Comparison of test data from Willis et al. (1965) and predictions using analytic method for granular soil and wheels with b = 38 mm (connected points are test data; thick lines are predictions)

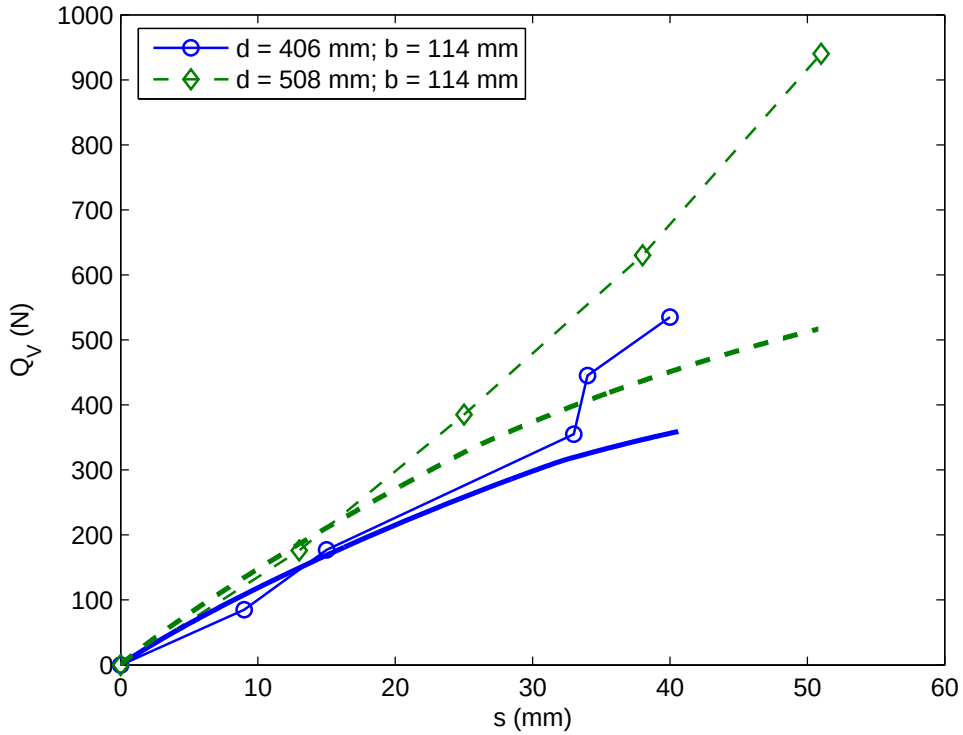

Figure 7.14. Comparison of test data from Willis et al. (1965) and predictions using analytic method for granular soil and wheels with b = 114 mm (connected points are test data; thick lines are predictions)

7.3 Comparison of Predictions and Data from Full Scale Field Tests

Some attempt is made in this section to make a meaningful comparison between the limited data collected from full scale field tests (Section 5.4) and the theoretical predictions. Rut depths and DCP readings were measured at two sites. An effort is made to relate the DCP data to the strength parameters required for the predictions using preexisting correlations from the literature. The correlated parameters are used subsequently to develop predictions for the rut depth.

7.3.1 Cohesive Soil

Penetration rate (*PR*) from DCP tests at the field site with cohesive soil are shown in Fig. 7.15. To arrive at a single *PR* which characterizes the soil, a spatially-weighted average over the first 0.5 m (1.6 ft) of soil is taken. For the DCP test conducted in the rut, the average *PR* is computed as 52 mm/blow (2.0 in./blow), and for the test conducted just outside the rut, the average *PR* is 41 mm/blow (1.6 in./blow). To relate *PR* to soil cohesion, *PR* is first correlated to the california bearing ratio (CBR) using the correlation given by Coonse (1999). The correlation by Coonse is used, since it lies within 1-4% of the mean trend computed from correlations proposed in a total of nine different papers (Roy 2007). The correlated CBR is subsequently related to cohesion using a correlation given by Gregory and Cross (2007).

Coonse (1999) gives that CBR is related to *PR* through

$$CBR = 338.8\left(PR\left[\frac{1}{mm}\right]\right)^{-1.14} \tag{7.1}$$

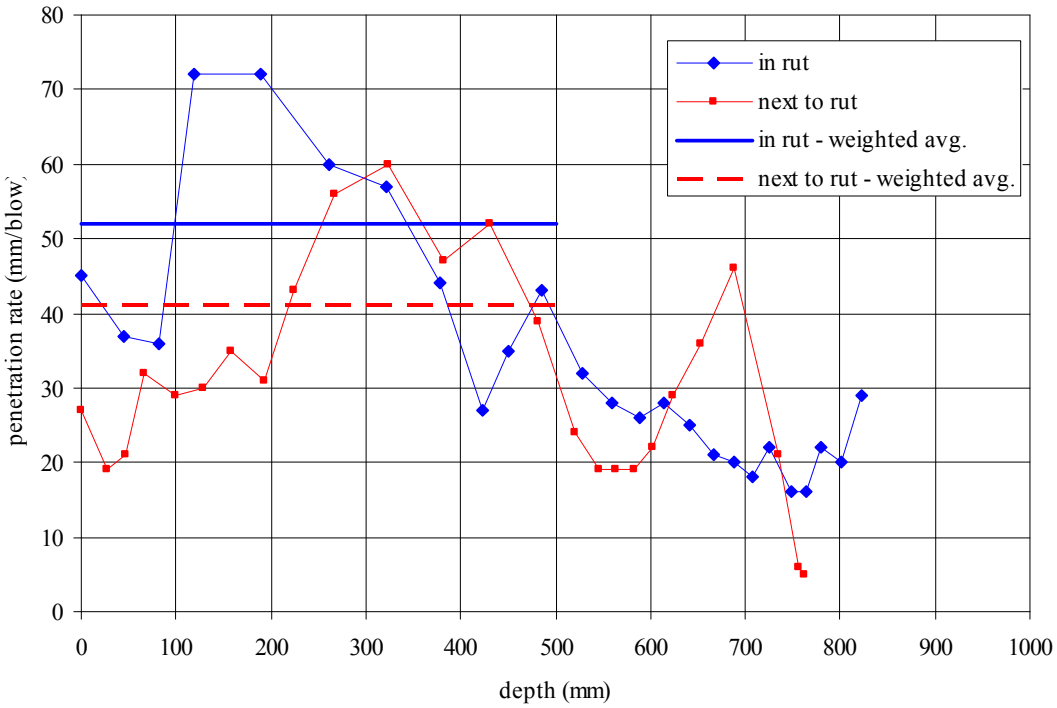

Figure 7.15. DCP readings at field site with cohesive soil

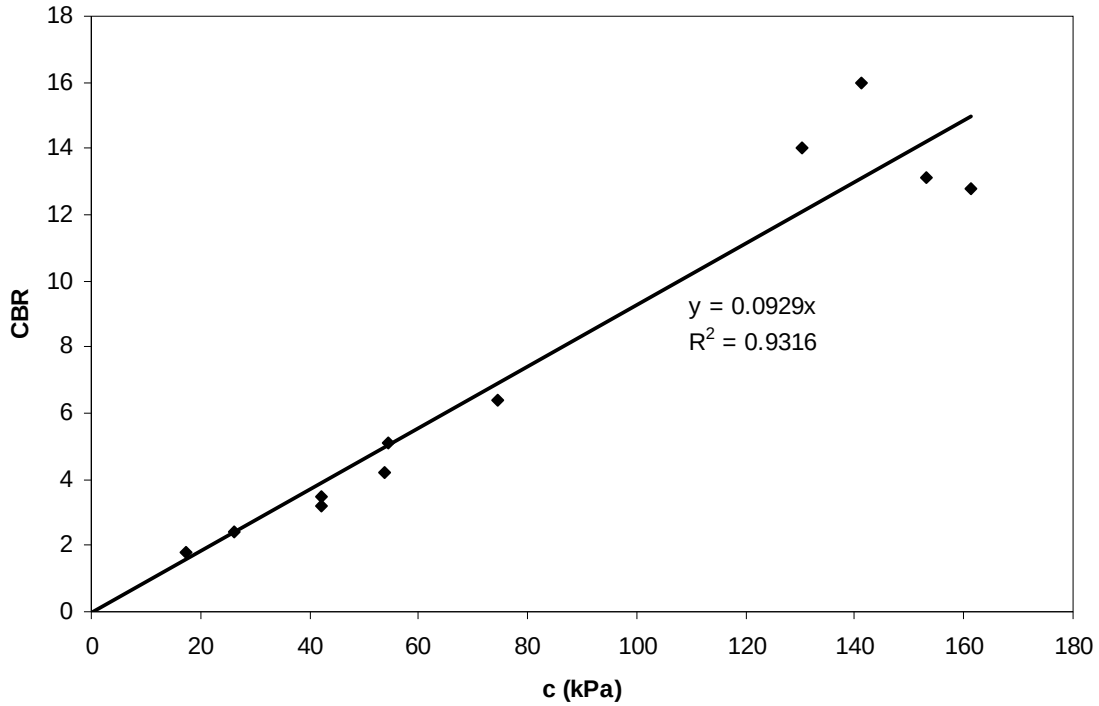

Figure 7.16. Correlation between measured CBR and measured cohesion using data from Gregory and Cross (2007)

Gregory and Cross (2007) proposed that CBR is related linearly to the undrained shear strength (or cohesion) of clay soils at or near saturation. The authors propose a theoretically-derived correlation which compares favorably with experimental data, although a direct correlation between measured CBR and measured soil cohesion c (Fig. 7.16) is used here. The least-squares linear regression for their data is

$$CBR = \left(0.0929 \frac{1}{kPa} \right) c \tag{7.2}$$

Eqs. (7.1) and (7.2) may be combined to ultimately relate c to PR as

$$c = 3650 \left(PR \left[\frac{1}{mm} \right] \right)^{-1.14} \left[kPa \right] \tag{7.3}$$

In this report, no claim is made that (7.3) can always provide a reliable relationship between cohesion and DCP penetration rate for a clay, although the correlation follows logically from two other correlations (Eqs. (7.1) and (7.2)) which are considered by others to be in good agreement with test data.

The average PR inside the rut of 52 mm/blow (2.0 in./blow) correlates to c = 40 kPa (5.8 psi) using Eq. (7.3). The average PR outside the rut of 41 mm/blow (1.6 in./blow) correlates to c = 53 kPa (7.7 psi). According to Das (2005), these values of cohesion represent clay of medium consistency (25 kPa < c < 50 kPa). It is important to realize that the correlation (7.3) only applies

to the undrained behavior of cohesive soils at or near saturation. When the soil is well below saturation or the soil is not fine-grained, internal friction is present and the correlation is inapplicable. Soil at the field site with cohesive soil appeared to be predominantly fine-grained, although the moisture content of 17.1% was below the moisture content at saturation.

Theoretical predictions are compared with the measured rut depth of about 90 mm (3.5 in.) measured in the field in Fig. 7.17. For the predictions, rebound of the soil is neglected, and the rut depth is considered identical to the sinkage s. Predicted s is plotted versus soil cohesion c to indicate sensitivity. Predicted sinkage for a rigid wheel of the same size and applied weight as the test roller wheel (d = 1.52 m (60 in.), b = 0.46 m (18 in.), and Q_V = 133.5 kN (15 tons)) is much greater than the measured rut depths, using the correlated values of cohesion and assuming $\phi = 0$. When internal friction ($\phi = 15°$) is included, the prediction becomes much more realistic. Internal friction, perhaps in the range ϕ = 10º to 20º, was almost certainly present for the cohesive soil.

The assumption of a rigid wheel is only an approximation for the tires on the test roller used at the field site. However, the analytic method also accommodates wheel flexibility through introduction of the flexibility parameter λ_r, incorporated through the relation

$$d_e = d + \lambda_r Q \tag{7.4}$$

where d_e is the so-called *equivalent wheel diameter* and Q is the total (inclined) wheel force (see Section 3.2.3).

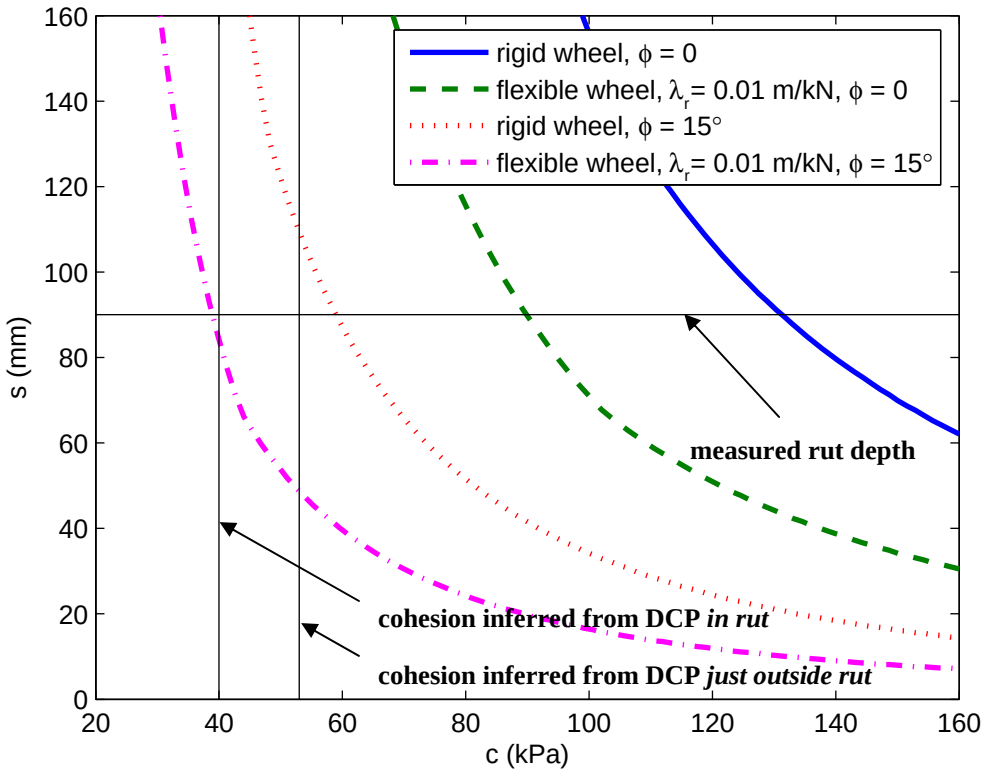

Figure 7.17. Comparison between predicted sinkage (rut depth) and measured rut depth from field test at site with cohesive soil

To obtain a rough estimate of λ_r, the results of numerical simulation for a pneumatic tire on cohesive performed are used. In Fig. 7.18, which shows for a simulated test roller tire with realistic inflation pressure and carcass stiffness that the equivalent wheel diameter is close to d_e = 2.6 m (8.5 ft), where the undeformed wheel diameter is d = 1.3 m (4.3 ft). The vertical component of force was specified at Q_V = 133.5 kN (15 tons) and the horizontal component determined from the simulation was $Q_H \approx$ 25 kN (2.8 tons), resulting in a total inclined force of Q = 136 kN (15.3 tons). The parameter λ_r for d = 1.3 m (4.3 ft), d_e = 2.6 m (8.5 ft), and Q = 136 kN (15.3 tons) is $\lambda_r \approx$ 0.01 m/kN (3.5 in/ton), using Eq. (7.4). While λ_r varies depending on soil type, wheel type, and inflation pressure, λ_r = 0.01 m/kN (3.5 in/ton) appears to be a reasonable first approximation for the tire of the test roller used at the field site.

Also shown in Fig. 7.17 are several predictions obtained using the analytic method for a rolling, flexible wheel with λ_r = 0.01 m/kN (3.5 in/ton). This has the effect of considerably reducing the sinkage as compared with the results for the rigid wheel. For a given soil cohesion, sinkage for the flexible wheel is about half of that when the wheel is rigid.

Too much uncertainty surrounds the data collected from the field to meaningfully evaluate the validity of the predictions. This section shows, however, that the predictions can accommodate likely scenarios occurring in the field.

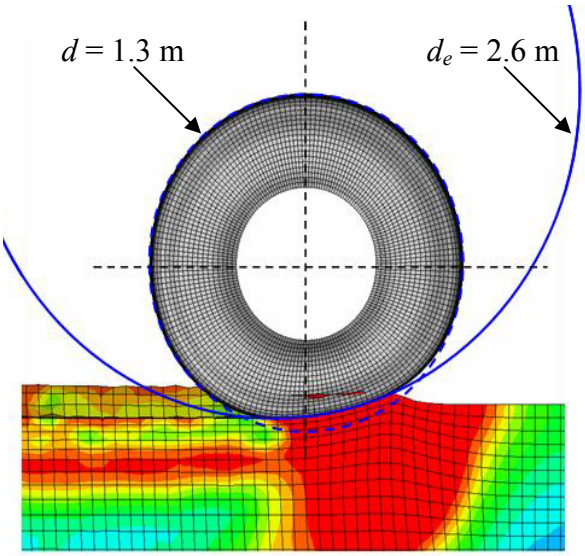

Figure 7.18. Deformed wheel configuration from numerical simulation of rolling pneumatic tire on cohesive soil (c = 100 kPa)

7.3.2 Granular Soil

Data was collected for two different ruts at the site with granular soil. The large rut measured about 120 mm (4.7 in.) in depth and the small rut measured approximately 70 mm (2.7 in.). DCP data collected for the large rut and small ruts is shown in Figs. 7.19 and 7.20. As in Section 7.3.1, a spatially-weighted average of the penetration rate *PR* is computed for the first 0.5 m (1.6 ft) of soil in order to obtain a single representative value. For the large rut, the average *PR* is 105 mm/blow (4.1 in./blow), 85 mm/blow (3.3 in./blow), and 25 mm/blow (1.0 in/blow) for the DCP readings taken in the rut, just outside the rut, and at the centerline of the roadway embankment, respectively. For the small rut, average *PR* is respectively 102 mm/blow (4.0 in./blow), 84 mm/blow (3.3 in./blow), and 30 mm/blow (1.2 in./blow).

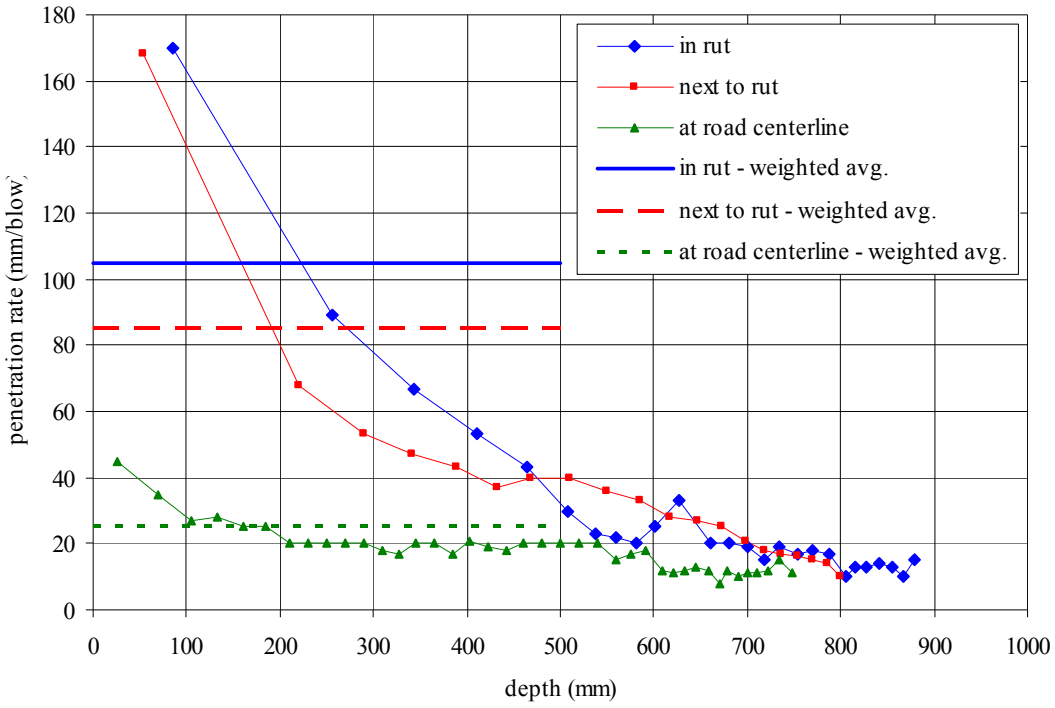

Figure 7.19. DCP readings for large rut at field site with granular soil

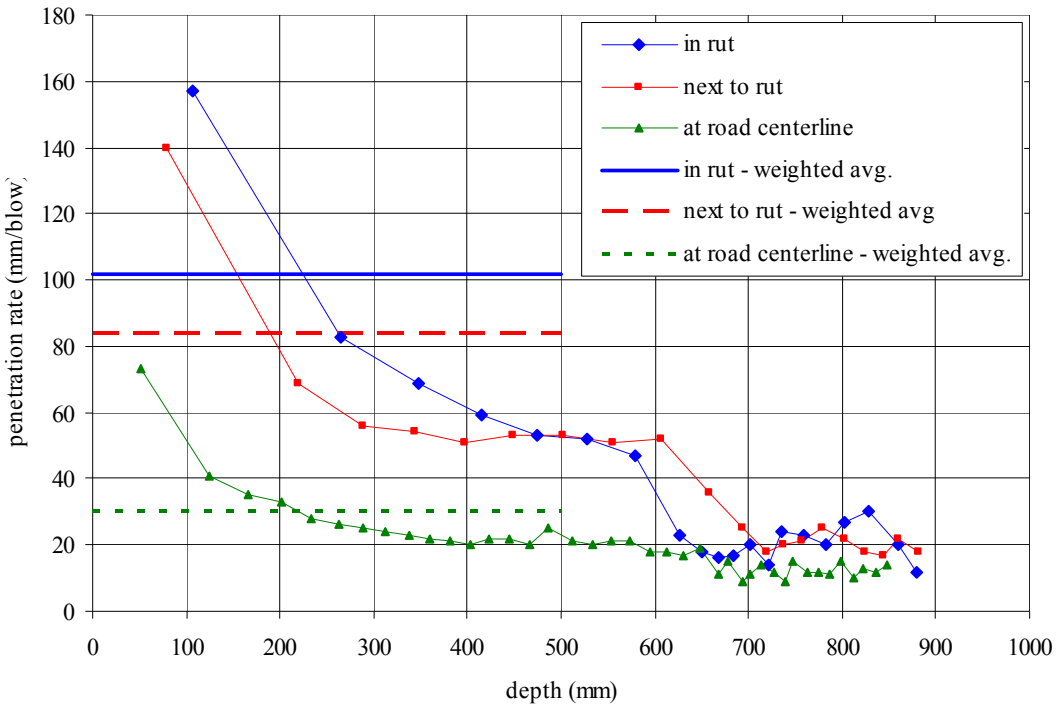

Figure 7.20. DCP readings for small rut at field site with granular soil

For a cohesionless sand, Ayers et al. (1989) gave the following correlations between deviatoric stress at failure $(\sigma_D)_f$ and PR for the given confining pressures σ_3:

$$(\sigma_D)_f = 285[kPa] - 3.48PR\left[\frac{kPa}{mm}\right] \quad \text{for} \quad \sigma_3 = 34.4\,kPa \tag{7.5}$$

$$(\sigma_D)_f = 692[kPa] - 6.35PR\left[\frac{kPa}{mm}\right] \quad \text{for} \quad \sigma_3 = 103\,kPa \tag{7.6}$$

$$(\sigma_D)_f = 1031[kPa] - 3.45PR\left[\frac{kPa}{mm}\right] \quad \text{for} \quad \sigma_3 = 207\,kPa \tag{7.7}$$

After computing $(\sigma_D)_f$ according to the correlations (7.5)-(7.7), the friction angle ϕ can be readily determined from the relationship

$$\phi = \sin^{-1}\left(\frac{(\sigma_D)_f}{(\sigma_D)_f + 2\sigma_3}\right) \tag{7.8}$$

The friction angle ϕ is independent of confining pressure for a linear failure envelope, so the presence of different equations for the three confining pressures indicates a nonlinear envelope.

When Eqs. (7.5)-(7.7) are used to correlate the values of average *PR* determined from the field measurements (Figs. 7.19 and 7.20), only Eq. (7.7) gives sensible results. Correlated values of ϕ using Eq. (7.8) are 38º, 40º, and 44º at the locations in the rut, just outside the rut, and at the embankment centerline, respectively, for both the large rut and the small rut. The correlations proposed by Ayers et al. are based on DCP readings ranging from 12 mm/blow (0.5 in/blow) to 31 mm/blow (1.2 in./blow) and friction angles (measured from triaxial compression tests) ranging from 44º to 51º. The correlated friction angles inside and just outside the ruts (38º and 40º, respectively) rely on data outside of this range, casting considerable doubt on the correlated values.

Fig. 7.21 plots several theoretical predictions for rut depth (considered the same as sinkage) using the analytic method for a rolling wheel, with wheel geometry and loading representing the current test roller (d = 1.57 m (60 in.), b = 0.46 m (18 in.), and Q_V = 133.5 kN (15 tons)). The unit weight is taken as γ = 20 kN/m^3 (127 pcf). The sinkage predictions are plotted versus friction angle to indicate the sensitivity to this parameter. The rut depths measured in the field are also shown. Two predictions are shown for a rigid wheel, and between these two predictions, the cohesion is varied from 0 to 1 kPa (0.15 psi). The latter is included to accommodate the possibility of a minute amount of cohesion introduced from moisture and fine particles. Two similar predictions are shown for a flexible wheel with λ_r = 0.01 m/kN (3.5 in./ton), as in Section 7.3.1.

Assuming a rigid wheel and c = 0 or c = 1 kPa (0.15 psi), the predicted rut depths using the correlated values of ϕ are greatly larger than the measured rut depths. When wheel flexibility is introduced, the sinkage drops to roughly half of that for a rigid wheel, and although the predicted rut depths remain larger than measured, the predictions approach the measured values.

The correlated values of ϕ are highly suspect, and as with the results from field testing at the site with cohesive soil (Section 7.3.1), the data from the field tests on granular soil neither validate nor invalidate the predictions using the analytic method. It is interesting to note, however, that the difference in the DCP readings (Figs. 7.19 and 7.20) taken for the large rut and small rut are fairly small, whereas the difference in the measured ruts is quite large. This sensitivity is supported by the theoretical predictions. In all of the predictions shown in Fig. 7.21, a mere 2º decrease in the friction angle is sufficient to cause the predicted rut depth to increase from 70 mm (2.7 in.) to 120 mm (4.7 in.).

7.4 Validity Assessment

Theoretical predictions using the approximate analytic method agree quite well with experimental data. When compared with data from the scaled field tests and supplemental data from Willis et al. (1965), the predictions for cohesive soil provide a good match to test results. For the scaled field tests, the Young's modulus of the soil was very low ($E_s \approx 2$ MPa), leading to some discrepancy arising from elastic effects that are disregarded using the analytic method. The analytic method provides an excellent match to the data obtained by Willis et al. for cohesive soil. The authors do not discuss elastic properties of the soil, though it is evident that the elastic stiffness of the soil was sufficiently large to eliminate noticeable elastic effects.

Predictions from numerical simulation for cohesive soil are similar to those obtained with the analytic method. When the elastic stiffness of the soil is very small (as in the case of the scaled field tests), the simulations are still capable of providing a very good match to experimental data.

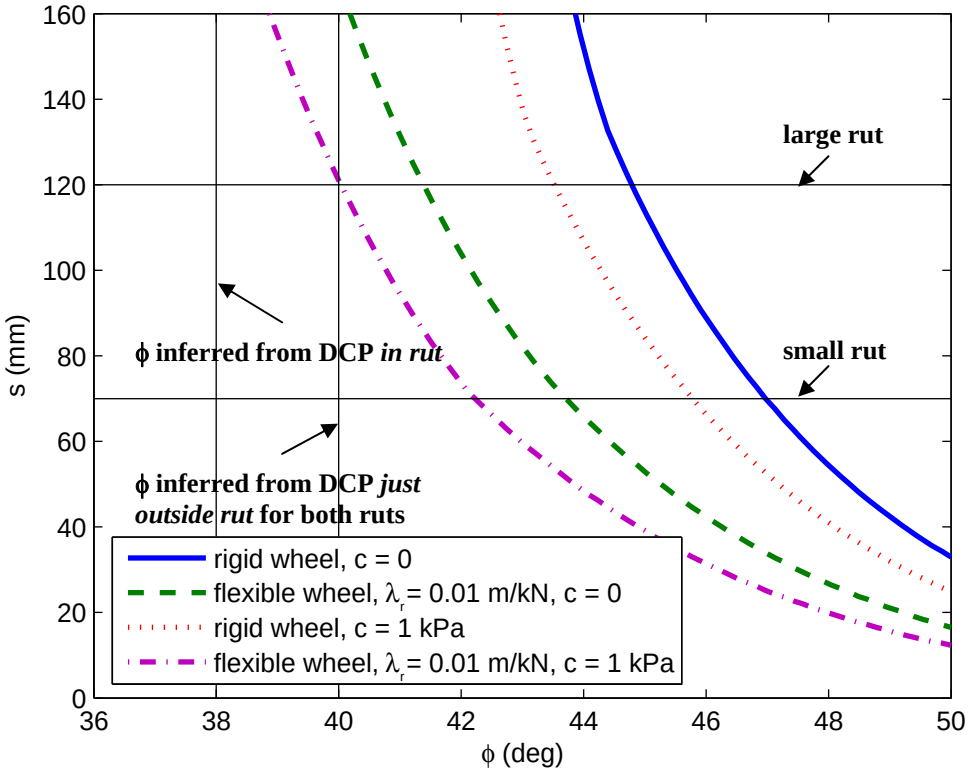

Figure 7.21. Comparison between predicted sinkage (rut depth) and measured rut depths from field tests at site with granular soil

Some minor differences between the predictions from numerical simulation and test data can be seen with the scaled field tests for the rolling wheel. This may be due to experimental error, but it may also arise from material behavior, such as hardening, that is disregarded in the simulations (and analytic method).

Results obtained from the scaled field tests on both loose and dense sand, for both indentation and rolling, are predicted very well using the analytic method, accepting there is some uncertainty involved in how to best match the Mohr-Coulomb strength parameters used in the models to the nonlinear failure envelope determined experimentally for the sand. The large increase in resistance to wheel penetration caused by the increase in soil density was captured very effectively by the theoretical predictions.

With the test data for granular material provided by Willis et al., the analytic method provides fair agreement. The trends in the test data were different both from the predictions using the analytic method and from the test data acquired from scaled field testing.

Partial results obtained from full scale field tests cannot provide conclusive evidence to validate (or invalidate) the theoretical predictions. The results of the full scale field tests fit within several conceivable scenarios accommodated by the theoretical predictions, although additional data is needed to ascertain the correct scenario (strength data for soil, flexibility characteristics for test roller tire, etc.).

For both the analytic method and the numerical simulations to be valid, the two approaches must at least agree with each other. Sinkage from several simulations with different material properties for a rolling, rigid wheel are shown in Fig. 7.22 together with predictions using the

analytic method. Simulation parameters were d = 1.52 m (60 in.), b = 0.46 m (18 in.), Q_V = 133.5 kN (15 tons), γ = 18 kN/m^3 (115 pcf), and E_s = 40 MPa (5800 psi). The simulation results correspond well with the predictions using the analytic method. With small s, there is some disagreement arising from elastic effects. Fig. 7.23 is the same as Fig. 7.22 except rut depth from the simulations is plotted instead of sinkage. The two methods coincide even at small s in this case. Whether sinkage or rut depth is taken from the simulations, the trends predicted by the two approaches are basically identical.

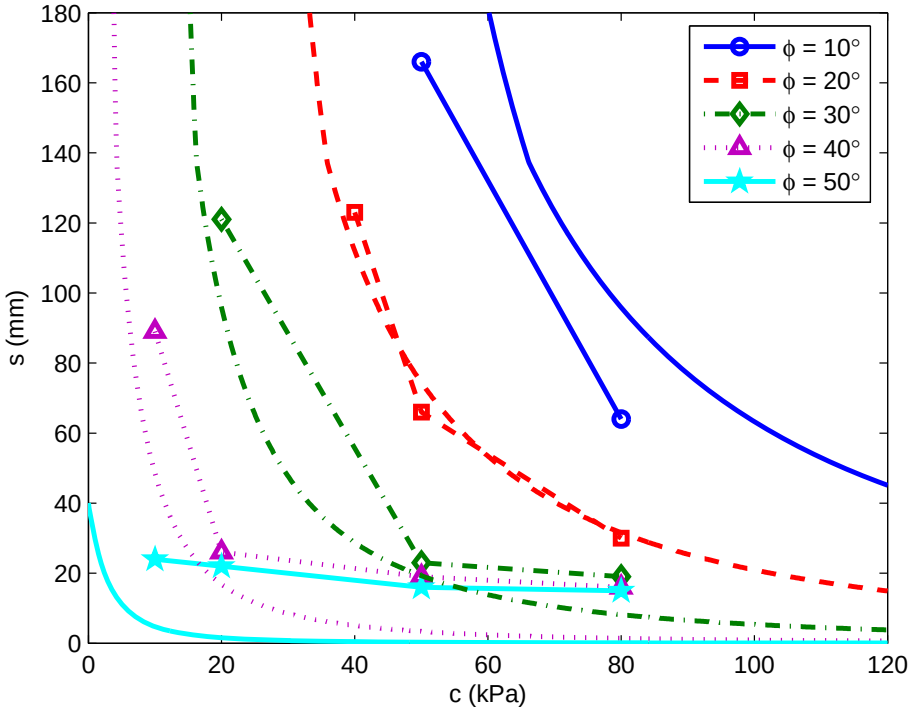

Figure 7.22. Comparison between sinkage from numerical simulation and predictions using analytic method for rolling, rigid wheel (connected points are from simulations; smooth curves are from analytic method)

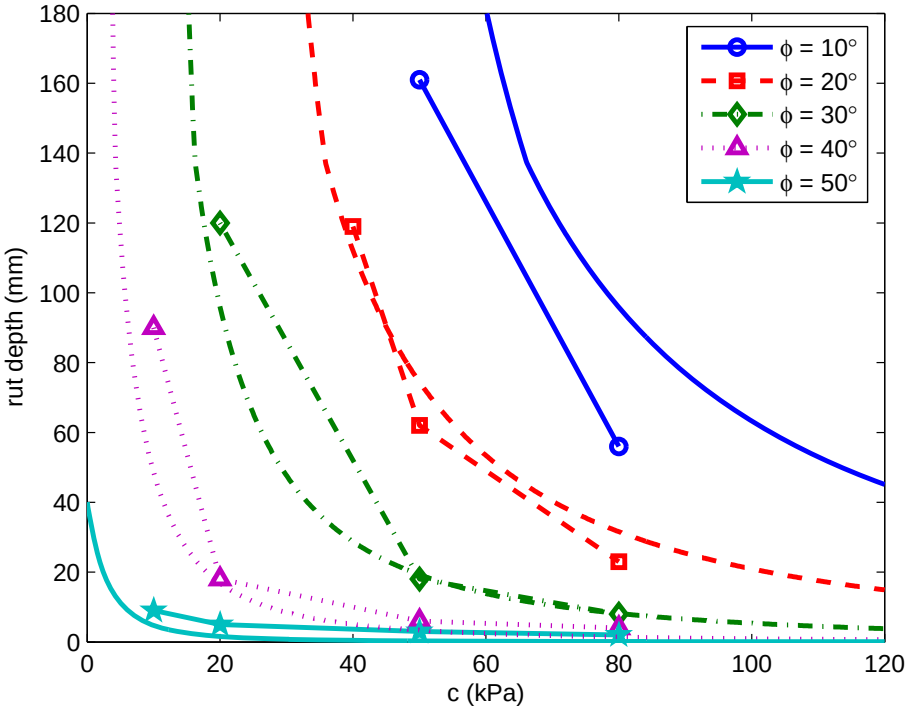

Figure 7.23. Comparison between rut depth from numerical simulation and predictions using analytic method for rolling, rigid wheel (connected points are from simulations; smooth curves are from analytic method)

Chapter 8

Conclusions and Recommendations

8.1 Conclusions

The following general conclusions may be drawn from the findings discussed in this report:

1. Test rolling is characterized by an elegant simplicity and has the potential to be a very successful tool for *in situ* characterization of some mechanical properties of subgrade materials in roadway embankments. As opposed to other tests used in road construction, test rolling is capable of providing a continuous record of measurement, and can be used to inspect large areas and detect weak (inadequately compacted) soils. In current Mn/DOT test rolling procedures (Minnesota 2000), no quantitative continuous record is taken and assessment is made based on visual observation.

2. The theoretical models developed in this project are, to the authors' knowledge, the first rigorously-developed tools for analyzing test rolling. Two theoretical approaches for analyzing and formulating models for test rolling were developed. The first is analytic, and the second is numerical, based on the commercial software ABAQUS. The advantage of the analytic approach, albeit more approximate, is its universality and ease in use. Accordingly, analytic expressions relate sinkage to strength parameters, or, inversely, the strength parameters to known sinkage and test roller configuration (weight and wheel geometry). The analytic expressions given in Chapter 3 are explicit or implicit, yet solvable using standard computation packages (e.g., Mathcad or MATLAB). The numerical simulations support the analytic expressions; however, no direct usage of the numerical simulations for evaluating soil strength parameters is proposed. Results from numerical simulations are case specific and do not serve as practical tools.

3. The theoretical models are approximate yet capture the essential elements of the wheel/soil interaction. Lab-scaled tests support the theoretical findings. The models provide means for realistic predictions of how much the wheel of a test roller with a given load and wheel geometry will penetrate (sink) on a soil with known material properties. The models also allow for analysis of the inverse problem, i.e., evaluating soil properties from measured wheel sinkage/rut depth. The theoretical predictions appear to be fairly accurate for sinkage-to-diameter ratios $0.01 \delta s/d \delta 0.08$.

4. An alternative to using the analytic expressions are graphs relating soil strength parameters, wheel geometry and weight, and the sinkage of a wheel. Examples of such graphs are shown in Appendices H-K.

5. Soil deformation induced by a test roller is primarily permanent. Permanent deformation is associated with soil failure, and is related to soil strength parameters, namely friction angle (ϕ) and cohesion (c). These parameters are essential in the theoretical models developed. The predominance of permanent deformation implies that test rolling is a means of evaluating *in situ* soil strength properties rather than elastic properties such as resilient modulus. Test rolling can thus be interpreted as a continuous measurement of soil strength properties. Other methods like the DCP test can only provide point information on soil strength.

6. Unit weight and moisture content, which are often used exclusively as quality assurance measures for soil compaction, play an indirect role in the theoretical models. A substantial increase in friction angle can be observed when sand is compacted from a loose state to a dense state, as demonstrated in the laboratory testing (Section 6). Proper control of moisture content allows one to maximize the density, and consequently the strength, by facilitating compaction. For cohesive soil, increased density and decreased moisture content tend to increase cohesion.

7. The ability to infer soil strength parameters from test rolling using the models developed depends on the type of the soil. If the strength of the soil is characterized by one parameter only, either friction angle (e.g., sand) or cohesion (e.g., clay), it is possible to assess this parameter from measuring the sinkage/rut of one wheel. If, however, the soil possesses both parameters (e.g., sand with fines), it is not possible to evaluate them using a measurement from one wheel. The measurements from two wheels of different sizes, or two identical wheels carrying different weights, are necessary to determine the friction angle and cohesion of the soil with some confidence. If one of the parameters is known, it again is possible to evaluate the second one from measurements with one wheel.

8. The influence depth of a rolling wheel, or the depth at which an underlying layer begins to influence sinkage, depends on soil type (granular or cohesive), layer position (strong over weak versus weak over strong), and the relative strength of the layers, as well as the wheel force and geometry. The influence depth determined approximately in the context of the analytic method agrees favorably with the results from numerical simulation and can be used to predict influence depth for arbitrary test roller weight and wheel sizes. Influence depth in the case of dense sand overlying weak clay was found to be greater (about twice for the cases considered) than in the case of strong clay overlying weak clay. Influence depth for a relatively weak layer overlying a strong layer was found to be small relative to the influence depth for a strong layer over a weak layer. Using the analytic method, influence depth appears to be only moderately affected by wheel size, though strongly affected by wheel weight. The influence depth of the test roller currently specified by Mn/DOT varies from 1.2 m (4 ft) to 0.6 m (2 ft).

9. The theoretical predictions suggest that larger wheel weight leads to greater sensitivity of the sinkage with respect to a small variation in soil strength, when the wheel geometry and soil strength are fixed. That is, when the wheel weight is large, a small variation in soil strength can lead to a relatively large change in sinkage, whereas the change in sinkage resulting from the same variation with a small wheel weight is relatively small. Larger wheel weights also lead to greater sensitivity to weak underlying layers (i.e., the depth at which a weak underlying layer affects sinkage is larger).

10. Both the numerical simulations and the analytic method show that wheel flexibility can influence sinkage substantially. Flexibility for a pneumatic tire is determined by tire construction and inflation pressure. Theoretical predictions incorporating a very rough approximation to the deformability of the tire on the present Mn/DOT test roller indicate that sinkage may be around half of that induced by a rigid wheel of the same geometry. As this deformability is generally unknown, accurate theoretical prediction in the case of a flexible wheel is difficult. Variability in construction of the pneumatic tires on the test roller currently used by Mn/DOT can lead to large differences in the test rolling results.

11. For rigid wheels, the following approximate relationships hold true between the sinkage, wheel weight, wheel width, and wheel diameter and can be used to assess the consequences in modifying the present configuration of the test rolling equipment :
    a. The relationship between sinkage and wheel weight for granular soils is linear. In cohesive soils this relationship is quadratic. This means that reducing the test roller weight by half will reduce the sinkage by one half in granular soils, and by one fourth in cohesive soils.
    b. Sinkage is inversely proportional to the width of the wheel for granular soils and inversely proportional to the width squared for cohesive soils. Thus, reducing wheel width by half leads to a two-fold increase in sinkage on granular soils and to a four-fold increase in sinkage on cohesive soils.
    c. Sinkage is inversely proportional to wheel diameter for both granular and cohesive soils. This implies a two-fold increase in sinkage in either soil for wheels whose diameter is reduced by half.

12. The scaled field tests were of good quality and provided reliable data for validating the theoretical models, although emphasis in this project was placed more on development of theoretical models rather than validation. As with all theoretical work, the predictions can only be trusted fully after they have been compared with exhaustive experimental data. The model predictions should ultimately be compared to results obtained from well-controlled field tests.

Along with general conclusions given above, illustrative examples are given in Appendix O to demonstrate the usefulness of the theoretical predictions. In one example, the performance of several prospective test rollers is evaluated. In another example, synthetic data from a given test roller is interpreted in terms of strength properties of the soil.

8.2 Recommendations

In addition to the general findings summarized in Section 8.1, the following recommendations are made:

1. Test rolling is conceptually a good test for *in situ* characterization of the strength properties of subgrade materials. Test rolling is not well suited to determination of soil elastic properties, which are the properties commonly used to predict long term pavement performance. Small-strain test methods (e.g., those involving light weight deflectometers and the emerging intelligent compactors) are more appropriate than test rolling for measuring soil elastic properties.

2. The theoretical models can be used for evaluating the effects of test roller modifications and interpreting test roller sinkage/rut in terms of soil strength properties. However, the accuracy of the models has not been thoroughly confirmed against experimental data, and the predictions should only be regarded as approximate. The models are not intended for use with $s/d \tau 0.1$. Sinkage/rut predictions using the analytic method apply to homogeneous soils, as well as layered soils for which the uppermost soil layer is of sufficient thickness such that deformation occurs only in the uppermost layer (i.e., the soil failure mechanism beneath the wheel does not extend into the underlying layers).

3. Test rollers with different weights and wheel geometries can provide similar results. A relatively light test roller with small wheels, when operated on a given soil, can provide similar information regarding soil strength as a heavy test roller with large wheels, like the one presently used by Mn/DOT. However, the influence depth of a light test roller is generally less than the influence depth of a heavy test roller.

4. Rigid wheels (or nearly rigid) are the preferred wheel type for test rolling. Wheel flexibility only obscures field measurements and adds unwarranted complexity to the test rolling process. For a rigid wheel, axle displacement is identical to sinkage, which is a feature that lends convenience to measurement automation. A steel or solid rubber tire could be implemented on a specialized test rolling device like the one presently used, although a pneumatic tire with a suitably stiff construction and sufficiently high inflation pressure may be capable of resembling a rigid wheel (cf. Bekker 1960).

5. A towed wheel, with no applied torque, is preferred over a driven wheel for test rolling. In the case of a driven wheel, sinkage depends also on the applied torque (cf. Freitag 1965), which is both unknown (without special instrumentation) and variable. The theoretical models developed pertain to a towed wheel.

6. A test roller wheel should travel ahead, or be offset from, driving wheels, as the driving wheels tend to damage the soil. Test rolling measurements on damaged soil are obscured by two factors: (1) the reference surface from which measurements are taken is disturbed, sometimes significantly, and (2) sinkage cannot be attributed exclusively to soil strength, since some sinkage arises from the effects of damage. A configuration in which the test rolling wheels travel ahead of the driving wheels may be achieved by pushing, rather than pulling, a test rolling device, or simply using the front (steerage) axle of a standard vehicle such as a dump truck. Caution should be used in the latter case, since the distribution of vehicle weight on the wheels can vary considerably when the vehicle is operating on soft material.

7. A test roller may be outfitted with two or more offset wheels with different weights or geometries (or both) in order to use the test rolling technique to infer the two strength parameter ϕ and c of a soil. With sinkage measured from a single wheel, test rolling cannot, in general, provide enough information to deduce ϕ and c when both are present.

8. An extensive program to validate the proposed theoretical models with experimental data from field tests should be undertaken. In addition to validating the models, such a program will reveal potential improvements.

References

ABAQUS Version 6.6 Documentation (2006). ABAQUS, Inc., Providence, RI.

ASTM Standard D3080 (2004), "Standard test method for direct shear tests of soils under consolidated drained conditions," ASTM International, West Conshohocken, PA.

ASTM Standard D2166 (2006), "Standard test method for unconfined compressive strength of cohesive soil," ASTM International, West Conshohocken, PA.

ASTM Standard D2850 (2003), "Standard test method for unconsolidated-undrained triaxial compression tests on cohesive soils," ASTM International, West Conshohocken, PA.

ASTM Standard D6951 (2003), "Standard test method for use of the dynamic cone penetrometer in shallow pavement applications," ASTM International, West Conshohocken, PA.

Minnesota Department of Transportation (2000). *Standard Specifications for Construction*. Specification 2111. Minnesota Department of Transportation, St. Paul, MN.

Abebe, A. T., Tanaka, T., and Yamazaki, M. (1989). "Soil compaction by multiple passes of a rigid wheel relevant for optimization of traffic." *Journal of Terramechanics*, 26(2), 139-148.

Abu-Hamdeh, N. H., Abu-Ashour, J. S., Al-Jalil, H. F., Khdair, A. I., and Reeder, R. C. (2000). "Soil physical properties and infiltration rate as affected by tire dynamic load and inflation pressure." *Transactions of the ASAE*, 43(4), 785-792.

Adebiyi, O. A., Koike, M., Konaka, T., Yuzawa, S., and Kuroishi, I. (1991). "Compaction characteristics for the towed and driven conditions of a wheel operating in an agricultural soil." *Journal of Terramechanics*, 28(4), 371-382.

Arvidsson, J., and Ristic, S. (1996). "Soil stress and compaction effects for four tractor tyres." *Journal of Terramechanics*, 33(5), 223-232.

Ayers, M. E., Thompson, M. R., and Uzarski, D. R. (1989). "Rapid shear strength evaluation of in situ granular materials." *Transportation Research Record*, 1227, 134-146.

Bekker, M. G. (1956). *Theory of Land Locomotion*, Universtiy of Michigan Press, Ann Arbor, MI.

Bekker, M. G. (1960). *Off-the-Road Locomotion*, University of Michigan Press, Ann Arbor, MI.

Bekker, M. G. (1969). *Introduction to Terrain-Vehicle Systems*, University of Michigan Press, Ann Arbor, MI.

Block, W. A. (1991). "Analysis of soil stress under rigid wheel loading," Ph.D. Thesis, Auburn University, Auburn, AL.

Block, W. A., Johnson, C. E., Bailey, A. C., Burt, E. C., and Raper, R. L. (1994). "Soil stress measurement under rigid wheel loading." *Transactions of the ASAE*, 37(6), 1753-1756.

Botta, G. F., Jorajuria, D., and Draghi, L. M. (2002). "Influence of axle load, tyre size and configuration on the compaction of a freshly tilled clay." *Journal of Terramechanics*, 39(1), 47-54.

Bygdén, G., Eliasson, L., and Wästerlund, I. (2004). "Rut depth, soil compaction and rolling resistance when using bogie tracks." *Journal of Terramechanics*, 40(3), 179-190.

Caquot, A., and Kerisel, J. (1953). "Sur le terme de surface dans le calcul des gondations en milieu pulverulent." *Third International Conference on Soil Mechanics and Foundation Engineering*, Zürich, 336-337.

Çarman, K. (1994). "Tractor forward velocity and tire load effects on soil compaction." *Journal of Terramechanics*, 31(1), 11-20.

Chen, W. F. (1975). *Limit Analysis and Soil Plasticity*, Elsevier, Amsterdam.
Chi, L., Tessier, S., and Lague, C. (1993). "Finite element prediction of soil compaction induced by various running gears." *Transactions of the ASAE,* 36(3), 629-636.
Chiroux, R. C., Foster, W. A., Johnson, C. E., Shoop, S. A., and Raper, R. L. (2005). "Three-dimensional finite element analysis of soil interaction with a rigid wheel." *Applied Mathematics and Computation,* 162(2), 707-722.
Chung, T. J., and Lee, J. K. (1975). "Dynamics of viscoelastoplastic soil under a moving wheel." *Journal of Terramechanics*, 12(1), 15-31.
Coonse, J. (1999). "Estimating California Bearing Ratio of cohesive piedmont residual soil using the scala dynamic cone penetrometer." MS Thesis. North Carolina State University, Raleigh, N.C.
Crovetti, J. A. (2002). *Comprehensive Subgrade Deflection Acceptance Criteria - Executive Summary*. Report No. WI/SPR-05-02, Wisconsin Department of Transportation, Madison, WI.
Das, B.M. (1983). *Advanced Soil Mechanics*, McGraw-Hill, New York.
Das, B.M. (1995). *Principles of Foundation Engineering*, 3rd Ed., PWS, Boston.
Das, B. M. (2005). *Fundamentals of Geotechnical Engineering*, Thomson, Toronto.
De Beer, E. E. (1970). "Experimental determination of the shape factors and bearing capacity factors of sand." *Geotechnique*, 20(4), 387-411.
Dagan, G., and Tulin, M. P. (1969). "A study of the steady flow of a rigid-plastic clay beneath a driven wheel." *Journal of Terramechanics*, 6(2), 9-27.
Davich, P., Labuz, J. F., Guzina, B. B., and Drescher, A. (2004). *Small Strain and Resilient Modulus Testing of Granular Soils*. MN-RC 2004-39, Minnesota Department of Transporation, St. Paul, MN.
Duncan, J. M., and Chang, C. Y. (1970). "Nonlinear analysis of stress and strain in soils." *Journal of the Soil Mechanics and Foundation Division*, ASCE, 96(SM5), 1629-1653.
Elsamny, M. K., and Ghobarah, A. A. (1972). "Stress field under slipping rigid wheel." *Journal of the Soil Mechanics and Foundation Division*, ASCE*,* 98(SM1), 13-25.
Evans, I. (1964). "The sinkage of tracked vehicles on soft ground." *Journal of Terramechanics*, 1(2), 33-43.
Freitag, D.R. (1965). "An analysis of the performance of pneumatic tires on soft soils." PhD Thesis. Auburn University, Auburn, AL.
Fujimoto, Y. (1977). "Performance of elastic wheels on yielding cohesive soils." *Journal of Terramechanics*, 14(4), 191-210.
Gassman, P. W., Erbach, D. C., and Melvin, S. W. (1989). "Analysis of track and wheel soil compaction." *Transactions ASAE*, 32(1), 23-29.
Gee-Clough, D. (1979). "The effect of wheel width on the rolling resistance of rigid wheels in sand." *Journal of Terramechanics*, 15(4), 161-184.
Gee-Clough, D. (1991). "Soil-vehicle interaction (B)." *Journal of Terramechanics*, 28(4), 289-296.
Gregory, G.H, and Cross, S.A. (2007). "Correlation of California Bearing Ratio with shear strength parameters." *Transportation Research Record*, No. 1989, 148-153.
Hansen, J. B. (1970). "A revised and extended formula for bearing capacity." Danish Geotechnical Institute, *Bulletin 28*, Copenhagen.
Hetherington, J. G., and Littleton, I. (1978). "The rolling resistance of towed, rigid wheels in sand." *Journal of Terramechanics*, 15(2), 95-105.

Karafiath, L. L. (1971). "Plasticity theory and the stress distribution beneath wheels." *Journal of Terramechanics*, 8(2), 49-60.
Karafiath, L. L., and Nowatzki, E. A. (1978). *Soil Mechanics for Off-Road Vehicle Engineering*, Tans Tech Publications, Clausthal, Germany.
Kim, K. U., and Shin, B. S. (1986). "Modeling motion resistance of rigid wheels." *Journal of Terramechanics*, 22(4), 225-236.
Kogure, K. (1976). "External motion resistance caused by rut sinkage of a tracked vehicle." *Journal of Terramechanics*, 13(1), 1-14.
Krick, G. (1969). "Radial and shear stress distribution under rigid wheels and pneumatic tires operating on yielding soils with consideration of tire deformation." *Journal of Terramechanics*, 6(3), 73-98.
Lansing, D. L. (1966). *The displacements in an elastic half space due to a moving concentrated normal load*. Report No. R-238, National Aeronautics and Space Administration, Washington, D.C.
Liu, C. H., and Wong, J. Y. (1996). "Numerical simulations of tire-soil interaction based on critical state soil mechanics." *Journal of Terramechanics*, 33(5), 209-221.
Maciejewski, J., and Jarzebowski, A. (2004). "Experimental analysis of soil deformation below a rolling rigid cylinder." *Journal of Terramechanics,* 41(4), 223-241.
Maclaurin, E. B. (1987). "Soil-vehicle interaction." *Journal of Terramechanics*, 24(4), 281-294.
McRae, J. L. (1964). "Theory for a towed wheel in soil." *Journal of Terramechanics*, 1(4), 31-53.
Meyerhof, G. G. (1963). "Some recent research on bearing capacity of foundations." *Canadian Geotechnical Journal*, 1(1), 16-26.
Meyerhof, G.G. (1974). “Ultimate bearing capacity of footings on sand layer overlying clay.” *Canadian Geotechnical Journal*, 11(2), 223-229.
Meyerhof, G.G., and Hanna, A.M. (1978). “Ultimate bearing capacity of foundations on layered soil under inclined load.” *Canadian Geotechnical Journal*, 15(4), 565-572.
Meyerhof, G. G., and Koumoto, T. (1987). "Inclination factors for bearing capacity of shallow footings." *Journal of Geotechnical Engineering*, 113(9), 1013-1018.
Muro, T. (1993). "Braking performances of a towed rigid wheel on a soft ground based on the analysis of soil-compaction." *Soils and Foundations*, 33(2), 91-104.
Muro, T., He, T., and Miyoshi, M. (1998). "Effects of a roller and a tracked vehicle on the compaction of a high lifted decomposed granite sandy soil." *Journal of Terramechanics*, 35(4), 265-293.
Nakashima, H., and Wong, J. Y. (1993). "A three-dimensional tire model by the finite element method." *Journal of Terramechanics*, 30(1), 21-34.
Nowatzki, E. A., and Karafiath, L. L. (1974). "General yield conditions in a plasticity analysis of soil-wheel interaction." *Journal of Terramechanics*, 11(1), 29.
Onafeko, O., and Reece, A. R. (1967). "Soil stresses and deformations beneath rigid wheels." *Journal of Terramechanics*, 4(1), 59-80.
Osetinsky, A., and Shmulevich. (2004). “Traction performance simulation of a pushed/pulled driven wheel.” *Transactions of the ASAE*, 47(4), 981-994.
Perumpral, J. V., Liljedahl, J. B., and Perloff, W. H. (1971). "A numerical method for predicting the stress distribution and soil deformation under a tractor wheel." *Journal of Terramechanics*, 8(1), 9-22.

Poletayev, A. F. (1964). "The compaction of soil under a rolling wheel." *Journal of Terramechanics*, 1(3), 7-17.
Pollock, D., Perumpral, J. V., and Kuppusamy, T. (1986). "Finite element analysis of multipass effects of vehicles on soil compaction." *Transactions ASAE*, 29(1), 45-50.
Prandtl, L. (1921). "Über die Eindringungsfestigkeit (Härte) plastischer Baustoffe und die Festigkeit von Schneiden." *Zeitschrift für angewandte Mathematik und Mechanik*, 1(1), 15-20.
Przeslawski, P. A. (2004). "Characterization of granular base materials using portable vibratory deflectometer and bender element testing," MS Thesis, University of Minnesota, Minneapolis, MN.
Qun, Y., Sunrong, G., and Guyuan, Y (1987). "On the modeling and simulation of tire-soil systems." *Ninth International Conference of the International Society for Terrain-Vehicle Systems*, Barcelona, 257-266.
Raghavan, G. S. V., and McKyes, E. (1978). "Statistical models for predicting compaction generated by off-road vehicular traffic in different soil types." *Journal of Terramechanics*, 15(1), 1.
Raghavan, G. S. V., McKyes, E., and Beaulieu, B. (1978). "Clay soil compaction due to wheel slip." *Transactions ASAE*, 21(4), 646-649.
Reissner, H. (1924). "Zum Erddruckproblem." *First International Congress of Applied Mechanics*, Delft, 295-311.
Roberts, A. M. (1971). "Further two-dimensional effects of cylinders rolling on an elastic half-space." *Quarterly of Applied Mathematics,* April, 17-28.
Roy, B.K. (2007). "New look at DCP test with a link to AASHTO SN concept." *Journal of Transportation Engineering*, 133(4), 264-274.
Saliba, J. E. (1990). "Elastic-viscoplastic finite-element program for modeling tire/soil interaction." *Journal of Aircraft*, 27(4), 350-357.
Schwanghart, H. (1991). "Measurement of contact area, contact pressure and compaction under tires in soft soil." *Journal of Terramechanics*, 28(4), 309-318.
Shibly, H., Iagnemma, K., and Dubowsky, S. (2005). "An equivalent soil mechanics formulation for rigid wheels in deformable terrain, with application to planetary exploration rovers." *Journal of Terramechanics*, 42(1), 1-13.
Swenson, J. N., Guzina, B. B., Labuz, J. F., and Drescher, A. (2006). *Moisture effects on PVD and DCP measurements*. MN/RC-2006-26, Minnesota Department of Transportation, Research Services Section, St. Paul, MN.
Terzaghi, K. (1943). *Theoretical Soil Mechanics*, Wiley, New York.
Turnbull, W. J., and Foster, C. R. (1956). "Stabilization of materials by compaction." *Journal of the Soil Mechanics and Foundation Division*, ASCE, 82(SM2), 1-23.
Vesic, A. S. (1973). "Analysis of ultimate loads of shallow foundations." *Journal of the Soil Mechanics and Foundation Division*, ASCE, 99(SM1), 45-73.
W.A. Foster, J., Johnson, C. E., Raper, R. L., and Shoop, S. A. (1995). "Soil deformation and stress analysis under a rolling wheel." *Proceedings of the 5th North American ISTVS Conference/Workshop*, Saskatoon, Canada, 194-203.
Willis, B. M. D., Barret, F. M., and Shaw, G. J. (1965). "An investigation into rolling resistance theories for towed rigid wheels." *Journal of Terramechanics*, 2(1), 24-53.
Windisch, E. J., and Yong, R. N. (1970). "The determination of soil strain-rate behaviour beneath a moving wheel." *Journal of Terramechanics*, 7(1), 55-67.

Wong, J. Y. (1989). *Terramechanics and Off-Road Vehicles*, Elsevier, New York.
Wong, J. Y. (2001). *Theory of Ground Vehicles*, John Wiley and Sons, Inc., New York.
Wong, J. Y., Garber, M., and Preston-Thomas, J. (1984). "Theoretical prediction and experimental substantiation of the ground pressure distribution and tractive performance of tracked vehicles." *Proceedings of the Institution of Mechanical Engineers, Part D: Transport Engineering*.
Yong, R. N., and Fattah, E. A. (1976). "Prediction of wheel-soil interaction and performance using the finite element method." *Journal of Terramechanics*, 13(4), 227-240.
Yong, R. N., Fattah, E. A., and Boonsinsuk, P. (1978). "Analysis and prediction of tyre-soil interaction and performance using finite elements." *Journal of Terramechanics*, 15(1), 43-63.
Zhu, M., and Michalowski, R.L. (2005). “Shape factors for limit loads on square and rectangular footings.” *Journal of Geotechnical and Geoenvironmental Engineering*, 131(2), 223-231.

Appendix A: Summary of Formulas

This appendix summarizes the equations resulting from the analytic method (Section 3.2) and is intended as an aid for practical implementation. Formulas relating weight on a wheel, wheel geometry, wheel flexibility, sinkage, and soil properties are listed for the cases of an indenting (non-rolling) rigid wheel, an indenting flexible wheel, a rolling rigid wheel, and a rolling flexible wheel. Formulas for influence depth (the depth at which a weak or strong layer begins to affect sinkage) are also presented.

Variables:

b wheel width

c soil cohesion (Mohr-Coulomb) for homogenous soil

c_1 soil cohesion (Mohr-Coulomb) of upper layer in layered soil

c_2 soil cohesion (Mohr-Coulomb) of lower layer in layered soil

d wheel diameter

ϕ soil friction angle (Mohr-Coulomb) for homogeneous soil

ϕ_1 soil friction angle (Mohr-Coulomb) of upper layer in layered soil

ϕ_2 soil friction angle (Mohr-Coulomb) of lower layer in layered soil

γ soil unit weight for homogenous soil

γ_1 soil unit weight of upper layer in layered soil

H influence depth

η coefficient for equivalent foundation depth; use $\eta = 6$ (see Section 3.5 for details)

λ_i wheel flexibility coefficient for wheel indentation

λ_r wheel flexibility coefficient for wheel rolling

K_s factor depending on ϕ in influence depth computations

N_c bearing capacity factor; $N_c = \left(N_q - 1\right)\cot\phi$

N_q bearing capacity factor; $N_q = \tan^2\left(\pi/4 + \phi/2\right)e^{\pi\tan\phi}$

N_γ bearing capacity factor; $N_\gamma = 2\left(N_q + 1\right)\tan\phi$

N_{q1} bearing capacity factor for layered soil; $N_{q1} = \tan^2\left(\pi/4 + \phi_1/2\right)e^{\pi\tan\phi_1}$

$N_{\gamma 1}$ bearing capacity factor for layered soil; $N_{\gamma 1} = 2\left(N_{q1} + 1\right)\tan\phi_1$

Q total wheel force; $Q = \sqrt{Q_V^2 + Q_H^2}$

Q_H horizontal component of wheel force

Q_V vertical component of wheel force (wheel weight)

s wheel sinkage

Indentation of rigid, right-cylindrical wheel:

$$Q_V = 2b\sqrt{ds - s^2}\left\{cN_c\left(1 + 2\frac{\sqrt{ds - s^2}}{b}\frac{N_q}{N_c}\right)\left(1 + 0.03\frac{\eta s}{\sqrt{ds - s^2}}\right)\right.$$
$$+ 0.17\gamma\eta s N_q\left(1 + 2\frac{\sqrt{ds - s^2}}{b}\tan\phi\right)\left[1 + 0.17\tan\phi\left(1 - \sin\phi\right)^2\frac{\eta s}{\sqrt{ds - s^2}}\right]$$
$$\left. + \gamma\sqrt{ds - s^2}N_\gamma\left(1 - 0.8\frac{\sqrt{ds - s^2}}{b}\right)\right\}$$

for $2\sqrt{ds - s^2} < b$ and

$$Q_V = 2b\sqrt{ds - s^2}\left\{cN_c\left(1 + 0.5\frac{b}{\sqrt{ds - s^2}}\frac{N_q}{N_c}\right)\left(1 + 0.07\frac{\eta s}{b}\right)\right.$$
$$+ 0.17\gamma\eta s N_q\left(1 + 0.5\frac{b}{\sqrt{ds - s^2}}\tan\phi\right)\left[1 + 0.33\tan\phi\left(1 - \sin\phi\right)^2\frac{\eta s}{b}\right]$$
$$\left. + \gamma b N_\gamma\left(0.5 - 0.1\frac{b}{\sqrt{ds - s^2}}\right)\right\}$$

for $2\sqrt{ds - s^2} \geq b$.

Steady-state rolling of rigid, right cylindrical wheel (inclined footing method):

$$Q_V = b\sqrt{ds}\cos\left(\sqrt{\frac{s}{d}}\right)\left\{cN_c\left(1 + \frac{\sqrt{ds}}{b}\frac{N_q}{N_c}\right)\left(1 + 0.07\frac{\eta s}{\sqrt{ds}}\right)\left(\frac{N_q e^{-2\sqrt{\frac{s}{d}}\tan\phi} - 1}{N_q - 1}\right)\right.$$
$$+ \left[0.17\gamma\eta s N_q\left(1 + \frac{\sqrt{ds}}{b}\tan\phi\right)\left(1 + 0.33\tan\phi\left(1 - \sin\phi\right)^2\frac{\eta s}{\sqrt{ds}}\right)\right.$$
$$\left.\left. + \gamma\sqrt{ds}N_\gamma\left(0.5 - 0.2\frac{\sqrt{ds}}{b}\right)\right]\left[1 - \tan\left(\sqrt{\frac{s}{d}}\right)\right]^2\right\}$$

for $2\sqrt{ds} < b$ and

$$Q_V = b\sqrt{ds}\cos\left(\sqrt{\frac{s}{d}}\right)\left\{cN_c\left(1+\frac{b}{\sqrt{ds}}\frac{N_q}{N_c}\right)\left(1+0.07\frac{\eta s}{b}\right)\left(\frac{N_q e^{-2\sqrt{\frac{s}{d}}\tan\phi}-1}{N_q-1}\right)\right.$$

$$+\left[0.17\gamma\eta s N_q\left(1+\frac{b}{\sqrt{ds}}\tan\phi\right)\left(1+0.33\tan\phi\left(1-\sin\phi\right)^2\frac{\eta s}{b}\right)\right.$$

$$\left.\left.+\gamma b N_\gamma\left(0.5-0.2\frac{b}{\sqrt{ds}}\right)\right]\left[1-\tan\left(\sqrt{\frac{s}{d}}\right)\right]^2\right\}$$

for $2\sqrt{ds} \geq b$

Indentation of flexible, right-cylindrical wheel:

$$Q_V = 2b\sqrt{s\left(d+\lambda_i Q_V\right)-s^2}\left\{cN_c\left(1+2\frac{\sqrt{s\left(d+\lambda_i Q_V\right)-s^2}}{b}\frac{N_q}{N_c}\right)\right.$$

$$\times\left[1+0.03\frac{\eta s}{\sqrt{s\left(d+\lambda_i Q_V\right)-s^2}}\right]+0.17\gamma\eta N_q s\left(1+2\frac{\sqrt{s\left(d+\lambda_i Q_V\right)-s^2}}{b}\tan\phi\right)$$

$$\times\left[1+0.17\tan\phi\left(1-\sin\phi\right)^2\frac{\eta s}{\sqrt{s\left(d+\lambda_i Q_V\right)-s^2}}\right]+\gamma N_\gamma\sqrt{s\left(d+\lambda_i Q_V\right)-s^2}$$

$$\left.\times\left(1-0.8\frac{\sqrt{s\left(d+\lambda_i Q_V\right)-s^2}}{b}\right)\right\}$$

for $2\sqrt{s\left(d+\lambda_i Q_V\right)-s^2} < b$ and

$$Q_V = 2b\sqrt{s\left(d+\lambda_i Q_V\right)-s^2}\left\{cN_c\left(1+0.5\frac{b}{\sqrt{s\left(d+\lambda_i Q_V\right)-s^2}}\frac{N_q}{N_c}\right)\right.$$

$$\times\left[1+0.07\frac{\eta s}{b}\right]+0.17\gamma\eta N_q s\left(1+0.5\frac{b}{\sqrt{s\left(d+\lambda_i Q_V\right)-s^2}}\tan\phi\right)$$

$$\left.\times\left[1+0.33\tan\phi\left(1-\sin\phi\right)^2\frac{\eta s}{b}\right]+\gamma b N_\gamma\left(0.5-0.1\frac{b}{\sqrt{s\left(d+\lambda_i Q_V\right)-s^2}}\right)\right\}$$

for $2\sqrt{s\left(d+\lambda_t Q_V\right)-s^2} \geq b$.

Steady-state rolling of flexible, right-cylindrical wheel (inclined footing method):

$$Q = b\sqrt{s\left(d+\lambda_r Q\right)}\left\{cN_c\left(1+\frac{\sqrt{s\left(d+\lambda_r Q\right)}}{b}\frac{N_q}{N_c}\right)\left(1+0.07\frac{\eta s}{\sqrt{s\left(d+\lambda_r Q\right)}}\right)\left(\frac{N_q e^{-2\sqrt{\frac{s}{d+\lambda_r Q}}\tan\phi}-1}{N_q-1}\right)\right.$$
$$+\left[0.17\gamma\eta s N_q\left(1+\frac{\sqrt{s\left(d+\lambda_r Q\right)}}{b}\tan\phi\right)\left(1+0.33\tan\phi\left(1-\sin\phi\right)^2\frac{\eta s}{\sqrt{\left(d+\lambda_r Q\right)s}}\right)\right.$$
$$\left.\left.+\gamma\sqrt{s\left(d+\lambda_r Q\right)}N_\gamma\left(0.5-0.2\frac{\sqrt{s\left(d+\lambda_r Q\right)}}{b}\right)\right]\left[1-\tan\left(\sqrt{\frac{s}{d+\lambda_r Q}}\right)\right]^2\right\}$$

for $\sqrt{s\left(d+\lambda_r Q\right)} < b$

$$Q = b\sqrt{s\left(d+\lambda_r Q\right)}\left\{cN_c\left(1+\frac{b}{\sqrt{s\left(d+\lambda_r Q\right)}}\frac{N_q}{N_c}\right)\left(1+0.07\frac{\eta s}{b}\right)\left(\frac{N_q e^{-2\sqrt{\frac{s}{(d+\lambda_r Q)}}\tan\phi}-1}{N_q-1}\right)\right.$$
$$+\left[0.17\gamma\eta s N_q\left(1+\frac{b}{\sqrt{s\left(d+\lambda_r Q\right)}}\tan\phi\right)\left(1+0.33\tan\phi\left(1-\sin\phi\right)^2\frac{\eta s}{b}\right)\right.$$
$$\left.\left.+\gamma b N_\gamma\left(0.5-0.2\frac{b}{\sqrt{s\left(d+\lambda_r Q\right)}}\right)\right]\left[1-\tan\left(\sqrt{\frac{s}{d+\lambda_r Q}}\right)\right]^2\right\}$$

for $\sqrt{s\left(d+\lambda_r Q\right)} \geq b$. After solving the preceding equations numerically, the total wheel force is resolved into its vertical and horizontal components using

$$Q_V = Q\cos\left(\sqrt{\frac{s}{d+\lambda_r Q}}\right) \quad , \quad Q_H = Q\sin\left(\sqrt{\frac{s}{d+\lambda_r Q}}\right)$$

Influence Depth for Dense Sand over Weak Clay (rolling wheel):

$$H = \frac{-\alpha_2 + \sqrt{\alpha_2^2 - 4\alpha_1\alpha_3}}{2\alpha_1}$$

$$\alpha_1 = \left(1 + \frac{B}{L}\right)\frac{\gamma_1 K_s \tan\phi_1}{B}$$

$$\alpha_2 = 0.33\left(1 + \frac{B}{L}\right)\frac{\gamma_1 \eta s K_s \tan\phi_1}{B}$$

$$\alpha_3 = 5.14\left(1 + 0.2\frac{B}{L}\right)c_2 + 0.17\eta\gamma_1 - 0.5\left(1 - 0.4\frac{B}{L}\right)\gamma_1 B N_{\gamma 1} - 0.17\gamma_1 \eta s N_{q1}$$

$$\left.\begin{matrix} B = \sqrt{ds} \\ L = b \end{matrix}\right\} \text{ for } \sqrt{ds} \le b \quad ; \quad \left.\begin{matrix} B = b \\ L = \sqrt{ds} \end{matrix}\right\} \text{ for } \sqrt{ds} > b$$

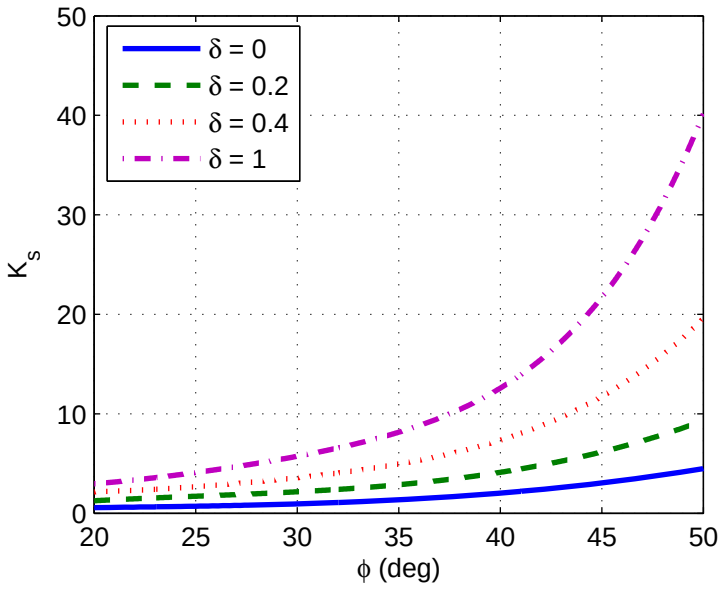

Figure A1. Variation of K_s with ϕ_1 for various $\delta = (10.28c_2)/(\gamma_1 B N_{\gamma 1})$ according to Das (1995)

Influence Depth for Strong Clay over Weak Clay (rolling wheel):

$$H = 2.57\sqrt{ds}\,\frac{\left(1+0.2\dfrac{\sqrt{ds}}{b}\right)}{\left(1+\dfrac{\sqrt{ds}}{b}\right)}\,\frac{\left(1-\dfrac{c_2}{c_1}\right)}{\left(\dfrac{c_1}{c_a}\right)} \quad \text{for} \quad \sqrt{ds} \le b$$

$$H = 2.57b\,\frac{\left(1+0.2\dfrac{b}{\sqrt{ds}}\right)}{\left(1+\dfrac{b}{\sqrt{ds}}\right)}\,\frac{\left(1-\dfrac{c_2}{c_1}\right)}{\left(\dfrac{c_1}{c_a}\right)} \quad \text{for} \quad \sqrt{ds} > b$$

$$\frac{c_a}{c_1} = 0.321\left(\frac{c_2}{c_1}\right)^3 - 1.023\left(\frac{c_2}{c_1}\right)^2 + 1.08\left(\frac{c_2}{c_1}\right) + 0.621$$

Use previous Q_V-s relationships for homogenous soil to obtain H versus Q_V.

Influence Depth for Weak Layer over Strong Layer (rolling wheel):

$H = \sqrt{ds}$ for $\sqrt{ds} \le b$

$H = b$ for $\sqrt{ds} > b$

Use previous Q_V-s relationships for homogenous soil to obtain H versus Q_V.

Appendix B: Parameters Used In Numerical Simulations of Indentation

Table B1. Parameters used in numerical simulations of indentation

case no.	d (m)	b (m)	ϕ_{DP} (deg)	c_{DP} (kPa)	E (MPa)	ν	γ (kN/m^3)	μ
1	1.524	0.4572	0.0	100.0	40	0.35	20	0.8
2	1.524	0.4572	0.0	200.0	40	0.35	20	0.8
3	1.524	0.4572	0.0	400.0	40	0.35	20	0.8
4	1.524	0.4572	27.5	97.3	40	0.35	20	0.8
5	1.524	0.4572	27.5	194.6	40	0.35	20	0.8
6	1.524	0.4572	27.5	389.3	40	0.35	20	0.8
7	1.524	0.4572	45.4	35.6	40	0.35	20	0.8
8	1.524	0.4572	45.4	89.1	40	0.35	20	0.8
9	1.524	0.4572	45.4	178.2	40	0.35	20	0.8
10	1.524	0.4572	55.2	29.9	40	0.35	20	0.8
11	1.524	0.4572	55.2	74.9	40	0.35	20	0.8
12	1.524	0.4572	60.5	21.8	40	0.35	20	0.8
13	1.524	0.4572	0.0	200.0	40	0.35	14	0.8
14	1.524	0.4572	27.5	194.6	40	0.35	14	0.8
15	1.524	0.4572	45.4	89.1	40	0.35	14	0.8
16	1.524	0.4572	55.2	29.9	40	0.35	14	0.8
17	1.524	0.4572	60.5	21.8	40	0.35	14	0.8
18	1.524	0.4572	0.0	200.0	40	0.35	20	0.4
19	1.524	0.4572	27.5	194.6	40	0.35	20	0.4
20	1.524	0.4572	45.4	89.1	40	0.35	20	0.4
21	1.524	0.4572	55.2	29.9	40	0.35	20	0.4
22	1.524	0.4572	60.5	21.8	40	0.35	20	0.4
23	1.524	0.3048	0.0	200.0	40	0.35	20	0.8
24	1.524	0.3048	27.5	194.6	40	0.35	20	0.8
25	1.524	0.3048	45.4	89.1	40	0.35	20	0.8
26	1.524	0.3048	55.2	29.9	40	0.35	20	0.8
27	1.524	0.3048	60.5	21.8	40	0.35	20	0.8
28	1.372	0.4572	0	200	50	0.3	20	0
29	1.372	0.4572	0	200	50	0.1	20	0
30	1.372	0.4572	0	200	50	0.45	20	0

Table B2. Mohr-Coulomb parameters matching Drucker-Prager parameters in triaxial compression

case no.	ϕ **(deg)**	c **(kPa)**
1	0.0	50.0
2	0.0	100.0
3	0.0	200.0
4	13.9	46.1
5	13.9	92.2
6	13.9	184.5
7	25.7	16.9
8	25.7	42.3
9	25.7	84.6
10	35.5	14.8
11	35.5	37.1
12	43.1	11.5
13	0.0	100.0
14	13.9	92.2
15	25.7	42.3
16	35.5	14.8
17	43.1	11.5
18	0.0	100.0
19	13.9	92.2
20	25.7	42.3
21	35.5	14.8
22	43.1	11.5
23	0.0	100.0
24	13.9	92.2
25	25.7	42.3
26	35.5	14.8
27	43.1	11.5
28	0.0	100.0
29	0.0	100.0
30	0.0	100.0

Appendix C: Parameters Used In Numerical Simulations of Rolling

Table C1. Parameters used in numerical simulations of rolling

case no.	d (m)	b (m)	ϕ_{DP} (deg)	c_{DP} (deg)	E (MPa)	ν	γ (kN/m^3)	μ
1	1.524	0.4572	0.0	100.0	40	0.35	20	0.8
2	1.524	0.4572	0.0	200.0	40	0.35	20	0.8
3	1.524	0.4572	0.0	400.0	40	0.35	20	0.8
4	1.524	0.4572	27.5	97.3	40	0.35	20	0.8
5	1.524	0.4572	27.5	194.6	40	0.35	20	0.8
6	1.524	0.4572	27.5	389.3	40	0.35	20	0.8
7	1.524	0.4572	45.4	35.6	40	0.35	20	0.8
8	1.524	0.4572	45.4	89.1	40	0.35	20	0.8
9	1.524	0.4572	45.4	178.2	40	0.35	20	0.8
10	1.524	0.4572	55.2	29.9	40	0.35	20	0.8
11	1.524	0.4572	55.2	74.9	40	0.35	20	0.8
12	1.524	0.4572	60.5	21.8	40	0.35	20	0.8
13	1.524	0.4572	0.0	200.0	15	0.35	20	0.8
14	1.524	0.4572	27.5	194.6	15	0.35	20	0.8
15	1.524	0.4572	45.4	89.1	15	0.35	20	0.8
16	1.524	0.4572	55.2	29.9	15	0.35	20	0.8
17	1.524	0.4572	60.5	21.8	15	0.35	20	0.8
18	1.524	0.4572	0.0	200.0	60	0.35	20	0.8
19	1.524	0.4572	27.5	194.6	60	0.35	20	0.8
20	1.524	0.4572	45.4	89.1	60	0.35	20	0.8
21	1.524	0.4572	55.2	29.9	60	0.35	20	0.8
22	1.524	0.4572	60.5	21.8	60	0.35	20	0.8
23	1.524	0.4572	0.0	200.0	40	0.35	14	0.8
24	1.524	0.4572	27.5	194.6	40	0.35	14	0.8
25	1.524	0.4572	45.4	89.1	40	0.35	14	0.8
26	1.524	0.4572	55.2	29.9	40	0.35	14	0.8
27	1.524	0.4572	60.5	21.8	40	0.35	14	0.8
28	1.524	0.4572	0.0	200.0	40	0.35	20	0.4
29	1.524	0.4572	27.5	194.6	40	0.35	20	0.4
30	1.524	0.4572	45.4	89.1	40	0.35	20	0.4
31	1.524	0.4572	55.2	29.9	40	0.35	20	0.4
32	1.524	0.4572	60.5	21.8	40	0.35	20	0.4
33	1.524	0.3048	0.0	200.0	40	0.35	20	0.8
34	1.524	0.3048	27.5	194.6	40	0.35	20	0.8
35	1.524	0.3048	45.4	89.1	40	0.35	20	0.8
36	1.524	0.3048	55.2	29.9	40	0.35	20	0.8
37	1.524	0.3048	60.5	21.8	40	0.35	20	0.8
38	1.2192	0.3048	0.0	200.0	40	0.35	20	0.8
39	1.2192	0.3048	27.5	194.6	40	0.35	20	0.8
40	1.2192	0.3048	45.4	89.1	40	0.35	20	0.8
41	1.2192	0.3048	55.2	29.9	40	0.35	20	0.8
42	1.2192	0.3048	60.5	21.8	40	0.35	20	0.8
43	1.524	0.4572	45.4	89.1	20	0.35	20	0.8

Table C2. Mohr-Coulomb parameters matching Drucker-Prager parameters in triaxial compression

case no.	ϕ (deg)	c (deg)
1	0.0	50.0
2	0.0	100.0
3	0.0	200.0
4	13.9	46.1
5	13.9	92.2
6	13.9	184.5
7	25.7	16.9
8	25.7	42.3
9	25.7	84.6
10	35.5	14.8
11	35.5	37.1
12	43.1	11.5
13	0.0	100.0
14	13.9	92.2
15	25.7	42.3
16	35.5	14.8
17	43.1	11.5
18	0.0	100.0
19	13.9	92.2
20	25.7	42.3
21	35.5	14.8
22	43.1	11.5
23	0.0	100.0
24	13.9	92.2
25	25.7	42.3
26	35.5	14.8
27	43.1	11.5
28	0.0	100.0
29	13.9	92.2
30	25.7	42.3
31	35.5	14.8
32	43.1	11.5
33	0.0	100.0
34	13.9	92.2
35	25.7	42.3
36	35.5	14.8
37	43.1	11.5
38	0.0	100.0
39	13.9	92.2
40	25.7	42.3
41	35.5	14.8
42	43.1	11.5
43	25.7	42.3

Appendix D: Parameters Used In Numerical Simulations of Rolling on Layered Soil

Table D1. Parameters used in numerical simulations of rolling on layered soil

case no.	d **(m)**	b **(m)**	ν	γ **(kN/m^3)**	μ
1	1.524	0.4572	0.35	20	0.8
:	:	:	:	:	:
20	1.524	0.4572	0.35	20	0.8

Table D2. Parameters used in numerical simulations of rolling on layered soil

	Layer No.								
	1			**2**			**3**		
Case No.	E **(kPa)**	ϕ_{DP} **(º)**	c_{DP} **(kPa)**	E **(kPa)**	ϕ_{DP} **(º)**	c_{DP} **(kPa)**	E **(kPa)**	ϕ_{DP} **(º)**	c_{DP} **(kPa)**
1	40	45.4	35.6	40	55.2	29.9	40	55.2	29.9
2	40	45.4	35.6	40	45.4	35.6	40	55.2	29.9
3	40	55.2	29.9	40	45.4	35.6	40	45.4	35.6
4	40	55.2	29.9	40	55.2	29.9	40	45.4	35.6
5	40	0.0	100.0	40	0.0	200.0	40	0.0	200.0
6	40	0.0	100.0	40	0.0	100.0	40	0.0	200.0
7	40	0.0	200.0	40	0.0	100.0	40	0.0	100.0
8	40	0.0	200.0	40	0.0	200.0	40	0.0	100.0
9	20	45.4	89.1	60	45.4	89.1	60	45.4	89.1
10	20	45.4	89.1	20	45.4	89.1	60	45.4	89.1
11	60	45.4	89.1	20	45.4	89.1	20	45.4	89.1
12	60	45.4	89.1	60	45.4	89.1	20	45.4	89.1
13	40	61.6	18.5	40	61.6	18.5	40	61.6	18.5
14	40	61.6	18.5	40	61.6	18.5	10	0	18.5
15	40	61.6	18.5	10	0	18.5	10	0	18.5
16	40	61.6	18.5	40	0	555	40	0	555
17	40	0	300	40	0	300	40	0	300
18	40	0	300	40	0	300	10	0	20
19	40	0	300	10	0	20	10	0	20
20	40	0	300	40	0	600	40	0	600

Table D3. Mohr-Coulomb parameters matching Drucker-Prager parameters in triaxial compression

	Layer No.								
	1			**2**			**3**		
Case No.	***E* (kPa)**	**ϕ (°)**	***c* (kPa)**	***E* (kPa)**	**ϕ (°)**	***c* (kPa)**	***E* (kPa)**	**ϕ (°)**	***c* (kPa)**
1	40	30	20	40	45	20	40	45	20
2	40	30	20	40	30	20	40	45	20
3	40	45	20	40	30	20	40	30	20
4	40	45	20	40	45	20	40	30	20
5	40	0	50	40	0	100	40	0	100
6	40	0	50	40	0	50	40	0	100
7	40	0	100	40	0	50	40	0	50
8	40	0	100	40	0	100	40	0	50
9	20	30	50	60	30	50	60	30	50
10	20	30	50	20	30	50	60	30	50
11	60	30	50	20	30	50	20	30	50
12	60	30	50	60	30	50	20	30	50
13	40	45	10	40	45	10	40	45	10
14	40	45	10	40	45	10	10	0	10
15	40	45	10	10	0	10	10	0	10
16	40	45	10	40	0	300	40	0	300
17	40	0	150	40	0	150	40	0	150
18	40	0	150	40	0	150	10	0	10
19	40	0	150	10	0	10	10	0	10
20	40	0	150	40	0	300	40	0	300

Appendix E: Correlation Coefficients for Numerical Simulations of Indentation

Table E1. Correlation coefficients for numerical simulations of indentation

case no.	κ_1	κ_2	κ_3	κ_4	R^2
1	2.85	28.7	-253.9	1009.0	0.999
2	2.54	74.1	-673.5	2905.8	0.998
3	1.57	139.0	-943.3	3209.0	0.999
4	1.80	74.6	-449.3	1478.5	0.999
5	0.95	128.8	-579.2	1529.2	1.000
6	0.00	197.0	-620.7	1382.5	1.000
7	0.80	74.5	-169.9	-38.7	0.999
8	0.37	123.4	-81.1	-515.6	1.000
9	0.00	173.9	-50.6	-339.2	1.000
10	1.98	87.1	1005.4	-4818.9	1.000
11	1.77	136.2	861.0	-2311.9	1.000
12	0.47	124.8	1415.6	-1716.1	1.000
13	4.47	97.3	-806.5	3150.4	0.999
14	0.64	194.7	-1079.2	3928.8	1.000
15	1.38	168.6	-46.6	-1264.0	1.000
16	3.66	114.6	1483.3	-7697.9	1.000
17	0.73	176.1	1900.1	-2206.9	1.000
18	3.33	65.1	-549.9	2170.3	0.998
19	1.16	127.8	-649.3	2125.3	0.999
20	0.46	124.5	-196.5	154.0	1.000
21	1.84	90.7	905.7	-4949.7	1.000
22	0.00	130.8	1345.6	-2197.3	1.000
23	1.70	49.1	-440.4	1847.9	0.999
24	0.00	95.4	-456.8	1190.0	0.999
25	0.00	88.8	-58.3	-604.5	1.000
26	0.79	64.5	713.8	-3784.2	1.000
27	0.00	91.9	899.8	-398.8	1.000

Appendix F: Correlation Coefficients for Numerical Simulations of Rolling

Table F1. Correlation coefficients for numerical simulations of rolling

case no.	κ_1	κ_2	κ_3	κ_4	R^2
1	2.92	12.2	-205.9	1075.9	0.981
2	4.01	37.7	-579.4	3269.2	0.992
3	3.06	105.1	-1377.5	7227.1	0.994
4	2.95	44.4	-599.1	3078.3	0.992
5	2.61	95.8	-1052.8	4940.5	0.998
6	0.00	190.7	-1804.2	8365.0	0.999
7	2.53	44.1	-547.9	2633.5	0.991
8	1.40	110.6	-1057.8	4009.4	0.997
9	0.00	175.2	-1115.3	3101.1	0.998
10	0.00	128.3	-1059.3	4708.2	0.997
11	0.00	160.9	-52.7	-3014.4	0.998
12	0.00	131.3	1459.1	-8044.1	0.999
13	0.00	59.9	-693.2	3441.4	0.996
14	0.00	78.9	-513.4	1671.3	0.999
15	0.00	73.9	-324.9	770.5	0.999
16	0.00	58.0	244.5	-2318.5	0.999
17	0.12	58.7	809.7	-1576.6	0.999
18	5.34	27.7	-456.4	2481.7	0.993
19	4.31	96.6	-1305.4	7060.2	0.991
20	3.93	107.4	-1239.1	5624.2	0.995
21	0.00	153.6	-1663.5	8726.1	0.993
22	3.46	125.5	2874.8	-22640.7	0.998
23	5.62	56.7	-908.7	5231.8	0.993
24	3.33	143.4	-1694.6	8659.1	0.998
25	3.36	145.3	-1442.5	5910.9	0.995
26	0.00	185.2	-1851.3	9519.2	0.997
27	9.52	62.5	4317.8	-28389.5	0.999
28	4.35	31.7	-459.7	2406.9	0.993
29	1.93	102.0	-1254.4	6536.7	0.997
30	3.33	88.1	-963.5	4933.4	0.996
31	0.00	134.3	-1666.2	9605.6	0.994
32	6.63	39.3	3722.9	-29747.0	0.998
33	2.83	20.7	-293.4	1581.0	0.996
34	2.02	60.0	-610.7	2717.8	0.998
35	0.89	73.0	-737.5	3546.6	0.999
36	0.00	81.9	-722.6	3308.5	0.999
37	0.00	79.9	1660.4	-14595.5	1.000
38	4.62	28.3	-349.0	1635.4	0.993
39	3.56	84.3	-802.5	3406.1	0.997
40	1.31	109.3	-1033.5	4453.1	0.998
41	0.00	122.7	-934.6	3384.7	0.999
42	5.13	57.0	3364.7	-22593.5	0.999
43	0	88.6	-570.3	1807.5	0.998

Appendix G: Correlation Coefficients for Numerical Simulations of Rolling on Layered Soil

Table G1. Correlation coefficients for numerical simulations of rolling

κ_1	κ_2	κ_3	κ_4	R^2
1.14	61.7	-960.9	5865.0	0.977
1.69	54.6	-797.3	4602.5	0.978
0.00	134.2	-1405.7	6815.7	0.985
0.00	133.0	-1254.8	6232.1	0.992
2.80	13.9	-236.8	1309.8	0.982
2.97	12.7	-236.0	1399.9	0.975
3.95	38.7	-591.6	3283.9	0.990
4.30	35.9	-591.2	3541.0	0.977
0.00	93.1	-401.8	-309.1	0.997
0.00	85.3	-378.1	21.8	0.997
3.35	92.2	-970.5	4350.2	0.992
0.58	140.7	-1870.4	9785.0	0.982

Appendix H: Dimensional Plots Using Analytic Method for Indentation

Table H1. Summary of parameters used in dimensional plots for indentation

Figure No.	Q_V **(kN)**	d **(m)**	b **(m)**	γ **(kN/m^3)**
H1	130	1.524	0.6096	20
H2	65	1.524	0.6096	20
H3	130	1.524	0.4572	20
H4	65	1.524	0.4572	20
H5	130	1.524	0.3048	20
H6	65	1.524	0.3048	20
H7	130	1.524	0.6096	14
H8	65	1.524	0.6096	14
H9	130	1.524	0.4572	14
H10	65	1.524	0.4572	14
H11	130	1.524	0.3048	14
H12	65	1.524	0.3048	14
H13	130	1.2192	0.6096	20
H14	65	1.2192	0.6096	20
H15	130	1.2192	0.4572	20
H16	65	1.2192	0.4572	20
H17	130	1.2192	0.3048	20
H18	65	1.2192	0.3048	20
H19	130	1.2192	0.6096	14
H20	65	1.2192	0.6096	14
H21	130	1.2192	0.4572	14
H22	65	1.2192	0.4572	14
H23	130	1.2192	0.3048	14
H24	65	1.2192	0.3048	14
H25	130	0.9144	0.6096	20
H26	65	0.9144	0.6096	20
H27	130	0.9144	0.4572	20
H28	65	0.9144	0.4572	20
H29	130	0.9144	0.3048	20
H30	65	0.9144	0.3048	20
H31	130	0.9144	0.6096	14
H32	65	0.9144	0.6096	14
H33	130	0.9144	0.4572	14
H34	65	0.9144	0.4572	14
H35	130	0.9144	0.3048	14
H36	65	0.9144	0.3048	14

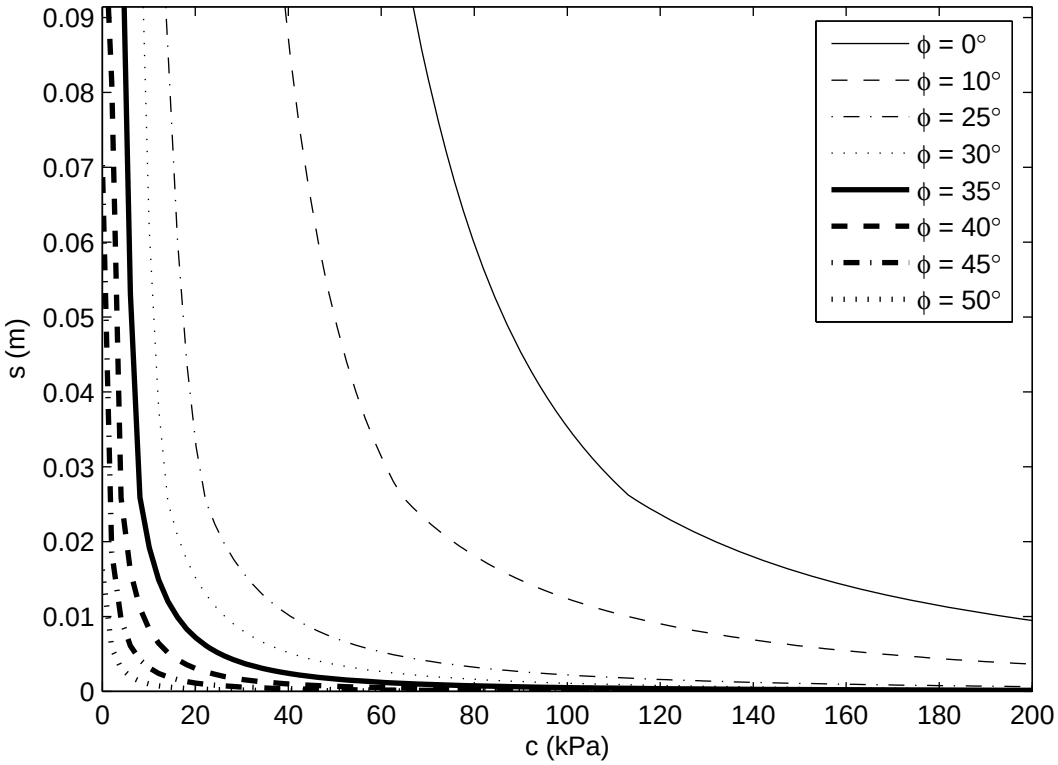

Figure H1. Analytic prediction for wheel indentation with Q_V = 130 kN, d = 1.524 m, b = 0.610 m, and γ = 20 kN/m^3

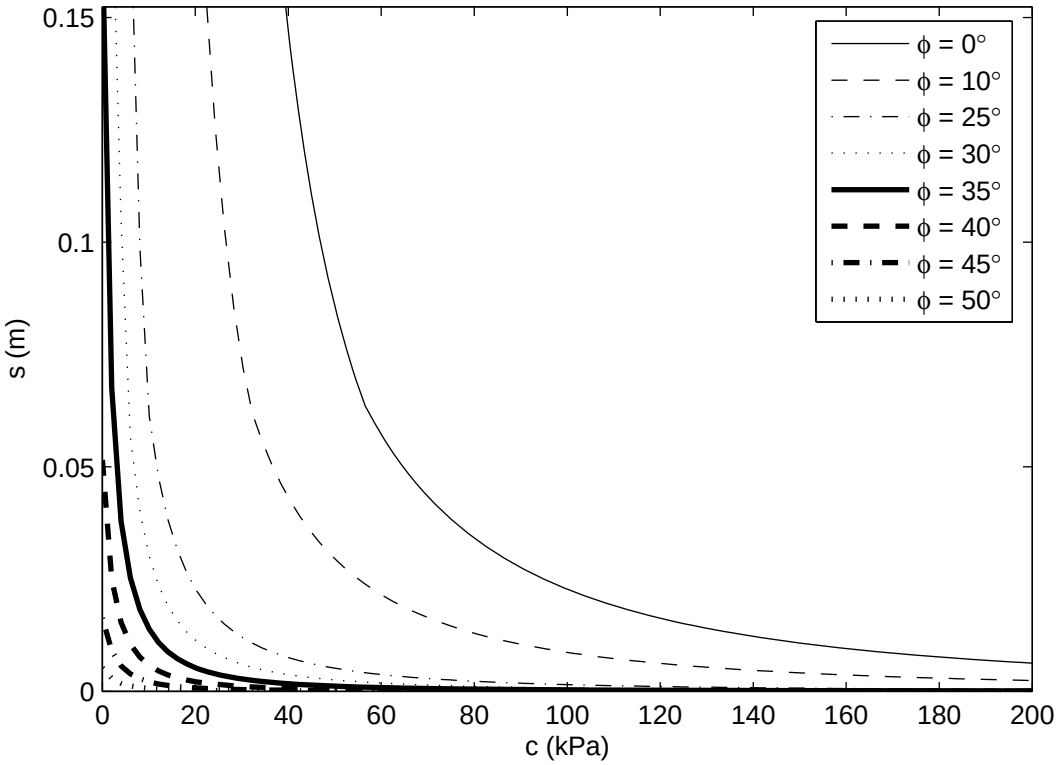

Figure H2. Analytic prediction for wheel indentation with Q_V = 65 kN, d = 1.524 m, b = 0.610 m, and γ = 20 kN/m^3

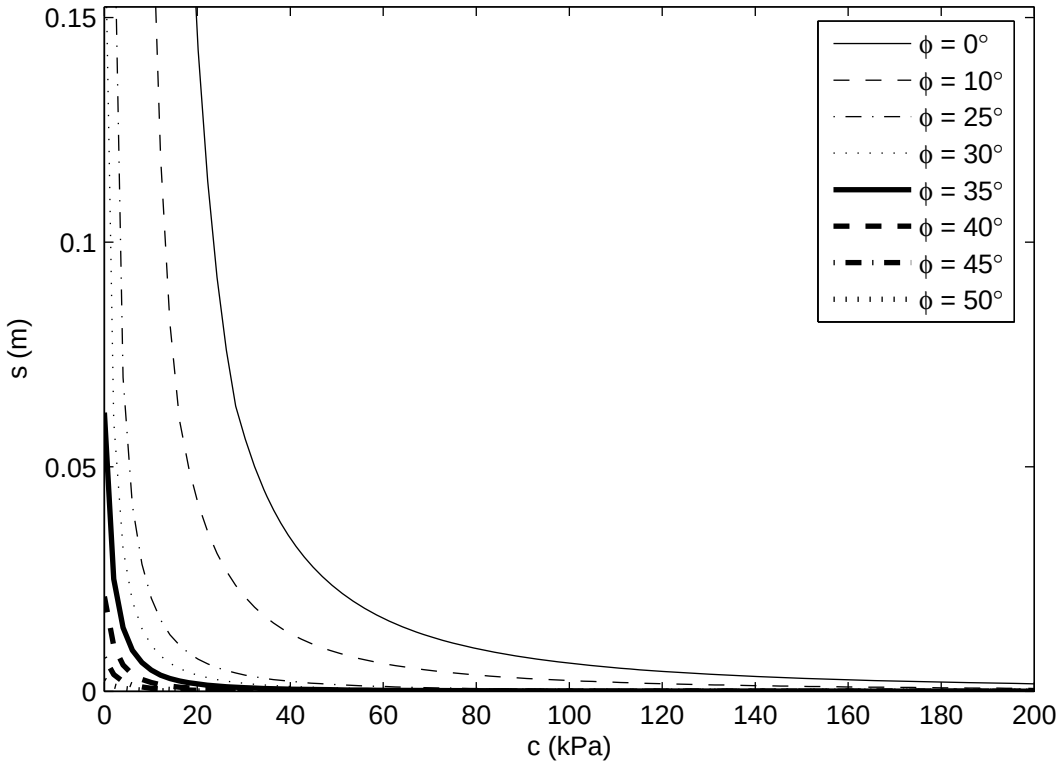

Figure H3. Analytic prediction for wheel indentation with Q_V = 130 kN, d = 1.524 m, b = 0.457 m, and γ = 20 kN/m^3

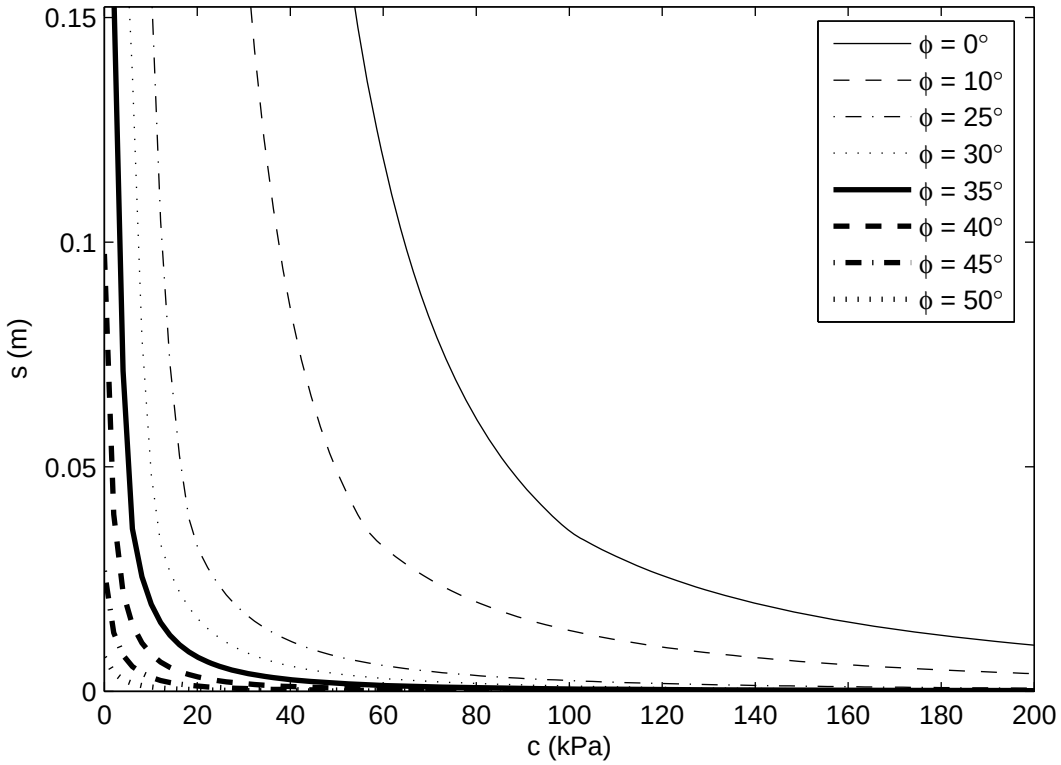

Figure H4. Analytic prediction for wheel indentation with Q_V = 65 kN, d = 1.524 m, b = 0.457 m, and γ = 20 kN/m^3

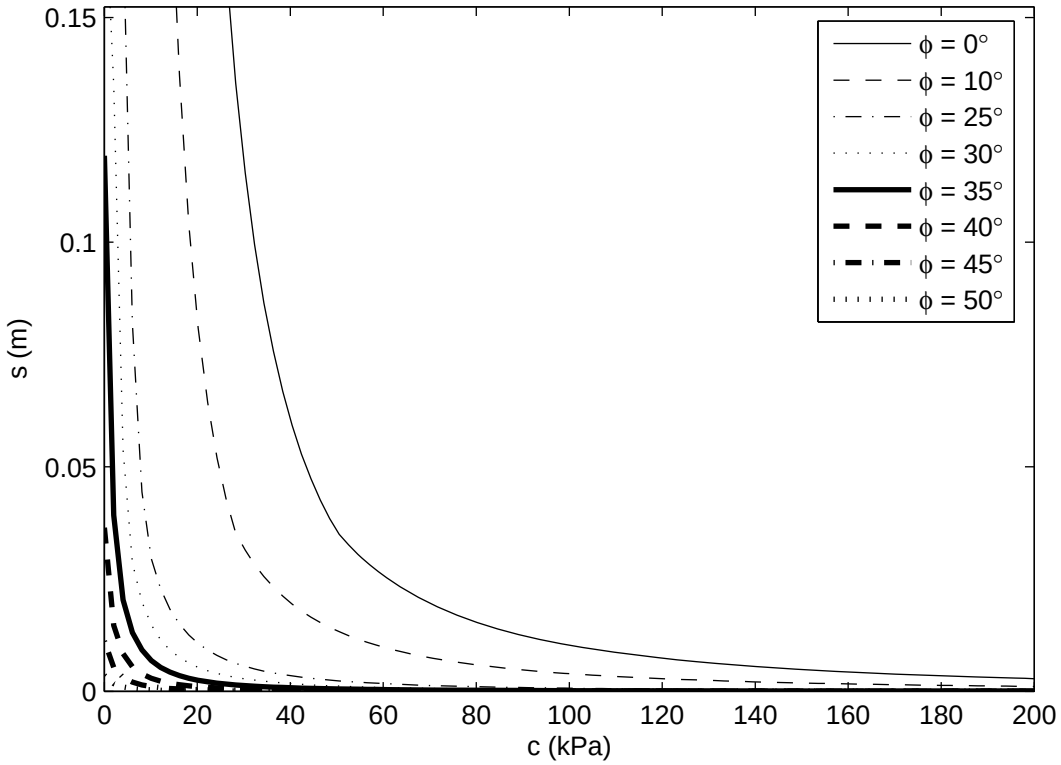

Figure H5. Analytic prediction for wheel indentation with Q_V = 130 kN, d = 1.524 m, b = 0.305 m, and γ = 20 kN/m^3

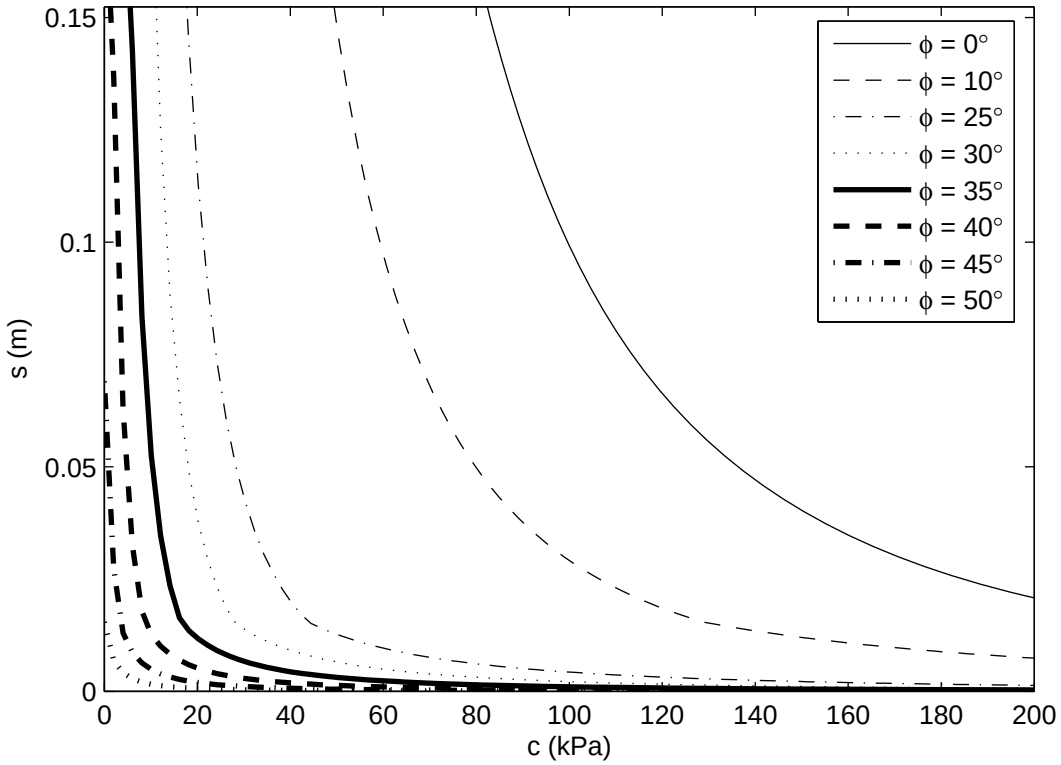

Figure H6. Analytic prediction for wheel indentation with Q_V = 65 kN, d = 1.524 m, b = 0.305 m, and γ = 20 kN/m^3

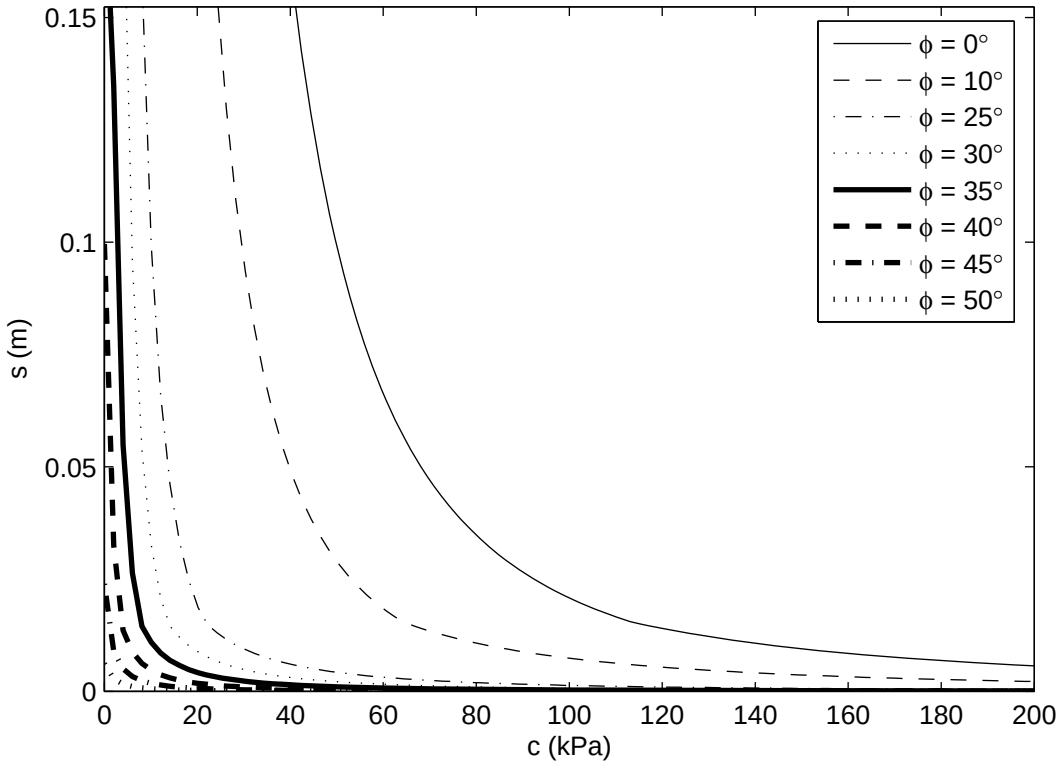

Figure H7. Analytic prediction for wheel indentation with Q_V = 130 kN, d = 1.524 m, b = 0.610 m, and γ = 14 kN/m^3

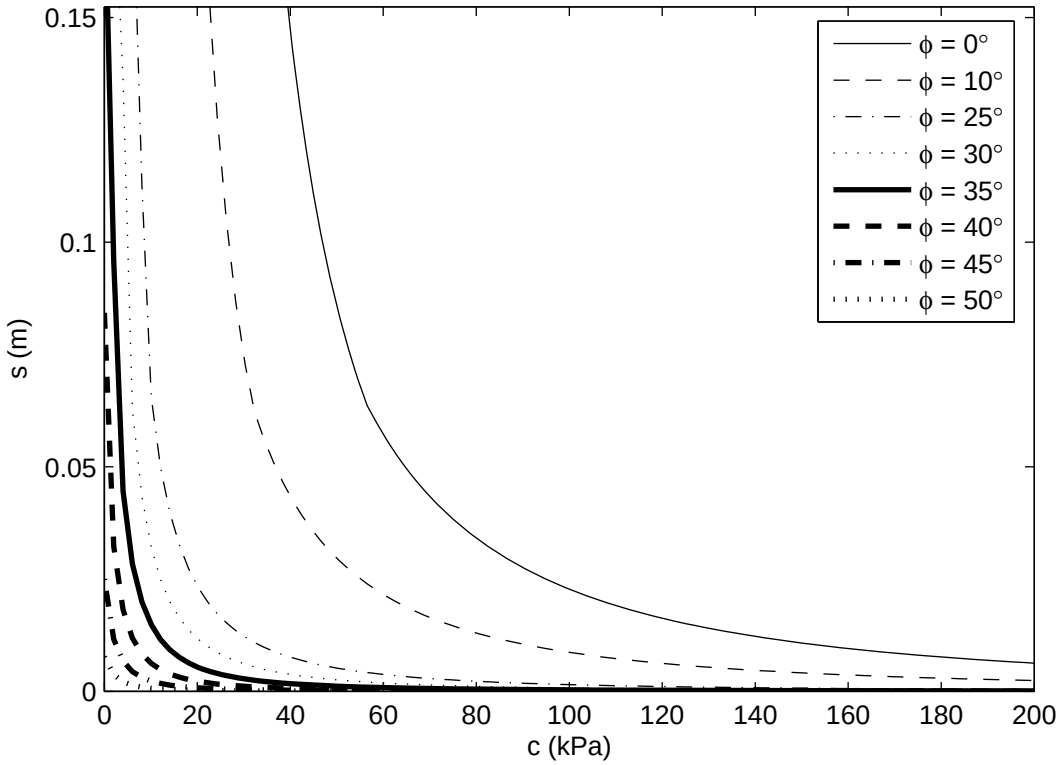

Figure H8. Analytic prediction for wheel indentation with Q_V = 65 kN, d = 1.524 m, b = 0.610 m, and γ = 14 kN/m^3

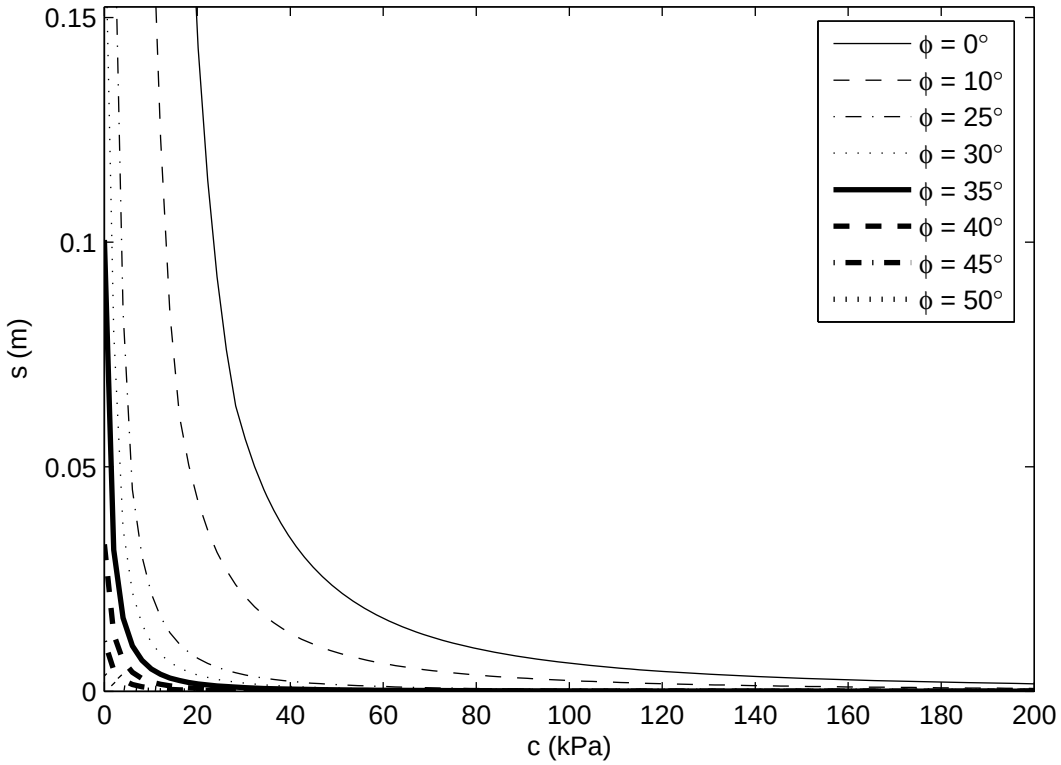

Figure H9. Analytic prediction for wheel indentation with Q_V = 130 kN, d = 1.524 m, b = 0.457 m, and γ = 14 kN/m^3

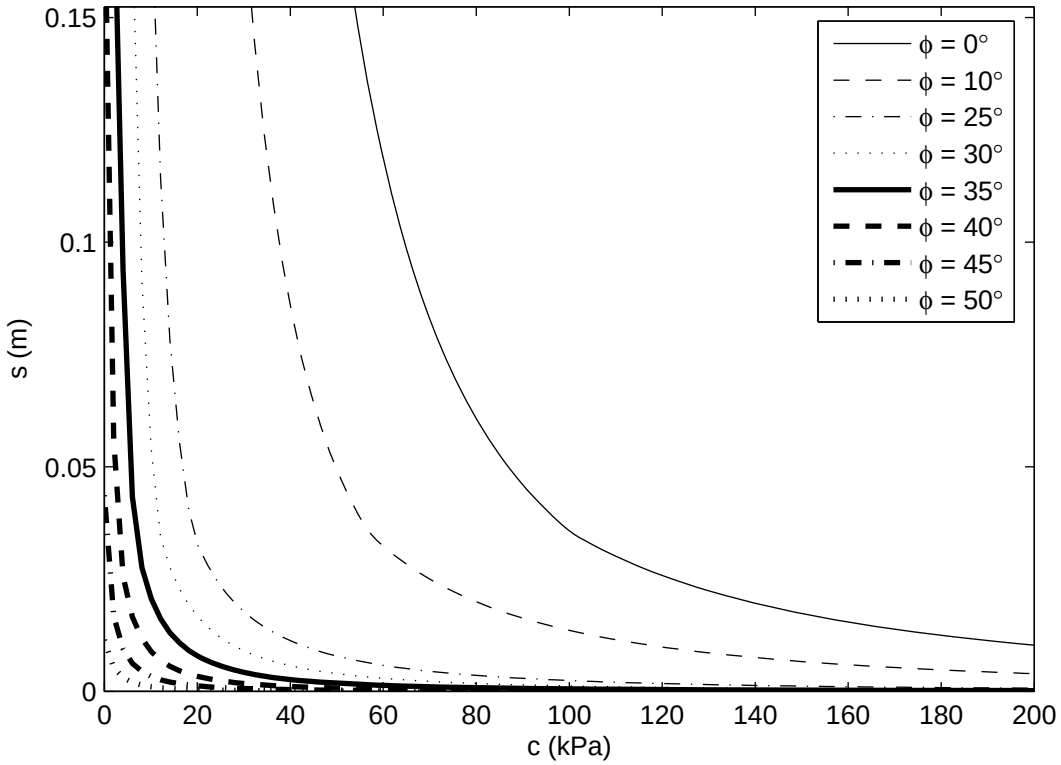

Figure H10. Analytic prediction for wheel indentation with Q_V = 65 kN, d = 1.524 m, b = 0.457 m, and γ = 14 kN/m^3

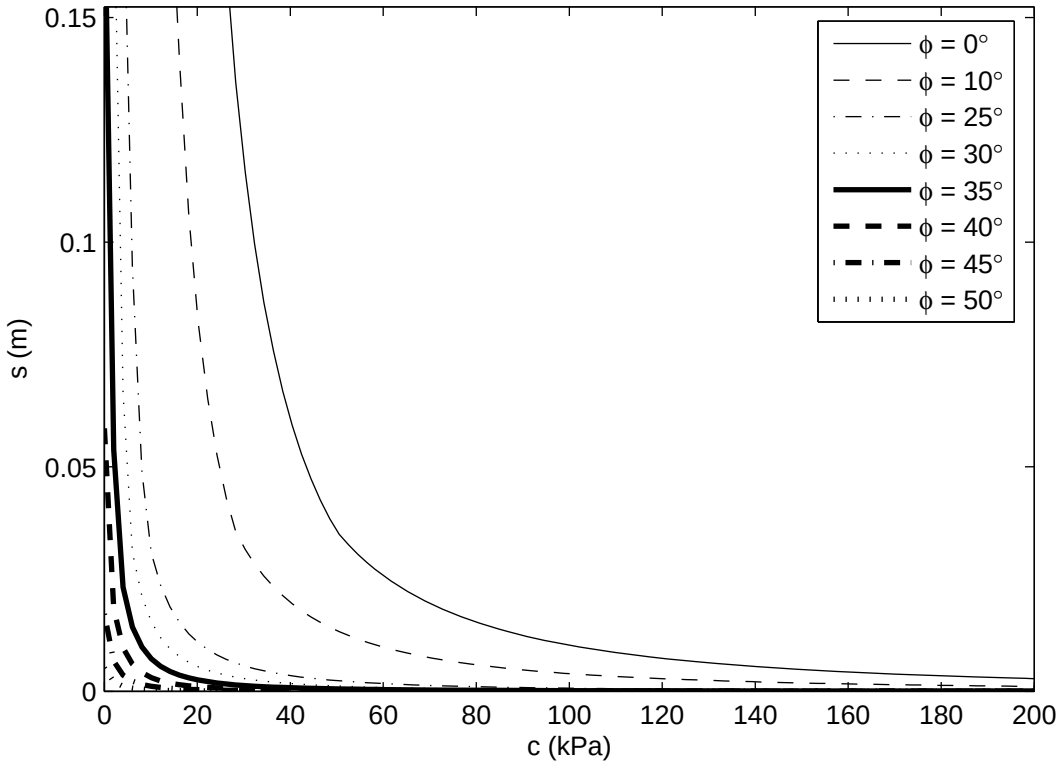

Figure H11. Analytic prediction for wheel indentation with Q_V = 130 kN, d = 1.524 m, b = 0.305 m, and γ = 14 kN/m^3

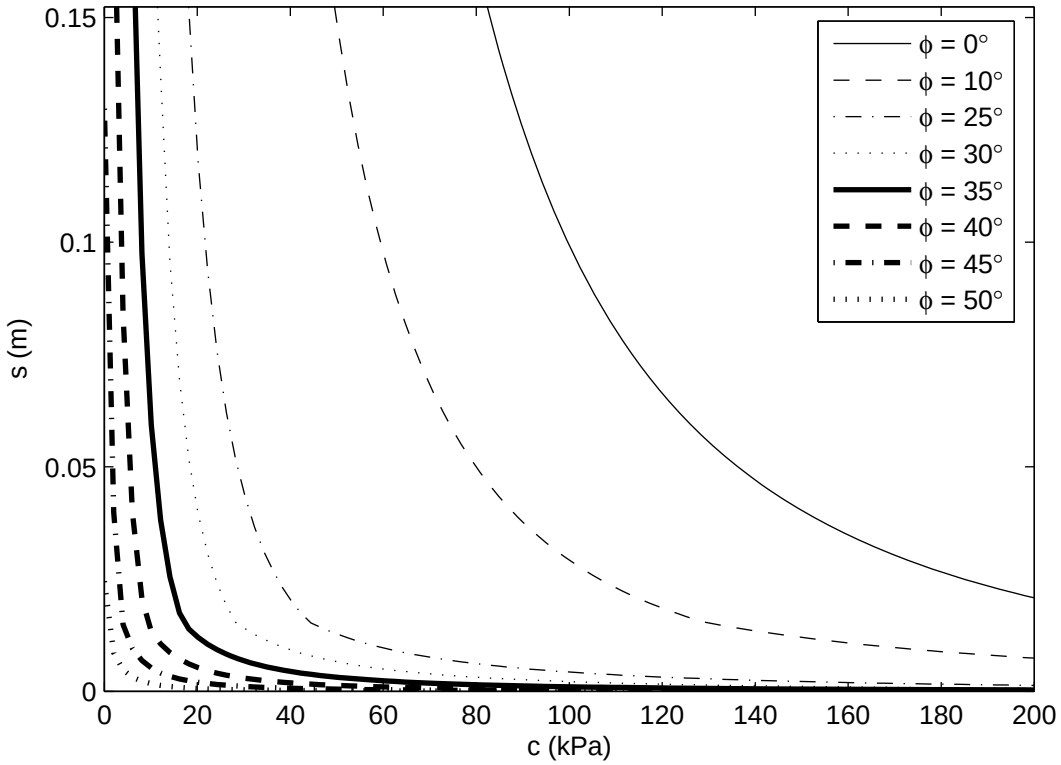

Figure H12. Analytic prediction for wheel indentation with Q_V = 65 kN, d = 1.524 m, b = 0.305 m, and γ = 14 kN/m^3

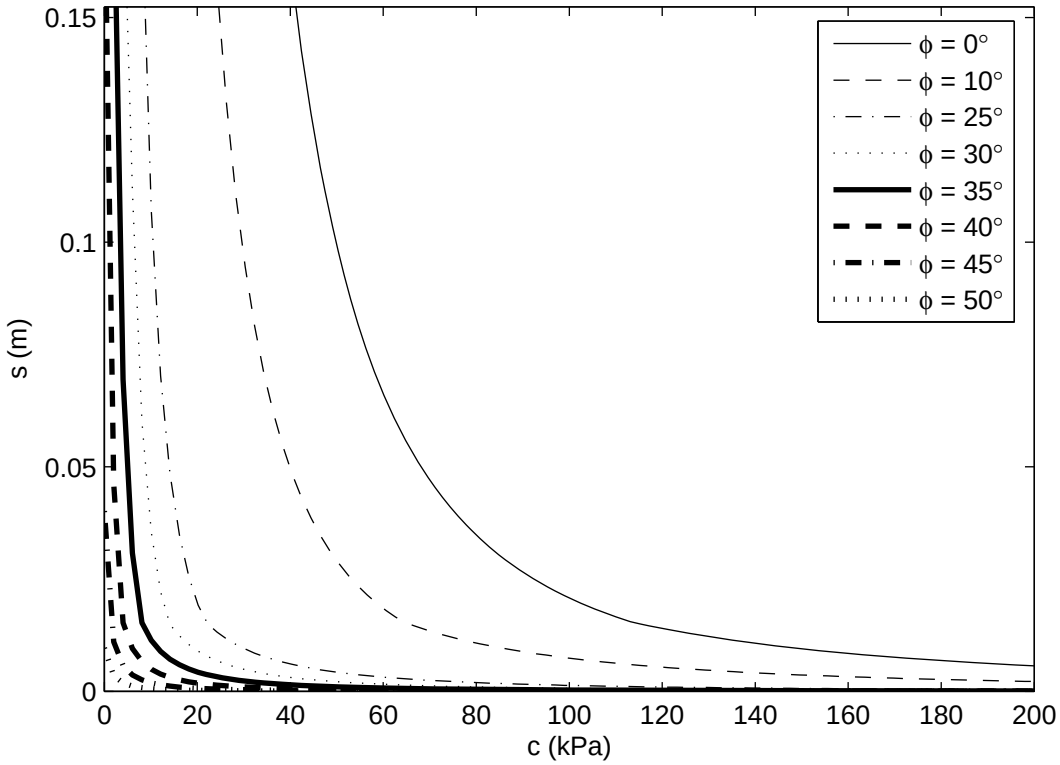

Figure H13. Analytic prediction for wheel indentation with Q_V = 130 kN, d = 1.219 m, b = 0.610 m, and γ = 20 kN/m^3

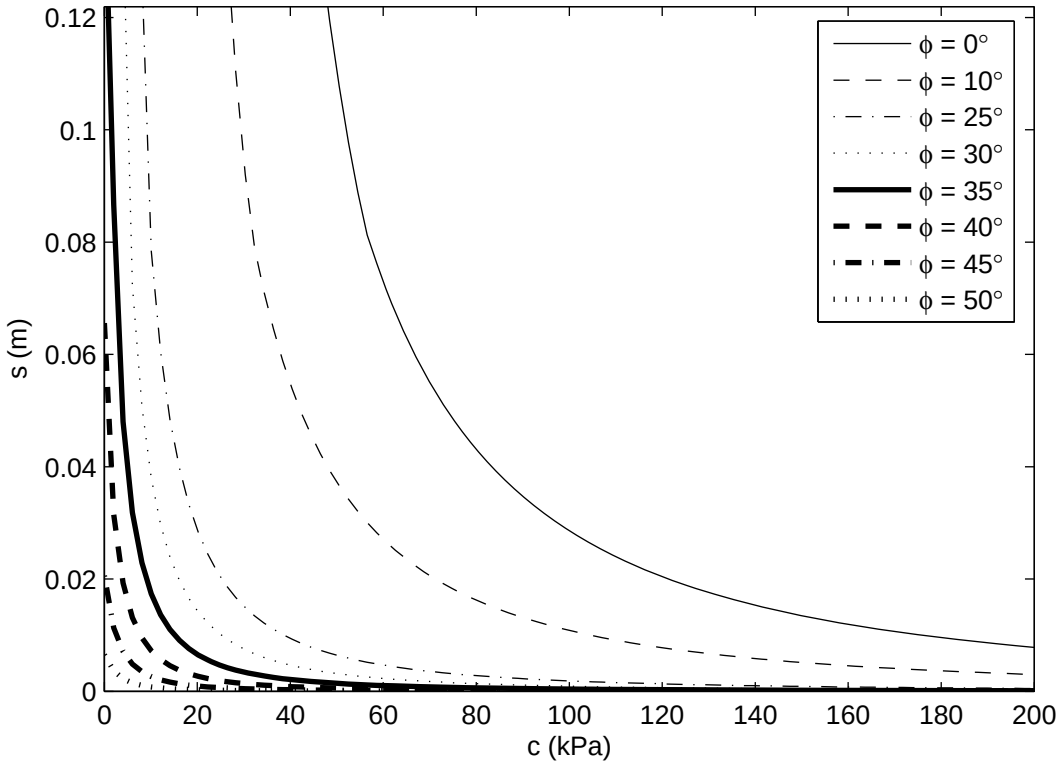

Figure H14. Analytic prediction for wheel indentation with Q_V = 65 kN, d = 1.219 m, b = 0.610 m, and γ = 20 kN/m^3

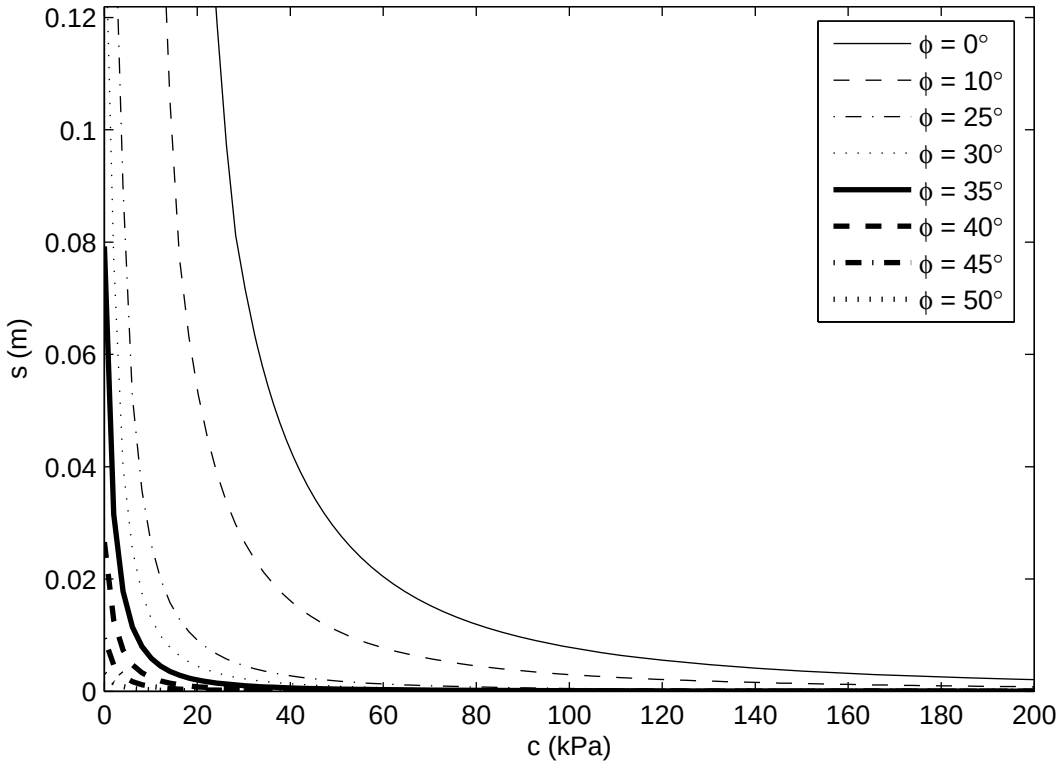

Figure H15. Analytic prediction for wheel indentation with Q_V = 130 kN, d = 1.219 m, b = 0.457 m, and γ = 20 kN/m^3

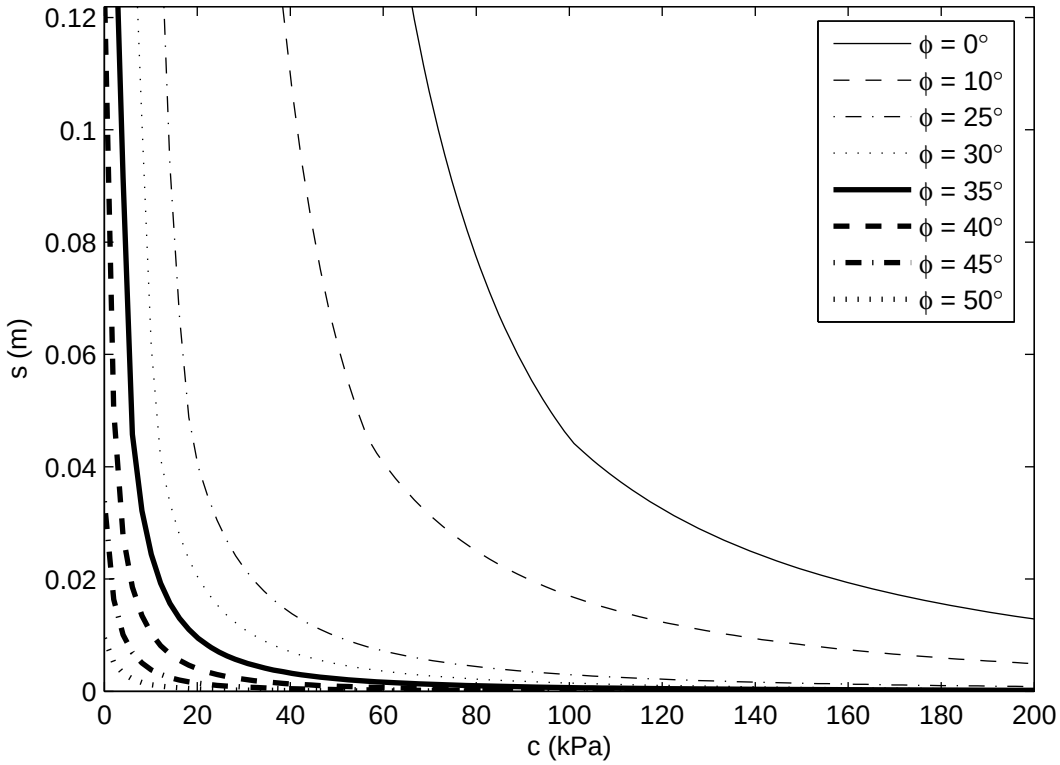

Figure H16. Analytic prediction for wheel indentation with Q_V = 65 kN, d = 1.219 m, b = 0.457 m, and γ = 20 kN/m^3

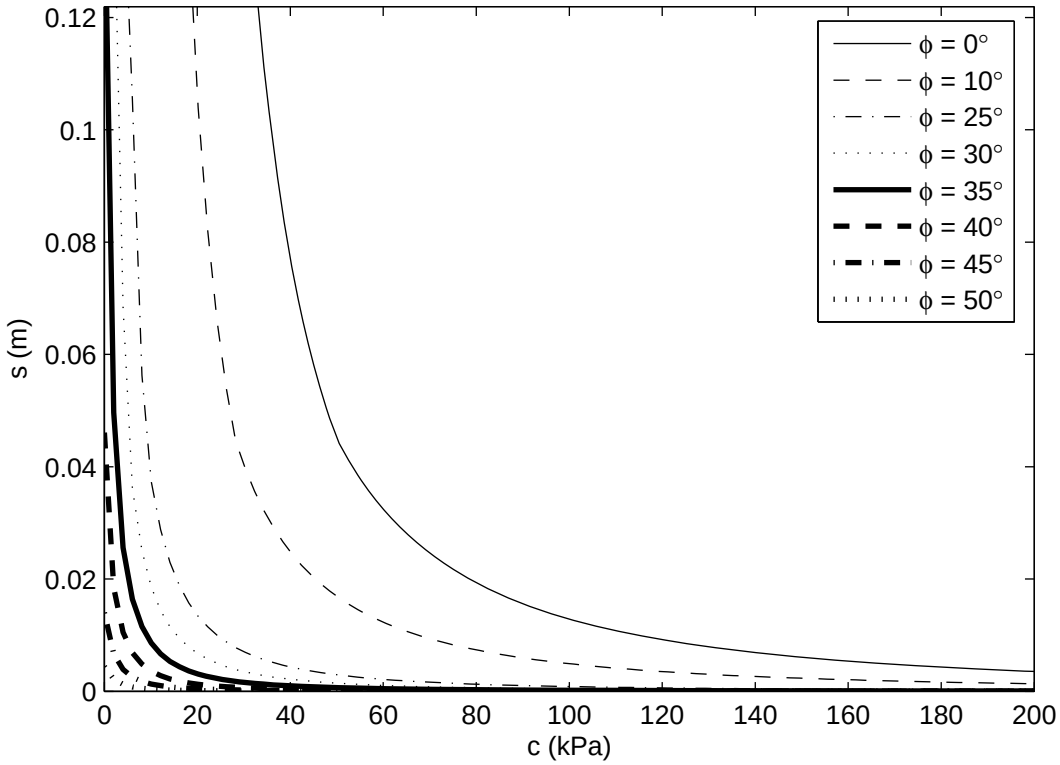

Figure H17. Analytic prediction for wheel indentation with Q_V = 130 kN, d = 1.219 m, b = 0.305 m, and γ = 20 kN/m^3

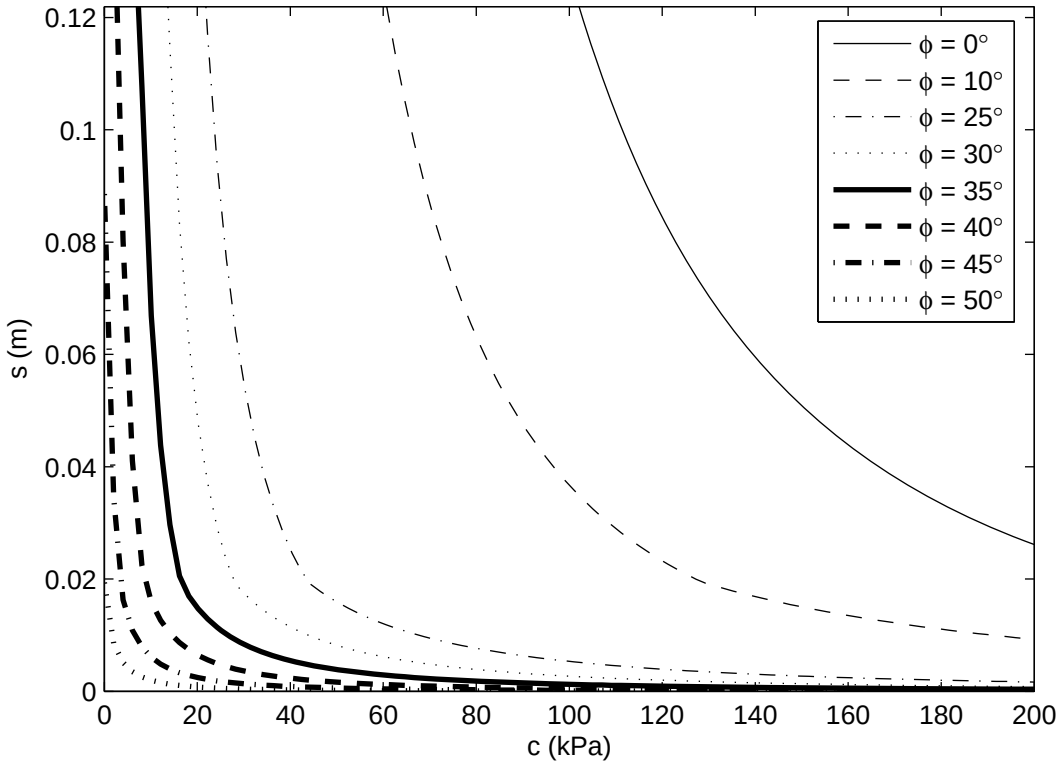

Figure H18. Analytic prediction for wheel indentation with Q_V = 65 kN, d = 1.219 m, b = 0.305 m, and γ = 20 kN/m^3

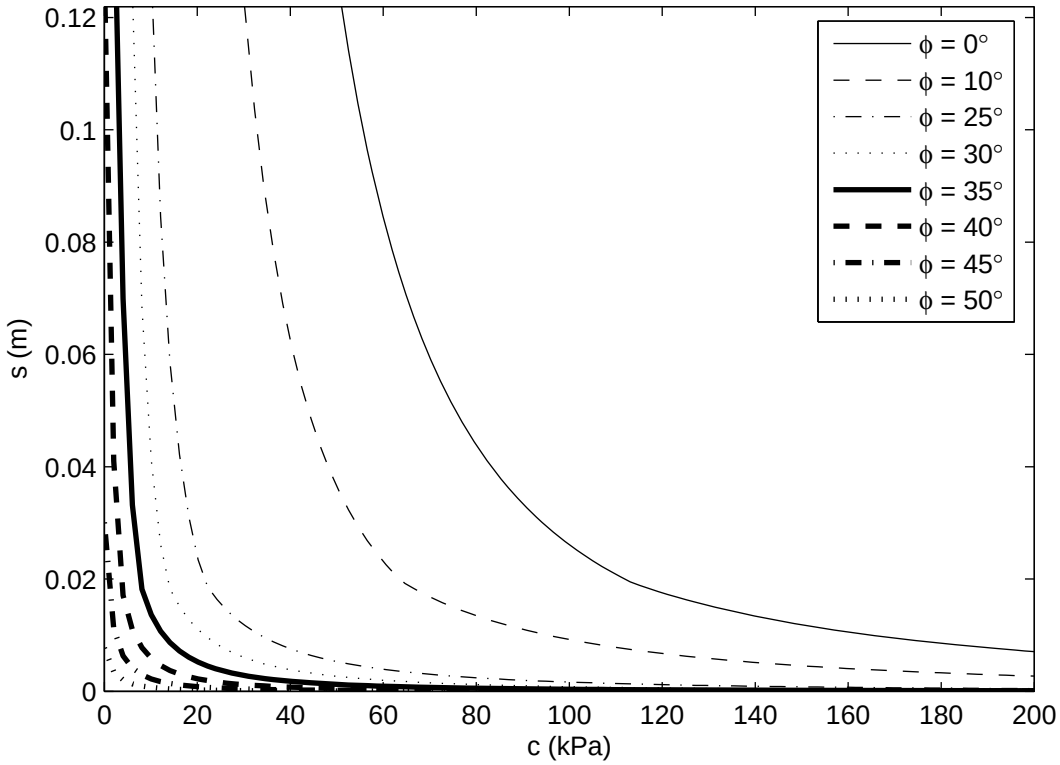

Figure H19. Analytic prediction for wheel indentation with Q_V = 130 kN, d = 1.219 m, b = 0.610 m, and γ = 14 kN/m^3

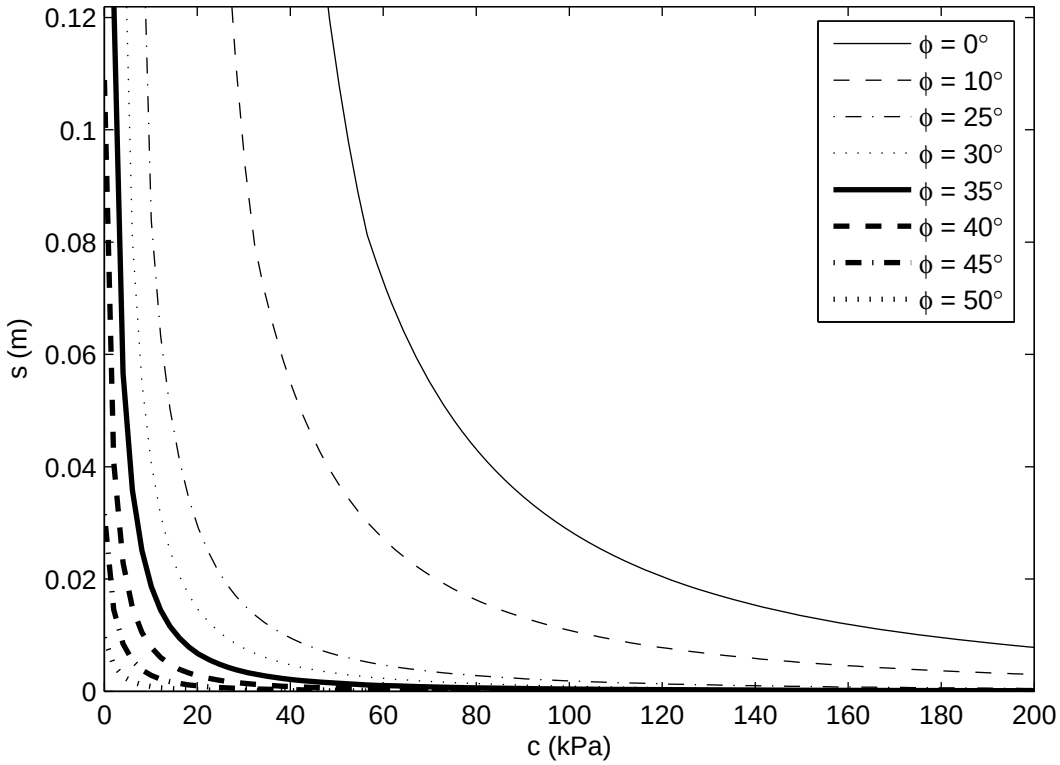

Figure H20. Analytic prediction for wheel indentation with Q_V = 65 kN, d = 1.219 m, b = 0.610 m, and γ = 14 kN/m^3

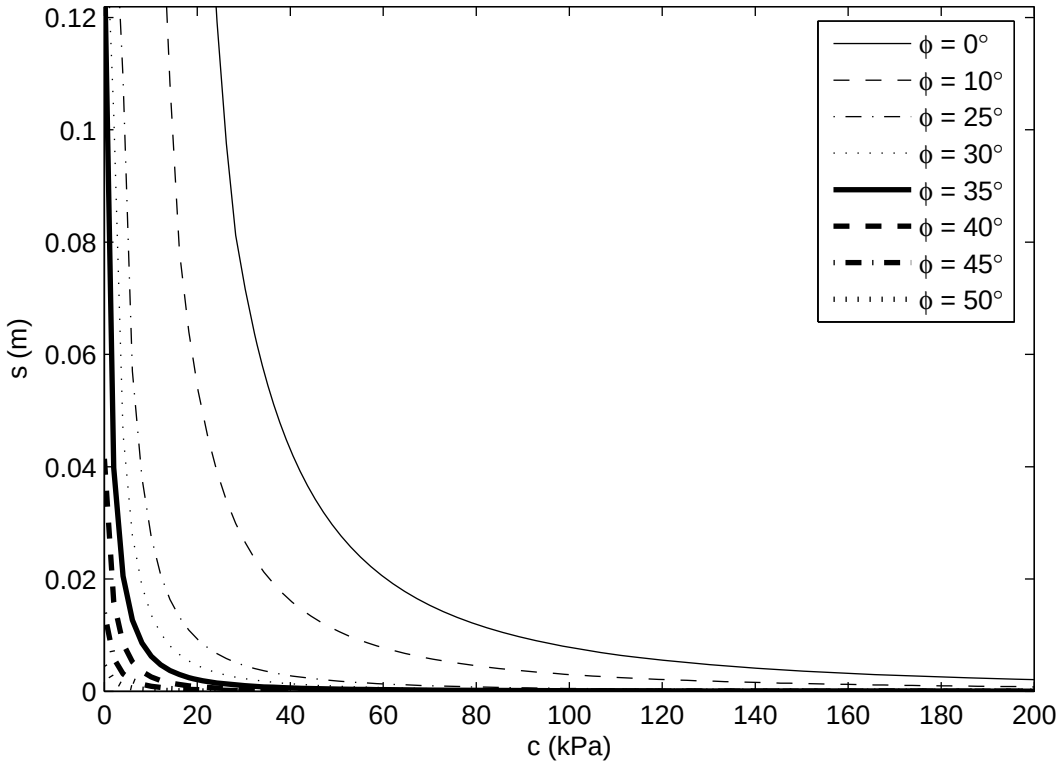

Figure H21. Analytic prediction for wheel indentation with Q_V = 130 kN, d = 1.219 m, b = 0.457 m, and γ = 14 kN/m^3

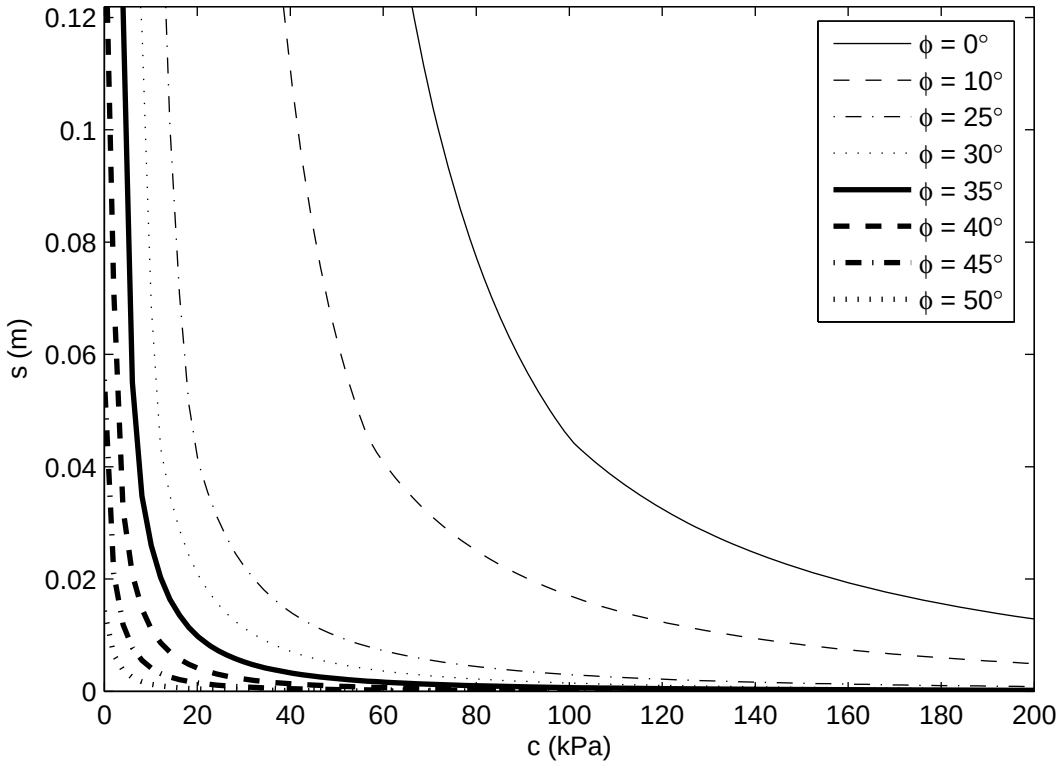

Figure H22. Analytic prediction for wheel indentation with Q_V = 65 kN, d = 1.219 m, b = 0.457 m, and γ = 14 kN/m^3

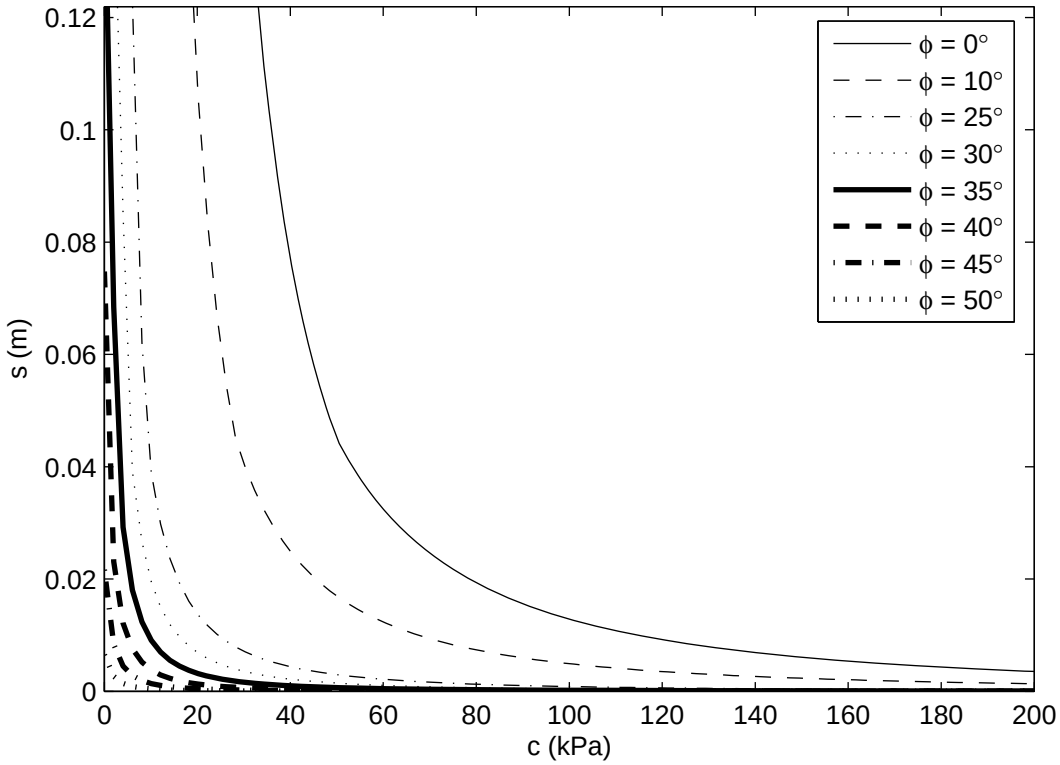

Figure H23. Analytic prediction for wheel indentation with Q_V = 130 kN, d = 1.219 m, b = 0.305 m, and γ = 14 kN/m^3

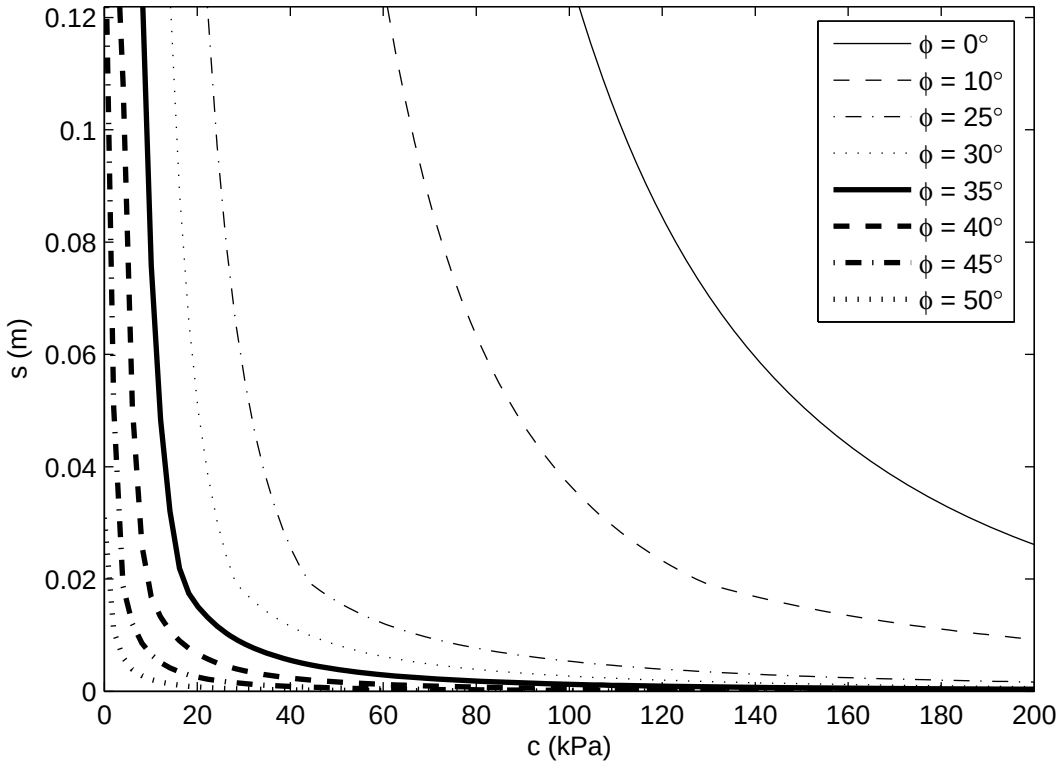

Figure H24. Analytic prediction for wheel indentation with Q_V = 65 kN, d = 1.219 m, b = 0.305 m, and γ = 14 kN/m^3

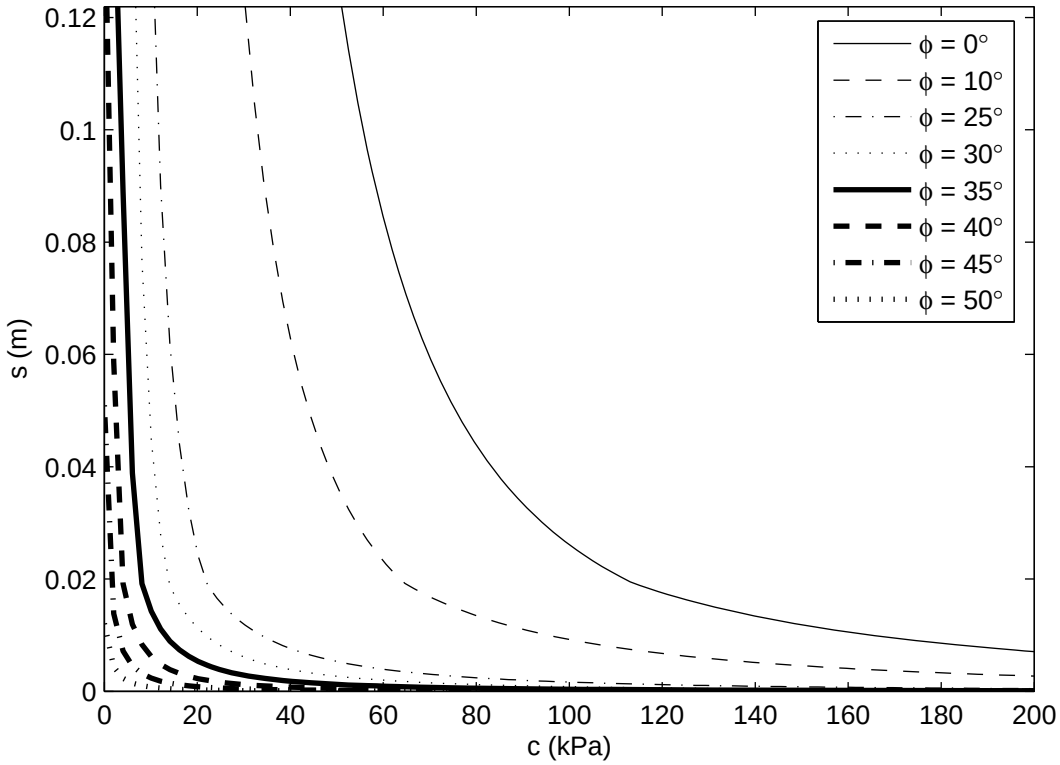

Figure H25. Analytic prediction for wheel indentation with Q_V = 130 kN, d = 0.914 m, b = 0.610 m, and γ = 20 kN/m^3

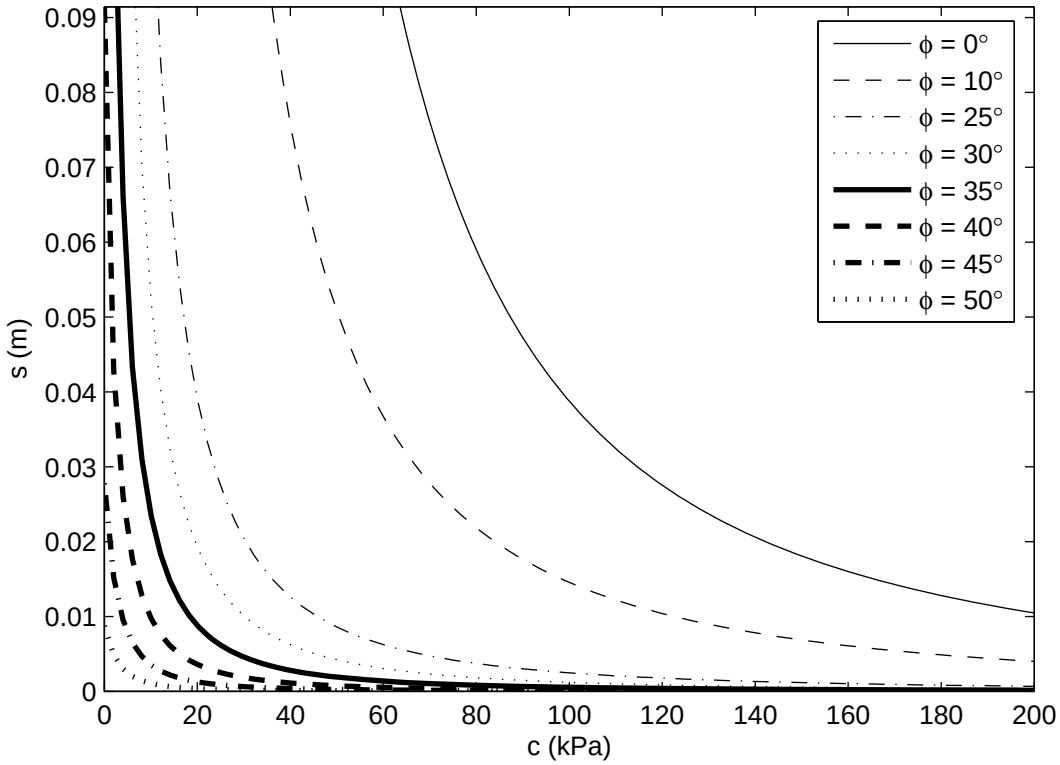

Figure H26. Analytic prediction for wheel indentation with Q_V = 65 kN, d = 0.914 m, b = 0.610 m, and γ = 20 kN/m^3

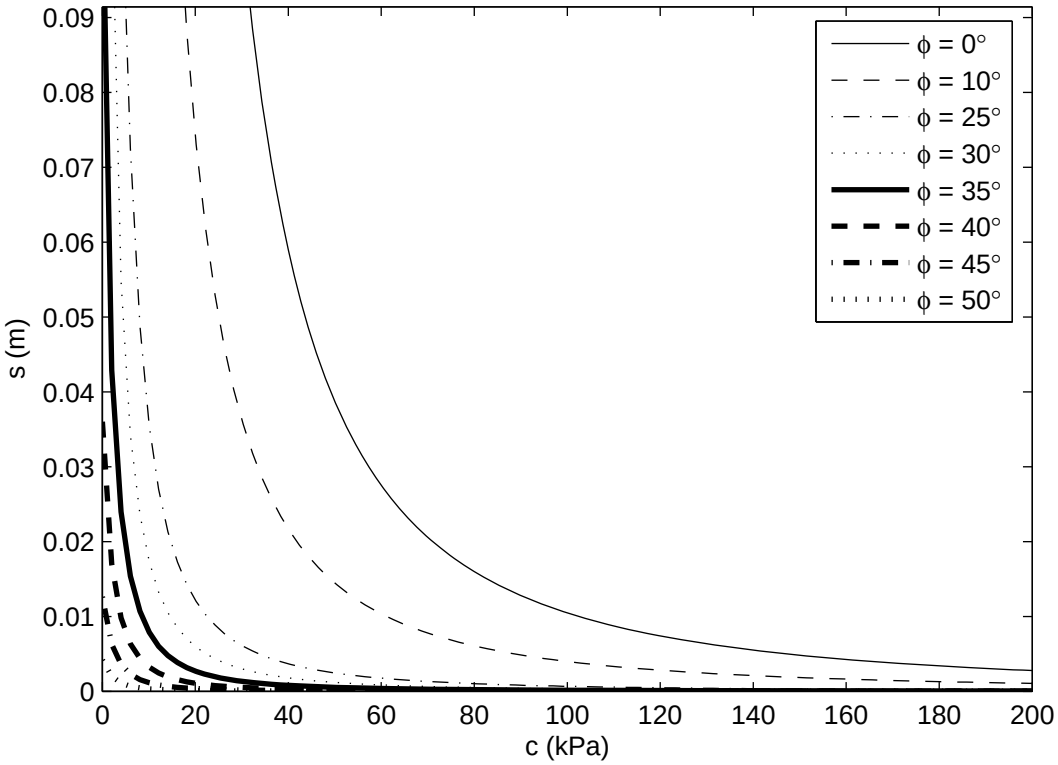

Figure H27. Analytic prediction for wheel indentation with Q_V = 130 kN, d = 0.914 m, b = 0.457 m, and γ = 20 kN/m^3

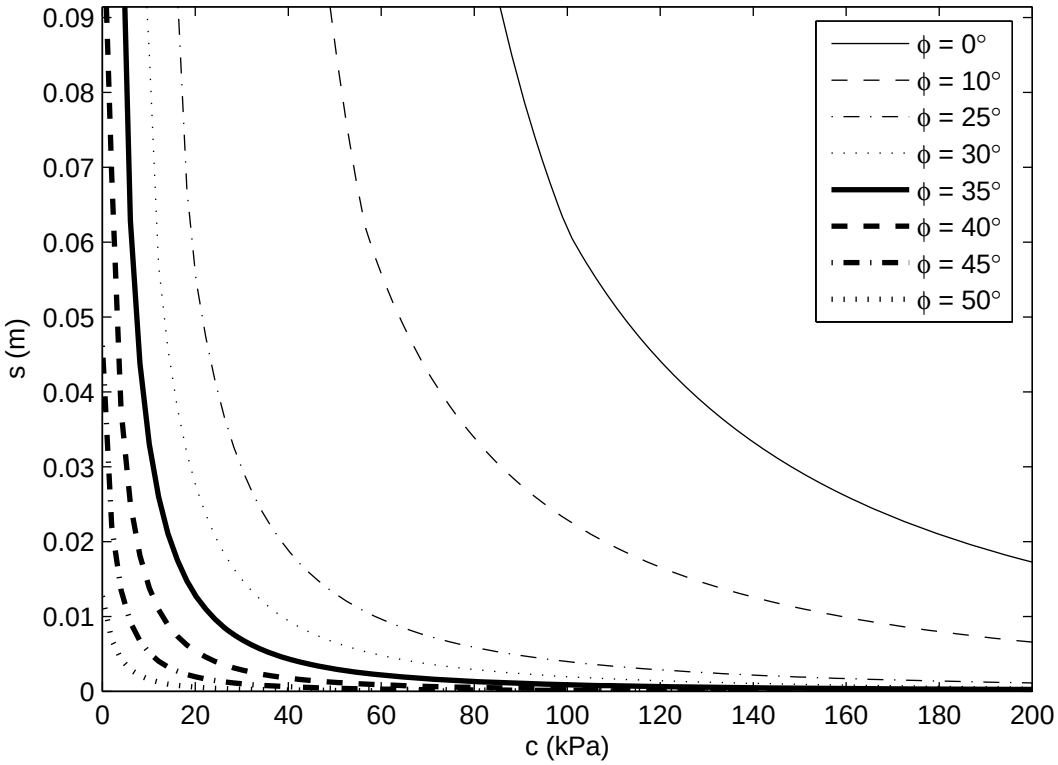

Figure H28. Analytic prediction for wheel indentation with Q_V = 65 kN, d = 0.914 m, b = 0.457 m, and γ = 20 kN/m^3

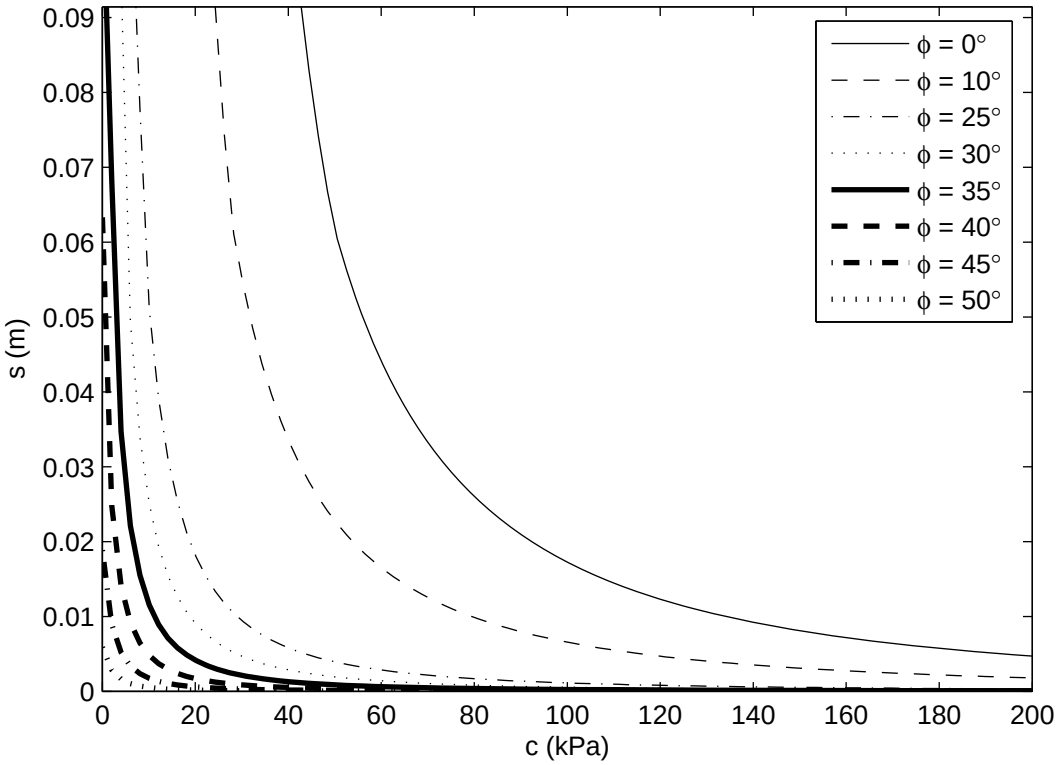

Figure H29. Analytic prediction for wheel indentation with Q_V = 130 kN, d = 0.914 m, b = 0.305 m, and γ = 20 kN/m^3

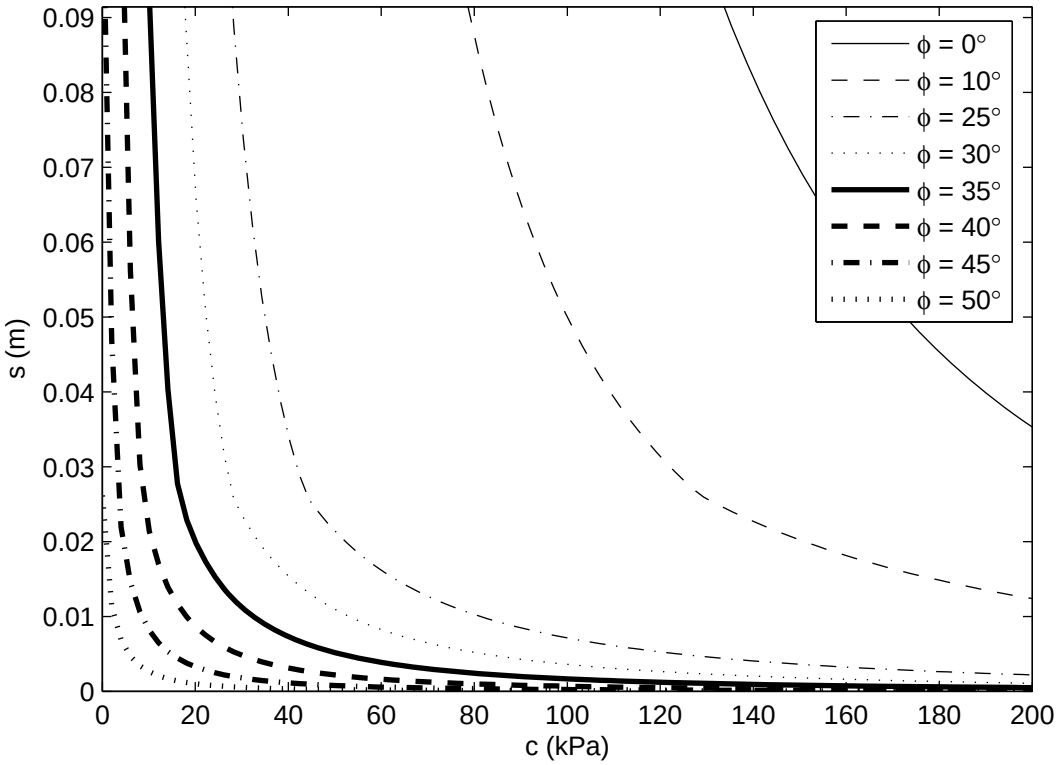

Figure H30. Analytic prediction for wheel indentation with Q_V = 65 kN, d = 0.914 m, b = 0.305 m, and γ = 20 kN/m^3

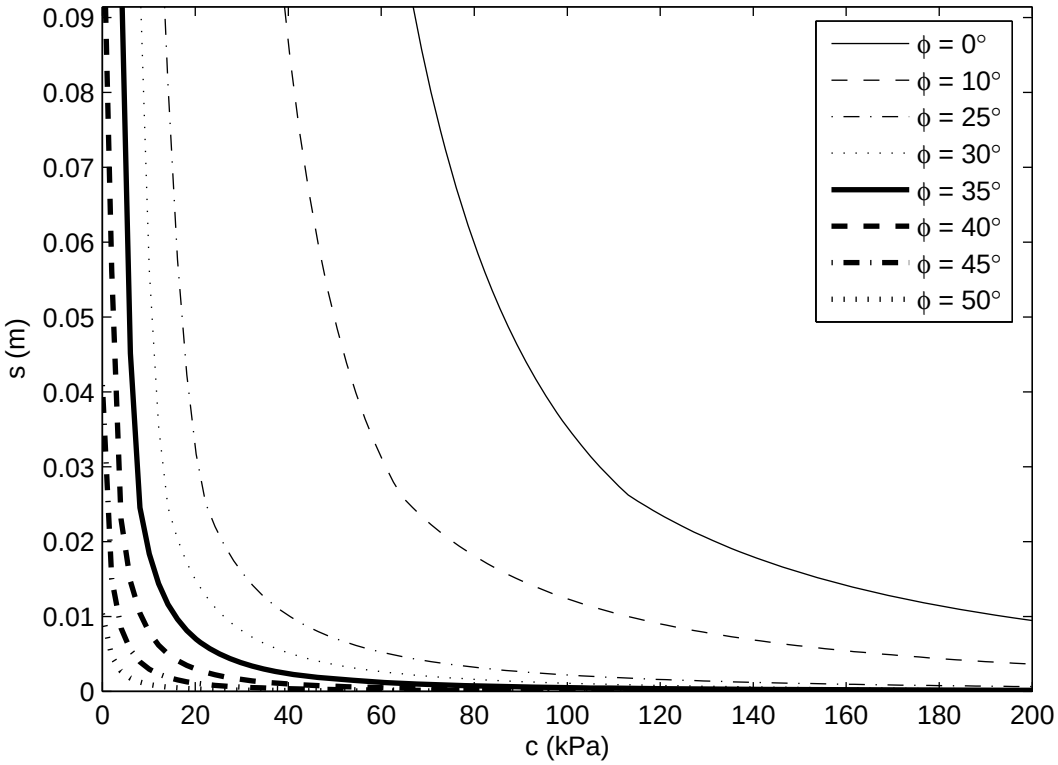

Figure H31. Analytic prediction for wheel indentation with Q_V = 130 kN, d = 0.914 m, b = 0.610 m, and γ = 14 kN/m^3

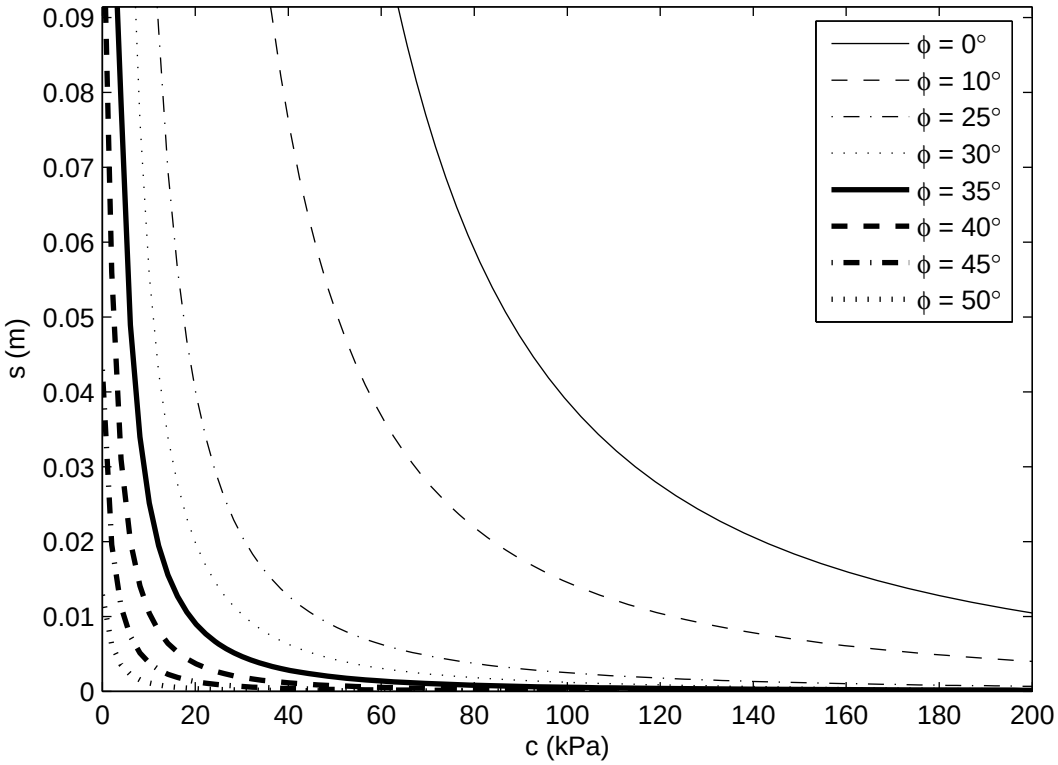

Figure H32. Analytic prediction for wheel indentation with Q_V = 65 kN, d = 0.914 m, b = 0.610 m, and γ = 14 kN/m^3

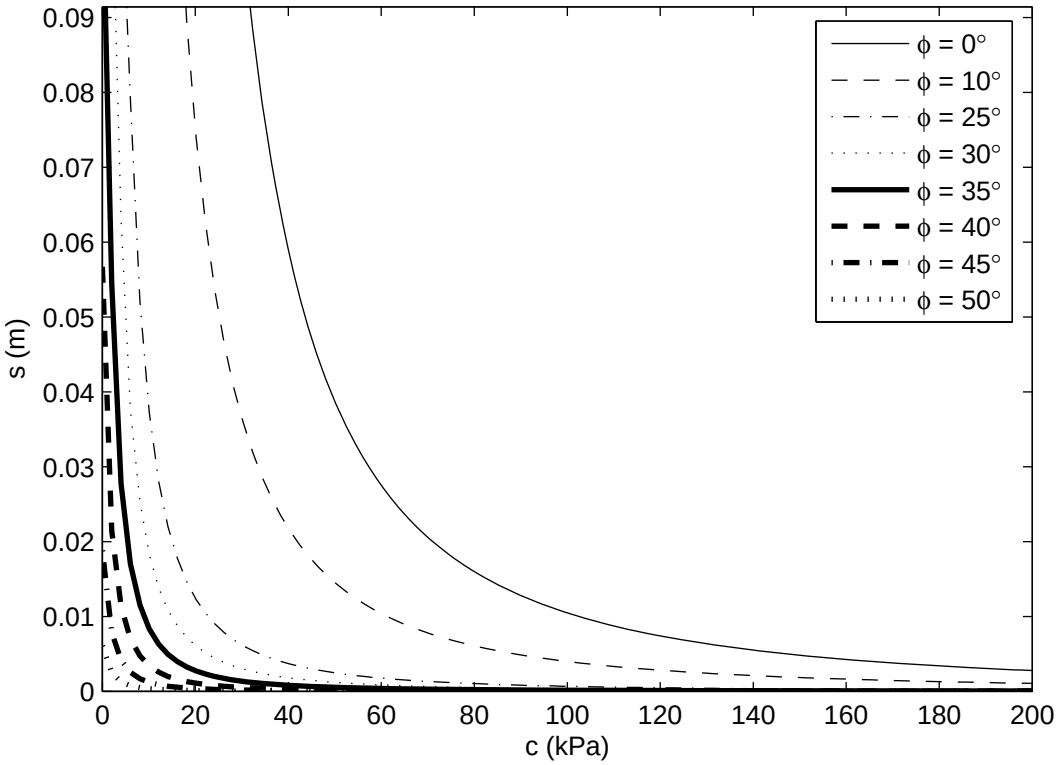

Figure H33. Analytic prediction for wheel indentation with Q_V = 130 kN, d = 0.914 m, b = 0.457 m, and γ = 14 kN/m^3

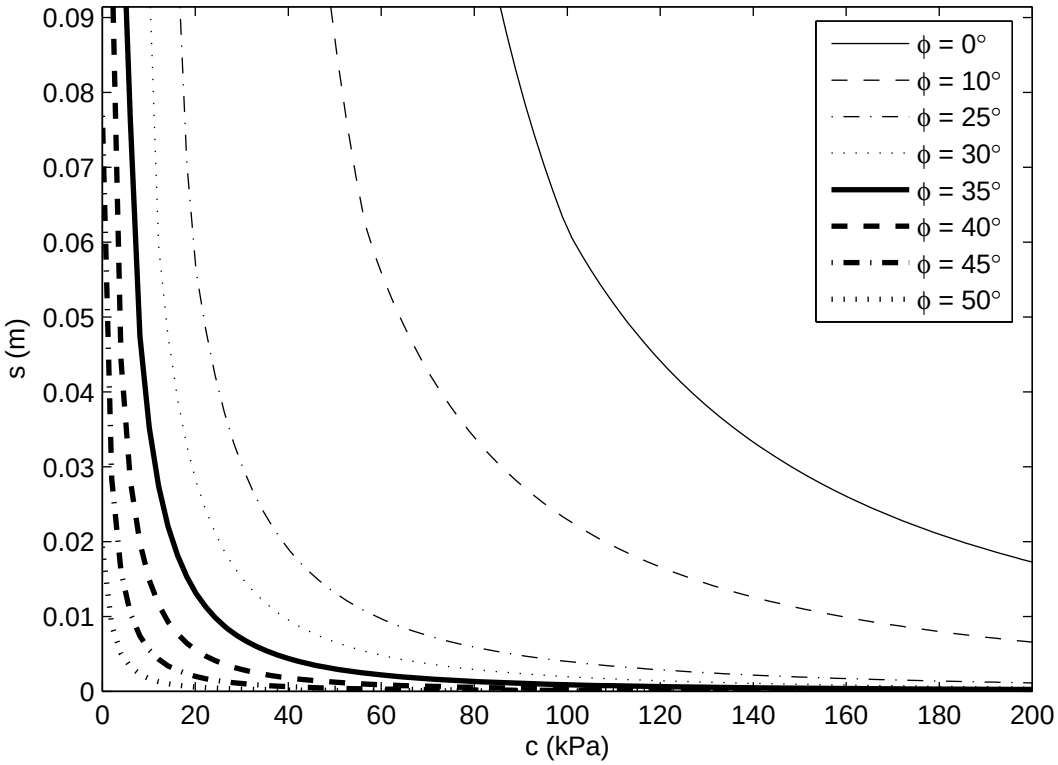

Figure H34. Analytic prediction for wheel indentation with Q_V = 65 kN, d = 0.914 m, b = 0.457 m, and γ = 14 kN/m^3

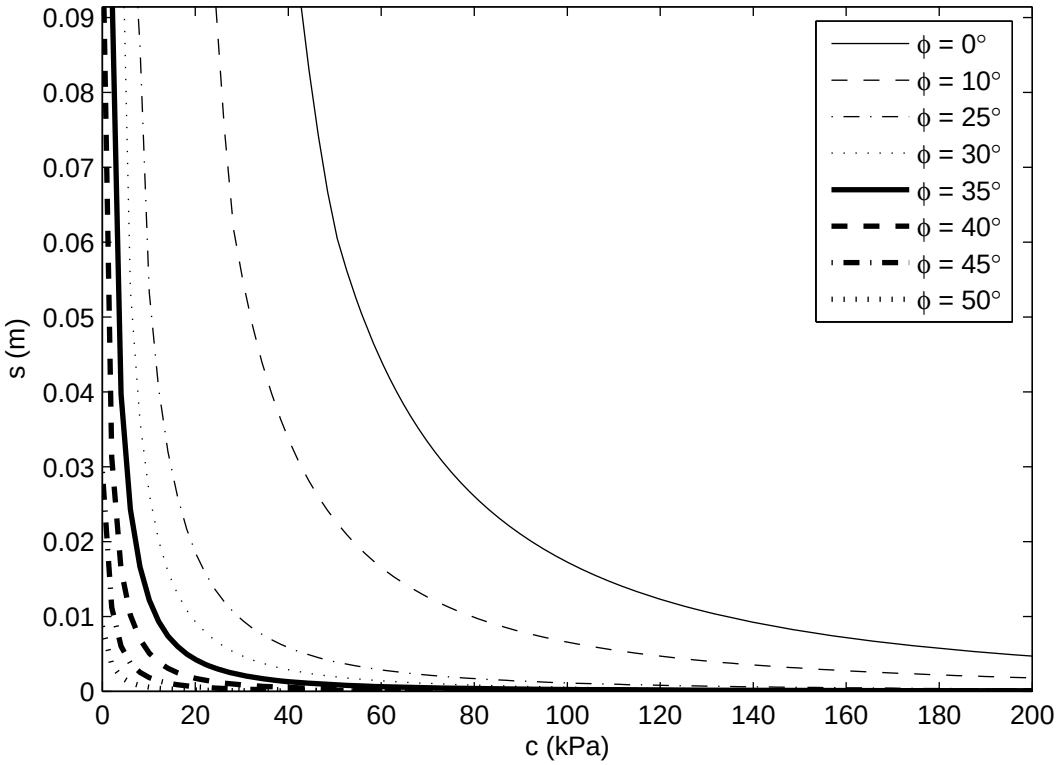

Figure H35. Analytic prediction for wheel indentation with Q_V = 130 kN, d = 0.914 m, b = 0.305 m, and γ = 14 kN/m^3

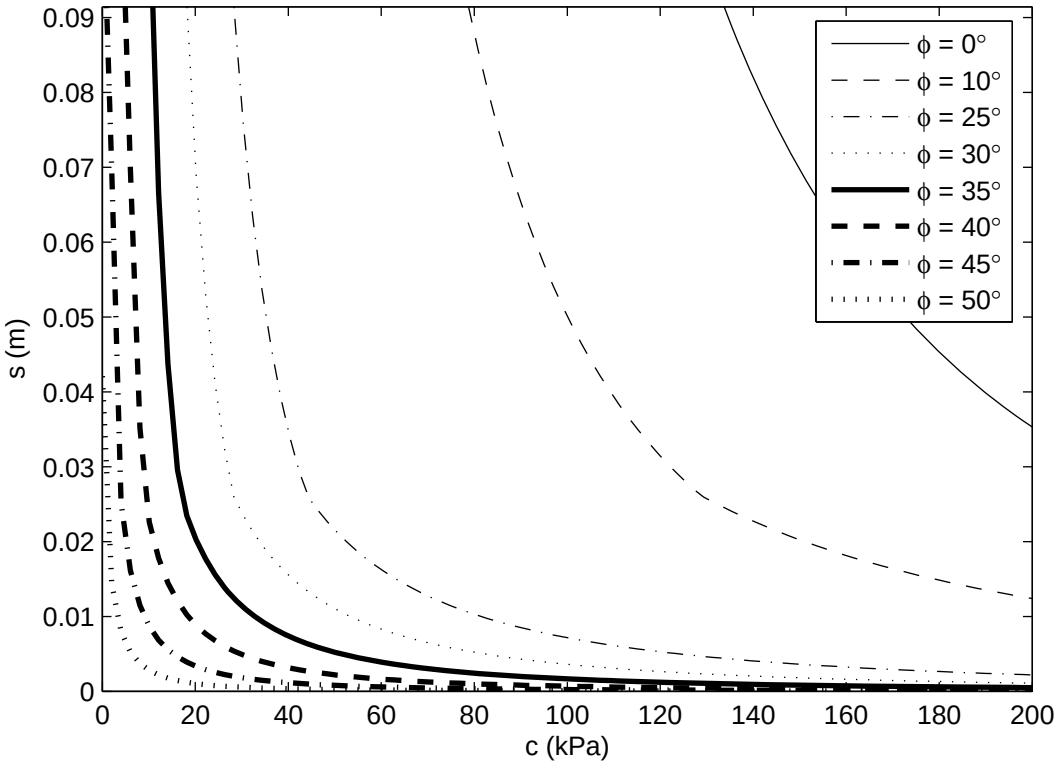

Figure H36. Analytic prediction for wheel indentation with Q_V = 65 kN, d = 0.914 m, b = 0.305 m, and γ = 14 kN/m^3

Appendix I: Dimensional Plots Using Analytic Method for Steady-State Rolling

Table I1. Summary of parameters used in dimensional plots for steady-state rolling

Figure No.	Q_V **(kN)**	d **(m)**	b **(m)**	γ **(kN/m^3)**
I1	130	1.524	0.6096	20
I2	65	1.524	0.6096	20
I3	130	1.524	0.4572	20
I4	65	1.524	0.4572	20
I5	130	1.524	0.3048	20
I6	65	1.524	0.3048	20
I7	130	1.524	0.6096	14
I8	65	1.524	0.6096	14
I9	130	1.524	0.4572	14
I10	65	1.524	0.4572	14
I11	130	1.524	0.3048	14
I12	65	1.524	0.3048	14
I13	130	1.2192	0.6096	20
I14	65	1.2192	0.6096	20
I15	130	1.2192	0.4572	20
I16	65	1.2192	0.4572	20
I17	130	1.2192	0.3048	20
I18	65	1.2192	0.3048	20
I19	130	1.2192	0.6096	14
I20	65	1.2192	0.6096	14
I21	130	1.2192	0.4572	14
I22	65	1.2192	0.4572	14
I23	130	1.2192	0.3048	14
I24	65	1.2192	0.3048	14
I25	130	0.9144	0.6096	20
I26	65	0.9144	0.6096	20
I27	130	0.9144	0.4572	20
I28	65	0.9144	0.4572	20
I29	130	0.9144	0.3048	20
I30	65	0.9144	0.3048	20
I31	130	0.9144	0.6096	14
I32	65	0.9144	0.6096	14
I33	130	0.9144	0.4572	14
I34	65	0.9144	0.4572	14
I35	130	0.9144	0.3048	14
I36	65	0.9144	0.3048	14

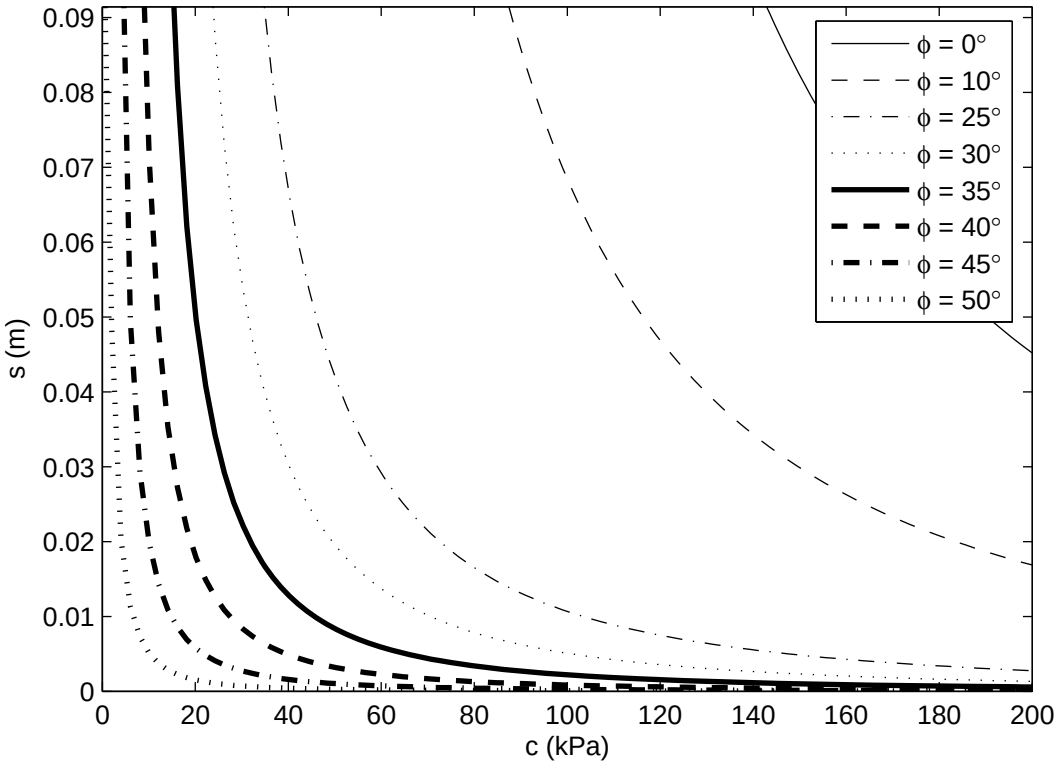

Figure I1. Analytic prediction for wheel rolling with Q_V = 130 kN, d = 1.524 m, b = 0.610 m, and γ = 20 kN/m^3

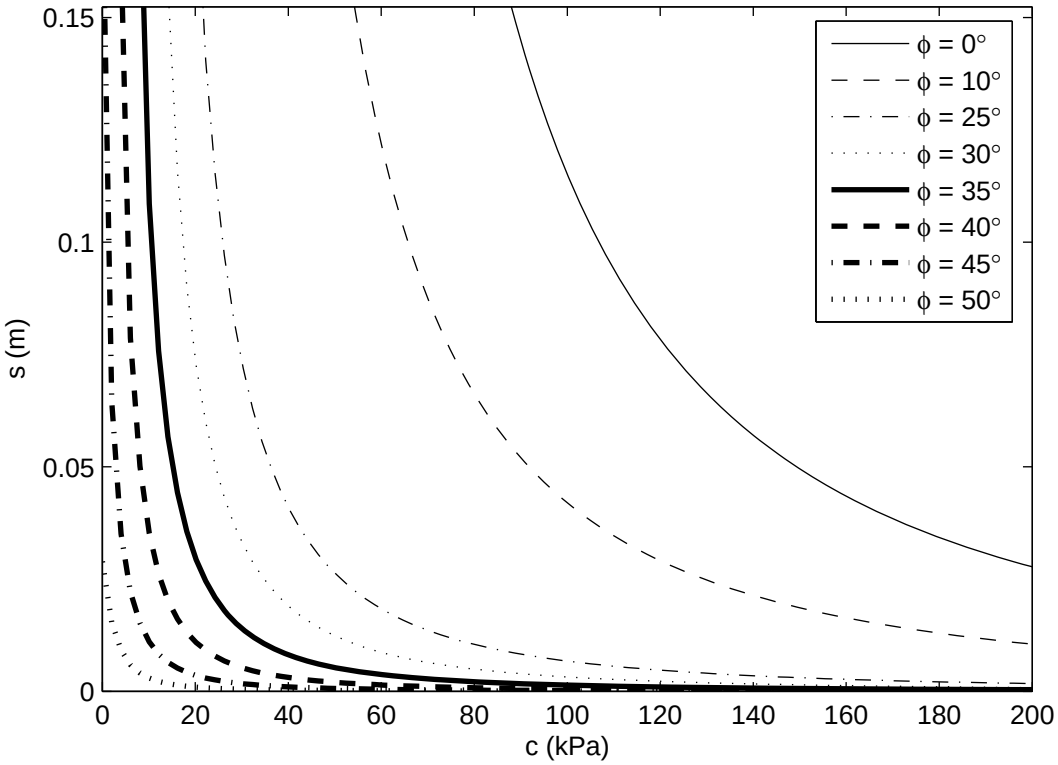

Figure I2. Analytic prediction for wheel rolling with Q_V = 65 kN, d = 1.524 m, b = 0.610 m, and γ = 20 kN/m^3

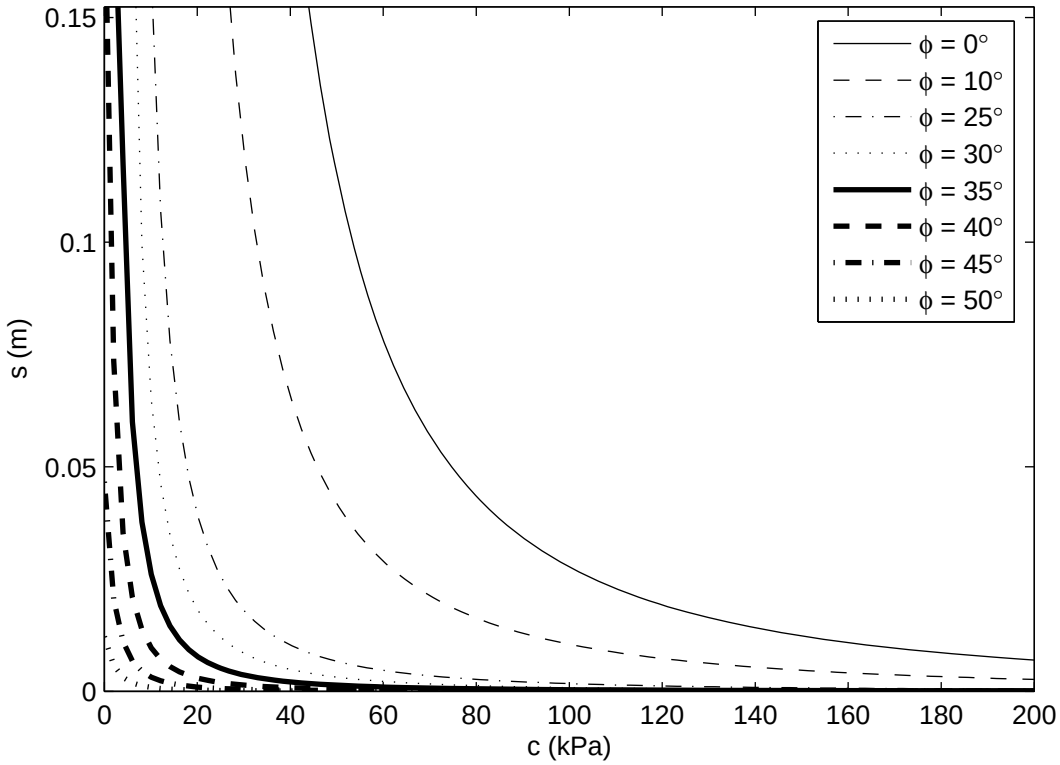

Figure I3. Analytic prediction for wheel rolling with Q_V = 130 kN, d = 1.524 m, b = 0.457 m, and γ = 20 kN/m^3

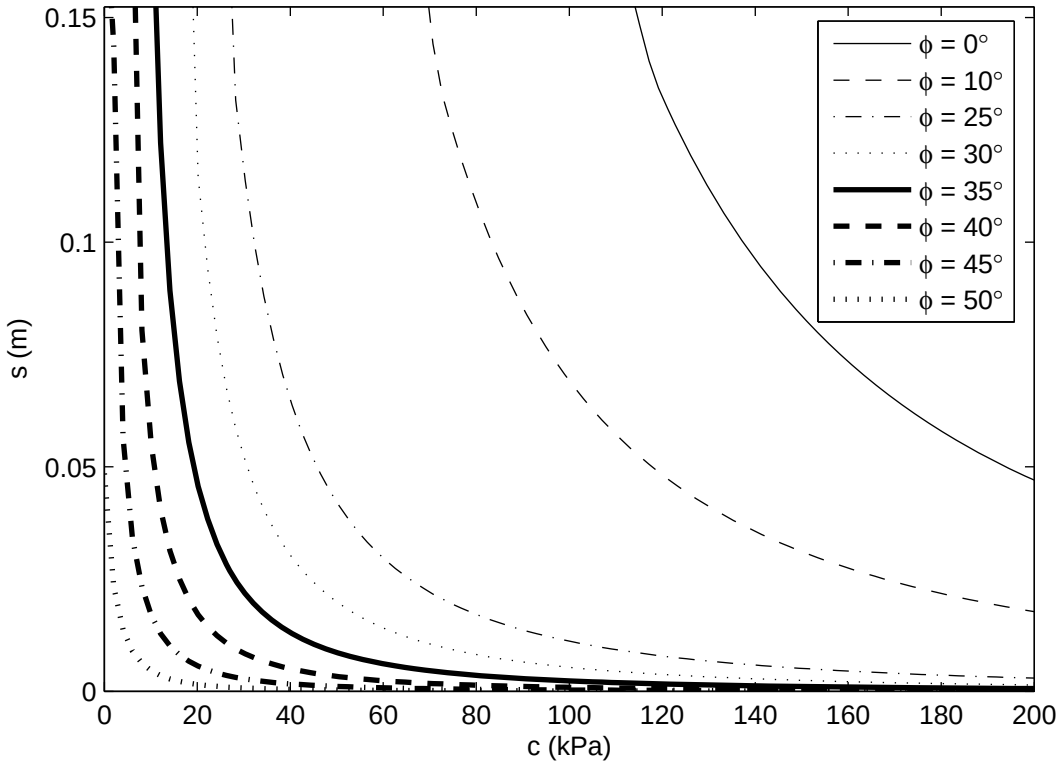

Figure I4. Analytic prediction for wheel rolling with Q_V = 65 kN, d = 1.524 m, b = 0.457 m, and γ = 20 kN/m^3

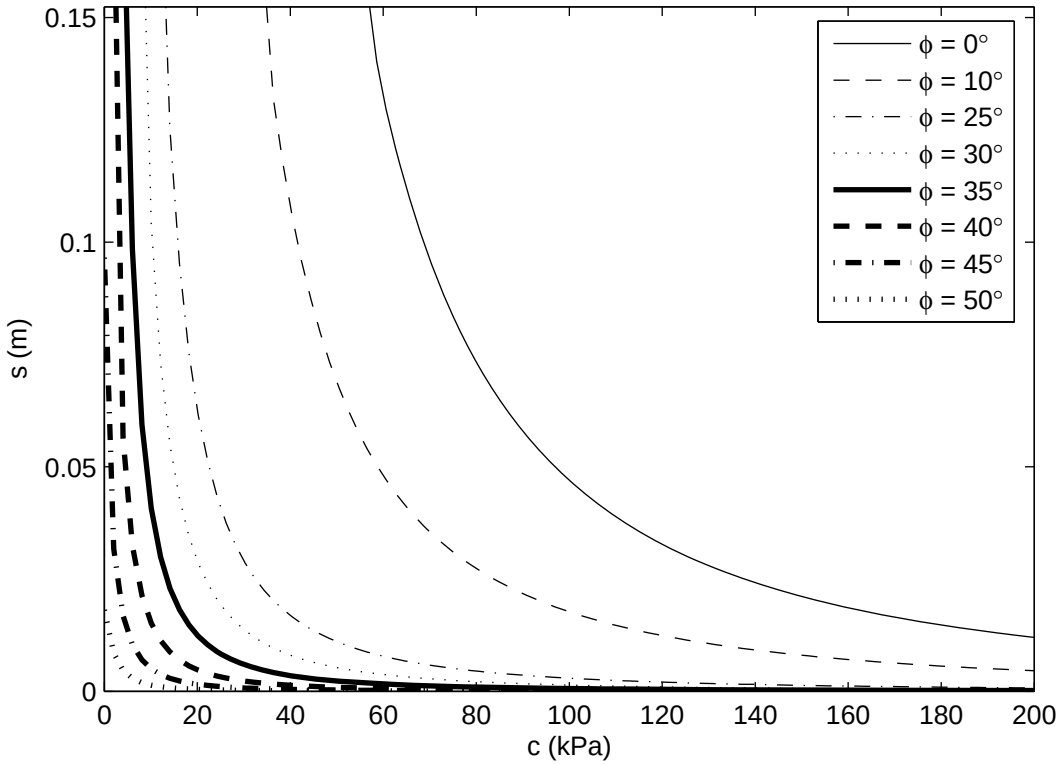

Figure I5. Analytic prediction for wheel rolling with Q_V = 130 kN, d = 1.524 m, b = 0.305 m, and γ = 20 kN/m^3

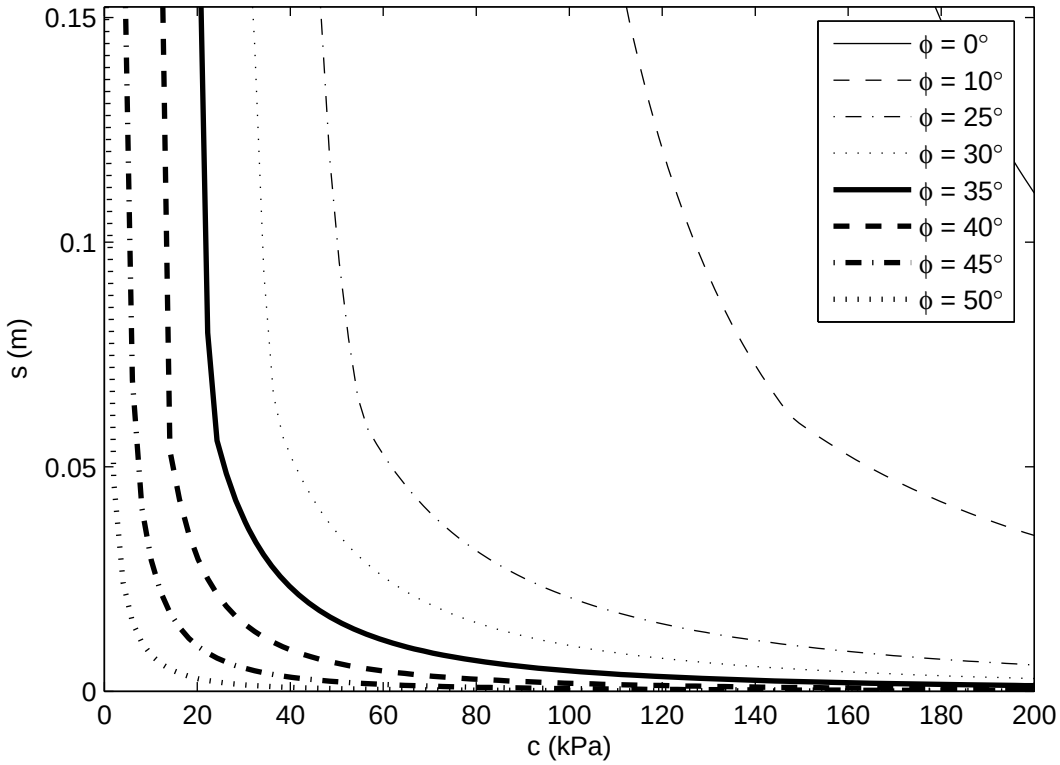

Figure I6. Analytic prediction for wheel rolling with Q_V = 65 kN, d = 1.524 m, b = 0.305 m, and γ = 20 kN/m^3

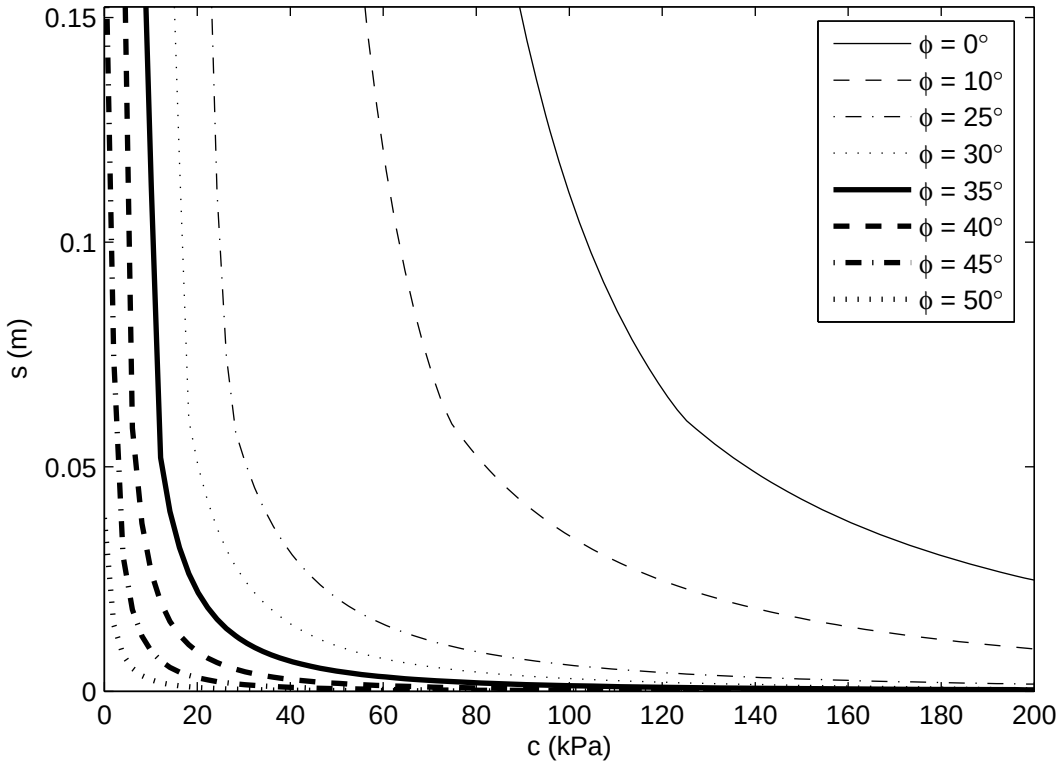

Figure I7. Analytic prediction for wheel rolling with Q_V = 130 kN, d = 1.524 m, b = 0.610 m, and γ = 14 kN/m^3

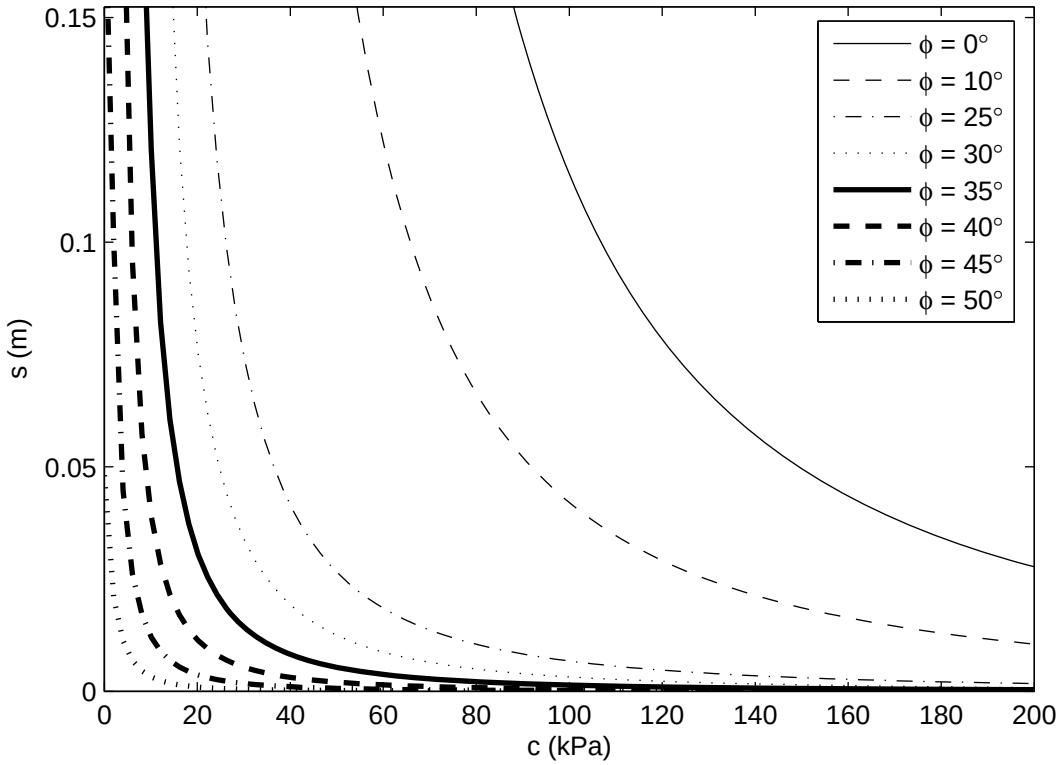

Figure I8. Analytic prediction for wheel rolling with Q_V = 65 kN, d = 1.524 m, b = 0.610 m, and γ = 14 kN/m^3

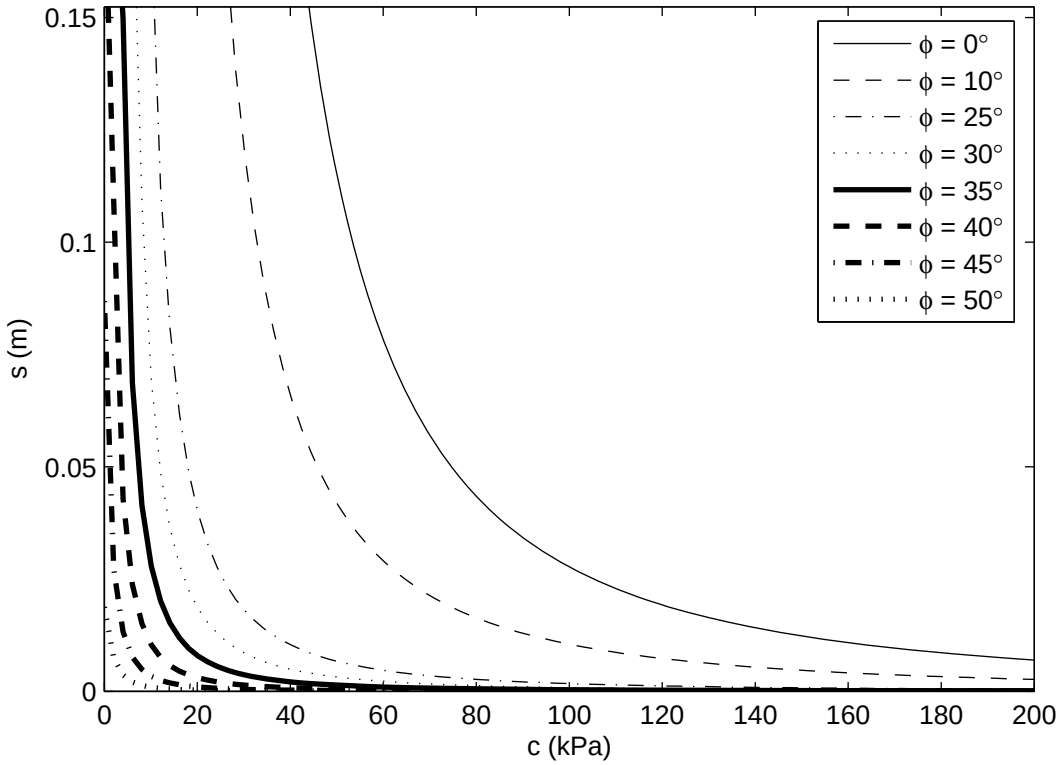

Figure I9. Analytic prediction for wheel rolling with Q_V = 130 kN, d = 1.524 m, b = 0.457 m, and γ = 14 kN/m^3

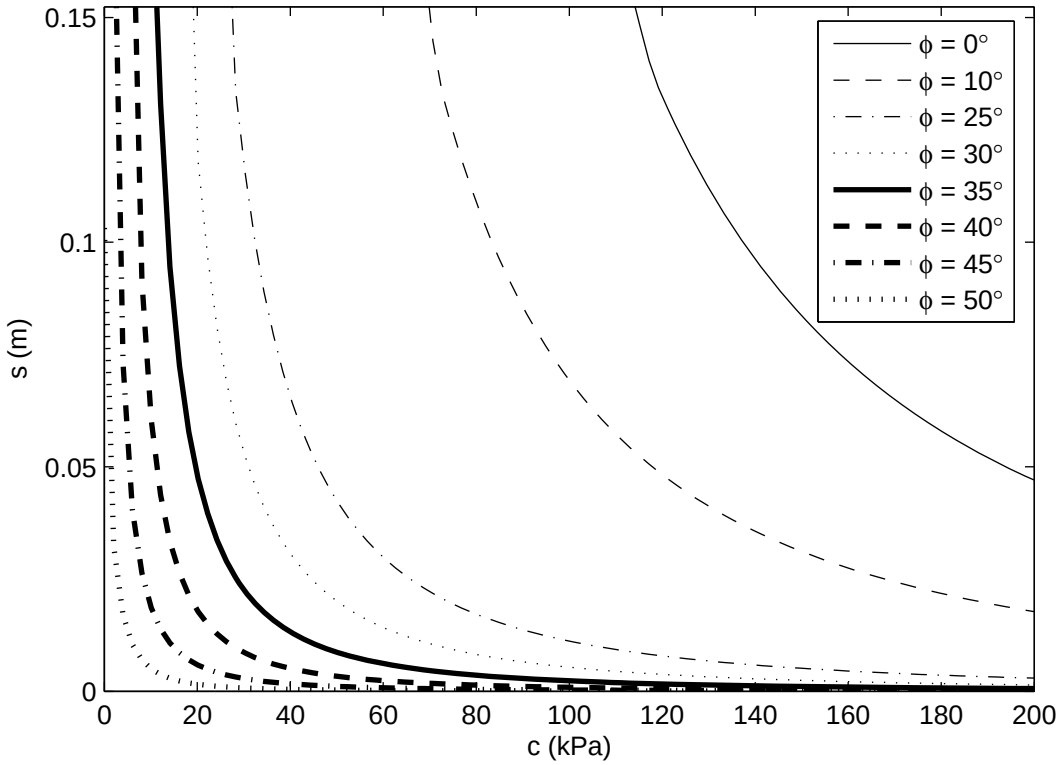

Figure I10. Analytic prediction for wheel rolling with Q_V = 65 kN, d = 1.524 m, b = 0.457 m, and γ = 14 kN/m^3

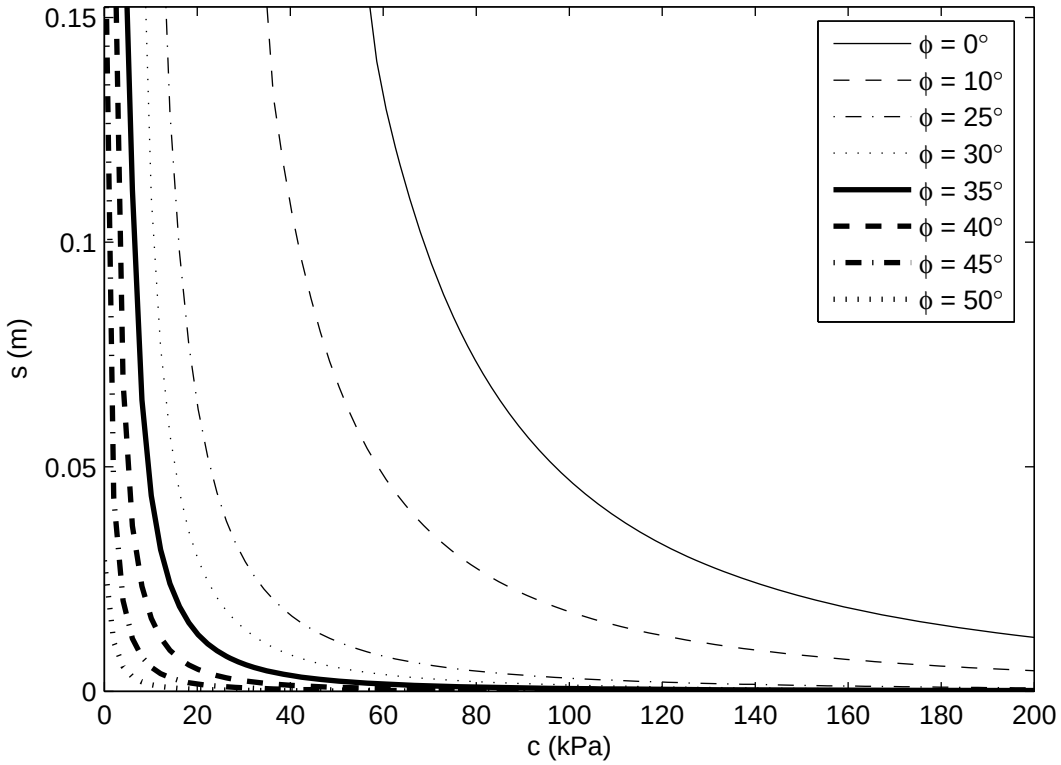

Figure I11. Analytic prediction for wheel rolling with Q_V = 130 kN, d = 1.524 m, b = 0.305 m, and γ = 14 kN/m^3

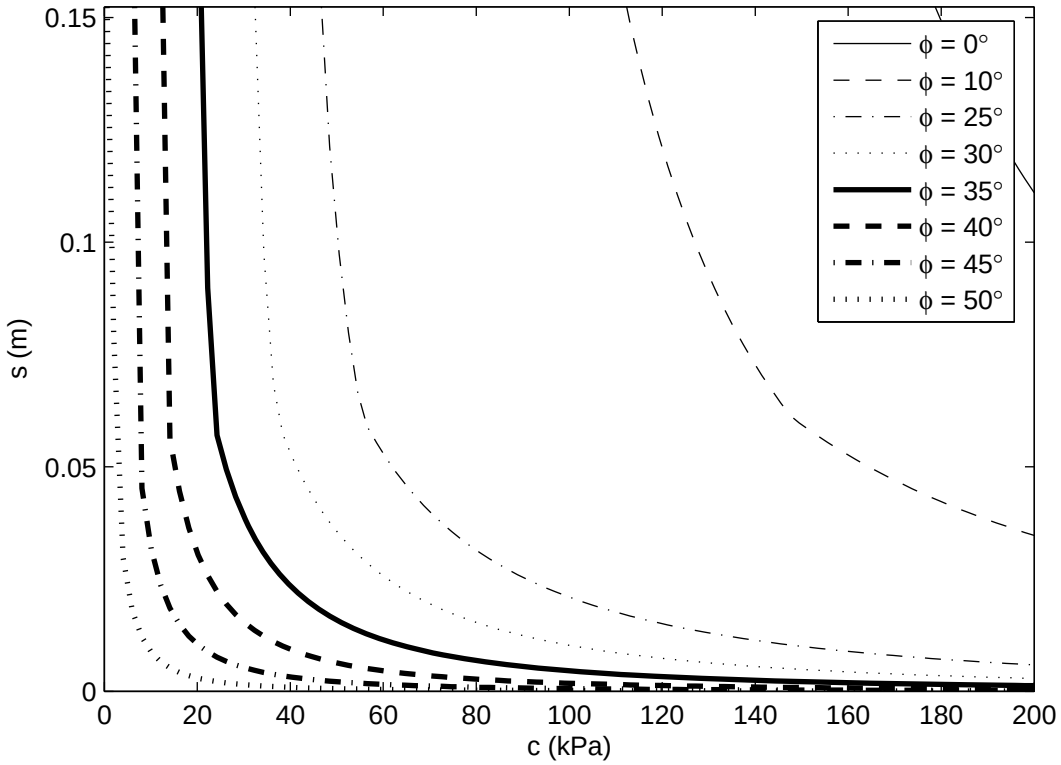

Figure I12. Analytic prediction for wheel rolling with Q_V = 65 kN, d = 1.524 m, b = 0.305 m, and γ = 14 kN/m^3

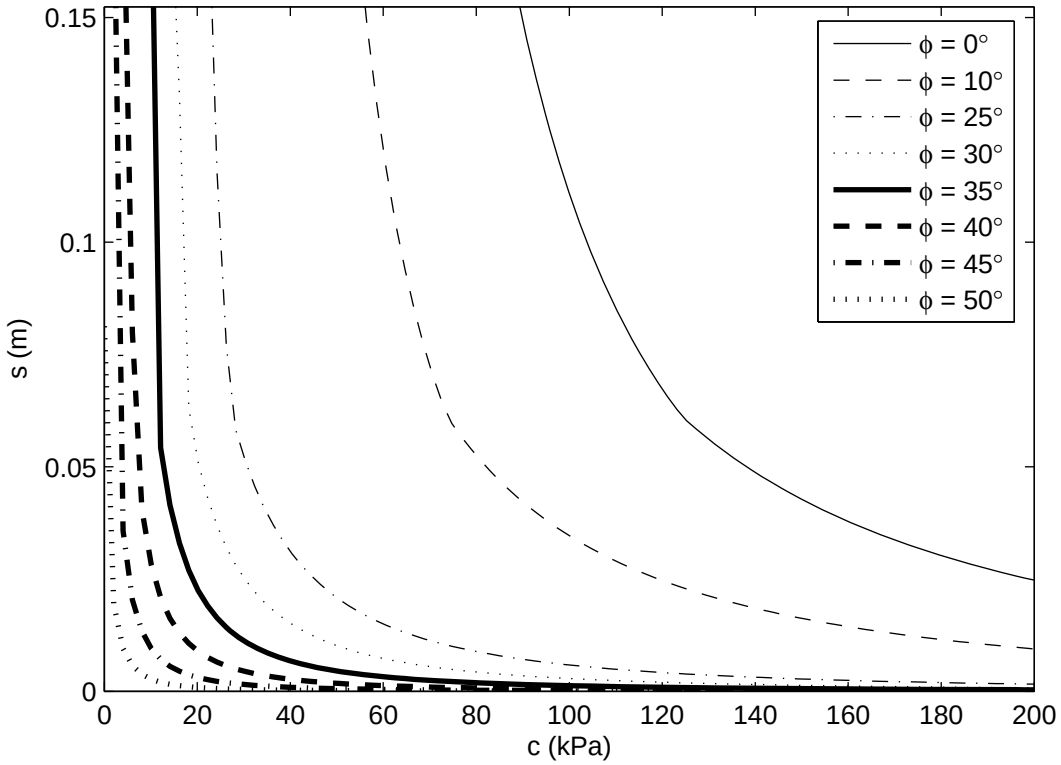

Figure I13. Analytic prediction for wheel rolling with Q_V = 130 kN, d = 1.219 m, b = 0.610 m, and γ = 20 kN/m^3

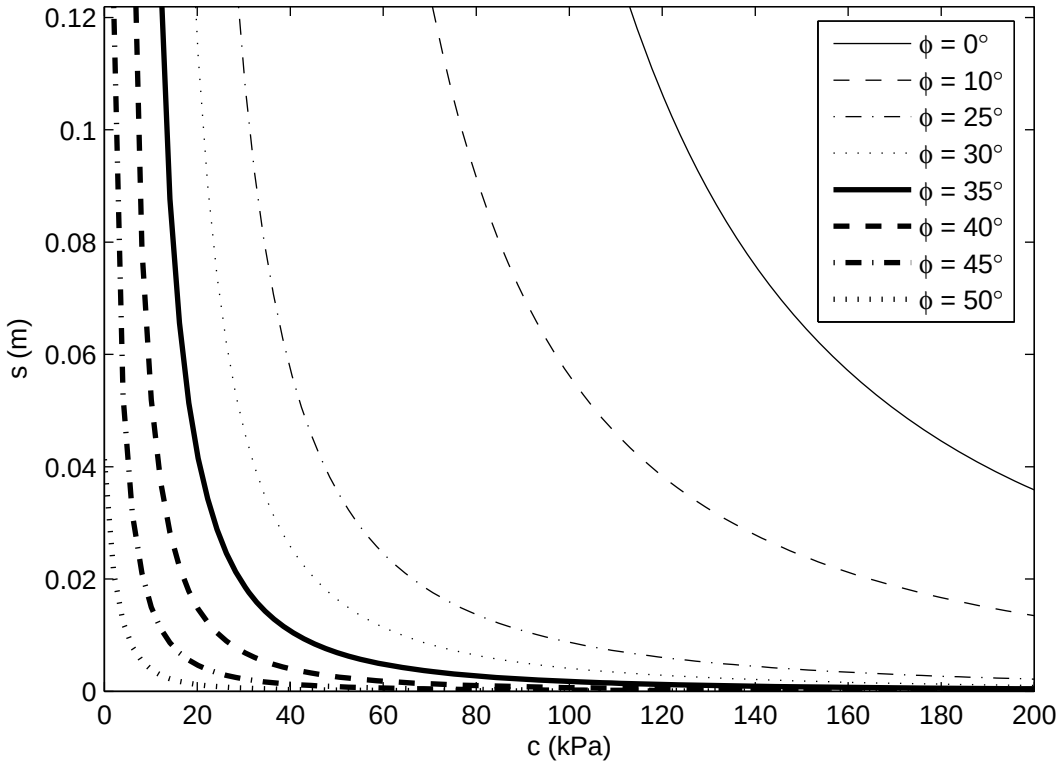

Figure I14. Analytic prediction for wheel rolling with Q_V = 65 kN, d = 1.219 m, b = 0.610 m, and γ = 20 kN/m^3

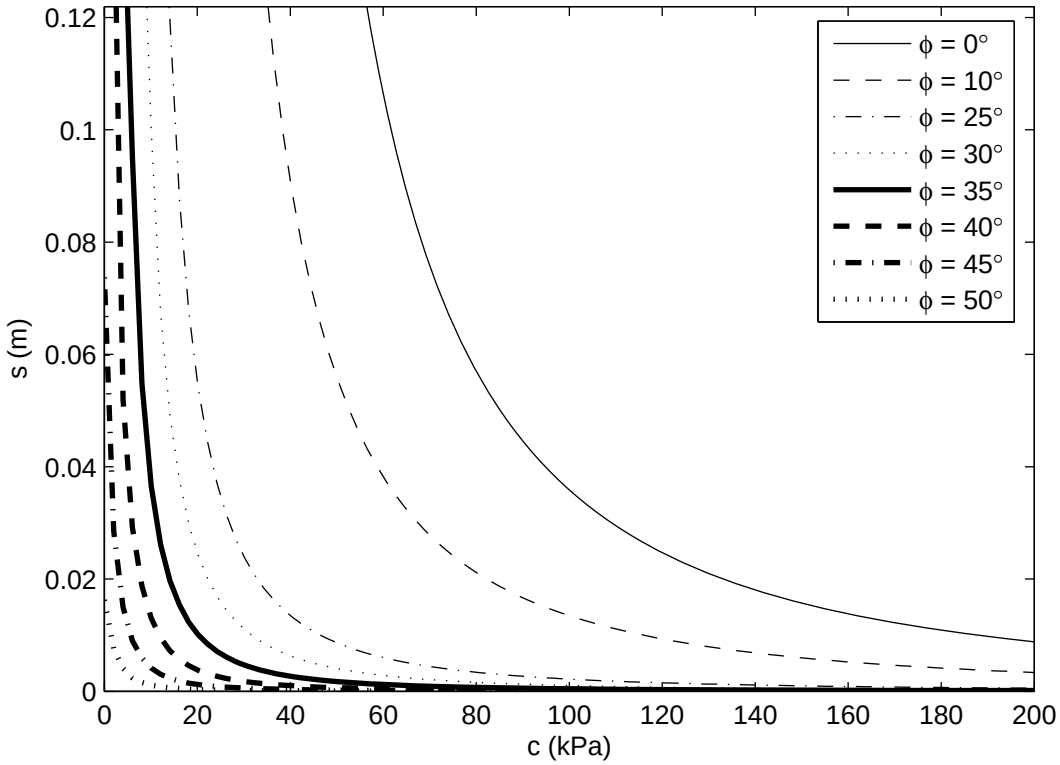

Figure I15. Analytic prediction for wheel rolling with
Q_V = 130 kN, d = 1.219 m, b = 0.457 m, and γ = 20 kN/m^3

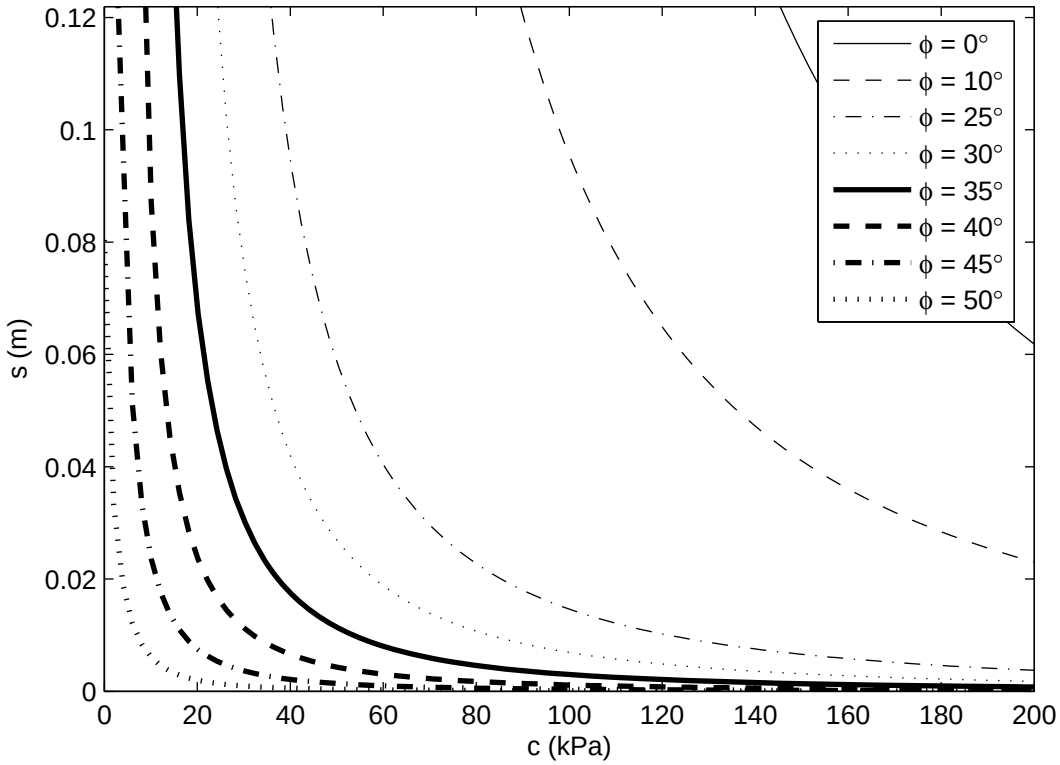

Figure I16. Analytic prediction for wheel rolling with
Q_V = 65 kN, d = 1.219 m, b = 0.457 m, and γ = 20 kN/m^3

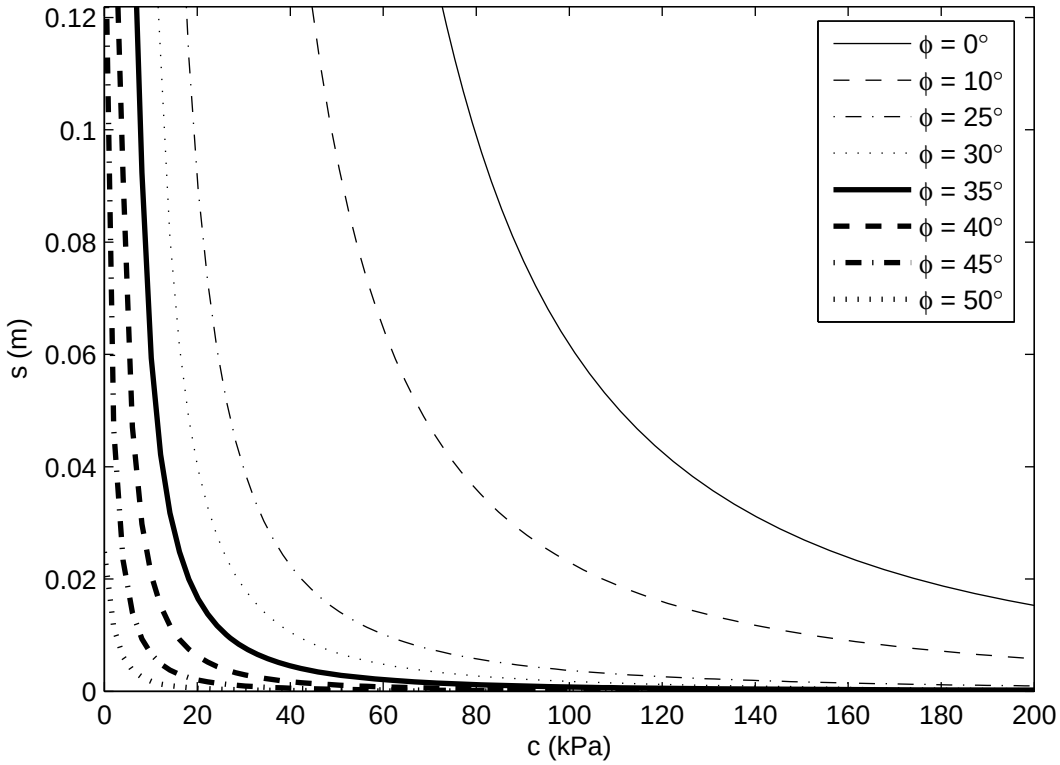

Figure I17. Analytic prediction for wheel rolling with
Q_V = 130 kN, d = 1.219 m, b = 0.305 m, and γ = 20 kN/m^3

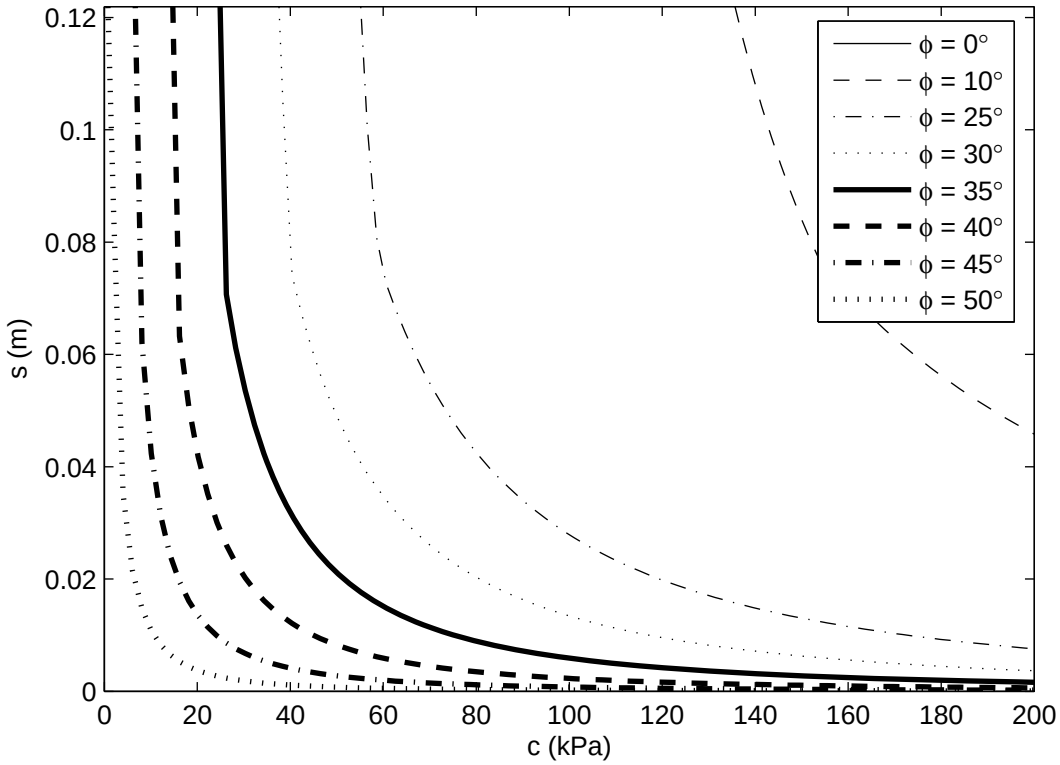

Figure I18. Analytic prediction for wheel rolling with
Q_V = 65 kN, d = 1.219 m, b = 0.305 m, and γ = 20 kN/m^3

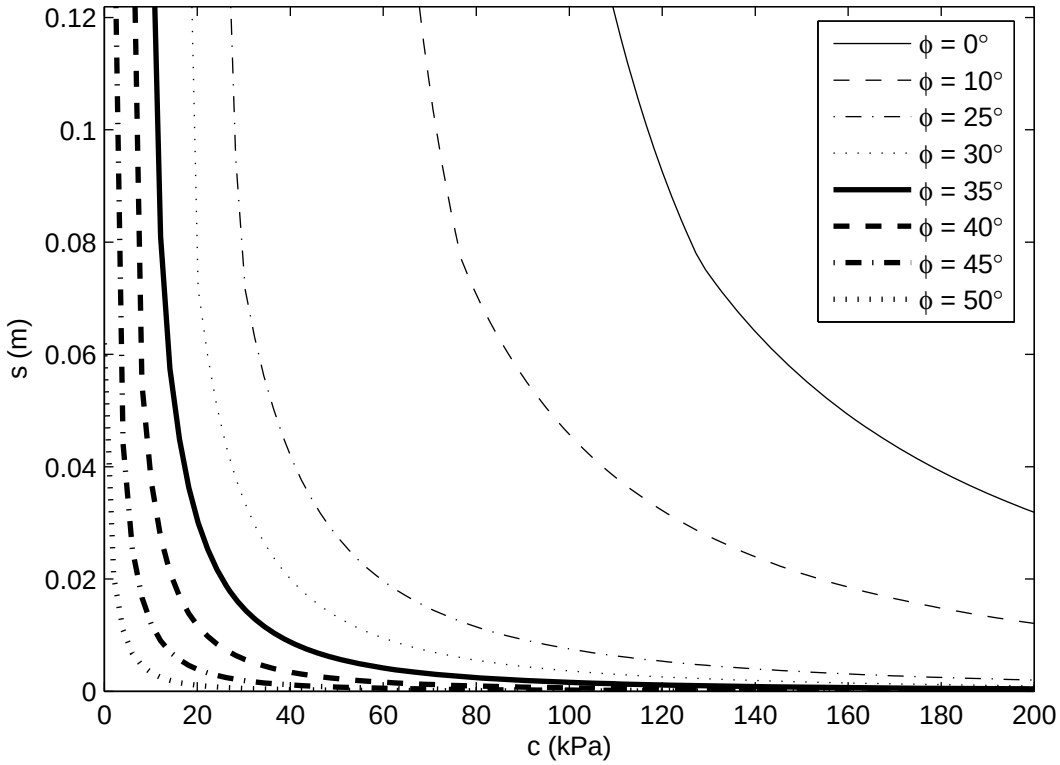

Figure I19. Analytic prediction for wheel rolling with
Q_V = 130 kN, d = 1.219 m, b = 0.610 m, and γ = 14 kN/m^3

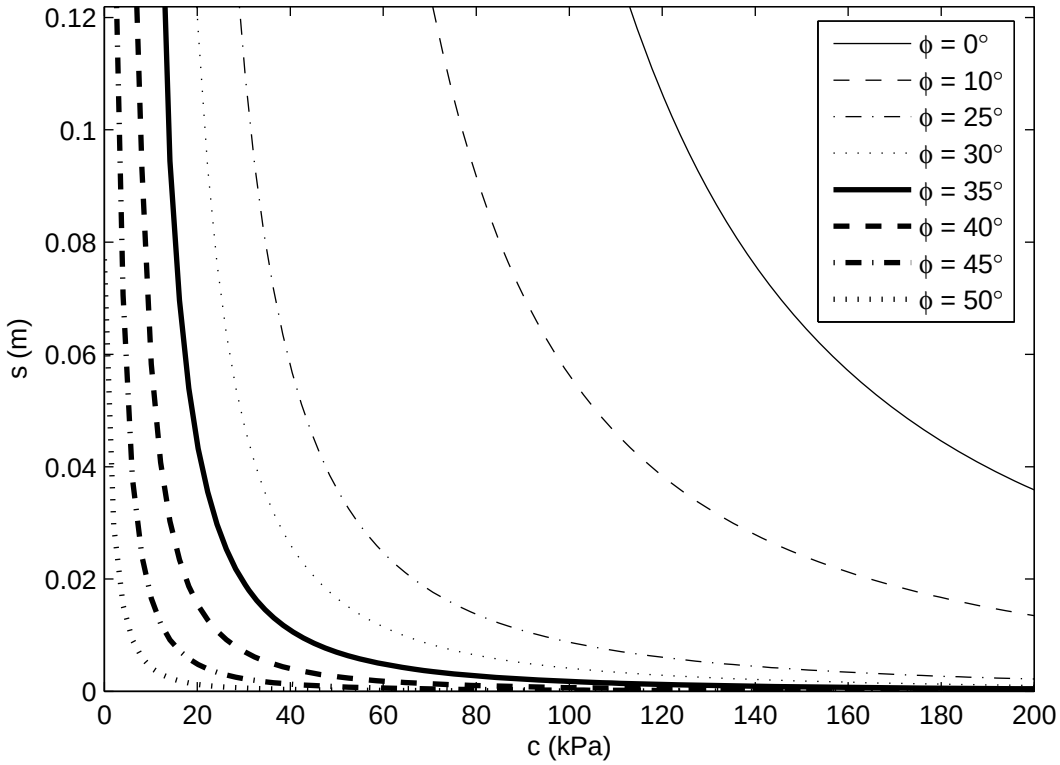

Figure I20. Analytic prediction for wheel rolling with
Q_V = 65 kN, d = 1.219 m, b = 0.610 m, and γ = 14 kN/m^3

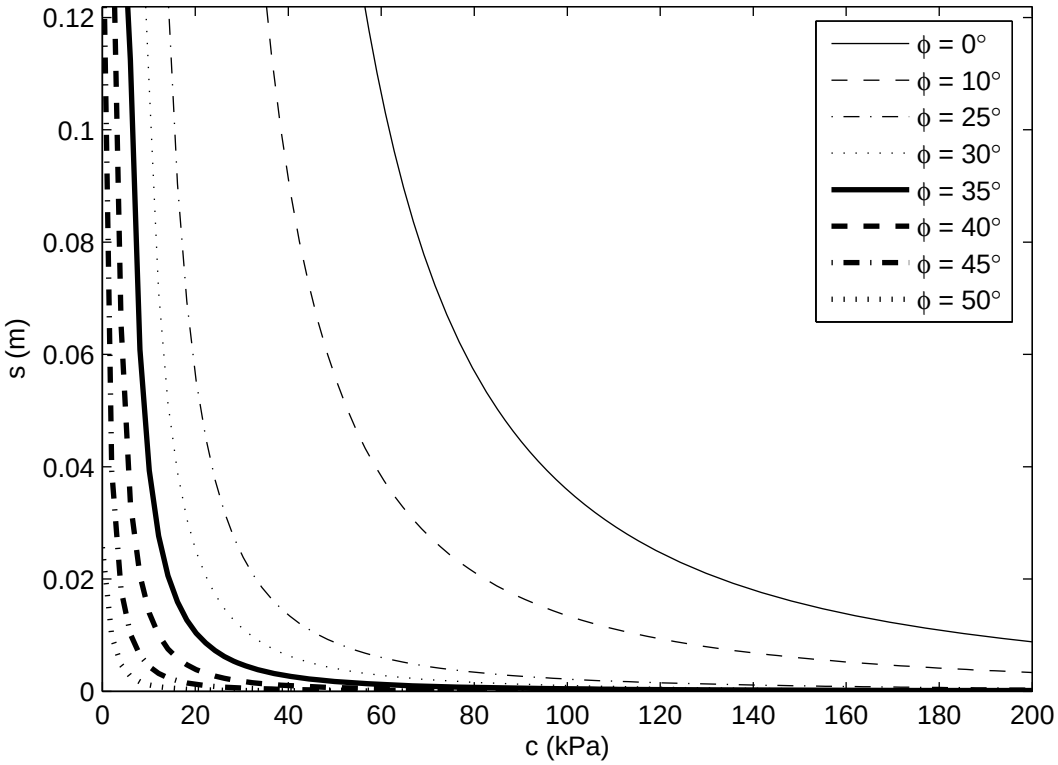

Figure I21. Analytic prediction for wheel rolling with
Q_V = 130 kN, d = 1.219 m, b = 0.457 m, and γ = 14 kN/m^3

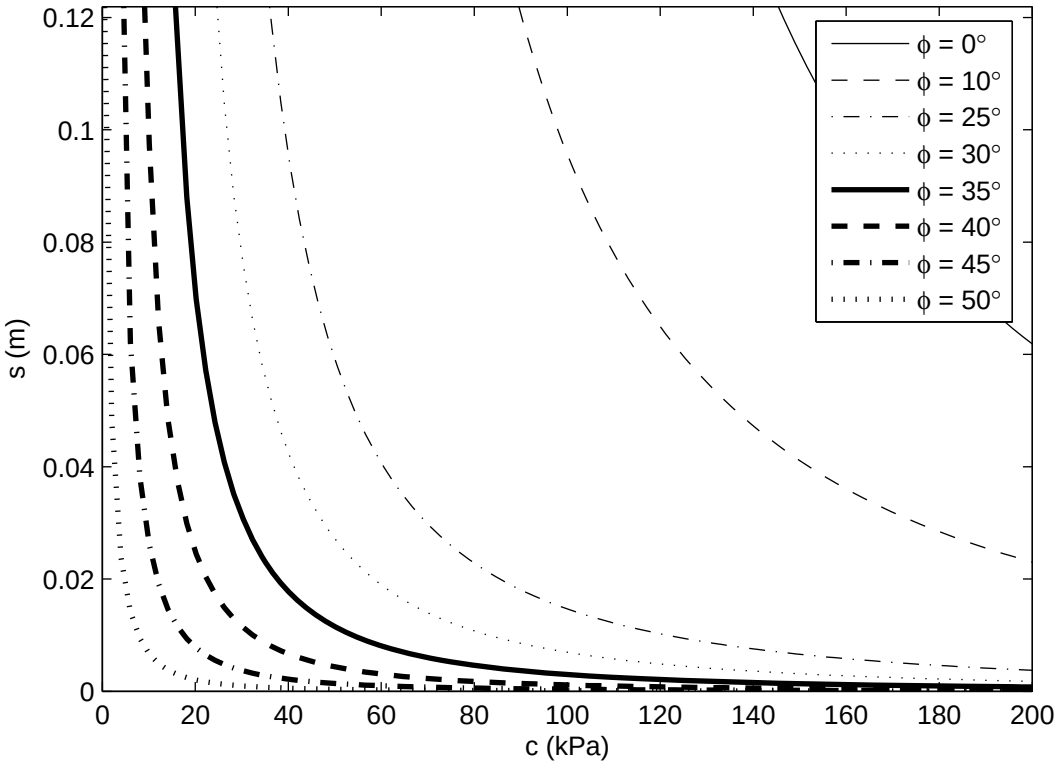

Figure I22. Analytic prediction for wheel rolling with
Q_V = 65 kN, d = 1.219 m, b = 0.457 m, and γ = 14 kN/m^3

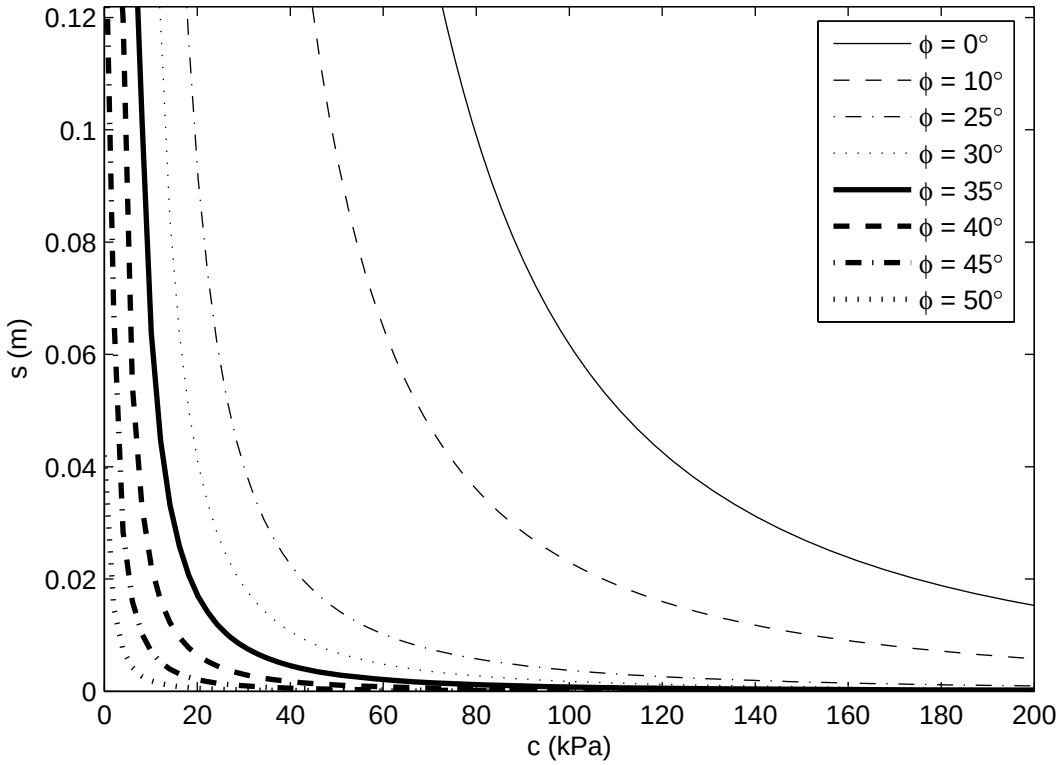

Figure I23. Analytic prediction for wheel rolling with
Q_V = 130 kN, d = 1.219 m, b = 0.305 m, and γ = 14 kN/m^3

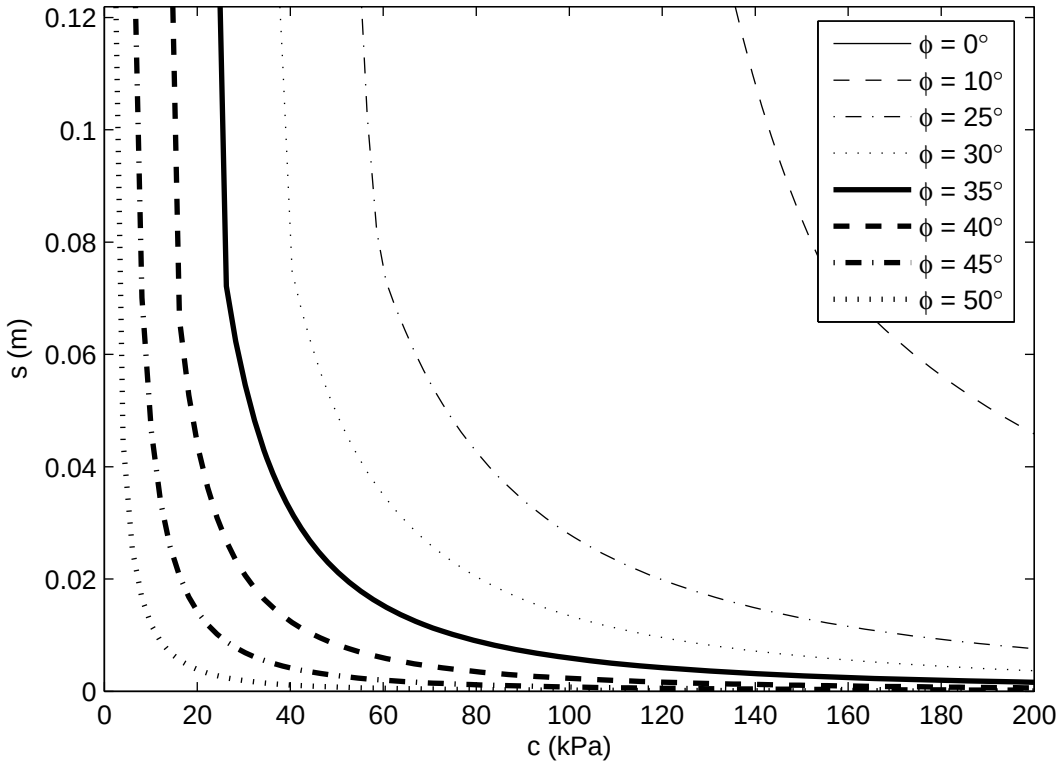

Figure I24. Analytic prediction for wheel rolling with
Q_V = 65 kN, d = 1.219 m, b = 0.305 m, and γ = 14 kN/m^3

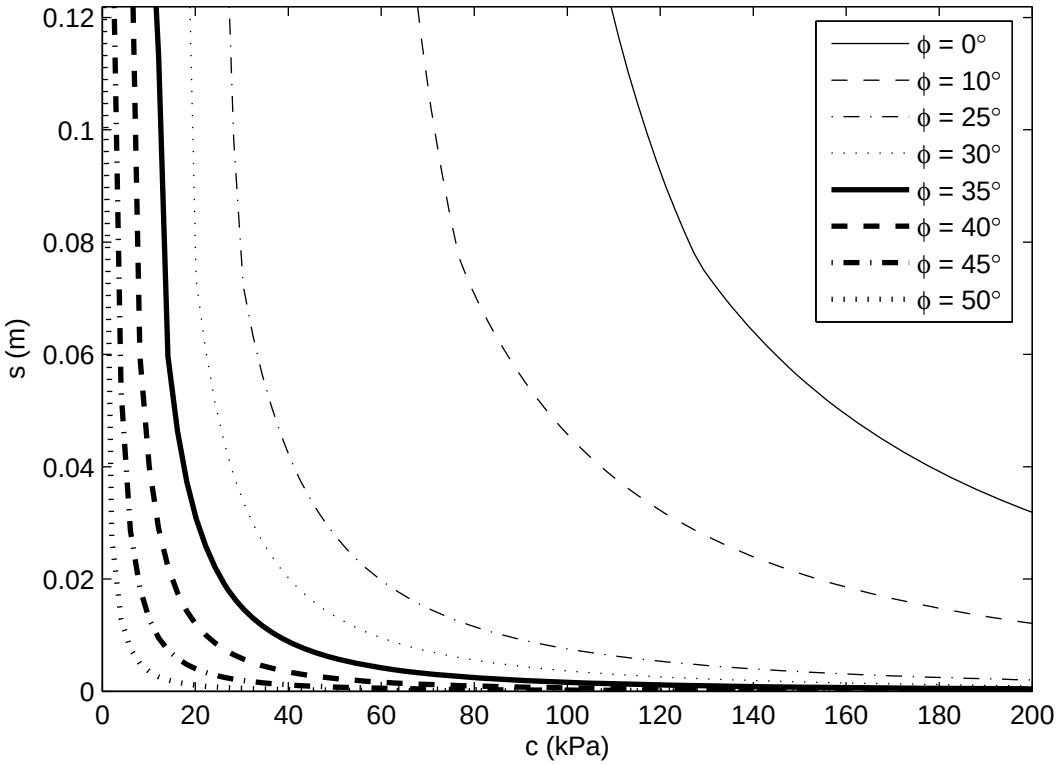

Figure I25. Analytic prediction for wheel rolling with
Q_V = 130 kN, d = 0.914 m, b = 0.610 m, and γ = 20 kN/m^3

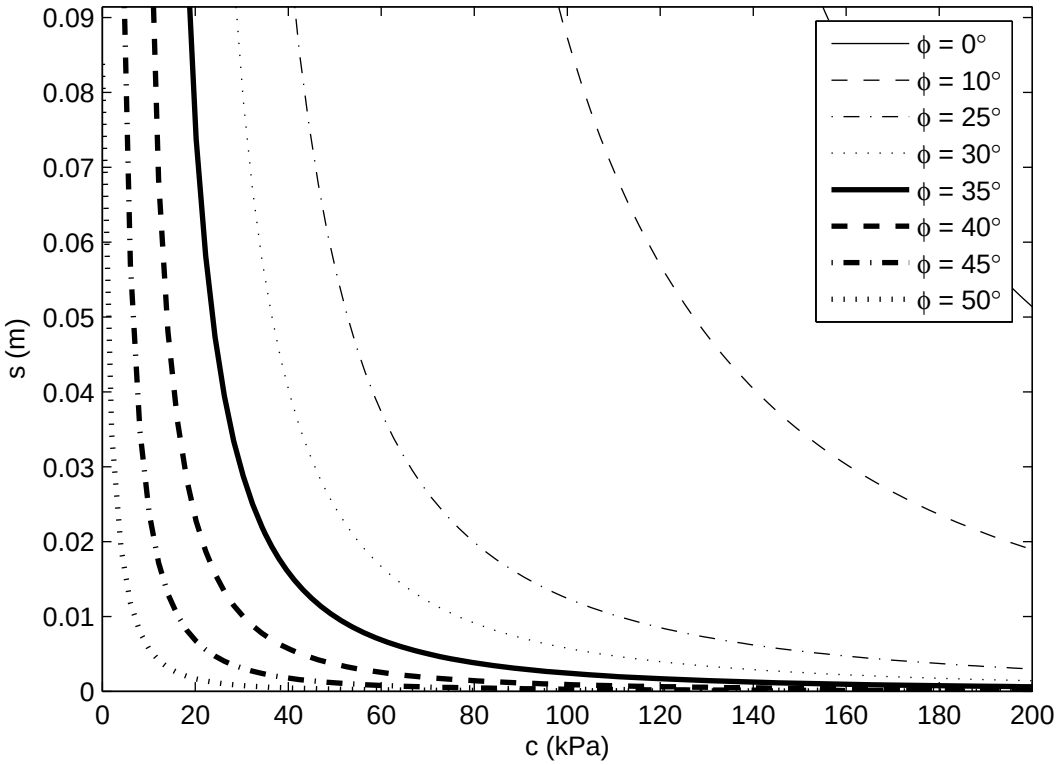

Figure I26. Analytic prediction for wheel rolling with
Q_V = 65 kN, d = 0.914 m, b = 0.610 m, and γ = 20 kN/m^3

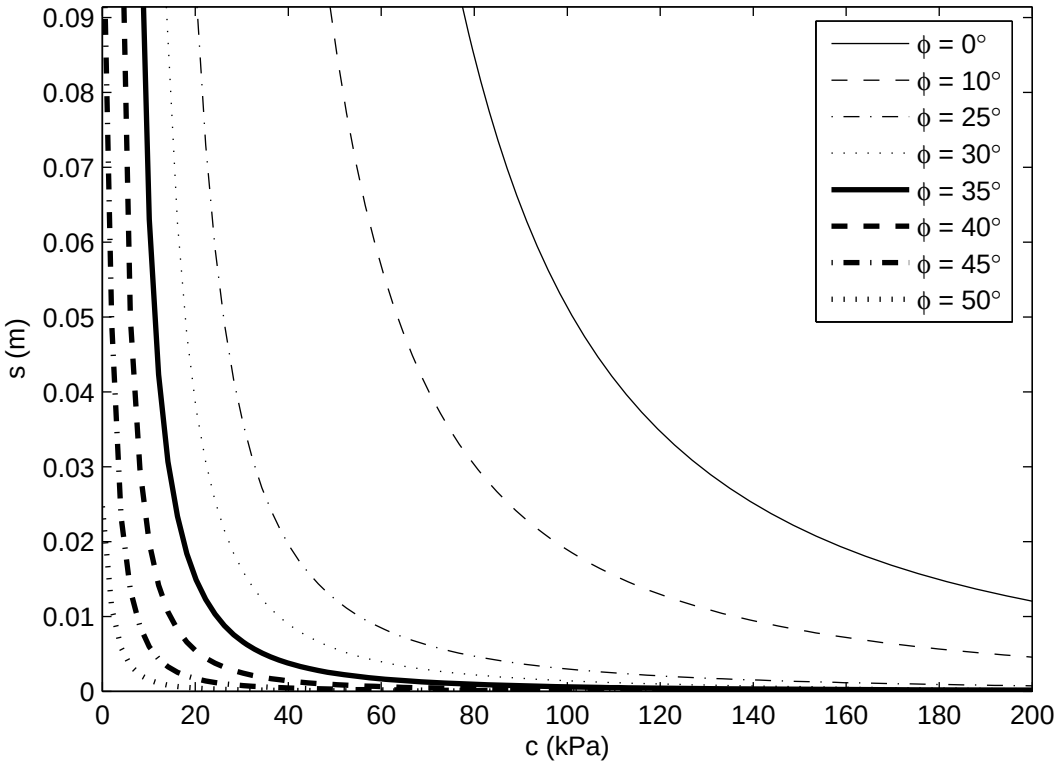

Figure I27. Analytic prediction for wheel rolling with Q_V = 130 kN, d = 0.914 m, b = 0.457 m, and γ = 20 kN/m^3

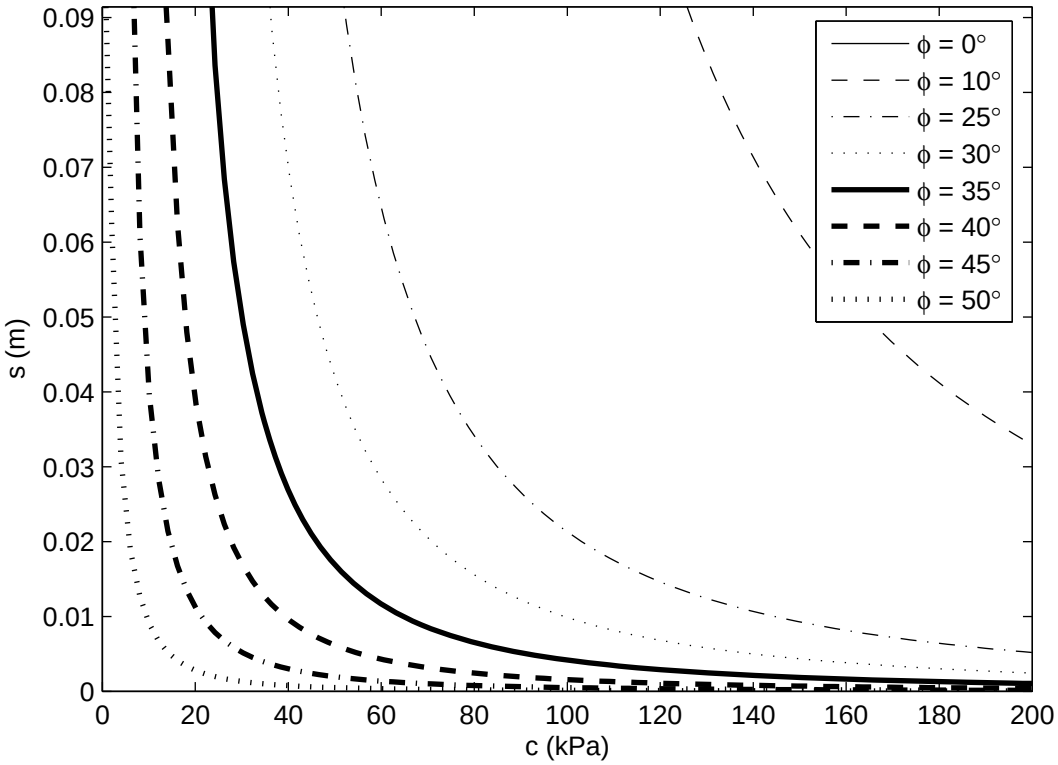

Figure I28. Analytic prediction for wheel rolling with Q_V = 65 kN, d = 0.914 m, b = 0.457 m, and γ = 20 kN/m^3

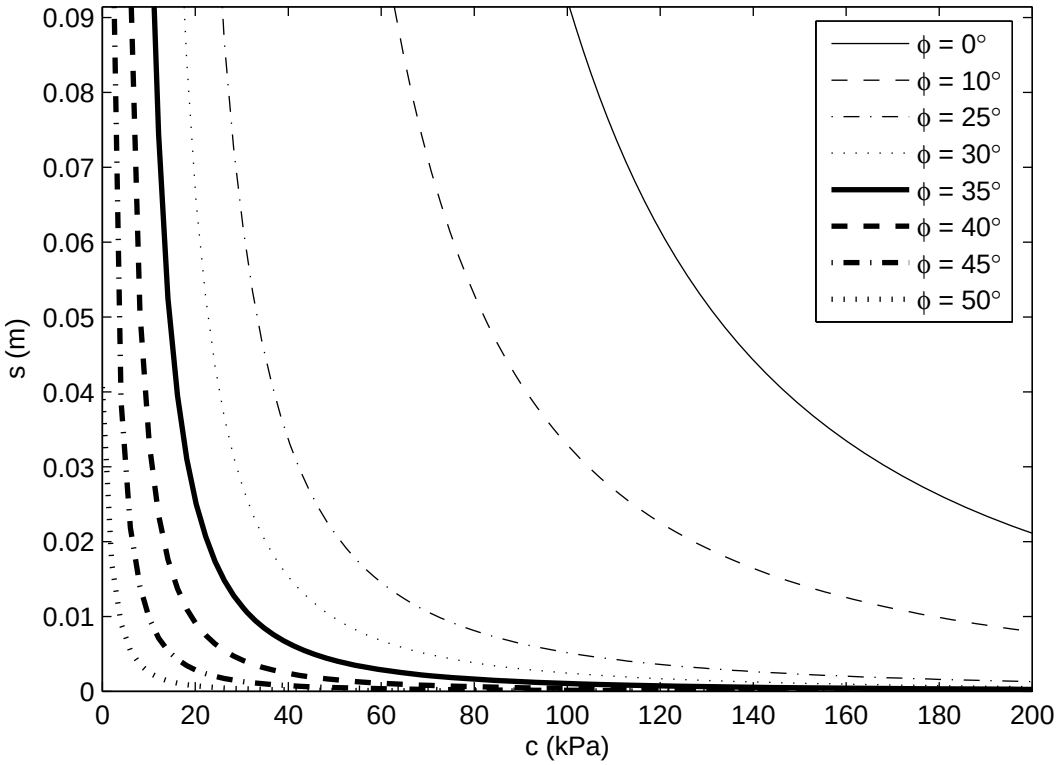

Figure I29. Analytic prediction for wheel rolling with Q_V = 130 kN, d = 0.914 m, b = 0.305 m, and γ = 20 kN/m^3

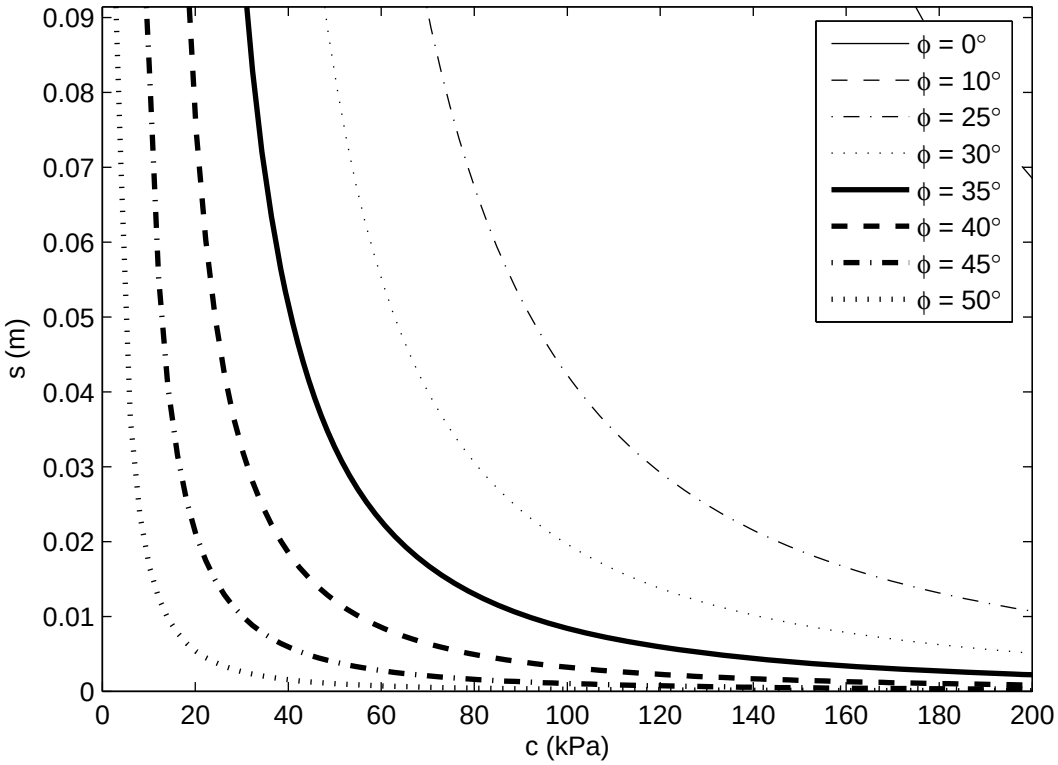

Figure I30. Analytic prediction for wheel rolling with Q_V = 65 kN, d = 0.914 m, b = 0.305 m, and γ = 20 kN/m^3

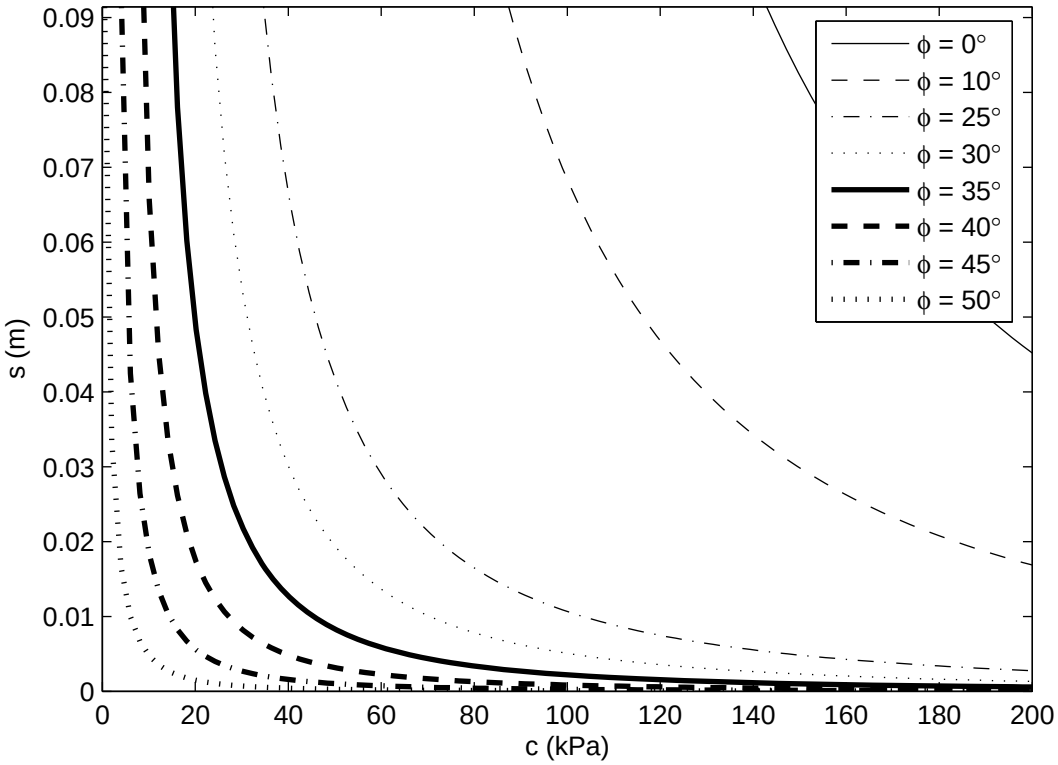

Figure I31. Analytic prediction for wheel rolling with Q_V = 130 kN, d = 0.914 m, b = 0.610 m, and γ = 14 kN/m^3

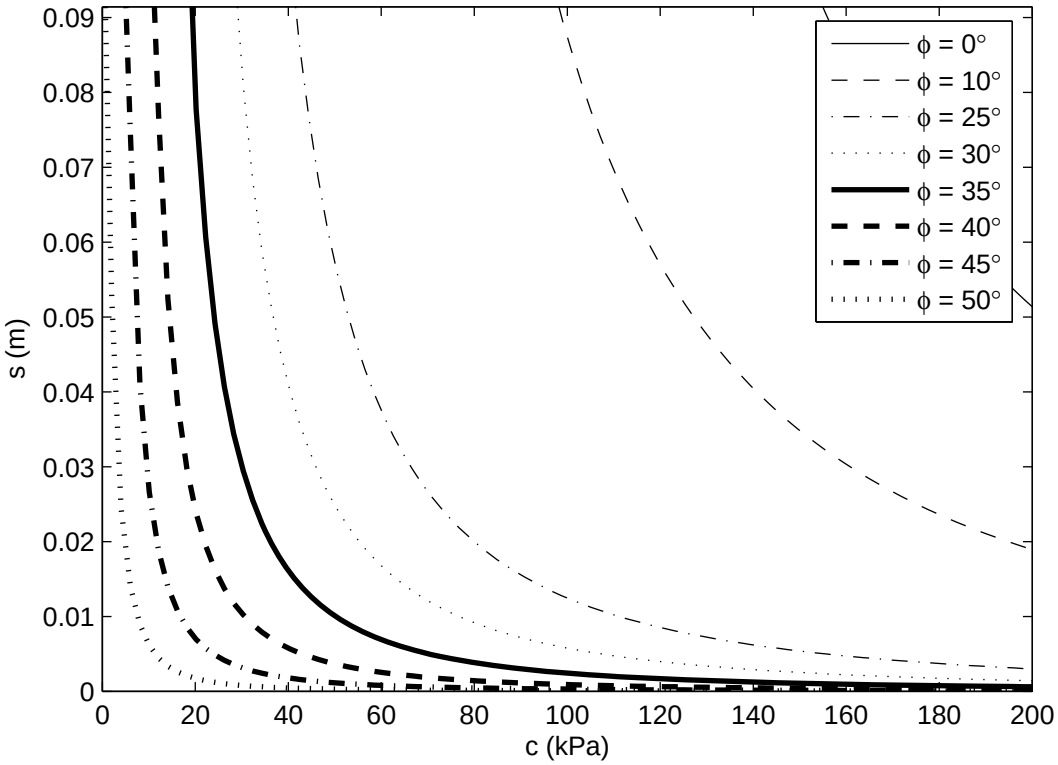

Figure I32. Analytic prediction for wheel rolling with Q_V = 65 kN, d = 0.914 m, b = 0.610 m, and γ = 14 kN/m^3

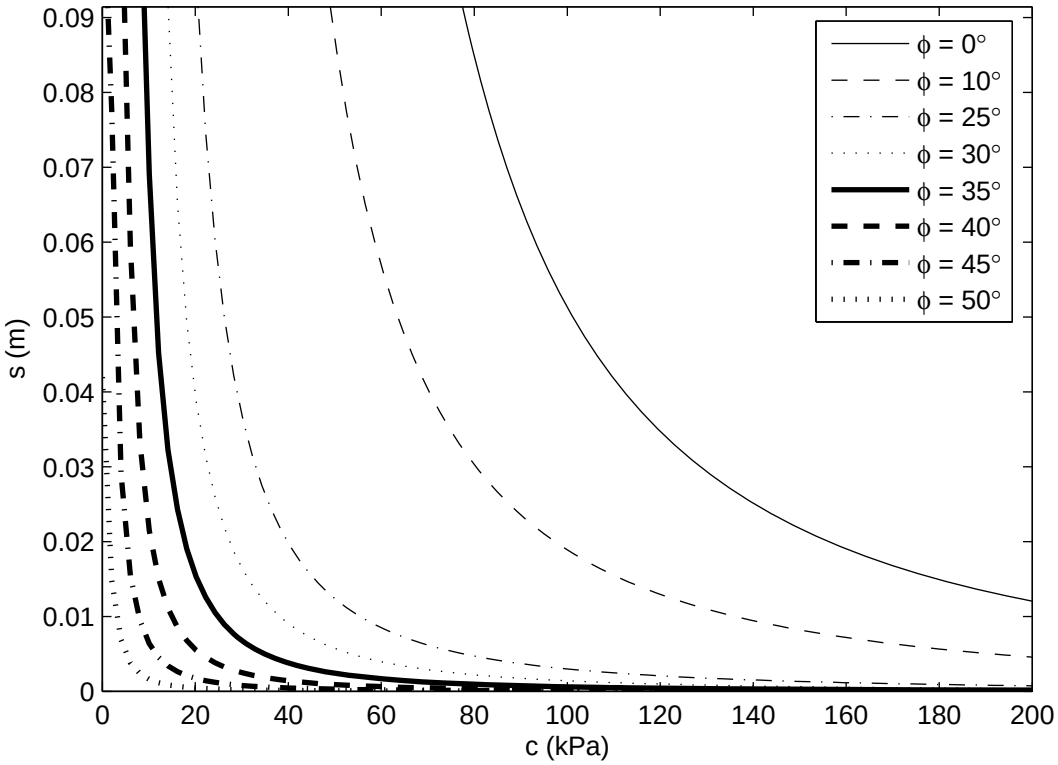

Figure I33. Analytic prediction for wheel rolling with Q_V = 130 kN, d = 0.914 m, b = 0.457 m, and γ = 14 kN/m^3

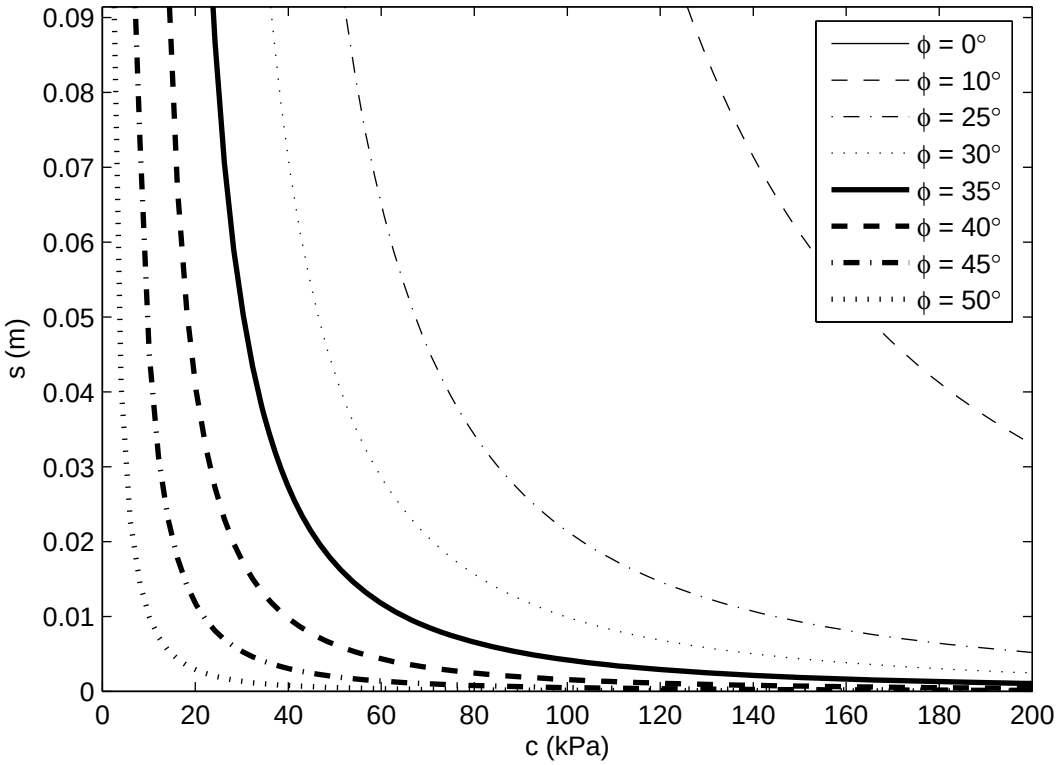

Figure I34. Analytic prediction for wheel rolling with Q_V = 65 kN, d = 0.914 m, b = 0.457 m, and γ = 14 kN/m^3

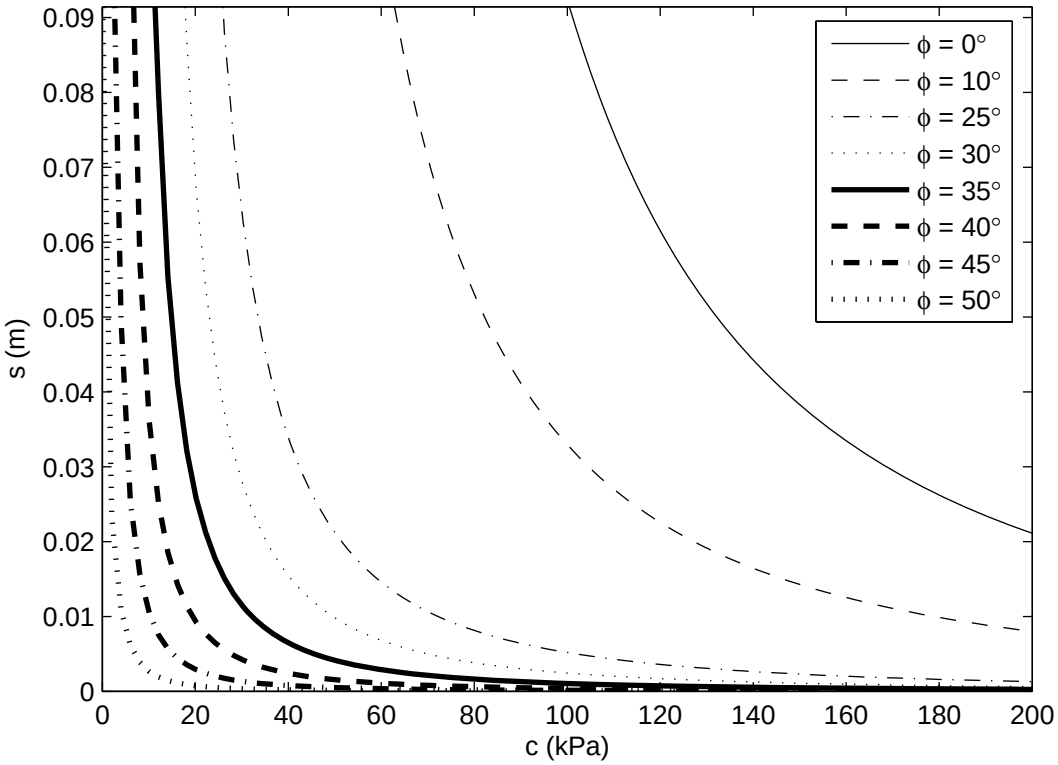

Figure I35. Analytic prediction for wheel rolling with
Q_V = 130 kN, d = 0.914 m, b = 0.305 m, and γ = 14 kN/m^3

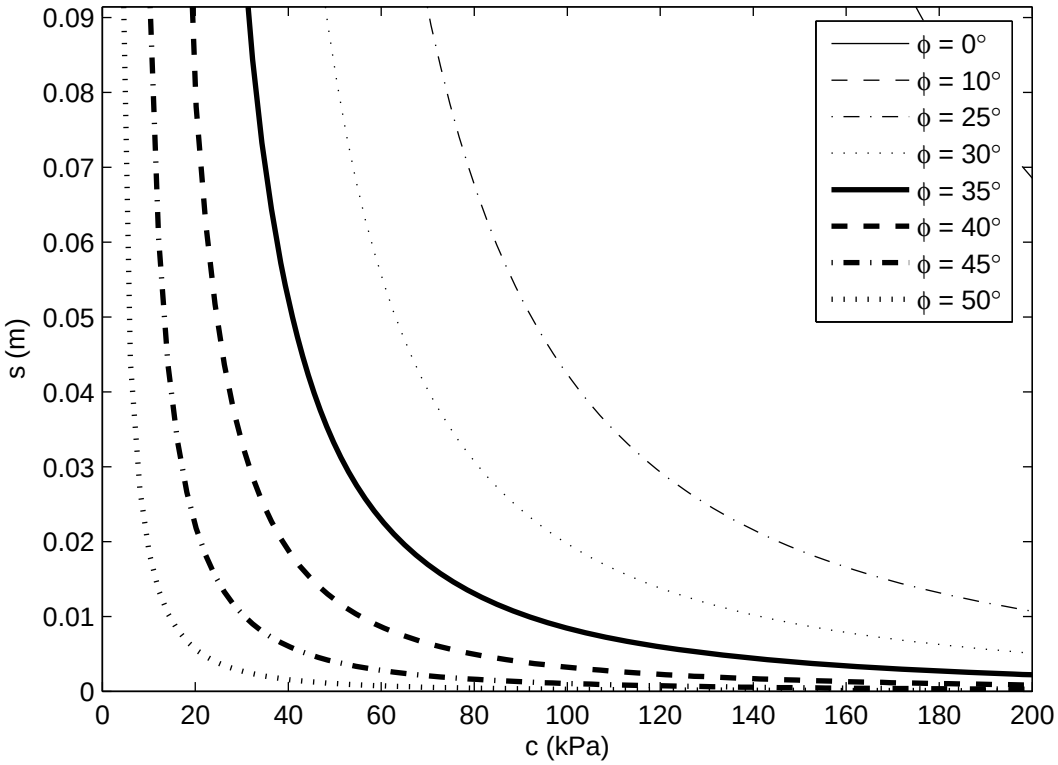

Figure I36. Analytic prediction for wheel rolling with
Q_V = 65 kN, d = 0.914 m, b = 0.305 m, and γ = 14 kN/m^3

Appendix J: Dimensional Plots of Results from Numerical Simulations of Indentation

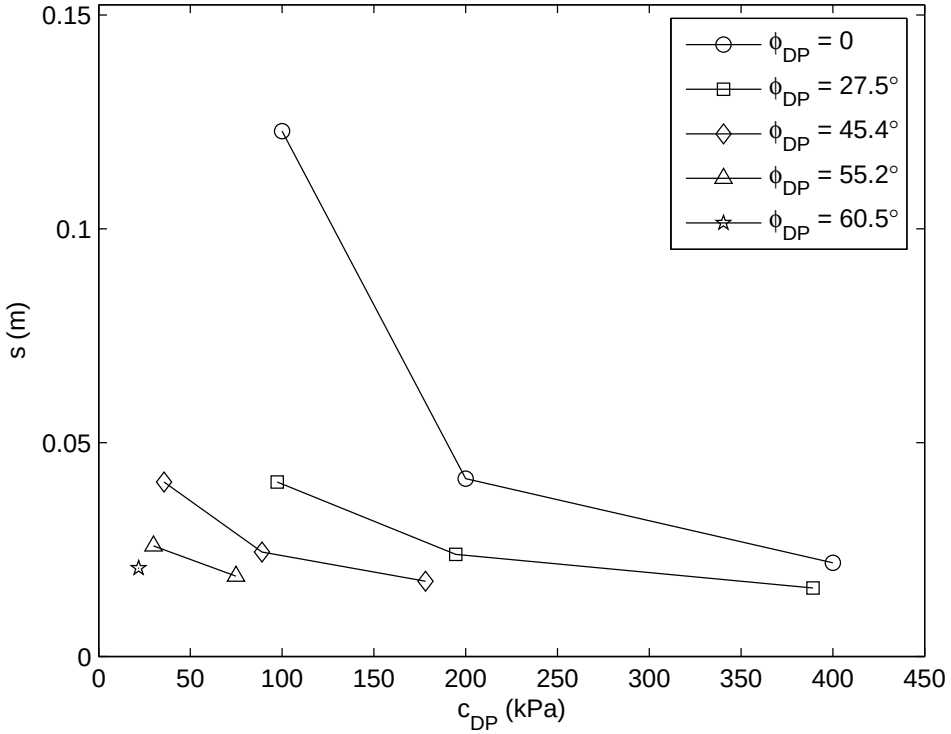

Figure J1. Results of numerical simulations of indentation; cases 1-12; Q_V = 142 kN (d = 1.524 m, b = 0.457 m, and E = 40 MPa)

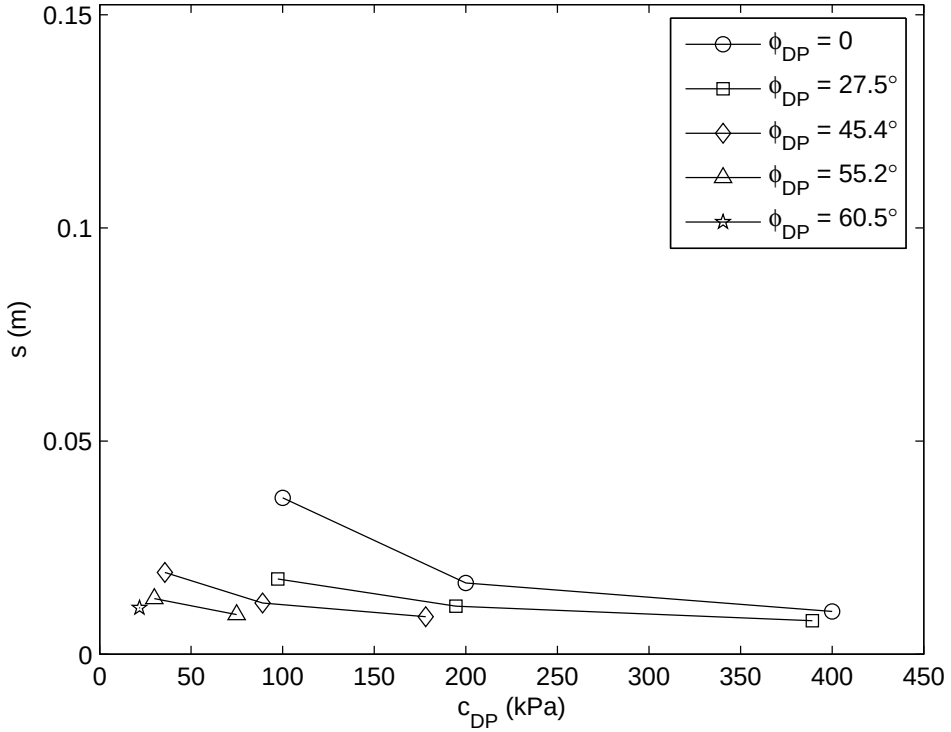

Figure J2. Results of numerical simulations of indentation; cases 1-12; Q_V = 71 kN (d = 1.524 m, b = 0.457 m, and E = 40 MPa)

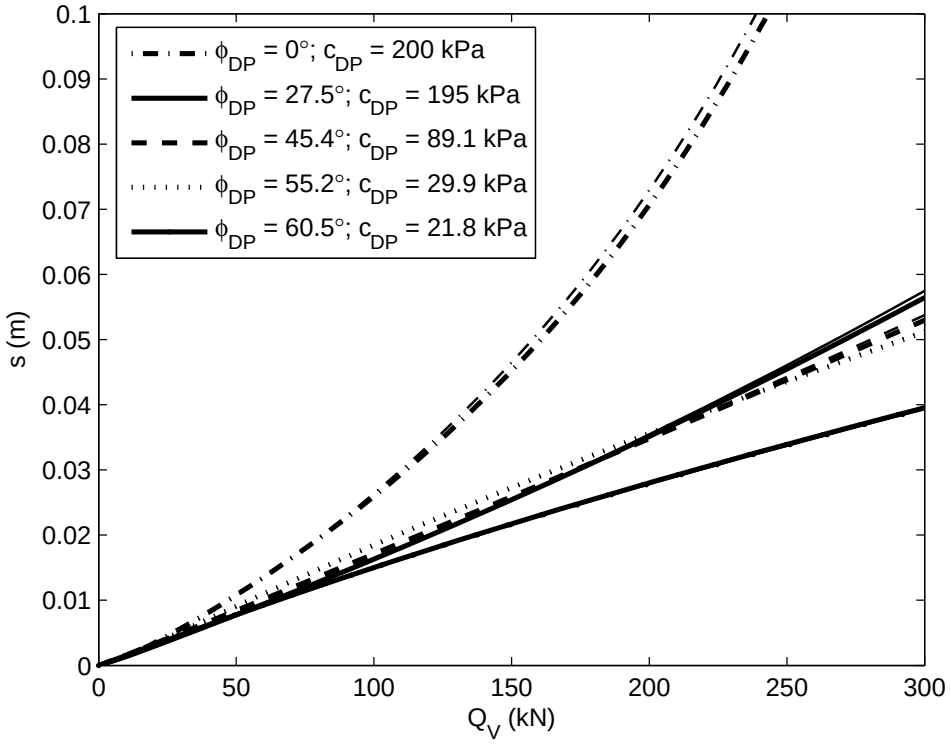

Figure J3. Effect of friction on indentation; heavy lines are with $\mu = 0.8$ and fine lines are with $\mu = 0.4$ ($d = 1.524$ m, $b = 0.457$ m, and $E = 40$ MPa)

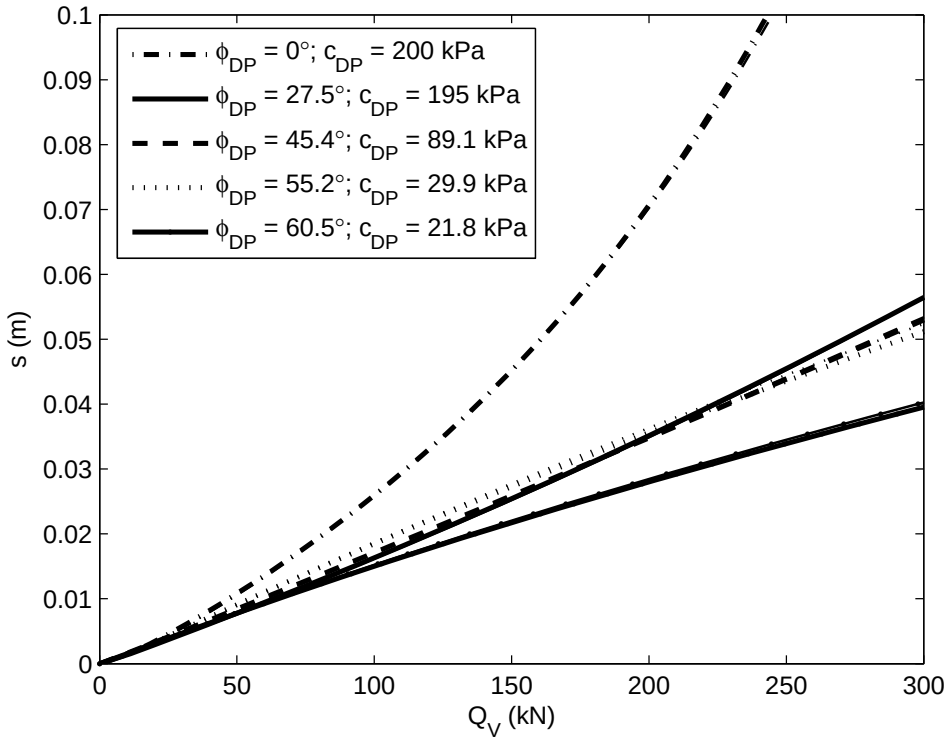

Figure J4. Effect of unit weight on indentation; heavy lines are with $\gamma = 20$ kN/m^3 and fine lines are with $\gamma = 14$ kN/m^3 ($d = 1.524$ m, $b = 0.457$ m, and $E = 40$ MPa)

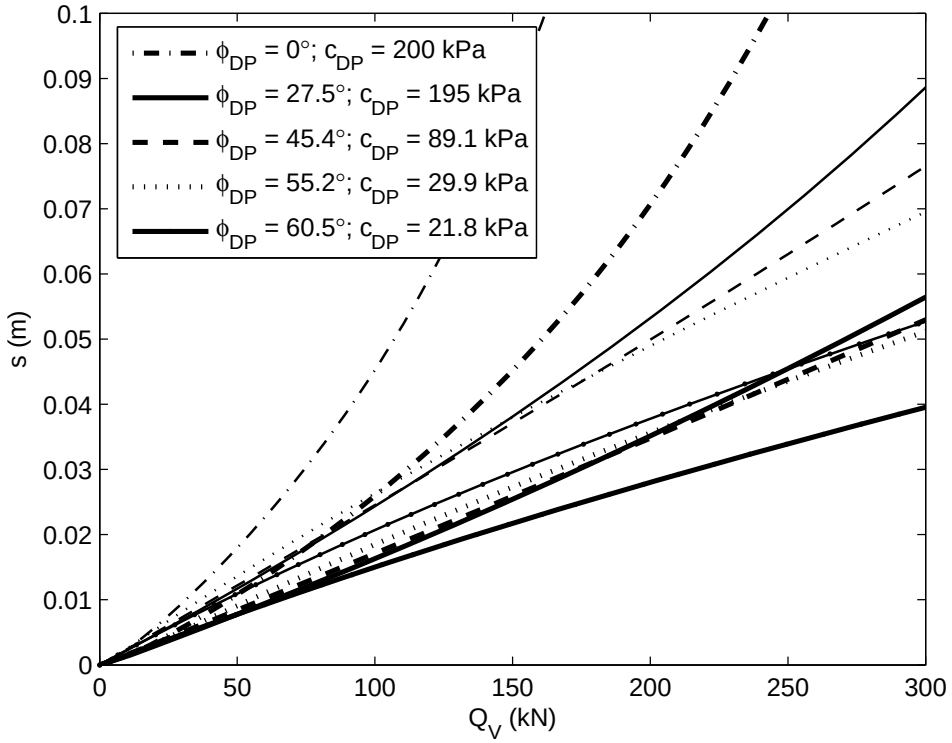

Figure J5. Effect of wheel width on indentation; heavy lines are with b = 0.457 m and fine lines are with b = 0.305 m (d = 1.524 m and E = 40 MPa)

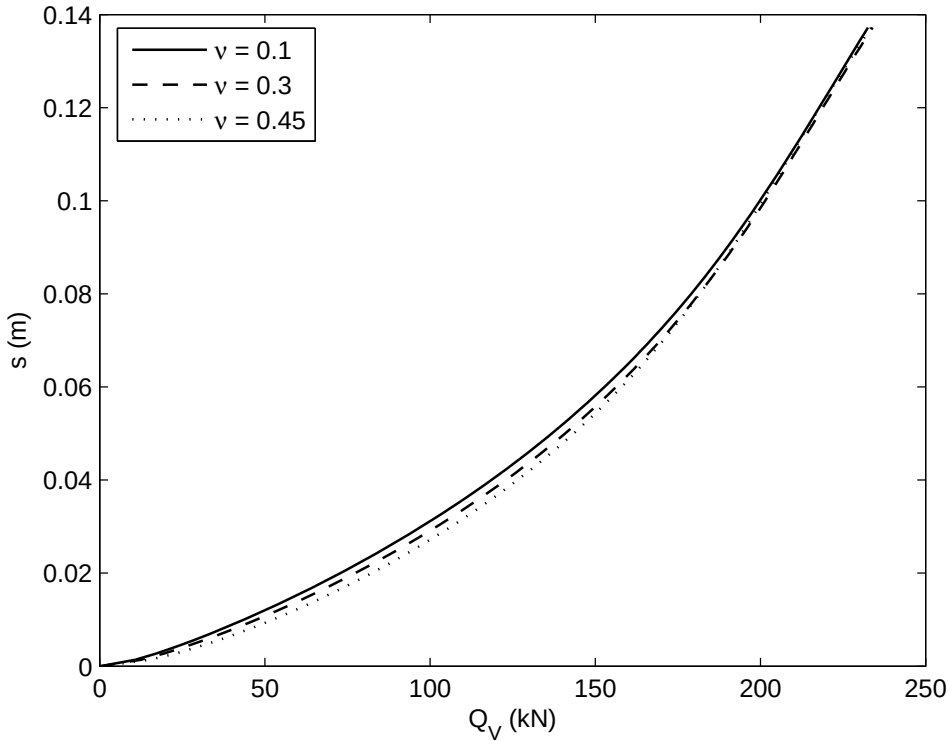

Figure J6. Effect of Poisson's ratio (d = 1.372 m, b = 0.457 m, ϕ_{DP} = 0, c_{DP} = 200 kPa, and E = 50 MPa)

Appendix K: Dimensional Plots of Results from Numerical Simulations of Rolling

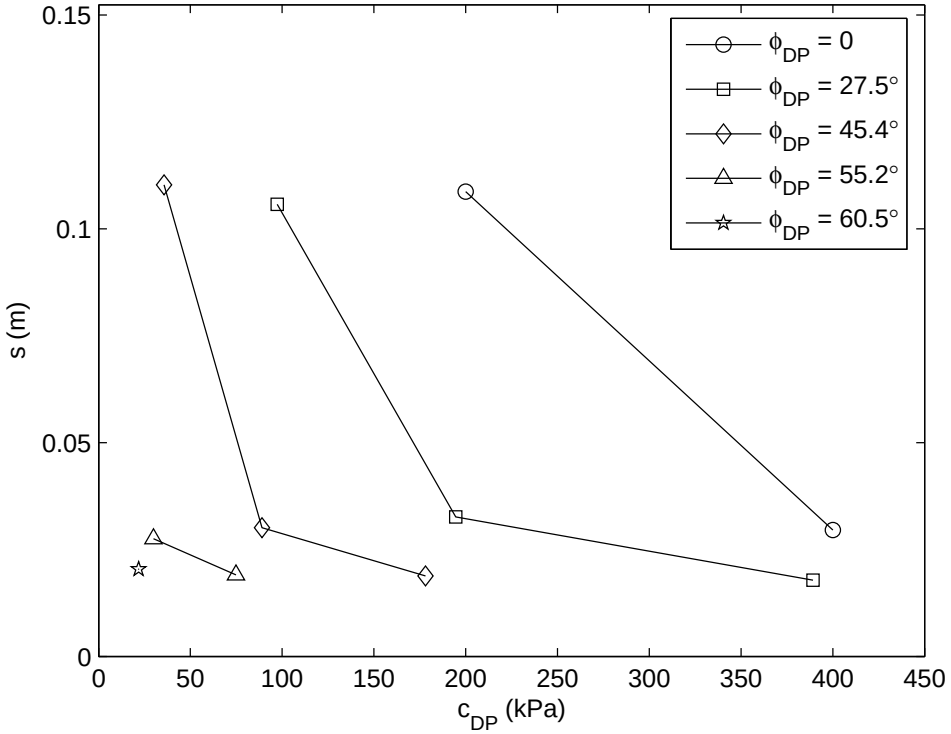

Figure K1. Results of numerical simulations of rolling; cases 1-12; Q_V = 142 kN (d = 1.524 m, b = 0.457 m, and E = 40 MPa)

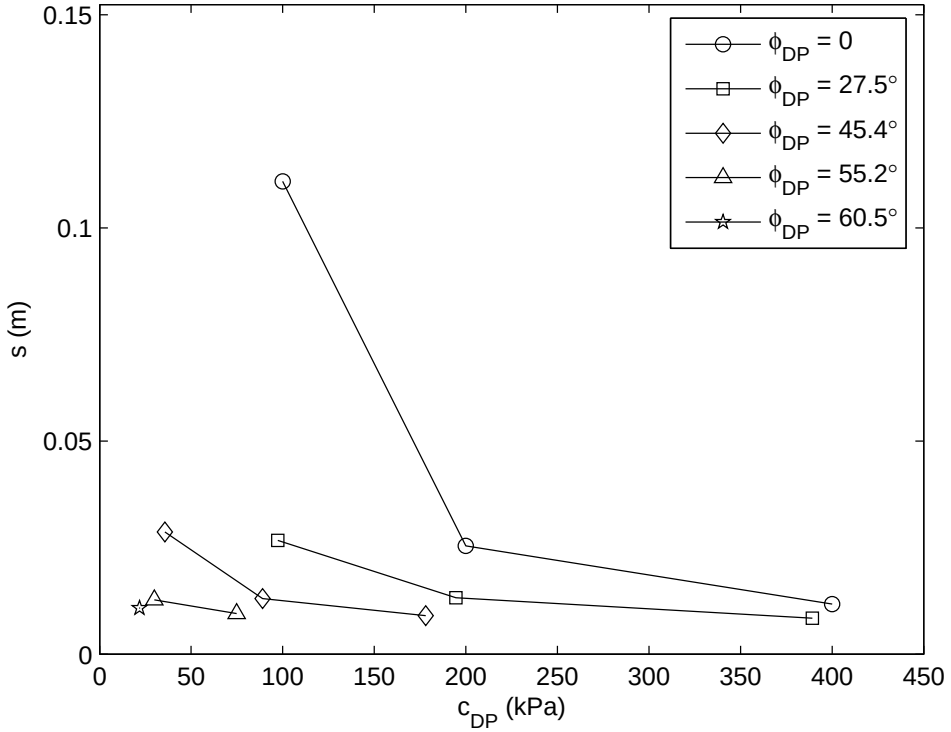

Figure K2. Results of numerical simulations of rolling; cases 1-12; Q_V = 71 kN (d = 1.524 m, b = 0.457 m, and E = 40 MPa)

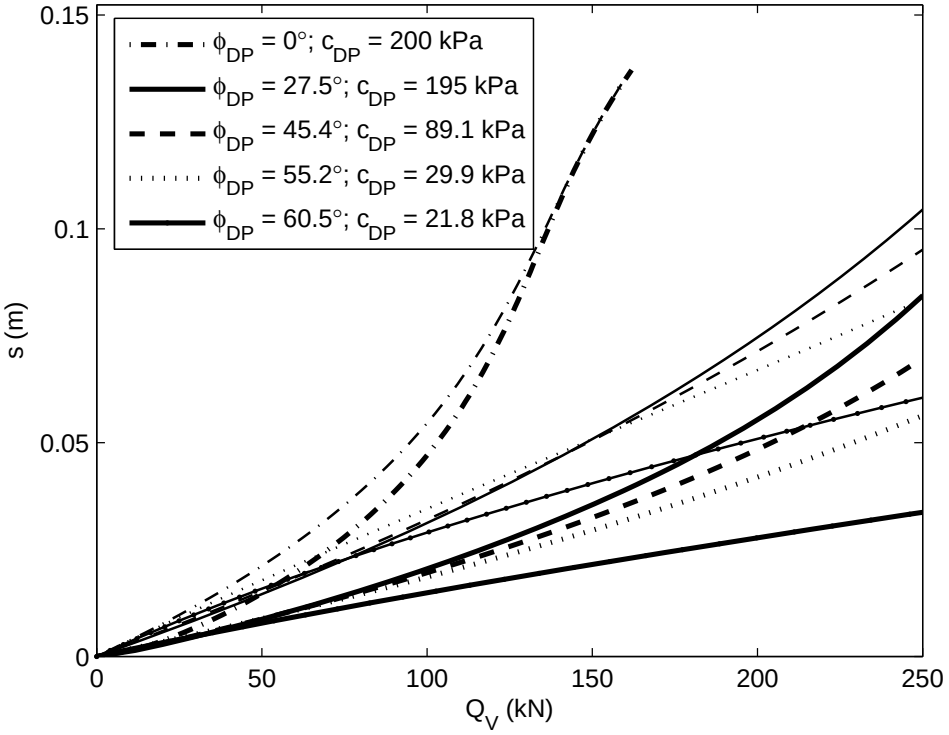

Figure K3. Effect of Young's modulus on rolling; heavy lines are with E = 40 MPa and fine lines are with E = 15 MPa (d = 1.524 m, b = 0.457 m)

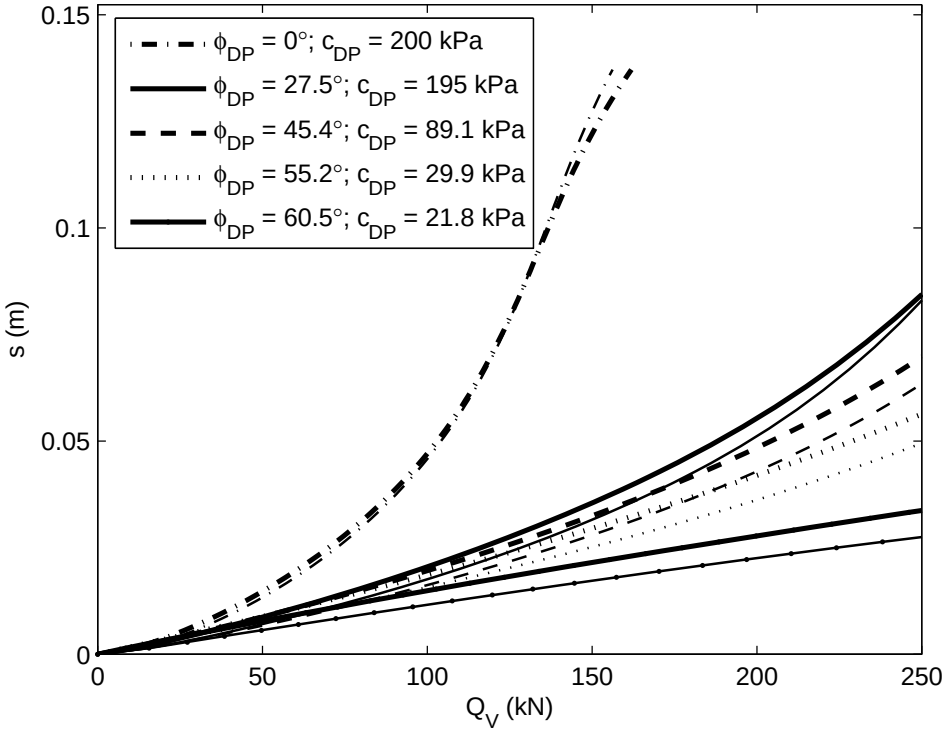

Figure K4. Effect of Young's modulus on rolling; heavy lines are with E = 40 MPa and fine lines are with E = 60 MPa (d = 1.524 m, b = 0.457 m)

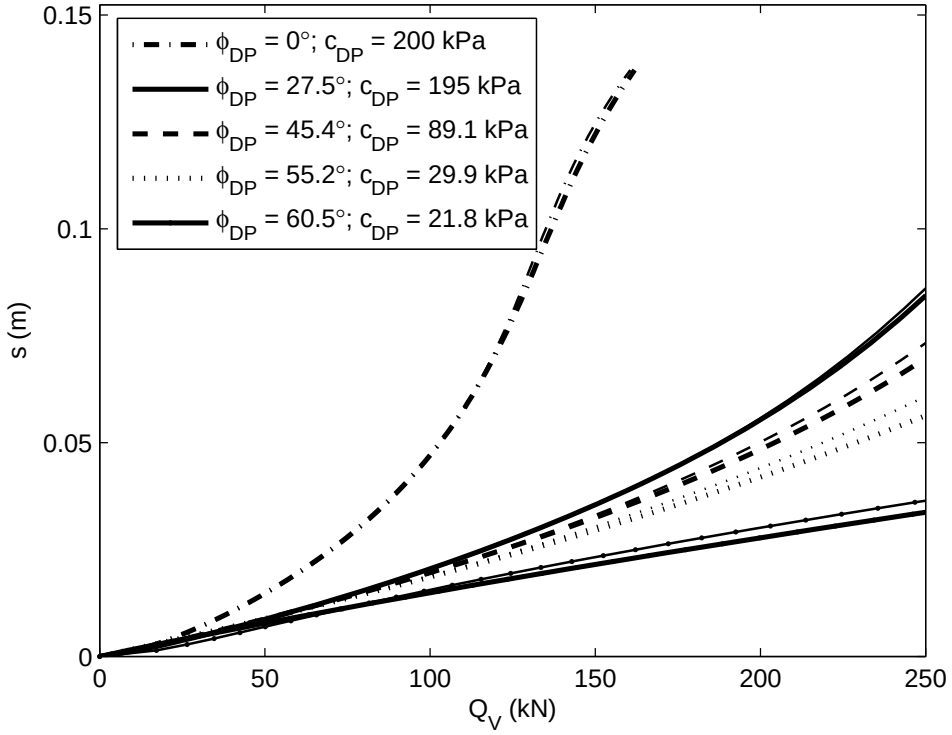

Figure K5. Effect of unit weight on rolling; heavy lines are with $\gamma = 20$ kN/m^3 and fine lines are with $\gamma = 14$ kN/m^3 ($d = 1.524$ m, $b = 0.457$ m, and $E = 40$ MPa)

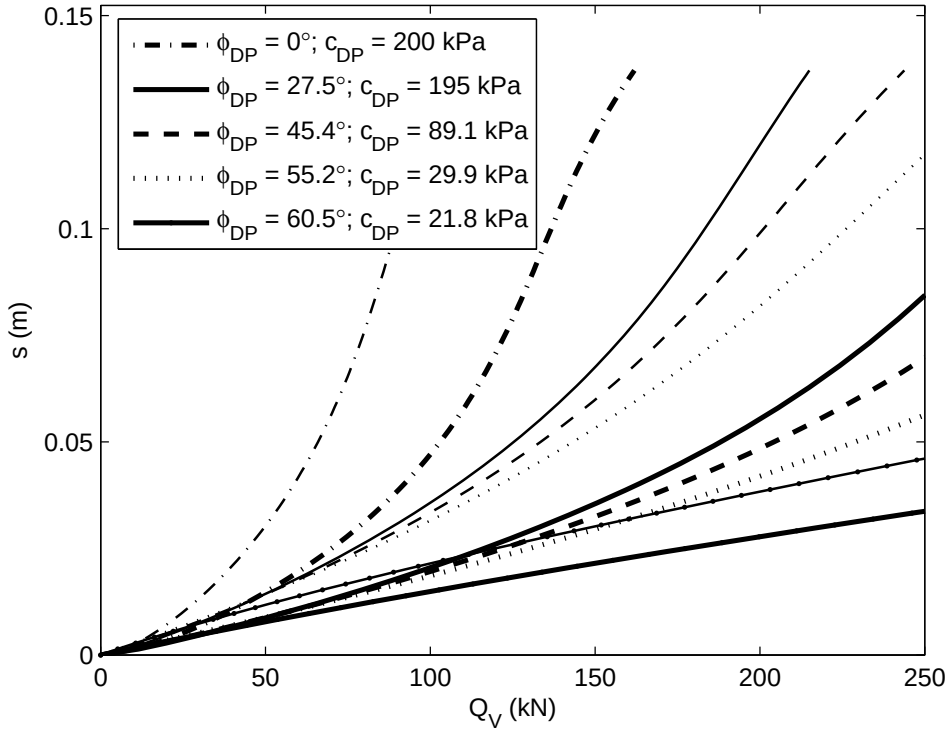

Figure K6. Effect of wheel width on rolling; heavy lines are with $b = 0.457$ m and fine lines are with $b = 0.306$ m ($d = 1.524$ m and $E = 40$ MPa)

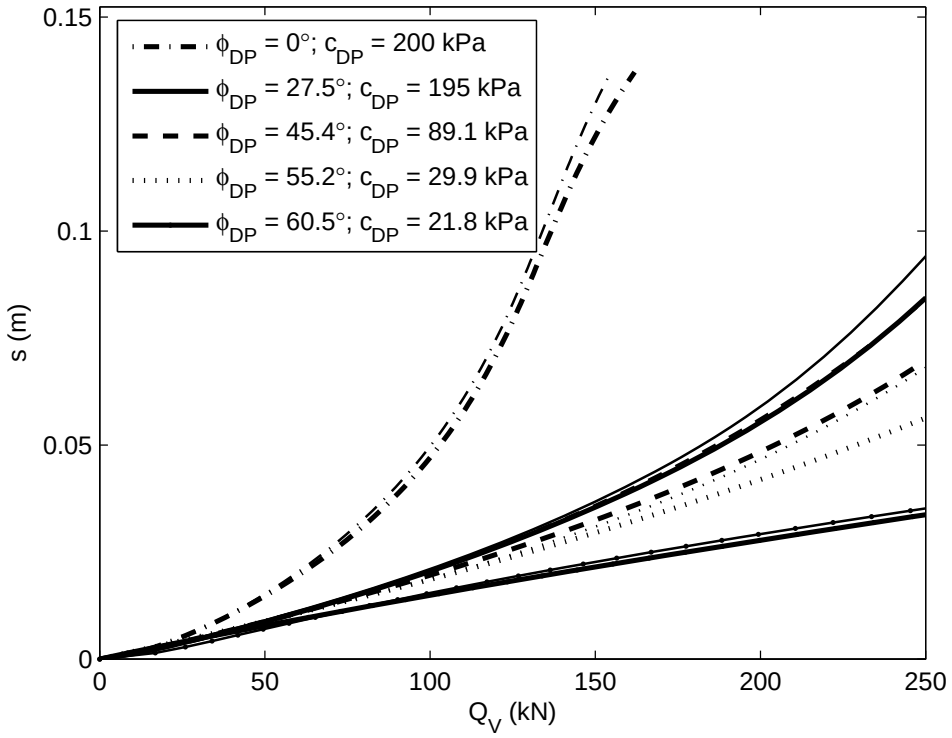

Figure K7. Effect of friction on rolling; heavy lines are with $\mu = 0.8$ and fine lines are with $\mu = 0.4$ ($d = 1.524$ m, $b = 0.457$ m, and $E = 40$ MPa)

Appendix L: Dimensional Plots of Results from Numerical Simulations of Rolling on Layered Soil

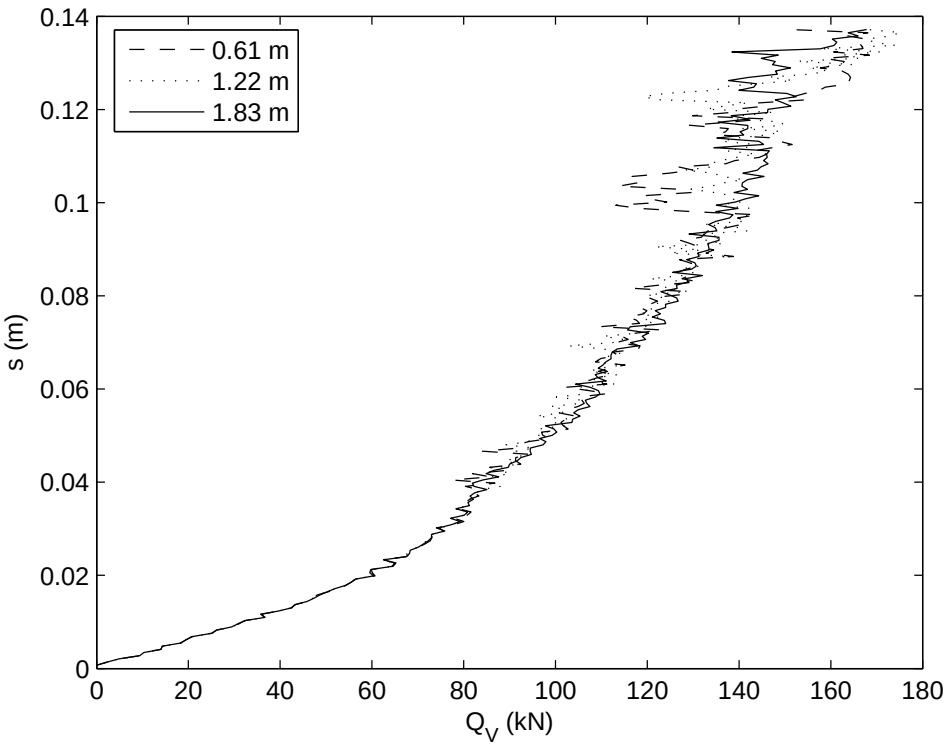

Figure L1. Effect of layering on sinkage with frictional soil: weak over strong; E = 40 kPa, ϕ_{DP} = 45.4º, and c_{DP} = 35.6 kPa in top layer (thickness shown in legend); E = 40 kPa, ϕ_{DP} = 55.2º, and c_{DP} = 29.9 kPa in bottom layer

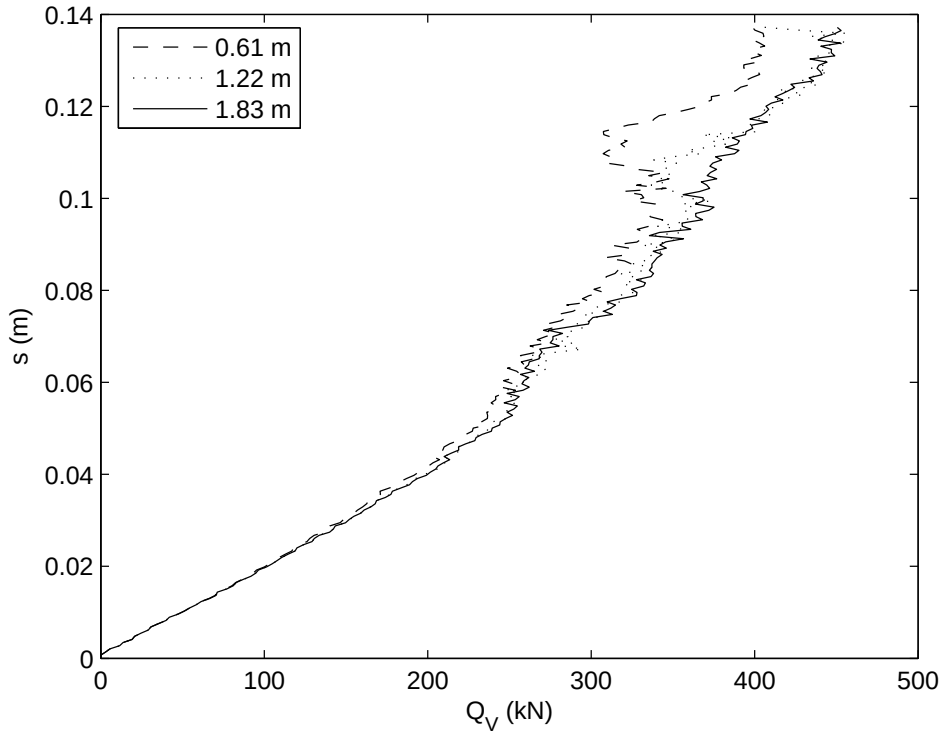

Figure L2. Effect of layering on sinkage with frictional soil: strong over weak; E = 40 MPa, ϕ_{DP} = 55.2º, and c_{DP} = 29.9 kPa in top layer (thickness shown in legend); E = 40 MPa, ϕ_{DP} = 45.4º, and c_{DP} = 35.6 kPa in bottom layer

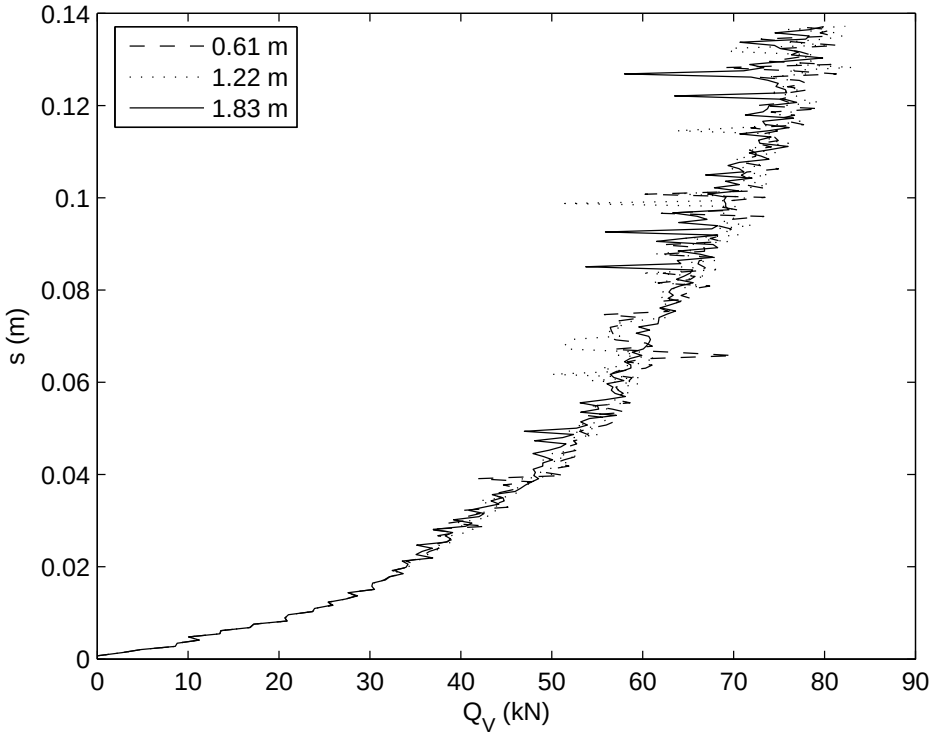

Figure L3. Effect of layering on sinkage with cohesive soil: weak over strong; E = 40 MPa, ϕ_{DP} = 0, and c_{DP} = 100 kPa in top layer (thickness shown in legend); E = 40 MPa, ϕ_{DP} = 0, and c_{DP} = 200 kPa in bottom layer

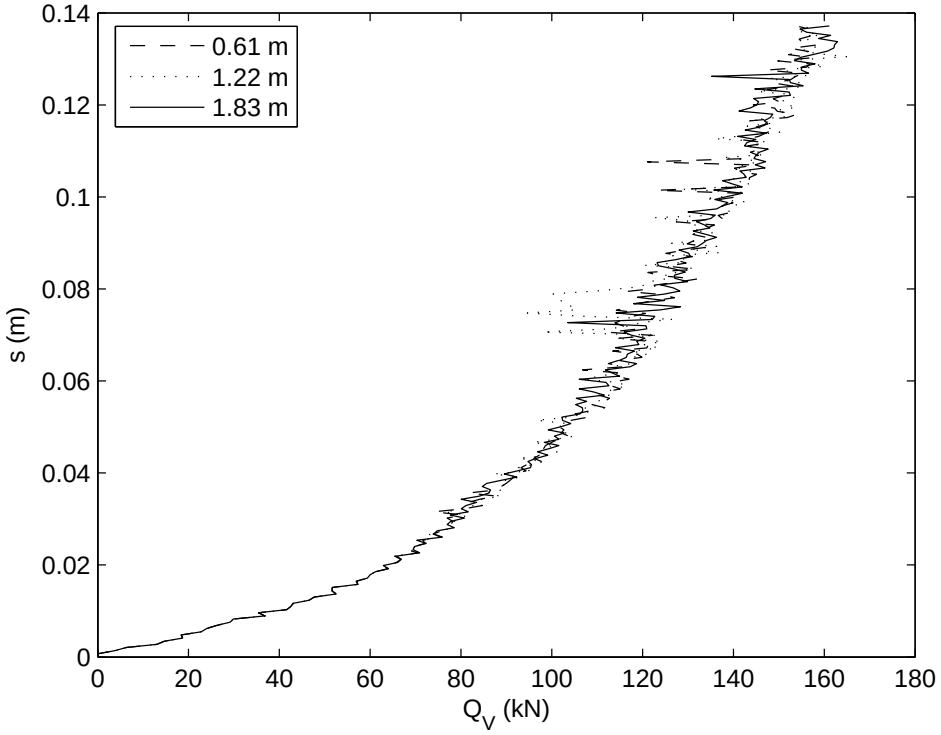

Figure L4. Effect of layering on sinkage with cohesive soil: strong over weak; E = 40 MPa, ϕ_{DP} = 0, and c_{DP} = 200 kPa in top layer (thickness shown in legend); E = 40 MPa, ϕ_{DP} = 0, and c_{DP} = 100 kPa in bottom layer

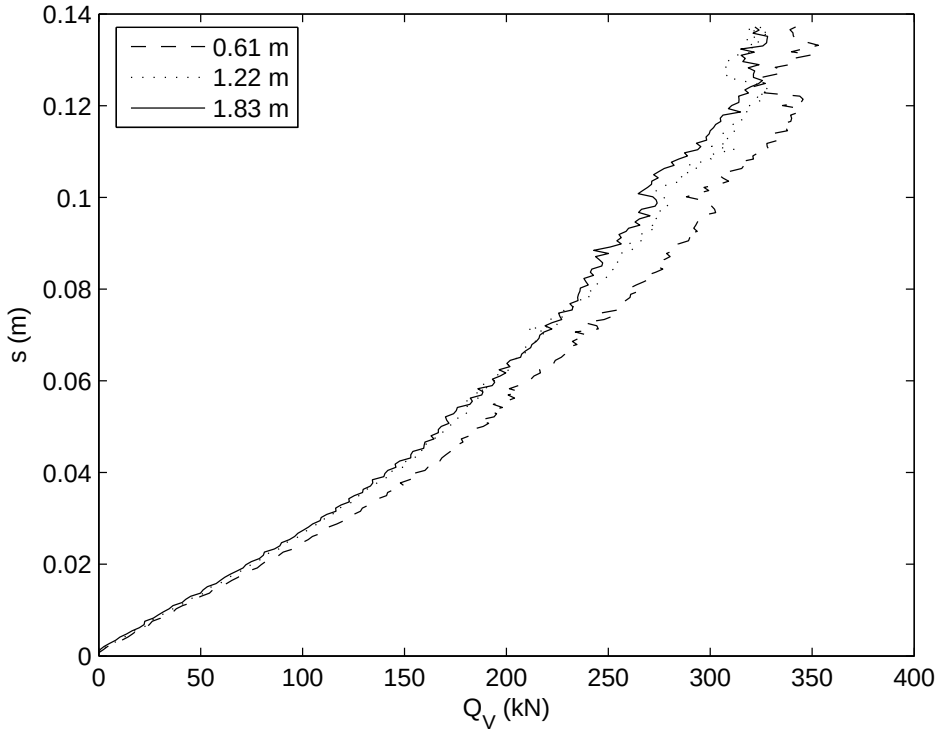

Figure L5. Effect of layering on sinkage: flexible over stiff; E = 20 MPa, ϕ_{DP} = 45.4º, and c_{DP} = 89.1 kPa in top layer (thickness shown in legend); E = 60 MPa, ϕ_{DP} = 45.4º, and c_{DP} = 89.1 kPa in bottom layer

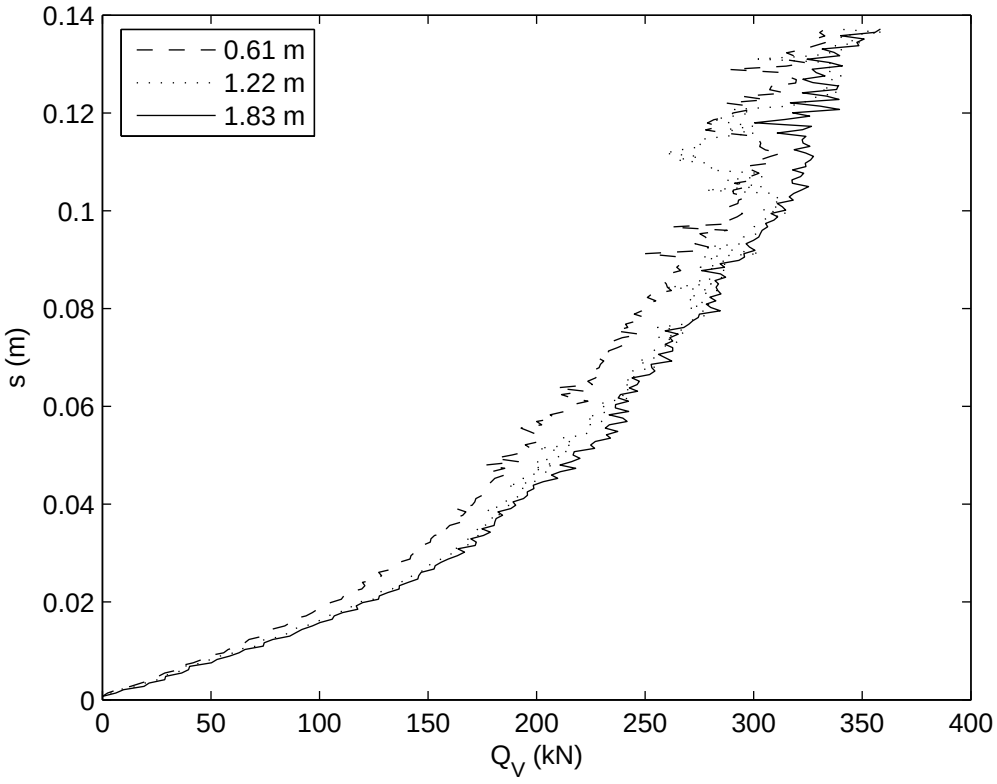

Figure L6. Effect of layering on sinkage: stiff over flexible; E = 60 MPa, ϕ_{DP} = 45.4º, and c_{DP} = 89.1 kPa in top layer (thickness shown in legend); E = 20 MPa, ϕ_{DP} = 45.4º, and c_{DP} = 89.1 kPa in bottom layer

Appendix M: DCP Data from Full Scale Field Tests

Table M1. DCP readings at test site with granular soil; large rut

	in rut	next to rut	at road centerline
blow count	**penetration depth (mm)**	**penetration depth (mm)**	**penetration depth (mm)**
0	85	53	25
1	255	221	70
2	344	289	105
3	411	342	132
4	464	389	160
5	507	432	185
6	537	469	210
7	560	509	230
8	582	549	250
9	602	585	270
10	627	618	290
11	660	646	310
12	680	673	328
13	700	698	345
14	719	719	365
15	734	737	385
16	753	754	402
17	770	770	423
18	788	785	442
19	805	799	460
20	815	809	480
21	828	--	500
22	841	--	520
23	855	--	540
24	868	--	560
25	878	--	575
26	893	--	592
27	--	--	610
28	--	--	622
29	--	--	633
30	--	--	645
31	--	--	658
32	--	--	670
33	--	--	678
34	--	--	690
35	--	--	700
36	--	--	711
37	--	--	722
38	--	--	734
39	--	--	749
40	--	--	760

Table M2. DCP readings at test site with granular soil; small rut

	in rut	next to rut	at road centerline
Blow Count	**penetration depth (mm)**	**penetration depth (mm)**	**penetration depth (mm)**
0	107	79	52
1	264	219	125
2	347	288	166
3	416	344	201
4	475	398	234
5	528	449	262
6	580	502	288
7	627	555	313
8	650	606	337
9	668	658	360
10	684	694	382
11	701	719	403
12	721	737	423
13	735	757	445
14	759	778	467
15	782	803	487
16	802	825	512
17	829	843	533
18	859	860	553
19	879	882	574
20	891	900	595
21	--	--	613
22	--	--	631
23	--	--	648
24	--	--	667
25	--	--	678
26	--	--	693
27	--	--	702
28	--	--	713
29	--	--	727
30	--	--	739
31	--	--	748
32	--	--	763
33	--	--	775
34	--	--	787
35	--	--	798
36	--	--	813
37	--	--	823
38	--	--	836
39	--	--	848
40	--	--	862

Table M3. DCP readings at test site with cohesive soil

	in rut	next to rut
blow count	**penetration depth (mm)**	**penetration depth (mm)**
0	0	0
1	45	27
2	82	46
3	118	67
4	190	99
5	262	128
6	322	158
7	379	193
8	423	224
9	450	267
10	485	323
11	528	383
12	560	430
13	588	482
14	614	521
15	642	545
16	667	564
17	688	583
18	708	602
19	726	624
20	748	653
21	764	689
22	780	735
23	802	756
24	822	762
25	851	767

Appendix N: Data on Granular Soil from Full Scale Field Tests

Minnesota Department of Transportation

Office of Materials and Road Research

Relative Density Test Grading & Base Construction

S. P. No: 1017-12 **Proj. File No:** **161.210.2.8**

Test Identification Data						
Date Sampled	10/5/06	Date Tested	10/5/06	Time (military)	18:20	
Test No.	DP10D159			Verf. C omp. ID		
Soil Class or 3138 Class	Sel. Gran. Mod.	Sample ID	0610051820CJB010	Work Type	Mainline	
Station	1200+46	Material ID	Sel. Gran. Mod.	Postion from center line:	7' lt CL	
Depth Below Grade (ft)	0	Location	EB212	Lot No.		
Coordinates	- ° - 'N	Elevation		Bridge No.		
	- ° - 'W	DP #	10	Source	MnDOT, TH 41 Pit	
Sampled By	Chris Braaten	Submitted By	Chris Braaten	Use of material	SGM	
Activity ID	C0.2110	Material	SGMB	Test Type	QAT	
Lab Supervisor	Lee McLaughlin	Remarks		Split	Yes	

Volume Determination (sand cone)

A. Wt. Sand & Container Before (g)	6000
B. Wt. Sand & Container After (g)	2477.3
C. Wt. Sand in Funnel & Hole A-B (g)	3522.7
D. Wt. Sand in Funnel (from Calib) (g)	1614.9
E. Wt. Sand in in Hole C-D (g)	1907.8

Inplace Dry Density Determination (Field Density Test)

Container No.	
- Burner Method -	
F. Wt. Wet Soil + Pan (g)	851.6
G. Wt. Dry Soil + Pan (g)	821.6
H. Wt Moisture F-G (g)	30
J. Wt Pan (g)	381.5
K. Wt. Wet Soil F-J (g)	470.1
- Speedy Method -	
M. Dial Reading	
N. Sample Size Factor	
P. % Moisture - Wet Wt. H/K*100 or M*N (g)	6.4
R. Total Wt. Wet Mat. From Hole (g)	2749.0
S. Wt.Moist. in Mat. from Hole R x P/100 (g)	175.4
T. Dry Wt.of Mat. from Hole R - S (g)	2573.6
U. Unit Wt. of Sand (lb/ft^3)	95.0
V. Dry Density (lb/ft^3) T/E x U	128.2

Relative Density Determination

W. Std Maximum Density (lb/ft^3)	122.2
Specs.	100
Relative Density % V/W x 100	105
Curve No.	123
Status	**Pass**

N1

Form 000-1021-1 July 24, 2006, Rev 1

Minnesota Department of Transportation

Office of Materials and Road Research

Relative Density Test Grading & Base Construction

S. P. No: 1017-12 **Proj. File No:** **161.210.2.8**

Test Identification Data						
Date Sampled	10/5/06	Date Tested	10/5/06	Time (military)	18:00	
Test No.	DP10D158			Verf. C omp. ID		
Soil Class or 3138 Class	Sel. Gran. Mod.	Sample ID	0610051800CJB010	Work Type	Mainline	
Station	1192+15	Material ID	Sel. Gran. Mod.	Postion from center line:	CL	
Depth Below Grade (ft)	0	Location	EB212	Lot No.		
Coordinates	- ° - 'N	Elevation		Bridge No.		
	- ° - 'W	DP #	10	Source	MnDOT, TH 41 Pit	
Sampled By	Chris Braaten	Submitted By	Chris Braaten	Use of material	SGM	
Activity ID	C0.2110	Material	SGMB	Test Type	QAT	
Lab Supervisor	Lee McLaughlin	Remarks		Split	Yes	

Volume Determination (sand cone)

A. Wt. Sand & Container Before (g)	6000
B. Wt. Sand & Container After (g)	3252.1
C. Wt. Sand in Funnel & Hole A-B (g)	2747.9
D. Wt. Sand in Funnel (from Calib) (g)	1614.9
E. Wt. Sand in in Hole C-D (g)	1133

Inplace Dry Density Determination (Field Density Test)

Container No.	
- Burner Method -	
F. Wt. Wet Soil + Pan (g)	710.7
G. Wt. Dry Soil + Pan (g)	681.9
H. Wt Moisture F-G (g)	28.8
J. Wt Pan (g)	250
K. Wt. Wet Soil F-J (g)	460.7
- Speedy Method -	
M. Dial Reading	
N. Sample Size Factor	
P. % Moisture - Wet Wt. H/K*100 or M*N (g)	6.3
R. Total Wt. Wet Mat. From Hole (g)	1636.6
S. Wt.Moist. in Mat. from Hole R x P/100 (g)	102.3
T. Dry Wt.of Mat. from Hole R - S (g)	1534.3
U. Unit Wt. of Sand (lb/ft^3)	95.0
V. Dry Density (lb/ft^3) T/E x U	128.6

Relative Density Determination

W. Std Maximum Density (lb/ft^3)	122.2
Specs.	100
Relative Density % V/W x 100	105
Curve No.	123
Status	**Pass**

N2

Form 000-1021-1 July 24, 2006, Rev 1

Minnesota Department of Transportation

Office of Materials and Road Research

Relative Density Test Grading & Base Construction

S. P. No: 1017-12 **Proj. File No:** **161.210.2.8**

Test Identification Data							
Date Sampled	10/5/06	Date Tested	10/5/06	Time (military)	11:15		
Test No.	DP10D156			Verf. C omp. ID			
Soil Class or 3138 Class	Sel. Gran. Mod.-	Sample ID	0610051115TMS010	Work Type	Mainline		
Station	1183+43	Material ID	Sel. Gran. Mod.	Postion from center line:	13'RT		
Depth Below Grade (ft)	0	Location	WB 212	Lot No.			
Coordinates	- ° - 'N	Elevation		Bridge No.			
	- ° - 'W	DP #	10	Source	Hansen Pit		
Sampled By	Tina Siebert	Submitted By	Tina Siebert	Use of material	Sel Gran Mod		
Activity ID	C0.2110	Material	Sel. Gran.	Test Type	QAT		
Lab Supervisor	Lee McLaughlin	Remarks				Split	Yes

Volume Determination (sand cone)

A. Wt. Sand & Container Before (g)	6000
B. Wt. Sand & Container After (g)	2375.2
C. Wt. Sand in Funnel & Hole A-B (g)	3624.8
D. Wt. Sand in Funnel (from Calib) (g)	1614.9
E. Wt. Sand in in Hole C-D (g)	2009.9

Inplace Dry Density Determination (Field Density Test)

Container No.	
- Burner Method -	
F. Wt. Wet Soil + Pan (g)	826.6
G. Wt. Dry Soil + Pan (g)	780.3
H. Wt Moisture F-G (g)	46.3
J. Wt Pan (g)	241.6
K. Wt. Wet Soil F-J (g)	585
- Speedy Method -	
M. Dial Reading	
N. Sample Size Factor	
P. % Moisture - Wet Wt. H/K*100 or M*N (g)	7.9
R. Total Wt. Wet Mat. From Hole (g)	2696.8
S. Wt.Moist. in Mat. from Hole R x P/100 (g)	213.4
T. Dry Wt.of Mat. from Hole R - S (g)	2483.4
U. Unit Wt. of Sand (lb/ft^3)	95.0
V. Dry Density (lb/ft^3) T/E x U	117.4

Relative Density Determination

W. Std Maximum Density (lb/ft^3)	114
Specs.	100
Relative Density % V/W x 100	103
Curve No.	80
Status	**Pass**

Minnesota Department of Transportation

Office of Materials and Road Research

Relative Density Test Grading & Base Construction

S. P. No: 1017-12 **Proj. File No:** **161.220.1.8**

Test Identification Data							
Date Sampled	10/5/06	Date Tested	10/5/06	Time (military)	11:53		
Test No.	DP002D204			Verf. C omp. ID			
Soil Class or 3138 Class	Sel. Gran. Mod.	Sample ID	0610051153LJM002	Work Type	Mainline		
Station	1205+66	Material ID	Sel. Gran. Mod.	Postion from center line:	CL		
Depth Below Grade (ft)	0	Location	WB212	Lot No.			
Coordinates	- ° - 'N	Elevation		Bridge No.			
	- ° - 'W	DP #	2	Source	On-Site Borrow		
Sampled By	Lee McLaughlin	Submitted By	Tina Siebert	Use of material	Sel Gran Mod		
Activity ID	C0.2110	Material	Sel. Gran.	Test Type	QAT		
Lab Supervisor	Lee McLaughlin	Remarks				Split	Yes

Volume Determination (sand cone)

A. Wt. Sand & Container Before (g)	6000
B. Wt. Sand & Container After (g)	2847.5
C. Wt. Sand in Funnel & Hole A-B (g)	3152.5
D. Wt. Sand in Funnel (from Calib) (g)	1416.9
E. Wt. Sand in in Hole C-D (g)	1735.6

Inplace Dry Density Determination (Field Density Test)

Container No.	
- Burner Method -	
F. Wt. Wet Soil + Pan (g)	815.0
G. Wt. Dry Soil + Pan (g)	785.2
H. Wt Moisture F-G (g)	29.8
J. Wt Pan (g)	241.4
K. Wt. Wet Soil F-J (g)	573.6
- Speedy Method -	
M. Dial Reading	
N. Sample Size Factor	
P. % Moisture - Wet Wt. H/K*100 or M*N (g)	5.2
R. Total Wt. Wet Mat. From Hole (g)	2127.2
S. Wt.Moist. in Mat. from Hole R x P/100 (g)	110.5
T. Dry Wt.of Mat. from Hole R - S (g)	2016.7
U. Unit Wt. of Sand (lb/ft^3)	95.0
V. Dry Density (lb/ft^3) T/E x U	110.4

Relative Density Determination

W. Std Maximum Density (lb/ft^3)	109.3
Specs.	100
Relative Density % V/W x 100	101
Curve No.	96
Status	**Pass**

Minnesota Department of Transportation

Office of Materials and Road Research

Relative Density Test Grading & Base Construction

S. P. No: 1017-12 **Proj. File No:** **161.220.1.8**

Test Identification Data							
Date Sampled	10/5/06	Date Tested	10/5/06	Time (military)	11:30		
Test No.	DP002D203			Verf. C omp. ID			
Soil Class or 3138 Class	Sel. Gran. Mod.	Sample ID	0610051130TMS002	Work Type	Mainline		
Station	1194+69	Material ID	Sel. Gran. Mod.	Postion from center line:	18'RT		
Depth Below Grade (ft)	0	Location	WB 212	Lot No.			
Coordinates	- ° - 'N	Elevation		Bridge No.			
	- ° - 'W	DP #	2	Source	Hansen Pit		
Sampled By	Tina Siebert	Submitted By	Tina Siebert	Use of material	Sel Gran Mod		
Activity ID	C0.2110	Material	SGMB	Test Type	QAT		
Lab Supervisor	Lee McLaughlin	Remarks				Split	Yes

Volume Determination (sand cone)

A. Wt. Sand & Container Before (g)	6000
B. Wt. Sand & Container After (g)	2448.7
C. Wt. Sand in Funnel & Hole A-B (g)	3551.3
D. Wt. Sand in Funnel (from Calib) (g)	1614.9
E. Wt. Sand in in Hole C-D (g)	1936.4

Inplace Dry Density Determination (Field Density Test)

Container No.	
- Burner Method -	
F. Wt. Wet Soil + Pan (g)	826
G. Wt. Dry Soil + Pan (g)	799.6
H. Wt Moisture F-G (g)	26.4
J. Wt Pan (g)	309
K. Wt. Wet Soil F-J (g)	517
- Speedy Method -	
M. Dial Reading	
N. Sample Size Factor	
P. % Moisture - Wet Wt. H/K*100 or M*N (g)	5.1
R. Total Wt. Wet Mat. From Hole (g)	2565.0
S. Wt.Moist. in Mat. from Hole R x P/100 (g)	131.0
T. Dry Wt.of Mat. from Hole R - S (g)	2434.0
U. Unit Wt. of Sand (lb/ft^3)	95.0
V. Dry Density (lb/ft^3) T/E x U	119.4

Relative Density Determination

W. Std Maximum Density (lb/ft^3)	114.1
Specs.	100
Relative Density % V/W x 100	105
Curve No.	80
Status	**Pass**

Minnesota Department of Transportation

Office of Materials and Road Research

Relative Moisture Test Grading & Base Construction

S. P. No: 1017-12 **Proj. File No:** **161.210.2.8**

Test Identification Data					
Date Sampled	10/5/06	Date Tested	10/5/06	Time (military)	11:15
Test No.	DP10M155			Verf. C omp. ID	
Soil Class or 3138 Class	Sel. Gran. Mod	Sample ID	0610051115TMS010	Work Type	Mainline
Station	1183+43	Material ID	Sel. Gran. Mod.	Postion from center line:	13'RT
Depth Below Grade (ft)	0	Location	WB 212	Lot No.	
Coordinates	- ° - 'N	Elevation		Bridge No.	
	- ° - 'W	DP #	10	Source	Hansen Pit
Sampled By	Tina Siebert	Submitted By	Tina Siebert	Use of material	Sel Gran Mod
Activity ID	C0.2110	Material	Sel. Gran.	Test Type	QAT
Lab Supervisor	Lee McLaughlin	Remarks		Split	Yes

Burner Method

- Burner Method -	
A. Wt. Wet Material + Pan	825
B. Wt. Dry Material + Pan	797.1
C. Wt Moisture A-B	27.9
D. Wt Pan	242.8
E. Wt. Dry Soil B-D	554.3

Speedy Method

- Speedy Method -	
F. Dial Reading	
G. Sample Size Factor	
H. % Moisture Wet Wt. [C / (A-D)]*100	4.8
J. % Moisture Dry Wt. C/E x 100 *	5.0

Relative Moisture Determination

Minimum Specs	
Maximum Specs	102
K. Standard Optimum Moisture	13.1
L. Relative Moisture % J/K x 100	38
Curve No.	80
Status	**Pass**

Minnesota Department of Transportation

Office of Materials and Road Research

Relative Moisture Test Grading & Base Construction

S. P. No: 1017-12 **Proj. File No:** **161.220.1.8**

Test Identification Data					
Date Sampled	10/5/06	Date Tested	10/5/06	Time (military)	11:53
Test No.	DP002M205			Verf. C omp. ID	
Soil Class or 3138 Class	Sel. Gran. Mod	Sample ID	0610051153LJM002	Work Type	Mainline
Station	1205+66	Material ID	Sel. Gran. Mod.	Postion from center line:	CL
Depth Below Grade (ft)	0	Location	WB212	Lot No.	
Coordinates	- ° - 'N	Elevation		Bridge No.	
	- ° - 'W	DP #	2	Source	On-Site Borrow
Sampled By	Lee McLaughlin	Submitted By	Tina Siebert	Use of material	Sel Gran Mod
Activity ID	C0.2110	Material	Sel. Gran.	Test Type	QAT
Lab Supervisor	Lee McLaughlin	Remarks		Split	Yes

Burner Method

- Burner Method -	
A. Wt. Wet Material + Pan	814.3
B. Wt. Dry Material + Pan	792.2
C. Wt Moisture A-B	22.1
D. Wt Pan	374.8
E. Wt. Dry Soil B-D	417.4

Speedy Method

- Speedy Method -	
F. Dial Reading	
G. Sample Size Factor	
H. % Moisture Wet Wt. [C / (A-D)]*100	5.0
J. % Moisture Dry Wt. C/E x 100 *	5.3

Relative Moisture Determination

Minimum Specs	
Maximum Specs	102
K. Standard Optimum Moisture	11.6
L. Relative Moisture % J/K x 100	46
Curve No.	96
Status	**Pass**

Minnesota Department of Transportation

Office of Materials and Road Research

Relative Moisture Test Grading & Base Construction

S. P. No: 1017-12 **Proj. File No:** **161.220.1.8**

Test Identification Data					
Date Sampled	10/5/06	Date Tested	10/5/06	Time (military)	11:30
Test No.	DP002M204			Verf. C omp. ID	
Soil Class or 3138 Class	Sel. Gran. Mod	Sample ID	0610051130TMS002	Work Type	Mainline
Station	1194+69	Material ID	Sel. Gran. Mod.	Postion from center line:	18'RT
Depth Below Grade (ft)	0	Location	WB 212	Lot No.	
Coordinates	- ° - 'N	Elevation		Bridge No.	
	- ° - 'W	DP #	2	Source	Hansen Pit
Sampled By	Tina Siebert	Submitted By	Tina Siebert	Use of material	Sel Gran Mod
Activity ID	C0.2110	Material	SGMB	Test Type	QAT
Lab Supervisor	Lee McLaughlin	Remarks		Split	Yes

Burner Method

- Burner Method -	
A. Wt. Wet Material + Pan	826.2
B. Wt. Dry Material + Pan	804
C. Wt Moisture A-B	22.2
D. Wt Pan	376.6
E. Wt. Dry Soil B-D	427.4

Speedy Method

- Speedy Method -	
F. Dial Reading	
G. Sample Size Factor	
H. % Moisture Wet Wt. [C / (A-D)]*100	4.9
J. % Moisture Dry Wt. C/E x 100 *	5.2

Relative Moisture Determination

Minimum Specs	
Maximum Specs	102
K. Standard Optimum Moisture	13.1
L. Relative Moisture % J/K x 100	40
Curve No.	80
Status	**Pass**

Minnesota Department of Transportation

Office of Materials and Road Research

Relative Moisture Test Grading & Base Construction

S. P. No: 1017-12 **Proj. File No:** **161.210.2.8**

Test Identification Data					
Date Sampled	10/5/06	Date Tested	10/5/06	Time (military)	18:20
Test No.	DP10M158			Verf. C omp. ID	
Soil Class or 3138 Class	Sel. Gran. Mod.	Sample ID	0610051820CJB010	Work Type	Mainline
Station	1200+46	Material ID	Sel. Gran. Mod.	Postion from center line:	7' lt CL
Depth Below Grade (ft)	0	Location	EB212	Lot No.	
Coordinates	- ° - 'N	Elevation		Bridge No.	
	- ° - 'W	DP #	10	Source	MnDOT, TH 41 Pit
Sampled By	Chris Braaten	Submitted By	Chris Braaten	Use of material	SGM
Activity ID	C0.2110	Material	SGMB	Test Type	QAT
Lab Supervisor	Lee McLaughlin	Remarks		Split	Yes

Burner Method

- Burner Method -	
A. Wt. Wet Material + Pan	708.5
B. Wt. Dry Material + Pan	687.5
C. Wt Moisture A-B	21
D. Wt Pan	242.9
E. Wt. Dry Soil B-D	444.6

Speedy Method

- Speedy Method -	
F. Dial Reading	
G. Sample Size Factor	
H. % Moisture Wet Wt. [C / (A-D)]*100	4.5
J. % Moisture Dry Wt. C/E x 100 *	4.7

Relative Moisture Determination

Minimum Specs	
Maximum Specs	102
K. Standard Optimum Moisture	7.9
L. Relative Moisture % J/K x 100	60
Curve No.	123
Status	**Pass**

Minnesota Department of Transportation

Office of Materials and Road Research

Relative Moisture Test Grading & Base Construction

S. P. No: 1017-12 **Proj. File No:** **161.210.2.8**

Test Identification Data					
Date Sampled	10/5/06	Date Tested	10/5/06	Time (military)	18:00
Test No.	DP10M157			Verf. C omp. ID	
Soil Class or 3138 Class	Sel. Gran. Mod.	Sample ID	0610051800CJB010	Work Type	Mainline
Station	1192+15	Material ID	Sel. Gran. Mod.	Postion from center line:	CL
Depth Below Grade (ft)	0	Location	EB212	Lot No.	
Coordinates	- ° - 'N	Elevation		Bridge No.	
	- ° - 'W	DP #	10	Source	MnDOT, TH 41 Pit
Sampled By	Chris Braaten	Submitted By	Chris Braaten	Use of material	SGM
Activity ID	C0.2110	Material	SGMB	Test Type	QAT
Lab Supervisor	Lee McLaughlin	Remarks		Split	Yes

Burner Method

- Burner Method -	
A. Wt. Wet Material + Pan	601.4
B. Wt. Dry Material + Pan	575.5
C. Wt Moisture A-B	25.9
D. Wt Pan	129
E. Wt. Dry Soil B-D	446.5

Speedy Method

- Speedy Method -	
F. Dial Reading	
G. Sample Size Factor	
H. % Moisture Wet Wt. [C / (A-D)]*100	5.5
J. % Moisture Dry Wt. C/E x 100 *	5.8

Relative Moisture Determination

Minimum Specs	
Maximum Specs	102
K. Standard Optimum Moisture	7.9
L. Relative Moisture % J/K x 100	73
Curve No.	123
Status	**Pass**

Appendix O: Illustrative Examples

Illustrative Example No. 1: Prospective Test Roller Performance Evaluation

In this example, the theoretical models are used to compare the performance of several possible test rollers with varying wheel sizes and weights. "Performance" is here loosely defined as the sensitivity of a test roller, in terms of sinkage, to soils encountered in road construction. It is supposed that two different wheel geometries are being considered for use in test rolling: (1) a large wheel with d = 1.52 m (60 in.) and b = 0.46 m (18 in.); and (2) a small wheel with d = 1.12 m (44 in.) and b = 0.30 m (12 in.). To evaluate how these different wheels perform, the graphs shown in Figs. O1 and O2 were generated using the formulas developed for a rolling, rigid wheel. These graphs show how sinkage varies as a function of soil strength for several different wheel weights. Fig. O1 is for a cohesive soil and plots sinkage versus cohesion. Fig. O2 is for a granular soil and plots sinkage versus friction angle.

The maximum acceptable sinkage s_{max} of a test roller on a roadway embankment is related to the minimum acceptable soil strength. In this example, the minimum allowable cohesion for a cohesive material is taken as c_{min}= 170 kPa (25 psi), and the minimum allowable friction angle for a granular soil is ϕ_{min} = 48º. Although ϕ_{min} = 48º is very large compared to typical values of ϕ observed in natural soil deposits, this value appears to be warranted, given the quality and compaction level of the soils used in construction, and is consistent with the range in ϕ measured experimentally by Ayers et al. (1989). Both c_{min} = 170 kPa (25 psi) and ϕ_{min} = 48º correlate roughly to a maximum DCP penetration rate of 15 mm/blow (0.6 in./blow) using the correlations mentioned in Section 7.3.2.

Figs. O1 and O2 readily give s_{max} corresponding to c_{min} and ϕ_{min} for the different wheel geometries and wheel weights, as well as revealing sensitivity of sinkage to soil strength at the values s_{max}. The values of s_{max} for the various test roller configurations are summarized in Table O1. It is evident that similar performance can be achieved with different test rollers. For example, a test roller with the large wheel and Q_V = 100 kN (11 tons) has similar s_{max} as compared with the small wheel and Q_V = 50 kN (5.5 tons), where $s_{max} \approx$ 30 mm (1.2 in.) for the cohesive soil and $s_{max} \approx$ 45 mm (1.8 in.) for the granular soil in both cases. It is also shown, for the large wheel and small wheel respectively, that the wheel weight should be greater than 60 kN (7 tons) and 30 kN (3.5 tons) for the sinkage to be of the order s = 10 mm (0.4 in.).

Figs. O3 and O4 give predictions for how the influence depth H varies with wheel weight using the approach given in Section 3.4. Fig. O3 is for the cohesive soil and gives H for a passing soil with c = 170 kPa (25 psi) overlying weak clay with c = 10 kPa (1.5 psi). Fig. O4 gives H for the sand (ϕ = 48º) when it overlies a weak clay with c = 10 kPa (1.5 psi). The influence depths at the selected weights shown in Figs. O1 and O2 are also tabulated in Table O1.

Figs. O1 and O2, together with Table O1, provide a fairly complete picture of the consequences of choosing one test roller configuration over another. Although this example pertains to specific data, such a comparison between different prospective configurations can be easily generated.

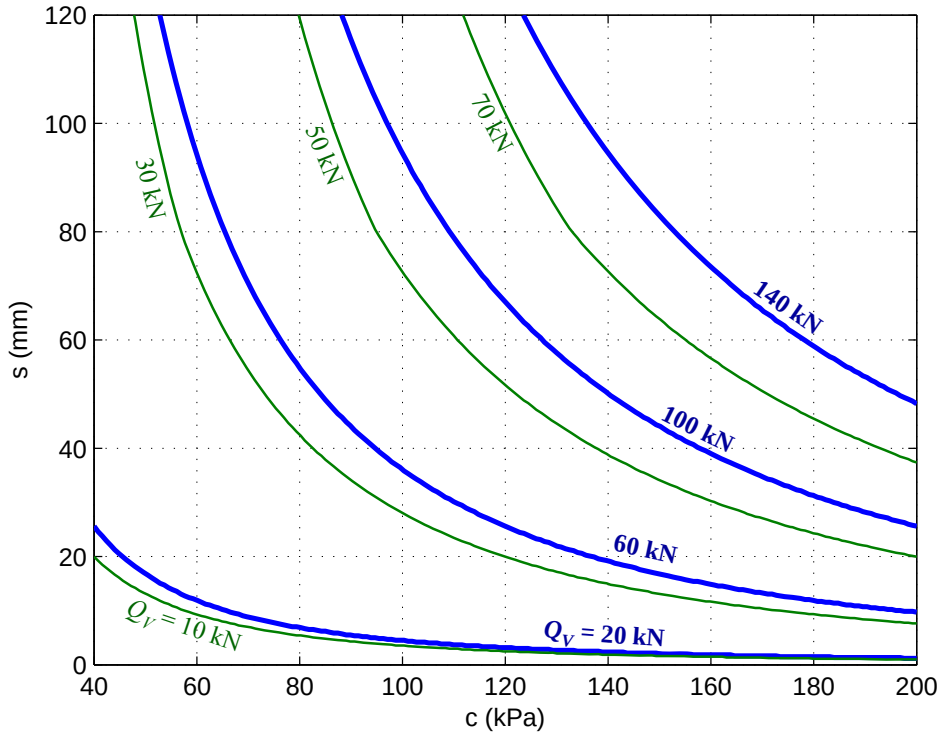

Figure O1. Sinkage predicted for cohesive soil ($\phi = 0$) using analytic method for rolling, rigid wheel (thick lines are for d = 1.52 m and b = 0.46 m; thin lines are for d = 1.12 m and b = 0.30 m)

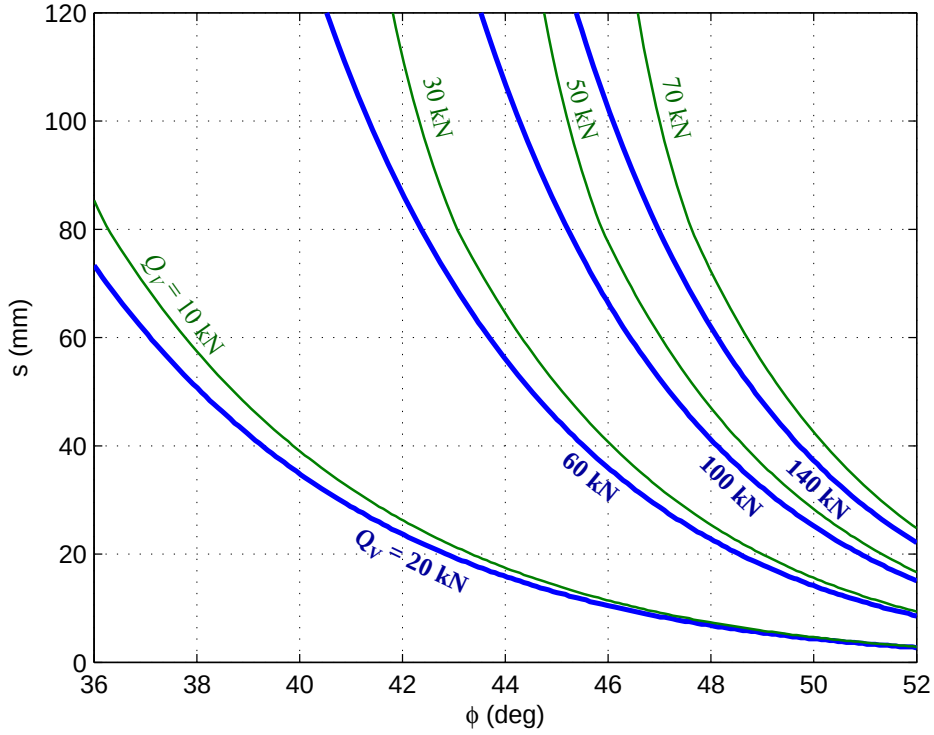

Figure O2. Sinkage predicted for granular soil (c = 0 and γ = 20 kN/m^3) using analytic method for rolling, rigid wheel (thick lines are for d = 1.52 m and b = 0.46 m; thin lines are for d = 1.12 m and b = 0.30 m)

Table O1. Predicted maximum allowable sinkage s_{max} and influence depth H for several prospective test rollers (rigid wheel; s_{max} based on c_{min} = 170 kPa for cohesive soil and ϕ_{min} = 48º for granular soil)

wheel geometry	**Q_V (kN)**	**s_{max} (mm)**		**H (m)**	
		cohesive	granular	cohesive	granular
d = 1.52 m, b = 0.46 m	140	65	62	0.75	1.50
	100	35	41	0.60	1.25
	60	13	23	0.40	0.95
	20	2	7	0.15	0.50
d = 1.12 m, b = 0.30 m	70	50	73	0.55	1.20
	50	27	47	0.45	1.05
	30	10	26	0.30	0.80
	10	1	7	0.15	0.45

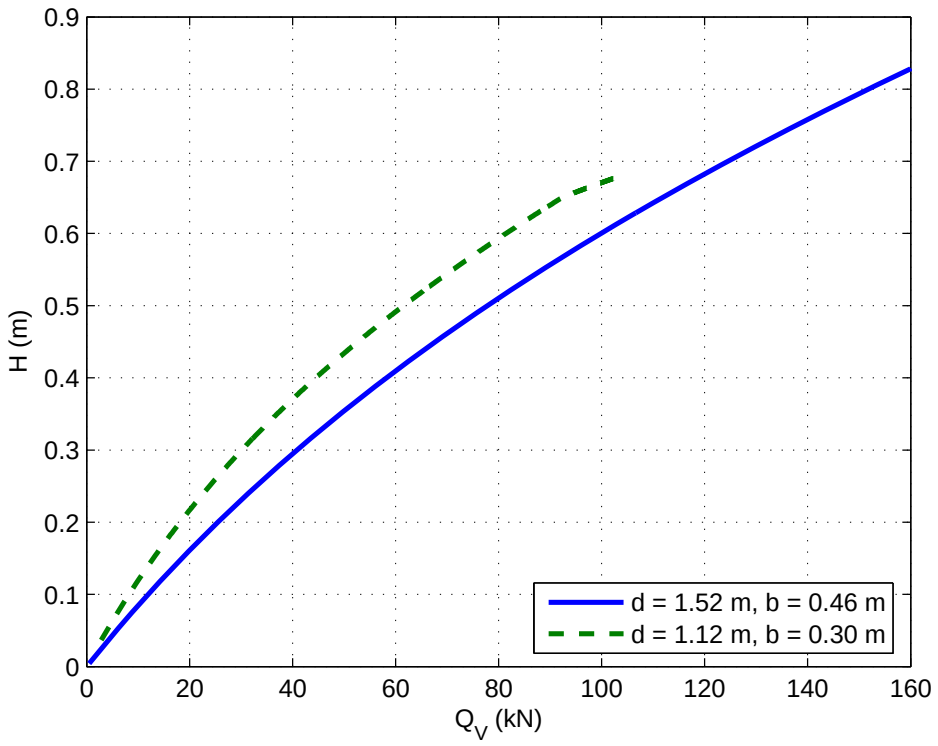

Figure O3. Influence depth H versus Q_V for strong clay (ϕ = 0 and c = 170 kPa) overlying weak clay (ϕ = 0 and c = 10 kPa)

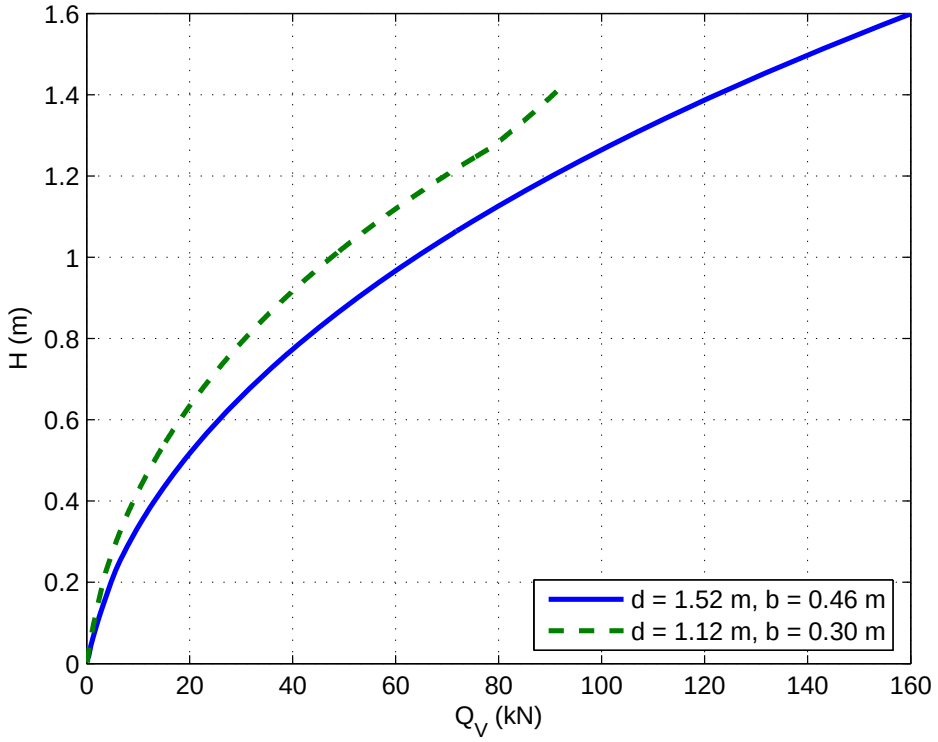

Figure O4. Influence depth H versus Q_V for dense sand ($\phi = 48°$, $c = 0$, and $\gamma = 20$ kN/m^3) overlying weak clay ($\phi = 0$ and $c = 10$ kPa)

Illustrative Example No. 2: Interpretation of Test Rolling Measurements

This example shows how the theoretical models may be used to interpret data collected from a test roller of a given configuration. Suppose that a test roller with $d = 1.12$ m (44 in.), $b = 0.30$ m (12 in.), and wheel weight $Q_V = 50$ kN (5.5 tons) is automated with instrumentation to collect a continuous record of sinkage along an embankment, such as the one shown in Fig. O5a. If the material is sand ($c = 0$), the unknown soil strength parameter is ϕ, which can be deduced from the sinkage using the formula for a rolling, rigid wheel.

Fig. O5b shows ϕ interpreted from the record of sinkage with the aid of the formula from the analytic method. The otherwise obscure test roller measurement is thus translated into a universal strength quantity. Taking, for example, a minimum acceptable strength $\phi_{min} = 48°$ as in the previous example, the failing regions are clearly identified.

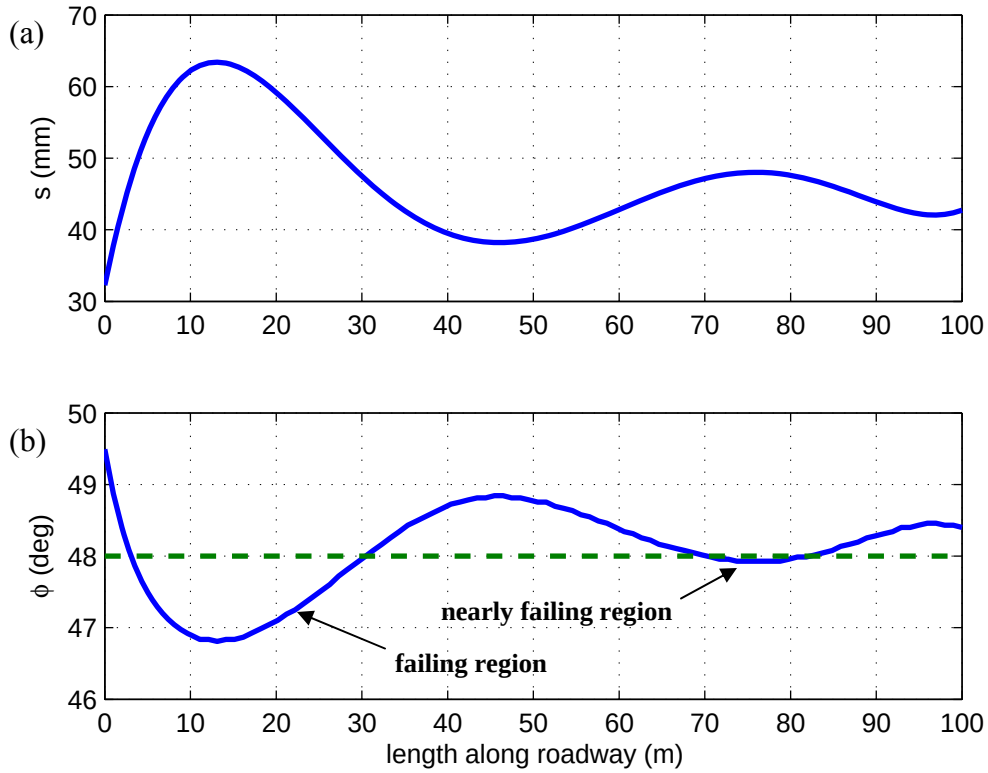

Figure O5. Example of using theoretical predictions to interpret test rolling measurements on granular soil: (a) continuous record of sinkage; (b) interpretation of sinkage in terms of ϕ from analytic method